

=====

Growth, phases and correlation effects of single-layer MoS₂ and VS₂

In a u g u r a l - D i s s e r t a t i o n

zur

Erlangung des Doktorgrades

der Mathematisch-Naturwissenschaftlichen Fakultät

der Universität zu Köln

vorgelegt von

Camiel van Efferen

aus Delft

Köln 2023

Erster Berichterstatter: Prof. Dr. Thomas Michely
Zweiter Berichterstatter: Prof. Dr. Paul van Loosdrecht
Dritter Berichterstatter: Prof. Dr. Alexander Khajetoorians

Vorsitzender der Prüfungskommission: Prof. Dr. Dr. (hc) Sanjay Mathur
Tag der mündlichen Prüfung: 03.11.2023

Die vorliegende Dissertation wurde von der Mathematisch-Naturwissenschaftlichen Fakultät der Universität zu Köln angenommen.

Abstract

In this thesis the two-dimensional materials MoS_2 and VS_2 are investigated in their single-layer form. Different phases, dependent on the synthesis parameters, substrate or temperature are explored, with an emphasis on the correlated electronic and magnetic states that are present in these materials. Scanning tunnelling microscopy is used to obtain structural information with atomic-scale spatial resolution, while scanning tunnelling spectroscopy is employed to measure the local density of states. Experimental results on correlated phenomena are compared to density functional theory and numerical renormalization group calculations performed by cooperation partners.

Single-layer VS_2 was predicted to be a strongly-correlated material, with a possibly coexisting magnetic and charge density wave ground state. However, the metastability of VS_2 makes it a difficult material to grow, and an experimental realisation of a freestanding single layer was yet to be achieved. We successfully synthesized single-layer VS_2 on the weakly interacting graphene on Ir(111) substrate, using the molecular beam epitaxy method. With the scanning tunnelling microscope, we find a charge density wave with a unit cell of $9 \times \sqrt{3}R30^\circ$. It is an unusual charge density wave, as it involves a symmetry reduction from a hexagonal to a rectangular unit cell and is present even at room temperature. Using the experimental data as the basis for density-functional theory calculations, we find that the charge density wave transition leads to a drastic reconfiguration of the band structure. Contrary to the intuitive Peierls picture of a charge density wave, which is driven by the electrons at the Fermi level, we find that the formation of the charge density wave can be best explained with non-linear coupling between transverse and longitudinal phonon modes. The most striking feature of this phase is a large, full gap in the unoccupied density of states, which is measured with scanning tunnelling spectroscopy. Additionally, x-ray magnetic circular dichroism spectra show that there is no net magnetization in small islands of VS_2 , which could be explained by a coexistence of the charge density wave with an antiferromagnetic spin density wave.

The metastability of VS_2 can, however, also be utilized to create new compounds, since it can readily transform to V-rich phases via intercalation or desulphurization. Previously, the introduction of sulphur defects and the intercalation of vanadium atoms have been shown to lead to phase transitions or magnetism in similar compounds. We combine scanning tunnelling microscopy with X-ray photoelectron spectroscopy to demonstrate the synthesis of two new vanadium based materials on graphene on Ir(111). By annealing single-layer VS_2 in ultra-high vacuum, we can create the one-dimensional patterned material V_4S_7 , which has ordered rows of sulphur vacancies running along its surface. By increasing the amount of vanadium and sulphur on the sample sufficiently, we can

alternatively grow ultimately thin V_5S_8 , which has a 2×2 layer of vanadium atoms intercalated between sheets of VS_2 . In the thinnest V_5S_8 -derived structures, a $\sqrt{3} \times \sqrt{3}$ CDW is found at low temperatures, which is investigated with scanning tunnelling spectroscopy.

While the semiconducting properties of single-layer MoS_2 have been extensively studied, there are many open questions regarding its metallic state, which can only be reached by significant gating or doping. As typical back-gating cannot achieve this due to breakdown effects, MoS_2 was previously made metallic using ionic liquids or doped via sulphur vacancies. However, these methods tend to lead to disorder and charge inhomogeneities. We instead exploit the unique properties of the graphene on Ir(111) substrate to adjust the MoS_2 Fermi level without these drawbacks. Taking oxygen as a *p*-dopant and europium as a *n*-dopant, we intercalate these atoms between graphene and Ir(111). As a result of oxygen taking up electrons from, or europium donating electrons to graphene, the Fermi level of MoS_2 is electrostatically shifted while remaining chemically pristine. Intercalating oxygen under graphene leads *p*-doping of MoS_2 , inducing a downwards Fermi level shift of 0.45 eV. Using europium, we can *n*-dope MoS_2 , shifting its Fermi level up by about 0.8 eV, inducing a metal-insulator transition. Due to the enhanced screening of the metallic state, a giant band gap renormalization of 0.67 eV takes place. We further explore the effect of the additional charge on the one-dimensional metallic states in MoS_2 mirror twin boundaries. The depletion and charging via the substrate is shown to shift the periodicity of the states, while preserving their one-dimensional nature. Additional DFT calculations reproduce the metal-insulator transition and the shifts of the graphene Dirac point and MoS_2 conduction band.

The Kondo effect, where the spin of a magnetic impurity is screened by the itinerant electrons in a metal, is one of the best understood phenomena in many-body physics. Its microscopic description allows one to predict the properties of the system at any energy scale, using only a few parameters. Nevertheless, these parameters, which pertain to the magnetic impurity, are inaccessible in the standard scanning tunnelling microscopy realisation of the Kondo effect, which makes use of magnetic adatoms on metal surfaces. We present a unique Kondo system in the mirror twin boundaries of single-layer MoS_2 . Using voltage pulses applied with the tip of the scanning tunnelling microscope, the doubly occupied, degenerate one-dimensional metallic states in the mirror twin boundaries can be shifted to the Fermi level, where they split due to strong Coulomb interactions. This leads to the formation of a singly occupied state with spin-1/2. Coupling of the magnetic moment of this state to electrons in the substrate results in a Kondo resonance at the Fermi level. Our ability to resolve the spectral function of the full Kondo system, consisting of the magnetic mirror twin boundary states together with the resonance, allows us to compare the experimental data directly with numerical renormalization group calculations. Another benefit of this system is that the variety of boundary lengths and energy states leads to a wide range of accessible Kondo coupling strengths, with Kondo temperatures spanning six orders of magnitude. We also resolve the relation between the magnetic states and the resonance in real space for the first time.

When single-layer MoS_2 is made metallic, theoretical and experimental works find evidence for

strong electron-phonon coupling, which can lead to various correlation effects, like superconductivity or the formation of polarons, a quasiparticle consisting of an excess charge carrier (electron or hole) localized within a potential well formed by the ions of the lattice. We provide a scanning tunnelling microscopy and density functional theory study of electron-phonon coupling effects in metallic single-layer MoS₂. Conductance spectra of two metallic MoS₂ samples, with europium or caesium intercalated below the graphene substrate, show series of evenly-spaced peaks around the Fermi level. Density functional theory calculations for *n*-doped single-layer MoS₂ demonstrate strong coupling between the occupied K-band of MoS₂ and the unoccupied Q-band via a M-phonon, with an energy corresponding to the conductance peak spacing. The coupling is shown to be strong enough to lead to the formation of polarons. We fit the conductance spectra to get an estimate of the electron-phonon coupling strength. We furthermore show that the conductance peaks, related to the local creation of polarons with the STM tip, can be shifted by charges at the edges of the MoS₂ islands. We use this dependence on the local environment to confine polarons to a quantum well, which allows us to image them directly with the scanning tunnelling microscope.

In the Scientific Appendix, two additional studies on single-layer MoS₂ are presented. With transport studies exhibiting signs of localization effects in MoS₂, which could lead to a Coulomb gap at the Fermi level, we conducted low-temperature (0.35 K) scanning tunnelling spectroscopy measurements of metallic MoS₂ on the graphene/europium/Ir(111) sample. The spectra reveal a V-shaped gap at the Fermi level. The gap is only present on MoS₂ and is absent on graphene. It does not respond to external magnetic fields, ruling out that it has a superconducting origin. Instead, it is found that the gap size depends on the area of the MoS₂ islands, which is in line with it being a Coulomb gap driven primarily by electron-electron correlations.

Finally, we have investigated single-layer MoS₂ on hBN/Ir(111). Exchanging graphene for the large band gap insulator hBN leads to a substantial band gap increase in MoS₂, at least in regions where sulphur intercalation below hBN flattens out the strong hBN/Ir(111) moiré. In these regions, we can resolve the maximum of the valence band at the K-point with constant-current scanning tunnelling spectroscopy, further pointing towards an enhanced decoupling from the substrate compared to graphene/Ir(111). Simultaneously, in regions with less or no sulphur intercalation, the moiré of hBN/Ir(111) modulates the band structure of MoS₂, giving rise to possible localized states in the quantum wells formed by the moiré potential.

Deutsche Kurzzusammenfassung

(German abstract)

In dieser Arbeit werden die zweidimensionalen Materialien MoS_2 und VS_2 in ihrer Einzelschichtform untersucht. Unterschiedliche Phasen, abhängig von den Syntheseparametern, dem Substrat oder der Temperatur, werden erforscht, wobei der Schwerpunkt auf den korrelierten elektronischen und magnetischen Zuständen liegt, die in diesen Materialien vorhanden sind. Rastertunnelmikroskopie wird verwendet, um strukturelle Informationen mit atomarer räumlicher Auflösung zu erhalten, während Rastertunnel-Spektroskopie eingesetzt wird, um die lokale Zustandsdichte zu messen. Experimentelle Ergebnisse zu korrelierten Phänomenen werden mit Dichtefunktionaltheorie und numerischen Renormierungsgruppen-Berechnungen verglichen, die von Kooperationspartnern durchgeführt wurden.

Die Einzelschicht von VS_2 wurde vorhergesagt, ein stark korreliertes Material zu sein, bei dem möglicherweise ein koexistierender magnetischer und ladungsdichtewellenartiger Grundzustand auftritt. Die Metastabilität von VS_2 führt jedoch dazu, dass es schwierig herzustellen ist, und eine experimentelle Realisierung einer freistehenden Einzelschicht war bislang noch nicht gelungen. Wir haben erfolgreich eine Einzelschicht von VS_2 auf dem schwach wechselwirkenden Graphen auf einem Ir(111)-Substrat synthetisiert, indem wir die Molekularstrahlepitaxiemethode verwendet haben. Mit dem Rastertunnelmikroskop finden wir eine Ladungsdichtewelle mit einer Elementarzelle von $9 \times \sqrt{3}R30^\circ$. Es handelt sich um eine ungewöhnliche Ladungsdichtewelle, da sie eine Symmetriereduktion von einer hexagonalen zu einer rechteckigen Elementarzelle aufweist und sogar bei Raumtemperatur vorhanden ist. Basierend auf den experimentellen Daten als Grundlage für Dichtefunktionaltheorie-Berechnungen finden wir heraus, dass der Übergang zur Ladungsdichtewelle zu einer drastischen Neugestaltung der Bandstruktur führt. Im Gegensatz zum intuitiven Peierls-Bild einer Ladungsdichtewelle, die von den Elektronen im Fermi-Niveau angetrieben wird, stellen wir fest, dass die Bildung der Ladungsdichtewelle am besten durch eine nichtlineare Kopplung zwischen transversalen und longitudinalen Phononmoden erklärt werden kann. Das auffälligste Merkmal dieser Phase ist eine große, vollständige Lücke in der unbesetzten Zustandsdichte, die mit Rastertunnel-Spektroskopie gemessen wird. Darüber hinaus zeigen Spektren der zirkularen Röntgenmagnetdichroismus, dass in kleinen Inseln von VS_2 keine Nettomagnetisierung vorhanden ist, was durch eine Koexistenz der Ladungsdichtewelle mit einer antiferromagnetischen Spin-Dichtewelle erklärt werden könnte.

Die Metastabilität von VS_2 kann jedoch auch genutzt werden, um neue Verbindungen herzustellen,

da es leicht in V-reiche Phasen überführt werden kann, indem es interkaliert oder desulfuriert wird. Es wurde bereits gezeigt, dass die Einführung von Schwefeldefekten und die Interkalation von Vanadiumatomen zu Phasenübergängen oder Magnetismus in ähnlichen Verbindungen führen können. Wir kombinieren Rastertunnelmikroskopie mit Röntgenfotoelektronenspektroskopie, um die Synthese von zwei neuen auf Vanadium basierenden Materialien auf Graphen auf Ir(111) zu demonstrieren. Durch das Glühen der Einzelschicht von VS_2 im Ultrahochvakuum können wir das eindimensionale strukturierte Material V_4S_7 herstellen, das geordnete Reihen von Schwefelvakanzstellen entlang seiner Oberfläche aufweist. Durch die Erhöhung der Menge an Vanadium und Schwefel auf der Probe können wir alternativ letztendlich dünnes V_5S_8 herstellen, das eine 2×2 -Schicht von Vanadiumatomen zwischen Schichten von VS_2 interkaliert hat. In den dünnsten V_5S_8 -abgeleiteten Strukturen wird bei niedrigen Temperaturen eine $\sqrt{3} \times \sqrt{3}$ -Ladungsdichtewelle gefunden, die mit Rastertunnel-Spektroskopie untersucht wird.

Während die halbleitenden Eigenschaften der Einzelschicht von MoS_2 umfassend untersucht wurden, gibt es viele offene Fragen bezüglich ihres metallischen Zustands, der nur durch erhebliches Gateing oder Dotierung erreicht werden kann. Da typisches Back-Gating aufgrund von Durchbrucheffekten dies nicht erreichen kann, wurde MoS_2 zuvor mithilfe ionischer Flüssigkeiten metallisch gemacht oder über Schwefelvakanz-Dotierung dotiert. Diese Methoden neigen jedoch dazu, zu Unordnung und Ladungsungleichgewichten zu führen. Stattdessen nutzen wir die einzigartigen Eigenschaften des Graphens auf dem Ir(111)-Substrat, um das Fermi-Niveau von MoS_2 ohne diese Nachteile anzupassen. Unter Verwendung von Sauerstoff als *p*-Dotiermittel und Europium als *n*-Dotiermittel interkalierten wir diese Atome zwischen Graphen und Ir(111). Als Ergebnis nimmt Sauerstoff Elektronen von Graphen auf oder Europium spendet Elektronen an Graphen, wodurch das Fermi-Niveau von MoS_2 elektrostatisch verschoben wird, während es chemisch unverändert bleibt. Die Interkalation von Sauerstoff unter Graphen führt zur *p*-Dotierung von MoS_2 , was eine Abwärtsverschiebung des Fermi-Niveaus von 0.45 eV bewirkt. Mit Europium können wir MoS_2 *n*-dotieren, wobei sich sein Fermi-Niveau um etwa 0.8 eV nach oben verschiebt und ein Metall-Isolator-Übergang induziert wird. Aufgrund der verbesserten Abschirmung des metallischen Zustands wird eine erhebliche Bandlückenrenormierung von 0.67 eV gemessen. Wir erforschen weiterhin die Auswirkung der zusätzlichen Ladung auf die eindimensionalen metallischen Zustände an den Zwillingsgrenzen von MoS_2 . Die Depletion und Ladung über das Substrat führen zur Verschiebung der Periodizität der Zustände, während ihre eindimensionale Natur erhalten bleibt. Zusätzliche DFT-Berechnungen reproduzieren den Metall-Isolator-Übergang sowie die Verschiebungen des Graphen-Dirac-Punkts und des MoS_2 -Leitungsbandes.

Der Kondo-Effekt, bei dem der Spin eines magnetischen Verunreinigungs Zustands von den beweglichen Elektronen in einem Metall abgeschirmt wird, ist eines der am besten verstandenen Phänomene in der Vielteilchenphysik. Die mikroskopische Beschreibung ermöglicht es, die Eigenschaften des Systems bei jeder Energieskala vorherzusagen, unter Verwendung weniger Parameter. Diese Parameter, die sich auf die magnetische Verunreinigung beziehen, sind jedoch in der

herkömmlichen Realisierung des Kondo-Effekts mit Hilfe von magnetischen Adatomen auf Metalloberflächen, die die Rastertunnelmikroskopie verwendet, nicht zugänglich. Wir präsentieren ein einzigartiges Kondo-System in den Zwillingsgrenzen der Einzelschicht von MoS_2 . Durch das Anlegen von Spannungspulsen mit der Spitze des Rastertunnelmikroskops können die doppelt besetzten, entarteten eindimensionalen metallischen Zustände in den Zwillingsgrenzen zum Fermi-Niveau verschoben werden, wo sie sich aufgrund starker Coulomb-Wechselwirkungen aufspalten. Dies führt zur Bildung eines einfach besetzten Zustands mit Spin $1/2$. Die Kopplung des magnetischen Moments dieses Zustands an Elektronen im Substrat führt zu einer Kondo-Resonanz am Fermi-Niveau. Unsere Fähigkeit, die spektrale Funktion des vollständigen Kondo-Systems, bestehend aus den magnetischen Spiegeltwin-Grenzflächenzuständen zusammen mit der Resonanz, aufzulösen, ermöglicht es uns, die experimentellen Daten direkt mit numerischen Renormierungsgruppen-Berechnungen zu vergleichen. Ein weiterer Vorteil dieses Systems besteht darin, dass die Vielfalt der Grenzflächenlängen und Energiezustände zu einer breiten Palette von zugänglichen Kondo-Kopplungsstärken führt, wobei die Kondo-Temperaturen sechs Größenordnungen umspannen. Wir können auch erstmals die Beziehung zwischen den magnetischen Zuständen und der Resonanz im Realraum auflösen.

Wenn die Einzelschicht MoS_2 metallisch gemacht wird, finden theoretische und experimentelle Arbeiten Hinweise auf starke Elektron-Phonon-Kopplung, die zu verschiedenen Korrelationseffekten führen kann, wie Superfluidität oder der Bildung von Polaronen, einem Quasiteilchen, das aus einem Überschuss an Ladungsträgern (Elektronen oder Löchern) besteht, das sich in einem Potentialtopf bildet, der durch die Ionen des Gitters gebildet wird. Wir bieten eine Studie zur Elektron-Phonon-Kopplung in der metallischen Einzelschicht MoS_2 mittels Rastertunnelmikroskopie und Dichtefunktionaltheorie. Leitfähigkeitsspektren von zwei metallischen MoS_2 -Proben, in die unterhalb des Graphen-Substrats Europium oder Cäsium interkaliert wurden, zeigen eine Serie von gleichmäßig verteilten Peaks um das Fermi-Niveau herum. Dichtefunktionaltheorie-Berechnungen für n -dotierte Einzelschicht MoS_2 zeigen eine starke Kopplung zwischen dem besetzten K-Band von MoS_2 und dem unbesetzten Q-Band mittels eines M-Phonons, mit einer Energie, die dem Abstand der Leitfähigkeitspeaks entspricht. Die Kopplung ist stark genug, um zur Bildung von Polaronen zu führen. Wir passen die Leitfähigkeitsspektren an, um eine Schätzung für die Stärke der Elektron-Phonon-Kopplung zu erhalten. Darüber hinaus zeigen wir, dass die Leitfähigkeitspeaks, die mit der lokalen Erzeugung von Polaronen mit der STM-Spitze zusammenhängen, durch Ladungen an den Rändern der MoS_2 -Inseln verschoben werden können. Wir nutzen diese Abhängigkeit von der lokalen Umgebung, um Polaronen in einem Quantentopf zu begrenzen, was es uns ermöglicht, sie direkt mit dem Rastertunnelmikroskop abzubilden.

Im wissenschaftlichen Anhang werden zwei zusätzliche Studien zur Einzelschicht MoS_2 vorgestellt. Transportstudien zeigen Anzeichen von Lokalisierungseffekten in MoS_2 , die zu einer Coulomb-Lücke am Fermi-Niveau führen könnten. Daher führten wir Rastertunnel-Spektroskopiemessungen an metallischem MoS_2 auf der Graphen/Europium/Ir(111)-Probe bei niedrigen Temperaturen (0.35 K) durch. Die Spektren zeigen eine V-förmige Lücke am Fermi-Niveau. Die Lücke ist nur in MoS_2

vorhanden und fehlt im Graphen. Sie reagiert nicht auf externe Magnetfelder, was eine superleitende Herkunft ausschließt. Stattdessen stellt sich heraus, dass die Lückengröße von der Fläche der MoS₂-Inseln abhängt, was darauf hinweist, dass es sich um eine Coulomb-Lücke handelt, die hauptsächlich durch Elektron-Elektron-Korrelationen verursacht wird.

Schließlich haben wir Einzelschicht MoS₂ auf hBN/Ir(111) untersucht. Der Austausch von Graphen gegen den Isolator hBN mit großer Bandlücke führt zu einer deutlichen Zunahme der Bandlücke in MoS₂, zumindest in Regionen, in denen Schwefel-Intercalation unter hBN das starke hBN/Ir(111)-Moiré glättet. In diesen Regionen können wir das Maximum des Valenzbands am K-Punkt mit konstantem Strom in der Rastertunnel-Spektroskopie auflösen, was auf eine verbesserte Entkopplung vom Substrat im Vergleich zu Graphen/Ir(111) hinweist. Gleichzeitig moduliert in Regionen mit weniger oder keiner Schwefel-Intercalation das Moiré von hBN/Ir(111) die Bandstruktur von MoS₂, was möglicherweise zu lokalisierten Zuständen in den durch das Moiré-Potential gebildeten Quantentöpfen führt.

Frequently used Acronyms and Abbreviations

1D	-	one-dimensional
2D	-	two-dimensional
3D	-	three-dimensional
CB	-	conduction band
CC	-	constant current
CDW	-	charge density wave
CH	-	constant height
CVD	-	chemical vapour deposition
DFT	-	density-functional theory
EPC	-	electron-phonon coupling
FSN	-	Fermi surface nesting
Gr	-	graphene
hBN	-	hexagonal boron nitride
LEED	-	Low-energy electron diffraction
MBE	-	molecular beam epitaxy
SPT	-	structural phase transition
STM	-	scanning tunnelling microscope
STS	-	scanning tunnelling spectroscopy
TMDC	-	transition metal dichalcogenide
UHV	-	ultra-high vacuum
XPS	-	X-ray photoelectron spectroscopy
VB	-	valence band
vdW	-	van der Waals

Contents

Deutsche Kurzzusammenfassung (<i>German abstract</i>)	v
Frequently used Acronyms and Abbreviations	ix
I Introduction and Background	1
1 Motivation	3
2 Transition Metal Dichalcogenides	7
2.1 Structure and growth of transition metal dichalcogenides	7
2.2 Molybdenum disulphide	13
2.3 Vanadium disulphide	17
3 Electronic and Magnetic Interactions	21
3.1 Electron-phonon coupling	21
3.2 Screening	27
II Experimental Results	31
4 Manuscript [1]: A full gap above the Fermi level: the charge density wave of monolayer VS₂	33
4.1 Supporting information	43
5 Manuscript [2]: Novel 2D vanadium sulphides: synthesis, atomic structure engineering and charge density waves	65
5.1 Supporting information	101
6 Manuscript [3]: Metal-insulator transition in monolayer MoS₂ via contactless chemical doping	117
6.1 Supporting information	131

Contents

7 Manuscript [4]: Modulated Kondo screening along magnetic mirror twin boundaries in monolayer MoS₂ on graphene	151
7.1 Supporting information	177
8 Manuscript 5: Real-space observation and tunneling spectroscopy of polarons in monolayer MoS₂	219
8.1 Supporting information	249
III Discussion	261
9 Discussion	263
9.1 What makes a charge density wave: the case of single-layer VS ₂	263
9.2 Mind the gap: CDW gaps measured with STM	266
9.3 The blessings and curses of a metastable material	267
9.4 Doping single-layer MoS ₂ : a material of many phases	269
9.5 The various uses of a tunable, fully resolved Kondo system	272
9.6 Seeing polarons: manifestations of strong electron-phonon coupling in STM	274
IV Appendix	279
A Scientific Appendix	281
A.1 Coulomb gap in metallic single-layer MoS ₂	282
A.2 Single-layer MoS ₂ on h-BN on Ir(111)	287
A.3 CPlot: plotting, analysing, filtering and managing Nanonis files	292
B List of publications (<i>Liste der Teilpublikationen</i>)	299
Bibliography	303
Acknowledgements (<i>Danksagung</i>)	341
Erklärung zur Dissertation	345
Lebenslauf (<i>Curriculum Vitae</i>)	347

PART I

Introduction and Background

CHAPTER 1

Motivation

Physics is the science of reduction. From the folding of proteins to the crashing of waves on the beach, from the movement of galaxies to the fall of a feather: it all comes down to four fundamental interactions. Nothing happens that should not, ultimately, fit into the microscopic causal chains connecting physical events with prior events via the four forces of nature.

In many cases, determining the precise microscopic origins of physical phenomena is both extremely difficult and impractical. Most of physics is concerned with cases involving more than a couple of particles in vacuum and even our best models cannot fully capture all the interactions between them. Macroscopic events are, instead, governed by statistics. We do not need to know the exact processes that underlie most phenomena we encounter in our daily lives: to predict the weather days in advance, or to calculate the current going through a wire. As long as the number of particles is large enough, we can use emergent properties, like temperature and resistance, to adequately describe what is happening. It is often enough to know that, on a deeper level, the phenomenological laws of thermodynamics or conductance should follow from a complete description of the microscopic constituents of the world.

Two dimensional (2D) materials inhabit the space between single particles described solely by fundamental forces and macroscopic objects ruled by statistics. An electron living in two dimensions is neither the elementary particle found in the standard model; nor is it the bland carrier of current that moves through three dimensional cables. In vacuum, a particle is free because it is alone. In a three dimensional material, it is free because there are so many other particles that their total influence is nearly cancelled out - the effects of any particle on their surroundings and vice versa are *screened*. In matter with less than three dimensions, electrons are decidedly not free. They are in close proximity, but without the benefit of screening - which is ineffective in lower dimensions - they cannot ignore each other. As a consequence, they end up being correlated with one another, forming new ordered states of matter with their own emergent physics.

In 2D materials, the quest for reduction, which is in the end the pursuit of understanding, takes on a particularly beautiful form. Most of the basic terminology of condensed matter physics consists of emergent phenomena: quasiparticles such as holes, polarons, excitons or phonons, or ordered phases such as superconductivity. The lack of screening in lower dimensions only gives rise to more of such many-body effects, like spinons and chargons, charge density waves and fractional charges. But here,

Chapter 1 Motivation

a full description based on lower-lying interactions, rooted in electrodynamics and quantum theory, does not feel so out of reach. Since they are all surface, we can access low-dimensional systems with extreme local precision - nothing is hidden. So, the emergent macroscopic properties can be matched with their local microscopic counterparts. In addition, we can grow 2D materials under clean, ultra-high vacuum conditions, making them as close as possible to the intrinsic materials considered in theoretical models based on fundamental interactions. We can even add disorder, defects or charge in a controlled way, to reveal their effects or manipulate the properties of the material. This unprecedented control over these systems simplifies them to such an extent, that it allows us to compare experiment directly with *ab-initio* theories based on the exact microscopic processes out of which they arise.

This undertaking can be regarded as the recurring theme of this thesis. Using the scanning tunnelling microscope, which consists of an atomically sharp, metal tip brought in very close proximity to the surface of a 2D material, we can image the individual atoms of which the material is composed. The atomic resolution of the structure of materials is made possible by a quantum tunnelling current between tip and sample, which is extremely distance-dependent. As the tip is moved over the surface, the current will fall and rise with the 'landscape' of atoms beneath it. This current has another, even more remarkable virtue: it contains information on the local density of states of the sample. With the STM, we thus see not only where the atoms are sitting, but also what the electrons in the material are doing. The behaviour of the electrons can be resolved in both space and energy. In some cases, the STM can even be used to directly observe other types of quasiparticles, like phonons or Cooper pairs. In most of the Chapters of this thesis, the data obtained with STM is directly compared to first-principles theory performed by our collaborators.

The correlated physics of low-dimensional materials is explored by means of two materials. VS_2 and MoS_2 are transition metal dichalcogenides (TMDCs), layered materials with weak van der Waals (vdW) forces acting between molecular sheets of transition metals bound to planes of chalcogen (S, Se, Te) atoms above and below. Since the coupling between layers is so feeble, these materials are always semi-2D, even in their bulk form. Nevertheless, it is worthwhile to remove even the last vestiges of the third dimension and isolate them as single layers, which can lead to the development of completely new physics [5]. Considering the single-layer variants of VS_2 and MoS_2 , it turns out that they have an impressive range of correlated phenomena to offer, neatly divided between the two of them.

Single-layer MoS_2 is a direct band gap semiconductor, where the holes in the valence band can couple strongly to excited electrons in the conduction band. These electron-hole pairs form quasiparticles called excitons, which have particularly high binding energies in MoS_2 [6]. The band edges of single-layer MoS_2 are spin-orbit split due to the lack of inversion symmetry, giving rise to valley physics, which makes use of the opposing spin states of particles moving in opposite directions [7]. Strong n -doping of MoS_2 can lead to a metal-insulator transition. In its metallic state, coupling between the electrons and the phonons of the crystal lattice could lead to the formation of another

quasiparticle: a polaron [8]. And if it is doped sufficiently, it can also become superconducting [9], with indications that this is of the unusual Ising-type, where the spin-orbit splitting of the bands protects the Cooper pairs from breaking in in-plane magnetic fields [10].

Single-layer VS_2 is an intrinsic metal and a promising material for strongly correlated physics [11]. Unlike MoS_2 , it was not yet synthesized in its freestanding form, due to the metastability of bulk VS_2 , which rather grows in S-deficient structures with V atoms intercalated between layers of VS_2 [12]. Predictions for single-layer VS_2 have generally focused on its purported ferromagnetic ground state [13], which is relatively rare in two-dimensional materials [14]. It was further predicted to undergo a charge density wave (CDW) transition, where the lattice periodically distorts to accommodate a standing wave of electrons, possibly accompanied by a spin density wave, where the magnetic moments are periodically modulated with a period related to the CDW [11].

In order to perform STM measurements on these materials, we first need a suitable substrate, one that allows a current to flow between tip and sample. In other words, we need a metal. Growing TMDCs directly on a metal is counter-productive: due to the dangling bonds at the surface of the metal, it could hybridize with the TMDC, altering its electronic properties as a consequence of orbital overlap. Hybridization, as well as screening from the bulk metal, would act against the intrinsic 2D nature of the TMDC, and can lead to the suppression of the correlated effects we aim to investigate. We therefore use a buffer layer between VS_2 and MoS_2 and our metallic substrate, which is a Ir(111) crystal. Graphene (Gr), a 2D sheet of carbon atoms, is selected as buffer; it shields the materials of interest from the metal, while still allowing a tunnelling current to pass. In this way we obtain what we call quasi-freestanding TMDCs in our STM [15].

The research we have performed on VS_2 is contained in two Chapters. In Chapter 4 we demonstrate the first quasi-freestanding synthesis of single-layer VS_2 . We find a unique, one-dimensional CDW in the material, which has a transition temperature above room temperature. Unlike most other CDW systems, it has a full gap in the unoccupied density of states, which we resolve with the STM. We compare our experimental findings to first principles calculations. The excellent agreement allows us to determine the microscopic origin of the CDW as mode-mode coupling between phonons. In Chapter 5, we instead focus on obtaining new vanadium and sulphur based compounds. We create single-layers of V_4S_7 , a material with ordered one-dimensional sulphur vacancies, which might host one-dimensional physics, as well as having possible catalytic properties. We also synthesize self-intercalated 2D variants of V_5S_8 , which have extra V atoms between layers of VS_2 and are promising candidates for magnetic interactions. In the V_5S_8 -derived structures, we observe a CDW at temperatures below 110 K.

Our studies of MoS_2 are found in the remaining three Chapters and two Appendices. In Chapter 6 we show how we can use our graphene on iridium substrate to control the Fermi level and band gap of MoS_2 . By intercalating either oxygen or europium between graphene and iridium, we can achieve very strong *p*- or *n*-doping of MoS_2 without chemically changing anything in MoS_2 itself. Using europium, we are able to make single-layer MoS_2 metallic, which is accompanied by a drastic band

Chapter 1 Motivation

gap renormalization. This theme of controlling the properties of MoS_2 is continued in Chapter 7, where we use voltage pulses applied with the STM tip to make one-dimensional defects in MoS_2 magnetic. In their magnetic state, they couple to the electrons from the substrate, leading to a Kondo resonance. We are able to measure for the first time the complete spectral function of the Kondo system with the STM, which allows us to compare our data directly with the microscopic Anderson model. In Chapter 8 we investigate the properties of metallic MoS_2 , which we obtained using the method of Chapter 6. In its metallic state we directly observe the effects of strong-electron phonon coupling in the tunnelling current, pointing towards the presence of polarons. Our findings are compared with first-principles calculations, which indeed find a (meta-)stable polaronic ground state for our system. Staying with metallic MoS_2 , we additionally find a small gap at the Fermi level when we cool down to very low temperatures. This is described in Appendix A.1. We argue that it is a Coulomb gap, driven by strong electron-electron correlations. Finally, in Appendix A.2, we exchange the graphene buffer layer of our substrate with hexagonal boron nitride (hBN), which is an insulating 2D material. The effect on the properties of MoS_2 is dual: depending on the amount of sulphur intercalation between hBN and iridium, it makes MoS_2 either more freestanding - with the band gap extremely close to its theoretical limit - or it modulates the properties of MoS_2 in an ordered fashion, leading to possible moiré physics.

This thesis is structured as follows: Part I provides background information on the concepts and materials relevant to this work. In Chapter 2, 2D materials are introduced. Their history, crystal structure and practical aspects of their synthesis are discussed. Afterwards, single-layer MoS_2 and VS_2 are presented in more detail. Chapter 3 focuses on the electronic interactions which lie at the heart of this thesis. They are divided into two categories: electron-phonon coupling, from which the polarons of Chapter 8 and charge density waves of Chapters 4 and 5 arise; and screening, which causes the band gap renormalization of Chapter 6 and the Kondo effect encountered in Chapter 7.

Part II contains five manuscripts, of which the first and third (Chapters 4 and 6) are published. The fourth manuscript (Chapter 7) has been accepted for publication, while the second manuscript (Chapter 5) is under review and can thus be considered close to being finished. The fifth manuscript, of Chapter 8, is in the final state before submission, with the theoretical calculations and experimental work completed.

In Part III, we discuss the results of the manuscripts, focusing on further experiments that could be conducted and including a broader consideration of our work in the context of current and past research.

In Part IV, the Appendices can be found. Apart from the Scientific Appendices mentioned above, it contains a manual for a Python-based application for data analysis and visualisation, developed during my PhD. It is freely available for download (<https://github.com/cavaern/CPlot>).

CHAPTER 2

Transition Metal Dichalcogenides

This Chapter should serve as a brief introduction to transition metal dichalcogenides, a class of materials with inherently two-dimensional properties. First the concept of a two-dimensional material will be introduced, followed by a discussion of the crystal and electronic structure of transition metal dichalcogenides. Their synthesis will be reviewed, as well as the dependence of their properties on the substrate and internal defects. Afterwards, the two materials investigated in this thesis, MoS₂ and VS₂, will be treated of in more detail. For a full review of transition metal dichalcogenides, the reader is referred to Ref. [5]. An excellent overview of the electronic properties of MoS₂ from a theoretical perspective is presented in Ref. [16], while growth methods of MoS₂ focused on applications are summed up in the short review of Ref. [17]. Most reviews of VS₂ concentrate on its applications in battery technology. A recent review of the various applications of VS₂ is given in Ref. [18].

2.1 Structure and growth of transition metal dichalcogenides

Most of the fascinating properties of TMDCs stem from the fact that they are 2D materials. Before we delve into the topic, we should therefore establish what that precisely means. Any material can, in principle, be thinned down, whittled away until nothing is left but a single layer of atoms. But could we really create a 2D layer of, say, iron in this way? The answer is negative. Iron, being a three-dimensional (3D) material, is unstable without the strong bonding interactions between its layers. As a result, it will not form a flat layer, but cluster together into balls.

We can try to remedy the situation. Perhaps we take a suitable substrate, a bulk metal crystal, which will keep the iron atoms in place while we perform our thinning procedure. Now our experiment might indeed be called a success. We end up with a layer of iron atoms firmly attached to the metallic bulk. But what we have created could be better described as a 3D crystal with some iron on its surface, than a proper 2D layer of iron. We cannot transfer the iron layer to another substrate, we cannot even think of its properties independent from the bulk metal, due to the strong hybridization between the two. And for a long time, this was supposed to be the only way for 2D materials to exist: as an integral part of a larger 3D structure [19].

An actual 2D material would be fully content to stay two-dimensional. If it would be created in space, it could float as a single layer through vacuum. If put on a substrate, it can be removed again and put on top of another. Its properties would not be tied to those of the material it rests on. And

around 1960, it was discovered that such materials indeed exist [5].

True to their nature, these types of materials are never really 3D, with much stronger intra- than interlayer bonding. In their bulk form, they consist of 2D layers bound only weakly together by vdW forces. TMDCs are a class of such layered materials, composed of a transition metal atom M and two chalcogen atoms (S, Se, or Te) X with stoichiometry MX_2 . They have been studied extensively in bulk and ultrathin form in the 1960s [20] and by 1986 suspensions of single layers of TaS_2 , NbS_2 and MoS_2 had been produced [21, 22].

However, theoretical doubts persisted about the possibility of single-layers under ambient conditions. It was argued that any 2D material would be inherently unstable due to thermodynamical fluctuations [23, 24]. Only with the discovery of Gr, a 2D sheet of carbon atoms, in 2004 [25], quickly followed by other freestanding 2D crystals like single-layer hBN [26], those doubts were quelled. Using the techniques developed during Gr-related research, new ways to study single-layers of TMDCs opened up and the field of 2D materials came into being.

Electronic and structural properties of TMDCs

Due to the great variety of electronic properties found in the various TMDC materials, paired with the weak electronic screening inherent to electronic confinement to two dimensions and the ability to stack them together to form heterostructures, TMDCs have been of continuous interest to fundamental research. In their now accessible single-layer form, TMDCs have been known to host a variety of phenomena, like charge density waves [27], two-dimensional superconductivity [28], valley polarization [7, 29], the quantum spin Hall effect [30] and heavy fermions [31].

Single-layer TMDCs are also hailed as promising materials for applications, especially the semiconductors MoS_2 and WSe_2 [32], whose electronic properties can be controlled with their dimensionality, strain, doping and via the substrate [33–36]. Compared to regular semiconducting materials, they are less sensitive to the formation of interfacial defects as their inherent 2D nature leads them to have few dangling bonds at the surface [37]. They further provide the possibility of ultimately thin transistors, enabling improved electrostatic control and reduced short-channel effects, which are two of the main issues plaguing current ultrascaled devices [38].

TMDCs can exist in different structural phases, which depend on the coordination sphere of the transition metal atoms [5]. The most common ones are the trigonal prismatic (2H) and the octahedral (1T) coordination. The 2H-phase is characterized by AbA stacking of covalently bonded atomic layers, with the chalcogen atoms (position designated by capital letters) on top of each other in the direction perpendicular to the layer and shifted relative to the metal atom (position indicated with lower case letter) [39]. The 1T-phase instead has an AbC stacking order. In most phases, the chalcogen atoms form a hexagonal lattice which gives TMDCs a threefold symmetry. The digit in front of the phases indicates the number of layers needed to comprise a unit cell of the bulk material. For representations of the 2H- and 1T-phases, see the MoS_2 structure in Fig. 2.1 and the VS_2 structure in Fig. 2.2, respectively.

2.1 Structure and growth of transition metal dichalcogenides

The electronic configuration of TMDCs is linked to the number of electrons in the transition metal d-orbital, which can be partially or fully filled, depending on the choice of transition metal and coordination phase [40]. The choice of chalcogen atom does not influence the electronic properties to the same degree, though the heavier the chalcogen, the smaller the band gap in the insulating (fully filled d-orbital) phases tends to be [41]. Most TMDCs can be realised in various metastable phases, with drastically different properties [5]; taking single-layer MoS₂ as an example, its stable 2H-phase is a semiconductor with a large band gap exceeding 2 eV, while the metastable 1T-phase is metallic [42]. In the sections related to MoS₂ 2.2 and VS₂ 2.3, which can be regarded as archetypical 2H- and 1T-phase TMDCs, their crystallographic and electronic properties will be discussed in more detail.

Preparing single-layer TMDCs

There are many ways to prepare single-layer TMDCs, each with their own unique advantages and limitations. A good overview of current synthesis methods can be found in recent review papers [43,44]. In Ref. [15], the growth process of single-layer TMDCs developed within our group is demonstrated in detail.

Exfoliation

The first method is perhaps the most straightforward: exfoliation. This can be done either mechanically - using adhesive tape as was used for the first isolation of Gr [25, 26] - or chemically, for instance using organic solvents for liquid-phase exfoliation - this was the method used to create the first TMDC single layers [21, 22]. Mechanical exfoliation is fast, requiring only a bulk crystal, maybe some scotch tape, and a proper optical microscope, but it is also non-scalable and the deposition of the material can be challenging to get right - there is always the problem of residue from the adhesive sticking to the layer. Chemical exfoliation involves sonication or shear to overcome the vdW forces between layers. It is performed in a liquid to ensure that the obtained layers dissolve instead of re-aggregating [44]. It generally produces high-quality materials, but suffers from fragmentation of the layers, leading to a wide size distribution [45].

Exfoliation is a top-down method: one starts with a bulk crystal and aims to isolate a single layer. Most of the other methods used are bottom-up approaches, where the desired material is synthesized directly in its single-layer form. Many of these can be classified under vapour phase deposition methods, which allow high levels of control over the exact amount deposited. I will discuss two of them in more detail. Information about other methods like physical vapour deposition, atomic layer deposition, and pulsed laser deposition can be found for instance in Ref. [32].

Chemical Vapour Deposition

Chemical vapour deposition (CVD) takes place in a tube furnace, where a target substrate is placed downstream from a chalcogen source (classically, this is a powder, but the chalcogen can also be applied in gas form [44]). As the furnace gets heated under a carrier gas, the S powder evaporates and reacts with a precursor powder containing a transition metal (like MoO_3). This leads to a stream of TMDC molecules that travel along with the carrier gas onwards to the hot substrate, where they combine to form the desired structure. Using this method, μm -sized TMDC single-layers can be grown on different substrates [46–48]. After growth, the material can be transferred either together with the substrate or exfoliated. CVD is relatively cheap and easy - it does not require a vacuum chamber or intensive labour and allows the use of many, readily available precursors. More than any other method it holds the promise of industrial-scale implementation. But the very things that make it scalable and cheap are also its downsides. The near-ambient pressures involved in the process and the high substrate temperature lead to contamination and defect formation, while the many parameters involved lead to enormously diverse results [49]. In general, the conditions of CVD are not ideal for fundamental research, which requires tight control over the synthesis outcome. In particular, a prerequisite for a direct comparison between first-principles theory and experiment is the pristine nature of the investigated material. Adsorbates or defects stemming from CVD growth, which strongly influence the properties of 2D materials [50], would preclude an unambiguous determination of their intrinsic properties.

Molecular Beam Epitaxy

The method used in this thesis is called reactive molecular beam epitaxy (MBE). MBE occurs under ultra-high vacuum (UHV) conditions, where beams of neutral atoms or molecules are directed towards a (heated) substrate [51]. The high melting temperature of many transition metals necessitates the use of electron beam evaporation, which requires high voltages and temperatures not needed in CVD. MBE typically takes place on weakly-interacting substrates, making full use of the lack of dangling bonds at the surfaces of TMDCs, as this removes the need for the lattice to match to that of the substrate, which is necessary in conventional growth of heterostructures [52]. In effect, this means that the material can be grown quasi-freestanding [15], with its lattice constant and symmetry not affected by the substrate. The weak vdW interaction with the substrate is enough to control the orientation of the layer, thereby preventing the sample from exhibiting multiple orientations and angle mismatches (polycrystallinity) [41, 53, 54]. MBE is generally performed in UHV systems which allow *in situ* characterization, using for instance LEED or STM. The UHV conditions also make it ideal for research purposes, especially those which involve local characterization, as the number of defects or adsorbates is kept at a minimum. The challenge of MBE growth of TMDCs lies in the low sticking coefficient of S and Se at the temperatures needed for metal surface diffusion. This problem is partially alleviated by using vdW substrates such as Gr, which enhance surface diffusion [15, 55–57]. Nevertheless, MBE growth typically results in smaller domains than those obtained with CVD. MBE

growth does allow for easy incorporation of (magnetic) dopant atoms or alloying of materials, by simultaneous evaporation of elemental metal atoms [58–62].

Substrate interaction in TMDCs

The great advantage of 2D materials is that they are extremely thin. They are all surface. This fact makes them highly susceptible to their environment, which can be leveraged to achieve a high level of control over their properties. It also makes them particularly difficult to work with. Their properties will depend heavily on external sources of disorder, mainly stemming from the substrate, as well as internal imperfections (defects). Whether this is a boon or a curse will hinge on our ability to control these parameters.

For the substrate there are - very broadly - three options available. The TMDC can be placed on a metal substrate, which facilitates easy growth, but leads to strong hybridization between the TMDC and the substrate. It is also possible to use an insulating substrate. This is necessary for most device applications, but the lack of screening can lead to strong disorder unless the substrate is of very high quality. Finally, one could opt for a vdW substrate. This would lead to a more involved growth process, due to the lack of catalytic activity of the substrate, but the weak interaction with the substrate reduces a main source of external disorder, so that the intrinsic qualities of the TMDC can be preserved.

Metallic substrates

As for metallic substrates, high-quality single-layer TMDCs have been successfully grown directly on Au already before the isolation of Gr. Originally, the islands obtained on Au were small [63]. While this made them interesting for their catalytic properties, which are enhanced at island edges [64], the need for large areas of single-layer TMDCs remained. With improvements in the CVD growth technique, large single-crystals of e.g. WS_2 and MoS_2 were eventually grown on Au(111) [65, 66]. With the MBE technique, the Au substrate has mainly been used to grow S-based TMDCs, since S has a high vapor pressure under UHV conditions, so that crystalline S cannot be used as a source material for the evaporation of elemental S. With a catalytic substrate like Au(111), there is no need for elemental S, since molecules like H_2S can be decomposed on the surface. In this way, the metallic TMDCs TaS_2 , VS_2 and NbS_2 were grown on Au(111). However, in each of these cases the strong interactions with the substrate led to the suppression of predicted electronic properties like CDWs or superconductivity [12, 67, 68].

Insulating substrates

For device applications, TMDCs are often grown on semiconducting substrates like SiO_2 [48]. Such substrates have the downside, that they can introduce substantial extrinsic disorder to the single-layer TMDC [69]. This can be remedied either by depositing a high- κ dielectric like HfO_2 on top of

the TMDC, so that it can screen charge impurities in the substrate and passivate charged impurities within the TMDC layer itself [70]; or by encapsulating the layer in hBN, to increase the distance between the TMDC and the substrate [71]. However, TMDCs grown on inert substrates tend to also have many intrinsic defects like S vacancies, antisite defects, adatoms and dislocations [72]. These lead to localized in-gap states and a strong decrease in the carrier mobility [73].

vdW substrates

This latter point brings us to the third type of substrate, which mainly has benefits for a scientist interested in the intrinsic properties of single-layer TMDCs. Already among the pioneering works on the growth of epitaxial TMDC films using MBE was a study demonstrating the successful growth of NbSe₂ on a cleaved 2H-MoS₂ surface [53]. Despite the lattice mismatch and the weak vdW forces between the materials, the adlayer shows a strong preference for alignment with the substrate axes. With the epitaxial alignment secured, the large surface mobility of the evaporated metal atoms and the minimal substrate interaction make vdW materials the substrate of choice for MBE [74]. However, since the growth is not primarily driven by the catalytic activity of the substrate, nucleation and expansion of adlayers can take place on top of the first TMDC layer. Using these substrates therefore tends to result in multilayer structures. To prevent substantial second and higher layer growth, single-layer films often cover but a portion of the substrate and consist of many small islands due to low surface diffusion of the chalcogen atoms. Originally, the growth of TMDCs on vdW substrates was mainly focused on Se-based compounds; this has lately shifted to include the S-, and Te-based materials [75].

In this thesis we apply MBE growth on Gr/Ir(111) to grow VS₂ and MoS₂, using pyrite (FeS₂) as a UHV-compatible S source [15]. Gr is chemically inert, binds weakly to any adlayer via vdW forces and screens poorly due to its 2D and semi-metallic nature [76]. To preserve these qualities, it is crucial that the Gr layer does not interact too strongly with the bulk metallic crystal necessary for most STM setups. On Ir(111), Gr can be grown epitaxially as a single-crystalline layer with an extremely low defect density [77–79]. The interaction between Gr and Ir(111) is weak enough that the Gr layer is physisorbed and its band structure close to pristine [80,81]. As a result, the single-layer TMDCs we grow on this substrate are quasi-freestanding, with properties close to those expected from first-principles calculations [15, 82].

Defects in TMDCs

But no matter how careful we grow and what substrate we choose, no growth is perfect. Whether exfoliated or grown with CVD or MBE, the resulting crystal will not be flawless. As a result of the second law of thermodynamics, every crystal will intrinsically have a temperature-dependent number of vacancy defects [83,84]. Growing TMDCs using the vapor phase methods involves the nucleation of small domains which merge together as more and more material is deposited on the substrate. This will typically result in polycrystalline films, with grain boundaries separating the original nuclei.

In the end, TMDCs will exhibit a variety of intrinsic and extrinsic defects besides vacancies and grain boundaries, like adatoms and substitutional impurities [48].

These defects can cause strain, store charge, break the lattice symmetry, scatter carriers, dope the material, host in-gap states, contain exotic states of matter or act as current filters. Defects can affect the optical and electronic properties of TMDCs [85, 86]. Understanding their role in shaping TMDCs is crucial, first from a fundamental point of view, but increasingly for practical applications as well.

Individual defects in 2D materials can act for instance as optically active sites, which behave as single-photon emitters [87]. The emission process can be tuned using a gate voltage [88]. They can also be used at catalytic sites instead of noble metal catalysts - which are expensive - in *e.g.* the hydrogen evolution reaction, with catalysis occurring at edges, S vacancies and grain boundaries [89]. Point and line defects in TMDCs can induce magnetism [90, 91], while S vacancies natively *n*-dope microcleaved few-layers of MoS₂ [73]. But they have downsides as well, mainly on the transport properties of materials. MoS₂ transport, *e.g.*, is hindered by charged impurities [92] and CVD grown single-layer MoS₂ has considerably lower carrier mobility compared to exfoliated samples due to imperfections stemming from the growth process [72].

The defects investigated in this thesis are mirror twin grain boundaries (MTBs). They form when two domains of a TMDC rotated by 60° grow together. Instead of other types of grain boundaries, their unique symmetry relation with the crystal allows them to have a regular atomic structure. They can thus be regarded as 1D structures embedded in a 2D crystal. Like other grain boundaries, they are mainly associated with impaired device performance [93, 94], though a slight increase in the in-plane conductivity was also reported for flakes of single-layer MoS₂ connected by a MTB [85]. From a microscopic point of view, the increased resistance across MTBs could be understood as a consequence of the band bending observed in STM [95], while the increased conductance could be related to band gap narrowing near the boundaries [96] and/or to the presence of mid-gap states in the MTB [97].

Density-functional theory (DFT) calculations predict that MTBs in 2D S-based TMDCs host 1D electronic bands [98]. This is a consequence of the polar nature of these materials, which results in polar charges accumulating at crystal discontinuities, which are cancelled out by the free charges that form the band [99, 100]. It was originally thought that the 1D band would lead to a pure Peierls CDW state in MoSe₂ MTBs [101]. However, the strong electron-electron correlations in MoS₂ and MoSe₂ MTBs instead lead to the formation of a Tomonaga-Luttinger liquid, where independent charge- and spin-density waves emerge out of fractionalized bosonic collective modes [102–104].

2.2 Molybdenum disulphide

Out of all the TMDCs, MoS₂ is probably the best known and most researched. It is a naturally occurring compound, silvery-black in its mineral form molybdenite. For a long time it was mainly

investigated for its tribological properties and used as a dry lubricant [105]. Other applications are petroleum desulfurization [106]; catalysis, especially involving hydrogen generation [64, 107]; and photovoltaics, with MoS₂ layers showing one order of magnitude higher absorption of sunlight compared to regular solar cell materials [108, 109]. MoS₂ has also been touted as an efficient electrode for high capacity batteries [110, 111]. Recently, the focus has shifted, with current research looking into its possible application in nanoelectronics [38], with the first single-layer MoS₂ transistor exhibiting a room-temperature current on/off ratio exceeding 1×10^8 and mobility of $\sim 20 \text{ cm}^2 \text{ V}^{-1} \text{ s}^{-1}$ [112]. Due to its large band gap, low in-plane dielectric field and atomic uniformity, single-layer MoS₂ transistors can be scaled down below the Si transistor scaling limit of $\sim 5 \text{ nm}$ gate lengths [113], recently crossing even the 1 nm mark [114].

Excitons and valleys

Two interesting transitions take place when bulk MoS₂ is thinned down to a single-layer. The first is due to the loss of inversion symmetry in the single layer, causing spin-orbit interactions to split the MoS₂ bands and allowing valley-dependent physics forbidden in regular materials [7]. The second transition is from an indirect to a direct band gap semiconductor [6, 33, 115, 116], with strongly enhanced excitonic binding energies [117].

Spin-orbit splitting

MoS₂ preferably crystallizes in the 2H-structure, see Fig. 2.1a. Unlike the 1T phase, the inversion center of the 2H phase lies in the middle between two planes. As a result, 2H-phase TMDCs lose inversion symmetry when they are thinned down to a single layer [7]. Because of the broken inversion symmetry, spin-orbit interactions split the MoS₂ valence bands by 160 meV and the conduction band by a couple of meV [7, 29, 119].

This can be understood if we consider a simple, non-magnetic, centrosymmetric crystal. Here each electronic state with energy E has a momentum \mathbf{k} and spin \uparrow or \downarrow . Since we have time-reversal symmetry, Kramer's degeneracy holds. If we flip the arrow of time, all angular momenta (which includes the electron spin) are reversed along with the linear direction of motion. This can be expressed as $E(\mathbf{k}, \uparrow) = E(-\mathbf{k}, \downarrow)$. In our crystal, we also have inversion symmetry for every state, such that: $E(\mathbf{k}, \uparrow) = E(-\mathbf{k}, \uparrow)$. This leads to a fourfold degeneracy for each momentum state $|\mathbf{k}|$.

Lifting inversion symmetry while preserving time reversal symmetry leads to a particular condition, which allows the spin splitting of states of opposite momentum. The magnitude of the splitting is determined by spin-orbit coupling [7]. Looking at the 2H-structure from above, we can see that inversion symmetry is broken in the real-space directions that connect nearest Mo atoms, see the red line in Fig. 2.1a, which translate to the ΓK direction in the Brillouin zone, which is depicted in Fig. 2.1b. Along the ΓM direction, inversion symmetry is preserved (green line in Fig. 2.1a); the same holds for spin components which lie in the plane. We thus end up with spin-splitting at the Q and K points of the MoS₂ band structure, which due to orbital effects is most pronounced at the

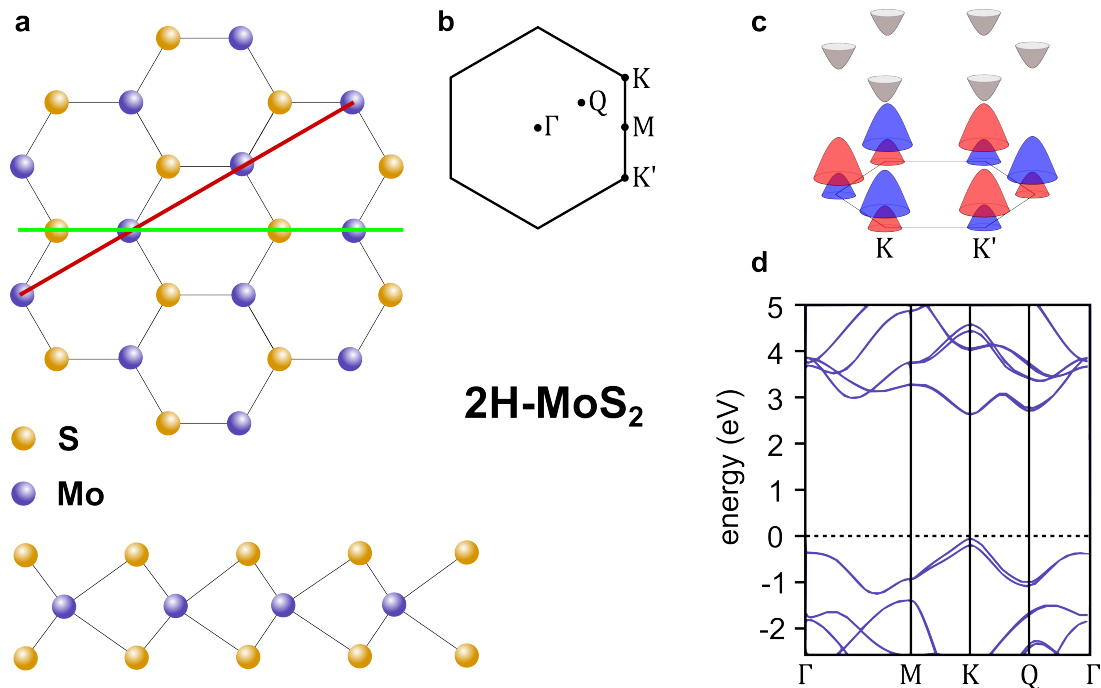


Figure 2.1: Atomic and electronic structure of single-layer 2H-MoS₂. **a** Top and side view of the atomic structure of the trigonal prismatic (2H) phase of MoS₂. The green line lies along a direction of inversion symmetry (ΓM), while the red line demarcates a direction where this symmetry is lifted (ΓK). **b** Hexagonal 2D Brillouin zone, with the high symmetry locations indicated. **c** Schematic representation of the band edges of single-layer MoS₂, showing the spin splitting of the bands at the K and K' points. Red and blue colours indicate up and down spin polarization. **d** Complete band structure of single-layer 2H-MoS₂. Panel c is adapted from Ref. [5]. Panel d is adapted from Ref. [118].

top of the valence band, see Fig. 2.1c,d. These band extrema are called valleys and the lifting of the spin-degeneracy and the coupling of the spin and valley degrees of freedom give rise to valley physics, like photo-induced charge Hall, spin Hall and valley Hall effects [7].

Indirect-direct band gap transition

MoS₂ is an indirect band gap semiconductor right up to the point where the penultimate layer is removed. It then undergoes an indirect-to-direct band gap transition [6, 33, 115, 116]. The transition can be traced back to the different orbitals that comprise the states at different points in the band structure. While the conduction band states at the K point are predominantly composed of strongly localized d orbitals at Mo sites, the states near Γ and Q originate from a combination of Mo d orbitals and antibonding p_z orbitals on S atoms. The former are rather insensitive to the number of layers because of their strong localization, whereas the latter two have strong interlayer coupling and energies that depend heavily on layer thickness [6]. As a result, the MoS₂ band gap shrinks with increasing layer number, as the bonding interactions at the Γ and Q points lead to the formation of new states within the former band gap. The edges of the direct band gap of single-layer MoS₂ are located at the K -points, see Fig. 2.1d [120–122], while the indirect band gap of the multilayer goes

from the Γ -point in the valence band to the conduction band edge at the K or Q-point, depending on the exact number of layers and strain [6, 123, 124].

In single-layer TMDCs the weak 2D screening also leads to strong binding between electrons and holes, which form bound states called excitons. While the binding energy of excitons E_b in classical (3D) systems like GaAs quantum wells is in the meV range, this shoots up by one to two orders of magnitude in single-layer TMDCs [125–128]. Since the creation of a bound electron-hole pair is energetically more favourable than creating a free electron, the optical band gap of single-layer MoS₂ is considerably lower than the electronic band gap E_{gap} [6, 33], since photons will be absorbed as soon as they have the energy $E_{\text{gap}} - E_b$, with $E_b \sim 500$ meV [129].

Localization and superconductivity

While its innate form might be semiconducting, there are two ways to access metallic phases in MoS₂. One is to induce a phase transition to the metallic 1T-phase, which has a completely different band structure; the other involves doping 2H-MoS₂ until the Fermi level reaches the valence or conduction band, leaving the band structure of the 2H-phase intact.

While the 1T-phase of MoS₂ is not stable at room temperature [130], it can be induced under certain conditions, like electron beam irradiation [131], plasmonic hot electron transfer [132] and chemical doping [133], specifically when MoS₂ is doped via Li intercalation [134–136]. A comprehensive review of 1T-MoS₂ can be found in Ref. [137]. For the purposes of this thesis, we will confine ourselves to the properties of metallic 2H-MoS₂, since that is the phase obtained using our contactless gating method discussed in Chapter 6.

Most of the studies on metallic 2H-MoS₂ are performed in transport setups, where a combination of a backgate and vacuum annealing is used to *n*-dope MoS₂. Vacuum annealing of CVD-grown single-layer MoS₂ leads to significant *n*-doping of the sample, attributed to doping from S vacancies [138]. While the process is not completely elucidated yet, it can be argued that it removes O substitutions at the S vacancy sites that are formed during the CVD process, which otherwise passivate the defects [139]. Transport in single-layer MoS₂ has two clearly demarcated regimes. Above a critical charge density of $\approx 1 \times 10^{13} \text{ cm}^{-2}$ the conductivity of the layer increases with decreasing temperature - a clear sign of metallic behavior; while below that threshold an insulating state characterized by variable-range hopping is found [70, 138, 140]. The regimes are separated by a metal-insulator transition with a localization-driven quantum critical point [140, 141]. There is ample evidence of long-range Coulomb scattering in single-layer MoS₂, both in the metallic [142, 143] and insulating state [143, 144], which could lead to the observed localization effects.

Doping MoS₂ even further, to $\approx 1 \times 10^{14} \text{ cm}^{-2}$, results in the emergence of superconductivity, with a T_c of $1 - 2$ K [9, 145, 146]. Like the superconductivity found in bulk MoS₂ samples, it is unconventional; the spin-valley locking at the *K* and *Q* points of the BZ protects the superconducting state from in-plane magnetic fields [10, 147, 148]. Superconductivity in single-layer MoS₂ differs from its bulk counterpart in its lower transition temperature, which in the bulk lies around 10 K. The

difference is tentatively attributed to the relative positions of the Q and K conduction band minima. While metallic single-layer MoS_2 starts out with only a single band at the K -point crossing the Fermi level [149, 150], in bulk MoS_2 the band at the Q -point might cross E_F first or near-simultaneously with the K -band when the metal-insulator transition takes place [6, 115, 116, 145], with significant consequences for the electron phonon coupling - which couples between K and Q - that leads to the superconductivity [145].

2.3 Vanadium disulphide

Among the many uses of MoS_2 mentioned in the previous chapter was its potential as an efficient electrode material for rechargeable batteries [151]. However, at least so far as 2H-phase of MoS_2 is considered, its semiconducting nature intrinsically limits its electrochemical performance [152]. VS_2 is a member of the metallic TMDC family. It preferentially grows in the 1T-phase, where the bottom S atoms are staggered with respect to those in the top layer, see Fig. 2.2a,b. It has a strongly dispersing band crossing the Fermi surface between M and K, which become nearly flat in the Γ K direction, see Fig. 2.2c.

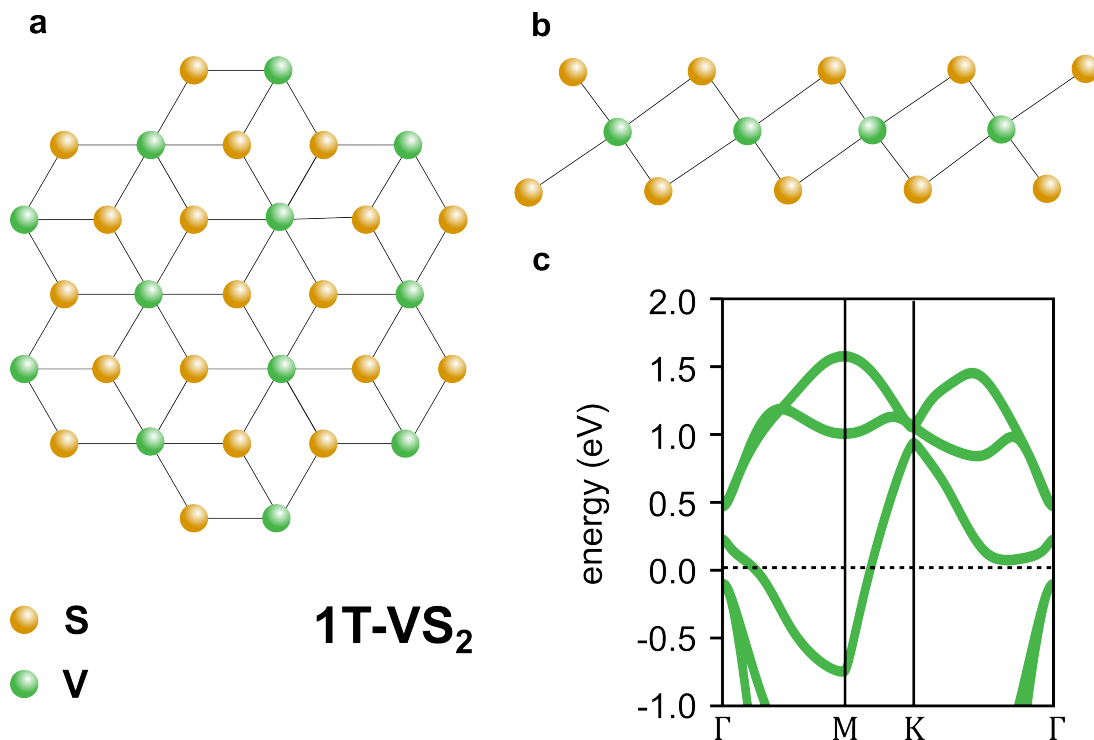


Figure 2.2: Atomic and electronic structure of single-layer 1T- VS_2 . **a,b** Top and side view of the atomic structure of the octahedral (1T) phase of VS_2 . **c** Band structure of single-layer 1T- VS_2 . Panel c is adapted from Ref. [153].

1T- VS_2 is a clear frontrunner among 2D materials as far as application for high-performance batteries is concerned [18]. It can easily be (de)intercalated with metal ions due to its large interlayer

spacing and consequentially weak interlayer interactions; the V atoms can continuously adjust their valence state; and it has high surface activity. Especially the first two characteristics give it one of the highest theoretical capacities (it can store many metal ions) combined with fast reaction kinetics (diffusion through the material is easy) [154,155]. Apart from its promise as a supercapacitor [156] - which can store up to two orders of magnitude more energy per unit volume or mass than electrolytic capacitors, moisture sensor [157], cathode material for Li-ion batteries [158] and a host of other types of batteries [152], 1T-VS₂ can be applied in catalysis setups [159,160].

A promising candidate for strongly correlated physics

From a more fundamental point of view, single-layer VS₂ is of interest because of its potential for strongly correlated physics, due to the localized nature of its d electrons [11]. This has led to a flurry of theoretical activity, mainly focused on the predicted ferromagnetic ground state of single-layer VS₂ [13,161,162].

Because VS₂ is such a strongly correlated material, with most of its properties like its phonon dispersion, magnetic moment and stability dependent on the effective Hubbard parameter U_{eff} [162], methods like DFT find many possible ground states for the material, all separated by small energy barriers. Generally, it is found that in the 1T-phase is more stable in the bulk, while the 2H-phase is stable in the single-layer limit, so that a layer-dependent coordination-phase transition should take place. In their single-layer form, both 1T- and 2H-VS₂ are predicted to be ferromagnetic [11,161,162]. While most studies find larger magnetic moments in the 2H phase, a recent study using both DFT+ U and hybrid DFT calculations using the Heyd-Scuseria-Ernzerhof functional found equal magnetic moments in both phases [163]. Nevertheless, because the putative larger moments and the stability in *ab-initio* calculations, the 2H-phase has gotten considerably more attention from theorists than the 1T-phase.

Before we discuss the experimental realizations of VS₂, another prediction bears mentioning. A full account of the electronic correlations in single-layer VS₂ results in the emergence of possible CDW ground states. These could coexist with different magnetic and non-magnetic states, all strongly dependent on the value of U_{eff} [11]. CDWs and (non-)magnetic states were found for both 2H- and 1T-VS₂. For the 1T-phase, the most likely CDW would have a periodicity of $q = \frac{2}{3}\Gamma\text{K}$.

A challenging synthesis

Compared to other TMDCs, VS₂ is more laborious to grow. The property that makes it a promising battery electrode - its weak interlayer interaction - also causes it to have no thermodynamically stable bulk polymorph. While the 1T-phase is indeed *more* stable than the 2H-phase in the bulk, it is not the most stable configuration. Instead, it prefers to grow in S-deficient structures with V atoms self-intercalated between the S layers [20,164,165]. It also desulpherizes already at temperatures below 600 K [166].

The difficulties arising from the synthesis translate directly to an inability to unambiguously determine the electronic ground state of bulk 1T-VS₂. When prepared using deintercalation of Li from LiVS₂, a CDW phase was found below 305 K in magnetic and NMR studies [166, 167]. From transmission electron microscopy, the periodicity of this CDW has been reported to be either $\sqrt{3} \times \sqrt{3}$ [168] or $3\sqrt{3} \times 3\sqrt{3}$ [169]. Other methods of preparing bulk VS₂, like high pressure synthesis [165, 170] and chemical vapor transport [171], find no CDW or a 4×4 coexisting with a $\sqrt{6} \times \sqrt{6}$ CDW, respectively. There is some agreement however, that the main phonon instability responsible for the CDW should be $q = \frac{2}{3}\Gamma K$ [11, 169–171].

As for monolayer 1T-VS₂, it was first synthesized on Au(111) using MBE [12]. Though monolayer 1T-VS₂, like the bulk, was predicted to have a CDW with $q = \frac{2}{3}\Gamma K$ [11], this was not observed, likely due to the strong substrate interaction with gold, which also suppresses the CDW in other TMDCs [67, 68]. In Chapter 4 of this thesis, the first MBE synthesis of single-layer 1T-VS₂ on the weakly-interacting substrate Gr/Ir(111) is demonstrated, which exhibits the predicted CDW [1]. This result was reproduced on bilayer Gr using a combination of MBE growth of VTe₂ and a topotactic reaction to replace Te with S atoms [172].

Single- and few-layer 2H-VS₂ has only very recently been grown on a sapphire substrate using CVD. The samples showed the predicted semiconducting behaviour in transport and exhibited ferromagnetism above room temperature in magneto-optic Kerr effect measurements [173].

CHAPTER 3

Electronic and Magnetic Interactions

This Chapter aims to provide a succinct overview of the electronic and magnetic interactions relevant to this thesis. First, electron-phonon coupling will be briefly introduced, followed by an in-depth treatment of polarons and charge density waves, which arise out of strong electron-phonon interactions. The second topic of this Chapter concerns screening effects, which are discussed in the context of band gap renormalization and the Kondo effect. A thorough review of electron-phonon coupling from a theoretical standpoint can be found in Ref. [174], while Ref. [175] contains a recent overview of polaron studies, which takes in both experimental and theoretical works. An older, but still particularly relevant review of charge density waves is given in Ref. [176]. For the Kondo effect, the review of Ref [177] provides an excellent discussion of the underlying physics in the case of magnetic adatoms.

3.1 Electron-phonon coupling

Once an electron is taken out of vacuum and put into any real material, it seemingly ceases to be an electron. If you measure it, you will find that it can no longer be regarded as a particle with the exact electron mass m_e , or the precise electronic g -factor. Under the right conditions, not even its charge will seem to correspond to the electron charge e , but appear fractionalized, or doubled.

This is possible, not because the nature of fundamental particles changes when moving through a material, but because an assembly of many elementary particles can have emergent properties which can differ greatly from those of the particles from which it is composed. These emergent properties will have their own quantized carriers, which, not being fundamental, are called quasiparticles. In this way, the electron in a crystal is not properly an electron; instead, it is a quasiparticle composed of an electron interacting with other electrons and the atomic nuclei of the crystal.

The coupling between electrons and phonons, which are quantized lattice vibrations, is one of best studied instances of many-particle physics. Electron-phonon coupling (EPC) lies at the heart of many macroscopic effects, like the temperature dependence of the electrical conductivity in metals and the carrier mobility in semiconductors [174]. It is responsible for BCS-type superconductivity and contributes to optical absorption in indirect band gap semiconductors. In this thesis, I am interested in cases were this interaction becomes sufficiently strong for more exotic phenomena to occur. We will encounter polarons, quasiparticles constituted of slow electrons dragging a cloud of lattice deformation with them as they plod through the crystal. Though they are apparently

Chapter 3 Electronic and Magnetic Interactions

ubiquitous - their presence is inferred in many different materials - they are rarely observed with local techniques like the scanning tunneling microscope. The second EPC interaction driven effect we will study is the charge density wave, where the lattice distorts to accommodate a particular charge ordering of the electrons. Charge density waves have been measured extensively with scanning tunneling microscopy. However, the focus in STM literature has been on the effect of the CDW at the states near the Fermi level. In fact, the CDW can transform the entire band structure, with energy gains distributed throughout the occupied states, see also Sections 9.1 and 9.2 of the Discussion.

For our discussion we will start with the Holstein (or Frölich) Hamiltonian, which is the simplest model for electrons interacting with a single, optical phonon mode:

$$H_{\text{Hol}} = \sum_{\mathbf{k}} \epsilon_{\mathbf{k}} a_{\mathbf{k}}^{\dagger} a_{\mathbf{k}} + \sum_{\mathbf{q}} \hbar \omega_{\mathbf{q}} b_{\mathbf{q}}^{\dagger} b_{\mathbf{q}} + \frac{1}{\sqrt{N}} \sum_{\mathbf{k}, \mathbf{q}} g_{\mathbf{q}} a_{\mathbf{k}+\mathbf{q}}^{\dagger} a_{\mathbf{k}} (b_{-\mathbf{q}}^{\dagger} + b_{\mathbf{q}}), \quad (3.1)$$

with $\epsilon_{\mathbf{k}}$ the energy state of the electron in state \mathbf{k} , $a_{\mathbf{k}}^{\dagger}$ and $a_{\mathbf{k}}$ the creation and annihilation operators for \mathbf{k} , $\omega_{\mathbf{q}}$ the frequency of the phonon mode in state \mathbf{q} , $b_{\mathbf{q}}^{\dagger}$ and $b_{\mathbf{q}}$ the creation and annihilation operators for phonon \mathbf{q} , N the number of lattice sites per unit length and $g_{\mathbf{q}}$ the electron-phonon coupling constant. The Hamiltonian thus consists of (1) a term describing electrons in a parabolic band with a dispersion $\epsilon_{\mathbf{k}} = \frac{\hbar^2 k^2}{2m^*}$, where m^* is the effective mass; (2) a term for a single phonon mode with energy $\hbar \omega_{\mathbf{q}}$, classically taken to be an optical phonon in the Einstein model (so that $\omega_{\mathbf{q}} = \Omega$ is a constant for all \mathbf{q}); and (3) a term for the coupling between electrons and phonons, governed by a coupling constant g , which can in principle depend on both \mathbf{k} and \mathbf{q} , but is often taken to be constant. The simplified model nicely captures the intuitive picture of a many-body interaction: if we want to calculate the energy of electronic states, they will inevitably have a contribution stemming from the lattice via the interaction term. Vice versa will the energy of the phonon mode Ω depend, in part, on its interaction with electronic states.

Three fundamental phenomena of condensed matter physics can be described using this model. Polarons are quasiparticles formed due to the mass enhancement of electrons dressed by the lattice vibrations. Superconductivity arises from the attractive coupling between electrons mediated by phonons. And charge density waves emerge out of the softening of the phonon mode due to the interaction with the electrons. It goes outside the scope of this thesis to answer why in particular systems one interaction is selected over the others. Instead, we will explore under which conditions electrons and phonons work together to form either polarons or charge density waves.

Polarons

Let's first consider the effect of EPC on the electronic subsystem, for the case of a single electron with dispersion $\epsilon_{\mathbf{k}} = \frac{\hbar^2 k^2}{2m}$. Placing an electron anywhere in a lattice with strong EPC will, provided the electron moves slow enough, cause the surrounding ions to assume shifted equilibrium positions, an idea first described by Landau in 1933 [178], see Fig. 3.1a. These altered positions create a potential well for the carrier. If the electronic energy gain E_p provided by the deformation is higher than the

3.1 Electron-phonon coupling

strain placed on the deformed lattice E_{strain} (proportional to the characteristic phonon energy $\hbar\Omega$ of the interaction [176]), the electron will become self-trapped, gaining an energy E_b - the binding energy of the polaron, see Fig. 3.1b. It will only be able to move if the ions accommodate its movement, otherwise the energy barrier separating it from the next lattice site will be too high. Calculating the electron energy from Eq. 3.1 for $T = 0$ (no thermally excited phonons), we find [179–181]:

$$\tilde{\epsilon}(k) = \epsilon(k) - E_p - \frac{\hbar^2 k^2}{2m} \lambda + \dots \quad (3.2)$$

where $E_p = \frac{1}{N} \sum_{\mathbf{q}} \frac{g^2}{\hbar\Omega + E(q)} > 0$ and $\lambda = \frac{2g^2 n_0}{\hbar\Omega}$, the dimensionless electron-phonon coupling constant, with n_0 the density of electron states at the Fermi level. Discarding higher order terms and using $1 - \lambda \approx \frac{1}{1+\lambda}$, we obtain:

$$\tilde{\epsilon}(k) = -E_p - \frac{\hbar^2 k^2}{2m(1+\lambda)} = -E_p + \frac{\hbar^2 k^2}{2m^*}. \quad (3.3)$$

From this we see that the effect of EPC on the electrons is twofold. Not only does it lower the energy of the electron by a constant E_p , but it also enhances the effective mass $m \rightarrow m^* = m(1 + \lambda)$. In this simple model, the essence of a polaron is captured. Going back to the idea of Landau, the mass enhancement can be regarded as a consequence of the electron dragging the potential well formed by the ions, slowing its process through the lattice.

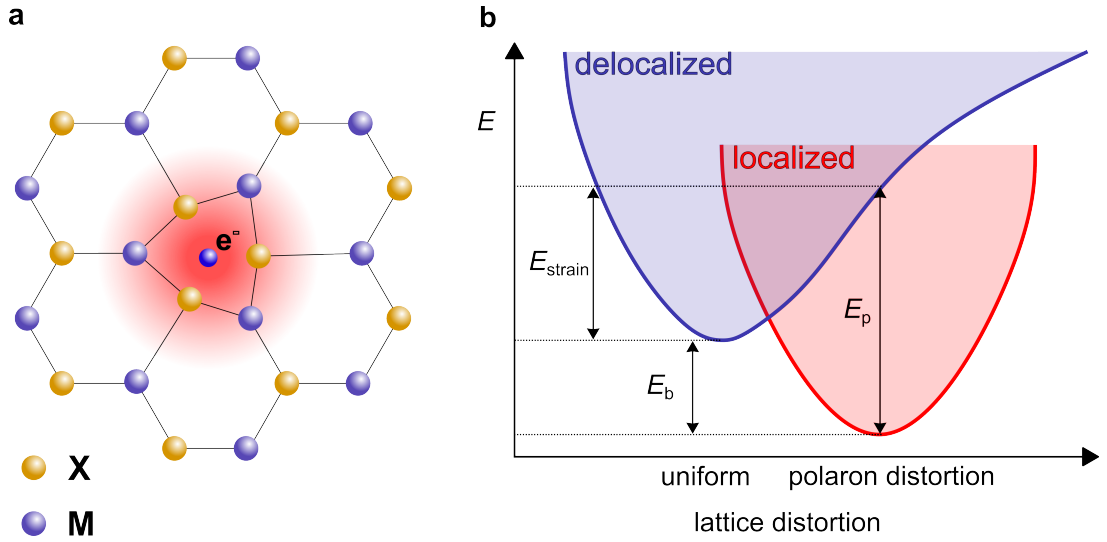


Figure 3.1: Basic properties of polarons. **a** Schematic illustration of the polarization (red) caused by the self-trapping of an electron (blue dot) at a lattice site and formation of a (small) polaron. The lattice is a standard 2H-phase MX_2 lattice. **b** Configuration coordinate diagram depicting the energy balance as a function of lattice distortion for a delocalized electron and for a localized polaron. E_{strain} is the structural energy, E_b the polaron binding energy and E_p is the electronic energy. Panel **a** adapted from Ref. [8]. Panel **b** adapted from Ref. [182].

We can now distinguish two regimes: a weak-coupling regime where $E_b < \hbar\Omega$ and a strong

Chapter 3 Electronic and Magnetic Interactions

coupling regime for $E_b > \hbar\Omega$. Self-trapping only occurs in the strong-coupling regime, because the carrier sees the potential well as essentially static (delocalized lattice excitations are rare, since the localized polaronic state is energetically preferred) [183]. Once we have reached the self-trapped regime, one can further distinguish between large and small polarons. ‘Large’ and ‘small’ are defined in terms of the size of the atomic lattice constant a . In the case that the polaron radius is on the order of the lattice constant, the binding energy of the polaron will be large (≈ 1 eV below E_F) and its motion will be incoherent. The latter statement means that it can only move via phonon-assisted hops - a process that becomes more likely with increasing temperature. If on the other hand the polaron radius greatly exceeds a , the binding energy is small (≈ 10 meV below E_F) and its movement is coherent - it essentially behaves like a regular carrier, except for its enhanced mass. As the temperature increases its mobility will therefore be reduced, as the probability of scattering from phonons becomes more likely [175]. The two regimes are used mainly when we think about polarons in a doped insulator, where the bound states will reside within the band gap of the material.

Another important distinction is made between systems where $\hbar\Omega \approx E_F$ and those where $\hbar\Omega \ll E_F$, with E_F the energy of the electrons at the Fermi level, relative to the bottom of the parabolic band [174]. This distinction is relevant in the case of doped semiconducting systems, where we consider how EPC changes the electron dispersion. When $\hbar\Omega \ll E_F$, the EPC will typically lead to kinks in the band structure, located at $E_F - \hbar\Omega$ [184]. At the kink, the electron velocity changes abruptly, as the electrons with energies below and above $E_F - \hbar\Omega$ have drastically different experiences while moving through the lattice. The former do not have enough energy to emit a phonon; as a consequence, they are surrounded by a cloud of virtual phonons which augment their mass, taking away kinetic energy from the carrier. The latter can emit real phonons, which makes the virtual processes less likely. Correspondingly, they have a lower mass and shorter lifetime than their low-energy counterparts [185]. Now, for systems with $\hbar\Omega \approx E_F$, a different scenario occurs. In these systems strong EPC leads to a parabolic band with enhanced mass and n polaronic satellites of the band shifted down by $n\hbar\Omega$ [186–188]. This condition is fulfilled for degenerately doped semiconductors close to the conduction band minimum.

In closing the discussion on polarons, it needs to be remarked that in many cases polarons are described not by the Holstein Hamiltonian, but with the Landau-Pekar model, which has a Schrödinger-type equation [189]:

$$E_0\phi(r) = \left(-\frac{\nabla^2}{2m} - e^2 \left(\frac{1}{\varepsilon_\infty} - \frac{1}{\varepsilon_0} \right) \int dr' \frac{|\phi(r')|^2}{|r' - r|} \right) \phi(r), \quad (3.4)$$

where ε_0 and ε_∞ are the static (electronic and ionic) and high-frequency (electronic) dielectric constants and E_0 the polaron ground-state energy. In this model the dimensionless electron-phonon interaction is represented by:

$$\alpha = e^2 \left(\frac{1}{\varepsilon_\infty} - \frac{1}{\varepsilon_0} \right) \sqrt{\frac{m}{2\Omega}}. \quad (3.5)$$

This model has drawbacks, like the fact that bound polarons are only obtained for $\varepsilon_0 > \varepsilon_\infty$ (which holds only for polar crystals, while polarons also exist in nonpolar crystals). More fundamentally, it is meant to describe large polarons, but it is formally only justified in case of strong EPC such that the polaron radius is small. Nevertheless, it is the basis for the most successful modern DFT approaches to predicting polaron formation in materials, even if it is limited to zone-center (low momentum), polar phonons [175, 190–192].

Charge density waves

Due to EPC, phonons are able to slow down the electrons by trapping them in wells of positive ionic charges. But how will this interaction affect the phonons themselves? To provide a rather extreme answer to that question, we will consider a half-filled 1D chain of metallic atoms with lattice spacing a at $T = 0$, see Fig. 3.2a. We let it interact with an acoustic phonon of momentum \mathbf{q} . In this scenario, we have two processes. Either an electron absorbs a phonon, exciting the electron to a state above the Fermi level, after which the phonon is re-emitted without change of its frequency; or we could have a second phonon being emitted and the original phonon absorbed afterwards. Going back to the Hamiltonian of Eq. 3.1, we get an expression for the phonon energy [176, 193]:

$$\omega_{\mathbf{q}}^2 = \Omega^2 \left(1 - 4 \frac{|g|^2}{\hbar\omega_{\mathbf{q}}} \sum_{\mathbf{k}} \frac{1}{L} \frac{f_{\mathbf{k}+\mathbf{q}} - f_{\mathbf{k}}}{E_{\mathbf{k}} - E_{\mathbf{k}+\mathbf{q}}} \right), \quad (3.6)$$

with L the length of the chain. We can recognize the static Lindhart function for the electronic susceptibility $\chi_0(\mathbf{q}) = \frac{1}{L} \frac{f_{\mathbf{k}+\mathbf{q}} - f_{\mathbf{k}}}{E_{\mathbf{k}} - E_{\mathbf{k}+\mathbf{q}}}$ in the expression. This means that the phonon energy at momentum \mathbf{q} is directly dependent on $\chi_0(\mathbf{q})$. For a 1D chain, $\chi_0(\mathbf{q})$ actually diverges for $\mathbf{q} = 2\mathbf{k}_F$. This follows from the consideration that if we have one electron in state $\mathbf{k} = \mathbf{k}_F$ and an empty state at $\mathbf{k} = -\mathbf{k}_F$, they are connected by a phonon of momentum $\mathbf{q} = 2\mathbf{k}_F$, see Fig. 3.2a. In that case, the numerator in the Lindhart function becomes 1, while the denominator $\rightarrow 0$. This singularity is called a Kohn anomaly. Due to the divergence, the only requirement for $\omega_{\mathbf{q}} = 0$ is that $g > 0$. A phonon mode with zero energy cost leads to a static deformation of the lattice, which will per necessity occur in 1D for finite EPC. The periodic lattice deformation will lead to a reduction of the Brillouin zone, accompanied by the opening of a gap 2Δ in the electronic density of states, see Fig. 3.2b. The gap lowers the energy of occupied electron states, which is how the system gains the energy needed to overcome the lattice deformation cost (strain). The gap separates two electronic states of equal \mathbf{k} , which are called charge density waves, since they consist of periodic charge accumulations with a periodicity of $2\mathbf{k}_F$.

So far we have considered an ideal situation. But when the temperature and dimensionality of the material are increased, the divergence of χ_0 is rapidly suppressed [195]. The effect of the dimensionality in particular is relevant, since the 1D argument holds only because all states at the Fermi level are coupled by the very same phonon, with momentum q . This phenomenon is called Fermi surface nesting. In a 2D or 3D Fermi surface, this condition is generally not fulfilled; at best

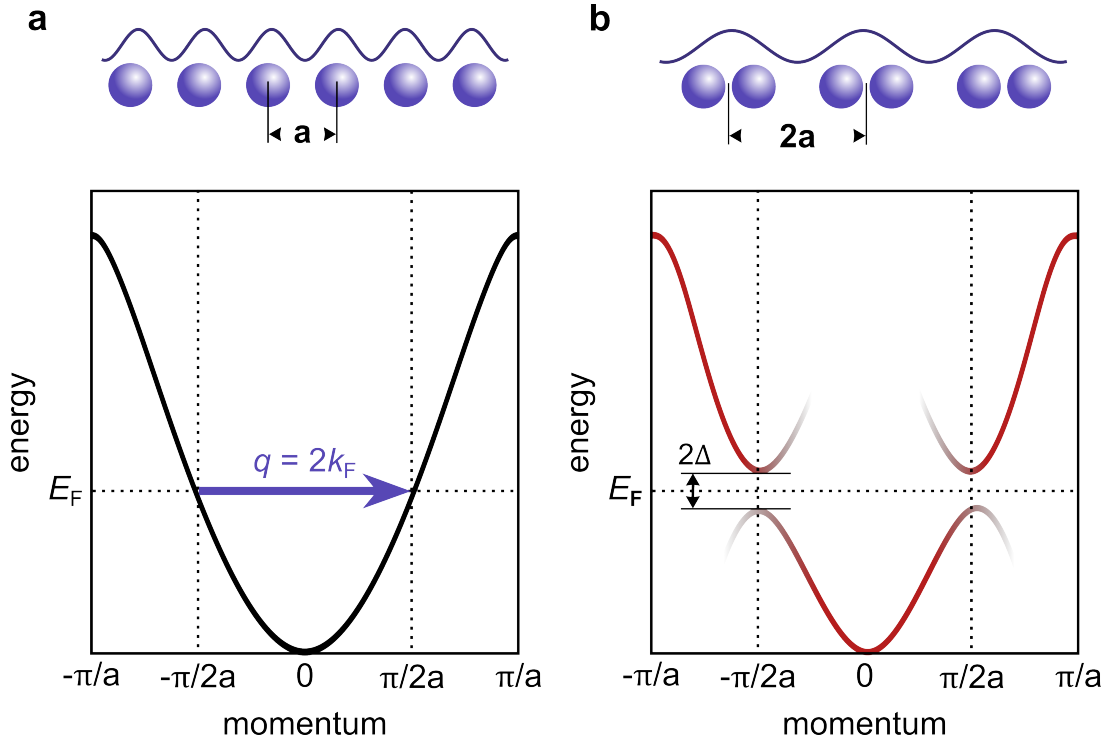


Figure 3.2: 1D charge density wave. a,b Schematic illustration of CDW formation in 1D. A 1D chain with atomic spacing a spontaneously distorts with a periodicity $q = 2k_F$. As a result, the real space lattice and charge density gain a $2a$ periodic modulation in real space. In the band structure, the increased lattice spacing leads to a halving of the BZ; as a consequence, a gap 2Δ opens up at the Fermi level, resulting in net energy gain. Figure adapted from Ref. [194].

parts of the Fermi surface will be nested with a single q vector, which means that the energy gain can stem only from a subset of the electrons. More general, the condition for the formation of a periodic lattice deformation can therefore be written as:

$$4 \frac{|g_{\mathbf{k},\mathbf{q}}|^2}{\hbar\omega_{\mathbf{q}}} - 2U_{\mathbf{q}} + V_{\mathbf{q}} > \frac{1}{\chi_0(\mathbf{q})}, \quad (3.7)$$

where the Coulomb energy $U_{\mathbf{q}}$ and the exchange energy $V_{\mathbf{q}}$ are taken into account. Note that the exchange energy is actually attractive due to the electron phonon coupling, favoring the distortion because it will lead to local increases in the electron charge density, while the Coulomb energy works against the distortion because it involves local decreases of the ionic distances [176]. Since χ_0 will not diverge in real systems, it is the consideration of the above elements that determines whether a charge density wave will form. Crucially, the EPC term $g_{\mathbf{k},\mathbf{q}}$ is not constant in real materials and depends on both \mathbf{q} and \mathbf{k} . Though this cannot be analytically obtained, a DFT-based approach allows one to calculate for nested parts of the Fermi surface whether $g_{\mathbf{k},\mathbf{q}}$ is significant enough to have an effect on the phonons. DFT can also consider higher-order processes like phonon-phonon coupling [1] and allows access the total energy gain of the system, which is not limited to the gap

opening at the Fermi level, but distributed throughout the occupied states [195]. For a more detailed discussion on CDW formation in real systems, see Section 9.1.

3.2 Screening

The screening of electric fields by mobile carriers is a prime example of a renormalized interaction. If we would naively apply the Coulomb potential of any point charge q , $V(r) = \frac{q}{4\pi\epsilon r}$, with ϵ the permittivity, to a fluid of charge carriers, we end up with one of the many infinities that plague physics. Because even though the Coulomb force $\mathbf{F} = \frac{q_1 q_2}{4\pi\epsilon|r|^2} \hat{\mathbf{r}}$ between two particles in the fluid diminishes with distance as $\frac{1}{r^2}$, the average number of particles at each distance r is proportional to r^2 . As a result, any charge fluctuation would transmit its effect at effectively infinite distance throughout the fluid.

Luckily, nature abhors infinities as much as vacuums. In the fluid, the charge of a single carrier is screened by the surrounding carriers. We can imagine this as the negative charges in the fluid moving away from a negative point charge we put in, effectively surrounding it by a region of relative positive charge. On a large length scale, these two charges (the negative point charge and the relative positive charge around it) will cancel out. In this way, the Coulomb potential is renormalized; one replaces $\frac{1}{r}$ with $\frac{1}{r} e^{-k_0 r}$, where k_0 is the Thomas–Fermi wave vector. This has the result of making the Coulomb potential short-ranged: carriers only interact with their immediate neighbours in the fluid.

A second type of screening occurs through dielectric materials. In that case, it is not due to the rearrangement of freely moving carriers, but via the polarizability of the material. Any electric field will generate dipoles in a dielectric, which will set up an internal electric field reducing the total field in the material. The latter effect is especially relevant for 2D semiconductors, where the properties will largely depend on the dielectric properties of the substrate or possible encapsulating layers.

Band gap renormalization

In 2D the field lines of all charges extend into the vacuum. As a result, all screening, both electronic and dielectric, will have to occur within the layer or the substrate. Due to this considerable weakening of screening compared to 3D materials, the quasiparticle band gap in single-layer TMDCs is expected to increase [196]. It furthermore leads to the formation of strongly bound electron-hole pairs called excitons [126, 197]. These excitons come in many flavors: there are bright and spin-forbidden dark excitons [198] and composite excitons called trions [199, 200]. They can also couple to other quasiparticles like polarons, plasmons or polaritons [201–203] and have been investigated in heterostructures of TMDCs, where they can arise due to the moiré formed between the TMDC layers [204–206]. The weak screening also makes it easy to engineer the band gap, by changing the dielectric environment [207], essentially swapping the vacuum for a dielectric or metal.

In single-layer MoS₂, all these effects are encountered, but for the purposes of this thesis, we focus

on control of the electronic band gap E_{gap} of MoS_2 via the substrate. The electronic band gap of a material can be characterized as the sum of the energies needed to separately tunnel an electron and a hole into it [197]. Since the two will be mutually attracted to one another by the Coulomb force, they need to be brought far enough away from each other to overcome this attraction. The distance at which Coulomb forces are active is set by the screening. The stronger the screening, the smaller the range at which the Coulomb force is effective and the less energy is required to separate the electron and hole. In this intuitive picture, the concept of band gap renormalization is captured.

The consequences of substrate screening on the band gap of MoS_2 are made clear when considering the varying band gap size of MoS_2 on different weakly-interacting substrates (so that strain or hybridization should not strongly affect the properties of MoS_2): 2.01 eV on Gr/SiC [208], 2.20 eV on Gr/Au [209] and 1.90–2.40 eV on graphite [95, 210, 211]. While our substrate of Gr/Ir(111) is screening ostensibly less than many others, with $E_{\text{gap}} = 2.53 \pm 0.08$ eV [82], it is still quite far from the predicted freestanding value of $E_{\text{gap}} \approx 2.8$ eV [125, 212]. Ways to control the band gap via the substrate, by changing its screening properties, for instance via doping, should simultaneously result in control over the exciton binding energies, which are also intimately linked to screening [197].

Kondo screening

Electrons are however not only able to screen charge; they can also screen the spin of a localized state. The microscopic process via which this occurs is however quite different from the electronic mechanism sketched above.

The discovery of spin screening started with the observation that impure gold wires had a small up-tick in their resistivity below a critical temperature, around 4 K [213]. This sounds innocent enough, but it broke with the fundamental understanding that the lower the temperature, the less scattering should take place, since any phonons that can scatter electrons are successively frozen out. As a result, metals should conduct ever better the lower the temperature, until a plateau of conductivity is reached, determined by the amount of defects, which scatter independent of the temperature.

It was quickly figured out that this effect was related to the presence of *magnetic* defects in the metal, but it would take thirty years before someone was able to understand and explain what was happening. In 1964 Jun Kondo showed that at low enough temperatures, a new type of scattering became possible [214]. In this process an electron in the magnetic impurity temporarily exchanges its spin state with that of an electron in the metal. Like the virtual boson exchanges that increase the mass of an electron under the influence of EPC, see section 3.1, this process is classically forbidden. The electron of the impurity is often far away from the Fermi level (several eV). However, Heisenberg's uncertainly principle allows tunnelling processes between the impurity and the metal to take place as long as, within the time scale set by the uncertainty principle, no energy is lost. In other words, as long as an impurity electron tunnels to the metal while a conduction electron tunnels into the impurity, this is quantum mechanically perfectly in order. If the tunnelling involves a spin exchange process, this changes the energy spectrum of the system. A single exchange leads to a tiny

change, but if many of these exchange processes are taken together (many-body effect) a resonant state is formed at the Fermi level. This resonance can scatter conduction electrons near the Fermi level, leading to the increase in resistivity [215]. For the effect to be significant compared to other scattering processes, it is essential that most conduction electrons have energies near the Fermi level, otherwise they (1) will not form the resonance and (2) will not scatter off it.

While Kondo's theory was able to make sense of the increase of resistivity, it also predicted, quite unphysically, that the resistance would become infinite as $T \rightarrow 0$. From the framework of Anderson, discussed below, it could be shown that Kondo's model was valid above a certain critical temperature, later called the Kondo temperature T_K . Below T_K , the magnetic moment of the impurity is effectively screened due to the interaction with the conduction electrons, so further enhancement of the resonance is halted. Essentially, all properties of a single-impurity Kondo effect are collected in this single parameter T_K , from which its behavior at any temperature T can be predicted using the numerical renormalization group technique [216].

While the Kondo model explains the resistivity increase due to this interaction, the microscopic understanding of the Kondo effect is often phrased in term of the Anderson Hamiltonian for a single impurity coupled to an electron bath [217]:

$$H = \sum_{k,\sigma} \epsilon_k c_{k\sigma}^\dagger c_{k\sigma} + \sum_{\sigma} \epsilon d_{\sigma}^\dagger d_{\sigma} + U d_{\uparrow}^\dagger d_{\uparrow} d_{\downarrow}^\dagger d_{\downarrow} + \sum_{k,\sigma} V_k (d_{\sigma}^\dagger c_{k\sigma} + c_{k\sigma}^\dagger d_{\sigma}). \quad (3.8)$$

In the Hamiltonian, we have a term for the kinetic energy of the conduction electrons with energy ϵ_k , momentum k , spin σ and annihilation and creation operators $c_{k\sigma}^\dagger c_{k\sigma}$; this is followed by a term describing the impurity level with energy ϵ , which is split by Coulomb repulsion U ; and finally, a hybridization term coupling the two, with a coupling potential V_k .

Originally, Anderson's model was used to explain why it is at all possible to have a localized spin on the impurity. He showed that it is crucial that the Coulomb interaction is only weakly screened on the atomic length scale, which allows, in the case that $\epsilon_d \ll E_F \ll \epsilon_d + U$, to have a spin localized at the impurity [217]. With local charge fluctuations thus suppressed at low temperatures, only the abovementioned virtual spin-flip processes are possible.

Schrieffer and Wolff later derived the effective Kondo coupling ρJ between the conduction electrons and the impurity state [218]:

$$\rho J = \frac{\gamma_0}{2\pi} \left(\frac{1}{\epsilon + U} - \frac{1}{\epsilon} \right) = \frac{\gamma_0 U}{2\pi |\epsilon| |\epsilon + U|}, \quad (3.9)$$

with J an effective antiferromagnetic exchange coupling, ρ the density of states of the electron bath and γ_0 the broadening of the localized impurity state due to hybridization with the substrate [219]. Using the Schrieffer-Wolff expression, we draw in Fig. 3.3a the density of states of a magnetic impurity with U , ϵ and $\gamma = 2\gamma_0$ coupled to a metal. In Fig. 3.3b, the two possible spin-flip processes that lead to the formation of the resonance are depicted.

In most experiments, the parameters of the Anderson model are not directly accessible. Instead, a

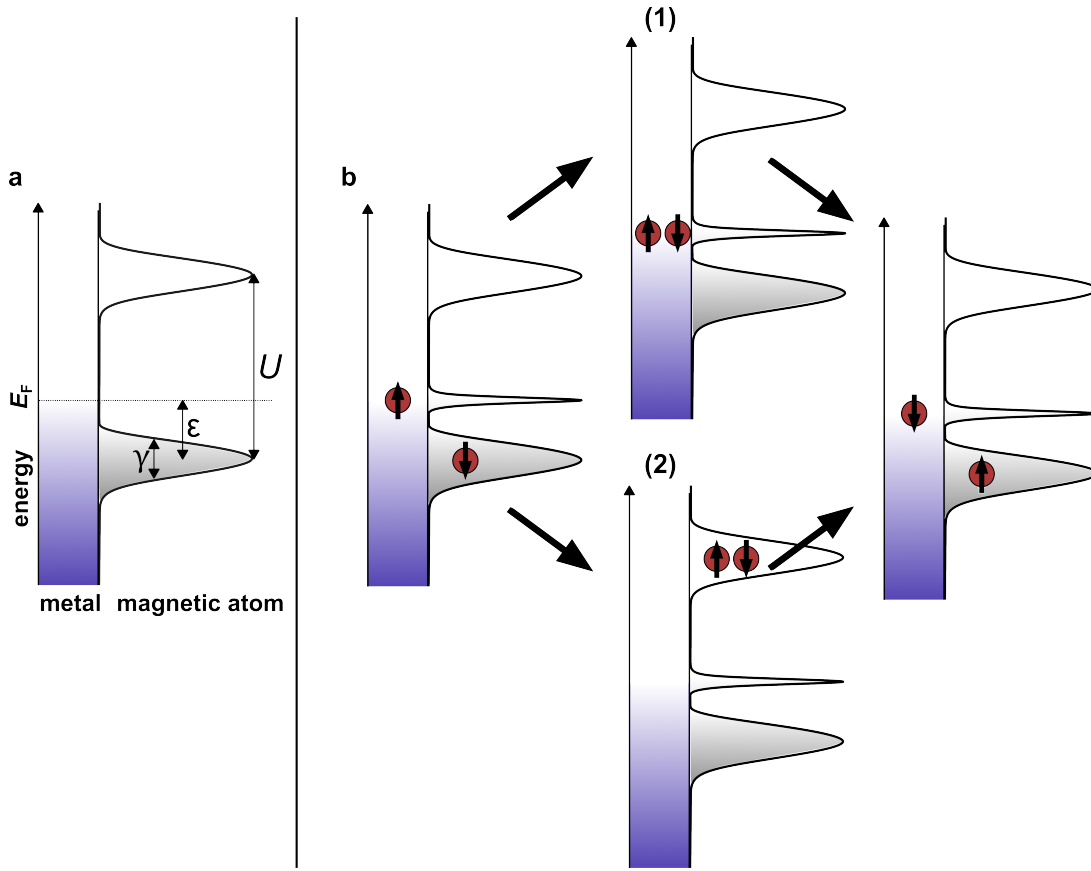


Figure 3.3: Kondo screening. **a** Schematic drawing of the density of states of magnetic adatom on top of a metallic substrate. U is the Coulomb energy, ϵ the distance from the filled state of the adatom to the Fermi level and γ the full width at half maximum of the impurity states. **b** The spin of the singly-occupied state of the adatom can be flipped by an electron from the substrate via process (1) or (2). During the process the adatom is briefly either empty (1) or doubly occupied (2). As a result of many of these processes, a Kondo resonance forms at the Fermi level. Figure adapted from Ref. [177].

fit to the resonance gives ρJ , from which the Kondo temperature T_K can be obtained via: [216,220]

$$k_B T_K = D_{\text{eff}} \sqrt{2\rho J} e^{-1/2\rho J}, \text{ for } \rho J \ll 1, \quad (3.10)$$

where $D_{\text{eff}} = w\sqrt{\pi}U/4$, the effective half-bandwidth for the Anderson model and w the universal Wilson number $w = e^{C+1/4}/\pi^{3/2} = 0.4128$, with $C = 0.577216$ being Euler's constant. As we will see later in Chapter 7, the Kondo temperature can also be obtained directly from the Anderson model parameters, given here for the general case that $\epsilon \neq U/2$:

$$k_B T_K = \gamma_0 \sqrt{U/4} \gamma_0 e^{-\pi|\epsilon||\epsilon+U|/U\gamma_0}. \quad (3.11)$$

PART II

Experimental Results

CHAPTER 4

Manuscript [1]: A full gap above the Fermi level: the charge density wave of monolayer VS_2









This chapter wholly consists of the above-named publication, published in Nature Communications on 25th November 2021, available online.

This publication was a collaborative effort from multiple groups, spanning almost five years of research, with the first growth studies of VS_2 performed in February 2017 by J. Hall. The experiments were proposed by T. Wehling and T. Michely. Sample growth and STM measurements were conducted at the TUMAI and TSTM systems in Cologne. The growth procedure of the samples at TUMAI was developed by J. Hall, with the growth parameters adapted for use in TSTM by C. van Efferen. Room temperature STM measurements were carried out by J. Hall, with assistance from T. Wekking at TUMAI; low-temperature measurements were performed by C. van Efferen with assistance from E. Plaar. The XMCD measurements were performed and analysed by F. Huttmann and S. Kraus, with support from N. Rothenbach, K. Ollefs, L. M. Arruda, N. Brookes, K. Kummer and H. Wende. The ab-initio DFT calculations were conducted by J. Berges, A. Schobert and G. Schönhoff, with support from E. van Loon and T. Wehling. Analysis of STM data was performed by C. van Efferen and J. Hall; the STS data was analysed by C. van Efferen. The interpretation of the results was discussed in depth by C. van Efferen, J. Berges, E. van Loon, T. Wehling and T. Michely.

C. van Efferen and J. Berges wrote the manuscript based on a draft by J. Hall and finalised it in close collaboration with T. Wehling and T. Michely. Some of the results shown in this Chapter can be found in the doctoral thesis of J. Hall [221] and the Bachelor's thesis of E. Plaar.

The first three authors have similar contributions to this publication.

A full gap above the Fermi level: the charge density wave of monolayer VS_2

Camiel van Efferen ^{1✉}, Jan Berges ², Joshua Hall¹, Erik van Loon ², Stefan Kraus¹, Arne Schobert², Tobias Wekking¹, Felix Huttmann¹, Eline Plaar¹, Nico Rothenbach³, Katharina Ollefs ³, Lucas Machado Arruda ⁴, Nick Brookes⁵, Gunnar Schönhoff², Kurt Kummer ⁵, Heiko Wende ³, Tim Wehling ^{2,6} & Thomas Michely¹

In the standard model of charge density wave (CDW) transitions, the displacement along a single phonon mode lowers the total electronic energy by creating a gap at the Fermi level, making the CDW a metal-insulator transition. Here, using scanning tunneling microscopy and spectroscopy and ab initio calculations, we show that VS_2 realizes a CDW which stands out of this standard model. There is a full CDW gap residing in the unoccupied states of monolayer VS_2 . At the Fermi level, the CDW induces a topological metal-metal (Lifshitz) transition. Non-linear coupling of transverse and longitudinal phonons is essential for the formation of the CDW and the full gap above the Fermi level. Additionally, x-ray magnetic circular dichroism reveals the absence of net magnetization in this phase, pointing to coexisting charge and spin density waves in the ground state.

¹II. Physikalisches Institut, Universität zu Köln, Zùlpicher Straße 77, 50937 Köln, Germany. ²Institut für Theoretische Physik, Bremen Center for Computational Materials Science, and MAPEX Center for Materials and Processes, Universität Bremen, Otto-Hahn-Allee 1, 28359 Bremen, Germany. ³Fakultät für Physik und Center für Nanointegration Duisburg-Essen (CENIDE), Universität Duisburg-Essen, Carl-Benz-Straße, 47057 Duisburg, Germany. ⁴Institut für Experimentalphysik, Freie Universität Berlin, Arnimallee 14, 14195 Berlin, Germany. ⁵European Synchrotron Research Facility (ESRF), Avenue des Martyrs 71, CS 40220, 38043 Grenoble Cedex 9, France. ⁶Institute of Theoretical Physics, Universität Hamburg, Notkestraße 9-11, 22607 Hamburg, Germany. ✉email: efferen@ph2.uni-koeln.de

The many-body ground states of two-dimensional (2D) materials, wherein the reduced dimensionality leads to the enhancement of correlation effects, have been extensively researched in recent years. Of particular interest are the coexistence or competition between charge density waves (CDWs), as found in many 2D transition metal dichalcogenides (TMDCs), with superconducting and magnetic phases^{1,2}. Since these phases can be strongly dependent on the substrate^{3,4} or the defect density^{5,6}, the intrinsic properties of 2D materials are difficult to determine experimentally. In addition, CDWs themselves are the subject of an ongoing controversy regarding the driving force behind the CDW transition and the exact structure of the electronic system in the CDW phase of 2D materials^{7,8}.

Peierls' explanation for the CDW in a one-dimensional chain of atoms states that periodic lattice distortions open an electronic gap at the nesting wavevector. This gap at the Fermi level lowers the energy of the occupied states and thus the total energy, while increasing the energy of the unoccupied states that do not contribute to the total energy. Thus, this gapping mechanism requires the gap to be at the Fermi level. However, in many (quasi-)2D cases, CDWs form in the complete or partial absence of Fermi-surface nesting, suggesting that the driving mechanism behind their formation lies beyond a simple electronic disturbance⁹, and it has been questioned whether the concept of nesting is essential for understanding CDW formation^{10–12}. Instead, a strong and wavevector-dependent electron–phonon coupling is often predicted to be the driving force behind the transition⁷. For these CDWs, spectral reconstructions are not limited to a small energy window around the Fermi energy, but can occur throughout the entire electronic structure, opening the door to novel spectral fingerprints of the CDW. A full gap could occur away from the Fermi energy. However, even for the well-studied strong-coupling TMDCs 2H-NbSe₂^{9,13,14} and 1T-TaS₂^{7,15–17}, no experimental verification of a clear CDW gap located away from the Fermi energy has been provided to date. Furthermore, at the Fermi energy, the undistorted phase and the CDW can have different Fermi-surface topologies, with the implication that the transition is a metal–metal Lifshitz transition¹⁸.

Metallic 1T-VS₂ is not only a promising electrode material in lithium-ion batteries^{19,20}, but also a prototypical *d*¹ system, expected to host strongly correlated physics²¹. It is stated to be a CDW material^{22,23} and a candidate for 2D magnetism^{24,25} with layer-dependent properties²⁶, making it a model system for investigating complex ground states. Although difficult to synthesize, bulk 1T-VS₂ has been well studied, with many authors finding a CDW transition at around 305 K when it was prepared via the de-intercalation of Li^{22,23,27–29}. However, recent powder samples prepared under high pressure show no CDW transition³⁰. Based on their finding of a phonon instability at $2/3 \bar{\Gamma}\bar{K}$ corresponding to the experimental CDW wavevector of Li de-intercalated bulk samples²³, Gauzzi et al. point out that bulk “VS₂ is at the verge of CDW transition”³⁰ but not a CDW material. Due to a similar difficulty in synthesis, the properties of monolayer 1T-VS₂ have proven equally elusive³¹. Theoretical calculations had predicted ferromagnetism and a CDW with a wavevector of $2/3 \bar{\Gamma}\bar{K}$ ^{21,25}. When it was first synthesized however, scanning tunneling microscope (STM) measurements did not reveal a CDW³¹, presumably due to strong hybridization with the Au(111) substrate, similar to the case of 2H-TaS₂ on Au(111)^{4,32,33}.

Here we report the growth of VS₂ monolayers on the inert substrate graphene (Gr) on Ir(111) via a two-step molecular beam epitaxy (MBE) synthesis developed for sulfur-based TMDCs³⁴. Using a combination of STM, scanning tunneling spectroscopy (STS), and ab initio density functional theory (DFT) calculations, we determine the spatial and electronic structure of monolayer

VS₂. We observe a $\mathbf{q} \approx 2/3 \bar{\Gamma}\bar{K}$ CDW as the electronic ground state at 7 K, which remains stable up to room temperature. A full gap in the density of states (DOS), residing completely in the unoccupied states, is measured via STS. From DFT and density functional perturbation theory (DFPT), we find that, although a transverse phonon mode initially becomes unstable in the harmonic approximation, the final CDW has a substantial admixture of longitudinal modes. The calculations are in excellent agreement with experiment, regarding both the electronic structure of the CDW phase and the spatial charge distribution observed on the VS₂ islands.

X-ray magnetic circular dichroism (XMCD) measurements at 7 K and 9 T robustly show vanishing total net magnetization. The coupling of the CDW to a spin density wave (SDW), energetically favored in DFT calculations, could explain this observation, providing interesting prospects for future research on the interplay of CDWs and magnetism.

Results

CDW in monolayer VS₂. The typical morphology of the MBE-grown monolayer VS₂ islands on Gr/Ir(111) is shown in the large-scale STM image in Fig. 1a. The islands were grown by room-temperature deposition of vanadium in a sulfur background pressure of $P_{\text{S}}^{\text{g}} = 1 \times 10^{-8}$ mbar and subsequently annealed at 600 K in the same sulfur pressure. Annealing to temperatures of 800 K and above leads to the formation of a variety of sulfur-depleted phases, which are not under concern here. Similar observations were made by Arnold et al.³¹, who established monolayer stoichiometric 1T-VS₂ on Au(111) by annealing in a sulfiding gas at 670–700 K, while sulfur-depleted monolayer phases form when annealed to the same or higher temperature in the absence of sulfiding species. We also note that depending on growth temperature and sulfur pressure bilayer samples without any monolayer islands evolve.

The monolayer islands are fully covered by a striped superstructure which is present regardless of island size or defect density and occurs in domains, typically separated by grain boundaries. In the topograph of Fig. 1b, taken at 7 K, the VS₂ lattice is resolved, exhibiting the hexagonal arrangement of top layer sulfur atoms as protrusions. We find that monolayer VS₂ has a lattice constant of $a_{\text{VS}_2} = (3.21 \pm 0.02)$ Å, in good agreement with the bulk lattice constant of 3.22 Å of 1T-VS₂^{27,35}. The similarity of the lattice constants indicates also the absence of epitaxial strain, consistent with the random orientation of the VS₂ with respect to the Gr.

The stripes of the superstructure have an average periodicity of $(2.28 \pm 0.02)a_{\text{VS}_2}$. Close analogues to this structure have previously been observed in stoichiometric monolayer VSe₂. There, a superstructure of identical symmetry is attributed to a CDW^{3,36–38} [compare Supplementary Fig. 1]. The superstructure is found to persist up to room temperature, as can be concluded from the STM topograph in Fig. 1c, taken at 300 K. At this temperature, the superstructure appears spontaneously only on larger islands, suggesting that the transition temperature between the superstructure and the undistorted phase is not far above room temperature. Indeed, on smaller islands the STM tip can be used to reversibly switch between the undistorted (1×1) structure and the superstructure, shown in Supplementary Fig. 2. This directly excludes the possibility that the superstructure is due to a sulfur-depleted phase. We conclude that the superstructure is most likely a CDW in a stoichiometric monolayer of 1T-VS₂.

For the DFT calculations below, the experimental wave pattern must be approximated by a commensurate structure. A close approximation with periodicity $2.25a_{\text{VS}_2}$ is overlaid on the atomic resolution image in Fig. 1b. It locally matches the

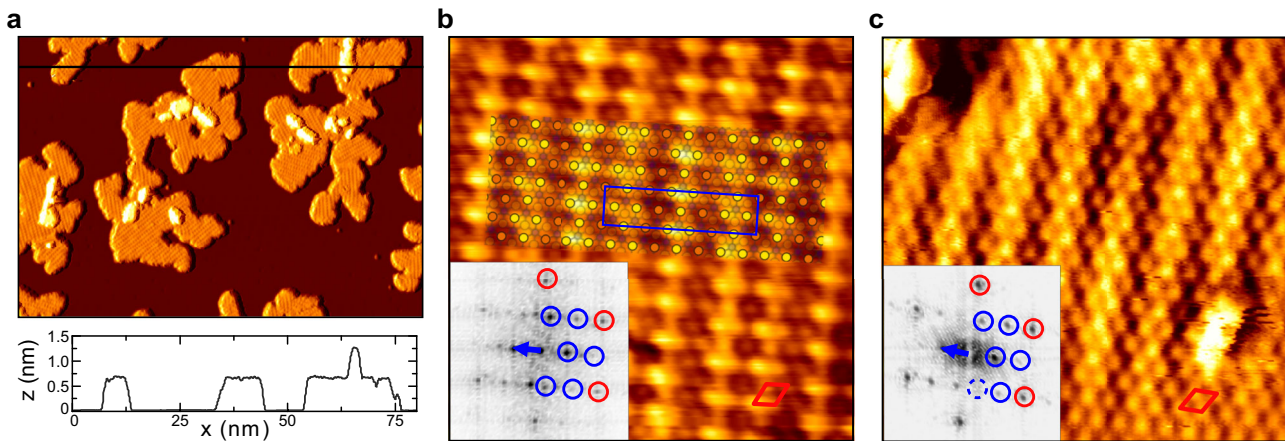


Fig. 1 Structure of VS₂ on Gr/Ir(111) at 7 and 300 K. **a** Large-scale 7 K STM topograph of monolayer VS₂ islands with small bilayers present. A height profile along the horizontal black line is shown below the image. **b, c** Atomically resolved STM images of monolayer VS₂ at 7 K (**b**) and 300 K (**c**). The Fourier transform of each image is shown as an inset, with the 1×1 VS₂ structure in red and the superstructure spots indicated in blue. In **b**, an atomic model for the $9 \times \sqrt{3}R30^\circ$ superstructure is included as an overlay. The model depicts the top sulfur atoms, with their apparent height in STM coded in orange (low) and yellow (high). Measurement parameters: **a** $80 \times 50 \text{ nm}^2$, $I_t = 0.8 \text{ nA}$, $V_t = -800 \text{ meV}$, **b** $6 \times 6 \text{ nm}^2$, $I_t = 0.6 \text{ nA}$, $V_t = 400 \text{ meV}$, **c** $6 \times 6 \text{ nm}^2$, $I_t = 1.0 \text{ nA}$, $V_t = -1000 \text{ meV}$.

incommensurate CDW quite well. The blue box indicates the corresponding $9 \times \sqrt{3}R30^\circ$ unit cell. The Fourier transform of the topograph is shown as inset in Fig. 1b, with the wavevector of the CDW indicated (blue arrow). The same is done for the 300 K topograph in Fig. 1c. Within the margin of error, the wavevector is found to be temperature independent, with $\mathbf{q}_{\text{CDW}(7\text{K})} = (0.656 \pm 0.006) \overline{\Gamma\text{K}}$ and $\mathbf{q}_{\text{CDW}(300\text{K})} = (0.65 \pm 0.03) \overline{\Gamma\text{K}}$. Since the wavevector of the $9 \times \sqrt{3}R30^\circ$ unit cell, $\mathbf{q}_{9 \times \sqrt{3}R30^\circ} = 2/3 \overline{\Gamma\text{K}} \approx 0.667 \overline{\Gamma\text{K}}$, is slightly larger than the experimental value, we will in the following also consider another unit cell of size $7 \times \sqrt{3}R30^\circ$, with a slightly smaller wavevector $\mathbf{q}_{7 \times \sqrt{3}R30^\circ} = 9/14 \overline{\Gamma\text{K}} \approx 0.643 \overline{\Gamma\text{K}}$. With the experimental wavevector lying in between $\mathbf{q}_{7 \times \sqrt{3}R30^\circ}$ and $\mathbf{q}_{9 \times \sqrt{3}R30^\circ}$, calculations with these two unit cells should capture the essential features of the incommensurate structure and provide a check on any artefacts or errors arising from using them for computational purposes (cf. Supplementary Fig. 3).

Energetics of lattice instabilities. Ab initio DFPT calculations of the acoustic phonon dispersion of undistorted monolayer 1T-VS₂ confirm that a structural instability and corresponding tendencies toward CDW formation exist for the experimental wavevector. Figure 2a shows that the longitudinal-acoustic and transverse-acoustic modes feature imaginary frequencies in several parts of the Brillouin zone. In other words, the Born-Oppenheimer energy surface is a downwards-opening parabola for small atomic displacements in the direction of these modes, as seen in Fig. 2b (triangle marks). At the experimental wavevector between $\mathbf{q} = 2/3 \overline{\Gamma\text{K}}$ and $\mathbf{q} = 9/14 \overline{\Gamma\text{K}}$, we find an instability of the transverse-acoustic branch. However, the dominant instability within the harmonic approximation (i.e., DFPT), is located at $\mathbf{q} = 1/2 \overline{\Gamma\text{M}}$ in the longitudinal-acoustic branch.

To go beyond the harmonic approximation, we have performed structural relaxations on appropriate unit cells. The resulting atomic positions are shown in Fig. 2c–e. On the aforementioned $9 \times \sqrt{3}R30^\circ$ and $7 \times \sqrt{3}R30^\circ$ unit cells, which can approximately host an integer multiple of the observed wavelength, the vanadium atoms are displaced from their symmetric positions by up to 8% of the lattice constant, while

the positions of the sulfur atoms remain almost unchanged, see Fig. 2c, d. The associated energy gains amount to about 23 meV per VS₂ formula unit (cf. ref. 21). The magnitude of these distortions and energy gains is similar to other octahedral TMDCs but exceeds by far what is found in trigonal-prismatic TMDCs^{7,39}. For instance, on the DFT level, the maximum displacement in the $\sqrt{13} \times \sqrt{13}$ CDW of 1T-NbSe₂ is 8.8% of the lattice constant with an energy gain of 57 meV per formula unit⁴⁰, while in the 3×3 CDW of 2H-NbSe₂ distortions and energy gain amount to only 2.3% of the lattice constant and 3.7 meV per formula unit⁴¹.

The vanadium displacement has components in both the transverse and longitudinal direction (vertical and horizontal in Fig. 2c, d), even though the instability of the phonons at $\mathbf{q} = 2/3 \overline{\Gamma\text{K}}$ and $\mathbf{q} = 9/14 \overline{\Gamma\text{K}}$ is of transverse character (white arrows in Fig. 2c, d). As a consequence, all longitudinal displacement components must stem from non-linear mode-mode coupling beyond the harmonic approximation. The admixture of longitudinal displacement components stems mainly from wavevectors $\mathbf{q} = 4/3 \overline{\Gamma\text{K}}$ and $\mathbf{q} = 9/7 \overline{\Gamma\text{K}}$, which are also commensurate with the $9 \times \sqrt{3}R30^\circ$ and the $7 \times \sqrt{3}R30^\circ$ unit cells, respectively. The admixed longitudinal modes at $\mathbf{q} = 4/3 \overline{\Gamma\text{K}}$ and $\mathbf{q} = 9/7 \overline{\Gamma\text{K}}$ are stable in the harmonic approximation and the non-linear admixture is not related to any nesting or Peierls physics (cf. Supplementary Fig. 4e, f).

We also find a distorted ground state on a 4×4 unit cell, see Fig. 2e. This structure is commensurate to the six wavevectors $\mathbf{q} = 1/2 \overline{\Gamma\text{M}}$, where we have instabilities in the longitudinal-acoustic branch arising from near perfect Fermi-surface nesting, see Supplementary Fig. 4a. However, here the displacements amount to only 4% of the lattice constant with a corresponding energy gain below 4 meV per 1T-VS₂ formula unit—much less than what is found for the $7 \times \sqrt{3}R30^\circ$ or $9 \times \sqrt{3}R30^\circ$ CDW structures. Thus, the DFT total energies of the fully relaxed structures are in line with the experimentally observed CDW patterns.

To illustrate the significance of the non-linear mode-mode coupling, in Fig. 2b, we also show the Born-Oppenheimer energy surfaces for displacements toward the relaxed structures (circle marks). The energy curve of the 4×4 structure is steeper in the vicinity of the origin. In other words, the 4×4 structure wins for

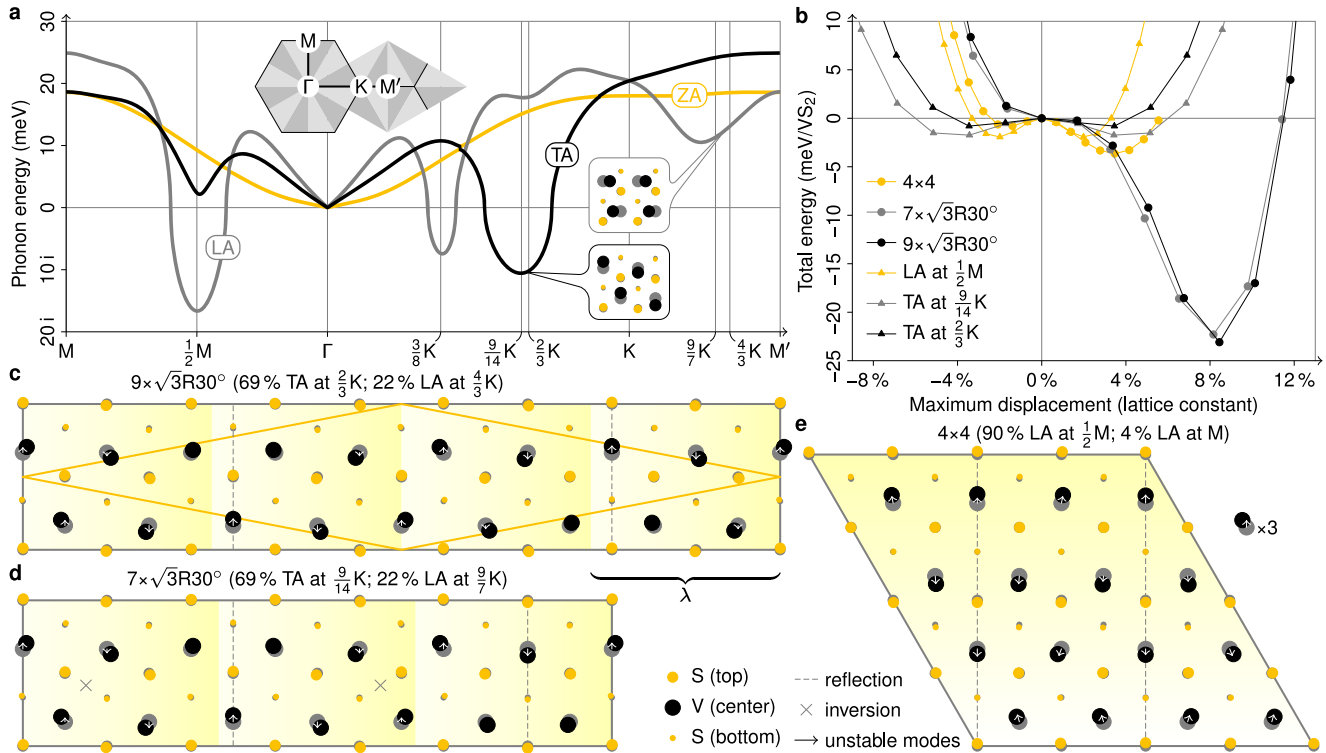


Fig. 2 Lattice instabilities in monolayer 1T-VS₂ from first principles. **a** Acoustic phonon dispersion from DFPT. LA, TA, and ZA stand for dominant longitudinal, transverse, and out-of-plane atomic displacements. The insets show selected displacement patterns corresponding to indicated modes. **b** Total energy from DFT as a function of the displacement amplitude for atomic displacements toward relaxed crystal structures and their projections onto soft phonon modes. **c–e** Relaxed crystal structures on $9 \times \sqrt{3}R30^\circ$, $7 \times \sqrt{3}R30^\circ$, and 4×4 unit cells from DFT. Vanadium and sulfur atoms are represented by black and yellow dots, their undistorted positions by gray shadows. Arrows represent the projections of the atomic displacements onto soft phonon modes. (Only arrows longer than 2% of the lattice constant are shown.) The contributions of different phonon modes are quantified in the figure titles. The displacements in **c**, **d** are drawn to scale, those in **e** have been magnified by a factor of three for better visibility. The primitive cell of the structure in **c**, which is in agreement with the results of ref. ²¹, is outlined in yellow. Dashed lines and crosses mark reflection planes and inversion centers.

small displacements. However, for larger displacements, the structures corresponding to the experimental wavevector reach by far the lowest values. These large energy gains at large displacements are inaccessible without non-linear mode–mode coupling, i.e., without the contribution of stable phonon modes (triangle marks). In the next section, we will address the non-linear regime of the distortions in a quantitative manner.

Non-linear mode–mode coupling. We decompose the entirety of atomic displacements of the relaxed $7 \times \sqrt{3}R30^\circ$ structure as $\mathbf{u} + \mathbf{v}$, where \mathbf{u} points in the direction of the unstable transverse–acoustic phonon modes at $\mathbf{q} = \pm 9/14 \bar{1}\bar{K}$ and the orthogonal complement $\mathbf{v} \perp \mathbf{u}$ combines contributions from all other phonon modes. The unstable modes account for $|\mathbf{u}|^2 / |\mathbf{u} + \mathbf{v}|^2 \approx 69\%$ of the total displacement only. In Fig. 2b, we have already seen one-dimensional cross sections of the Born–Oppenheimer energy surface, $E(\alpha\mathbf{u})$ and $E(\beta(\mathbf{u} + \mathbf{v}))$, where α and β are dimensionless scaling factors. Now, we will consider the full 2D Born–Oppenheimer surface spanned by \mathbf{u} and \mathbf{v} . Figure 3 shows $E(x\mathbf{u} + y\mathbf{v})$, where the minimum at $x = y = 1$ corresponds to the $7 \times \sqrt{3}R30^\circ$ structure and $x = y = 0$ is the undistorted structure. A fourth-order polynomial fit,

$$\frac{E(x\mathbf{u} + y\mathbf{v})}{\text{meV}/\text{VS}_2} \approx -25x^2 + 29y^2 + 34x^3 - 99x^2y - 20xy^2 - 12y^3 + 0.1x^4 + 44x^3y + 13x^2y^2 + 4.8xy^3 + 7.2y^4, \quad (1)$$

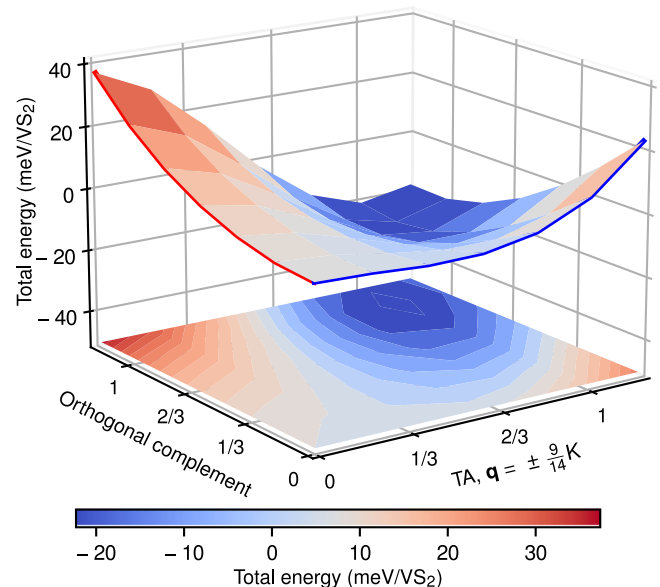


Fig. 3 Born–Oppenheimer energy surface for the $7 \times \sqrt{3}R30^\circ$ structure of 1T-VS₂. The axes represent the projection of the full CDW displacement onto the transverse–acoustic (TA) phonon modes at $\mathbf{q} = \pm 9/14 \bar{1}\bar{K}$ and the orthogonal complement, which combines all other contributing modes. The full CDW displacement is located at the point (1, 1). The forces resulting from this energy surface are predominantly non-linear and coupled in both directions.

accurately describes the DFT Born Oppenheimer surface. Here, the first and second line give rise to linear and non-linear forces $\mathbf{F} = -\nabla E$, respectively. It turns out that the non-linear part of the forces is dominated by mode-mode coupled terms^{42–44} (dependent on both x and y). The energy reduction stems largely from the x^2y and xy^2 terms above, which correspond to a shift of the minimum of the potential-energy surface toward finite positive y upon finite displacement in x direction and a softening of the effective spring constant in y direction for finite positive x , respectively. Note that within the harmonic approximation the x^2 (y^2) term lowers (raises) the energy.

The decisive role of mode-mode coupling terms x^2y and xy^2 distinguishes 1T-VS₂ from systems like 2H-NbSe₂ or 2H-TaS₂, where a single mode can be employed to describe anharmonicities, and distortions along a single effective coordinate suffice to explain the relaxation pattern of the full CDW and associated energy gains (cf. Supplementary Fig. 5).

The non-linear mode-mode coupling also manifests in monolayer 1T-VTe₂, which is isoelectronic to monolayer 1T-VS₂. Monolayer 1T-VTe₂ in experiment realizes a 4×4 CDW⁴⁵ in contrast to monolayer 1T-VS₂. In line with experiment, the comparison of DFT total energies in the fully relaxed supercells (Supplementary Table 1) reveals a clear preference of the 4×4 structure in 1T-VTe₂. At the harmonic level, this is likely related to a shift of the lattice instabilities, especially in the transverse-acoustic branch, toward smaller wavevectors in 1T-VTe₂ as compared to 1T-VS₂ (cf. Fig. 2a and Supplementary

Fig. 6a), which can be traced back to differences in the Fermi surface (cf. Supplementary Figs. 4 and 6b–g). At the harmonic level, a CDW with $7 \times \sqrt{3}R30^\circ$ structure of monolayer 1T-VS₂ is not expected, as Supplementary Fig. 6a shows. The small energy gain and still appreciable distortions obtained from the relaxation of a $7 \times \sqrt{3}R30^\circ$ structure of monolayer 1T-VS₂ (Supplementary Table 1) despite the stability on the harmonic level suggest that non-linear mode-mode coupling is also effective, here.

Full CDW gap in the unoccupied states. To better understand this CDW phase, we determined the electronic structure of monolayer VS₂ by a combination of STS experiments and simulated dI/dV maps based on the ab initio calculations using the $7 \times \sqrt{3}R30^\circ$ and $9 \times \sqrt{3}R30^\circ$ unit cells. STS spectra were used to locally probe the DOS of monolayer VS₂ at 7 K (black line) and 78.5 K (purple line), shown in Fig. 4a. Both spectra were taken with a clean Au tip in the middle of VS₂ islands. The most prominent feature is the gap located at about 0.175 eV, which is absent in calculations of undistorted monolayer VS₂²¹. At 7 K, the dI/dV signal vanishes completely, corresponding to a full gap in the DOS. At 78.5 K, this gap is not fully open, appearing as a wide depression with a finite value at its minimum. In most other characteristic features the spectra agree qualitatively.

While the lack of energy resolution at 78.5 K certainly smears out the spectra and the gap, the reason for its absence is not immediately evident. When discussing the band structure below,

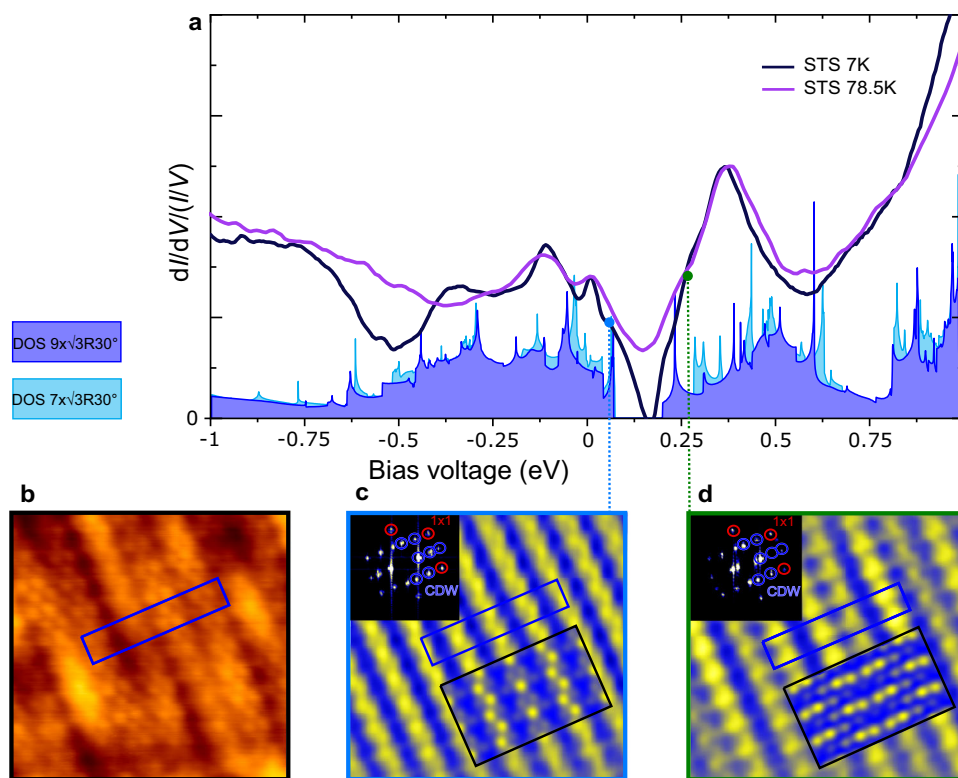


Fig. 4 Spatially and electronically resolved CDW phase in monolayer VS₂. **a** Scanning tunneling spectroscopy (STS) dI/dV spectra taken with a Au tip on monolayer VS₂ at 78.5 K (purple) and 7 K (black). The spectra are plotted along with the DFT-calculated density of states (DOS) for the $7 \times \sqrt{3}R30^\circ$ (cyan) and $9 \times \sqrt{3}R30^\circ$ (indigo) CDW phases of monolayer 1T-VS₂. **b** Atomically resolved STM topograph of monolayer VS₂ taken at $V_t = 175$ meV. **c, d** Fourier-filtered dI/dV conductance maps of the same region as in **b**, taken at $V_t = 75$ meV (**c**) and $V_t = 275$ meV (**d**). A linear yellow (maximum) to blue (minimum) color scale is used to depict the dI/dV intensity. The blue box indicates the same location in **b–d** and corresponds to a single $9 \times \sqrt{3}R30^\circ$ unit cell of the CDW. In the same color scale, DFT-simulated dI/dV maps below (**c**) and above (**d**) the gap of the charge density wave (CDW) are overlaid as insets. The maps show the integrated DOS from 0 to 137 meV (**c**) and from 137 to 275 meV (**d**). Additionally, the Fourier transforms of the conductance maps are shown in the upper-left corners with the 1×1 (red) and CDW peaks (blue) highlighted by circles. Measurement parameters: $f = 777.7$ Hz, **a** $T = 78.5$ K, $I_t = 0.3$ nA, $V_{r.m.s.} = 6$ meV and $T = 7$ K, $I_t = 0.45$ nA, $V_{r.m.s.} = 4$ meV, **b–d** $T = 7$ K, 5.5×5.5 nm², $I_t = 0.3$ nA, $V_{r.m.s.} = 10$ meV.

it will be seen that the width and existence of the full gap depend on the magnitude of the lattice distortions, which may already be diminished at 78.5 K.

In the same figure, *ab initio* calculations for the DOS of VS_2 , structurally relaxed in the $7 \times \sqrt{3}R30^\circ$ (cyan) or $9 \times \sqrt{3}R30^\circ$ (indigo) unit cell, are shown. Both unit cells feature quite similar structures, as expected for close-lying \mathbf{q} vectors. Most striking, for both cases a full gap in the unoccupied states is predicted. They only differ in size: 0.13 eV and 0.21 eV for the $9 \times \sqrt{3}R30^\circ$ and $7 \times \sqrt{3}R30^\circ$ unit cell, respectively. The location of the gap matches the STS data. That the width of the gap in the spectrum is smaller than in DFT might stem from the ground-state calculation assumed in DFT, overestimating the vanadium atom displacement at realistic temperatures. Note also that while many of the characteristic features of calculated and measured DOS (peaks, minima) seem to agree, the experimental spectra appear to be compressed with respect to the DFT calculated DOS. This quasiparticle renormalization is indicative of strong electron–electron correlations beyond the approximations of DFT (compare Supplementary Fig. 7).

With theory and experiment largely agreeing on the electronic structure, we turn to the relation between the gap and the CDW measured on the VS_2 islands. For that purpose, dI/dV conductance maps were taken on either side of the gap (both in the unoccupied states), in the location shown in Fig. 4b. The maps help to distinguish structural from electronic contributions, providing a close approximation of the spatial distribution of the DOS at the selected energies. As shown in Fig. 4c, d, we find two different DOS distributions on either side of the gap (see Supplementary Fig. 8 for the in-gap DOS). Both distributions are locked into the distorted lattice periodicity. They are out-of-phase, as seen in the blue unit cell drawn in the same location in

Fig. 4b–d: The DOS maxima below the gap correspond to DOS minima above the gap and vice versa. This behavior is perfectly analogous to that for a CDW with a symmetric gap around the Fermi level⁴. Simulated dI/dV maps derived from the DFT DOS for a $9 \times \sqrt{3}R30^\circ$ CDW are shown as an overlay in Fig. 4c, d. In Fig. 4c, the simulation reproduces both the alternating rows of single and zigzag atoms and the DOS minima between the rows. Its counterpart in Fig. 4d shows higher DOS contrast than experiment, but presents the same qualitative features. With the simulated maps based on the displacement patterns of Fig. 2c, the close agreement with experiment emphasizes the need to look beyond the harmonic approximation to understand this type of CDW.

Band structure and Fermi-surface topology. To deepen our understanding of the system, we calculated the spin-degenerate band structure, density of states, and Fermi surface of monolayer 1T- VS_2 with DFT. The results are shown in Fig. 5 and the Supplementary Movies. In the undistorted case, we find a single electronic band at the Fermi level, which strongly disperses between M and K and features a Van Hove singularity in the unoccupied states, as shown in Fig. 5a. The Fermi surface, depicted in Fig. 5b, consists of cigar-shaped electron pockets around the M points. For small distortions, partial gaps open at the Fermi level (e.g., between M and K). With increasing amplitude of the distortion, the gaps become larger and the bands are heavily reconstructed also for high energies. Only then, a full gap as observed in STS at 7 K emerges (cf. Supplementary Movie 1).

The presence of the CDW is therefore in the first place correlated with the gap between M and K, which opens already for small displacements and results in a partial gapping of the

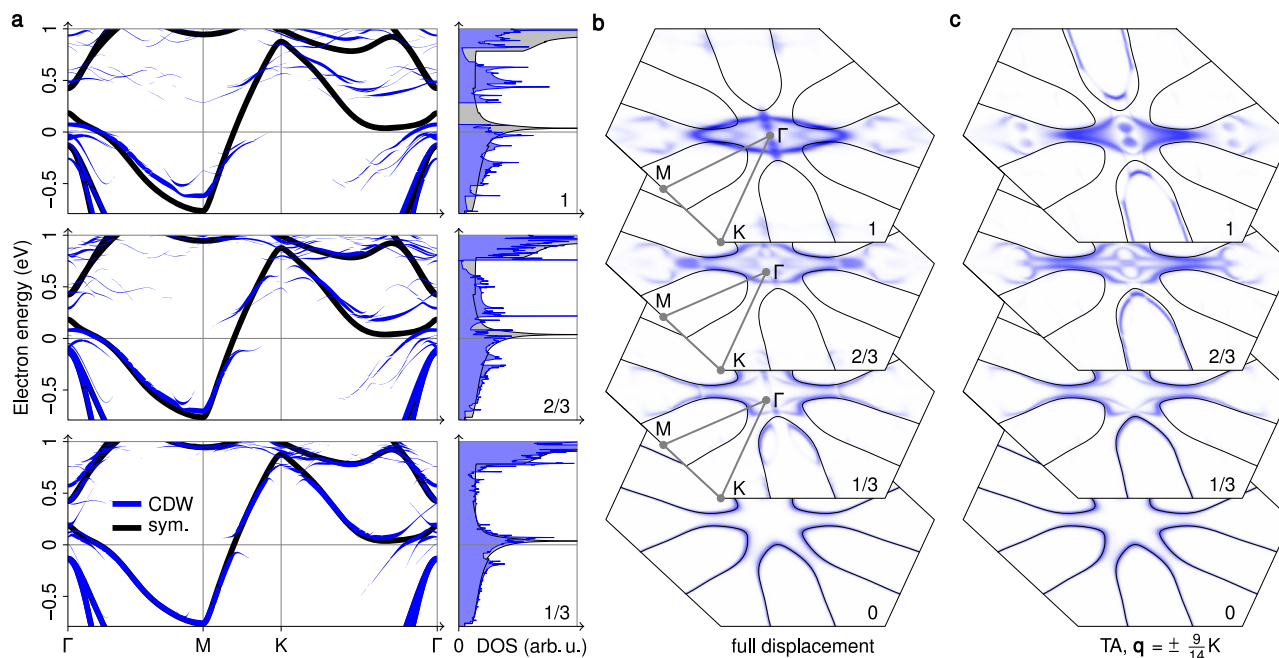


Fig. 5 Electronic structure of monolayer 1T- VS_2 from DFT. Data for the undistorted structure and the $7 \times \sqrt{3}R30^\circ$ CDW is shown in black and blue, respectively. The CDW data has been unfolded to the Brillouin zone of the undistorted structure. Here, the linewidth/saturation corresponds to the overlap of CDW and undistorted wave functions for the same \mathbf{k} point. Analogous results for 1T- VSe_2 and the $9 \times \sqrt{3}R30^\circ$ CDW are shown in Supplementary Fig. 3. **a** Electronic band structure and density of states (DOS) for 0%, 1/3, 2/3, and 100% of the displacements of the relaxed CDW structure. Please note that since the CDW breaks the C_3 symmetry, the chosen path, indicated in **b**, does not represent the full Brillouin zone. The bands along an extended path are shown in Supplementary Fig. 9. **b**, **c** Lifshitz transition. The Fermi surface is shown for displacements toward the relaxed CDW structure (**b**) and its projection onto unstable transverse-acoustic (TA) phonon modes (**c**). The Supplementary Movies 1 and 2 show animations of the transitions in **b** and **c**, respectively (including bands, DOS, and structures).

total DOS. Presumably it is the associated gain in electronic energy that initially drives the CDW transition. Since the full gap only starts to open at 70% of the final displacements, the experimental observation of a full gap above the Fermi level is an indication that the displacements in the experiments do not fall much below the calculated ones.

At the Fermi level, there is no complete gap even at large distortion, since the downwards-dispersing bands along Γ -M are only slightly shifted downwards and remain above the Fermi level near Γ . On the other hand, the originally flat portion of the band structure between Γ and K now disperses downwards and crosses the Fermi level. The preservation of states near Γ that mask the partial gap at the Fermi level can be understood in terms of band characters and degeneracies, as shown in Supplementary Fig. 10. Altogether, the Fermi surface is reconstructed and not completely destroyed by the lattice distortion. The CDW transition is thus a metal-metal Lifshitz transition with a change in Fermi-surface topology, instead of the usual metal-insulator Peierls transition.

As shown in Fig. 5c, we cannot understand this Fermi-surface reconstruction based on a single unstable mode: The displacements expected from the harmonic approximation (\mathbf{u} in Eq. (1)) only induce gaps in two-third of the cigar-shaped electron pockets (cf. Supplementary Movie 2). The other component \mathbf{v} couples to segments of the Fermi surface that are not affected by \mathbf{u} , i.e., the remaining third of the electron pockets (cf. Supplementary Movie 3). Together, they transform the Fermi surface from multiple cigar-shaped electron pockets around the M points to the single elliptical hole pocket around Γ visible in Fig. 5b. The decomposition of the CDW contains modes at more than one wavevector \mathbf{q} , so several approximate Fermi-surface nesting conditions and electron-phonon coupling matrix elements play a role (Supplementary Fig. 4b, c, e, f), enabling the CDW to affect distinct parts of the Fermi surface.

Magnetic properties of monolayer VS₂. Prompted by the prediction of ferromagnetism for monolayer 1T-VS₂ in its $\mathbf{q} = 2/3 \bar{\Gamma}\text{K}$ CDW phase²¹, we also examined the magnetic properties of VS₂, by means of X-ray magnetic circular dichroism (XMCD). The monolayer VS₂ samples were grown in situ and investigated with STM beforehand to make sure that the same phase and decent coverage were obtained. A STM topograph of the sample investigated by XMCD is shown in Supplementary Fig. 11. The blue curve in Fig. 6a represents the X-ray absorption spectrum averaged over both helicities and external field directions. The overall line shape is very similar to previous bulk crystal measurements²³ and clearly fits to a $3d^1$ configuration⁴⁶. The red signal in Fig. 6a is the XMCD magnified by a factor of 10, where no signal above the noise level is visible. This implies that the total magnetization vanishes. Sum rule analysis would yield an upper

bound of $0.02\mu_B$ per vanadium atom. Since it cannot be strictly applied to the case of the $V_{2,3}$ edges⁴⁷, this analysis yields only a zero-order estimate of the upper bound, but we can safely conclude that neither ferromagnetic nor paramagnetic behavior is present in this system.

We investigated magnetic order in monolayer VS₂ using spin-polarized DFT. We were able to stabilize both ferromagnetic and SDW structures within the $7 \times \sqrt{3}R30^\circ$ unit cell. In fact, magnetically ordered CDW phases are preferred over nonmagnetic CDW phases by energies of the order of 1 meV per VS₂ unit. Figure 6b shows the most favorable SDW pattern in the $7 \times \sqrt{3}R30^\circ$ CDW phase. The magnetic moments on vanadium reach $\pm 0.18\mu_B$, those on sulfur only $\pm 0.01\mu_B$ and are thus not shown. While the CDW alone reduces the total energy to -22.7 meV per VS₂ unit with respect to the symmetric structure, the SDW lowers this value by another 1.5 to -24.2 meV. Interestingly, without the CDW, a similar SDW with larger local moments of up to $\pm 0.51\mu_B$ (shown in Fig. 6c) leads to an energy reduction of 7.1 meV. As already suggested by previous calculations of ferromagnetism in the $9 \times \sqrt{3}R30^\circ$ structure of 1T-VS₂²¹, there is a competition between the lattice distortion and the formation of local moments. Although a full account of magnetism needs to go beyond the DFT level, in view of the good agreement between our ab initio results and the experimental STS and XMCD data, the formation of coupled CDW-SDW state in 1T-VS₂ is plausible. This presumption is further supported by comparison of the calculated DOS in the CDW-SDW state to the STS shown in Supplementary Fig. 12: the SDW formation on top of the CDW leads to a reduction of the gap size and the DOS of the coupled CDW-SDW is even in better agreement with the experiment than the non-spin-polarized CDW DOS.

Discussion

Both the electronic and magnetic results for VS₂ shed some light on the properties of the isoelectronic compound VSe₂, which displays a CDW of the same periodicity^{3,38,48}. Our calculations strongly suggest that also for this system non-linear effects are relevant and that a full gap opens in the unoccupied states (compare Supplementary Fig. 3). A full gap at the Fermi level, as proposed for 1T-VSe₂^{6,38,48,49}, would be unlikely to intrinsically occur for a CDW with the observed wavevector. The strong similarity between our calculations and experimental data, especially for those VSe₂ systems where only the $7 \times \sqrt{3}R30^\circ$ CDW is observed^{36,37}, lends credence to our analysis (compare Supplementary Fig. 13). It is possible that the simultaneous occurrence of a 4×1 CDW^{3,6}, perhaps due to substrate-induced strain⁵⁰, causes an additional gap opening near the Fermi level as a result of the interplay between the CDWs. In any case, similar to VS₂, the presence of a SDW coupled to the $7 \times \sqrt{3}R30^\circ$ CDW

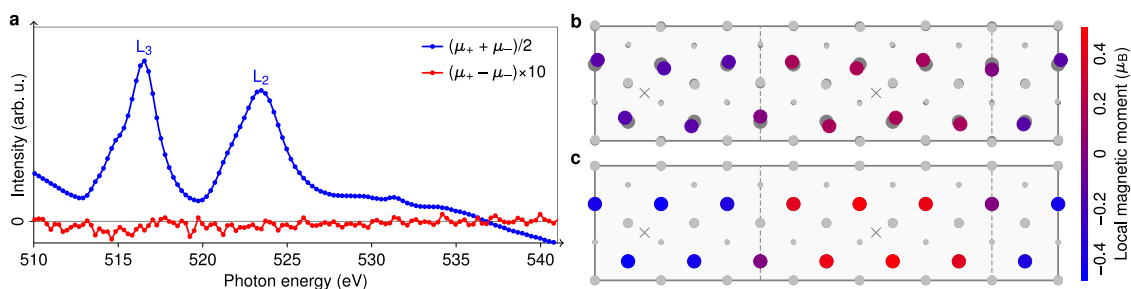


Fig. 6 Magnetic properties of monolayer 1T-VS₂. **a** Plotted in blue is the X-ray absorption signal averaged over both helicities and directions of the B field. The corresponding XMCD is shown in red. All measurements have been conducted in B fields of ± 9 T and at a temperature of 7 K. **b, c** Possible SDW pattern with **(b)** and without CDW **(c)**.

could explain the absence of net magnetization in XMCD experiments^{37,38,48}. Spin-polarized STM or XMLD might be able to detect the magnetic ground state for both VS₂ and VSe₂.

In conclusion, VS₂ defies the common phenomenology of CDW formation, as the complete CDW gap occurs above the Fermi level, there is giant non-linear longitudinal–transverse mode–mode coupling, and the CDW formation is accompanied by a change of the Fermi-surface topology. The unconventional CDW appears to host further electronic correlations as signalled by the quasiparticle renormalization and magnetic-moment formation. In this respect, it is reminiscent of correlated phases in superlattice structures such as Star of David phases⁷, moiré superlattices⁵¹, and doped cuprate superconductors⁵². In the latter class, lattice anharmonicities are central to boosting superconductivity under THz optical driving⁴⁴. The case of VS₂ presents new terrain: A metal–metal Lifshitz transition from non-linear electron–lattice effects in the strong-coupling regime is intertwined with electronic correlations. We note that the full gap in the DOS, situated within 0.2 eV from the Fermi level, opens up the possibility of inducing a metal–insulator transition upon mild gating or doping (e.g., with Li). Finally, we are convinced that the excellent agreement of experiment and theory for the unconventional CDW of monolayer VS₂ with the full gap in the unoccupied states provides a paradigmatic case study of strong-coupling CDWs in general.

Methods

The Ir(111) crystal is cleaned by grazing incidence 1.5 keV Ar⁺ ion exposure and flash annealing to 1500 K. A closed monolayer of single-crystalline Gr on Ir(111) is grown by room temperature exposure of Ir(111) to ethylene until saturation, subsequent annealing to 1300 K, followed by exposure to 200 L ethylene at 1300 K⁵³.

The synthesis of vanadium sulfides on Gr/Ir(111) is based on a two-step MBE approach introduced in detail in ref. ³⁴ for MoS₂. In the first step, the sample is held at room temperature and vanadium is evaporated at a rate of $F_V = 2.5 \times 10^{16}$ atoms/(m²s) into a sulfur background pressure of $P_S^B = 1 \times 10^{-8}$ mbar built up by thermal decomposition of pyrite inside a Knudsen cell. This results in dendritic TMDC islands of poor epitaxy. To make the islands larger and more compact, the sample is flashed in a sulfur background to 600 K.

The VS₂ layers were analyzed by STM, STS, and low-energy electron diffraction (LEED) inside a variable temperature (30–700 K) ultrahigh vacuum apparatus and a low-temperature STM operating at 7 and 78.5 K. The software WSXM⁵⁴ was used for STM data processing. XMCD measurements have been conducted at the beamline ID32 of the European Synchrotron Radiation Facility (ESRF) in Grenoble, France. The VS₂ samples were grown in situ inside the preparation chamber and checked with LEED and STM before X-ray absorption spectroscopy measurements. To be surface sensitive, the measurements were conducted in the total-electron-yield mode under normal incidence. The measurement temperature was 7 K and fields of 9 T were used. The spectra were recorded at the L_{3,2} edges, i.e., using the dipole allowed transition from 2*p* states into the 3*d* shell potentially generating magnetism.

All DFT and DFPT calculations were performed using QUANTUM ESPRESSO^{55,56}. We apply the PBE functional^{57,58} and norm-conserving pseudopotentials from the PSEUDO-DOJO table^{59,60}. In the undistorted case, uniform meshes (including Γ) of $12 \times 12 \times \mathbf{q}$ and $24 \times 24 \times \mathbf{k}$ points are combined with a Fermi–Dirac smearing of 300 K. For a fixed unit-cell height of 15 Å, minimizing forces and in-plane pressure to below 1×10^{-5} Ry/Bohr and 0.1 kbar yields a lattice constant of 3.18 Å and a layer height (vertical sulfur–sulfur distance) of 2.93 Å. For the superstructure calculations, appropriate \mathbf{k} -point meshes of similar density are chosen, except for the precise total energies quoted in the section about magnetism and in Supplementary Table 1, which required four times as dense meshes. The average lattice constant of superstructures is kept fixed at the value of the symmetric structure. Fourier interpolation to higher \mathbf{k} resolutions (1000×1000 for calculations of the DOS) and the unfolding of electronic states is based on localized representations generated with WANNIER90⁶¹. For the visualization of the unfolded Fermi surfaces, a Fermi–Dirac broadening of 10 meV is used.

Data availability

All the data and methods are present in the main text and the supplementary materials. Any other relevant data are available from the authors upon reasonable request.

Code availability

Codes used in this work are available from the authors upon reasonable request.

Received: 18 December 2020; Accepted: 4 November 2021;
Published online: 25 November 2021

References

- Ugeda, M. M. et al. Characterization of collective ground states in single-layer NbSe₂. *Nat. Phys.* **12**, 92 (2016).
- Zheng, B.-X. et al. Stripe order in the underdoped region of the two-dimensional Hubbard model. *Science* **358**, 1155 (2017).
- Duvjir, G. et al. Emergence of a metal–insulator transition and high-temperature charge-density waves in VSe₂ at the monolayer limit. *Nano Lett.* **18**, 5432 (2018).
- Hall, J. et al. Environmental control of charge density wave order in monolayer 2H-TaS₂. *ACS Nano* **13**, 10210 (2019).
- Yu, W. et al. Chemically exfoliated VSe₂ monolayers with room-temperature ferromagnetism. *Adv. Mater.* **31**, 1903779 (2019).
- Chua, R. et al. Can reconstructed Se-deficient line defects in monolayer VSe₂ induce magnetism? *Adv. Mater.* **32**, 2000693 (2020).
- Rosnagel, K. On the origin of charge-density waves in select layered transition-metal dichalcogenides. *J. Phys. Condens. Matter* **23**, 213001 (2011).
- Li, Y. W. et al. Folded superstructure and degeneracy-enhanced band gap in the weak-coupling charge density wave system 2H-TaS₂. *Phys. Rev. B* **97**, 115118 (2018).
- Zhu, X., Guo, J., Zhang, J. & Plummer, E. W. Misconceptions associated with the origin of charge density waves. *Adv. Phys. X* **2**, 622 (2017).
- Johannes, M. D. & Mazin, I. I. Fermi surface nesting and the origin of charge density waves in metals. *Phys. Rev. B* **77**, 165135 (2008).
- Inosov, D. S. et al. Fermi surface nesting in several transition metal dichalcogenides. *New J. Phys.* **10**, 125027 (2008).
- Berges, J., van Loon, E. G. C. P., Schobert, A., Rösner, M. & Wehling, T. O. Ab initio phonon self-energies and fluctuation diagnostics of phonon anomalies: Lattice instabilities from Dirac pseudospin physics in transition metal dichalcogenides. *Phys. Rev. B* **101**, 155107 (2020).
- Borisenko, S. V. et al. Two energy gaps and Fermi-surface “arcs” in NbSe₂. *Phys. Rev. Lett.* **102**, 166402 (2009).
- Weber, F. et al. Extended phonon collapse and the origin of the charge-density wave in 2H-NbSe₂. *Phys. Rev. Lett.* **107**, 107403 (2011).
- Dardel, B. et al. Temperature-dependent pseudogap and electron localization in 1T-TaS₂. *Phys. Rev. B* **45**, 1462 (1992).
- Dardel, B. et al. Spectroscopic signatures of phase transitions in a charge-density-wave system: 1T-TaS₂. *Phys. Rev. B* **46**, 7407 (1992).
- Zwick, F. et al. Spectral consequences of broken phase coherence in 1T-TaS₂. *Phys. Rev. Lett.* **81**, 1058 (1998).
- Lifshitz, I. M. Anomalies of electron characteristics of a metal in the high pressure region. *Zh. Eksp. Teor. Fiz.* **38**, 1569 (1960).
- Ji, Q. et al. Metallic vanadium disulfide nanosheets as a platform material for multifunctional electrode applications. *Nano Lett.* **17**, 4908 (2017).
- Li, Q., Zhou, Q., Shi, L., Chen, Q. & Wang, J. Recent advances in oxidation and degradation mechanisms of ultrathin 2D materials under ambient conditions and their passivation strategies. *J. Mater. Chem. A* **7**, 4291 (2019).
- Isaacs, E. B. & Marianetti, C. A. Electronic correlations in monolayer VS₂. *Phys. Rev. B* **94**, 035120 (2016).
- Tsuda, T., Yasuoka, H., Kitaoka, Y. & Di Salvo, F. J. ⁵¹V NMR study of the phase transition in 1T-VS₂. *J. Magn. Magn. Mater.* **31–34**, 1101 (1983).
- Mulazzi, M. et al. Absence of nesting in the charge-density-wave system 1T-VS₂ as seen by photoelectron spectroscopy. *Phys. Rev. B* **82**, 075130 (2010).
- Ma, Y. et al. Evidence of the existence of magnetism in pristine VX₂ monolayers (X = S, Se) and their strain-induced tunable magnetic properties. *ACS Nano* **6**, 1695 (2012).
- Zhuang, H. L. & Hennig, R. G. Stability and magnetism of strongly correlated single-layer VS₂. *Phys. Rev. B* **93**, 054429 (2016).
- Zhang, H., Liu, L.-M. & Lau, W.-M. Dimension-dependent phase transition and magnetic properties of VS₂. *J. Mater. Chem. A* **1**, 10821 (2013).
- Murphy, D. W., Cros, C., Di Salvo, F. J. & Waszczak, J. V. Preparation and properties of Li_xVS₂ (0 ≤ x ≤ 1). *Inorg. Chem.* **16**, 3027 (1977).
- Magonov, S., Contow, H.-J., Hillebrecht, H., Drechsler, M. & Rotter, W. Atomic structure and superstructure of vanadium disulfide by scanning tunneling microscopy. *Optik* **83**, 60 (1989).
- Sun, X. et al. In situ unravelling structural modulation across the charge-density-wave transition in vanadium disulfide. *Phys. Chem. Chem. Phys.* **17**, 13333 (2015).
- Gauzzi, A. et al. Possible phase separation and weak localization in the absence of a charge-density wave in single-phase 1T-VS₂. *Phys. Rev. B* **89**, 235125 (2014).
- Arnold, F. et al. Novel single-layer vanadium sulphide phases. *2D Mater.* **5**, 045009 (2018).
- Sanders, C. E. et al. Crystalline and electronic structure of single-layer TaS₂. *Phys. Rev. B* **94**, 081404(R) (2016).

33. Lefcochilos-Fogelquist, H. M., Albertini, O. R. & Liu, A. Y. Substrate-induced suppression of charge density wave phase in monolayer 1H-TaS₂ on Au(111). *Phys. Rev. B* **99**, 174113 (2019).
34. Hall, J. et al. Molecular beam epitaxy of quasi-freestanding transition metal disulphide monolayers on van der Waals substrates: a growth study. *2D Mater.* **5**, 025005 (2018).
35. Feng, J. et al. Metallic few-layered VS₂ ultrathin nanosheets: high two-dimensional conductivity for in-plane supercapacitors. *J. Am. Chem. Soc.* **133**, 17832 (2011).
36. Chen, P. et al. Unique gap structure and symmetry of the charge density wave in single-layer VSe₂. *Phys. Rev. Lett.* **121**, 196402 (2018).
37. Coelho, P. M. et al. Charge density wave state suppresses ferromagnetic ordering in VSe₂ monolayers. *J. Phys. Chem. C* **123**, 14089 (2019).
38. Wong, P. K. J. et al. Evidence of spin frustration in a vanadium diselenide monolayer magnet. *Adv. Mater.* **31**, 1901185 (2019).
39. Miller, D. C., Mahanti, S. D. & Duxbury, P. M. Charge density wave states in tantalum dichalcogenides. *Phys. Rev. B* **97**, 045133 (2018).
40. Calandra, M. Phonon-assisted magnetic Mott-insulating state in the charge density wave phase of single-layer 1T-NbSe₂. *Phys. Rev. Lett.* **121**, 026401 (2018).
41. Lian, C.-S., Si, C. & Duan, W. Unveiling charge-density wave, superconductivity, and their competitive nature in two-dimensional NbSe₂. *Nano Lett.* **18**, 2924 (2018).
42. Först, M. et al. Nonlinear phononics as an ultrafast route to lattice control. *Nat. Phys.* **7**, 854 (2011).
43. Truitt, P. A., Hertzberg, J. B., Altunkaya, E. & Schwab, K. C. Linear and nonlinear coupling between transverse modes of a nanomechanical resonator. *J. Appl. Phys.* **114**, 114307 (2013).
44. Mankowsky, R. et al. Nonlinear lattice dynamics as a basis for enhanced superconductivity in YBa₂Cu₃O_{6.5}. *Nature* **516**, 71 (2014).
45. Wang, Y. et al. Evidence of charge density wave with anisotropic gap in a monolayer VTe₂ film. *Phys. Rev. B* **100**, 241404 (2019).
46. Brik, M. G., Ogasawara, K., Ikeno, H. & Tanaka, I. Fully relativistic calculations of the L_{2,3}-edge XANES spectra for vanadium oxides. *Eur. Phys. J. B* **51**, 345 (2006).
47. Scherz, A. et al. Relation between L_{2,3} XMCD and the magnetic ground-state properties for the early 3d element V. *Phys. Rev. B* **66**, 184401 (2002).
48. Feng, J. et al. Electronic structure and enhanced charge-density wave order of monolayer VSe₂. *Nano Lett.* **18**, 4493 (2018).
49. Bonilla, M. et al. Strong room-temperature ferromagnetism in VSe₂ monolayers on van der Waals substrates. *Nat. Nanotechnol.* **13**, 289 (2018).
50. Si, J. G. et al. Origin of the multiple charge density wave order in 1T-VSe₂. *Phys. Rev. B* **101**, 235405 (2020).
51. Cao, Y. et al. Correlated insulator behaviour at half-filling in magic-angle graphene superlattices. *Nature* **556**, 80 (2018).
52. Tranquada, J. M., Sternlieb, B. J., Axe, J. D., Nakamura, Y. & Uchida, S. Evidence for stripe correlations of spins and holes in copper oxide superconductors. *Nature* **375**, 561 (1995).
53. van Gestel, R. et al. Selecting a single orientation for millimeter sized graphene sheets. *Appl. Phys. Lett.* **95**, 121901 (2009).
54. Horcas, I. et al. WSXM: a software for scanning probe microscopy and a tool for nanotechnology. *Rev. Sci. Instrum.* **78**, 013705 (2007).
55. Giannozzi, P. et al. QUANTUM ESPRESSO: a modular and open-source software project for quantum simulations of materials. *J. Phys. Condens. Matter* **21**, 395502 (2009).
56. Giannozzi, P. et al. Advanced capabilities for materials modelling with QUANTUM ESPRESSO. *J. Phys. Condens. Matter* **29**, 465901 (2017).
57. Perdew, J. P., Burke, K. & Ernzerhof, M. Generalized gradient approximation made simple. *Phys. Rev. Lett.* **77**, 3865 (1996).
58. Perdew, J. P., Burke, K. & Ernzerhof, M. Generalized gradient approximation made simple. *Phys. Rev. Lett.* **78**, 1396(E) (1997).
59. Hamann, D. R. Optimized norm-conserving Vanderbilt pseudopotentials. *Phys. Rev. B* **88**, 085117 (2013).
60. van Setten, M. J. et al. The PSEUDO-DOJO: Training and grading a 85 element optimized norm-conserving pseudopotential table. *Comput. Phys. Commun.* **226**, 39 (2018).
61. Mostofi, A. A. et al. An updated version of wannier90: a tool for obtaining maximally-localised Wannier functions. *Comput. Phys. Commun.* **185**, 2309 (2014).

Acknowledgements

This work was funded by the Deutsche Forschungsgemeinschaft (DFG, German Research foundation) through CRC 1238 (project no. 277146847, subprojects A01 and B06). J.B., A.S., and T.We. acknowledge financial support by the DFG through EXC 2077, GRK 2247, and SPP 2244. T.We. acknowledges support via the European Graphene Flagship Core3 Project (grant agreement 881603). J.B., A.S., and T.We. acknowledge computational resources of the North-German Supercomputing Alliance (HLRN). E.v.L. is supported by the Central Research Development Fund of the University of Bremen. L.M.A. acknowledges financial support from CAPES (project no. 9469/13-3).

Author contributions

T.We. and T.M. conceived this work and designed the research strategy. J.H. and discovered the CDW and developed, with the assistance of T.We., the growth method. C.v.E. and E.P. conducted and analyzed the STS experiments. J.B., A.S., and G.S., with support from E.v.L. and T.We., performed ab initio calculations. F.H. and S.K., with support from N.R., K.O., L.A., N.B., K.K., and H.W., performed and analyzed the XMCD experiment. The results were discussed by all authors. C.v.E., J.B., J.H., E.v.L., S.K., T.We., and T.M. wrote the manuscript with input from all authors. The first three authors have comparable contributions to this work.

Funding

Open Access funding enabled and organized by Projekt DEAL.

Competing interests

The authors declare no competing interests.

Additional information


Supplementary information The online version contains supplementary material available at <https://doi.org/10.1038/s41467-021-27094-x>.

Correspondence and requests for materials should be addressed to Camielvan Efferen.

Peer review information *Nature Communications* thanks Matteo Calandra and the other, anonymous, reviewer(s) for their contribution to the peer review of this work. Peer reviewer reports are available.

Reprints and permission information is available at <http://www.nature.com/reprints>

Publisher's note Springer Nature remains neutral with regard to jurisdictional claims in published maps and institutional affiliations.

 **Open Access** This article is licensed under a Creative Commons Attribution 4.0 International License, which permits use, sharing, adaptation, distribution and reproduction in any medium or format, as long as you give appropriate credit to the original author(s) and the source, provide a link to the Creative Commons license, and indicate if changes were made. The images or other third party material in this article are included in the article's Creative Commons license, unless indicated otherwise in a credit line to the material. If material is not included in the article's Creative Commons license and your intended use is not permitted by statutory regulation or exceeds the permitted use, you will need to obtain permission directly from the copyright holder. To view a copy of this license, visit <http://creativecommons.org/licenses/by/4.0/>.

© The Author(s) 2021

4.1 Supporting information

Supplementary Information of “A full gap above the Fermi level: the charge density wave of monolayer VS₂”

Camiel van Efferen^{1*}, Jan Berges², Joshua Hall¹, Erik van Loon², Stefan Kraus¹, Arne Schobert², Tobias Wekking¹, Felix Huttmann¹, Eline Plaar¹, Nico Rothenbach³, Katharina Ollefs³, Lucas Machado Arruda⁴, Nick Brookes⁵, Gunnar Schönhoff², Kurt Kummer⁵, Heiko Wende³, Tim Wehling², Thomas Michely¹

¹*II. Physikalisches Institut, Universität zu Köln, Zùlpicher Straße 77, 50937 Köln, Germany*

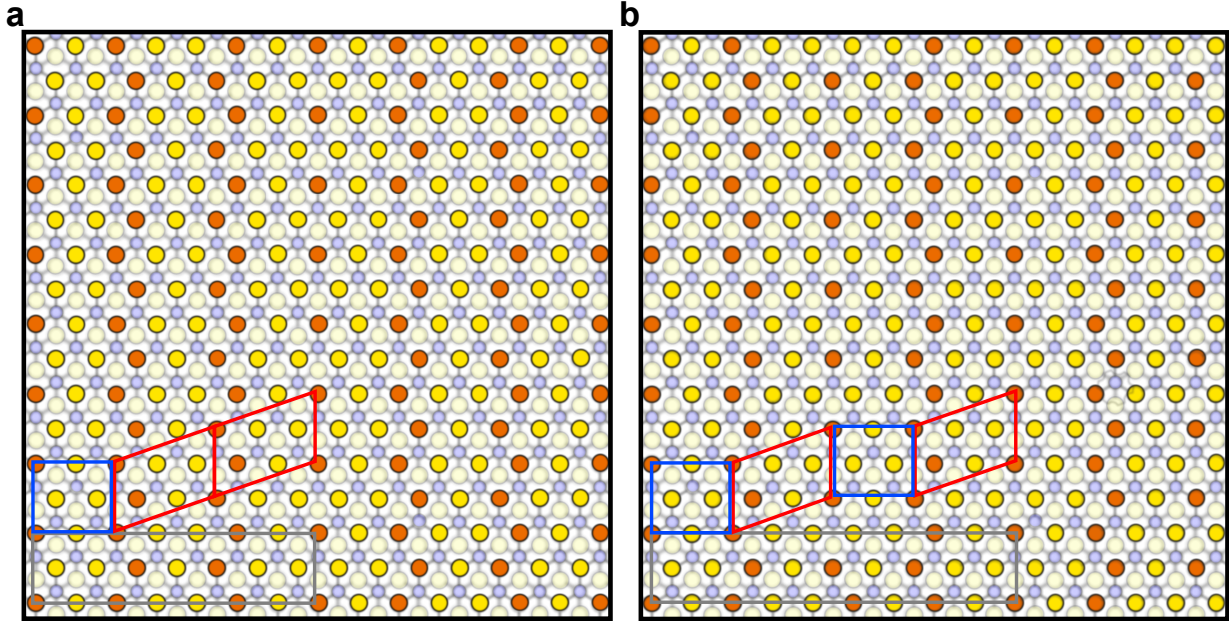
²*Institut für Theoretische Physik, Bremen Center for Computational Materials Science, and MAPEX Center for Materials and Processes, Otto-Hahn-Allee 1, Universität Bremen, 28359 Bremen, Germany*

³*Fakultät für Physik und Center für Nanointegration Duisburg-Essen (CENIDE), Universität Duisburg-Essen, Carl-Benz-Straße, 47057 Duisburg, Germany*

⁴*Institut für Experimentalphysik, Freie Universität Berlin, Arnimallee 14, 14195 Berlin, Germany*

⁵*European Synchrotron Research Facility (ESRF), Avenue des Martyrs 71, CS 40220, 38043 Grenoble Cedex 9, France*

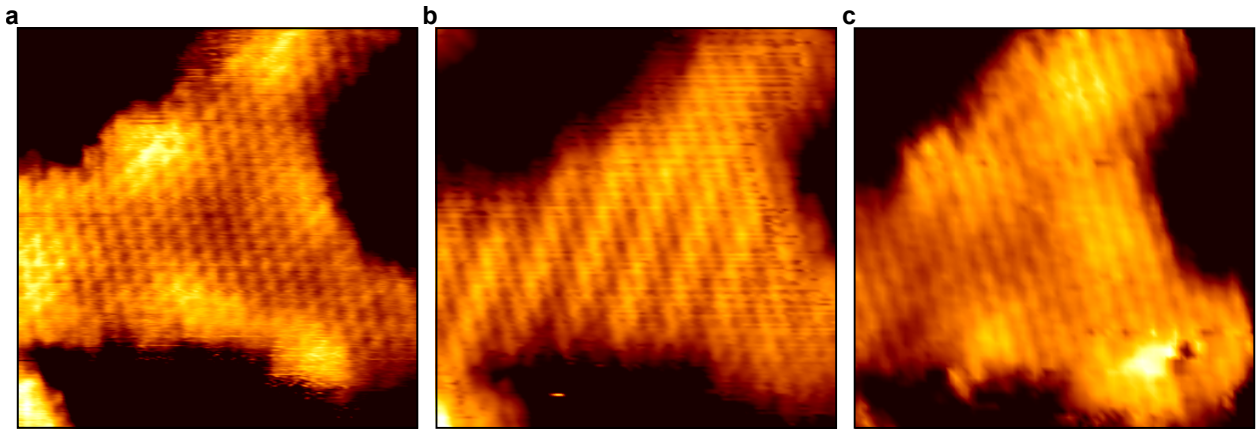
Supplementary Note 1: Unit cells



Supplementary Figure 1: Correspondence between unit cells in monolayer VSe_2 literature and the unit cells used in this paper. In **a** and **b**, models of the 1T- VS_2 atomic lattice are depicted with V atoms in blue and bottom-S atoms in faint yellow. $7 \times \sqrt{3}R30^\circ$ (**a**) and $9 \times \sqrt{3}R30^\circ$ (**b**) superstructures are visible in the top-S atoms, which are drawn in two colors to mimic the experimental apparent height in yellow (bright) and orange (dark). The dark gray rectangles indicate the $7 \times \sqrt{3}R30^\circ$ (**a**) and $9 \times \sqrt{3}R30^\circ$ (**b**) unit cells. The blue rectangle is a $2 \times \sqrt{3}R30^\circ$ unit, the red rhombus a $\sqrt{7}R19.1^\circ \times \sqrt{3}R30^\circ$.

In the isotopic material VSe_2 , a superstructure of same symmetry as in VS_2 , has been identified and attributed to a charge density wave (CDW)¹⁻⁴. In these studies, the superstructure was described by a combination of $2 \times \sqrt{3}R30^\circ$ and $\sqrt{7}R19.1^\circ \times \sqrt{3}R30^\circ$ units, which we mark in our model in [Supplementary Figure 1a, b](#) in blue and red, respectively. By the combination of a single $2 \times \sqrt{3}R30^\circ$ and two $\sqrt{7}R19.1^\circ \times \sqrt{3}R30^\circ$ units, the $7 \times \sqrt{3}R30^\circ$ CDW lattice can be described; two $2 \times \sqrt{3}R30^\circ$ units and two $\sqrt{7}R19.1^\circ \times \sqrt{3}R30^\circ$ units make up the $9 \times \sqrt{3}R30^\circ$ lattice.

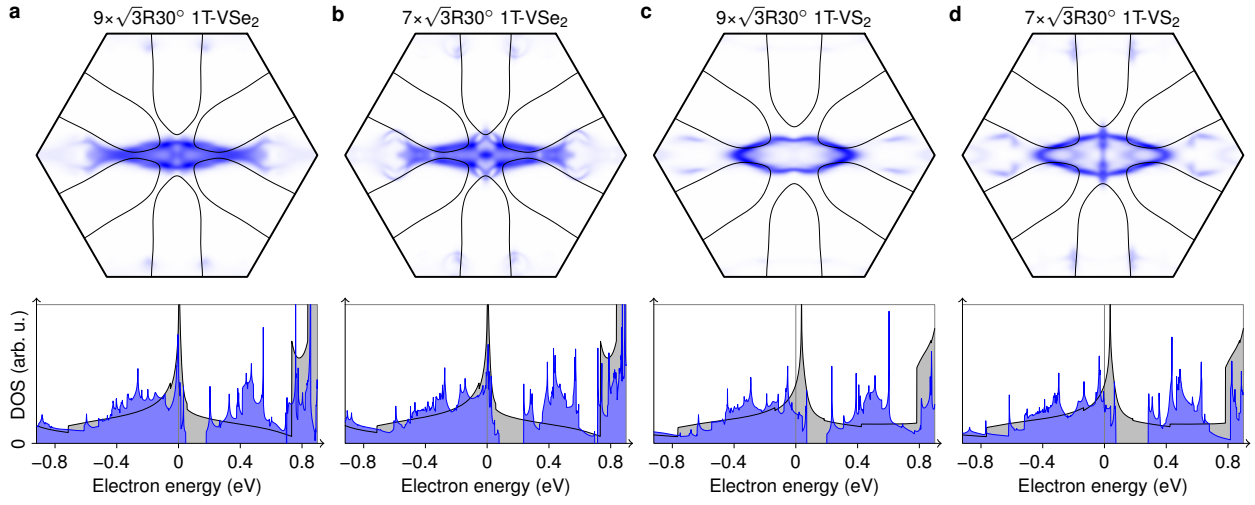
Supplementary Note 2: Tip-induced switching between distorted and undistorted phase



Supplementary Figure 2: Influence of STM tip on monolayer VS_2 : the two consecutive STM scans in panel **a** and **b** document the STM-tip-induced switch from the undistorted to the superstructure CDW phase. Scan **c** is taken 15 minutes later and shows no more signs of the superstructure. Images taken at 300 K. Measurement parameters: **a–c** $7 \times 7 \text{ nm}^2$, $I_t = 0.5 \text{ nA}$, $V_t = -90 \text{ meV}$.

The presence of the superstructure at room temperature can also be influenced by the scanning tunneling microscope (STM) tip. [Supplementary Figure 2a, b](#) shows two consecutive STM scans, taken at the same position, tunnelling current, and bias. In [Supplementary Figure 2a](#), the STM reveals only hexagonal atomic ordering inside the small VS_2 structure. In the successive STM scan in [Supplementary Figure 2b](#), the wave superstructure is observed in the same region, with the phase transition apparently triggered by the interaction with the STM tip. A subsequent STM scan taken about 15 minutes later, displayed in [Supplementary Figure 2c](#), again shows the absence of the superstructure.

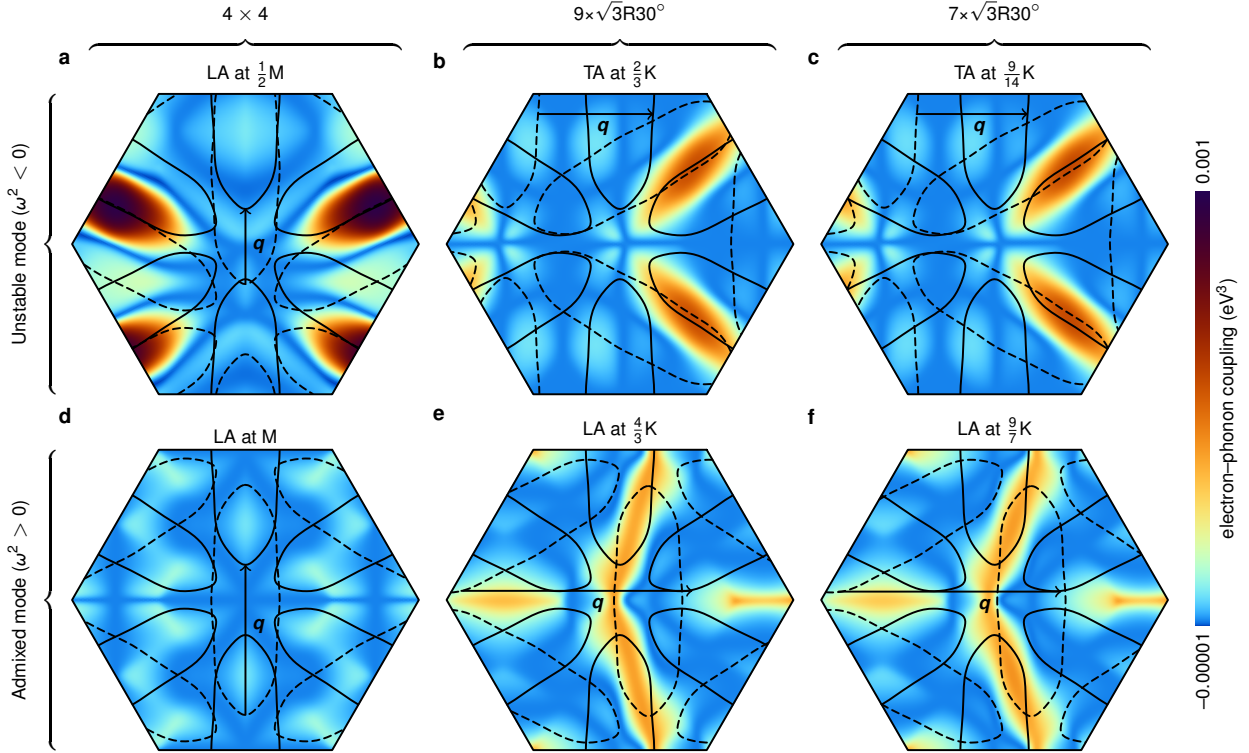
Supplementary Note 3: 1T-VSe₂ vs 1T-VS₂ and $9 \times \sqrt{3}R30^\circ$ vs $7 \times \sqrt{3}R30^\circ$



Supplementary Figure 3: Fermi surface and density of states (DOS) of monolayer **a, b** 1T-VSe₂ and **c, d** 1T-VS₂ in the undistorted phase as well as for the **a, c** $9 \times \sqrt{3}R30^\circ$ and **b, d** $7 \times \sqrt{3}R30^\circ$ CDW as obtained from DFT. The CDW data has been unfolded to the Brillouin zone of the undistorted structure. Here, the color saturation corresponds to the overlap of CDW and undistorted wave functions for the same **k** point.

In [Supplementary Figure 3a, b](#), we show the Fermi surface and density of states (DOS) of monolayer 1T-VSe₂ in the undistorted as well as $9 \times \sqrt{3}R30^\circ$ and $7 \times \sqrt{3}R30^\circ$ CDW phases from density functional theory (DFT). In VSe₂ a similar CDW as the one found in VS₂ has been reported repeatedly^{1,2,4-6}. As points of reference, corresponding results for monolayer 1T-VS₂ are displayed in [Supplementary Figure 3c, d](#). The results for the $9 \times \sqrt{3}R30^\circ$ and $7 \times \sqrt{3}R30^\circ$ cells agree qualitatively. Furthermore, our calculations suggest that 1T-VSe₂ and 1T-VS₂ are very similar in their electronic structure. In the distorted phase, 1T-VSe₂ will also have a full gap in the unoccupied states; at the Fermi energy, only a partial gap is expected. Though this has been observed in experiment^{2,3}, most studies on monolayer VSe₂ agree on a full gap located at the Fermi level^{1,4,6,7}. To our understanding, such a gap would require a filling of the downwards-dispersing bands near Γ , which are not gapped in the CDW configuration. According to our DFT calculations for both 1T-VS₂ and 1T-VSe₂ on a $9 \times \sqrt{3}R30^\circ$ ($7 \times \sqrt{3}R30^\circ$) supercell, $1/9 \approx 0.11$ ($1/7 \approx 0.14$) additional electrons would shift the gap to the Fermi energy (compare [Supplementary Figure 10a, b](#)). This charge could be provided by, e.g., the substrate or defects.

Supplementary Note 4: Nesting conditions and electron–phonon coupling

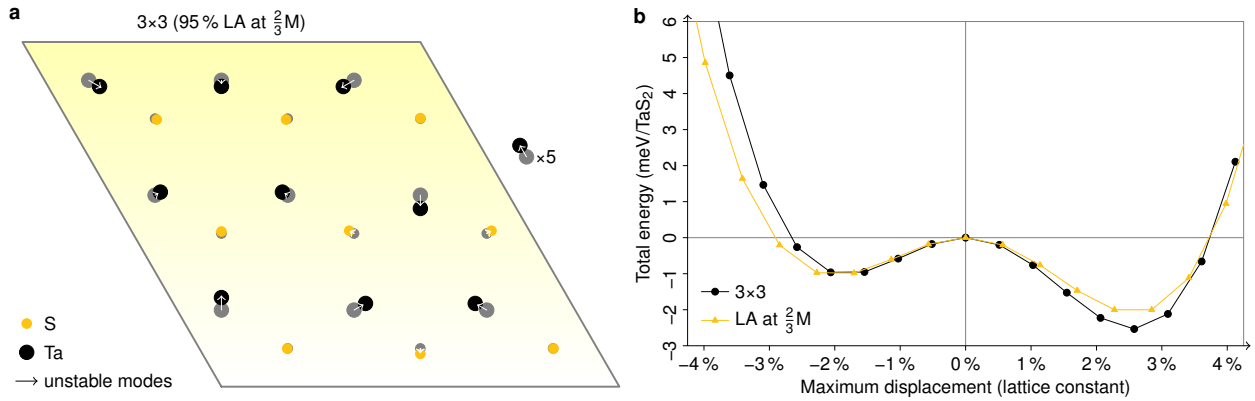


Supplementary Figure 4: Nesting conditions for different longitudinal– and transverse–acoustic (LA and TA) phonon wavevectors \mathbf{q} . We show the relevant electron–phonon coupling $2\omega_{\mathbf{q}}g_{\mathbf{k}+\mathbf{q},\mathbf{k}}\tilde{g}_{\mathbf{k},\mathbf{k}+\mathbf{q}}$ as a function of the electron wavevector \mathbf{k} (color scale) together with the original Fermi surface (solid lines) and the Fermi surface shifted by $-\mathbf{q}$ (dashed lines). Nesting parts of the Fermi surface can only have a strong effect on the phonons if they occur in \mathbf{k} -space regions with significant electron–phonon coupling (dark/brown spots). While the \tilde{g} from DFPT is fully screened, the partially screened g from constrained DFPT (cDFPT)⁸ excludes low-energy electronic screening (precisely, from within the isolated band at the Fermi level). Together with the bare electronic susceptibility χ_0 , they determine the phonon self-energy $\Pi = g^*\chi_0\tilde{g}$ responsible for the instabilities in the phonon dispersion. This analysis is equivalent to the fluctuation diagnostics in Ref. 9. The electron–phonon coupling has been obtained via the EPW code^{10,11}.

In Supplementary Figure 2a of the manuscript, we can observe two main instabilities in the acoustic phonon dispersion of monolayer 1T-VS₂ from density functional perturbation theory (DFPT): one in the longitudinal branch at $\mathbf{q} \approx 1/2\overline{\Gamma M}$ and one in the transverse branch at $\mathbf{q} \approx 2/3\overline{\Gamma K}$. A mode with momentum \mathbf{q} will be favoured if there is a large electron–phonon coupling matrix element connecting momenta \mathbf{k} and $\mathbf{k} + \mathbf{q}$ close to the Fermi surface. These nesting conditions are investigated in Supplementary Figure 4. In the longitudinal case, shown in Supplementary Figure 4a, we have almost perfect Fermi-surface nesting together with a strong electron–phonon coupling (cf. Fig. 5c, d of Ref. 12 for the case of 1T-VSe₂). This \mathbf{q} point is compatible with the formation

of a 4×4 CDW, as found, e.g., in bulk VSe_2 ¹³. Interestingly, despite these favorable conditions, this is not the preferred ground state of monolayer VS_2 . Instead, a CDW with a wavevector near $\mathbf{q} = 2/3 \overline{\Gamma\overline{K}}$ and $\mathbf{q} = 9/14 \overline{\Gamma\overline{K}}$ develops, which features only approximate nesting and a slightly reduced coupling strength, as seen in [Supplementary Figure 4b, c](#). As discussed in the main text, the formation of the CDW can only be understood considering non-linear mode–mode coupling. Phonon modes that appear stable in the harmonic approximation contribute significantly to the final atomic displacements, especially the longitudinal–acoustic modes for twice the momenta of the unstable modes, i.e., $\mathbf{q} = \text{M}$, $\mathbf{q} = 9/7 \overline{\Gamma\overline{K}}$, and $\mathbf{q} = 4/3 \overline{\Gamma\overline{K}}$, see [Supplementary Figure 4d–f](#). For both the harmonic ([Supplementary Figure 4b, c](#)) and the higher-order contributions ([Supplementary Figure 4e, f](#)) to the experimentally observed CDW, we find a similar situation of partially overlapping Fermi pockets in \mathbf{k} -space regions of considerable coupling, except that different pairs of pockets are involved.

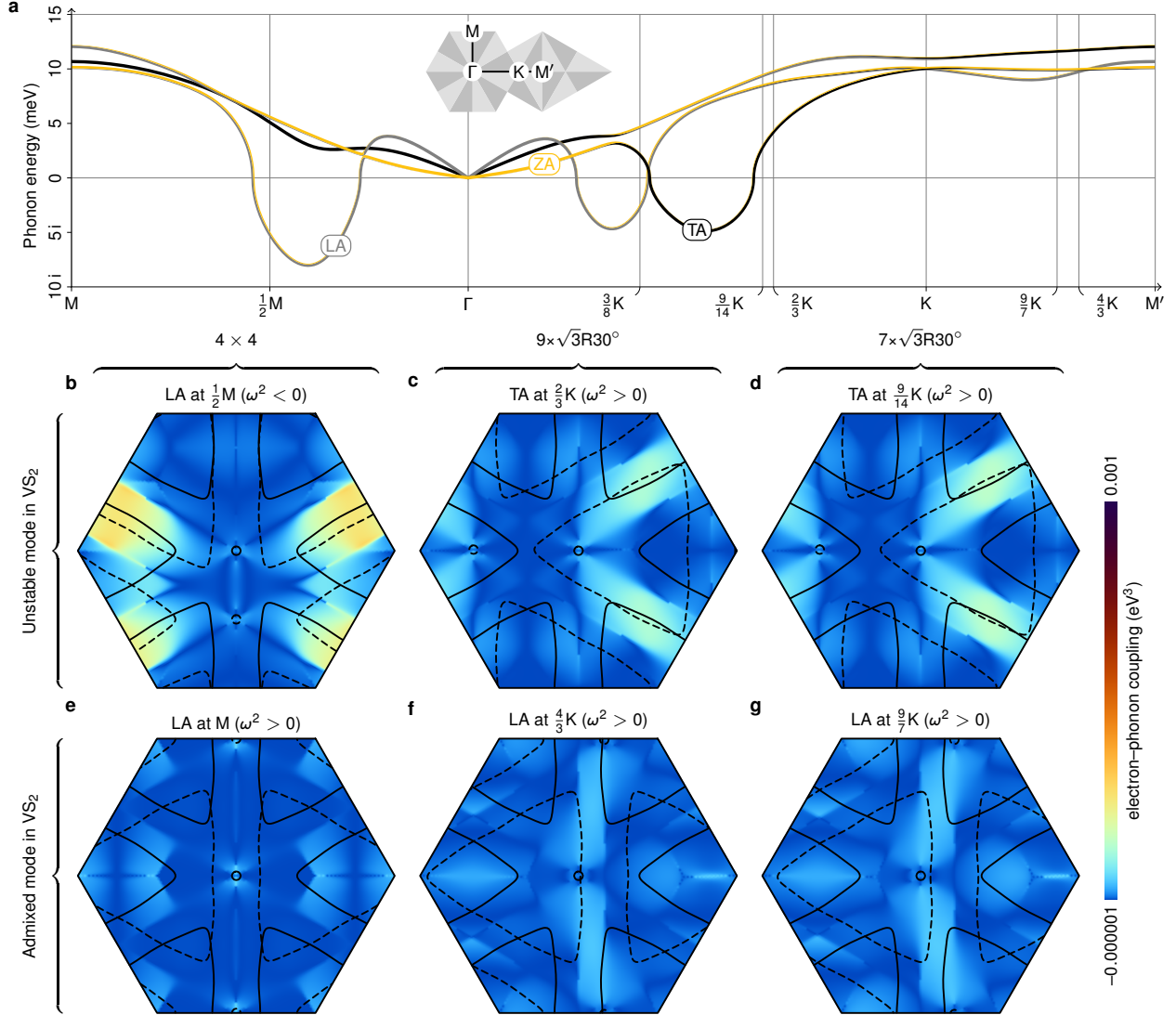
Supplementary Note 5: Born–Oppenheimer energy surface in TaS₂



Supplementary Figure 5: a CDW distortion in monolayer 2H-TaS₂ and **b** corresponding Born–Oppenheimer energy surface. Full circles indicate atomic positions and energies for displacements in the direction of the relaxed structure, arrows and triangle marks those for the projection onto the unstable longitudinal–acoustic (LA) phonon modes at the six wavevectors $\mathbf{q} = 2/3\overline{\Gamma M}$. The relaxed atomic displacements have been amplified by a factor of five for better visibility.

While the experimentally observed CDW in VS₂ can only be explained by the nonlinear coupling between soft and stable phonon modes, the 3×3 CDW in the trigonal–prismatic TMDCs is an example of a lattice instability that is determined essentially by a single unstable phonon mode. Analogous to Supplementary Figure 2b–e, [Supplementary Figure 5](#) shows the 3×3 CDW structure and the corresponding Born–Oppenheimer energy surface of monolayer 2H-TaS₂ from DFT: Here, the distortion along the leading unstable phonon normal-mode coordinate largely captures the energy gain associated with the full CDW relaxation. We used the same computational parameters as in Ref. 9.

Supplementary Note 6: Phonon dispersion, nesting conditions, and electron–phonon coupling in 1T-VTe₂



Supplementary Figure 6: **a** Longitudinal–, transverse– and z–acoustic (LA, TA and ZA) phonon dispersion of monolayer 1T-VTe₂. **b–g** Corresponding electron–phonon coupling $2\omega_{\mathbf{q}}g_{\mathbf{k}+\mathbf{q},\mathbf{k}}\tilde{g}_{\mathbf{k},\mathbf{k}+\mathbf{q}}$ together with the \mathbf{k} and $\mathbf{k} + \mathbf{q}$ Fermi surfaces (cf. Supplementary Figure 4).

The phonon dispersion of monolayer 1T-VTe₂ obtained from DFPT is shown in Supplementary Figure 6a. We find similar lattice instabilities as in the case of 1T-VS₂ (cf. Supplementary Figure 2a of the main text), albeit shifted to smaller $|\mathbf{q}|$. This shift, which is more pronounced for the transverse–acoustic instability in the $\overline{\Gamma K}$ direction than for the longitudinal–acoustic instability in the $\overline{\Gamma M}$ direction, can be traced back to differences in the Fermi surface (topology) rather than in the electron–phonon coupling, see Supplementary Figure 6b–g: Instead of the cigar-shaped electron pockets around the M points in 1T-VS₂ (cf. Supplementary Figure 4), we find triangular

hole pockets around the K points (as well as a small hole pocket at Γ) in 1T-VTe₂. In the latter case, the approximately parallel segments of the Fermi surface are closer together.

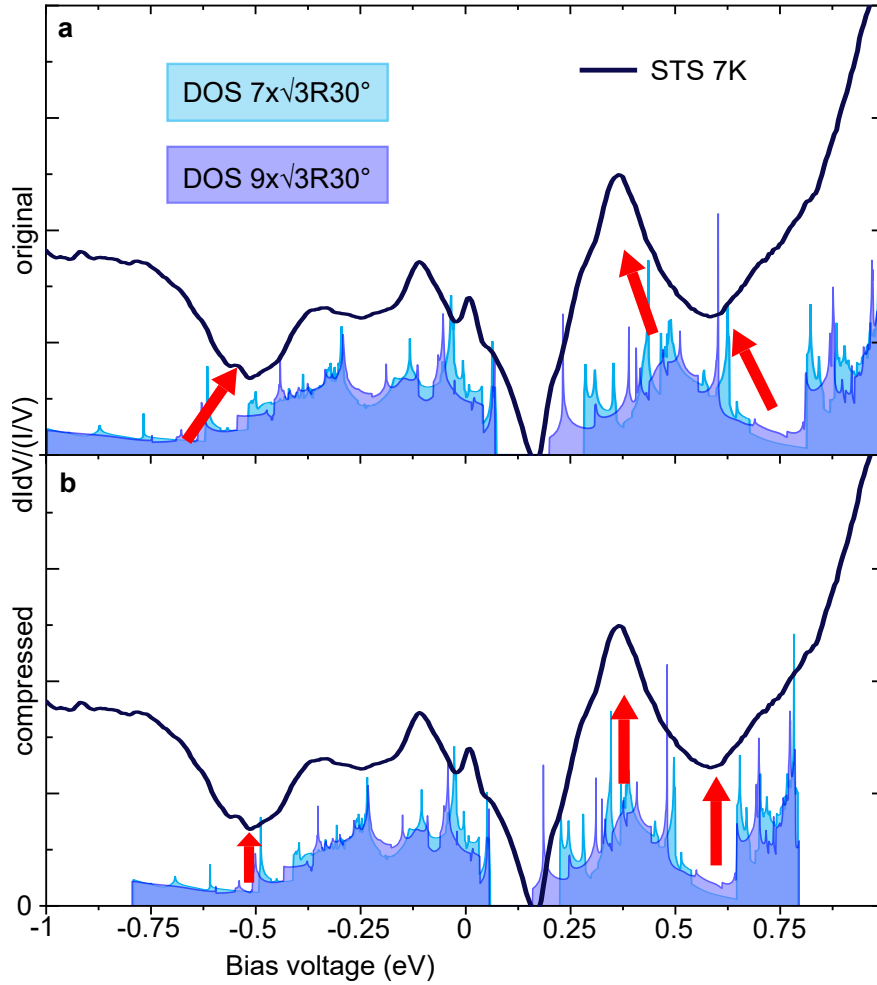
Supplementary Note 7: CDW energy gains in VS₂ vs VTe₂

Supplementary Table 1: Comparison of maximum atomic displacements and energy gains upon CDW formation for different materials and periodicities from DFT (PBE). All energies refer to a single VX₂ unit; the reference for the displacements is the lattice constant.

	1T-VS ₂		1T-VTe ₂	
4×4	4 %	3.4 meV	13 %	34.2 meV
$7 \times \sqrt{3}R30^\circ$	8 %	22.7 meV	6 %	2.5 meV

To compare the energy gains associated with CDW formation in 1T-VS₂ and in 1T-VTe₂ for the different periodicities, we performed structural relaxations on corresponding supercells in the framework of DFT (PBE). The energy gains reported in Table 1 show that in 1T-VS₂ the $7 \times \sqrt{3}R30^\circ$ CDW is favored over the 4×4 CDW; in 1T-VTe₂ vice versa. The DFT prediction is thus in line with experimental observation for both materials.

Supplementary Note 8: Compression of electronic spectrum



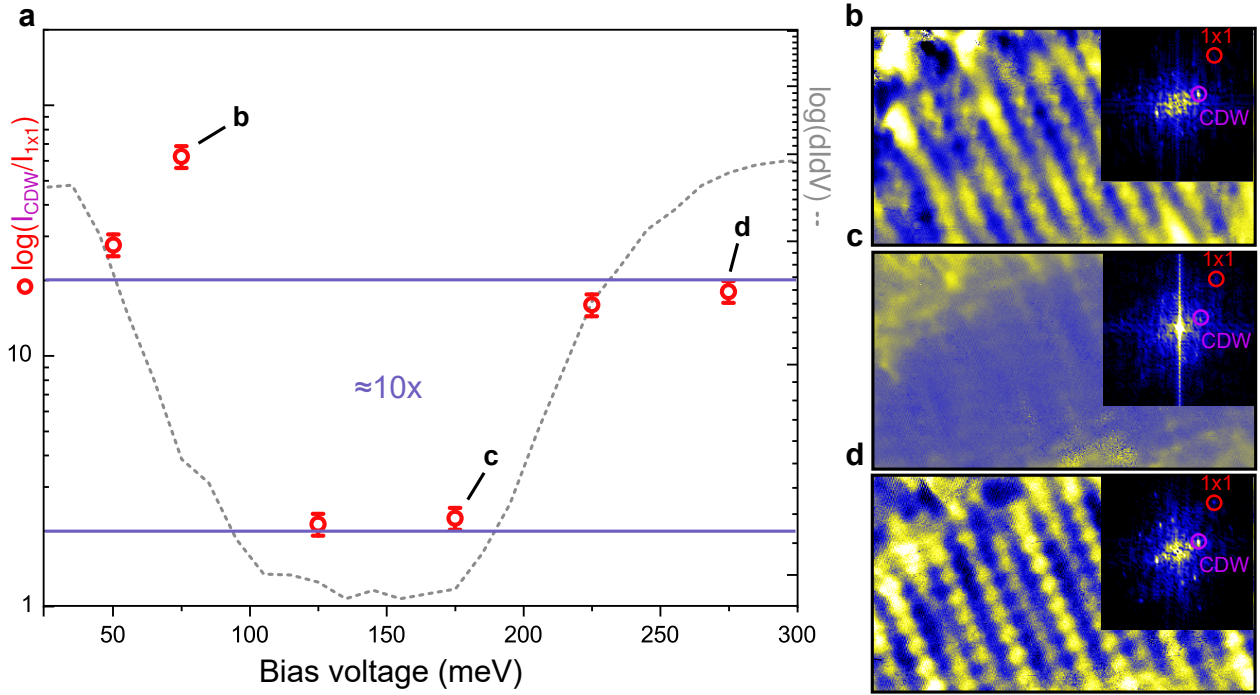
Supplementary Figure 7: Compression of experimental scanning tunneling spectroscopy (STS) data relative to density-functional theory (DFT)-calculated density of states (DOS). In **a**, the 7 K spectrum from the main manuscript is compared to the calculated DOS for the $7 \times \sqrt{3}R30^\circ$ and $9 \times \sqrt{3}R30^\circ$ unit cells. In **b**, the calculated DOS is compressed to about 80 % of its original width. The red arrows in **a, b** indicate three major features in the spectrum and DOS that can be harmonized between them when the DOS is compressed.

In Supplementary Figure 4a of the main text, the DOS from DFT appears to be wider than the experimental spectrum. Dynamic electronic correlation effects beyond DFT are a possible source of this discrepancy, since they can lead to band renormalization¹⁴. More precisely, they effect a mass enhancement of the electrons, i.e., the quasi-particle dispersions become flatter than what is expected from theories like DFT. In the case of purely local correlations¹⁵, this effect is described by a single renormalization factor Z or the corresponding mass enhancement factor $1/Z$. [Supplementary Figure 7](#) shows that we obtain a good match between experimental and theoretical spectra by setting $Z = 0.8$. This is indicative of moderate electronic correlations. For comparison, examples range

from diverging mass enhancement at Mott–Hubbard transitions, via mass enhancement factors of about 10 to 1000 in Kondo or heavy fermion systems, to enhancement factors between 1 and 10 in transition-metal compounds like metallic chromium or iron-based superconductors. The mass enhancement factor of $1/Z \approx 1.25$ puts VS_2 at similar electronic correlation strengths as, e.g., metallic chromium¹⁶.

The rise in the normalized dI/dV beyond -0.5 eV can be attributed to contributions from the graphene/Ir(111) substrate, which can come to dominate the signal for large V when the VS_2 has a small DOS. In this case, the graphene spectrum (not shown) diverges beyond the Ir(111) surface state at -190 meV .

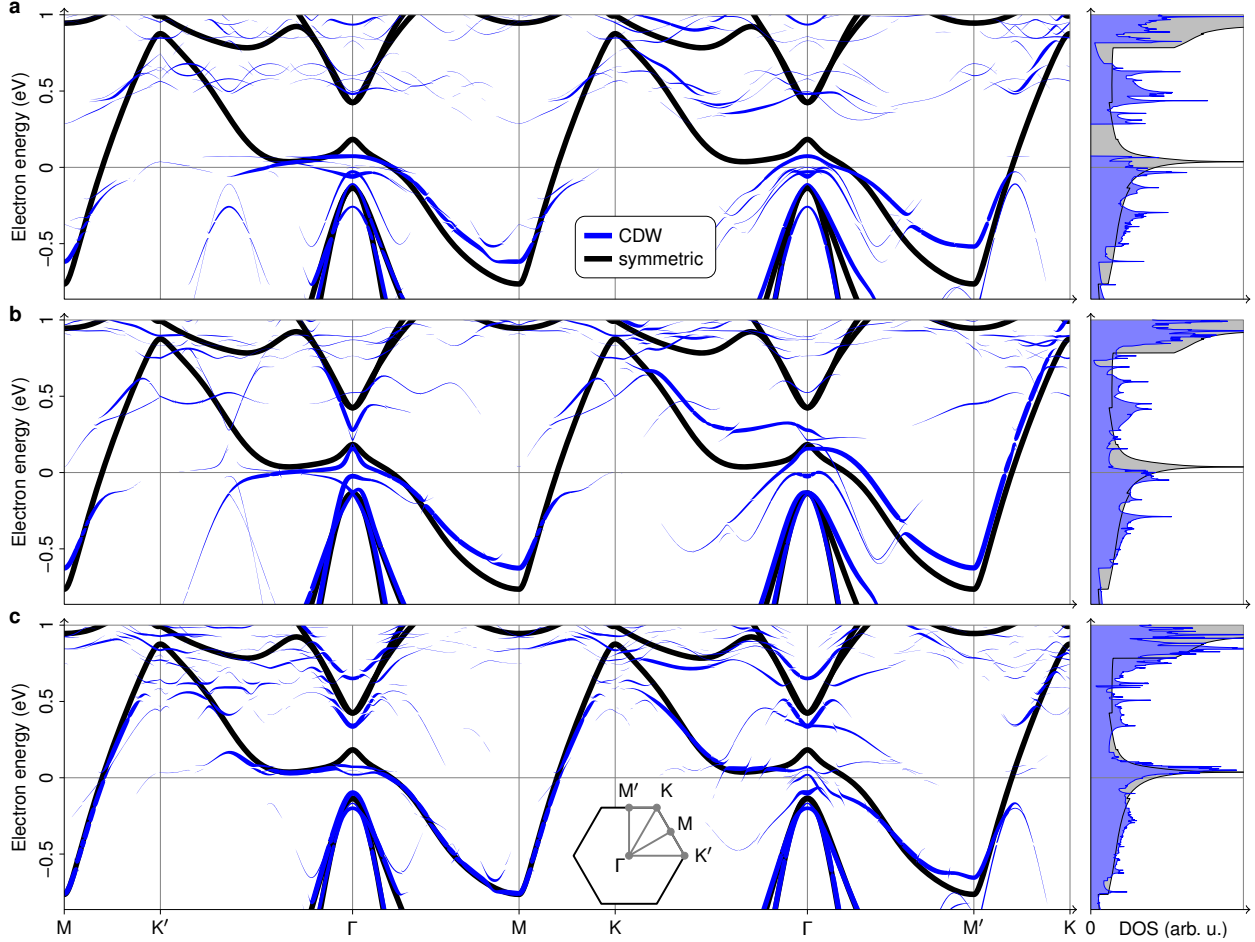
Supplementary Note 9: Suppression of CDW Fourier intensity within the gap



Supplementary Figure 8: Suppression of charge density wave (CDW) within the gap. **a** Logarithmic plot of the CDW intensity in the Fourier transform of dI/dV conductance maps, normalized to the 1×1 lattice intensity. Additionally, a dI/dV spectrum is plotted in order to indicate the location and width of the gap. **b–d** dI/dV conductance maps taken at the voltages indicated in **a**. Measurement settings: (maps) $9.5 \times 5.5 \text{ nm}^2$, $I_t = 0.3 \text{ nA}$, except for the map at 50 meV, which is taken at $I_t = 0.6 \text{ nA}$; (dI/dV spectrum) $f = 777.7 \text{ Hz}$, $I_t = 0.4 \text{ nA}$, $V_{\text{r.m.s.}} = 6 \text{ meV}$. All data taken at $T = 7 \text{ K}$.

Apart from the different charge distributions on either side of the gap discussed in the main manuscript, dI/dV maps taken within the gap show a clear suppression of the CDW. For a quantitative analysis, we have Fourier analyzed the dI/dV maps and normalized the CDW peak in the Fourier spectrum with respect to the 1×1 lattice peak intensity. The resulting value $R = I_{\text{CDW}}/I_{1 \times 1}$ is observed to fall by an order of magnitude within the gap. Since a gap of other than CDW origin would have the same value of R in- and outside of the gap region¹⁷, this is another clear indication of the relation between gap and CDW.

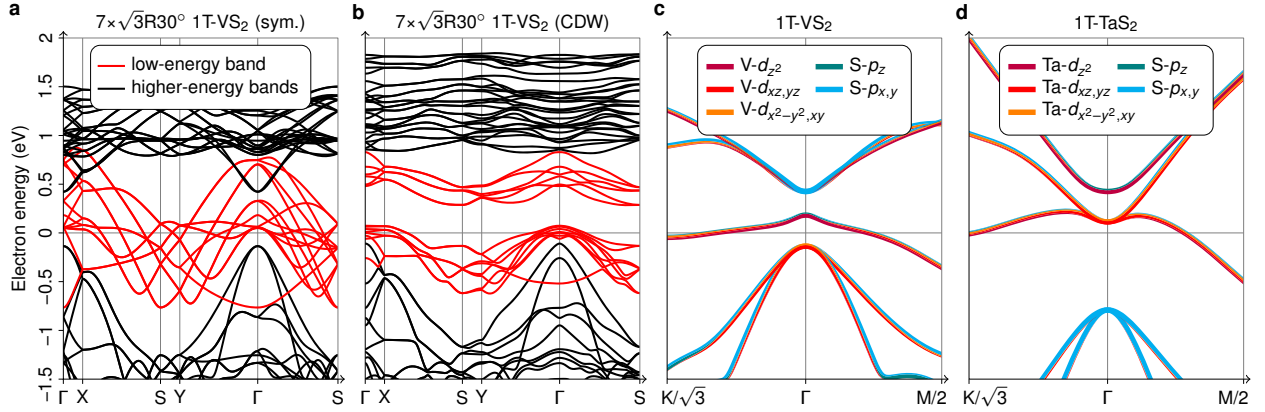
Supplementary Note 10: Bands along extended Brillouin-zone path



Supplementary Figure 9: Electronic band structure along an extended Brillouin-zone path and density of states (DOS) of monolayer 1T-VS₂ for **a** the full $7 \times \sqrt{3}R30^\circ$ charge density wave (CDW) displacements, **b** their projection onto unstable phonon modes, and **c** the orthogonal complement.

In Supplementary Figure 5a of the manuscript, we show the electronic band structure of monolayer 1T-VS₂ in the $7 \times \sqrt{3}R30^\circ$ phase along a selected high-symmetry path Γ -M-K- Γ of the undistorted phase only. Once the distortion breaks the C_3 symmetry, this path is not representative of the full Brillouin zone anymore. For completeness, in Supplementary Figure 9a, we thus reproduce the respective data along an extended path, again supplemented with the DOS. In Supplementary Figure 9b, c, we show the analogous results for the projection of the displacement onto the soft transverse-acoustic phonon modes at $\mathbf{q} = \pm 9/14 \overline{\Gamma\bar{K}}$ and the orthogonal complement. There are some salient differences between the electrons for the full and partial CDW displacement. In Supplementary Figure 9b, the gap between M' and K is missing; in turn, in Supplementary Figure 9c, there is no gap between M and K' as well as M and K. The combination of both displacement components is needed to open a full gap.

Supplementary Note 11: Preservation of states at the Fermi level

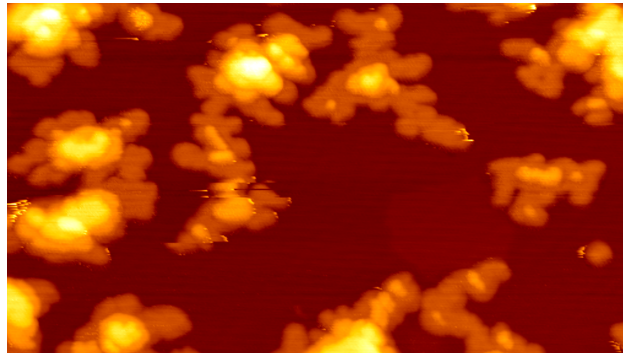


Supplementary Figure 10: **a, b** Band structure of symmetric and distorted 1T-VS₂ along path through Brillouin zone corresponding to $7 \times \sqrt{3}R30^\circ$ cell. The low-energy band is half-filled and splits into seven four-fold (including spin) bands between X and S. Thus, there must be $1/7$ unoccupied states per V atom below the gap. **c, d** Orbital-resolved low-energy electron dispersion of 1T-TaS₂ and 1T-VS₂ near Γ . In the case of 1T-VS₂ there is an avoided crossing between V-*d* and S-*p_{x,y}* bands.

The CDW does not create a complete gap at the Fermi level. For the commensurate structures used to approximate the incommensurate CDW, it is the combination of the electron count and the symmetry of the unit cell that guarantees a partially filled band, i.e., a metallic DOS. A complete gap at the Fermi level in the CDW would require the splitting of bands that must be degenerate by symmetry of the CDW structures (Supplementary Figure 10a, b), i.e., further symmetry breaking.

The particular form of the remaining spectral weight at the Fermi level resembling a downwards dispersing parabola around Γ in the CDW state (cf. Supplementary Figure 5) can be understood in terms of orbital band characters: In 1T-VS₂, we find an avoided crossing of V-*d* and S-*p_{x,y}* bands in the relevant region and thus a significant hybridization between these states (Supplementary Figure 10c). This is opposed to, e.g., the case of 1T-TaS₂, where the S-*p_{x,y}* states are much lower in energy (Supplementary Figure 10d). Now, while the *d*-type bands are heavily reconstructed due to the CDW, the *p* orbitals are less affected and can contribute to a new Fermi surface in the case of 1T-VS₂ in contrast to 1T-TaS₂.

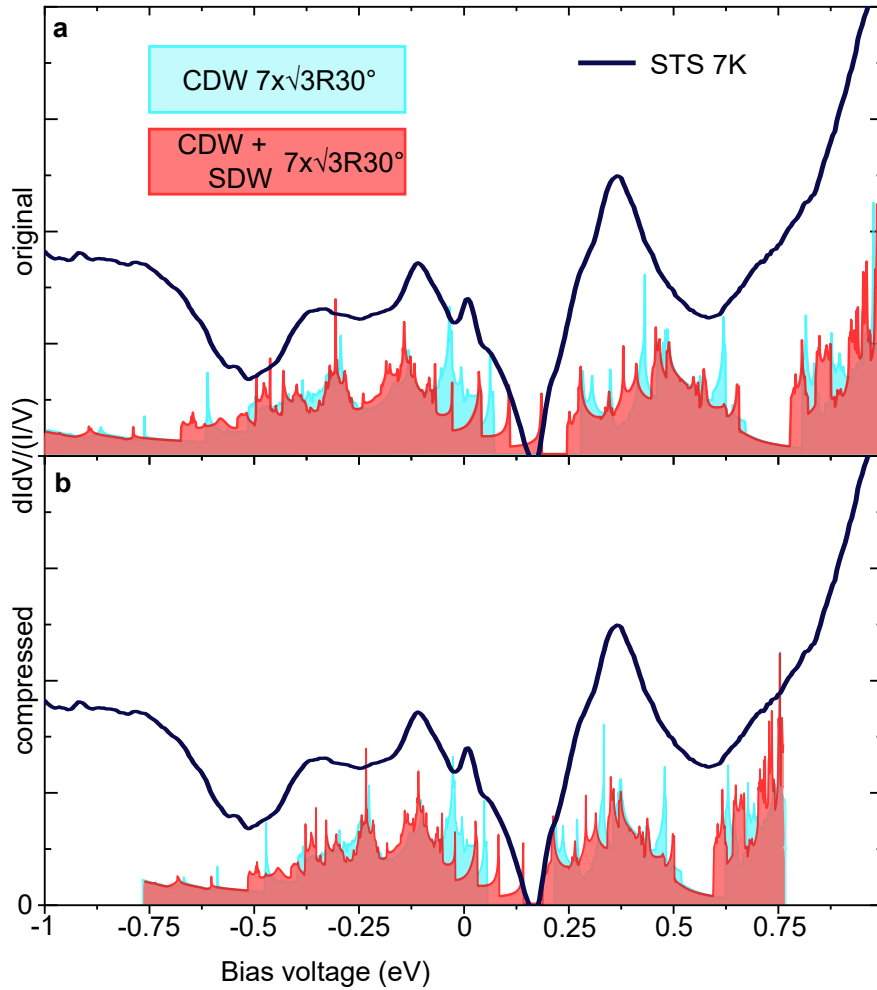
Supplementary Note 12: XMCD sample morphology



Supplementary Figure 11: Magnetic properties of VS_2 : STM topograph illustrating the sample morphology of the XMCD measured sample. Image size: $100 \times 50 \text{ nm}^2$.

In the main manuscript, we describe the magnetic properties of VS_2 as measured by x-ray absorption spectroscopy (XAS) and x-ray magnetic circular dichroism (XMCD). [Supplementary Figure 11](#) displays the sample morphology of the investigated sample. Like the samples shown in the main text, the island shape is dendritic. By comparison to substrate step edges, the monolayer height is measured to be 7 Å. The sample has a monolayer coverage of about 40%. Distinct height levels indicate up to three layers, with multilayer VS_2 making up approximately 25% of the total amount of VS_2 present on the surface.

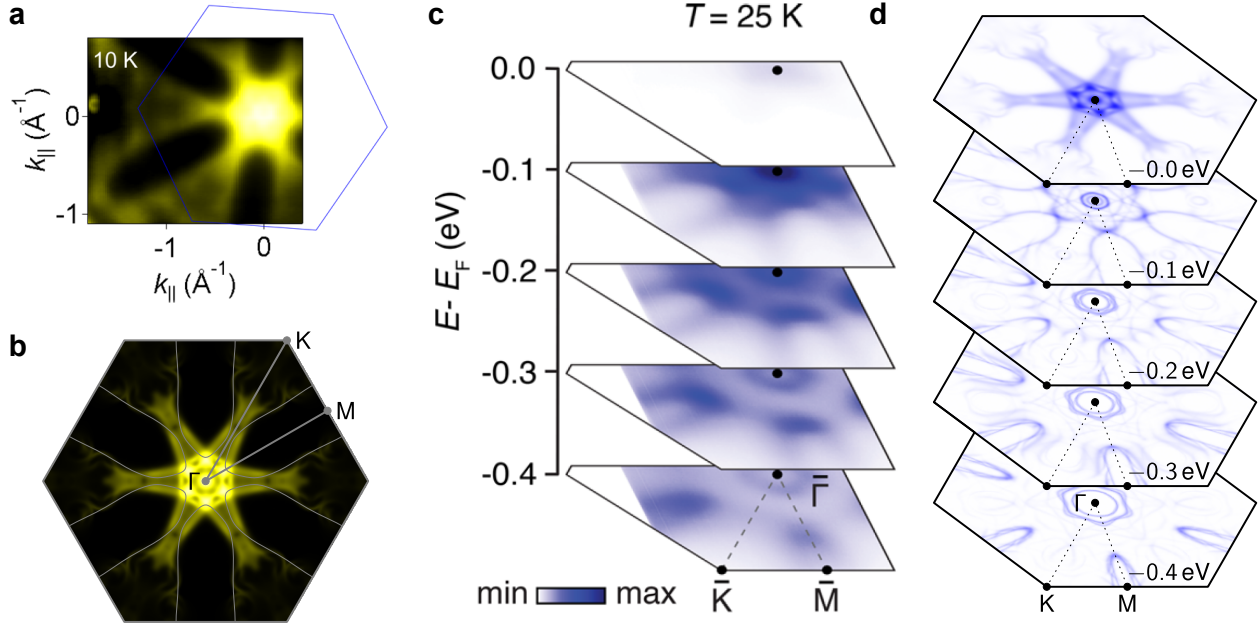
Supplementary Note 13: DOS for SDW



Supplementary Figure 12: **a** Scanning tunneling spectroscopy (STS) data taken with a Au tip on monolayer VS_2 at 7 K along with density-functional theory (DFT) calculated charge density wave (CDW) density of states (DOS) with (red) and without (cyan) SDW. **b** The same data after compressing calculated DOS to 80% of original size.

In [Supplementary Figure 12a](#), we show the DOS of the CDW structure with and without spin density wave (SDW), along with the experimental dI/dV spectra. The most prominent difference in the DOS is the reduction of the gap size. For the $7 \times \sqrt{3}R30^\circ$ structure, the gap shrinks from 0.21 eV to 0.06 eV when the CDW is coupled to a SDW. Since the CDW gap is indeed much larger in DFT than the experimental gap, this can be considered as an additional argument for the simultaneous presence of a SDW. Taking into account the compression of the experimental data, discussed under [Supplementary Figure 7](#), the DOS of the coupled CDW–SDW is in even better agreement with the experimental spectra, as seen in [Supplementary Figure 12b](#).

Supplementary Note 14: Comparison of DFT results with literature data for VSe₂



Supplementary Figure 13: Fermi surface of $7 \times \sqrt{3}R30^\circ$ CDW of monolayer 1T-VSe₂ averaged over regions of different CDW orientations and comparison to experiment. **a** Fermi surface reprinted with permission from Ref. 2 © 2018 American Physical Society. **b** Symmetrized Fermi surface calculated in this work. **c** Energy isolines reprinted with permission from Ref. 7 © 2018 American Chemical Society. **d** Symmetrized energy isolines calculated in this work.

In order to compare our DFT results for monolayer VSe₂ to existing ARPES studies, we have averaged our calculated Fermi surface of VSe₂ in the $7 \times \sqrt{3}R30^\circ$ CDW phase over all domains of the CDW with respect to the lattice. In this way, many of the familiar ARPES characteristics of VSe₂ are uncovered. If we compare to VSe₂ systems where only the $7 \times \sqrt{3}R30^\circ$ CDW was observed^{2,3}, we see that the experimental data in Supplementary Figure 13a, taken from Ref. 2, shows excellent agreement with our calculated Fermi surface in Supplementary Figure 13b. In particular, we observe the formation of gaps between M and K, while the rest of the Fermi surface remains intact. The apparent persistence of the six cigar-shaped electron pockets and the appearance of the hole pocket around Γ are visible in both theory and experiment. That the ARPES measurements show such small changes during the transition to the CDW phase can therefore be understood as stemming mostly from the fact that it is an averaging technique. More subtle changes to the band structure around Γ and the elliptic electron pockets cannot easily be compared by eye. All in all, our theoretical studies match very well to experimental ARPES reports of VSe₂ in the $7 \times \sqrt{3}R30^\circ$ phase^{2,3}.

It must however be noted that most publications on VSe₂ find, in contrast to our prediction, a full gap at the Fermi level^{1,4,6,7}. Monolayer VSe₂, especially in the light of recent works^{12,18,19}, seems to have a strong substrate-dependence. It is therefore likely that our calculation, which is based on freestanding VSe₂, does not capture the intricacies of all experimental systems. At the Fermi surface, an (additional) 4×1 CDW found on some substrates^{1,6,12,19}, might induce

an insulating state. A possible cause for the presence of different and competing CDW orders might be substrate-induced strain²⁰, which is not included in our DFT calculations. [Supplementary Figure 13c](#) shows the Fermi surface and constant-energy contours at higher binding energies of a VSe₂ system where the Fermi surface is fully gapped at 25 K, taken from Ref. 7. In this case, though our calculation in [Supplementary Figure 13d](#) does not predict the fully gapped surface, we see that it captures the features of the band structure away from the Fermi level quite well. The dissimilarities between VSe₂ systems with different CDW orders might therefore pertain mostly to the Fermi surface and the unoccupied states.

References

1. Duvjir, G. *et al.* Emergence of a metal–insulator transition and high-temperature charge-density waves in VSe₂ at the monolayer limit. *Nano Lett.* **18**, 5432 (2018). URL <https://doi.org/10.1021/acs.nanolett.8b01764>.
2. Chen, P. *et al.* Unique gap structure and symmetry of the charge density wave in single-layer VSe₂. *Phys. Rev. Lett.* **121**, 196402 (2018). URL <https://doi.org/10.1103/PhysRevLett.121.196402>.
3. Coelho, P. M. *et al.* Charge density wave state suppresses ferromagnetic ordering in VSe₂ monolayers. *J. Phys. Chem. C* **123**, 14089 (2019). URL <https://doi.org/10.1021/acs.jpcc.9b04281>.
4. Wong, P. K. J. *et al.* Evidence of spin frustration in a vanadium diselenide monolayer magnet. *Adv. Mater.* **31**, 1901185 (2019). URL <https://doi.org/10.1002/adma.201901185>.
5. Bonilla, M. *et al.* Strong room-temperature ferromagnetism in VSe₂ monolayers on van der Waals substrates. *Nat. Nanotechnol.* **13**, 289 (2018). URL <https://doi.org/10.1038/s41565-018-0063-9>.
6. Chua, R. *et al.* Can reconstructed Se-deficient line defects in monolayer VSe₂ induce magnetism? *Adv. Mater.* **32**, 2000693 (2020). URL <https://doi.org/10.1002/adma.202000693>.
7. Feng, J. *et al.* Electronic structure and enhanced charge-density wave order of monolayer VSe₂. *Nano Lett.* **18**, 4493 (2018). URL <https://doi.org/10.1021/acs.nanolett.8b01649>.
8. Nomura, Y. & Arita, R. Ab initio downfolding for electron-phonon-coupled systems: Constrained density-functional perturbation theory. *Phys. Rev. B* **92**, 245108 (2015). URL <https://doi.org/10.1103/PhysRevB.92.245108>.
9. Berges, J., van Loon, E. G. C. P., Schobert, A., Rösner, M. & Wehling, T. O. Ab initio phonon self-energies and fluctuation diagnostics of phonon anomalies: Lattice instabilities from Dirac pseudospin physics in transition metal dichalcogenides. *Phys. Rev. B* **101**, 155107 (2020). URL <https://doi.org/10.1103/PhysRevB.101.155107>.
10. Giustino, F., Cohen, M. L. & Louie, S. G. Electron-phonon interaction using Wannier functions. *Phys. Rev. B* **76**, 165108 (2007). URL <https://doi.org/10.1103/PhysRevB.76.165108>.
11. Poncé, S., Margine, E., Verdi, C. & Giustino, F. EPW: Electron–phonon coupling, transport and superconducting properties using maximally localized Wannier functions. *Comput. Phys. Commun.* **209**, 116 (2016). URL <https://doi.org/10.1016/j.cpc.2016.07.028>.

12. Chua, R. *et al.* Coexisting charge-ordered states with distinct driving mechanisms in monolayer VSe₂ (2021). URL <https://arxiv.org/abs/2104.12420>.
13. Williams, P. M. Phase transitions and charge density waves in the layered transition metal dichalcogenides. In Lévy, F. (ed.) *Crystallography and Crystal Chemistry of Materials with Layered Structures* (Reidel, Dordrecht, 1976). URL https://doi.org/10.1007/978-94-010-1433-5_2.
14. Giuliani, G. & Vignale, G. *Quantum Theory of the Electron Liquid* (Cambridge University Press, Cambridge, 2005). URL <https://doi.org/10.1017/CBO9780511619915>.
15. Georges, A., Kotliar, G., Krauth, W. & Rozenberg, M. J. Dynamical mean-field theory of strongly correlated fermion systems and the limit of infinite dimensions. *Rev. Mod. Phys.* **68**, 13 (1996). URL <https://doi.org/10.1103/RevModPhys.68.13>.
16. Qazilbash, M. M. *et al.* Electronic correlations in the iron pnictides. *Nat. Phys.* **5**, 647 (2009). URL <https://doi.org/10.1038/nphys1343>.
17. Ugeda, M. M. *et al.* Characterization of collective ground states in single-layer NbSe₂. *Nat. Phys.* **12**, 92 (2016). URL <https://doi.org/10.1038/nphys3527>.
18. Zong, J. *et al.* Observation of multiple charge density wave phases in epitaxial monolayer 1T-VSe₂ film. *Research Square* (2021). URL <https://doi.org/10.21203/rs.3.rs-498840/v1>.
19. Duvjir, G. *et al.* Multiple charge density wave phases of monolayer VSe₂ manifested by graphene substrates. *Nanotechnology* **32**, 364002 (2021). URL <https://doi.org/10.1088/1361-6528/ac06f3>.
20. Si, J. G. *et al.* Origin of the multiple charge density wave order in 1T-VSe₂. *Phys. Rev. B* **101**, 235405 (2020). URL <https://doi.org/10.1103/PhysRevB.101.235405>.

CHAPTER 5

Manuscript [2]: Novel 2D vanadium sulphides: synthesis, atomic structure engineering and charge density waves

This chapter wholly consists of the above-named manuscript, which is under review at ACS Nano, available online on arXiv.

The experiments were proposed by C. van Efferen, J. Hall and T. Michely. Sample growth and STM measurements were conducted at the TUMAIL, TSTM, MSTM systems in Cologne as well as the STM system at the MAX IV Laboratory in Lund. The growth procedure of the samples at TUMAIL was developed by J. Hall. The growth parameters were adapted for use in the other systems by C. van Efferen, W. Jolie and J. Fischer. Room temperature STM measurements were carried out by J. Hall, with assistance from T. Wekking at TUMAIL; 300–4 K STM measurements were performed by C. van Efferen and W. Jolie at TSTM and MSTM; room temperature and 110 K STM measurements were performed by N. Vinogradov in Lund. The XPS measurements were conducted by C. van Efferen, V. Boix, J. Fischer and T. Michely, with support from J. Knudsen and A. Preobrajenski. Analysis of STM data was performed by C. van Efferen and J. Hall; the STS data was analysed by C. van Efferen and W. Jolie. The interpretation of the results was discussed in depth by C. van Efferen, J. Fischer, W. Jolie, J. Knudsen and T. Michely. C. van Efferen wrote the manuscript, with advice and corrections from T. Michely.

Novel 2D vanadium sulphides: synthesis, atomic structure engineering and charge density waves

Camiel van Efferen,^{*,†} Joshua Hall,[†] Virgínia Boix,[‡] Tobias Wekking,[†] Nikolay Vinogradov,[¶] Alexei Preobrajenski,[¶] Jan Knudsen,[‡] Jeison Fischer,[†] Wouter Jolie,[†] and Thomas Michely[†]

[†]*II. Physikalisches Institut, Universität zu Köln, Zùlpicher StraÙe 77, 50937 Köln, Germany*

[‡]*Division of Synchrotron Radiation Research, Department of Physics, Lund University, P.O. Box 118, SE-221 00 Lund, Sweden*

[¶]*MAX IV Laboratory, Lund University, P.O Box 118, SE-221 00 Lund, Sweden*

E-mail: efferen@ph2.uni-koeln.de

Abstract

Two new ultimately thin vanadium rich 2D materials based on VS_2 are created via molecular beam epitaxy and investigated using scanning tunneling microscopy and X-ray photoemission spectroscopy. The controlled synthesis of stoichiometric single-layer VS_2 or either of the two vanadium-rich materials is achieved by varying the sample coverage and the sulphur pressure during annealing. Through annealing of small stoichiometric single-layer VS_2 islands without S pressure, S-vacancies spontaneously order in 1D arrays, giving rise to patterned adsorption. We provide an atomic model of the 1D patterned phase, with a stoichiometry of V_4S_7 . By depositing larger amounts of vanadium and sulphur, which are subsequently annealed in a S-rich atmosphere, self-intercalated ultimately thin V_5S_8 -derived layers are obtained, which host 2×2 V-layers between sheets of VS_2 . We provide atomic models for the thinnest V_5S_8 -derived

structures. Finally, we use scanning tunneling spectroscopy to investigate the charge density wave observed in the 2D V_5S_8 -derived islands.

Atomic structure engineering of two-dimensional (2D) materials in order to tailor their electronic and chemical properties or to create novel phases has been on the forefront of recent research. Various methods to achieve this have been explored, like the introduction of point or line defects¹⁻³, creating horizontal or vertical heterostructures^{4,5}, doping or gating⁶⁻⁹, as well as intercalation of native or foreign atoms between the layers^{10,11}.

The creation of defects has been particularly successful in engineering transition metal dichalcogenides (TMDCs)¹². Chalcogen vacancies alone can be used to dope TMDCs¹³, to develop or enhance a magnetic ground state^{14,15} or to gain increased surface reactivity^{16,17}. Vacancies can be created by extrinsic means like electron-beam irradiation^{13,18}, but can also spontaneously form under suitable conditions through thermal annealing^{15,16}.

Since TMDCs are layered materials, they are also easily intercalated, with additional metal atoms placed between the TMDC sheets¹¹. Intercalated atomic layers have been used to enhance electronic conductivity, induce ferromagnetism, phase transitions or Ising superconductivity in TMDCs¹⁹⁻²³. While these intercalants have been used extensively to intercalate bulk TMDCs^{10,19,21,22}, recently the focus has shifted to bilayer TMDC intercalation, being the thinnest intercalated material^{20,24,25}.

Among TMDCs, vanadium based compounds like VS_2 have attracted substantial theoretical research interest due to their predicted electronically correlated and magnetic ground states when thinned down to a single layer²⁶⁻²⁹. However, due to the lack of a stable bulk polymorph^{30,31}, VS_2 is a particularly challenging material to synthesize as a few-layer system and it was a late addition of the single-layer TMDCs when it was synthesized on Au(111)³² and on quasi-freestanding on Gr/Ir(111), where a $9 \times \sqrt{3}R30^\circ$ charge density wave (CDW) was found³³. Owing to the wealth of experiments performed on VS_2 and its sister compound VSe_2 showing the absence of net magnetic moment in these materials, it is commonly accepted that the theoretically predicted ferromagnetic ground state²⁶⁻²⁹ is not realized in pristine

single-layers of these materials^{15,33,34}.

In contrast, the stable compound V_5S_8 exhibits layer-dependent magnetism, which transforms with decreasing thickness from anti-ferromagnetic to ferromagnetic^{35–37}. These results have so far been limited to samples down to 3 nm thickness since this compound has not yet been realized in its minimum thickness configuration of two VS_2 layers sandwiching a 2×2 V intercalation layer. Transport measurements of bulk V_5S_8 show no increase in the resistivity at low temperatures, suggesting it does not have a CDW^{38,39}, though upon cooling down to 100 K, an anisotropic contraction of V-V bonds was observed using X-ray diffraction⁴⁰. Several studies also note that the magnetic moment of the intercalated V atoms can couple to the itinerant electrons in the VS_2 sheets, leading to a Kondo effect^{41,42}.

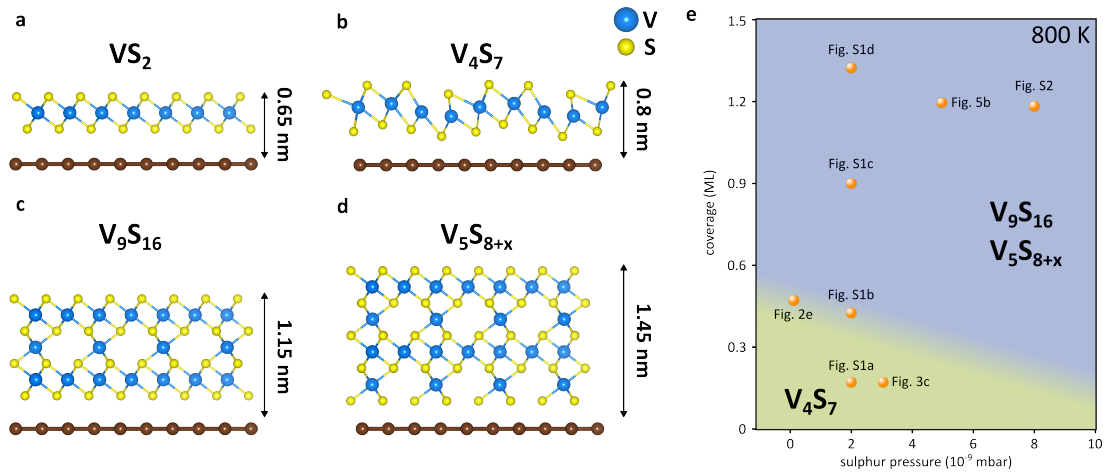


Figure 1: Atomic structures and phase diagram of VS_x compounds. **a-d** Atomic structure models of VS_2 , V_4S_7 , V_9S_{16} and V_5S_{8+x} , respectively. Below the structures, a Gr substrate layer is drawn; besides the images, the apparent height measured with STM is indicated. The suggested structure of V_4S_7 is based on DFT calculations of VSe_2 /HOPG in Ref. 16. For V_5S_{8+x} the actual configuration of the S atoms in the lowest layer is not known. **e** Schematic representation of phases present after annealing temperature of 800 K. With increasing initial coverage and annealing S pressure, the transition of VS_2 into V_4S_7 is suppressed. Instead, a 2×2 self-intercalated material is obtained, with stoichiometry V_9S_{16} or V_5S_{8+x} depending on the number of intercalation layers.

Here we explore two novel 2D vanadium-sulphide compounds, created using a two-step molecular beam epitaxy process. The synthesis consists of an initial growth step at room temperature and an annealing step at elevated temperature to enhance island shape and alignment. Depending on the amount of deposited material during growth, the temperature,

and the S pressure during annealing, three materials of different V:S stoichiometry are obtained. Since V deposition always takes place in large S excess, the deposited amount is characterized through the amount of V deposited - the V atoms stay on the surface, while excess S evaporates. The unit used is monolayer (ML), which characterizes the V amount needed to grow a full single layer of stoichiometric VS_2 , *i.e.* an amount of 1.12×10^{19} V atoms per m^2 . The synthesis is performed in each case on the inert graphene (Gr)/Ir(111) substrate, which preserves the intrinsic properties of the material under investigation^{43,44}.

Single-layer islands of stoichiometric and phase pure VS_2 are obtained when less than 0.5 ML are deposited at room temperature and annealed to a temperature not exceeding 600 K³³. Under these conditions, the resulting single-layer VS_2 is always present in the 1T phase, as depicted in Fig. 1a. When stoichiometric VS_2 is exposed to higher annealing temperatures, it gradually transforms into V_4S_7 , a process that is completed at an annealing temperature of ≈ 800 K. V_4S_7 has periodically arranged rows of S vacancies and an accompanying buckling of the lattice, see Fig. 1b. However, when the initial coverage during growth is larger, specifically when the islands resulting from the initial growth carry second layer islands of significant size, a different compound is formed upon annealing. It consists of layers of VS_2 self-intercalated with V atoms in a 2×2 pattern. The bulk stoichiometry of this phase would be V_5S_8 , which has a NiAs structure with ordered V vacancies every second layer (leaving a quarter of the V atoms to form the 2×2)⁴⁵. The V:S ratio of bulk V_5S_8 is a limit reached only when the number of layers goes to infinity. We obtain V_5S_8 -derived islands of minimal thickness, consisting of two layers of VS_2 with a 2×2 layer of V atoms intercalated in the van der Waals (vdWs) gap between the layer. Consequently the stoichiometry is V_9S_{16} , see Fig. 1c. We also find evidence for the presence of a doubly intercalated structure. In that case, a second 2×2 layer of V, passivated by S atoms, intercalated in the vdWs gap between the bottom VS_2 sheet and Gr, as depicted in Fig. 1d. We denote this structure as V_5S_{8+x} , since the precise amount of S saturating the V is unknown. To show the different growth regimes in S pressure and coverage needed to obtain either the vacancy row structure V_4S_7 or the 2D derivatives of

V_5S_8 , a schematic representation is shown in Fig. 1e, wherein the structures obtained after room temperature growth and subsequent annealing at a temperature of 800 K are collected.

In this study, the materials shown schematically in Fig 1 are investigated using scanning tunneling microscopy (STM) and X-ray photoemission spectroscopy (XPS). Furthermore, using low-temperature scanning tunneling spectroscopy (STS), a $(\sqrt{3} \times \sqrt{3})R30^\circ$ CDW is found in the 2D V_5S_8 -derived islands, with a transition temperature below 110 K. An overview of our results is given in Table 1.

Table 1: **Overview of VS_x compounds and their synthesis parameters.**

Growth parameters and properties of VS_x compounds				
stoichiometry	VS_2	V_4S_7	V_9S_{16}	V_5S_{8+x}
coverage (ML)	< 0.5	< 0.5	> 0.5	
annealing temperature (K)	≤ 600	≈ 800	≈ 800	
annealing S pressure (mbar)	$0 - 8 \times 10^{-9}$	$0 - 8 \times 10^{-9}$	5×10^{-9}	
purity	phase pure	phase pure	not phase pure, mixed with other V_5S_8 -derived structures	not phase pure, dominant with excess V
CDW, T_c	$9 \times \sqrt{3}R30^\circ$, > 300K	none, none	$(\sqrt{3} \times \sqrt{3})R30^\circ$, $\approx 110K$	
structure	T-phase TMDC	S-vacancy rows	2×2 - intercalation, V_5S_8 -derived	
apparent height (nm)	0.65	0.8	1.15	1.45
figure	2d	2f	5b	6d

Results

Creating 1D-patterned V_4S_7 from single-layer VS_2

In Fig. 2a the sample topography directly after growth at room temperature is shown. Dendritic first layer islands of 0.65 nm apparent height are visible, covered by small second

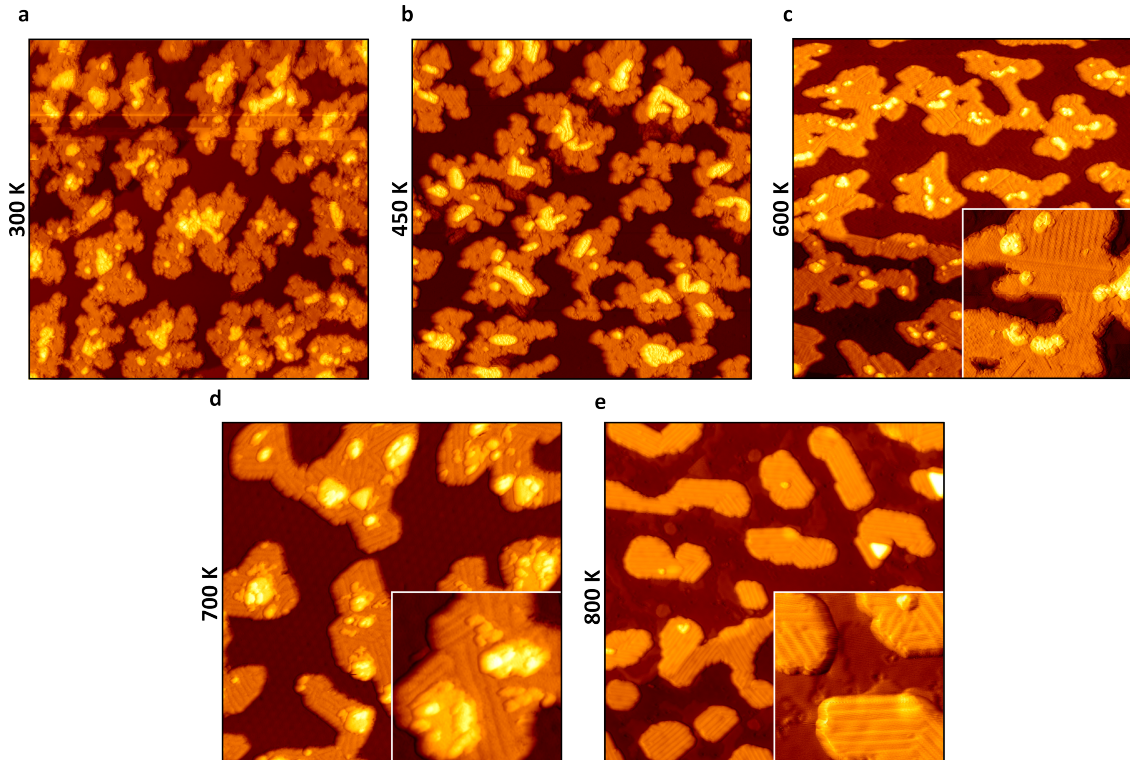


Figure 2: **Evolution of stoichiometric VS_2 with temperature.** **a** STM topograph of VS_2 islands directly after growth at 300 K. **b-e** STM topographs after annealing to the indicated temperatures. The insets in **c-e** are close-ups of the topographs, highlighting the different superstructures. All annealing was performed without S background pressure. Images taken at 300 K. Image information (image size, sample bias, tunneling current): main panels $80 \times 80 \text{ nm}^2$, inset $20 \times 20 \text{ nm}^2$. **a** -1.0 V , 210 pA ; **b** -1.0 V , 90 pA ; **c** -1.0 V , 100 pA , inset: -0.7 V , 550 pA ; **d** -1.2 V , 110 pA , inset: -1.2 V , 110 pA ; **e** -1.3 V , 10 pA , inset: -1.3 V , 10 pA .

layer islands. After annealing in vacuum to 450 K, see Fig. 2b, the single-layer islands are less rough, but dendritic shapes are still prevalent. After annealing to 600 K, in Fig. 2c, the islands are more compact with smoother edges. A superstructure, identified in previous work as a unidirectional charge density wave with an approximate unit cell of $9 \times \sqrt{3}R30^\circ$ ³³, covers all but the smallest regions of the islands. The CDW appears only after annealing to 600 K, as its formation requires sufficiently large islands of stoichiometric VS₂. The instability of the CDW on small islands of VS₂ has been documented in previous work³³.

Further annealing to 700 K, see Fig. 2d, leads to the dominant presence of a new type of striped superstructure (note that already at 600 K some stripes are present, compare Fig. 2c). The dark stripes have non-uniform spacing with a minimal width of ≈ 1 nm and several domains of different orientations, as can be seen in the inset. After annealing to 800 K, in Fig. 2e, the VS₂ islands are elongated but compact and display a well-ordered pattern of stripes. The stripes are generally aligned with the island edges and exhibit only three domains, rotated by 120°. The islands have an altered apparent height of 0.8 nm (see Supplementary Fig. 3 for line profiles of the relevant topographies). The area of the islands has decreased - correspondingly, patches of what are presumably S and V atoms intercalated under the Gr are visible. Annealing beyond 800 K leads to the formation of higher structures, discussed below, and elongated crystallites which are not studied in the present manuscript, see Supplementary Fig. 4.

Focussing on the stripe superstructure, Fig. 3a shows an atomically resolved topograph of the surface of a striped single-layer island. In the center of the image, a homogeneous area with evenly spaced stripes is visible. The unit cell is shown as a turquoise box. Its dimensions are (3.4 ± 0.1) Å along its short axis and (10.6 ± 0.1) Å along its long axis. The first number indicates a significant distortion from the original hexagonal lattice with $a_{\text{VS}_2} = 3.21 \pm 0.02$ Å³³. The line profile along the black line shows an apparent height corrugation of about 0.6 Å. Note that the contrast (two bright rows with visible atomic periodicity and a dark row with faint atomic periodicity) is merely one of several STM imaging contrasts. In the bottom left

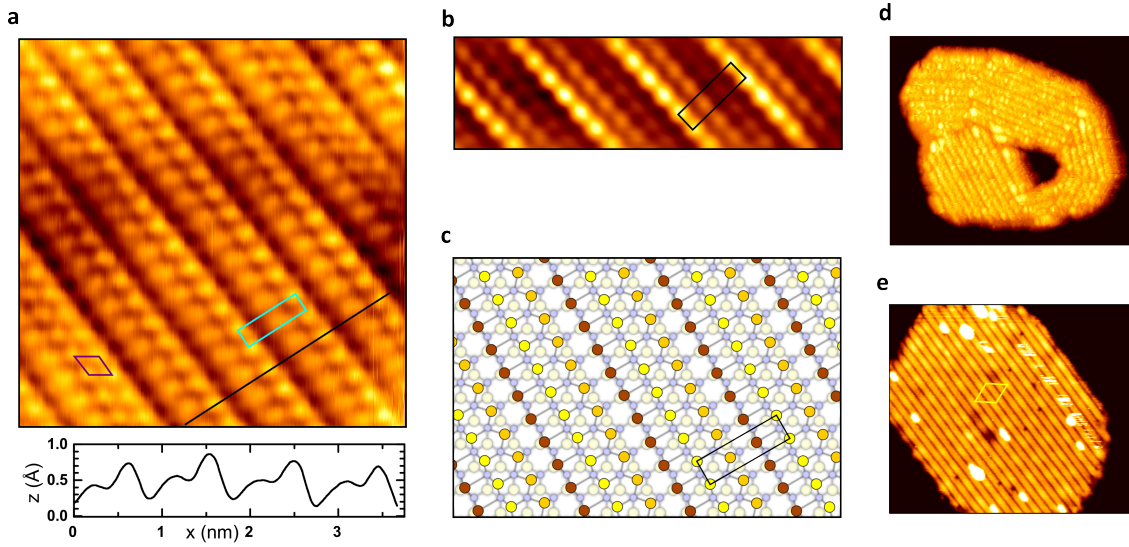


Figure 3: **Reconstruction of VS_2 into V_4S_7 through defect-row formation.** **a** Atomically resolved STM topograph of the stripes of non-uniform width. The unit cells of the hexagonal lattice (purple) and of the dominant striped superstructure (turquoise) are indicated. The black line indicates the position of the line profile at the bottom. **b** High-resolution STM topograph of the striped surface showing three atomic rows. **c** Atomistic model of the reconstructed surface with a faint yellow bottom S layer, blue V layer and intense coloured yellow, orange and brown top S layer. Only the top sulphur layer is reconstructed in this model; the V atom and bottom S plane are generic to the 1T phase. The unit cell is indicated. **d** STM topograph of a V_4S_7 island with dark stripes covered by adsorbates after annealing in S-rich environment to 800 K. **e** STM topograph of island surface after quick heating to 600 K. Most of the adsorbates have desorbed. The yellow rhombus indicates the Gr/Ir(111) moiré unit cell shining through the V_4S_7 island. Images taken at 300 K. Image information (image size, sample bias, tunneling current): **a** $6 \times 6 \text{ nm}^2$, -0.5 V , 1 nA ; **b** $7 \times 2 \text{ nm}^2$, -0.1 V , 0.5 nA ; **c** $35 \times 30 \text{ nm}^2$, -0.5 V , 10 pA ; **d** $30 \times 30 \text{ nm}^2$, -0.3 V , 20 pA .

of the image, a thicker row is visible, where the hexagonal VS₂ lattice can be observed, with its corresponding unit cell (purple rhombus).

Fig. 3b shows a high-resolution STM topograph of a homogeneously striped area, with the rectangular unit cell indicated. Here, the STM contrast allows identification of three rows with atomic periodicity of descending apparent height. Fig. 3c shows a proposed model of this reconstructed surface with the unit cell indicated. In the model, the atoms that form a rectangle are assumed to neighbour a row of S vacancies in the top layer, which leads to the observed symmetry, while the bottom S layer is assumed to be without vacancies. The validity of these assumptions will be discussed below. In this ball model the bottom S layer is assumed to be of a generic 1T structure.

If every fourth S row is removed from the top S layer without any other changes in the bonding distances of the V and lower S layer, one would expect a periodicity of $4 \times a_{\text{VS}_2} \times \sqrt{3}/2 = 1.11$ nm normal to the removed rows. This agrees reasonably well with our measured distance of 1.06 nm. The slightly shortened length is likely due to bond length changes and bond reorganization as a result of the S-row removal. The enhanced corrugation measured by STM indicates that this reorganization involves buckling. With every fourth row of surface S atoms missing, the stoichiometry of this phase amounts to V₄S₇.

Fig. 3d shows the result of annealing V₄S₇ to 800 K in a moderate sulphur background of $P_{\text{sulphur}}^{\text{a}} = 2 \times 10^{-9}$ mbar. Bright stripes of adsorbates are present on the island, with a spacing corresponding to the periodicity of the originally dark stripes. Subsequent annealing largely removes the adsorbates uncovering the dark stripes again, as shown in Fig. 3e. Only some bright adsorbate clusters are left. The moiré of Gr/Ir(111) (marked with a yellow rhombus) becomes apparent again after annealing.

We interpret the situation as follows: upon cooldown from the annealing step, residual S, which is hard to pump out, adheres to the islands. The subsequent brief heating in clean UHV causes desorption of these adsorbed S atoms. Irrespective of the details, the observations imply a modulated reactivity of the V₄S₇ island with a maximum along the dark stripes.

Note that for stoichiometric VS_2 islands such structured adsorption was never observed. Note also the reconstructed island edges in Fig. 3e, with the the stripes causing kinked edges in segments parallel and orthogonal to them. The stripe superstructure being imprinted on the step edge highlights that the structure is not of electronic but of structural origin.

In order to obtain additional information about the effect of annealing stoichiometric VS_2 , we performed high-resolution X-ray photoemission spectroscopy (XPS) of the S 2p core level. Fig. 4a shows the S 2p core-level spectra obtained for samples with increasing annealing temperatures in the absence of S pressure from bottom to top. Spin-orbit coupling of the S 2p level gives rise to an S $2p_{3/2}$ and S $2p_{1/2}$ doublet separated by 1.19(3) eV. At 500 K only a single S 2p doublet is visible, with peaks at 160.83(3) eV and 162.02(3) eV. As the annealing temperature is increased, more doublets become pronounced. In particular, the S 2p peak intensities shift toward higher binding energies. At the highest annealing temperature of 850 K the total intensity of the signal is significantly reduced.

Fitting the XPS spectra across the whole range of annealing temperatures requires five doublets, which will be discussed by reference to the lower binding energy $2p_{3/2}$ peak of the doublet. In Fig. 4b, a single component (160.83(3) eV, yellow) dominates the spectrum, denoted S_{VS_2} . In contrast, the 800 K spectrum in Fig. 4c is made up of multiple doublets of similar intensity. Crucially, two new doublets close to the original yellow component are present at 800 K, which we denote $S_{\text{V}_{4\text{S}7-1}}$ (161.13(3) eV, orange) and $S_{\text{V}_{4\text{S}7-2}}$ (161.47(3) eV, brown). Comparison to the 500 K spectrum furthermore reveals that the dark grey (162.53(3) eV) component S_{S} has disappeared, whereas the silver (162.03(3) eV) component S_{int} is still present and has larger relative intensity.

From STM images we know that at or below 600 K, mainly unperturbed (though defective) single-layer VS_2 islands are present (compare Fig. 2a,b,c). We therefore assign S_{VS_2} to stoichiometric VS_2 . S_{S} , which disappears rapidly when the sample is heated up from room temperature, we assign to sulphur species which react or desorb upon annealing. S_{int} , on the other hand, can be straightforwardly assigned to S atoms intercalated between Gr

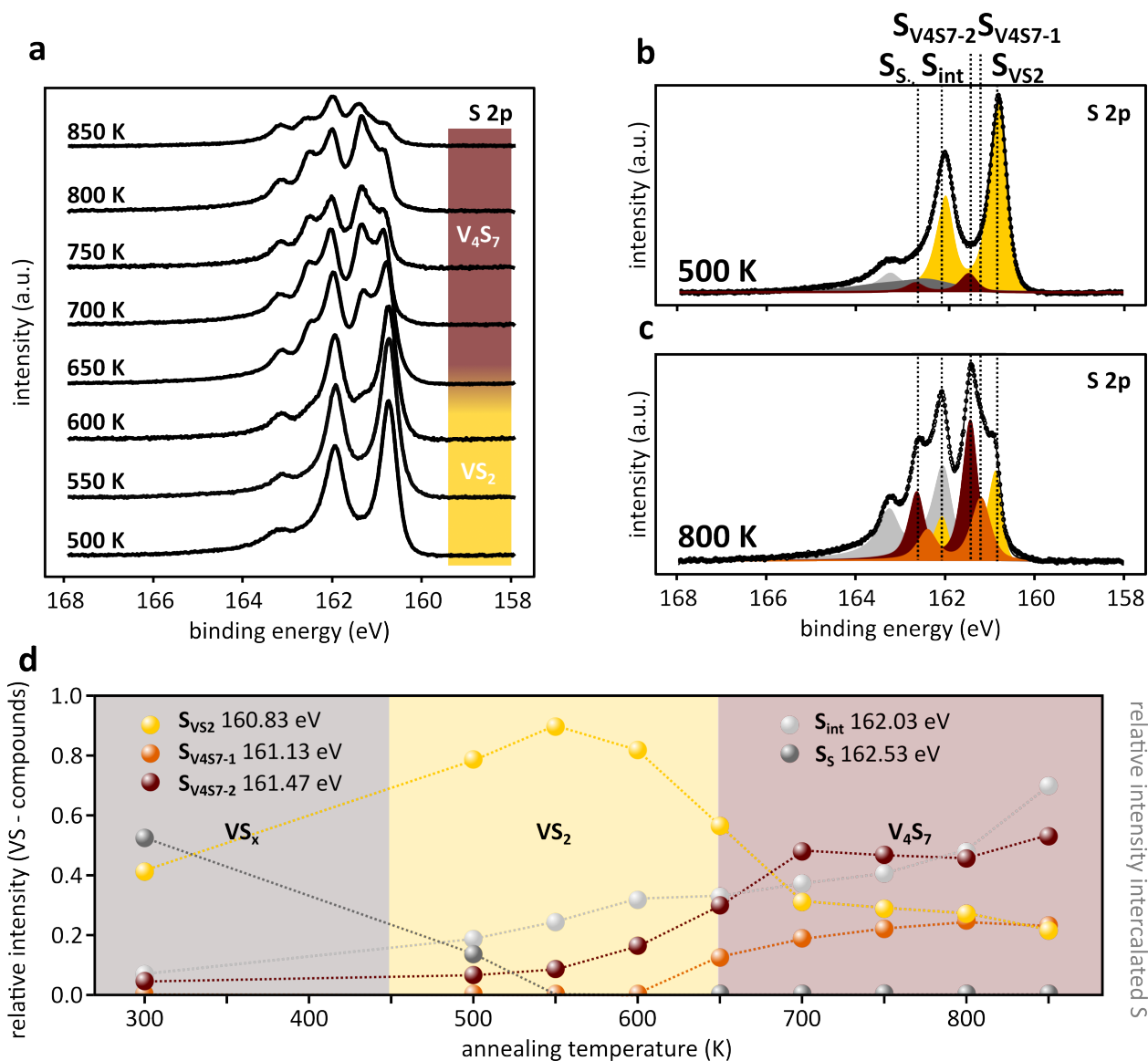


Figure 4: **XPS of single-layer VS_2 .** **a** Temperature resolved X-ray photoemission spectra (XPS) of S $2p_{3/2}$ and S $2p_{1/2}$ core-level spectra of VS_2 measured at a photon energy of $h\nu = 260$ eV. For each successive datapoint the sample was annealed to the indicated temperature without additional S and then measured at 300 K. **b**, **c** XPS spectra of S 2p core-level spectra fitted with 5 components. The fitted components are denoted as S_{VS_2} (yellow), $S_{V_4S_7-1}$ and $S_{V_4S_7-2}$ (orange and brown), S_{int} (silver) and S_S (dark grey), see text for discussion. The data points are represented by black circles and the overall fit by a solid black line. **d** Change of the relative intensities of the fit components during the entire annealing sequence as a function of temperature. Dashed lines to guide the eye. Note that the relative intensity of the intercalated S atoms S_{int} has been plotted on the right y-axis versus the total S signal of the atoms in the vanadium compound.

and Ir(111)⁴⁶. The presence of intercalated S atoms is inferred from STM images (see Supplementary Fig. 5) and low-energy electron diffraction (LEED), an example of which is shown in Fig. 6. The assignment is further based on the presence of this peak at the same location for all samples investigated in this study. Its high binding energy furthermore sets it apart from the peaks intrinsic to the vanadium sulphide compound. $S_{V_4S_7-1}$ and $S_{V_4S_7-2}$ finally, are related to the formation of the striped vacancy row V_4S_7 observed in STM, as these components are present in significant intensity only at higher annealing temperatures.

Plotting the relative intensities of all components against the annealing temperature in Fig. 4d, we can broadly distinguish three stages. At 300 K, stoichiometric VS_2 is coexisting with unreacted sulphur (compare Fig. 2a and Supplementary Fig. 6). Upon annealing to 500 K, the sulphur desorbs from the surface, leaving a sample consisting mainly of stoichiometric VS_2 , with about 90% of the vanadium sulphide intensity stemming from the S_{VS_2} component. Above 600 K, the sample undergoes a transition to V_4S_7 , with $S_{V_4S_7-1}$ and $S_{V_4S_7-2}$ becoming prominent with a ratio that tends to 1 : 2. Because of this ratio, we assign $S_{V_4S_7-2}$ to the two S atom rows that neighbour a missing S row (orange and brown atoms in Fig. 3c), and $S_{V_4S_7-1}$ to the other S atom row, which is not directly next to a missing S row (yellow atoms in Fig. 3c), see Supplementary Fig. 7. While S_{VS_2} is reduced in intensity and shifts to a slightly higher binding energy by ≈ 100 meV when the sample is annealed, it remains present up to 800 K, when the sample surface uniformly exhibits the striped superstructure. We infer that this signal stems from the bottom S atoms, which are in a chemical environment not too different to that of pristine VS_2 . At higher annealing temperatures, the S detached from VS_2 intercalates below Gr, which can be seen in Fig. 2e, leading to the strong increase in the relative intensity of the S_{int} component.

In conclusion, we interpret V_4S_7 to emerge gradually with increasing annealing temperature through loss of sulphur from the initial VS_2 islands and an accompanying reconstruction of the atomic lattice (compare Figs. 2c-e). At about 800 K, the density of the vacancy rows has reached a saturation, resulting in uniform V_4S_7 characterized by every fourth sulphur

top layer row missing. The XPS spectra, which show the appearance of new S 2p doublets at considerably higher binding energies, support this interpretation. In particular, two new S 2p components indicate that most of the top layer S atoms are in a different chemical environment compared to pristine VS_2 , which makes a different stoichiometry likely. The loss in S is accompanied with a substantial lattice reconstruction, also consistent with the reshaping of the islands, which reflect the vacancy row periodicity.

A sulphur depleted single-layer of V_4S_7 is in line with recent findings of similar chalcogen deficient single-layer phases in $\text{VS}_2/\text{Au}(111)$ ³² and VSe_2/HOPG ¹⁶. The latter in particular can be regarded as analogous to V_4S_7 , with periodically ordered rows of Se vacancies formed by removal of every fourth Se row. In STM and density-functional calculations, the authors of that study observe a distortion of the hexagonal lattice and buckling of the layer similar to the present case¹⁶.

The formation of chalcogen vacancy rows or line defects due to annealing, electron or laser beam irradiation seems a general feature in TMDCs⁴⁷⁻⁵⁰. In the case of single-layer VSe_2 , annealing-induced Se-vacancy rows were used to lift the spin-frustration of the material, leading to room-temperature ferromagnetism¹⁵. Since the CDW ground state responsible for the magnetic frustration⁵¹ is very similar in both stoichiometric single-layers of VS_2 and VSe_2 , it would be of great interest to track the effect of annealing VS_2 on its magnetic properties. In contrast to VSe_2 however, where it is possible to transform the patterned state back to stoichiometric VSe_2 *via* low-temperature annealing after deposition of Se atoms^{15,16}, low-temperature annealing in sulphur vapour did not recreate stoichiometric VS_2 from V_4S_7 . Depending on the coverage of the sample, either adsorbed S atoms on top of the patterned material were observed, depicted in Fig. 3d, or - in the case of larger coverage - higher structures were obtained, which will be discussed below.

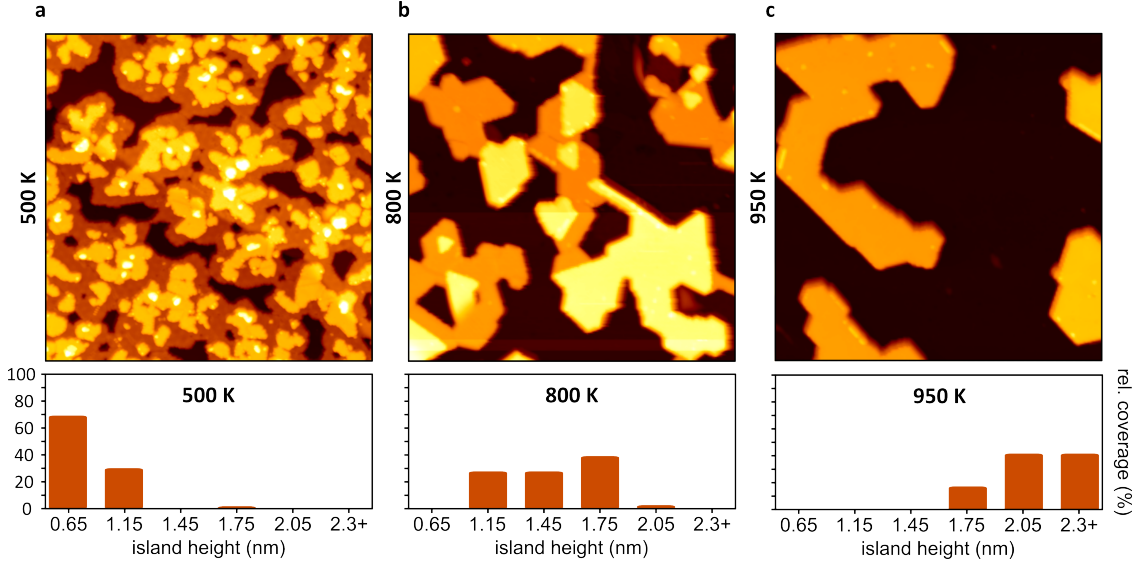


Figure 5: **Evolution of multiheight VS_x with temperature.** **a** STM topograph after deposition of ≈ 1.2 ML, annealed at 550 K in a S-rich atmosphere. **b** STM topograph after annealing to 800 K. **c** STM topograph after annealing to 950 K. Below the STM topographs in **a-c**, histograms of the relative coverage of islands of different apparent heights is shown. Images taken at 4–7 K.

STM parameters: **a-c** $80 \times 80 \text{ nm}^2$, **a** 1.0 V, 50 pA, **b** -1.0 V, 50 pA, **c** 1.0 V, 100 pA.

Self-intercalation of V atoms in multilayer VS_2

Instead of single-layer VS_2 or V_4S_7 , we can selectively grow a new 2D material by changing the growth conditions to favor higher structures. Already during growth at 300 K multilayer structures form (see Fig. 2a). As we deposit more material, a substantial fraction of the material will grow on top of single-layer VS_2 . When we then anneal in S-rich environment to about 800 K, structures with several height levels are created, which do not manifest S vacancies in their top layer.

In Fig. 5a-c the evolution of such a sample is depicted. After annealing ≈ 1.2 ML of VS_x to 550 K, the apparent height distribution shows the 0.65 nm apparent height characteristic for single-layer VS_2 , a significant area fraction of 1.15 nm height and some small areas of 1.75 nm apparent height, as shown in Fig. 5a. Annealing the sample to 800 K leads to a transformation of island shapes and apparent heights, shown in Fig. 5b. The island edges are straight, largely aligned to the dense packed directions of Gr. In addition, two new island apparent heights appear (1.45 nm and 2.05 nm), both 0.3 nm offset from the higher islands

already present at 550 K. The lowest islands are now 1.15 nm high. No single-layer VS_2 is present on the surface. While the different islands are generally sharply demarcated by step edges from one another, continuous transitions between them are also observed, like in the bottom left of Fig. 5b. These transitions will be discussed below. When the sample is further annealed to 950 K, as shown in Fig. 5c, only islands with apparent heights of 1.75 nm and up are observed. We thus find that as the annealing temperature increases, the island density goes down, while the average apparent island height increases, with island heights separated by ≈ 0.3 nm. The resulting sample cannot be understood as multilayer VS_2 , since the height of each VS_2 layer is ≈ 0.6 nm. We therefore refer to these samples as multiheight VS_x . Our investigation will focus on the lower two levels of 1.15 nm and 1.45 nm apparent height, which will be identified as 2D derivatives of V_5S_8 .

In the LEED pattern of the multiheight sample annealed at 800 K, where the apparent minimum island height is 1.15 nm, we find multiple ordered structures, see Fig. 6a. The Gr (black circle) and iridium (green circle) first order spots are visible, surrounded by hardly visible satellite spots from their moiré. Closer to the center, sharp $\sqrt{3} \times \sqrt{3}$ spots with respect to Ir $[(\sqrt{3} \times \sqrt{3})_{\text{Ir}}]$ are present, which stem from S intercalation under Gr. The VS_x spots (orange ellipses) are elongated, indicating a small epitaxial spread in orientation angles, which sets them apart from the perfectly oriented spots of the substrate. Besides the first order VS_x spots, two other sets of spots with the same elongation are visible, which are identified as first and second order spots of a 2×2 superstructure with respect to VS_x . The first order spots indicate a hexagonal symmetry with a lattice parameter of 3.23 ± 0.03 Å. This is close to the lattice parameter of stoichiometric VS_2 (3.21 ± 0.02 Å)^{33,52}. However, the strong 2×2 reflections are characteristic of V_5S_8 , a material of monoclinic symmetry which can be understood as a bulk crystal consisting of sheets of VS_2 with a 2×2 layer of V atoms in between⁴⁵.

An atomically resolved STM topograph, taken at room temperature, of a 1.15 nm high island after annealing to 800 K, depicted in Fig. 6b, shows that the material has preserved

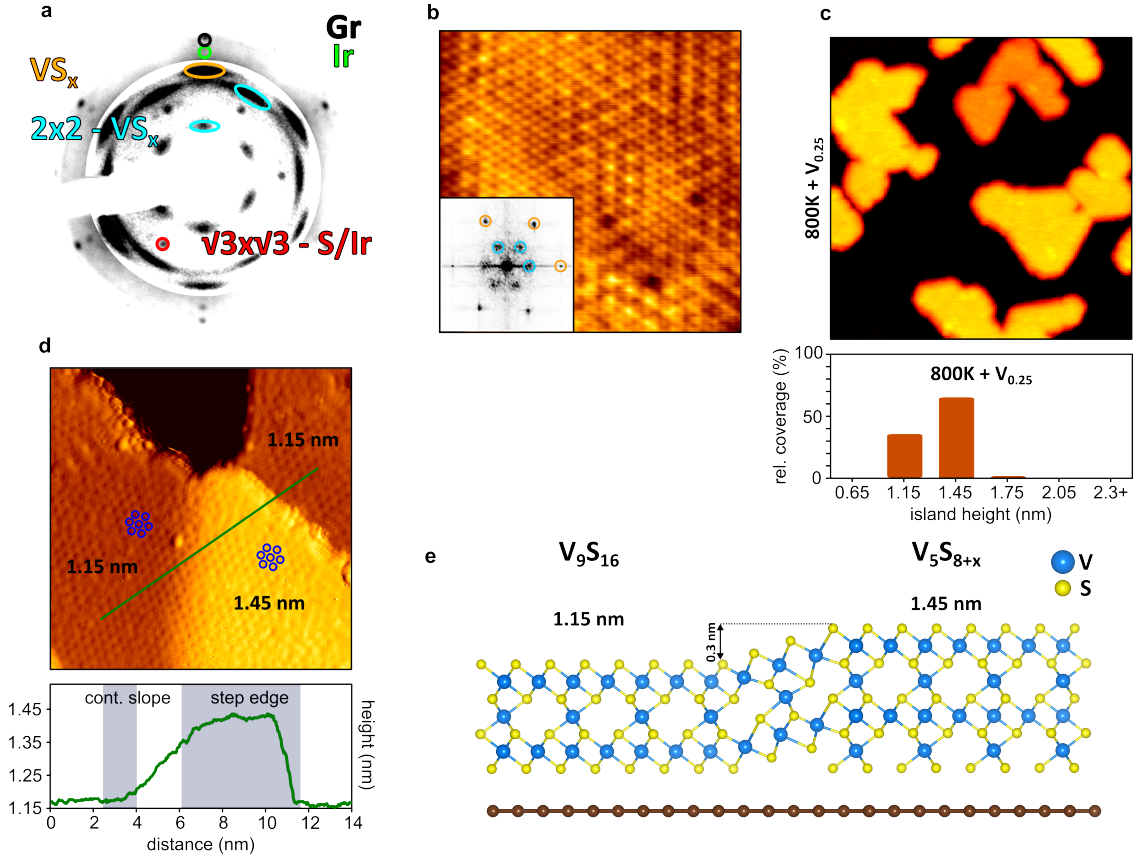


Figure 6: 2×2 self-intercalation in multiheight VS_x . **a** LEED image of VS_x after annealing to 800 K. Some Gr and Ir first order reflections are encircled black and green, respectively. Intercalated S (red) gives rise to a $\sqrt{3} \times \sqrt{3}$ superstructure with respect to Ir. Some first order reflections of VS_x (orange) and reflections of a 2×2 superstructure with respect to VS_x (light blue) are encircled. **b** Room temperature STM topograph of 1.15 nm island, with FFT as inset. A clear 2×2 superstructure is visible on the island. **c** STM topograph of VS_x sample, where 25% additional V atoms were deposited on a sample grown at 300 K and annealed to 500 K. After room temperature V deposition, the sample was subsequently annealed to 800 K in UHV (no S pressure). **d** STM topograph of 1.15 nm and 1.45 nm islands on sample without additional V atoms. A $(\sqrt{3} \times \sqrt{3})R30^\circ$ superstructure is highlighted with blue circles on both islands, see text. Below the topograph, a height profile taken along the green line is shown. **e** Side view of atomic structure model of 1.15 nm and 1.45 nm islands forming a continuous top layer. STM parameters: **b** 300 K, $10 \times 10 \text{ nm}^2$, -1.0 V , 200 pA; **c** 110 K, $80 \times 80 \text{ nm}^2$, 1.5 V , 550 pA; **d** 77 K, $16 \times 16 \text{ nm}^2$, -1.0 V , 200 pA LEED taken with 118 eV. The contrast of the inner part of the LEED image has been enhanced for clarity.

its hexagonal symmetry on the surface - as expected from the LEED pattern. At room temperature and under favorable imaging conditions, along with the atomic lattice, a 2×2 superstructure is visible. The superstructure is slightly disordered. This is evident also in the fast Fourier transform (FFT) shown in the inset of Fig. 6b, where the 2×2 spots (green circles) are broader than the atomic lattice spots (yellow circles). The presence of a (2×2) superstructure in STM is consistent with a 2×2 intercalation layer, as expected for V_5S_8 . The fact that it is hard to image and not present on all atomic resolution topographs obtained indicates that the 2×2 does not originate from the top layer, again as expected for an intercalation layer in a V_5S_8 -derived structure.

To confirm that it is straightforward to self-intercalate V into existing layers, we evaporated 25% additional V atoms on an already grown VS_x sample annealed to 500 K. Prior to V deposition, the sample was comparable to the sample shown in Fig. 5a, with uncovered single-layer VS_2 and some islands of 1.15 nm apparent height. The evaporation was performed in UHV, with no additional S added. After deposition, the sample was annealed to 800 K in UHV - so again without the addition of any S. The result is shown in Fig. 6c. Compared to Fig. 5b, which was annealed to the same temperature, the ratio of 1.45 nm islands to 1.15 nm islands has increased and little to no thicker layers have formed. Crucially, no V atoms or clusters are present on top of the islands or the Gr. The V atoms have been incorporated in the islands, changing their stoichiometry. In the LEED of this sample, a clear 2×2 signal can be distinguished, consistent with our interpretation of a 2×2 intercalation structure, see Supplementary Fig. 8.

No structural differences exist between the surfaces of the 1.15 nm and 1.45 nm islands. On the contrary, a continuous transition from one island type to the other is possible, as evinced in Fig. 6d. In the image, an island of 1.45 nm apparent height is seen to continuously transform into the island of 1.15 nm on the right hand side, while a step edge separates it from the 1.15 nm island in the upper left, as seen in the line profile below Fig. 6d. Because of this continuity, we conclude that the structure of the islands is essentially the same.

The thinnest possible form of V_5S_8 consists of two layers of VS_2 intercalated by a single 2×2 sheet of V atoms and has a stoichiometry of V_9S_{16} , see Fig. 1c. The second thinnest 2D V_5S_8 -derivative would then have a second intercalation layer under the lower S atoms. With these structures in mind, we give an atomic model that explains the continuity in Fig. 6e. Since V atoms below the island would be highly reactive, we presume that they are passivated by S atoms. This additional layer of V and S accounts for the 3 \AA apparent height difference between the islands, see in Fig. 6e. The stoichiometry of the thicker island, with two V intercalation layers, is dubbed V_5S_{8-x} , since the exact configuration of the bottom S atoms is not known. $2p_{3/2}$ and S $2p_{1/2}$

Using XPS we investigated the S2p core level of VS_x at different temperatures during an annealing experiment in a S-rich atmosphere corresponding to the STM sequence in Fig. 5. The result is displayed in Fig. 7a. After annealing to 500 K, the S_{VS_2} doublet at 160.83(3) eV and 162.02(3) eV is most prominent in the spectrum, indicating the dominant presence of stoichiometric VS_2 , see Fig. 7b. When the annealing temperature is increased, S_{VS_2} decreases in intensity and a new doublet $S_{V_5S_8}$ appears at the higher binding energy of 161.55(3) eV (brown in Fig. 7c). The total intensity of the signal is reduced significantly. However, unlike the annealing sequence in Fig. 4, where a small coverage of VS_2 was annealed without S pressure, the S_{VS_2} component in Fig. 7 remains dominant up to 800 K. When we fit the spectra, using the same fitting parameters for S_{VS_2} and S_{int} as for the fits of Fig. 4, we find that we obtain a reliable fit for a total of four peaks. Besides $S_{V_5S_8}$, we added a minor dark grey component S_x located at 163.30(10) eV, hardly visible in the spectra and of unknown origin. Additional XP spectra of the sample with extra V atoms, shown in Fig. 6c, can be found in Supplementary Fig. 9.

Tracking the relative intensities of all components in Fig. 7d, it becomes apparent that $S_{V_5S_8}$ is already present at the lowest investigated temperature and grows at the expense of S_{VS_2} , with an onset for the growth between 550–600 K. S_x remains of equal low intensity throughout the annealing process, while S_{int} grows as the annealing temperature is increased.

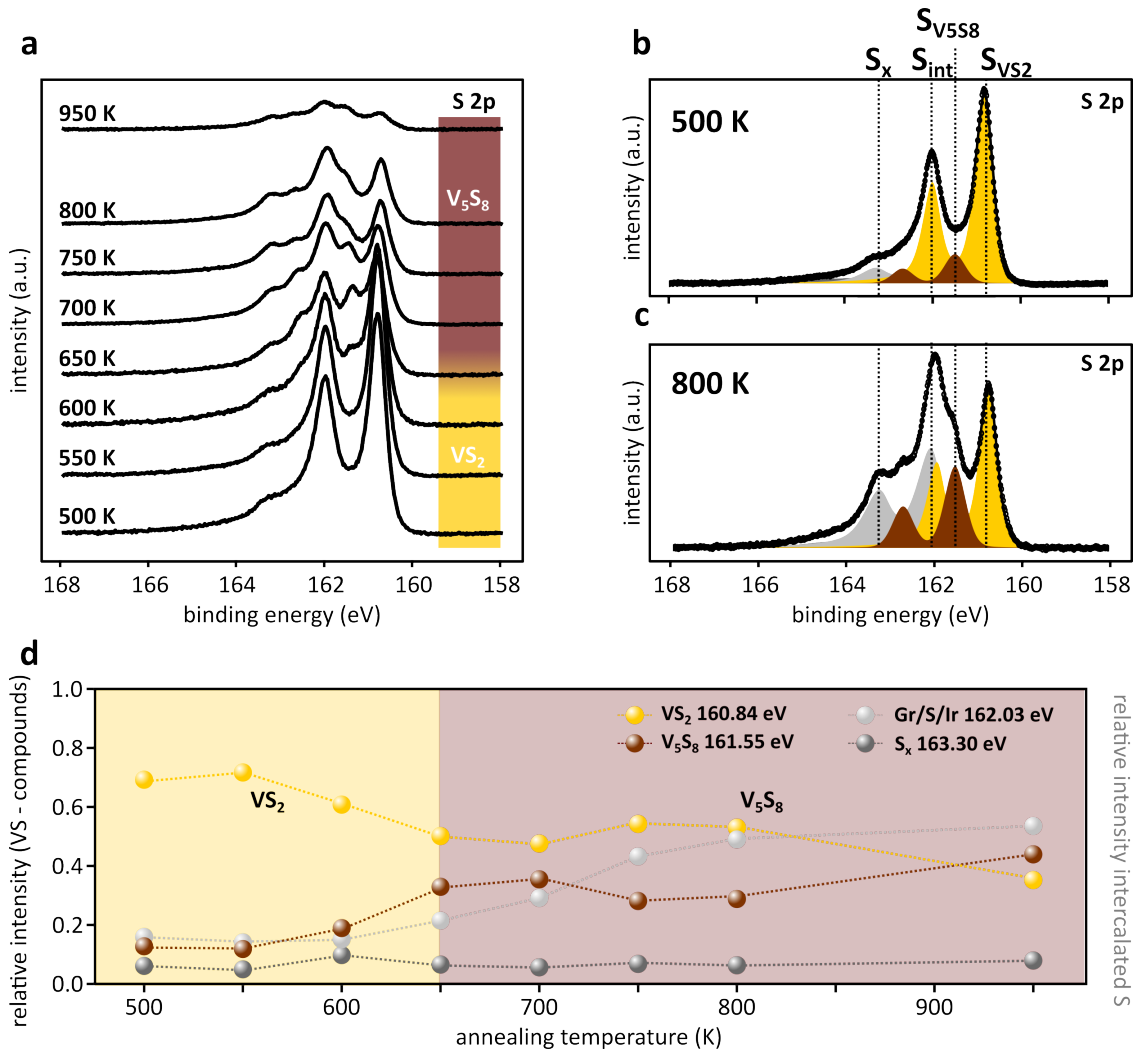


Figure 7: **XPS of multiheight VS_x .** **a,b,c** Temperature resolved X-ray photoemission spectra (XPS) of the S $2p_{3/2}$ and S $2p_{1/2}$ core-levels of VS_2 measured at a photon energy of $h\nu = 260$ eV. For each spectrum, the sample was annealed to the indicated temperature in a S background pressure of 3×10^{-9} mbar and then measured at 300 K. The XPS spectra are fitted with 4 components. The fitted components are S_{VS_2} (yellow), $S_{V_5S_8}$ (brown), S_{int} (silver) and S_x (dark grey), see text for discussion. The data points are represented by black circles and the overall fit by a solid black line. **d** Change of the relative intensities of the fit components as a function of temperature. Dashed lines are present to guide the eye. Note that the relative intensity of the intercalated S atoms S_{int} has been plotted on the right y-axis versus the total S signal of the atoms in the vanadium compound.

We interpret the two characteristic components in V_5S_8 -derived islands to stem from S atoms in two different chemical environments. S atoms bound only to 3 V neighbours as in VS_2 give rise to the S_{VS_2} component, which undergoes a small shift on the order of ≈ 100 meV towards lower binding energies upon intercalation, while S atoms next to the V 2×2 intercalation layer, being bound to more than 3 V, give rise to the $S_{V_5S_8}$ component. Although the 2×2 superstructure in STM and LEED alone could stem from a lattice distortion, the strong shift (≈ 700 meV) in the binding energy of the S atoms from the S_{VS_2} to the $S_{V_5S_8}$ doublet signals a more significant change in the chemical environment of the atoms.

Islands thicker than 1.45 nm are most likely also V_5S_8 -derived. Consequently, the number of S atoms bordering 2×2 -V planes increases upon annealing, causing the $S_{V_5S_8}$ component to rise, while the number of surface S atoms decreases, leading to the decrease of the S_{VS_2} component and the observed shift in relative ratio between the components. Since XPS is a surface sensitive technique, the S_{VS_2} component stemming from the top S atoms will generally outweigh XPS signals of S atoms deeper in the islands, which explains the dominant presence of S_{VS_2} even when most islands have one or more intercalation layers. We also cannot exclude the presence of (unintercalated/partially intercalated) vdWs gaps in the thicker islands. Their precise analysis lies beyond the scope of the manuscript.

Concerning the other components, the comparatively small increase in the relative intensity of S_{int} , compared to the increase of the same component in the XPS of single-layer VS_2 , is probably due to the presence of S-intercalation already after annealing at 500 K, since all annealing steps were performed in a S-rich environment (note the high intensity of the S intercalation spots in the LEED of Fig. 6a). The increase in the intensity of S_{int} is thus a measure of the reduced surface area of the islands, exposing more of the Gr. The S_x component has little weight and its origin cannot be uniquely determined. It could stem from adsorbed S, since it has a similarly high binding energy as the S_S component in the monolayer.

To summarize at this point, we interpret the islands formed when annealing a large (> 1 ML) deposited amount of VS_x in a S background pressure as being V_5S_8 -derived. This is indicated by the simultaneous presence of a 2×2 superstructure in LEED and STM and the new $S_{V_5S_8}$ component in the S 2p XPS spectra, with a binding energy 700 meV higher than S_{VS_2} . We are able to create a more pure minimal-thickness V_5S_8 sample *via* the evaporation of extra V atoms on a multiheight sample annealed to 500 K, and then annealing it to 800 K, as depicted in Fig. 6c.

We note finally that in similar fashion V_5Se_8 was previously procured from seed layers of VSe_2 during thin film growth⁵³, or by increasing the substrate temperature during growth or annealing of single-layer VSe_2 ^{54,55}. In a similar vein, the chemical vapor deposition growth of VS_2 nanosheets generally leads to the simultaneous presence of VS_2 and V_5S_8 ^{56,57}. In each case, the small differences in formation energy between the self-intercalated material and the TMDC are emphasized. Here, we showed that providing extra V atoms after an initial growth step can help to favor one phase over the other and enables one to grow phase pure ultrathin V_5S_8 -derived material down to the minimal thickness of 1.15 nm. These minimal thickness islands with a stoichiometry of V_9S_{16} can be considered as single layers of a new 2D material.

$(\sqrt{3} \times \sqrt{3})R30^\circ$ CDW in ultimately thin V_5S_8 -derived islands

When we cool down the multiheight sample, we find that the islands of 1.15 nm and 1.45 nm apparent height undergo a structural phase transition. In both island types, a pronounced superstructure with a periodicity of $5.5 \pm 0.1 \text{ \AA} = \sqrt{3}a_{VS_2}$ is observed in topography at temperatures ≤ 77 K. This superstructure can already be seen clearly in Fig. 6d, where the $(\sqrt{3} \times \sqrt{3})R30^\circ$ superstructure maxima are encircled in blue (see also Supplementary Fig. 10).

Upon heating the sample from 7 K back to room temperature, the $(\sqrt{3} \times \sqrt{3})R30^\circ$ superstructure vanishes and the atomic lattice becomes visible. As a measure of the strength of the superstructure, we take the relative peak intensity of the 1×1 Bragg peaks with respect

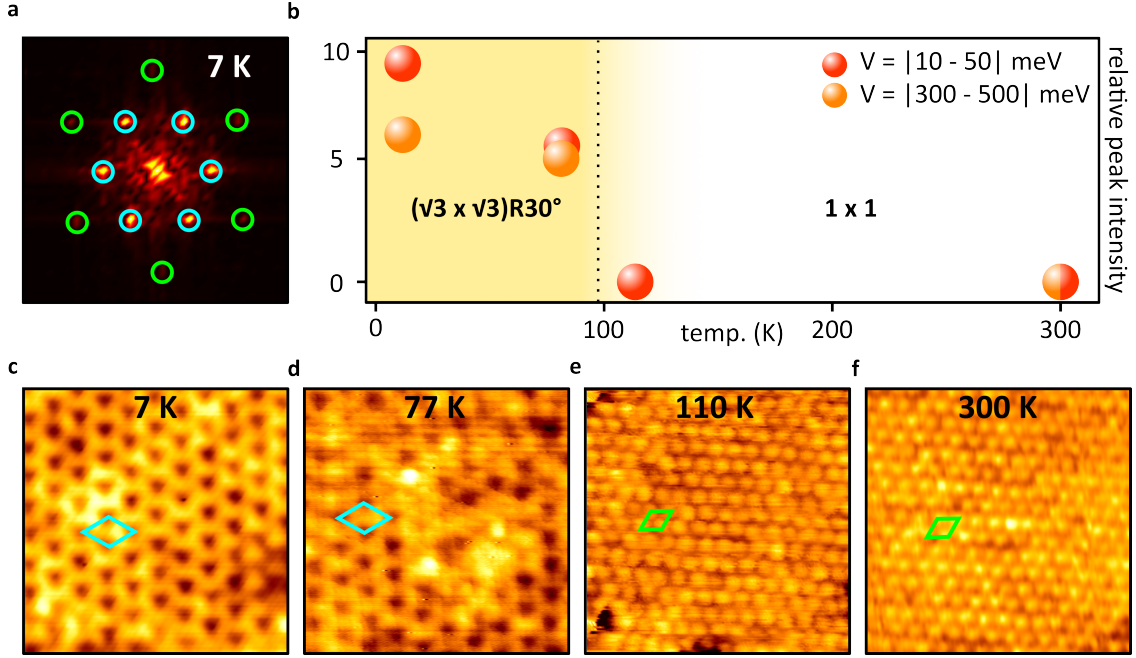


Figure 8: $(\sqrt{3} \times \sqrt{3})R30^\circ$ CDW transition in thin V_5S_8 -derived islands. **a** FFT of 1.15 nm V_9S_{16} island taken at 7 K, with the superstructure spots stemming from the $(\sqrt{3} \times \sqrt{3})R30^\circ$ and atomic lattice encircled in cyan and green, respectively. **b** Temperature dependence of $(\sqrt{3} \times \sqrt{3})R30^\circ$ CDW in V_9S_{16} . Thermal evolution of intensities of CDW peaks normalized to intensities of Bragg peaks, from FFTs of $5 \times 5 \text{ nm}^2$ STM topographs of 1.15 nm (V_9S_{16}) and 1.45 nm high (V_5S_{8+x}) islands. **c-f** Selected topographs at each temperature used in **a**, with the unit cells of the $(\sqrt{3} \times \sqrt{3})R30^\circ$ (cyan) and the atomic lattice (green) indicated. The STM topographies used for the analysis were taken both close to the Fermi level ($|10 - 50| \text{ meV}$) and far from it ($|300 - 500| \text{ meV}$), to make certain that the disappearance is not an artefact stemming from different tunneling conditions. STM/STS parameters: **c-f** All topographs $5 \times 5 \text{ nm}^2$; **c** -0.5 V , 50 pA ; **d** -0.5 V , 200 pA ; **e** 0.014 V , 500 pA ; **f** 0.010 V , 3 nA .

to that of the $(\sqrt{3} \times \sqrt{3})R30^\circ$ peaks⁵⁸. In the 7 K FFT shown in Fig 8a, these are encircled in green and cyan, respectively. Plotting the relative intensities for FFTs obtained at different temperatures in Fig 8b, the $(\sqrt{3} \times \sqrt{3})R30^\circ$ can be seen to disappear between 77 K and 110 K (see Supplementary Fig. 11 for all topographies and FFTs). Some representative topographies are shown Fig 8c-f, which make clear that the atomic lattice is recovered at 110 K. From the strong temperature dependence of the $(\sqrt{3} \times \sqrt{3})R30^\circ$ superstructure, we conclude that it is likely a charge density wave. This CDW is not to be confused with the one that develops in single-layer VS_2 , which is unidirectional and has a much higher transition temperature³³, see Table 1 for the differences.

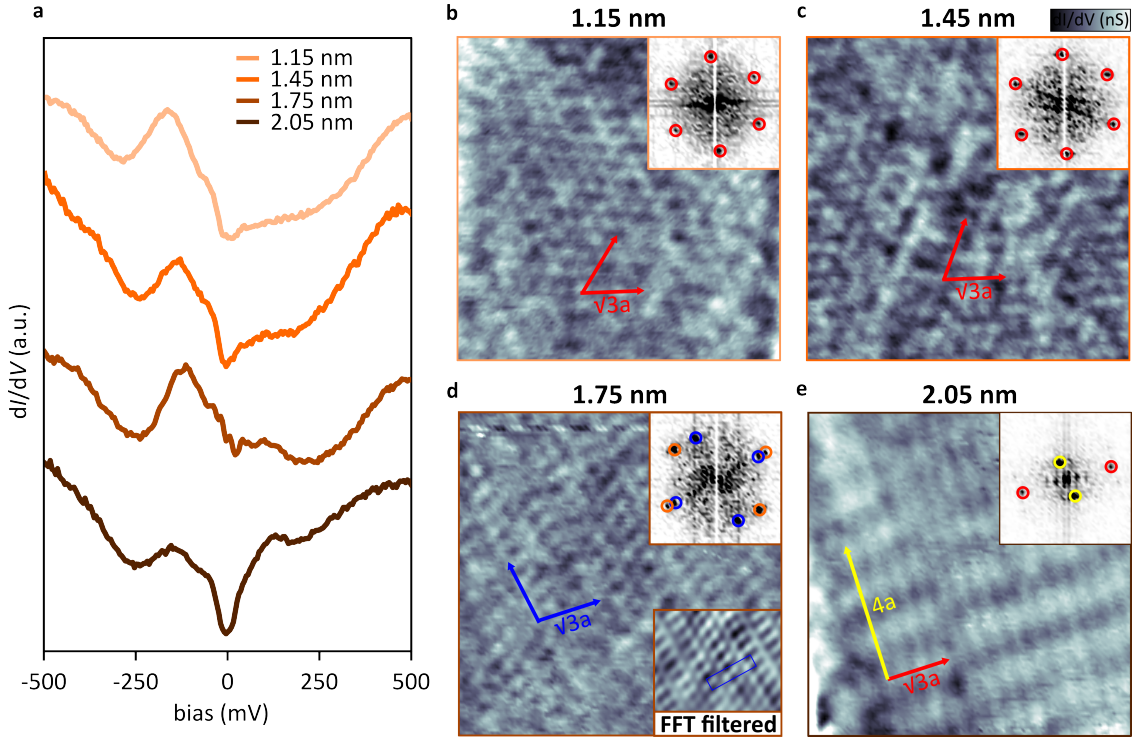


Figure 9: **Multiple CDW orders in V_5S_8 -derived islands.** **a** dI/dV spectra of islands of different apparent heights. **b-e** Constant-current dI/dV maps of different islands, all taken with $V_{\text{set}} = -0.5$ V. The insets show FFTs of the images. Note that the FFTs only display the superstructure, no atomic spots are present. The superstructure spots are encircled for emphasis. In the images, arrows are drawn to indicate the direction of particular periodicities. Each arrow has the size of three wavelengths of the corresponding structure. STM/STS parameters: **a** $V_{\text{stab}} = -500$ mV, $I_{\text{stab}} = 250$ pA; **b-e** 9×9 nm², -0.5 V, 100 pA. STS taken with $f_{\text{mod}} = 871$ Hz and $V_{\text{mod}} = 5$ mV. Maps obtained at 7 K.

Finally, turning towards the electronic structure of the multiheight islands, we see in

Fig. 9a that, in contrast to ML VS_2 , which hosts a CDW with a full gap above the Fermi level E_F ³³, dI/dV spectra taken on the thinnest V_5S_8 -derived islands (1.15 nm and 1.45 nm) show a partial gap around E_F , while a large density of states (DOS) peak is observed below E_F . Comparing dI/dV spectra of islands of different apparent heights, taken with the same tip, we see essentially no differences between islands of 1.15 nm and 1.45 nm apparent height, which is in line with the fact that both have the same $(\sqrt{3} \times \sqrt{3})R30^\circ$ CDW.

Islands of 1.75 nm, however, have a spectrum with no clear gap around E_F and instead a depression around 250 meV. At 2.05 nm apparent height, yet another spectrum is obtained, which lacks the large DOS below E_F that characterizes the other spectra and instead displays a more symmetric distribution of states on either side of E_F .

dI/dV maps taken on the islands at 7 K, as shown in Fig. 9b-e, reveal that these differences in electronic structure are accompanied by the presence of different CDWs. Note that all maps shown are taken at the same bias voltage $V_{\text{set}} = -0.5$ meV, with the same tip, see Supplementary Fig. 12 for an overview STM image showing all investigated islands. While the two lower islands both show the aforementioned $(\sqrt{3} \times \sqrt{3})R30^\circ$, the lattice symmetry is broken in the higher islands, which exhibit striped superstructures. Upon closer inspection, the 1.75 nm superstructure can be understood as a $(\sqrt{3} \times \sqrt{3})R30^\circ$ structure, together with dimerization along one of the high-symmetry directions of the lattice, which is highlighted in the inset Figs. 9d. The dimerization breaks the symmetry and leads to a distortion of the $\sqrt{3}a$ FFT spots. The superstructure of the 2.05 nm island shown in Fig. 9e, on the other hand, can be readily decomposed into a $\sqrt{3}a$ and a $4a$ component, which are orthogonal to one another.

These differences illustrate the complexity of the system and would require a further and more detailed investigation. However, regardless of the actual composition, this variety of superstructures of slightly differing thickness and stoichiometry is striking. It underscores both the ubiquity of CDWs in low-dimensional vanadium chalcogenides and the metastability of any particular periodicity. It can be seen as an analogue to the case of VSe_2 , which hosts

a plentitude of CDW phases, depending on its substrate and the number of layers⁵⁹⁻⁶³.

With respect to V_5S_8 in particular, the fact that it hosts a CDW when thinned down to its 2D limit could shed new light on the layer-dependence of its magnetism, which changes from anti-ferromagnetic to ferromagnetic when thinned down to 3.2 nm³⁵⁻³⁷. Since bulk V_5S_8 is not known to have a CDW, the interplay between the formation of the $(\sqrt{3} \times \sqrt{3})R30^\circ$ CDW and the magnetic structure would be a compelling subject for further study.

Conclusion

In conclusion, we have grown and investigated two novel 2D vanadium-sulphur compounds: V_4S_7 and V_9S_{16} , the latter being the thinnest possible V_5S_8 -derived material.

V_4S_7 is created from ML VS_2 by the formation of S-defects through annealing without additional sulphur vapor. At an annealing temperature of 800 K, the S defects have spontaneously ordered into a homogeneous array of 1D trenches. We have shown that this 1D pattern templates S adsorption and speculate that also other adsorbates can be templated through the vacancy row pattern.

V_5S_8 -derived islands are obtained automatically when a larger coverage (> 0.5 ML) of VS_x is grown. Second layer nucleation on top of single-layer VS_2 does not occur as bilayer VS_2 ; instead, V atoms intercalate between VS_2 layers in a 2×2 pattern and form V_9S_{16} . Annealing a mixture of single-layer VS_2 and V_9S_{16} in a S-rich atmosphere to 800 K leads to further self-intercalation of V atoms and the creation of a variety of structures of different apparent height. However, when additional V atoms are supplied after growth, phase-pure minimal thickness V_5S_8 -derived material is obtained as a mixture of V_9S_{16} of 1.15 nm thickness and V_5S_{8+x} with 1.45 nm thickness. Using low-temperature STM, these 2D V_5S_8 -derived structures were shown to undergo a CDW transition to a $(\sqrt{3} \times \sqrt{3})R30^\circ$ phase, which develops below 110 K, whereas the thicker islands were found to exhibit different superstructures, presumably all of CDW origin.

Our findings provide a recipe for the growth of two new single-layer vanadium compounds. Given the thickness dependent magnetic and electronic properties of V_5S_8 , having access to its 2D form is of particular interest for the further development of 2D magnetic materials.

Methods

The experiments were conducted in five ultra high vacuum systems (base pressure in the low 10^{-10} mbar range). Three systems were equipped with sample preparation facilities, scanning tunneling microscopy (STM) - operating at base temperatures given in the figure captions - and low energy electron diffraction (LEED). The fourth system was the FlexPES beamline endstation preparation chamber at MAX IV, Laboratory Lund, Sweden. There the samples were grown following the same recipes as in the STM system and sample quality was checked by LEED. The fifth system was an STM-only system, to which samples from FlexPES were transferred with a vacuum suitcase and then measured by STM at room temperature and 110 K.

Ir(111) was cleaned by cycles of noble gas sputtering (4.5 keV Xe^+ at 75° with respect to the surface normal or with 1 keV Ar^+ at normal incidence) and annealing to 1500 K. A closed monolayer of single-crystalline Gr on Ir(111) is grown by room temperature exposure of Ir(111) to ethylene until saturation, subsequent annealing to 1500 K and followed by exposure to 200 L ethylene at 1200 K⁶⁴.

The synthesis of vanadium sulphides on Gr/Ir(111) is based on a two-step molecular beam epitaxy approach introduced in detail in Ref.⁴³ for MoS_2 . In the first step, the sample is held at room temperature and V is evaporated at a rate of $F_V = 2.5 \times 10^{16}$ atoms $m^{-2}s^{-1}$ into a sulphur background pressure of $P_S^g = 5 \times 10^{-9}$ mbar built up by thermal decomposition of pyrite inside a Knudsen cell. In a second step, the sample is annealed to 800 K with or without S pressure.

The XPS experiments were conducted at the FlexPES beamline at MAX IV Laboratory,

Lund, Sweden⁶⁵. The S 2p core levels were measured with a photon energy of 260 eV. The measurements were conducted at room temperature with a spot size of $50 \times 50 \mu\text{m}$. The spectra for each sample were fitted simultaneously for all temperatures with pseudo-Voigt functions. The width, skew and ratio of Gaussian to Lorentzian contributions were fixed for each component, meaning that they were not allowed to vary between spectra taken at different annealing temperatures. The center energy of each component was granted a maximum deviation of $\pm 100 \text{ meV}$ to account for small shifts in the chemical environment between spectra while the intensities (total area) of the components were unconstrained. The fitting was performed with the lmfit module of python, using a basin hopping algorithm.

Acknowledgements

This work was funded by the Deutsche Forschungsgemeinschaft (DFG, German Research foundation) through CRC 1238 (project no. 277146847, subprojects A01 and B06). V.B. and J.K. acknowledge financial support from the Swedish Research Council (grant number 2017-04840). We acknowledge MAX IV Laboratory for time on Beamline FlexPES under Proposal 20210859. Research conducted at MAX IV, a Swedish national user facility, is supported by the Swedish Research council under contract 2018-07152, the Swedish Governmental Agency for Innovation Systems under contract 2018-04969, and Formas under contract 2019-02496.

References

- (1) Ma, Q.; Isarraraz, M.; Wang, C. S.; Preciado, E.; Klee, V.; Bobek, S.; Yamaguchi, K.; Li, E.; Odenthal, P. M.; Nguyen, A. Postgrowth tuning of the bandgap of single-layer molybdenum disulfide films by sulfur/selenium exchange. *ACS Nano* **2014**, *8*, 4672–4677.
- (2) Lin, Y.-C.; Björkman, T.; Komsa, H.-P.; Teng, P.-Y.; Yeh, C.-H.; Huang, F.-S.; Lin, K.-H.; Jadcak, J.; Huang, Y.-S.; Chiu, P.-W.; Krasheninnikov, A. V.; Suenaga, K. Three-

- Fold Rotational Defects in Two-Dimensional Transition Metal Dichalcogenides. *Nat. Commun.* **2015**, *6*, 6736.
- (3) Coelho, P. M.; Komsa, H.-P.; Coy Diaz, H.; Ma, Y.; Krasheninnikov, A. V.; Batzill, M. Post-Synthesis Modifications of Two-Dimensional MoSe₂ or MoTe₂ by Incorporation of Excess Metal Atoms into the Crystal Structure. *ACS Nano* **2018**, *12*, 3975–3984.
- (4) Huang, C.; Wu, S.; Sanchez, A. M.; Peters, J. J. P.; Beanland, R.; Ross, J. S.; Rivera, P.; Yao, W.; Cobden, D. H.; Xu, X. Lateral heterojunctions within monolayer MoSe₂–WSe₂ semiconductors. *Nat. Mater.* **2014**, *13*, 1096–1101.
- (5) Vaňo, V.; Amini, M.; Ganguli, S. C.; Chen, G.; Lado, J. L.; Kezilebieke, S.; Liljeroth, P. Artificial heavy fermions in a van der Waals heterostructure. *Nature* **2021**, *599*, 582–586.
- (6) Lin, Y.-C.; Dumcenco, D. O.; Huang, Y.-S.; Suenaga, K. Atomic mechanism of the semiconducting-to-metallic phase transition in single-layered MoS₂. *Nat. Nanotechnol.* **2014**, *9*, 391–396.
- (7) Sutter, E.; Huang, Y.; Komsa, H.-P.; Ghorbani-Asl, M.; Krasheninnikov, A. V.; Sutter, P. Electron-beam induced transformations of layered tin dichalcogenides. *Nano Lett.* **2016**, *16*, 4410–4416.
- (8) Wang, Y.; Xiao, J.; Zhu, H.; Li, Y.; Alsaied, Y.; Fong, K. Y.; Zhou, Y.; Wang, S.; Shi, W.; Wang, Y. Structural phase transition in monolayer MoTe₂ driven by electrostatic doping. *Nature* **2017**, *550*, 487–491.
- (9) van Efferen, C.; Murray, C.; Fischer, J.; Busse, C.; Komsa, H.-P.; Michely, T.; Jolie, W. Metal-insulator transition in monolayer MoS₂ via contactless chemical doping. *2D Mater.* **2022**, *9*, 25026.
- (10) Friend, R. H.; Yoffe, A. D. Electronic properties of intercalation complexes of the transition metal dichalcogenides. *Adv. Phys.* **1987**, *36*, 1–94.

- (11) Wan, J.; Lacey, S. D.; Dai, J.; Bao, W.; Fuhrer, M. S.; Hu, L. Tuning two-dimensional nanomaterials by intercalation: materials, properties and applications. *Chem. Soc. Rev.* **2016**, *45*, 6742–6765.
- (12) Hu, Z.; Wu, Z.; Han, C.; He, J.; Ni, Z.; Chen, W. Two-dimensional transition metal dichalcogenides: interface and defect engineering. *Chem. Soc. Rev.* **2018**, *47*, 3100–3128.
- (13) Komsa, H.-P.; Kotakoski, J.; Kurasch, S.; Lehtinen, O.; Kaiser, U.; Krasheninnikov, A. V. Two-Dimensional Transition Metal Dichalcogenides under Electron Irradiation: Defect Production and Doping. *Phys. Rev. Lett.* **2012**, *109*, 35503.
- (14) Yu, W. et al. Chemically Exfoliated VSe₂ Monolayers with Room-Temperature Ferromagnetism. *Adv. Mater.* **2019**, *31*, 1903779.
- (15) Chua, R.; Yang, J.; He, X.; Yu, X.; Yu, W.; Bussolotti, F.; Wong, P. K. J.; Loh, K. P.; Breese, M. B. H.; Goh, K. E. J.; Huang, Y. L.; Wee, A. T. S. Can Reconstructed Se-Deficient Line Defects in Monolayer VSe₂ Induce Magnetism? *Adv. Mater.* **2020**, *32*, 2000693.
- (16) Liu, Z.-L.; Lei, B.; Zhu, Z.-L.; Tao, L.; Qi, J.; Bao, D.-L.; Wu, X.; Huang, L.; Zhang, Y.-Y.; Lin, X.; Wang, Y.-L.; Du, S.; Pantelides, S. T.; Gao, H.-J. Spontaneous Formation of 1D Pattern in Monolayer VSe₂ with Dispersive Adsorption of Pt Atoms for HER Catalysis. *Nano Lett.* **2019**, *19*, 4897–4903.
- (17) Wang, X.; Zhang, Y.; Si, H.; Zhang, Q.; Wu, J.; Gao, L.; Wei, X.; Sun, Y.; Liao, Q.; Zhang, Z. Single-atom vacancy defect to trigger high-efficiency hydrogen evolution of MoS₂. *JACS* **2020**, *142*, 4298–4308.
- (18) Lin, J.; Pantelides, S. T.; Zhou, W. Vacancy-Induced Formation and Growth of Inversion Domains in Transition-Metal Dichalcogenide Monolayer. *ACS Nano* **2015**, *9*, 5189–5197.

- (19) Liu, X.-C.; Zhao, S.; Sun, X.; Deng, L.; Zou, X.; Hu, Y.; Wang, Y.-X.; Chu, C.-W.; Li, J.; Wu, J.; Ke, F.-S.; Ajayan, P. M. Spontaneous self-intercalation of copper atoms into transition metal dichalcogenides. *Sci. Adv.* **2023**, *6*, eaay4092.
- (20) Zhao, X. et al. Engineering covalently bonded 2D layered materials by self-intercalation. *Nature* **2020**, *581*, 171–177.
- (21) Wang, X.; Shen, X.; Wang, Z.; Yu, R.; Chen, L. Atomic-scale clarification of structural transition of MoS₂ upon sodium intercalation. *ACS Nano* **2014**, *8*, 11394–11400.
- (22) Tan, S. J. R.; Abdelwahab, I.; Ding, Z.; Zhao, X.; Yang, T.; Loke, G. Z. J.; Lin, H.; Verzhbitskiy, I.; Poh, S. M.; Xu, H. Chemical stabilization of 1T' phase transition metal dichalcogenides with giant optical Kerr nonlinearity. *JACS* **2017**, *139*, 2504–2511.
- (23) Zhang, H. et al. Tailored Ising superconductivity in intercalated bulk NbSe₂. *Nat. Phys.* **2022**, *18*, 1425–1430.
- (24) Kanetani, K.; Sugawara, K.; Sato, T.; Shimizu, R.; Iwaya, K.; Hitosugi, T.; Takahashi, T. Ca intercalated bilayer graphene as a thinnest limit of superconducting C₆Ca. *PNAS* **2012**, *109*, 19610–19613.
- (25) Lasek, K.; Coelho, P. M.; Zborecki, K.; Xin, Y.; Kolekar, S. K.; Li, J.; Batzill, M. Molecular Beam Epitaxy of Transition Metal (Ti-, V-, and Cr-) Tellurides: From Monolayer Ditellurides to Multilayer Self-Intercalation Compounds. *ACS Nano* **2020**, *14*, 8473–8484.
- (26) Ma, Y.; Dai, Y.; Guo, M.; Niu, C.; Zhu, Y.; Huang, B. Evidence of the Existence of Magnetism in Pristine VX₂ Monolayers (X = S, Se) and Their Strain-Induced Tunable Magnetic Properties. *ACS Nano* **2012**, *6*, 1695–1701.
- (27) Zhang, H.; Liu, L.-M.; Lau, W.-M. Dimension-dependent phase transition and magnetic properties of VS₂. *J. Mater. Chem. A* **2013**, *1*, 10821–10828.

- (28) Isaacs, E. B.; Marianetti, C. A. Electronic Correlations in Monolayer VS₂. *Phys. Rev. B* **2016**, *94*, 35120.
- (29) Zhuang, H. L.; Hennig, R. G. Stability and magnetism of strongly correlated single-layer VS₂. *Phys. Rev. B* **2016**, *93*, 54429.
- (30) Mulazzi, M.; Chainani, A.; Katayama, N.; Eguchi, R.; Matsunami, M.; Ohashi, H.; Senba, Y.; Nohara, M.; Uchida, M.; Takagi, H.; Shin, S. Absence of nesting in the charge-density-wave system 1T-VS₂ as seen by photoelectron spectroscopy. *Phys. Rev. B* **2010**, *82*, 75130.
- (31) Gauzzi, A.; Sellam, A.; Rousse, G.; Klein, Y.; Taverna, D.; Giura, P.; Calandra, M.; Loupiaz, G.; Gozzo, F.; Gilioli, E.; Bolzoni, F.; Allodi, G.; De Renzi, R.; Calestani, G. L.; Roy, P. Possible Phase Separation and Weak Localization in the Absence of a Charge-Density Wave in Single-Phase 1T-VS₂. *Phys. Rev. B* **2014**, *89*, 235125.
- (32) Arnold, F. et al. Novel Single-Layer Vanadium Sulphide Phases. *2D Mater.* **2018**, *5*, 045009.
- (33) van Efferen, C. et al. A full gap above the Fermi level: the charge density wave of monolayer VS₂. *Nat. Comm.* **2021**, *12*, 6837.
- (34) Coelho, P. M.; Nguyen Cong, K.; Bonilla, M.; Kolekar, S.; Phan, M.-H.; Avila, J.; Asensio, M. C.; Oleynik, I. I.; Batzill, M. Charge Density Wave State Suppresses Ferromagnetic Ordering in VSe₂ Monolayers. *J. Phys. Chem. C* **2019**, *123*, 14089–14096.
- (35) Hardy, W. J.; Yuan, J.; Guo, H.; Zhou, P.; Lou, J.; Natelson, D. Thickness-Dependent and Magnetic-Field-Driven Suppression of Antiferromagnetic Order in Thin V₅S₈ Single Crystals. *ACS Nano* **2016**, *10*, 5941–5946.

- (36) Niu, J.; Yan, B.; Ji, Q.; Liu, Z.; Li, M.; Gao, P.; Zhang, Y.; Yu, D.; Wu, X. Anomalous Hall effect and magnetic orderings in nanothick V_5S_8 . *Phys. Rev. B* **2017**, *96*, 75402.
- (37) Zhang, R.-Z.; Zhang, Y.-Y.; Du, S.-X. Thickness-dependent magnetic order and phase transition in V_5S_8 . *Chin. Phys. B* **2020**, *29*, 77504.
- (38) Nozaki, H.; Ishizawa, Y.; Saeki, M.; Nakahira, M. Electrical properties of V_5S_8 single crystals. *Phys. Lett. A* **1975**, *54*, 29–30.
- (39) Moutaabbid, H.; Le Godec, Y.; Taverna, D.; Baptiste, B.; Klein, Y.; Loupiau, G.; Gauzzi, A. High-Pressure Control of Vanadium Self-Intercalation and Enhanced Metallic Properties in $1T-V_{1+x}S_2$ Single Crystals. *Inorg. Chem.* **2016**, *55*, 6481–6486.
- (40) Bensch, W.; Koy, J. The single crystal structure of V_5S_8 determined at two different temperatures: anisotropic changes of the metal atom network. *Inorganica Chim. Acta* **1993**, *206*, 221–223.
- (41) Niu, J.; Zhang, W.; Li, Z.; Yang, S.; Yan, D.; Chen, S.; Zhang, Z.; Zhang, Y.; Ren, X.; Gao, P. Intercalation of van der Waals layered materials: A route towards engineering of electron correlation. *Chin. Phys. B* **2020**, *29*, 97104.
- (42) Zhou, Z.; Zhao, X.; Wu, L.; Liu, H.; Chen, J.; Xi, C.; Wang, Z.; Liu, E.; Zhou, W.; Pennycook, S. J. Dimensional crossover in self-intercalated antiferromagnetic V_5S_8 nanoflakes. *Phys. Rev. B* **2022**, *105*, 235433.
- (43) Hall, J.; Pielic, B.; Murray, C.; Jolie, W.; Wekking, T.; Busse, C.; Kralj, M.; Michely, T. Molecular Beam Epitaxy of Quasi-Freestanding Transition Metal Disulphide Monolayers on van der Waals Substrates: A Growth Study. *2D Mater.* **2018**, *5*, 025005.
- (44) Murray, C.; Jolie, W.; Fischer, J. A.; Hall, J.; van Efferen, C.; Ehlen, N.; Grüneis, A.; Busse, C.; Michely, T. Comprehensive Tunneling Spectroscopy of Quasifreestanding MoS_2 on Graphene on Ir(111). *Phys. Rev. B* **2019**, *99*, 115434.

- (45) Kawada, I.; Nakano-Onoda, M.; Ishii, M.; Saeki, M.; Nakahira, M. Crystal structures of V_3S_4 and V_5S_8 . *J. Solid State Chem.* **1975**, *15*, 246–252.
- (46) Pielić, B.; Hall, J.; Despoja, V.; Rakić, I. Š.; Petrović, M.; Sohani, A.; Busse, C.; Michely, T.; Kralj, M. Sulfur Structures on Bare and Graphene-Covered Ir(111). *J. Phys. Chem. C* **2020**, *124*, 6659–6668.
- (47) Komsa, H.-P.; Kurasch, S.; Lehtinen, O.; Kaiser, U.; Krasheninnikov, A. V. From Point to Extended Defects in Two-Dimensional MoS_2 : Evolution of Atomic Structure Under Electron Irradiation. *Phys. Rev. B* **2013**, *88*, 035301.
- (48) Lu, J.; Carvalho, A.; Chan, X. K.; Liu, H.; Liu, B.; Tok, E. S.; Loh, K. P.; Castro Neto, A. H.; Sow, C. H. Atomic Healing of Defects in Transition Metal Dichalcogenides. *Nano Lett.* **2015**, *15*, 3524–3532.
- (49) Elibol, K.; Susi, T.; Argentero, G.; Reza Ahmadpour Monazam, M.; Pennycook, T. J.; Meyer, J. C.; Kotakoski, J. Atomic Structure of Intrinsic and Electron-Irradiation-Induced Defects in $MoTe_2$. *Chem. Mater.* **2018**, *30*, 1230–1238.
- (50) Zhao, X.; Ji, Y.; Chen, J.; Fu, W.; Dan, J.; Liu, Y.; Pennycook, S. J.; Zhou, W.; Loh, K. P. Healing of Planar Defects in 2D Materials via Grain Boundary Sliding. *Adv. Mater.* **2019**, *31*, 1900237.
- (51) Wong, P. K. J. et al. Evidence of Spin Frustration in a Vanadium Diselenide Monolayer Magnet. *Adv. Mater.* **2019**, *31*, 1901185.
- (52) Murphy, D. W.; Cros, C.; Di Salvo, F. J.; Waszczak, J. V. Preparation and Properties of Li_xVS_2 . *Inorg. Chem.* **1977**, *16*, 3027–3031.
- (53) Nakano, M.; Wang, Y.; Yoshida, S.; Matsuoka, H.; Majima, Y.; Ikeda, K.; Hirata, Y.; Takeda, Y.; Wadati, H.; Kohama, Y.; Ohigashi, Y.; Sakano, M.; Ishizaka, K.; Iwasa, Y.

- Intrinsic 2D Ferromagnetism in V_5Se_8 Epitaxial Thin Films. *Nano Lett.* **2019**, *19*, 8806–8810.
- (54) Meng, Q.; Zong, J.; Tian, Q.; Chen, W.; Xie, X.; Yu, F.; Qiu, X.; Wang, K.; Zhang, Y.; Wang, P.; Li, F.-S.; Wang, C.; Zhang, Y. Selectable Growth and Electronic Structures of Monolayer 1T-VSe₂ and V_5Se_8 Films on Bilayer Graphene. *Phys. Status Solidi RRL* **2022**, *16*, 2100601.
- (55) Sumida, K.; Kusaka, S.; Takeda, Y.; Kobayashi, K.; Hirahara, T. Formation of monolayer V_5Se_8 from multilayer VSe₂ films via V- and Se-desorption. *Phys. Rev. B* **2022**, *106*, 195421.
- (56) Ji, Q.; Li, C.; Wang, J.; Niu, J.; Gong, Y.; Zhang, Z.; Fang, Q.; Zhang, Y.; Shi, J.; Liao, L.; Wu, X.; Gu, L.; Liu, Z.; Zhang, Y. Metallic Vanadium Disulfide Nanosheets as a Platform Material for Multifunctional Electrode Applications. *Nano Lett.* **2017**, *17*, 4908–4916.
- (57) Lee, S.-H.; Park, Y. C.; Chae, J.; Kim, G.; Kim, H. J.; Choi, B. K.; Lee, I. H.; Chang, Y. J.; Chun, S.-H.; Jung, M. Strong electron–phonon coupling driven charge density wave states in stoichiometric 1T-VS₂ crystals. *J. Mater. Chem. C* **2022**, *10*, 16657–16665.
- (58) Ugeda, M. M. et al. Characterization of collective ground states in single-layer NbSe₂. *Nat. Phys.* **2016**, *12*, 92–97.
- (59) Zhang, C.; Gong, C.; Nie, Y.; Min, K. A.; Liang, C.; Oh, Y. J.; Zhang, H.; Wang, W.; Hong, S.; Colombo, L.; Wallace, R. M.; Cho, K. Systematic study of electronic structure and band alignment of monolayer transition metal dichalcogenides in Van der Waals heterostructures. *2D Mater.* **2017**, *4*, 015026.
- (60) Duvjir, G.; Choi, B. K.; Thi Ly, T.; Lam, N. H.; Jang, K.; Dung, D. D.; Chang, Y. J.;

- Kim, J. Multiple charge density wave phases of monolayer VSe₂ manifested by graphene substrates. *Nanotechnology* **2021**, *32*, 364002.
- (61) Wang, Z.; Zhou, J.; Loh, K. P.; Feng, Y. P. Controllable phase transitions between multiple charge density waves in monolayer 1T-VSe₂ via charge doping. *Appl. Phys. Lett.* **2021**, *119*, 163101.
- (62) Chua, R.; Henke, J.; Saha, S.; Huang, Y.; Gou, J.; He, X.; Das, T.; van Wezel, J.; Soumyanarayanan, A.; Wee, A. T. S. Coexisting Charge-Ordered States with Distinct Driving Mechanisms in Monolayer VSe₂. *ACS Nano* **2022**, *16*, 783–791.
- (63) Fumega, A. O.; Diego, J.; Pardo, V.; Blanco-Canosa, S.; Errea, I. Anharmonicity Reveals the Tunability of the Charge Density Wave Orders in Monolayer VSe₂. *Nano Lett.* **2023**, *23*, 1794–1800.
- (64) van Gastel, R.; N'Diaye, A. T.; Wall, D.; Coraux, J.; Busse, C.; Buckanie, N. M.; zu Heringdorf, F.-J.; von Hoegen, M.; Michely, T.; Poelsema, B. Selecting a Single Orientation for Millimeter Sized Graphene Sheets. *Appl. Phys. Lett.* **2009**, *95*, 121901.
- (65) Preobrajenski, A.; Generalov, A.; Öhrwall, G.; Tchaplyguine, M.; Tarawneh, H.; Appelfeller, S.; Frampton, E.; Walsh, N. FlexPES: a versatile soft X-ray beamline at MAX IV Laboratory. *J. Synchrotron Radiat.* **2023**, *30*.

5.1 Supporting information

Supplementary Information of ‘Novel 2D vanadium sulphides: synthesis, atomic structure engineering and charge density waves’

Camiel van Efferen,^{*,†} Joshua Hall,[†] Virgínia Boix,[‡] Tobias Wekking,[†] Nikolay
Vinogradov,[¶] Alexei Preobrajenski,[¶] Jan Knudsen,[‡] Jeison Fischer,[†] Wouter
Jolie,[†] and Thomas Michely[†]

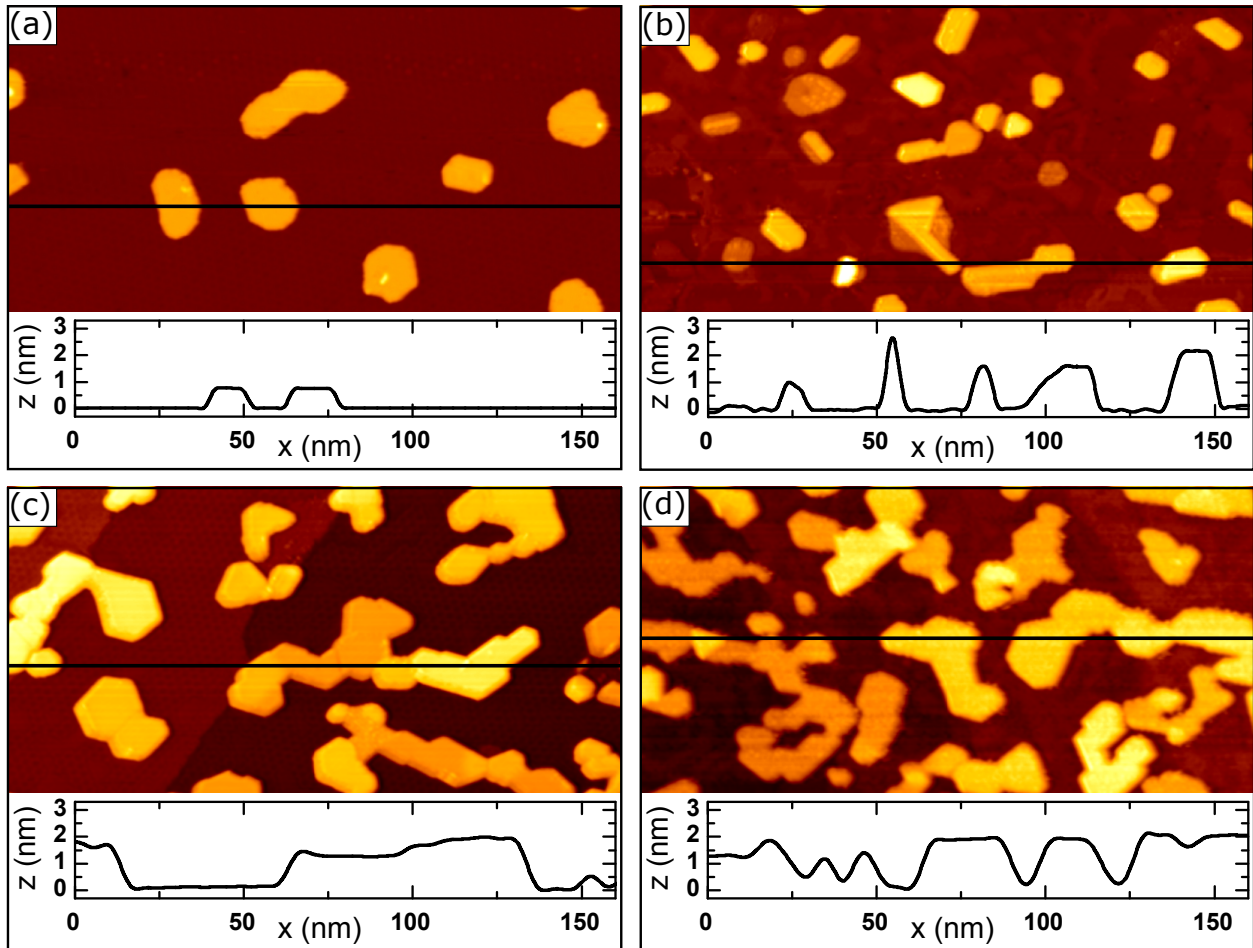
[†]*II. Physikalisches Institut, Universität zu Köln, Zùlpicher Straße 77, 50937 Köln, Germany*

[‡]*Division of Synchrotron Radiation Research, Department of Physics, Lund University, P.O.
Box 118, SE-221 00 Lund, Sweden*

[¶]*MAX IV Laboratory, Lund University, P.O Box 118, SE-221 00 Lund, Sweden*

E-mail: efferen@ph2.uni-koeln.de

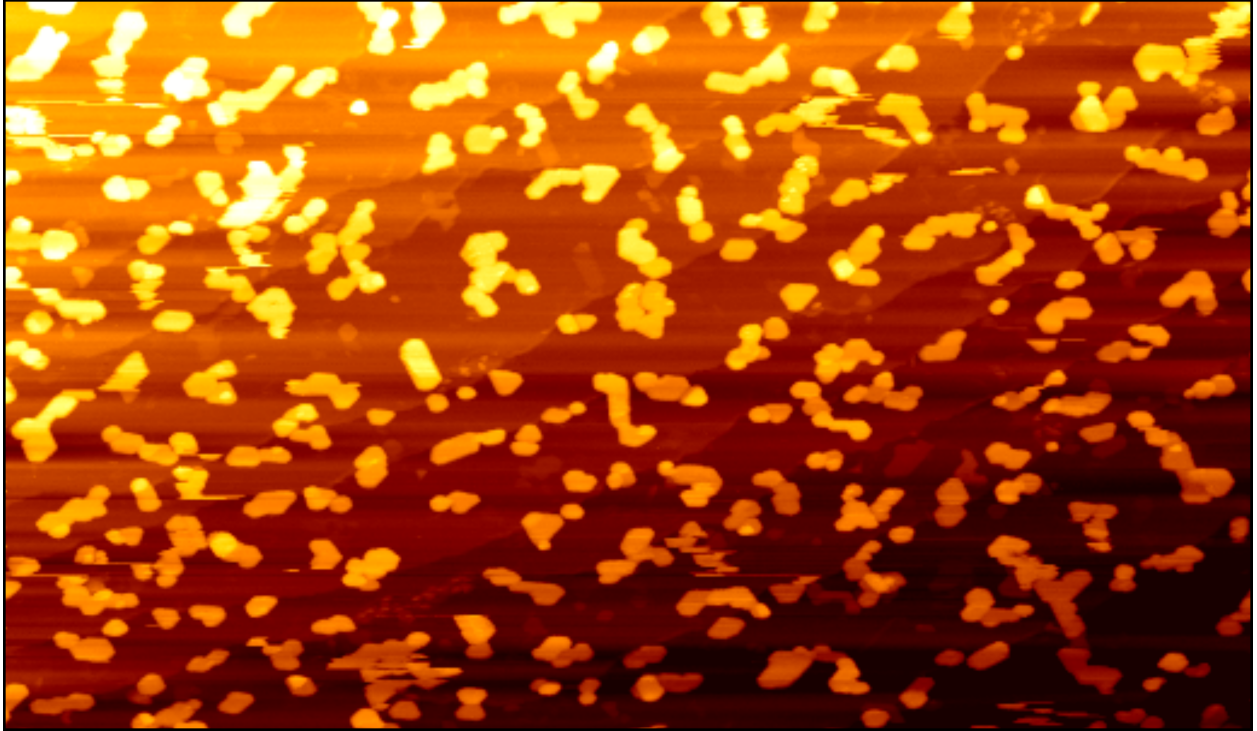
Supplementary Note 1: Transition from mono- to multi-layer growth mode



Supplementary Figure 1: Transition from mono- to multilayer growth mode. STM topographs after growth with identical synthesis parameters (growth temperature 300 K, S pressure during growth 5×10^{-9} mbar, annealing temperature 800 K, S pressure during annealing 2×10^{-9} mbar), but variation of deposition time, which results in a change in growth mode. **a** Deposition of 0.15 ML resulting in single-layer VS_2 islands. **b** Deposition of 0.45 ML results in a non phase-pure system of mixed single- and multilayer heights, which cover 20% of the surface area. **c** After depositing 0.9 ML no single-layer heights can be found anymore, multilayer islands cover about 30% of the surface. **d** Depositing 1.35 ML results in a sample with only multilayer islands that cover 45% of the Gr substrate.

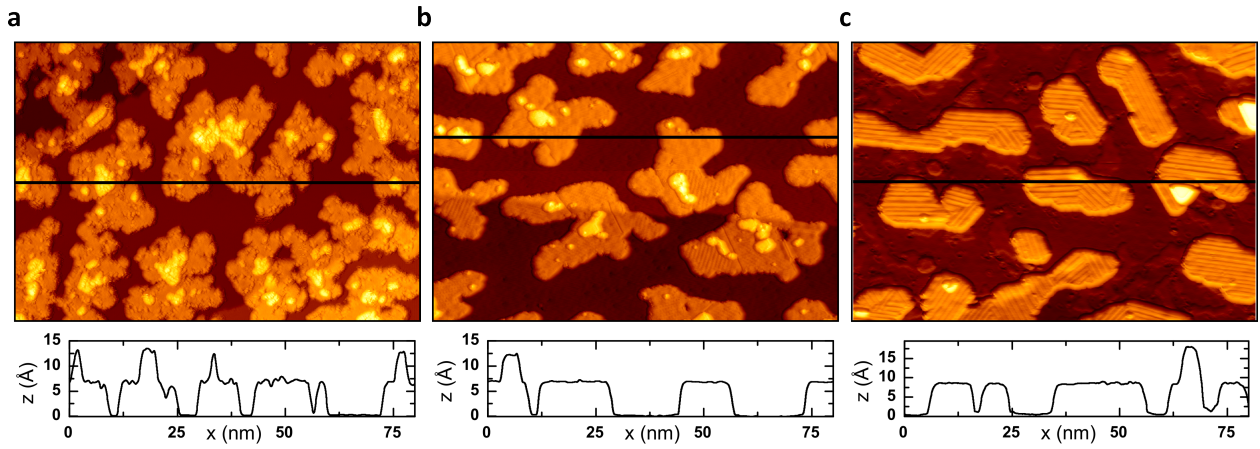
Image information (image size, sample bias, tunnelling current): **a** $160 \times 80 \text{ nm}^2$, 1.3 V, 20 pA, **b** $160 \times 80 \text{ nm}^2$, -1 V, 1 nA, **c** $160 \times 80 \text{ nm}^2$, -1 V, 0.5 nA, **d** $160 \times 80 \text{ nm}^2$, -0.7 V, 0.1 nA.

Supplementary Note 2: Formation of V_5S_8 at high S pressure



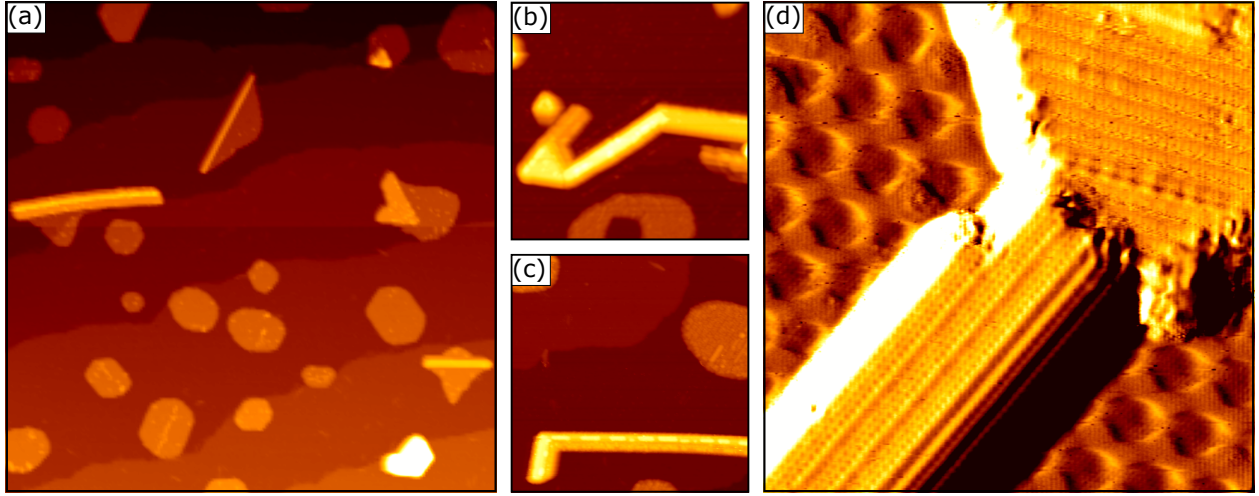
Supplementary Figure 2: Formation of V_5S_8 -derived islands at high S pressure. Annealing to 800 K after deposition of 1.2 ML V in a high S pressure $p_S^a = 8 \times 10^{-9}$ mbar, V_5S_8 -derived islands in a variety of heights are formed. Image information (image size, sample bias, tunnelling current): **a** $655 \times 385 \text{ nm}^2$, -0.02 V , 8 pA .

Supplementary Note 3: Line profiles of VS_x islands



Supplementary Figure 3: Line profiles of VS_x islands. **a** STM topograph of VS_2 islands directly after growth at 300 K. **b** STM topograph after annealing to 600 K. **c** STM topograph after annealing to 800 K. All annealing was performed without S background pressure. Images taken at 300 K. Image information (image size, sample bias, tunneling current): main panels $80 \times 80 \text{ nm}^2$, inset $20 \times 20 \text{ nm}^2$. **a** -1.0 V , 210 pA ; **b** -1.0 V , 100 pA ; **c** -1.3 V , 10 pA .

Supplementary Note 4: 1D crystallites of VS_x



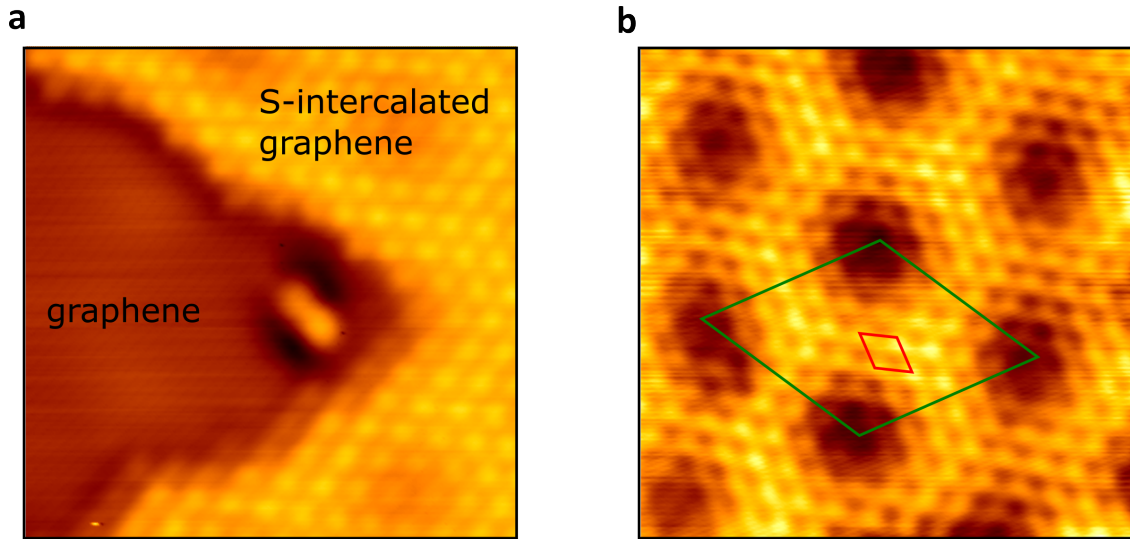
Supplementary Figure 4: 1D crystallites of VS_x . **a** After annealing to 900 K, 1D crystallites form at the edges of formerly single-layer VS_x . **b,c** Solitary 1D structures which show apparent heights of several nm. **d** At the atomic scale again striped reconstructions are visible, reminiscent of the striped surface of V_4S_7 .

Image information (image size, sample bias, tunnelling current): **a** $250 \times 250 \text{ nm}^2$, -0.3 V , 20 pA , **b** $80 \times 80 \text{ nm}^2$, -0.4 V , 10 pA , **c** $80 \times 80 \text{ nm}^2$, -1 V , 10 pA , **d** $20 \times 20 \text{ nm}^2$, -0.08 V , 0.4 nA .

The sulphur loss associated with elevated temperatures leads not only to vacancy superstructures but rather indicates the metastability of the VS_2 phase by a quick transition to thermodynamically more stable phases. In that regard, the striped sulphur vacancy row phase V_4S_7 readily transforms into elongated crystallites as illustrated in Fig. 4 when going to higher temperatures. In panel Fig. 4a, an overview of a formerly pure monolayer sample after annealing at 900 K in sulphur vapor is given. Besides the formation of small close to triangular-shaped bilayer islands, elongated bright structures form at the edge of an island strongly resembling rolled-up layers. Owing to their increased height of about 2–2.5 nm, but low surface contact area to Gr, these structures are easily dragged over the surface or picked up by the STM tip. In Fig. 4b,c, single, free-standing crystallites, which are not connected to any residual monolayer are shown. In STM, these structures have an apparent height of up to 3 nm and are again covered in adsorbates, which arrange periodically. This indicates a lattice rearrangement similar to the one observed for V_4S_7 and may also be resolved atomically

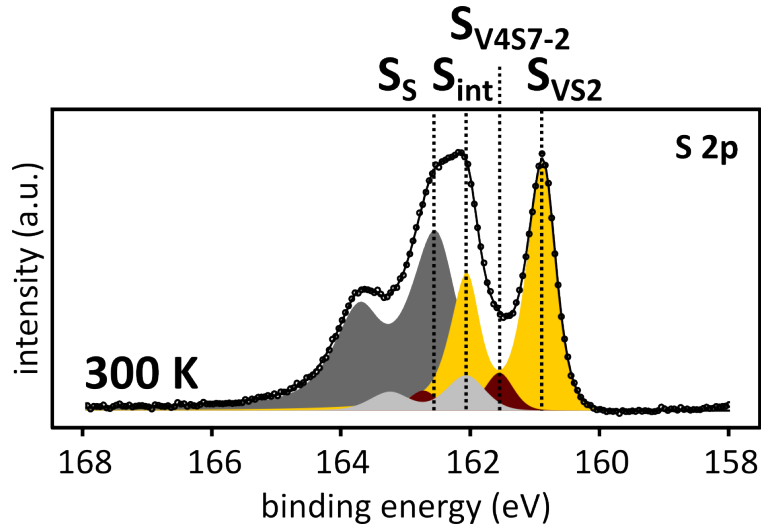
as shown in Fig. 4d. Here, the clean multilayer of 16 nm height shows striped ordering reminiscent of the monolayer analogue.

Supplementary Note 5: S intercalation below Gr



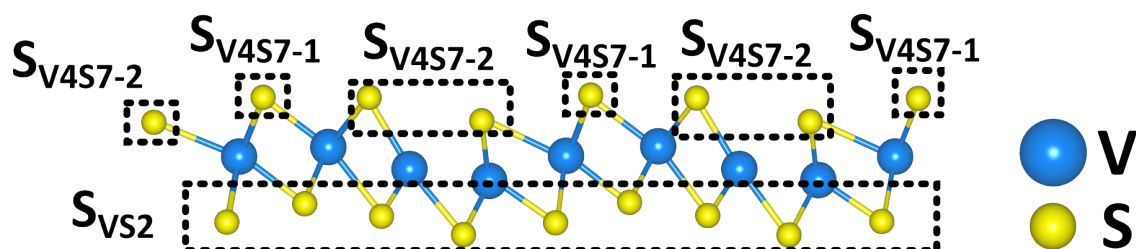
Supplementary Figure 5: S intercalation below Gr. After growth or annealing of VS_x , patches of $(\sqrt{3} \times \sqrt{3})R30^\circ$ S intercalation are visible below Gr. **a** STM topograph of partially intercalated graphene. **b** Patch of fully intercalated graphene. Visible are the moiré between graphene and $\text{Ir}(111)$ ¹ and the $(\sqrt{3} \times \sqrt{3})R30^\circ$ S intercalation². Both unit cells are drawn in the image, with the moiré unit cell in green ($a_{\text{moiré}} = 25.3 \text{ \AA}$) and the S intercalation in red ($a_{\text{S}(\sqrt{3} \times \sqrt{3})R30^\circ} = 4.3 \text{ \AA}$). Images taken at 7 K. STM parameters: **a** $6.2 \times 6.2 \text{ nm}^2$, -1.0 V , 50 pA ; **b** $6.4 \times 6.4 \text{ nm}^2$, -0.5 V , 100 pA .

Supplementary Note 6: 300 K XPS spectrum of S $2p_{3/2}$ and $2p_{1/2}$ core-level spectra of VS_2



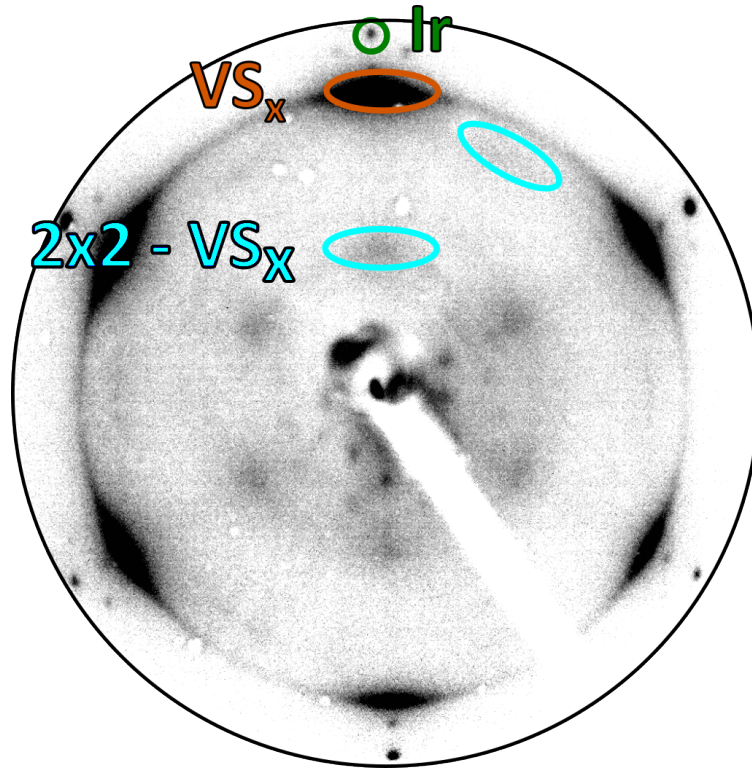
Supplementary Figure 6: 300 K XPS of S $2p_{3/2}$ and $2p_{1/2}$ core-level spectra of VS_2 . XP spectrum data measured at a photon energy of $h\nu = 260$ eV, fitted with 5 components, see text in main manuscript for discussion. The data points are represented by black circles and the overall fit by a solid black line. The $S_{V_4S_7-2}$ component is assumed to stem from edges and defects at this temperature.

Supplementary Note 7: Origin of $S_{V_4S_7-1}$ and $S_{V_4S_7-2}$ XPS components



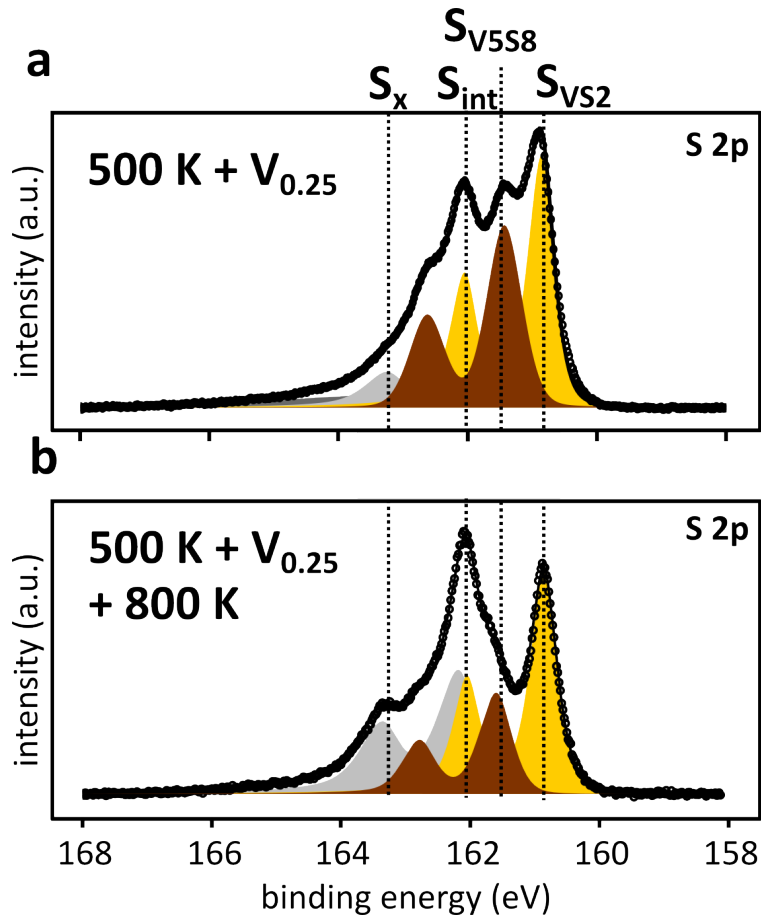
Supplementary Figure 7: Origin of $S_{V_4S_7-1}$ and $S_{V_4S_7-2}$ XPS components. Atomic structure models of V_4S_7 , with labeled boxes around three inequivalent atoms in the structure: 1) top S atoms that neighbour a missing S row, 2) top S atoms which do not sit directly next to a missing S row and 3) bottom S atoms. The box labels indicate which XPS components discussed in the main text correspond to the atoms.

Supplementary Note 8: LEED of phase-pure V_5S_8 -derived sample



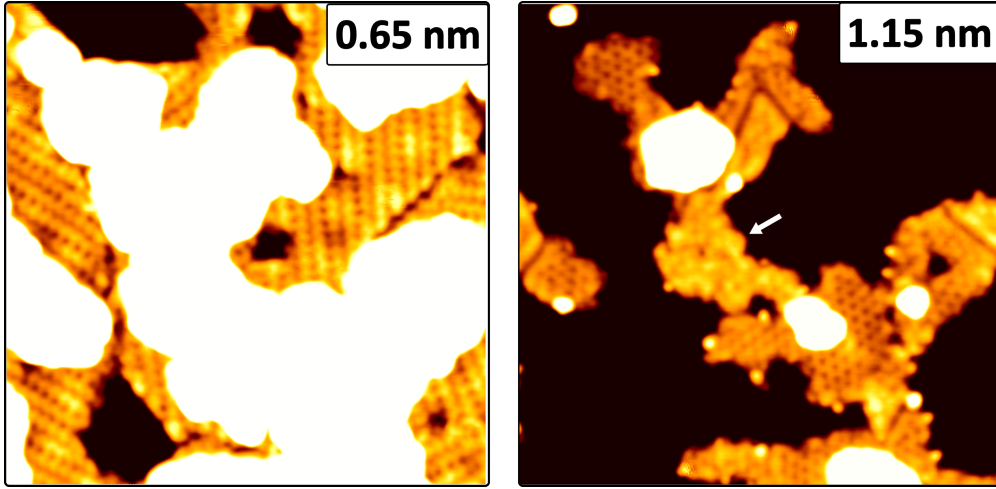
Supplementary Figure 8: LEED of phase-pure V_5S_8 -derived sample. a LEED pattern of VS_x sample, where 25% additional V atoms were deposited on a sample grown at 300 K and annealed to 500 K. After room temperature V deposition, the sample was subsequently annealed to 800 K in UHV (no S pressure). Indicated with colored circles are the Ir (green) first order reflections. First order reflections of VS_x (orange) and reflections of a 2×2 superstructure with respect to VS_x (cyan) are visible. Note that unlike the other LEED images shown in this work, this one was not taken with a microchannel plate LEED, leading to a reduced gain power. LEED taken with 85 eV.

Supplementary Note 9: XP spectra of S $2p_{3/2}$ and $2p_{1/2}$ core-level spectra of multiheight VS_x , with 25% extra V



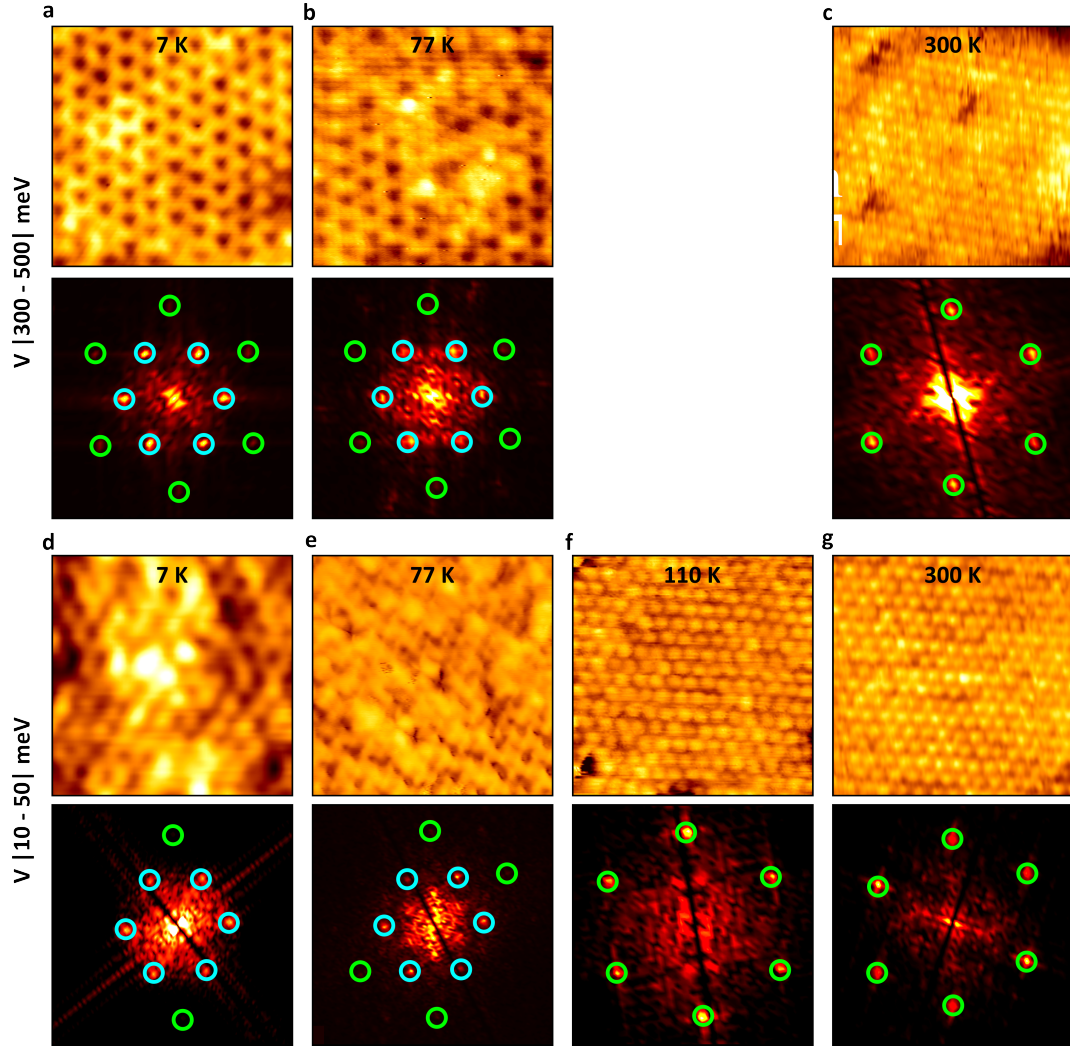
Supplementary Figure 9: XP spectra of S $2p_{3/2}$ and $2p_{1/2}$ core-level spectra of multiheight VS_x , with 25% extra V. **a XP spectrum of VS_x sample, where 25% additional V atoms were deposited on a VS_x sample grown at 300 K and annealed to 500 K. The spectrum was taken immediately after room temperature V deposition. **b** XP spectrum of the same sample, after a subsequent annealing step to 800 K in UHV (no S pressure). XP spectra measured at a photon energy of $h\nu = 260$ eV, fitted with 4 components, see text in main manuscript for discussion. The data points are represented by black circles and the overall fit by a solid black line.**

Supplementary Note 10: Single-layer VS_2 and V_9S_{16}



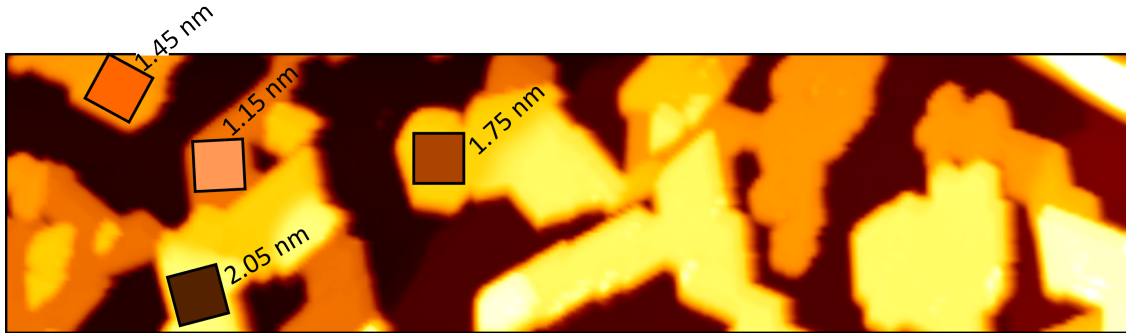
Supplementary Figure 10: Single-layer VS_2 and V_9S_{16} Low-temperature STM topograph of a multiheight sample annealed to 500 K, see Fig. 4a of the main text. On the left, the contrast is placed on single-layer VS_2 , which has an unidirectional CDW phase³. On the right, the same image is presented with the contrast placed on the higher islands. On most islands the $(\sqrt{3} \times \sqrt{3})R30^\circ$ superstructure has developed (see main text), characteristic for V_9S_{16} , while the island in the center looks disordered, indicated by a white arrow. Image taken at 4 K. STM parameters: $20 \times 20 \text{ nm}^2$, -1.0 V , 50 pA .

Supplementary Note 11: Temperature dependence of $(\sqrt{3} \times \sqrt{3})R30^\circ$ superstructure



Supplementary Figure 11: Temperature dependence of $(\sqrt{3} \times \sqrt{3})R30^\circ$ superstructure All topographs and FFTs used for graph in the top panel Fig. 6a of the main text. In the FFTs the Bragg peaks (green circles) and the $(\sqrt{3} \times \sqrt{3})R30^\circ$ spots (cyan circles) are indicated. The FFTs are rotated for the purpose of comparison. All topographs $5 \times 5 \text{ nm}^2$. STM parameters: **a** -0.5 V , 50 pA ; **b** -0.5 V , 200 pA ; **c** -0.3 V , 4.0 nA ; **d** -0.05 V , 100 pA ; **e** -0.01 V , 200 pA ; **f** 0.014 V , 500 pA ; **g** 0.01 V , 3.0 nA .

Supplementary Note 12: Location spectra and maps of multiheight sample



Supplementary Figure 12: Location of spectra and maps for multiheight sample. STM topograph of high-coverage sample with different islands heights. Indicated are the locations of the maps and spectra shown in Fig. 10 of the main text. All maps and spectra are taken with the same tip. Image taken at 7 K. STM parameters: a $200 \times 50 \text{ nm}^2$, -1.0 V , 100 pA .

References

- (1) N'Diaye, A. T.; Coraux, J.; Plasa, T. N.; Busse, C.; Michely, T. Structure of epitaxial graphene on Ir(111). *New J. of Phys.* **2008**, *10*, 043033.
- (2) Pielic, B.; Hall, J.; Despoja, V.; Rakić, I. Š.; Petrović, M.; Sohani, A.; Busse, C.; Michely, T.; Kralj, M. Sulfur Structures on Bare and Graphene-Covered Ir(111). *J. Phys. Chem. C* **2020**, *124*, 6659–6668.
- (3) van Efferen, C. et al. A full gap above the Fermi level: the charge density wave of monolayer VS_2 . *Nat. Comm.* **2021**, *12*, 6837.

CHAPTER 6

Manuscript [3]: Metal-insulator transition in monolayer MoS₂ via contactless chemical doping

This chapter wholly consists of the above-named publication, published in 2D Materials on 28th March 2022, available online.

The experiments were proposed by C. van Efferen, C. Murray, J. A. Fischer, T. Michely and W. Jolie. The growth and STM measurements took place at the TSTM system in Cologne. The Eu-intercalated sample was grown and measured by C. Murray and C. van Efferen. The O-intercalated sample was grown and measured by C. van Efferen and W. Jolie. Advice on MoS₂ growth was provided by J. Hall. The LEED, STM and STS data analysis was performed principally by C. van Efferen and C. Murray, with assistance from J. A. Fischer and W. Jolie. The DFT calculations were conducted by H. P. Komsa. The interpretation of the results was discussed in depth by C. van Efferen, C. Murray, H. P. Komsa, J. A. Fischer, T. Michely and W. Jolie.

C. van Efferen, C. Murray and W. Jolie wrote the manuscript, with advice and corrections from J. A. Fischer and T. Michely. Some of the results shown in this Chapter can be found in the Master's thesis of C. van Efferen and, to a minor extent, the doctoral thesis of W. Jolie [222].

The first two authors have similar contributions to this publication.

PAPER • OPEN ACCESS

Metal-insulator transition in monolayer MoS₂ via contactless chemical doping

To cite this article: Camiel van Efferen *et al* 2022 *2D Mater.* **9** 025026

View the [article online](#) for updates and enhancements.

You may also like

- [Theory of zero-field superconducting diode effect in twisted trilayer graphene](#)
Harley D Scammell, J I A Li and Mathias S Scheurer
- [Review of graphene for the generation, manipulation, and detection of electromagnetic fields from microwave to terahertz](#)
David A Katzmarek, Aiswarya Pradeepkumar, Richard W Ziolkowski et al.
- [Two-dimensional material-based printed photonics: a review](#)
Bibi Mary Francis, Joice Sophia Ponraj, Balaji Dhanabalan et al.



PAPER

Metal-insulator transition in monolayer MoS₂ via contactless chemical doping

OPEN ACCESS

RECEIVED

20 December 2021

REVISED

3 March 2022

ACCEPTED FOR PUBLICATION

11 March 2022




PUBLISHED

28 March 2022

Original Content from this work may be used under the terms of the [Creative Commons Attribution 4.0 licence](#).

Any further distribution of this work must maintain attribution to the author(s) and the title of the work, journal citation and DOI.



Camiel van Efferen^{1,4,*} , Clifford Murray^{1,4}, Jeison Fischer¹, Carsten Busse^{2,5} , Hannu-Pekka Komsa³ , Thomas Michely¹ and Wouter Jolie¹

¹ II. Physikalisches Institut, Universität zu Köln, Zùlpicher Straße 77, Köln, 50937, Germany

² Institut für Materialphysik, Westfälische Wilhelms-Universität Münster, Wilhelm-Klemm-Straße 10, 48149 Münster, Germany

³ Faculty of Information Technology and Electrical Engineering, University of Oulu, Pentti Kaiteran Katu 1, 90014 Oulu, Finland

⁴ These authors contributed equally to this work.

⁵ Present address: Department Physik, Universität Siegen, Walter-Flex-Str. 3, 57068 Siegen, Germany.

* Author to whom any correspondence should be addressed.

E-mail: efferen@ph2.uni-koeln.de

Keywords: metal–insulator transition, contactless doping, monolayer MoS₂, graphene substrate, density-functional theory, scanning tunneling microscopy/spectroscopy

Supplementary material for this article is available [online](#)

Abstract

Much effort has been made to modify the properties of transition metal dichalcogenide layers via their environment as a route to new functionalization. However, it remains a challenge to induce large electronic changes without chemically altering the layer or compromising its two-dimensionality. Here, a non-invasive technique is used to shift the chemical potential of monolayer MoS₂ through p- and n-type doping of graphene (Gr), which remains a well-decoupled 2D substrate. With the intercalation of oxygen (O) under Gr, a nearly rigid Fermi level shift of 0.45 eV in MoS₂ is demonstrated, whereas the intercalation of europium (Eu) induces a metal–insulator transition in MoS₂, accompanied by a giant band gap reduction of 0.67 eV. Additionally, the effect of the substrate charge on 1D states within MoS₂ mirror-twin boundaries (MTBs) is explored. It is found that the 1D nature of the MTB states is not compromised, even when MoS₂ is made metallic. Furthermore, with the periodicity of the 1D states dependent on substrate-induced charging and depletion, the boundaries serve as chemical potential sensors functional up to room temperature.

Metallic transition metal dichalcogenide (TMDC) monolayers show a plethora of many-body phenomena, such as charge density wave order [1], Mott insulating states [2] or superconductivity [3]. Understanding these correlated phases, as well as their dependence on external electric or magnetic fields, allows the creation of devices with tunable phase transitions [4]. While intrinsic TMDC metals are being extensively investigated, less is known about the metallic properties of intrinsic TMDC semiconductors such as MoS₂ and WS₂, mainly due to experimental difficulties in shifting the chemical potential close to the conduction or valence band.

Monolayer MoS₂ and WS₂ have electronic band gaps of more than 2.0 eV when resting on weakly interacting substrates (see [5] for a discussion of substrate-induced band gap variability in MoS₂). Hence, back-gated devices are typically unable to

bring the chemical potential close to the onset of the conduction or valence band before breakdown occurs [6, 7]. Larger shifts are obtained with ionic-liquid-gating. With this method, transport measurements showed that MoS₂ and WS₂ become superconducting when the chemical potential lies within the conduction band [8–13]. However, ionic-liquid-gating suffers from charge inhomogeneities [14]. At low temperatures this effect is exacerbated due to freezing of the liquid [15, 16]. The liquid also hampers complementary measurements using surface sensitive techniques. As a consequence, many open questions remain on the nature of the superconducting dome in MoS₂ [8–10, 17, 18] and WS₂ [12], the origin of the finite density of states within the superconducting gap [19], and on the properties of the (quasi-) metallic phase in between the insulating and superconducting phases [12].

Another method to obtain large shifts of the chemical potential is the introduction of foreign species. This is done through adsorption, elemental substitution or via intercalation between the 2D sheet and its substrate [20–25]. But the direct contact with the TMDC results in, like in the case of ion-gating, an entangled effect of charge redistribution and chemical hybridization [26], leading to non-universal, element-specific properties. Hence, an efficient method able to tune the chemical potential of TMDCs by large amounts without chemically altering it or leaving the surface inaccessible would be highly desirable. Such a method would make it possible to gain fundamental knowledge on the effect of charge on the band structure of TMDC semiconductors [13], ultimately enabling access to novel phases of matter, such as topological superconductivity [27].

Here, we introduce contactless chemical doping as a method to induce large shifts in the chemical potential of MoS₂, without disturbing its chemical environment. We chemically dope a Gr layer from below in order to shift the chemical potential of MoS₂ monolayer grown on top *in situ*. The doping is done through the use of intercalants, taking Eu and O as electron donor and acceptor respectively, to create high quality MoS₂/Gr/(Eu or O)/Ir(111) layered configurations. For both intercalants, it has been found that they are able to cause considerable shifts in the Dirac point of Gr (as far as $E_D = -1.38$ eV for Eu and up to $E_D = +0.68$ eV for O), without strong hybridization [28–31]. In this way, the chemical potential within the MoS₂ band structure can be controlled through the doping level of Gr and shifted far beyond what is possible in traditional back-gate device setups, without hybridization or loss of surface accessibility and quality. The MoS₂/doped Gr samples are analyzed experimentally with scanning tunneling microscopy (STM) and spectroscopy (STS) and theoretically with *ab initio* density functional theory (DFT) calculations. Additional attention is given to the effect of the Gr doping on the 1D states within mirror-twin boundaries (MTBs) in MoS₂, which can be filled and depleted via the substrate without compromising their 1D nature. Thereby, they can be used as chemical potential sensors.

1. Results

1.1. Metal–insulator transition in MoS₂

Our method is illustrated in figure 1(a). The initial heterostructure consists of three different materials: the 2D semiconductor MoS₂, the 2D semi-metal Gr, with the Dirac point close to Fermi level E_F , and the metallic Ir(111). Since foreign elements bind much more strongly to Ir(111) than to the van der Waals materials Gr and MoS₂, this arrangement enables us to intercalate these between Gr and Ir(111), while preserving the chemical environment of MoS₂. Here, the

concept is demonstrated for the case of Eu and O. The applicability of our method to other 2D semiconductors is demonstrated in the SI (figure S1 available online at stacks.iop.org/TDM/9/025026/mmedia).

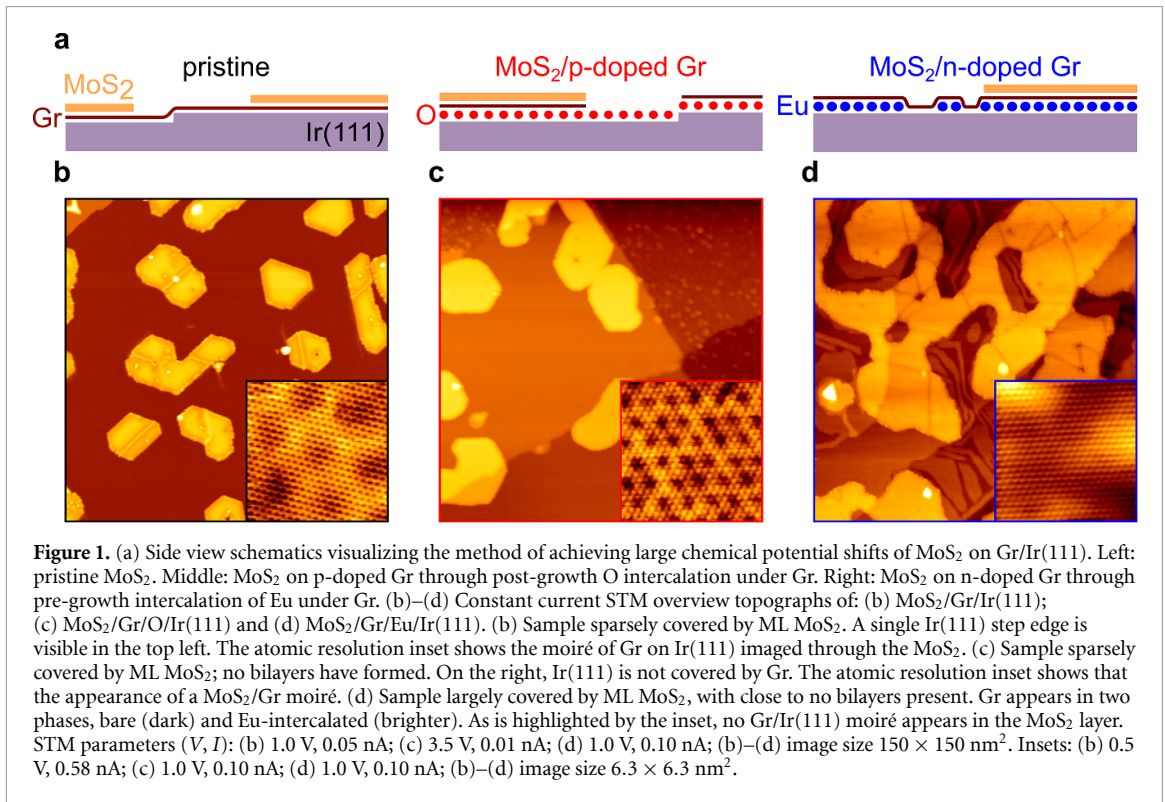
Concerning the choice of substrate, Gr is ideal as it fulfills the following requirements:

- It is a 2D material, creating the thinnest possible interface between MoS₂ and the intercalation layer.
- It has a low density of states (DOS) close to the Fermi energy, so large shifts of the band structure can be achieved with moderate carrier densities.
- Its work function is pinned to the band structure, i.e. energy shifts due to doping lead to equal shifts of the work function [32].
- The finite DOS allows for charge flow to MoS₂ when it becomes metallic.

Intercalating an electron donor such as Eu thus leads to an upward shift of the chemical potential in Gr via charge transfer. Similarly, the intercalation of an electron acceptor such as O causes the chemical potential of Gr to shift down in energy. These changes in the Gr substrate cause comparable shifts in the chemical potential of the top layer via workfunction alignment and/or charge transfer. The precise mechanisms by which the MoS₂ chemical potential is shifted for each intercalant will be discussed in detail below. In the following, we refer to MoS₂/Gr/Eu/Ir(111) (MoS₂/Gr/O/Ir(111)) as MoS₂ on n-doped (p-doped) Gr, while MoS₂/Gr/Ir(111) is referred to as pristine.

The STM topograph of figure 1(b) displays the pristine sample as a reference. Islands of monolayer (ML) MoS₂ are distributed on the Gr/Ir(111) substrate. The typical apparent height of the ML islands is 0.65 nm when tunneling into the MoS₂ conduction band. Apart from MTBs, which appear as bright lines, defects are largely absent. In the inset, an atomic resolution topograph of MoS₂ shows that the moiré of Gr/Ir(111) is visible through the MoS₂ layer, see SI (figure S2). This system has previously been investigated in detail in [5].

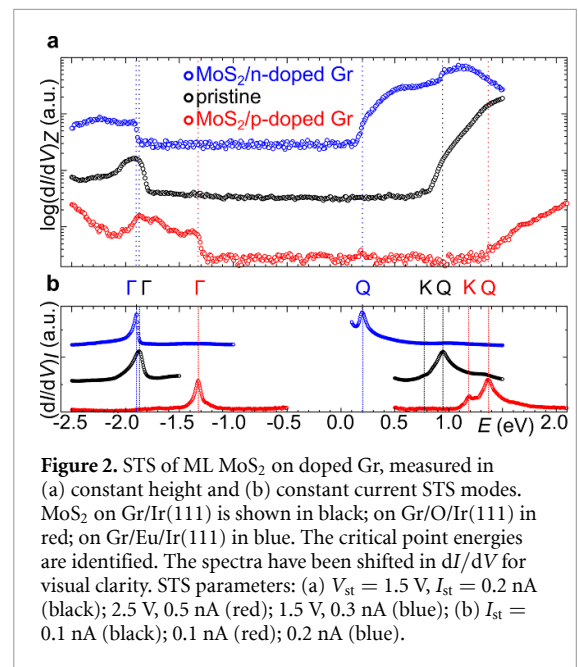
An STM image of MoS₂ on p-doped Gr is shown in figure 1(c). O was intercalated after the growth of MoS₂, as the O would etch Gr at the high temperatures employed in MoS₂ growth. The process is detailed in the section 3. The Gr layer is partially combusted, leaving uncovered areas (holes) in the graphene sheet, while the O atoms intercalate the subsisting Gr. An area where Gr was combusted is partly imaged in the top right of figure 1(c). After the process extended Gr patches remain, on which MoS₂ is found. The Gr layer is completely intercalated with a O-($2\sqrt{3} \times 2\sqrt{3}$)-R30° superstructure reported previously, see SI (figure S1) [33]. Since O-intercalation decouples Gr from Ir(111), the Gr/Ir(111) moiré



vanishes and a moiré between MoS₂ and Gr becomes visible as shown in the inset of figure 1(c).

Figure 1(d) is an STM topograph of the surface morphology of MoS₂ on n-doped Gr. The Gr layer not covered by MoS₂ is not uniformly intercalated: large intercalation areas and stripes of apparent height 0.30 nm are visible, similar to previous Gr/Eu/Ir(111) samples [34]. All investigated MoS₂ islands have an apparent height of around 0.70 nm relative to the higher (brighter in d) patches of Gr, under similar tunneling conditions as for the pristine sample, consistent with the absence of any Eu in between Gr and MoS₂. We thus infer that ML MoS₂ grows preferentially on top of Gr/Eu/Ir(111). A similar preference for adsorption on Eu-intercalated patches was observed for aromatic molecules [35]. The moiré of Gr/Ir(111) is no longer visible in the MoS₂ layer; instead, the layer shows slight apparent height modulations, due to a variation in the density of the intercalated Eu underneath Gr, see SI (figures S2 and S3).

We use STS to investigate how the band structure of MoS₂ is altered due to doping of the Gr substrate. The spectra in figures 2(a) and (b) are recorded in constant height and constant current mode on MoS₂, respectively. Constant height STS, in figure 2(a), is proportional to the local density of states and hence records the band gap position in energy. For pristine MoS₂ (black dots), the apparent valence band (VB) and conduction band (CB) edges are close to -1.8 eV and 0.9 eV, respectively. The doping of Gr leads to non-trivial energy shifts of these apparent band edges. The spectrum measured on MoS₂ on p-doped Gr displays a nearly rigid upward shift (≈ 450 meV)



of the apparent VB and CB edges (red dots). Since both band edges shifted by approximately the same amount, the p-doping of Gr leaves the MoS₂ band gap nearly unchanged with only a minor reduction of ≈ 20 meV. Upon n-doping, a considerable narrowing of the band gap is found, with the apparent CB edge shifting close to the Fermi energy, while the apparent VB edge remains at approximately the same location (blue dots). The shift of the apparent CB by ≈ 700 meV demonstrates a large shift of the chemical potential of MoS₂, whereas the lack of

Table 1. Critical point energies (eV) identified in ML MoS₂ on different substrates using constant current STS (averaged over multiple data sets), and the corresponding distance between the well-defined Γ and Q peaks in STS $E_{\Gamma-Q}$. For more details on the MoS₂/Gr/Ir(111) data, including the determination of the actual electronic bandgap $E_g = 2.53$ eV, see [5]. The location of the K-point of MoS₂ on n-doped Gr has been determined using quasiparticle interference mapping (see figure 3), since it is not accessible via constant current STS.

MoS ₂ on	Γ	K	Q	$E_{\Gamma-Q}$
Gr/Ir(111)	-1.87 ± 0.02	0.77 ± 0.02	0.90 ± 0.05	2.77 ± 0.05
Gr/Eu/Ir(111)	-1.90 ± 0.01	(-0.09 ± 0.01)	0.20 ± 0.01	2.10 ± 0.01
Gr/O/Ir(111)	-1.37 ± 0.04	1.22 ± 0.03	1.38 ± 0.03	2.75 ± 0.05

a significant shift of the apparent VB is indicative of a large band gap renormalization, as will be analyzed in more detail below.

Constant current STS detects the critical point energies in the band structure [5, 36]. It serves as a complementary method to constant height STS. The resulting spectra are shown in figure 2(b). We follow the analysis of [5] to identify the critical point energies of MoS₂. In the VB, the Γ -point band edge states cause a large peak [5], which is found in all three systems. The actual VB maximum at the K-point is not detected in MoS₂ because of its large parallel momentum, in-plane orbital character and close proximity in energy. Based on ARPES measurements, the VB K-point was estimated to lie 0.11 eV above the Γ -point energy of the VB [37, 38]. The CB minimum at the K-point, however, is dominated by out-of-plane orbitals and thus appears as a small shoulder [5, 39]. This shoulder is found in the pristine sample and in MoS₂ on p-doped Gr, but cannot be detected in MoS₂ on n-doped Gr with constant current STS, as the signal diverges near the Fermi energy. States from the CB Q-point edge cause a larger peak, which is reproducibly found in all three samples. For that reason, we specify the gap size $E_{\Gamma-Q}$, used for determining the renormalization energy, as the energetic distance between the well-defined VB Γ peak and the CB Q peak in constant current STS. The actual bandgap is expected to be at least 240 meV smaller, see [5]. The exact location of the critical point energies and estimated $E_{\Gamma-Q}$ gap sizes are listed in table 1.

Remarkably, we find that the CB of MoS₂ on n-doped Gr is effectively at the Fermi level. To address this point, we perform STS mapping to investigate the conduction band minimum (CBM) of MoS₂ on n-doped Gr. MoS₂ patches enclosed by grain boundaries and island edges host confined states, effectively forming a quantum well. Mapping these standing waves allows us to detect the quasiparticles close to the Fermi energy. Figure 3(a) displays STS maps of such a triangular quantum well, in which we identify quantized states [40]. The lowest state is pronounced already at -50 meV below the Fermi energy, providing the smoking gun for the metallic nature of MoS₂ on this substrate. In addition, more complex states appear at higher energies, as expected for an electron-like band.

Quasiparticle interference patterns around defects and confined quantum well states such as

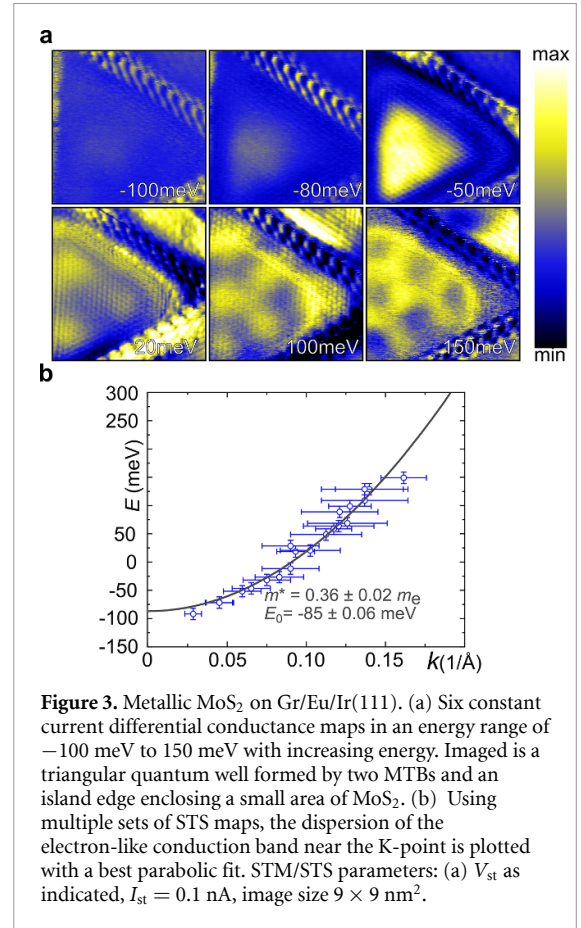
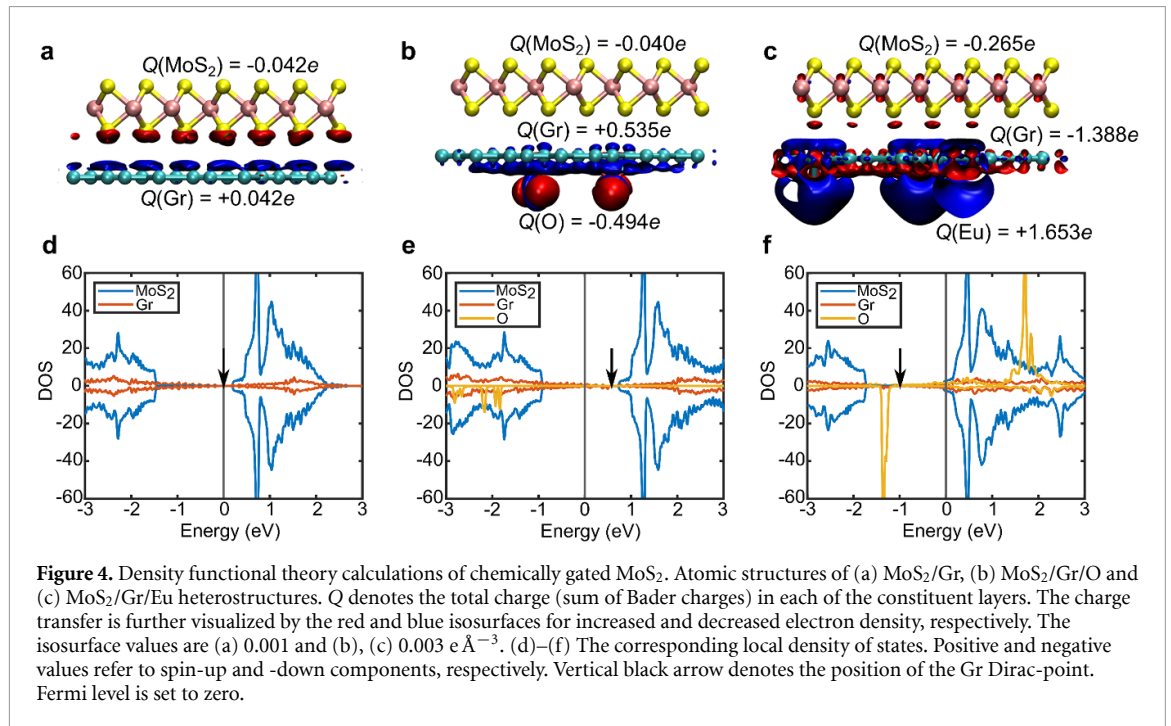


Figure 3. Metallic MoS₂ on Gr/Eu/Ir(111). (a) Six constant current differential conductance maps in an energy range of -100 meV to 150 meV with increasing energy. Imaged is a triangular quantum well formed by two MTBs and an island edge enclosing a small area of MoS₂. (b) Using multiple sets of STS maps, the dispersion of the electron-like conduction band near the K-point is plotted with a best parabolic fit. STM/STS parameters: (a) V_{st} as indicated, $I_{st} = 0.1$ nA, image size 9×9 nm².

those in figure 3(a) are used to determine the dispersion of the quasiparticles around the Fermi energy. The result is shown in figure 3(b). The different data sets and methods used to obtain these data points are shown and discussed in the SI (figure S4). We fit the data with a parabolic dispersion and find that the bottom of the band is located at -85 ± 6 meV. This is consistent with constant height STS measurements taken with small tip-sample distances, shown in the SI (figure S5). We further obtain an effective mass of $0.36 \pm 0.02 m_e$, which agrees with the calculated effective mass of 0.35 – $0.40 m_e$ at the K-point [41, 42].

1.2. DFT calculations and model of band shifts

We conducted DFT calculations to obtain a qualitative understanding of the mechanism through which the shifts of the chemical potential of MoS₂ are enabled. Our supercell includes the MoS₂ and Gr



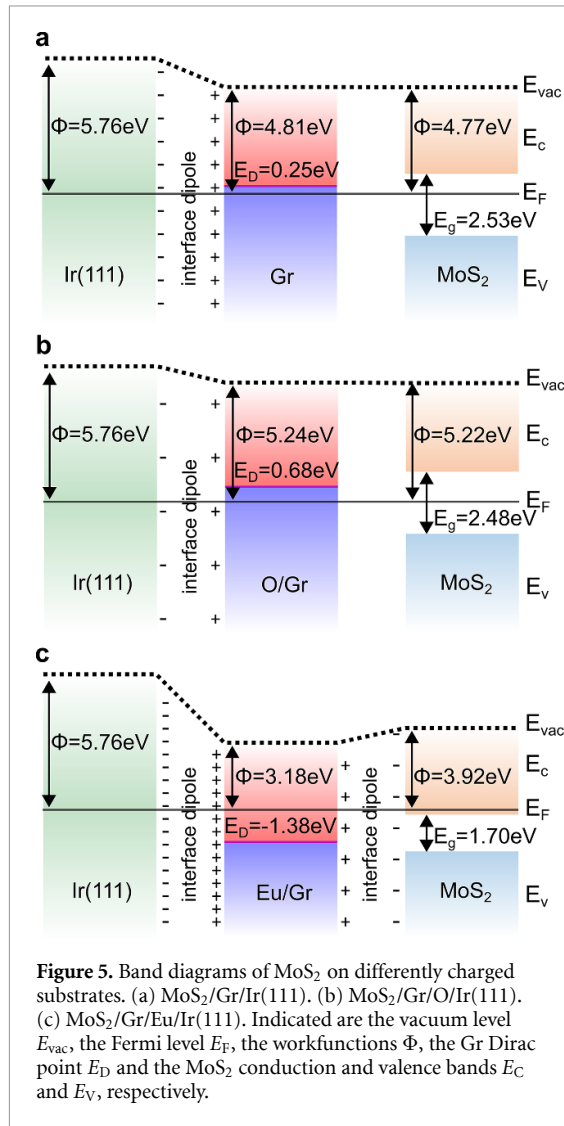
sheets, while the Ir(111) substrate was omitted. This simplified model of the experimental situation grasps the essentials at affordable computational effort. We also note that the renormalization of the fundamental bandgap due to screening is not accounted for in our DFT calculations. Since the band alignment is sensitive to strain in MoS₂ and Gr, we adopted a supercell model where strain was minimized.

Figures 4(a)–(c) show the structural models of the pristine heterostructure and the intercalated structures containing two O and two Eu dopants, respectively. The figures also show the total charge transfers, as obtained by summing up the Bader charges, and the charge density difference isosurfaces (defined as $\rho(\text{MoS}_2/\text{Gr}) - \rho(\text{MoS}_2) - \rho(\text{Gr})$ and $\rho(\text{MoS}_2/\text{Gr}/\text{dopants}) - \rho(\text{MoS}_2/\text{Gr}) - \rho(\text{dopants})$). In the case of the pristine heterostructure, the electronic structure at the interface is slightly perturbed by the presence of the other layers, which effectively yields a small charge transfer and an interface dipole induced potential shift of about 0.25 eV. In the case of the O-doped heterostructure, there is significant electron transfer from the Gr to O, while the MoS₂ layer is left mostly unaffected. This is in stark contrast to the Eu-doped heterostructure, where we find charge transfer from Eu to both Gr and MoS₂, albeit with the charge transfer to Gr still considerably larger. The charge transfer, induced dipoles and Dirac-point positions are listed in the SI (table S1).

Figures 4(d)–(f) show the DFT-calculated local densities of states projected onto the two or three constituent layers. We find that pristine MoS₂ is semiconducting, with the Fermi level 0.2 eV below CBM and the gap of 1.69 eV close to the value calculated for

an isolated monolayer [43]. Gr remains charge neutral, with the Fermi level coinciding with the Dirac-point, since the interface dipole is the result of modifications to the extensions of the Gr wave functions and not of charge transfer. In the case of the O-doped heterostructure Gr is p-type doped, with the Fermi level 0.58 eV below the Dirac-point and 0.75 eV below the MoS₂ CBM. Thus we find a near-rigid shift of the Gr and MoS₂ bands to higher energies, in agreement to our experiments. In the case of the Eu-doped heterostructure Gr is n-type doped, with the Fermi level 0.99 eV above the Dirac-point and 0.05 eV above MoS₂ CBM. This represents a strong deviation from a rigid shift picture, in which one would expect the Fermi level to lie 0.8 eV above the MoS₂ CBM. DFT thus reproduces the metal–insulator transition, as well as the shifts of the Gr Dirac point and MoS₂ conduction band found experimentally, including deviations from a rigid shift. Our DFT model thus captures the essence of our experimental observations, although the absence of the Ir substrate leads to a significantly lower density of dopants needed to obtain shifts comparable to the experiments.

The physics involved in the changes of band edge positions and bandgap width can be grasped in a model, accounting for workfunction alignment and interface dipole formation, as shown in figures 5(a)–(c). The MoS₂, Gr and Ir(111) band diagrams are sketched for the three samples. Two interfaces are considered: between (doped) Gr and Ir(111), and between (doped) Gr and MoS₂. If charge transfer is possible between the layers (e.g. the metal–metal junction between Gr and Ir), an interface dipole will be formed, as a result of workfunction differences.



If no charge transfer is possible because one of the materials is gapped (e.g. the metal–semiconductor junction between undoped Gr and MoS₂), the workfunctions of the two materials have to align through shifts in the position of the chemical potential with respect to the band structure and thus to the vacuum level.

Both types of interfaces are present in the pristine case sketched in figure 5(a). The Ir(111) workfunction $\Phi_{Ir} = 5.76$ eV [44] is considerably larger than the workfunction of pristine Gr $\Phi_{Gr} = 4.56$ eV [45]. Due to the difference in workfunctions, charge will flow from Gr to Ir until an interface dipole is formed, halting the flow of further charge carriers. As a result, Gr is slightly p-doped when grown on Ir(111), by about 0.1 eV [46]. Note that for physisorbed Gr with an intact Dirac cone, e.g. Gr on Ir(111), even strong doping does not change the energetic separation of the Dirac point from the vacuum level, it being identical to the workfunction of undoped Gr [47].

When ML MoS₂ is placed on top of Gr, the interface dipole between Gr and Ir is marginally changed due to a slight increase in the p-doping of Gr, from

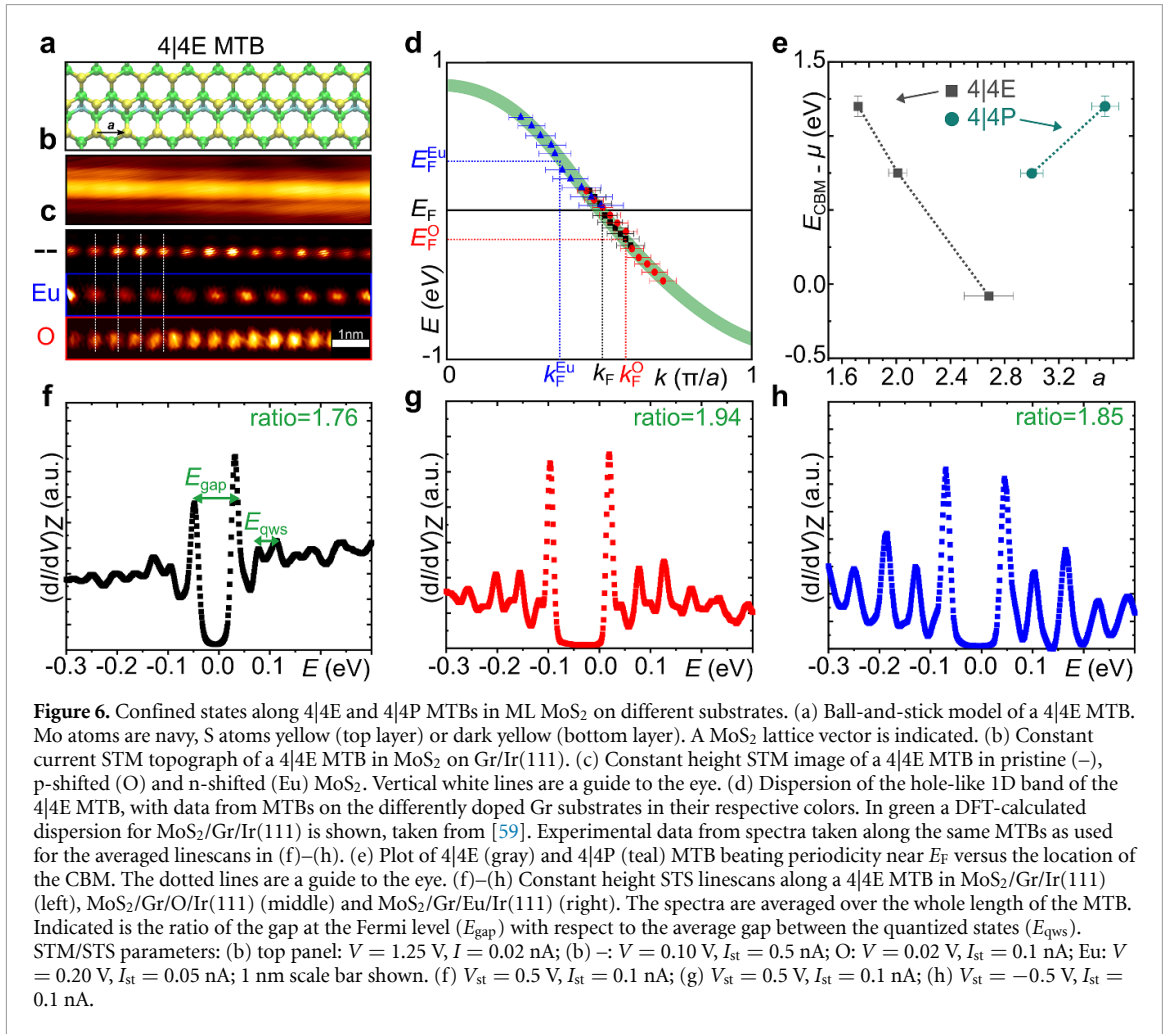
+0.1 eV to +0.25 eV [37], resulting in a Gr workfunction 4.56 eV + 0.25 eV = 4.81 eV. Between the interior of the MoS₂ layer and Gr no charge transfer is possible, as the Fermi level lies within the MoS₂ band gap. Therefore, with no dipole formed, the workfunctions of both materials have to align. The chemical potential of MoS₂ correspondingly shifts from the middle of the band gap closer to the CB. With the ML MoS₂ electron affinity $\chi \approx 4.0$ eV [48–52], and finding the conduction band edge E_c of MoS₂/Gr/Ir(111) in STS at 0.77 eV, the workfunction of MoS₂ on Gr/Ir(111) $\Phi_{MoS_2} = \chi + E_{CBM} = 4.77$ eV is indeed very close to that of Gr: $\Phi_{Gr} = 4.81$ eV.

When O is intercalated underneath Gr, shown in figure 5(b), the Dirac point moves to 0.68 eV [31] and the Gr workfunction changes to 4.56 eV + 0.68 eV = 5.24 eV. The interface dipole between Gr and Ir(111) becomes smaller. Following the previous considerations, the MoS₂ bands must follow the shift of the Dirac point, in order to keep the workfunctions of Gr and MoS₂ the same. The measured K-point shift in the MoS₂ CB of ≈ 450 meV is correspondingly close to the expected Gr Dirac point shift of 430 meV. The chemical potential of MoS₂ is thus directly set by that of Gr, as long as MoS₂ remains insulating.

Experimentally, we find that the size of the band gap E_g is only slightly reduced, when comparing the p-doped and pristine sample. Since MoS₂ is still insulating, the screening within the layer should not have changed. Gr, on the other hand, has an increased hole density on the order of 10^{13} cm⁻² due to an estimated Dirac point energy $E_D = -0.68$ eV [29]. Gr is thus expected to better screen electrostatic interactions in MoS₂. Previous experimental and theoretical work on TMDC/Gr heterostructures has however found that the effect of increased Gr carrier density on the band gap flattens off after $E_D = \pm 0.25$ eV [7, 53]. Since the Gr layer is already p-doped in the pristine MoS₂ sample [37], the observed renormalization of $\Delta E_g \approx 20$ meV seems to indicate that the substrate-induced renormalization is already close to saturation prior to O-intercalation.

For Eu-doped Gr, figure 5(c), the situation is decidedly different. Gr/Eu has its Dirac point at about -1.38 eV, see [28] and the SI (figure S6). The chemical potential difference between Eu-doped Gr and pristine MoS₂ is larger than the difference between pristine MoS₂ and the pristine CB edge. The MoS₂ potential will therefore shift in response to the Eu-doped Gr potential until it hits the CB and MoS₂ becomes metallic. Charge flows from Gr to MoS₂, creating an interface dipole, which reduces the shift of the MoS₂ CB minimum compared to the shift of the Dirac point of graphene.

In addition to the formation of an interface dipole, the charge carriers within MoS₂ are also able to efficiently screen within the layer, leading to the experimentally observed band gap reduction $\Delta E_g = 0.67$ eV. The renormalization of the bandgap



due to the metal–insulator transition is considerably larger than what is achieved via methods which only increase the carrier density in the substrate. In those cases, renormalization energies of at most 0.24 eV have been reported [7, 54].

1.3. Effect of charge on mirror twin boundaries

The presence of 0D defects (such as vacancies) or 1D defects (such as MTBs) in TMDCs will influence the shifts of the chemical potential induced via contactless chemical doping. In-gap states within these defects tend to weaken the impact of the work function difference due to local Fermi level pinning [55–57], which is absent away from these defects [58]. In the pristine sample, the presence of in-gap states below the Gr Fermi level in MoS₂ edges and MTBs leads to the accumulation of charge in the MTBs, causing band bending in the surrounding semiconductor [59]. With the doping of Gr potentially influencing the amount of charge that is transferred to the MTBs as well as the dielectric properties of the MoS₂/Gr heterostructure (e.g. by inducing a metal–insulator transition), it is worthwhile to disentangle the various effects of Gr doping on the MTB states and the electronic landscape surrounding them.

In MoS₂ two types of MTBs (4|4E and 4|4P) are present, formed between 180°-misoriented MoS₂ domains [60, 61]. A model and a constant current STM image of the 4|4E MTB are shown in figures 6(a) and (b), respectively. The 4|4P MTB is discussed in the SI (figure S4). In the pristine sample, the states within MTBs are strictly 1D, leading to strong electron–correlations and the emergence of Tomonaga–Luttinger liquid (TLL) behaviour [62]. In addition, since the states are located in boundaries of finite length, they are confined. Hence, when mapping the local density of states close to the Fermi energy, we expect a pronounced, sinusoidal beating pattern along the length of the MTB, resulting from quantized 1D electronic states, as shown in figure 6(c). The wavelength of this beating pattern is related to the confined states closest to the Fermi energy, $\lambda = \pi/k_F$ [62]. Therefore, if the charge donated by the Gr substrate shifts the Fermi level of the MTB band, the change in filling can be observed directly with STM, by imaging the periodicity of the states near E_F .

The constant height STM images in figure 6(c), taken near E_F , reveal the beating patterns found within 4|4E MTBs for MoS₂ on the differently doped substrates. In the pristine case, we find $\lambda_{\text{F}}^{\text{Gr}} = (2.01 \pm$

$0.04)a$ for the 4|4E MTBs, where $a = 0.315$ nm is the ML MoS₂ lattice constant [63]. For p-shifted MoS₂ the periodicity along the 4|4E MTBs has visibly decreased, $\lambda_F^O = (1.72 \pm 0.01)a$, while for n-shifted MoS₂, an increased periodicity of $\lambda_F^{Eu} = (2.69 \pm 0.11)a$ is measured.

The shifts in the beating periodicity can be understood from the band structure of the MTB. 4|4E MTBs host a hole-like band, which is shown in green in figure 6(d), based on DFT calculations discussed in [62]. With the Fermi level E_F in the pristine case bisecting the band at $k_F = \pi/2a$, this leads to the observed $2a$ periodicity. When the Gr substrate is n-doped, additional charge can flow into the boundary, raising the Fermi level to E_F^{Eu} and leading to an increased wavelength λ_F^{Eu} . For p-doping of Gr, the inverse happens: charge is extracted from the boundary, the Fermi level sinks to E_F^O and λ_F^O decreases. The quantitative relationship between k_F and the line charge in the boundary is given in the SI (table S2).

From the measured k values we find that the chemical potential shifts in the MTB are considerably smaller than those in Gr or MoS₂, with the Fermi level difference between the 4|4E on n- and p-doped Gr about 500 meV, see SI (table S2) for the exact values. In other words, the states within MTBs locally pin the Fermi level, while Fermi level pinning is absent in MoS₂ away from defects. This can be understood from previous considerations: the metal-metal interface between the MTB and Gr allows for charge transfer and thus the formation of an interface dipole. As a consequence, the MTB Fermi level will not shift as much as the chemical potential of MoS₂, which rigidly follows the Gr doping level until it becomes metallic. Note that the relation between λ_F and Fermi level is reversed for 4|4P MTBs, which host an electron-like band, see SI (figure S7).

Our findings are summarized in figure 6(e) in which we plot the position of the CBM of MoS₂ as a function of beating period for the two types of MTBs. This allows the identification of the Fermi wave vector of the MTB band and the position of the chemical potential μ with respect to the MoS₂ conduction band in a single STM image. Due to the close proximity of CBM and chemical potential in our n-shifted MoS₂ samples, we can also set a lower bound of $\lambda_F^{Eu} = (2.69 \pm 0.11)a$ for the beating pattern within 4|4E MTBs, for which the surrounding 2D material is metallic. As a consequence, the MTBs function as a sensor—they allow for a determination of the chemical potential of MoS₂ by measuring the periodicity of the MTB states near E_F . This method is also applicable at room temperature.

In figures 6(f)–(h) we display additional constant height STS linescans averaged along the length of 4|4E MTBs on all three substrates, respectively. The finite length of the MTBs leads to a series of peaks in the dI/dV spectra at the energetic location of the quantized states. The dominant lowest energy excitations

for a given wavevector are used to obtain the dispersion within the 4|4E MTBs, see figure 6(d) [62]. We find a pronounced gap E_{gap} around the Fermi level, consistent with the presence of a Coulomb blockade which pushes the states closest to E_F further apart [62]. The gap is almost twice as large as the energy spacing between the quantized states E_{qws} . We find that the ratio $E_{\text{gap}}/E_{\text{qws}}$, which eliminates the length-dependence of both parameters [64], has only minor substrate-dependence. This is surprising, since the presence of a Coulomb gap, which arises from strong electron–electron interactions, indicates that the 1D correlated states within 4|4E MTBs persist even when the surrounding MoS₂ is metallic.

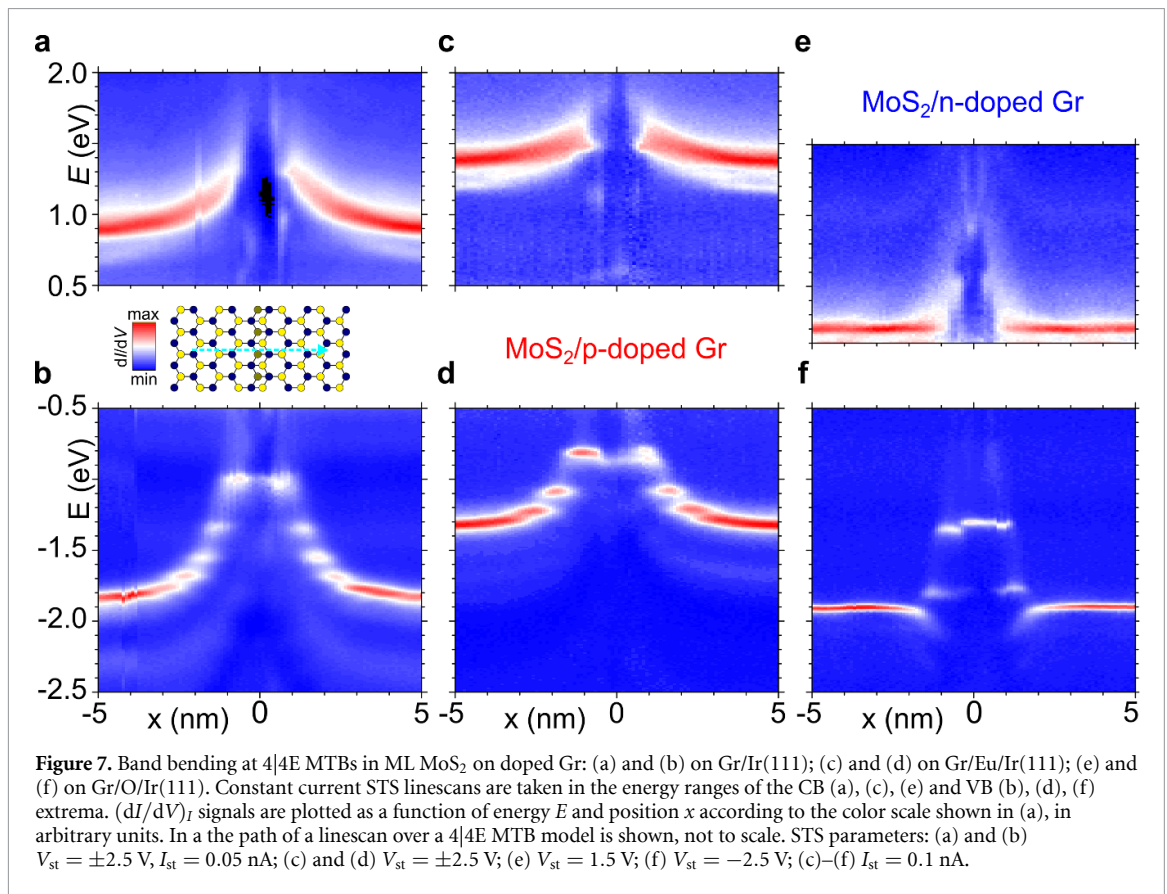
Moving away from the effects of the intercalation on the intrinsic MTB properties, we also investigated the region directly surrounding the boundaries, where the MoS₂ bands are bent under the influence of the MTB charge [59]. The magnitude of band bending must change if the amount of charge on the MTB is changed in consequence of Gr doping, while the shape of the bending provides insight into how the screening properties of MoS₂ are affected.

For reference, we take constant current STS linescans orthogonally crossing a 4|4E MTB in the pristine heterostructure. While figure 7(a) captures the behaviour of the CB edge, figure 7(b) captures that of the VB. Far away from the MTB, at $x = \pm 5$ nm, the unperturbed pristine band structure is observed. Approaching the MTB, located at $x = 0$ nm, both CB and VB are seen to bend upwards by at least 0.5 eV, indicating that the MTB is negatively charged. The bending is smooth in the CB but occurs stepwise at characteristic energies in the VB due to quantization effects [59].

On p-doped Gr, figures 7(c) and (d), the magnitude of the bending is severely reduced for both bands, while the spatial extent of the bending is similar to that of the pristine case. There are fewer quantized VB levels and the unperturbed band structure is recovered at $x = \pm 4$ nm. This can be understood from previous considerations: Gr is more p-doped, lowering its chemical potential. As a result, certain MTB states are now shifted above the Gr Fermi level and less charge can flow from Gr into the MTB, reflected in its smaller periodicity at E_F .

On n-doped Gr, shown in figures 7(e) and (f), the bending of the MoS₂ bands occurs in a much smaller range of $|2|$ nm on either side of the MTB. In figure 7(f) there are fewer quantized VB levels—only two—and their energy spacing is larger. The highest quantized state occurs at around -1.3 eV, compared to -1.0 eV found in the pristine sample. Additionally, the VB bends up steeply at $x \approx \pm 1.5$ nm from the boundary. The increase in band bending due to graphene n-doping is expected, as more charge is transferred into the MTB states.

The decrease of the spatial extent of band bending on the one hand is a sign of the metallic phase



of MoS₂ on Gr/Eu/Ir(111), which effectively screens the charge within the MTB. On the other hand, the steep band bending close to the MTB leaves the direct surrounding of the latter insulating, in line with the persistent Coulomb gap E_{gap} found experimentally.

2. Discussion

We have demonstrated a non-invasive method to strongly modify the electrostatic environment of ML MoS₂, applicable also to other TMDCs and van der Waals materials. We have shown that the doping of its Gr substrate can induce a metal–insulator transition in MoS₂ and enables the manipulation of metallic states within MTBs. In addition, the chemical potential shifts in MoS₂ can be monitored via MTB states and the screening environment around the boundaries. The backside functionalization of Gr leaves the TMDC top layer chemically pristine, thereby offering advantages over chemical doping or adatom techniques. Our contactless chemical doping method to shift the chemical potential of wide-bandgap semiconductors can be extended by other intercalants such as alkalis [65], other rare earth metals [66] or the p-dopant chlorine [67]. Continuous tuning of the chemical potential, analogous to gating, could be accomplished by using Li as intercalant [68, 69]. A combination of contactless gating for coarse adjustment of the chemical potential with electrostatic gating for fine adjustment represents another exciting

perspective. As the conductive Gr substrate is not suited to most technological applications, replacing it with an insulating layer such as hexagonal boron nitride presents a promising approach to achieve practical implementation of this method. We envision that contactless chemical doping will enable observation and characterization of novel states of matter using both local and global surface science techniques.

3. Methods

The samples were grown *in situ* in a preparation chamber with base pressure $p < 5 \times 10^{-10}$ mbar. Ir(111) is cleaned by 1.5 keV Ar⁺ ion erosion and annealing to temperatures $T \approx 1550$ K. Gr is grown on Ir(111) by two steps. First, room temperature ethylene exposure till saturation followed by 1370 K thermal decomposition gives well-oriented Gr islands. Second, exposure to 2000 l ethylene at 1370 K for 600 s yields a complete single-crystal Gr layer [70]. ML MoS₂ is grown by Mo deposition in an elemental S pressure of 1×10^{-8} mbar [71]. Subsequently, the sample is annealed to 1050 K in the same S background pressure. The Eu-intercalated sample is prepared in the order: Gr growth; Eu intercalation; MoS₂ growth. Eu is evaporated from a Knudsen cell onto the Gr/Ir(111) crystal kept at 720 K. Intercalation is confirmed by low-energy electron diffraction (LEED) [72]. After Eu intercalation no Eu is adsorbed on

Gr [72, 73]. Subsequently, the sample is annealed to 1075 K. Due to this annealing step, all Eu that could escape from underneath the Gr at the lower MoS₂ annealing temperature of 1050 K has already escaped. Thereby Eu contamination of MoS₂ during subsequent MoS₂ growth and annealing is prevented. The O-intercalated sample is prepared in the order: Gr growth; MoS₂ growth, O intercalation. O intercalation is achieved by exposing MoS₂/Gr/Ir(111) for 210 seconds at 770 K to 2×10^4 l of O₂ [30, 33]. No obvious increase in the density of point defects, such as oxygen substitutions [74], is observed in MoS₂ after oxygen intercalation.

STM and STS are carried out in the $T = 7$ K bath cryostat system after *in situ* transfer from the preparation chamber. STS is performed with the lock-in technique, at modulation frequency 619–777 Hz and modulation voltage $V_{\text{mod}} = 4$ mV_{rms}, with an experimental resolution of ≈ 10 meV or better [75]. We employ constant height (recording $(dI/dV)_Z$) and constant current ($(dI/dV)_I$) STS modes, where I is the tunneling current, V the bias voltage, and Z the tip-sample distance or height. In both modes dI/dV is recorded while V is ramped; see [5] for further explanation. Spectra are always taken away (> 6 nm) from defects, unless indicated otherwise.

All density functional theory calculations were carried out using the Vienna *Ab Initio* Simulation Package (VASP) [76, 77]. The plane wave cutoff was set to 400 eV throughout. We used the exchange-correlation functional of Perdew, Burke, and Ernzerhof (PBE) [78]. Van der Waals interactions are described using Grimme's semi-empirical corrections at the D2 level [79]. A 4×4 k-point mesh was used during structural optimization in the supercell, while the density of states is evaluated using a 16×16 mesh. The optimized lattice constants of MoS₂ and Gr are 3.18 Å and 2.468 Å, respectively. For a minimally strained heterostructure model, we used the same approach and model as in [39], wherein a 4×4 supercell of MoS₂ is interfaced with a $(6, 3) \times (6, 3)$ Gr cell (i.e. $\vec{a}_{\text{sc}} = 6\vec{a} + 3\vec{b}$, where \vec{a} and \vec{b} are the lattice vectors of Gr at an 120° angle). The dopants were placed as far from each other as possible within the supercell. The optimized geometry for O atoms was between graphene top- and hollow-sites. The optimized geometry for Eu atoms was on the graphene hollow site. The MoS₂ layer is kept unstrained and Gr layer is compressively strained by 0.8%. Finally, in order to avoid the buckling of Gr due to chemical interactions with the dopants, charging, or strain, the z -coordinates of C atoms were fixed.

Data availability statement

The data that support the findings of this study are available upon reasonable request from the authors.

Acknowledgments

This work was funded by the Deutsche Forschungsgemeinschaft (DFG, German Research Foundation)—Project Number 277146847—CRC 1238 (Subprojects A01 and B06). Support from the German Academic Exchange Service DAAD and the Academy of Finland via PPP Finland MODEST, Project IDs 57458732 (DAAD) and 321914 (Academy of Finland) is gratefully acknowledged. The authors thank CSC IT Center for Science for the generous grants of computer time.

ORCID iDs

Camiel van Efferen  <https://orcid.org/0000-0002-6237-8602>

Carsten Busse  <https://orcid.org/0000-0001-5522-0578>

Hannu-Pekka Komsa  <https://orcid.org/0000-0002-0970-0957>

References

- [1] Xi X, Zhao L, Wang Z, Berger H, Forró L, Shan J and Mak K F 2015 Strongly enhanced charge-density-wave order in monolayer NbSe₂ *Nat. Nanotechnol.* **10** 765–9
- [2] Chen Y *et al* 2020 Strong correlations and orbital texture in single-layer 1T-TaSe₂ *Nat. Phys.* **16** 218–24
- [3] Ugeda M M *et al* 2016 Characterization of collective ground states in single-layer NbSe₂ *Nat. Phys.* **12** 92–97
- [4] Li L, O'Farrell E, Loh K, Eda G, Özyilmaz B and Castro Neto A 2016 Controlling many-body states by the electric-field effect in a two-dimensional material *Nature* **529** 185–9
- [5] Murray C, Jolie W, Fischer J A, Hall J, van Efferen C, Ehlen N, Grüneis A, Busse C and Michely T 2019 Comprehensive tunneling spectroscopy of quasifreestanding MoS₂ on graphene on Ir(111) *Phys. Rev. B* **99** 115434
- [6] Nguyen P V *et al* 2019 Visualizing electrostatic gating effects in two-dimensional heterostructures *Nature* **572** 220–3
- [7] Qiu Z *et al* 2019 Giant gate-tunable bandgap renormalization and excitonic effects in a 2D semiconductor *Sci. Adv.* **5** eaaw2347
- [8] Ye J, Zhang Y J, Akashi R, Bahramy M S, Arita R and Iwasa Y 2012 Superconducting dome in a gate-tuned band insulator *Science* **338** 1193–6
- [9] Lu J M, Zheliuk O, Leermakers I, Yuan N F, Zeitler U, Law K T and Ye J T 2015 Evidence for two-dimensional Ising superconductivity in gated MoS₂ *Science* **350** 1353–7
- [10] Saito Y *et al* 2016 Superconductivity protected by spin-valley locking in ion-gated MoS₂ *Nat. Phys.* **12** 144–9
- [11] Saito Y, Nojima T and Iwasa Y 2017 Highly crystalline 2D superconductors *Nat. Rev. Mater.* **2** 16094
- [12] Lu J, Zheliuk O, Chen Q, Leermakers I, Hussey N E, Zeitler U and Ye J 2018 Full superconducting dome of strong Ising protection in gated monolayer WS₂ *Proc. Natl Acad. Sci.* **115** 3551–6
- [13] Wang L *et al* 2020 Correlated electronic phases in twisted bilayer transition metal dichalcogenides *Nat. Mater.* **19** 861–6
- [14] Ren Y, Yuan H, Wu X, Chen Z, Iwasa Y, Cui Y, Hwang H Y and Lai K 2015 Direct imaging of nanoscale conductance evolution in ion-gel-gated oxide transistors *Nano Lett.* **15** 4730–6
- [15] Jo S, Costanzo D, Berger H and Morpurgo A F 2015 Electrostatically induced superconductivity at the surface of WS₂ *Nano Lett.* **15** 1197–202

- [16] Costanzo D, Jo S, Berger H and Morpurgo A F 2016 Gate-induced superconductivity in atomically thin MoS₂ crystals *Nat. Nanotechnol.* **11** 339–44
- [17] Fu Y *et al* 2017 Gated tuned superconductivity and phonon softening in monolayer and bilayer MoS₂ *npj Quantum Mater.* **2** 52
- [18] Piatti E, De Fazio D, Daghero D, Tamalampudi S R, Yoon D, Ferrari A C and Gonnelli R S 2018 Multi-valley superconductivity in ion-gated MoS₂ layers *Nano Lett.* **18** 4821–30
- [19] Costanzo D, Zhang H, Reddy B A, Berger H and Morpurgo A F 2018 Tunnelling spectroscopy of gate-induced superconductivity in MoS₂ *Nat. Nanotechnol.* **13** 483–8
- [20] Helveg S, Lauritsen J V, Lægsgaard E, Stensgaard I, Njörskov J K, Clausen B S, Topsoe H and Besenbacher F 2000 Atomic-scale structure of single-layer MoS₂ nanoclusters *Phys. Rev. Lett.* **84** 951–4
- [21] Alidoust N *et al* 2014 Observation of monolayer valence band spin-orbit effect and induced quantum well states in MoX₂ *Nat. Commun.* **5** 4673
- [22] Zhang C, Johnson A, Hsu C-L, Li L-J and Shih C-K 2014 Direct imaging of band profile in single layer MoS₂ on graphite: quasiparticle energy gap, metallic edge states and edge band bending *Nano Lett.* **14** 2443–7
- [23] Kang M *et al* 2017 Universal mechanism of band-gap engineering in transition-metal dichalcogenides *Nano Lett.* **17** 1610–5
- [24] Katoch J *et al* 2018 Giant spin-splitting and gap renormalization driven by trions in single-layer WS₂/h-BN heterostructures *Nat. Phys.* **14** 355–9
- [25] Liu H *et al* 2020 Spontaneous chemical functionalization via coordination of Au single atoms on monolayer MoS₂ *Sci. Adv.* **6** eabc9308
- [26] Shao B, Eich A, Sanders C, Nganku A S, Bianchi M, Hofmann P, Khajetoorians A A and Wehling T O 2019 Pseudodoping of a metallic two-dimensional material by the supporting substrate *Nat. Commun.* **10** 180
- [27] Hsu Y-T, Vaezi A, Fischer M H and Kim E-A 2017 Topological superconductivity in monolayer transition metal dichalcogenides *Nat. Commun.* **8** 14985
- [28] Schumacher S *et al* 2013 The backside of graphene: manipulating adsorption by intercalation *Nano Lett.* **13** 5013–9
- [29] Larciprete R *et al* 2012 Oxygen switching of the epitaxial graphene-metal interaction *ACS Nano* **6** 9551–8
- [30] Grånäs E, Knudsen J, Schröder U A, Gerber T, Busse C, Arman M A, Schulte K, Andersen J N and Michely T 2012 Oxygen intercalation under graphene on Ir(111): energetics, kinetics and the role of graphene edges *ACS Nano* **6** 9951–63
- [31] Jolie W, Craes E, Petrović M, Atodiresei N, Caciuc V, Blügel S, Kralj M, Michely T and Busse C 2014 Confinement of Dirac electrons in graphene quantum dots *Phys. Rev. B* **89** 155435
- [32] Giovannetti G, Khomyakov P A, Brocks G, Karpan V M, van den Brink J and Kelly P J 2008 Doping graphene with metal contacts *Phys. Rev. Lett.* **101** 026803
- [33] Martínez-Galera A J *et al* 2016 Oxygen orders differently under graphene: new superstructures on Ir(111) *Nanoscale* **8** 1932–43
- [34] Schumacher S, Förster D, Rösner M, Wehling T and Michely T 2013 Strain in epitaxial graphene visualized by intercalation *Phys. Rev. Lett.* **110** 086111
- [35] Huttmann F *et al* 2015 Tuning the van der Waals interaction of graphene with molecules via doping *Phys. Rev. Lett.* **115** 236101
- [36] Zhang X *et al* 2015 Growth graphene on silver-copper nanoparticles by chemical vapor deposition for high-performance surface-enhanced Raman scattering *Appl. Surf. Sci.* **353** 63–70
- [37] Ehlen N *et al* 2019 Narrow photoluminescence peak of epitaxial MoS₂ on graphene/Ir(111) *2D Mater.* **6** 011006
- [38] Ehlen N 2017 private communication
- [39] Komsa H-P and Krasheninnikov A V 2013 Electronic structures and optical properties of realistic transition metal dichalcogenide heterostructures from first principles *Phys. Rev. B* **88** 085318
- [40] Li W-K and Blinder S M 1985 Solution of the Schrödinger equation for a particle in an equilateral triangle *J. Math. Phys.* **26** 2784–6
- [41] Cheiwchanchamnangij T and Lambrecht W R L 2012 Quasiparticle band structure calculation of monolayer, bilayer and bulk MoS₂ *Phys. Rev. B* **85** 205302
- [42] Qiu D Y, da Jornada F H and Louie S G 2013 Optical spectrum of MoS₂: many-body effects and diversity of exciton states *Phys. Rev. Lett.* **111** 216805
- [43] Komsa H-P and Krasheninnikov A V 2015 Native defects in bulk and monolayer MoS₂ from first principles *Phys. Rev. B* **91** 125304
- [44] Michaelson H B 1977 The work function of the elements and its periodicity *J. Appl. Phys.* **48** 4729–33
- [45] Yan H, Sun Y, He L, Nie J-C and Chan M H W 2012 Observation of Landau-level-like quantization at 77 K along a strained-induced graphene ridge *Phys. Rev. B* **85** 035422
- [46] Pletikosić I, Kralj M, Pervan P, Brako R, Coraux J, N'Diaye A T, Busse C and Michely T 2009 Dirac cones and minigaps for graphene on Ir(111) *Phys. Rev. Lett.* **102** 056808
- [47] Khomyakov P A, Giovannetti G, Rusu P C, Brocks G, van den Brink J and Kelly P J 2009 First-principles study of the interaction and charge transfer between graphene and metals *Phys. Rev. B* **79** 195425
- [48] Das S, Chen H-Y, Penumatcha A V and Appenzeller J 2013 High performance multilayer MoS₂ transistors with scandium contacts *Nano Lett.* **13** 100–5
- [49] Lee S Y *et al* 2016 Large work function modulation of monolayer MoS₂ by ambient gases *ACS Nano* **10** 6100–7
- [50] Hu C, Yuan C, Hong A, Guo M, Yu T and Luo X 2018 Work function variation of monolayer MoS₂ by nitrogen-doping *Appl. Phys. Lett.* **113** 041602
- [51] Zhang C *et al* 2016 Systematic study of electronic structure and band alignment of monolayer transition metal dichalcogenides in van der Waals heterostructures *2D Mater.* **4** 015026
- [52] Schlaf R, Lang O, Pettenkofer C and Jaegermann W 1999 Band lineup of layered semiconductor heterointerfaces prepared by van der Waals epitaxy: charge transfer correction term for the electron affinity rule *J. Appl. Phys.* **85** 2732
- [53] Riis-Jensen A C, Lu J and Thygesen K S 2020 Electrically controlled dielectric band gap engineering in a two-dimensional semiconductor *Phys. Rev. B* **101** 121110
- [54] Ugeda M M *et al* 2014 Giant bandgap renormalization and excitonic effects in a monolayer transition metal dichalcogenide semiconductor *Nat. Mater.* **13** 1091–5
- [55] Allain A, Kang J, Banerjee K and Kis A 2015 Electrical contacts to two-dimensional semiconductors *Nat. Mater.* **14** 1195–205
- [56] Diaz H C, Ma Y, Chaghi R and Batzill M 2016 High density of (pseudo) periodic twin-grain boundaries in molecular beam epitaxy-grown van der Waals heterostructure: MoTe₂/MoS₂ *Appl. Phys. Lett.* **108** 191606
- [57] Bampoulis P, van Bremen R, Yao Q, Poelsema B, Zandvliet H J W and Sotthewes K 2017 Defect dominated charge transport and Fermi level pinning in MoS₂/metal contacts *ACS Appl. Mater. Interfaces* **9** 19278–86
- [58] Le Quang T, Cherkez V, Nogajewski K, Potemski M, Dau M T, Jamet M, Mallet P and Veuillen J-Y 2017 Scanning tunneling spectroscopy of van der Waals graphene/semiconductor interfaces: absence of Fermi level pinning *2D Mater.* **4** 035019
- [59] Murray C, van Efferen C, Jolie W, Fischer J A, Hall J, Rosch A, Krasheninnikov A V, Komsa H-P and Michely T 2020 Band bending and valence band quantization at line defects in MoS₂ *ACS Nano* **14** 9176–87
- [60] Zou X, Liu Y and Yakobson B I 2013 Predicting dislocations and grain boundaries in two-dimensional metal-disulfides from the first principles *Nano Lett.* **13** 253–8

- [61] Komsa H-P and Krasheninnikov A V 2017 Engineering the electronic properties of two-dimensional transition metal dichalcogenides by introducing mirror twin boundaries *Adv. Electron. Mater.* **3** 1600468
- [62] Jolie W *et al* 2019 Tomonaga–Luttinger liquid in a box: electrons confined within MoS₂ mirror-twin boundaries *Phys. Rev. X* **9** 011055
- [63] Kormányos A, Burkard G, Gmitra M, Fabian J, Zólyomi V, Drummond N D and Fal'ko V 2015 $\mathbf{k} \cdot \mathbf{p}$ theory for two-dimensional transition metal dichalcogenide semiconductors *2D Mater.* **2** 022001
- [64] Yang X *et al* 2021 Manipulating Hubbard-type Coulomb blockade effect of metallic wires embedded in an insulator (arXiv:2104.08577)
- [65] Petrović M *et al* 2013 The mechanism of caesium intercalation of graphene *Nat. Commun.* **4** 2772
- [66] Klimovskikh I, Krivenkov M, Varykhalov A, Estyunin D and Shikin A 2019 Reconstructed Fermi surface in graphene on Ir(111) by Gd-Ir surface alloying *Carbon* **147** 182–6
- [67] Vinogradov N A, Simonov K, Generalov A, Vinogradov A, Vyalikh D, Laubschat C, Mårtensson N and Preobrajenski A 2012 Controllable p-doping of graphene on Ir (111) by chlorination with FeCl₃ *J. Phys.: Condens. Matter* **24** 314202
- [68] Schröder U A *et al* 2016 Core level shifts of intercalated graphene *2D Mater.* **4** 015013
- [69] Halle J, Néel N and Kröger J 2016 Filling the gap: Li-intercalated graphene on Ir(111) *J. Phys. Chem. C* **120** 5067–73
- [70] Coraux J *et al* 2009 Growth of graphene on Ir(111) *New J. Phys.* **11** 023006
- [71] Hall J, Pielic B, Murray C, Jolie W, Wekking T, Busse C, Kralj M and Michely T 2018 Molecular beam epitaxy of quasi-freestanding transition metal disulphide monolayers on van der Waals substrates: a growth study *2D Mater.* **5** 025005
- [72] Schumacher S *et al* 2014 Europium underneath graphene on Ir(111): intercalation mechanism, magnetism and band structure *Phys. Rev. B* **90** 235437
- [73] Schumacher S, Förster D F, Rösner M, Wehling T O and Michely T 2013 Strain in epitaxial graphene visualized by intercalation *Phys. Rev. Lett.* **110** 086111
- [74] Barja S *et al* 2019 Identifying substitutional oxygen as a prolific point defect in monolayer transition metal dichalcogenides *Nat. Commun.* **10** 1–8
- [75] Morgenstern M 2003 Probing the local density of states of dilute electron systems in different dimensions *Surf. Rev. Lett.* **10** 933–62
- [76] Kresse G and Furthmüller J 1996 Efficient iterative schemes for *ab initio* total-energy calculations using a plane-wave basis set *Phys. Rev. B* **54** 11169–86
- [77] Kresse G and Furthmüller J 1996 Efficiency of *ab-initio* total energy calculations for metals and semiconductors using a plane-wave basis set *Comput. Mater. Sci.* **6** 15–50
- [78] Perdew J P, Burke K and Ernzerhof M 1996 Generalized gradient approximation made simple *Phys. Rev. Lett.* **77** 3865
- [79] Grimme S 2006 Semiempirical GGA-type density functional constructed with a long-range dispersion correction *J. Comput. Chem.* **27** 1787

6.1 Supporting information

Metal-insulator transition in monolayer MoS₂ via contactless chemical doping

Camiel van Efferen^{1,5,*}, Clifford Murray^{1,5}, Jeison Fischer¹, Carsten Busse^{2,3}, Hannu-Pekka Komsa⁴, Thomas Michely¹, Wouter Jolie¹

¹*II. Physikalisches Institut, Universität zu Köln, Zùlpicher Straße 77, 50937 Köln, Germany*

²*Present address: Department Physik, Universität Siegen, Walter-Flex-Str. 3, 57068 Siegen, Germany*

³*Institut für Materialphysik, Westfälische Wilhelms-Universität Münster, Wilhelm-Klemm-Straße 10, 48149 Münster, Germany*

⁴*Faculty of Information Technology and Electrical Engineering, University of Oulu, Pentti Kaiteran katu 1, 90014 Oulu, Finland*

⁵*CvE and CM contributed equally to this work*

Contents

Contactless chemical doping of WS ₂	3
Intercalation structures	5
Effect of non-uniform Eu intercalation on MoS ₂	7
Fitting of the dispersion	9
Constant height STS of CB minimum	11
Field emission resonances on n-doped Gr	12
DFT results	14
Charging of MTBs	15
4 4P MTB	17

Contactless chemical doping of WS₂

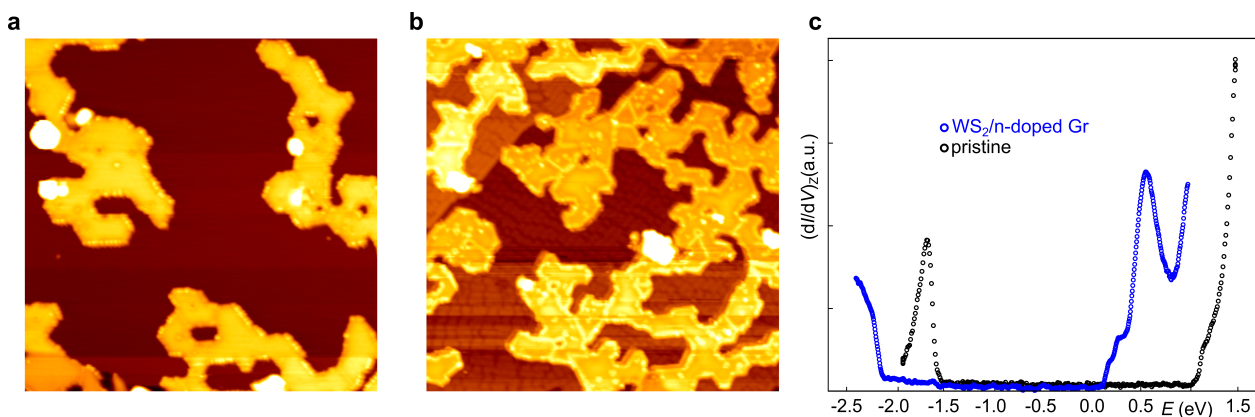


Figure S1: **a** Constant current STM overview topograph of WS₂/Gr/Ir(111) Sample has 0.4 ML coverage of monolayer WS₂ with few bilayers. **b** WS₂/Gr/Eu/Ir(111). Sample has 0.7 ML coverage of monolayer WS₂ with no bilayers present. A single Ir(111) step edge is visible in the upper left. Gr is fully intercalated. **c** Constant height STS of ML WS₂/Gr/Ir(111) (black) and ML WS₂/Gr/Eu/Ir(111) (blue). STM/STS parameters: **a** $V_{st} = 1.75$ V, $I_{st} = 0.03$ nA, image size 100×100 nm²; **b** $V_{st} = -2.0$ V, $I_{st} = 0.1$ nA, image size 100×100 nm²; **c** $V_{st} = 1.5$ V, $I_{st} = 0.4$ nA (black); $V_{st} = -2.5$ V, $I_{st} = 0.2$ nA (blue).

Contactless chemical gating of WS₂ is demonstrated in Fig. S1. The scanning tunneling microscopy (STM) topographs, displayed in Fig. S1a, b, present ML WS₂ islands on graphene (Gr) and on n-gated Gr, respectively. In the latter, Gr is fully intercalated by Eu. The Eu superstructure is identical to the one found after MoS₂ growth. It is discussed in Fig. S2.

Fig. S1b compares constant height spectra measured on WS₂/Gr/Ir(111) (referred to as pristine) and WS₂/Gr/Eu/Ir(111) (referred to as WS₂ on n-doped graphene). We see that the n-doping of Gr causes a considerable shift in the WS₂ band structure towards lower energies. The conduction band (CB) is shifted by 1 eV down to the Fermi energy. In contrast,

the valence band (VB) moved only by about 0.7 eV. The different energy shifts of the CB and VB indicate a band gap renormalization of ≈ 0.3 eV.

Intercalation structures

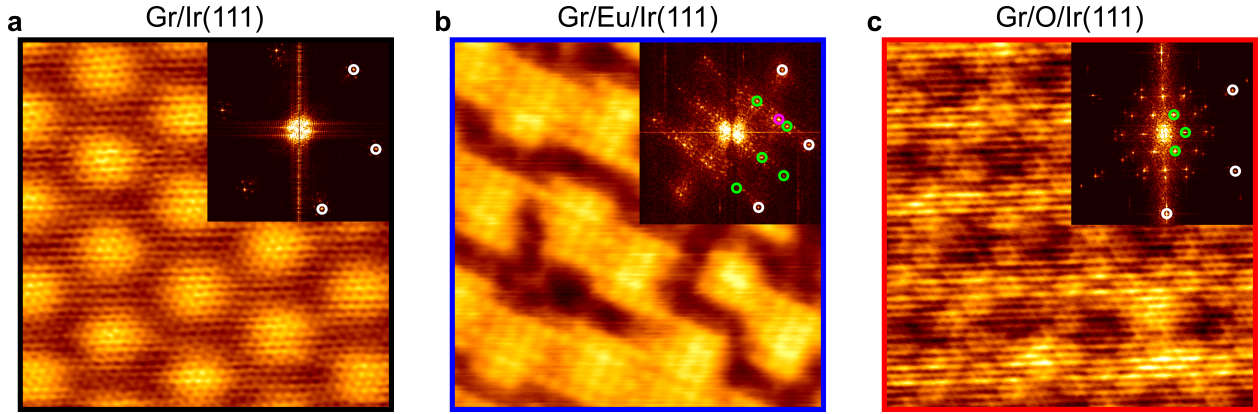


Figure S2: Constant current STM close-up topographs of the Gr substrates: **a** Gr/Ir(111), **b** Gr/Eu/Ir(111), **c** Gr/O/Ir(111). Insets show the Fourier transform (FT) of each image, with spots corresponding to Gr (white circled) and the superstructures (green circled) highlighted. STM parameters (V , I): **a** -0.15 V, 8.00 nA; **b** 0.30 V, 0.40 nA; **c** 0.01 V, 0.50 nA; **a-d** image size 10×10 nm².

In Fig. S2 we identify the graphene (Gr) intercalation structures on the atomic scale. For purpose of comparison, Fig. S2a shows a topograph of Gr/Ir(111) and, in the inset, the Fourier transform (FT) of the topograph. The Gr lattice and the moiré with Ir(111), of unit lengths 0.245 nm and 2.53 nm respectively, are visible in real space. In reciprocal space the brightest outer spots correspond to Gr (white circles).

The topograph in Fig. S2b shows an area of Gr/Eu/Ir. A rectangular lattice covers most of the image, with small trenches of presumably lower (or zero) Eu density in between. The apparent height of the higher density areas relative to the areas of low density is ≈ 50 pm. The higher density patches often coalesce along a single direction, leading to the formation of bright stripes. The Eu superstructure (green circles) is measured to have unit

lengths (0.426 ± 0.07) nm and (0.495 ± 0.06) nm, corresponding to a $c(4 \times 2)$ with respect to Gr. The superstructure spots also have satellites of the Gr/Ir(111) moiré unit length, and there are additional spots (pink circle), each resulting from the summation of vectors analogous to multiple scattering in LEED. Eu is known to form various hexagonally symmetric superstructures under Gr on Ir(111) ¹⁻³. The $c(4 \times 2)$ phase has not been reported previously, but we note that it has precisely the same density as the well-documented (2×2) phase, namely 25% with respect to the Gr lattice. Its electronic effect on Gr is also comparable, see Fig. S6.

In Fig. S2c the O intercalation structure is seen. It forms a $(2\sqrt{3} \times 2\sqrt{3})$ -R30° superstructure with respect to Ir(111), which was previously reported in Ref. 4. It has a density of 0.5 ML of O with respect to the Ir(111) surface.

Effect of non-uniform Eu intercalation on MoS₂

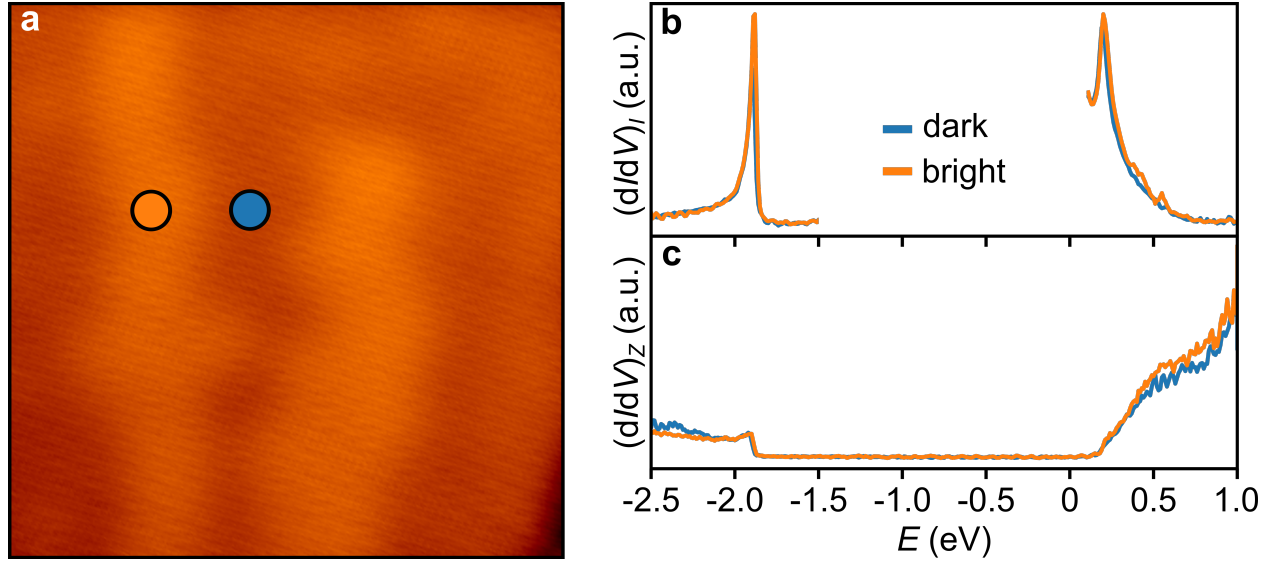


Figure S3: Spectroscopic investigation of bright and dark patches of MoS₂ on Eu-intercalated graphene. **a** Constant current STM topograph of MoS₂ on top of Eu-intercalated Gr. The orange and blue spot mark the locations of STS spectra. **b,c** Constant current (**b**) and constant height (**c**) STS taken at the locations indicated in **a**. The spectra are normalized to the signal strength at the stabilization voltage: dI/dV ($V = V_{\text{stab}}$). STM/STS parameters (V , I): **a** 0.80 V, 0.50 nA; **b** valence band: -2.50 V, 0.20 nA (dark), 0.50 nA (bright); conduction band: 1.10 V, 0.20 nA; **c** -2.50 V, 1.00 nA; **a-c** image size 14×14 nm².

We find small apparent height modulations in the MoS₂ layer on the Gr/Eu/Ir(111) substrate. The modulations on MoS₂ often appear as stripes, as in Fig. S3a, though individual patches are also found, see inset of Fig. 1d in the main manuscript. The stripes (or patches) have an apparent height of ≈ 50 pm and have no detectable effect on the electronic properties of MoS₂, as is shown in Fig. S3b,c,d, where dI/dV spectra taken on top and in between the bright areas show essentially no difference. We therefore rule out that they are caused by residual Eu atoms between MoS₂ and Gr, which would lead to strong energy shifts in the peak

positions. Instead, we attribute the effect to the density variations in the Eu intercalation of Gr, seen in Fig. S2b, which have the same apparent height of ≈ 50 pm as the modulations on MoS₂. The lack of electronic variation in MoS₂ is also in line with the near-uniform doping of Gr across the Eu-intercalated areas, see Fig. S6.

Fitting of the dispersion

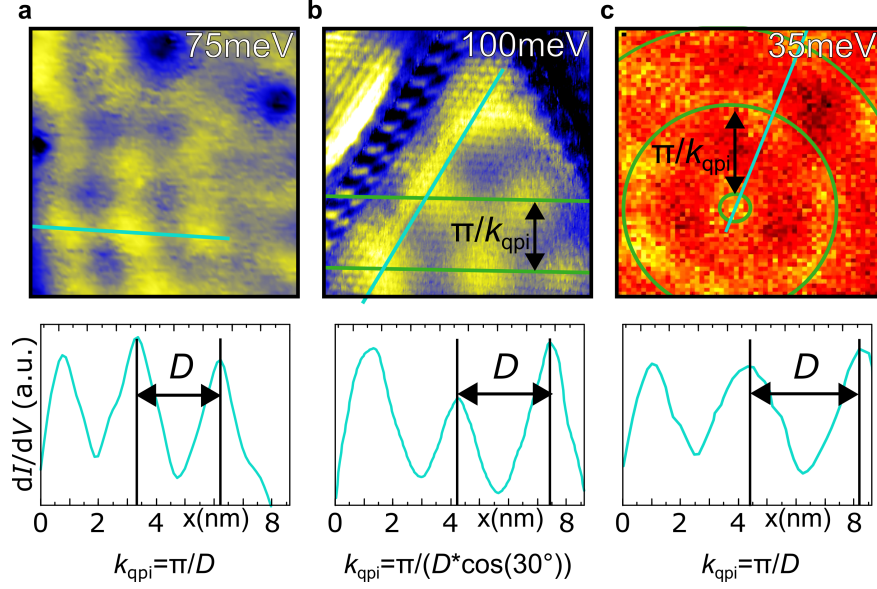


Figure S4: Extraction of the dispersion from STS data of n-shifted MoS₂. **a** Top panel: differential constant current conductance map. Quasiparticle interference patterns around defects are visible. A line profile (cyan line) is taken on maxima normal to a MoS₂ island edge. **b** Top panel: differential constant current conductance map of a triangular quantum well. A line profile is taken on the maxima parallel to an edge of the well. **c** Top panel: constant height STS grid at 35 meV of an approximately circular quantum well. A line profile is taken along maxima so that the line is normal to the circular wavefronts. **a-c** Lower panel: line profile along cyan line in top panel, with below it the relation of maxima along the line profile (D) and wavenumber (k_{qpi}). STM/STS parameters: **a** $I_{\text{st}}=0.1$ nA, image size 11×11 nm²; **b** $I_{\text{st}}=0.1$ nA, image size 9×9 nm²; **c** $I_{\text{st}}=0.4$ nA, image size 9.7×9.7 nm².

To determine the dispersion of the quasiparticles crossing the Fermi level, the real space wavelength of standing waves due to quasiparticle interference D can be measured. The exact relation between the maxima visible in differential conductance maps and the wavenumber k_{qpi} depends on the geometry of the scattering area. The most straightforward

case is depicted in Fig. S4a. When quasiparticles scatter from a (relatively) straight edge or boundary, the standing wave normal to the scatterer has a wavenumber $k_{\text{qpi}} = \pi/D$. Note that there are multiple scatters present in the area, which causes the behavior of the quasiparticle interference (QPI) to differ from that of a single wave-train scattering from a 1D defect ⁵.

In the case of a triangular quantum well, as in Fig. S4b, interference from the three straight edges leads to a more complicated pattern, which can be solved exactly, see Ref. 6. In real space, one can measure the wavefront along a straight edge, which is a factor of $\cos(30^\circ)$ larger than the wavelength of the quasiparticles.

We can approximate the area in Fig. S4c as a circular quantum well, leading to ringlike interference patterns. Exact solutions exist for a circular quantum well, see *e.g.* Ref. 7. In real space, one can measure the difference between the radii of the circular interference patterns to obtain k_{qpi} ⁸.

Constant height STS of CB minimum

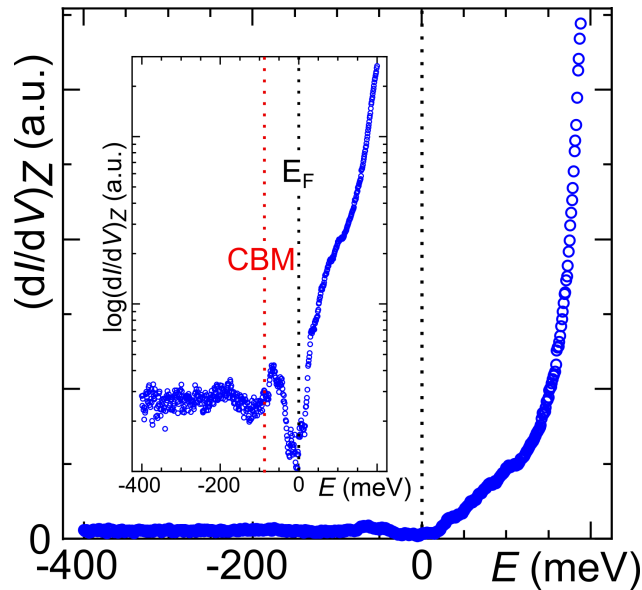


Figure S5: Constant height STS performed close to the surface. In the inset the same data is shown, plotted in a logarithmic scale. The CB minimum (red) and the Fermi level (black) are indicated. $V_{\text{st}}=0.2\text{ V}$, $I_{\text{st}}=0.5\text{ nA}$.

The CB minimum can also be measured with constant height STS when decreasing the tip-sample distance. We find that the differential conductance decreases towards the Fermi level when stabilizing at 0.2 eV but remains clearly above the noise level well into the occupied states. The signal disappears at -80 meV , marking the onset of the CB in agreement with our QPI analysis.

We find a pronounced gap around the Fermi level. While the origin of this gap remains unclear at present, we speculate that it is a consequence of phonon-mediated inelastic tunneling. A similar gap has been observed in graphene^{9,10}.

Field emission resonances on n-doped Gr

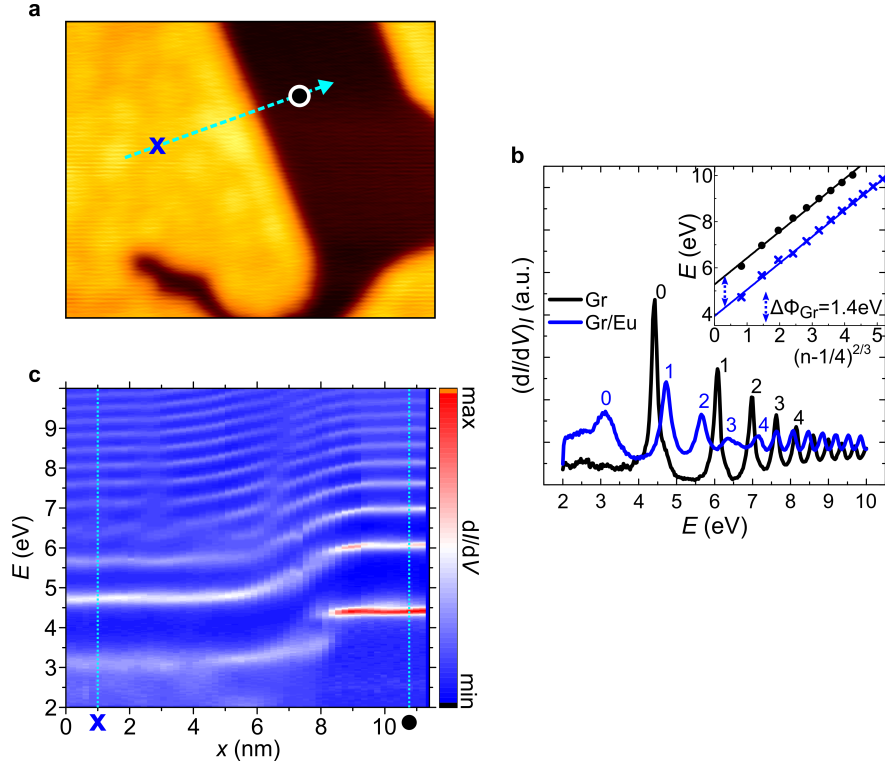


Figure S6: Field emission resonance (FER) spectroscopy on n-doped Gr. **a** STM topograph showing region of intercalated Gr (bright) and unintercalated Gr (dark). **b** FER spectroscopy recorded on Gr/Ir(111) (black) and Gr/Eu/Ir(111) (blue) at the locations marked in **a**. Resonant states are numbered n , and in the inset (right) plotted E against $(n - \frac{1}{4})^{\frac{2}{3}}$, see Ref. 11. The energy shift in the corresponding lines of best fit gives the difference in Gr work function $\Delta\Phi_{\text{Gr}} = (-1.4 \pm 0.1) \text{ eV}$. **c** Constant current linescan along the cyan line shown in **a**. STM and STS parameters (V , I): **a** $20 \times 16 \text{ nm}^2$, 1.0 V, 0.04 nA; **b**, **c** FER spectroscopy stabilization voltage $V_{\text{st}} = 2 \text{ V}$, $I_{\text{st}} = 0.1 \text{ nA}$.

Since the $c(4 \times 2)$ phase of Eu under Gr has not been observed before, we checked the doping level of Gr using field emission resonance (FER) spectroscopy. FER allows us to determine the change in the Gr work function due to the Eu intercalation layer. In Fig. S6a an area of partly intercalated Gr is shown. The bright patches are Eu-intercalated Gr and

the dark regions bare Gr. Constant current STS point spectra were taken at the cross and circle positions in Fig. S6a. The spectra are shown in Fig. S6b. The dI/dV peaks are resonant field emission states. In accordance with the method described by Lin *et al.* ¹¹, each state can be assigned an order n and an approximately linear energy shift between same-order states observed, see inset of Fig. S6b. This energy shift indicates a work function reduction $\Delta\Phi_{\text{Gr}} = (-1.4 \pm 0.1)$ eV on Eu-intercalated Gr. Assuming a rigid shift of the Dirac cone, this would mean that the Dirac point has shifted to -1.3 eV, compared to its value of 0.1 eV for Gr/Ir(111) ¹². This is in line with the ARPES-measured Dirac point of -1.36 eV for Gr/(2×2)-Eu/Ir(111) ³, and represents strong n-doping of Gr.

Looking at Fig. S6c, where a constant current STS linescan, taken along the line in Fig. S6a, is depicted, we find that the Eu-intercalated islands are near-uniformly doped, as the FER states show little change when going across the doped Gr region.

DFT results

Table S1: Charge transfers between MoS₂, Gr, and dopant (in units of e /supercell) calculated from Bader charges. Potential shifts induced over the heterostructures due to charge transfer (in units of V). Values for the doped systems are given relative to the pristine system, where it is 0.249 V. $E_D - E_F$ is the position of Dirac-point with respect to the Fermi level. The concentration of dopants is indicated as Eu x and O x , with x the number of dopant atoms per MoS₂ supercell.

	MoS ₂	Gr	dopant	ΔV	$E_D - E_F$
MoS ₂ /Gr	0.042	-0.042		0	0
MoS ₂ /Gr/Eu1	0.204	0.615	-0.820	0.934	-0.66
MoS ₂ /Gr/Eu2	0.265	1.388	-1.653	1.119	-0.99
MoS ₂ /Gr/O1	0.041	-0.352	0.311	-0.612	0.34
MoS ₂ /Gr/O2	0.040	-0.535	0.494	-0.940	0.58
MoS ₂ /Gr/O3	0.040	-0.703	0.663	-1.241	0.61

Charging of MTBs

MoS ₂ on	$k_F (\pi/a)$	$\lambda (e/a)$	$\Delta E_F (eV)$
freestanding (DFT) ¹³	0.63	-0.74	—
Gr (DFT) ¹³	0.54	-0.92	—
Gr/Ir (STM)	0.50	-1.00	0
Gr/Eu/Ir (STM)	0.37	-1.26	+0.33
Gr/O/Ir (STM)	0.58	-0.84	-0.19

Table S2: Fermi wavevectors k_F of the 4|4E MTB band in ML-MoS₂ on different substrates, and the associated line charge on the MTB, $\lambda = -\frac{2e}{\pi}(1 - k_F)$. See Ref. 13 for more details. The experimentally determined shifts of the Fermi level due to doping of the Gr substrate are given with respect to the pristine (undoped) case.

In previous work, DFT showed that a 4|4E MTB in a *freestanding* MoS₂ layer is approximately charge neutral, with a line charge $\lambda_{\text{MTB}}^{\text{band}}$ of about the same magnitude (but opposite polarity) as the polarization charge of the MTB $\lambda_{\text{MTB}}^{\text{pol}}$. This leads to $\lambda_{\text{MTB}} = \lambda_{\text{MTB}}^{\text{band}} - \lambda_{\text{MTB}}^{\text{pol}} \approx 0$. For details see Ref. 13. Placing the MoS₂ on Gr caused an increased MTB band filling due to Gr electron donation; comparing Fermi wavevectors before and after showed a changed line charge density of $\Delta\lambda = -\frac{2e}{\pi}(k_F - k'_F) = -0.18 e/a$ ¹³, see Table S2. In STM, a slightly larger value of $-0.26 e/a$ was obtained, as the observed Fermi wavevector was $k_F \approx (0.5) \pi/a$, instead of the DFT-predicted $k_F = (0.54) \pi/a$.

Using STM, we can similarly assess the change in band filling due to the Eu and O interlayer, relative to the unintercalated system. We find $\Delta\lambda_{Eu} = -\frac{2e}{\pi}(k_F^{\text{Gr}} - k_F^{\text{Eu}}) = -0.26 e/a$

and $\Delta\lambda_{\mathcal{O}} = -\frac{2e}{\pi}(k_{\text{F}}^{\text{Gr}} - k_{\text{F}}^{\text{O}}) = +0.16 e/a$, where k_{F}^{Gr} is the unintercalated experimental system.

In addition, we can use the shifts in k_{F} to estimate the shift in the Fermi level E_{F} of the MTB, relative to the pristine Gr/Ir(111) substrate. This is done in Fig. 6(d) of the main text, where overlapping k states between the three samples are used to map the dispersion of the 1D band. The results for the Fermi level of the MTB are shown in the last column of Table S2.

4|4P MTB

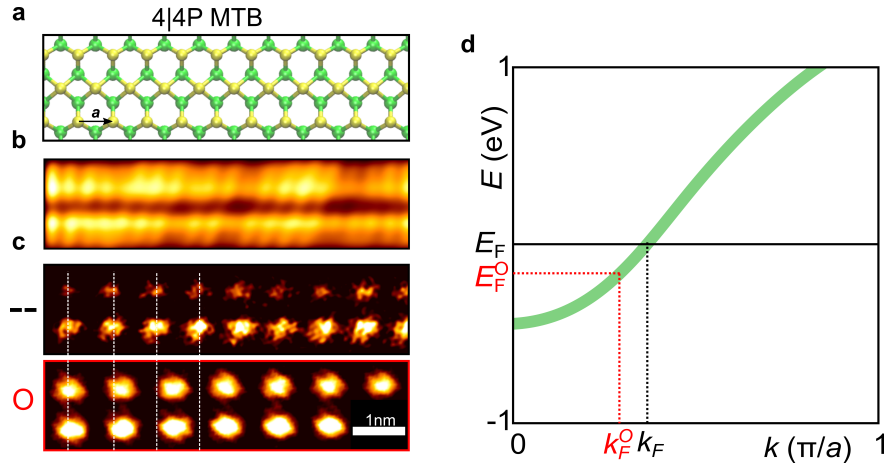


Figure S7: Confined states in 4|4P MTBs in ML-MoS₂ on different substrates. **a** Ball-and-stick model of 4|4P MTB. Mo atoms are navy, S atoms yellow (top layer) or dark yellow (bottom layer). A MoS₂ lattice vector is indicated. **b** Constant current STM topograph of 4|4P MTB in MoS₂ on Gr/Ir. **c** Constant height STM of 4|4P MTBs in pristine (-) MoS₂ and in MoS₂ on p-doped Gr (O). Vertical white lines are a guide to the eye. No 4|4P MTBs were found in MoS₂ on n-doped Gr. **d** Dispersion of the hole-like 1D band of the 4|4P MTB. Based on DFT calculations from Ref. 13. Fermi level and k -vector based on experimental data. STM/STS parameters: **b** $V=0.9$ V, $I=0.02$ nA; **c** top panel $V=0.1$ V, $I_{st}=0.1$ nA; bottom panel $V=0.04$ V, $I_{st}=0.1$ nA. 1 nm scale bar shown.

References

1. Förster, D. F., Wehling, T. O., Schumacher, S., Rosch, A. & Michely, T. Phase coexistence of clusters and islands: Europium on graphene. *New Journal of Physics* **14**, 023022 (2012).
2. Schumacher, S., Förster, D. F., Rösner, M., Wehling, T. O. & Michely, T. Strain in epitaxial graphene visualized by intercalation. *Phys. Rev. Lett.* **110**, 86111 (2013).
3. Schumacher, S. *et al.* Europium underneath graphene on Ir(111): Intercalation mechanism, magnetism, and band structure. *Phys. Rev. B* **90**, 235437 (2014). URL <https://link.aps.org/doi/10.1103/PhysRevB.90.235437>. 1409.4272.
4. Martínez-Galera, A. J. *et al.* Oxygen orders differently under graphene: new superstructures on Ir(111). *Nanoscale* **8**, 1932–1943 (2016). URL <http://xlink.rsc.org/?DOI=C5NR04976H>.
5. Crommie, M. F., Lutz, C. P. & Eigler, D. M. Imaging standing waves in a two-dimensional electron gas. *Nature* **363**, 524–527 (1993). URL <http://www.nature.com/doifinder/10.1038/363524a0>.
6. Li, W.-K. & Blinder, S. M. Solution of the schrödinger equation for a particle in an equilateral triangle. *J. Math. Phys.* **26**, 2784–2786 (1985).
7. Jolie, W. *et al.* Confinement of Dirac electrons in graphene quantum dots. *Phys. Rev. B* **89**, 155435 (2014). URL <http://link.aps.org/doi/10.1103/PhysRevB.89.155435>.

8. Jolie, W., Craes, F. & Busse, C. Graphene on weakly interacting metals: Dirac states versus surface states. *Phys. Rev. B* **91**, 115419 (2015). URL <https://link.aps.org/doi/10.1103/PhysRevB.91.115419>.
9. Zhang, Y. *et al.* Giant phonon-induced conductance in scanning tunnelling spectroscopy of gate-tunable graphene. *Nat. Phys.* **4**, 627–630 (2008). URL <http://www.nature.com/doi/10.1038/nphys1022>.
10. Natterer, F. D. *et al.* Strong Asymmetric Charge Carrier Dependence in Inelastic Electron Tunneling Spectroscopy of Graphene Phonons. *Phys. Rev. Lett.* **114**, 245502 (2015). URL <http://link.aps.org/doi/10.1103/PhysRevLett.114.245502>.
11. Lin, C. L. *et al.* Manifestation of work function difference in high order gundlach oscillation. *Phys. Rev. Lett.* **99**, 216103 (2007). URL <https://link.aps.org/doi/10.1103/PhysRevLett.99.216103>.
12. Pletikosić, I. *et al.* Dirac Cones and Minigaps for Graphene on Ir(111). *Phys. Rev. Lett.* **102**, 056808 (2009). URL <http://link.aps.org/doi/10.1103/PhysRevLett.102.056808><https://link.aps.org/doi/10.1103/PhysRevLett.102.056808>.
13. Murray, C. *et al.* Band Bending and Valence Band Quantization at Line Defects in MoS₂. *ACS Nano* **14**, 9176–9187 (2020). URL <https://pubs.acs.org/doi/10.1021/acsnano.0c04945>.

CHAPTER 7

Manuscript [4]: Modulated Kondo screening along magnetic mirror twin boundaries in monolayer MoS₂ on graphene

This chapter wholly consists of the above-named manuscript, which has been accepted by Nature Physics, pending minor revisions to comply with editorial and formatting guidelines. The version in this thesis is available online on arXiv.

The experiments were proposed by W. Jolie. The measurements were carried out by C. van Efferen, J. Fischer and W. Jolie at the TSTM and MSTM systems in Cologne. The analysis of the experimental data was performed by C. van Efferen, with support from W. Jolie. The NRG calculations were conducted by T. A. Costi. The interpretation of the results was discussed in depth by all authors.

C. van Efferen and W. Jolie wrote the main manuscript, with advice and corrections from T. Michely. Large portions of the supplement pertaining to the NRG results were written by T. A. Costi.

Modulated Kondo screening along magnetic mirror twin boundaries in monolayer MoS₂ on graphene

Camiel van Efferen^{1,*}, Jeison Fischer¹, Theo A. Costi^{2,3}, Achim Rosch⁴, Thomas Michely¹,
Wouter Jolie¹

¹*II. Physikalisches Institut, Universität zu Köln, Zùlpicher StraÙe 77, 50937 Köln, Germany*

²*Peter Grünberg Institut, Forschungszentrum Jùlich, 52425 Jùlich, Germany*

³*Institute for Advanced Simulation, Forschungszentrum Jùlich, 52425 Jùlich, Germany*

⁴*Institut für theoretische Physik, Zùlpicher StraÙe 77, 50937 Köln, Germany*

A many-body resonance emerges at the Fermi energy when an electron bath screens the magnetic moment of a half-filled impurity level. This Kondo effect, originally introduced to explain the abnormal resistivity behavior in bulk magnetic alloys ¹, has been realized in many quantum systems over the past decades, such as quantum dots ²⁻⁴, quantum point contacts ⁵⁻⁸, nanowires ⁹, single-molecule transistors ¹⁰⁻¹², heavy-fermion lattices ¹³⁻¹⁵, down to adsorbed single atoms ¹⁶⁻¹⁸. Here we describe a unique Kondo system which allows us to experimentally resolve the spectral function consisting of impurity levels and Kondo resonance in a large Kondo temperature range, as well as their spatial modulation. Our experimental Kondo system, based on a discrete half-filled quantum confined state within a MoS₂ grain boundary, in conjunction with numerical renormalization group calculations, enables us to test the predictive power of the Anderson model

which is the basis of the microscopic understanding of Kondo physics.

The Kondo effect of single magnetic atoms or molecules on metal surfaces has been the subject of intense research since it was first observed with the scanning tunnelling microscope (STM) by Madhavan et al. ¹⁶ and Li et al. ¹⁹. While the Kondo resonance has been well-characterized for numerous such systems ^{20,21}, the underlying atomic or molecular impurity levels that give rise to it have largely remained experimentally inaccessible. This is due to the dominant contribution of substrate states to the tunneling current, which lie in the same energy range as the localized d and f orbitals involved. Furthermore, the strong hybridization of the impurity states with these substrate states, electronvolts away from the Fermi energy, obscures the connection between Kondo resonance and impurity levels. While STM experiments for magnetic atoms on surfaces show that their behaviour close to the Fermi energy can often be understood in terms of the universal physics of the Kondo effect, the absence of a full characterization of their impurity levels and Coulomb interactions has led to a strong dependence on theoretical input to clarify the origin of the measured signals. For example, the line shapes around zero bias, observed in STM spectra for Co on noble metal surfaces ¹⁶ were considered as paradigms for a Kondo resonance, but have recently been argued by Bouaziz et al. to originate from exotic spin excitations rather than the Kondo effect ²². In consequence, theoretical predictions for the dependence of the Kondo resonance on energy position, strength of local interactions, and width of the impurity level ^{21,23} could not be tested due to the absence of experimental data.

A promising approach to enable local detection of the impurity levels is to spatially confine electrons, as done in a quantum dot ²⁻⁴. When a confined state at the Fermi energy E_F is filled with a single electron, strong Coulomb repulsion can lift the degeneracy of the energy level, leading to the formation of a singly occupied state below E_F mimicking the half-filled orbital of a magnetic atom. A Kondo resonance emerges when the non-degenerate states couple to an electron bath in close proximity ²⁻⁴. The advantages of the confinement approach are a small separation of the non-degenerate states, together with a large spatial extension of the confined wave function. In quantum dot systems these wavefunctions are, however, not accessible due to the lack of spatial resolution. Here we present a system where scanning tunneling spectroscopy (STS) and STM, with their unsurpassed energy and spatial resolution, can be used to track the Kondo resonance along with the impurity levels and the spatial modulation of their wavefunctions on the atomic scale. It enables us to compare experimental data with unsurpassed precision to predictions for the Anderson model of the Kondo effect obtained through numerical renormalization group (NRG) calculations.

Our Kondo system is realized in a MoS₂ mirror twin boundary (MTB), a line defect of finite length which hosts confined states in the band gap of the semiconducting two-dimensional (2D) material ²⁴⁻²⁶. Due to its one-dimensional nature, strong Coulomb interactions push the states around the Fermi energy apart and transform higher excitations into the bosonic spin- and charge excitations of a confined Tomonaga-Luttinger liquid ^{26,27}. The lowest-energy excitations of such a system can, however, simply be described by a single fermionic level which is either empty, singly occupied, or doubly occupied. Fig. 1a sketches the local density

of states around the Fermi energy of a MTB placed on a graphene substrate. The electron bath is represented by graphene's Dirac electrons, which exhibit a linear energy dependence close to the Dirac point ²⁸. The discrete energy levels sketched in Fig. 1a, right, are quantized states within the one-dimensional MoS₂ MTB. The two energy levels closest to the Fermi energy describe excitations, where a single electron is added to or removed from the MTB. When the highest occupied level is filled by a single electron, the strong Coulomb interaction U prohibits a second electron to enter, creating a spin- $\frac{1}{2}$ system localized along the MTB. This spin couples to the bath and creates through resonant spin-flip processes a Kondo resonance pinned to E_F , as we demonstrate below.

A MoS₂ monolayer island hosting two such MTBs is shown in Fig. 1b. The finite length of the MTBs leads to confined energy levels with a spacing inversely proportional to the length of the wire ²⁶. When the highest energy level is filled with two electrons, there is no unpaired magnetic moment and hence no Kondo effect. This situation is depicted in Fig.1c, which displays the averaged differential conductance dI/dV along a MTB. The dI/dV signal of the STM is proportional to the local density of states as a function of energy (given by the bias voltage). We find a series of peaks corresponding to quantized energy levels. Satellite peaks attributed to phonon-induced inelastic tunneling processes are observed at fixed energy intervals $|24.8| \pm 3.7$ meV and $|47.7| \pm 4.1$ meV from the main peaks ²⁵. The peaks closest to E_F exhibit an energy gap $E_{\text{gap}} = E_Q + U$, with E_Q the confinement energy and U the Coulomb energy 'penalty' incurred due to strong Coulomb interactions ^{26,29}. The standing waves corresponding to the energy levels closest to E_F are mapped in Fig.1d using a series of

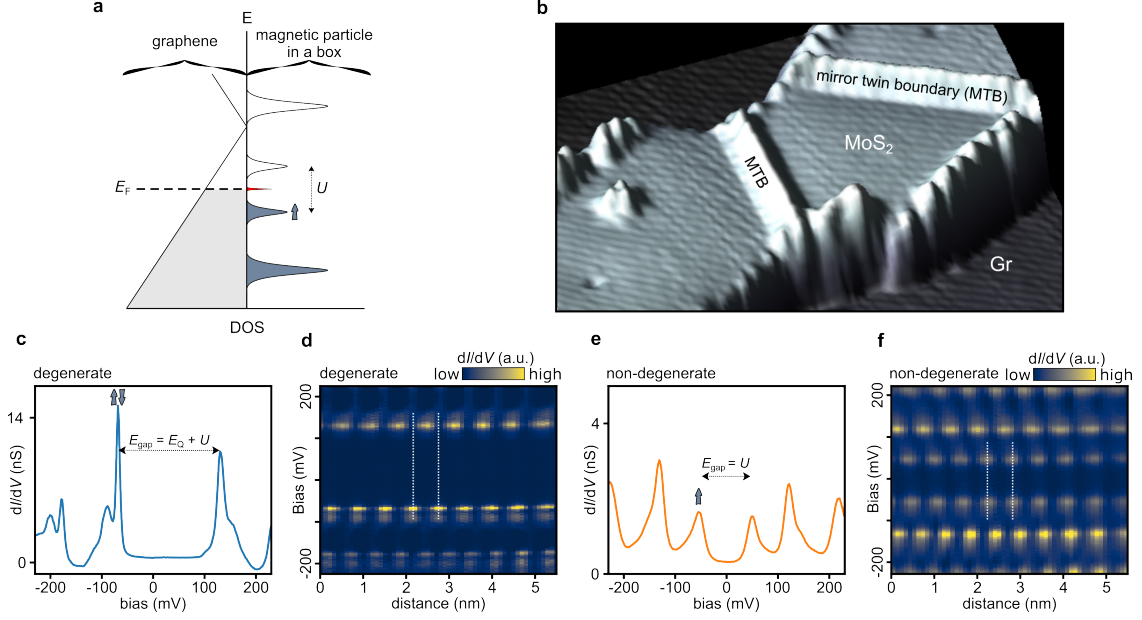


Figure 1: **Kondo effect within a MoS₂ MTB.** **a** Kondo coupling of graphene (bath) with the non-degenerate states (impurity) confined along a MoS₂ MTB. Indicated are the Fermi energy E_F and Coulomb energy U , see text. The electron inside the highest occupied states is symbolized by an arrow. **b** Atomically-resolved topography of a single-layer MoS₂ island on graphene, with two MTBs of lengths 7.1 nm (left) and 9.0 nm (right), separating mirror-symmetric domains. **c,e** Spatially averaged dI/dV spectra along a MTB of 8.6 nm before **c** and after **e** voltage pulses applied with the STM, being in a state that is either **c** degenerate or **e** non-degenerate. **d,f** Conductance colormaps showing spatially resolved dI/dV spectra along the MTB. Dashed white lines are added to highlight the phase relation between the states on either side of E_F in the middle of the boundary. STM/STS parameters: **b** $20 \times 20 \text{ nm}^2$, $V_{\text{set}} = 500 \text{ mV}$, $I_{\text{set}} = 10 \text{ pA}$; **c,d** $V_{\text{set}} = 500 \text{ mV}$, $I_{\text{set}} = 1.0 \text{ nA}$; **e,f** $V_{\text{set}} = 500 \text{ mV}$, $I_{\text{set}} = 0.5 \text{ nA}$. $V_{\text{mod}} = 2.5 \text{ mV}$.

dI/dV spectra taken along the MTB. These standing waves are out of phase in the center of the boundary, as expected for successive degenerate particle-in-a-box states (Supplementary Note 1).²⁶

The number of electrons within a MTB can be tuned with the help of the STM, either continuously with a back gate or stepwise via voltage pulses in the range $|V_{\text{pulse}}| = |1 - 2.5| \text{ eV}$ (Supplementary Note 2), as has been demonstrated previously for the isostructural 2D material MoSe_2 ^{29,30}. Fig. 1e shows the spectrum obtained on the same boundary after such a voltage pulse. The gap at E_F is now reduced to the pure Coulomb energy U , splitting the formerly degenerate energy level at the Fermi energy. The splitting leads to a singly occupied state below E_F that is energetically separated from the doubly occupied state by U , which in the single electron picture is the unoccupied state visible just above E_F . In the spatially resolved series of dI/dV spectra shown in Fig. 1f, the non-degenerate nature of the energy levels closest to E_F is visible as an in-phase beating of the two standing waves above and below the Fermi energy, which would collapse to a degenerate standing wave without Coulomb interaction U .

In between the two non-degenerate states, a narrow zero-bias peak (ZBP) is found in dI/dV spectra, as shown in Fig. 2a,b. The ZBP shows a relatively low intensity compared to the non-degenerate peaks (Fig. 2a) but becomes well visible when the tip-sample distance is reduced (Fig. 2b). No significant change in width and height (relative to the background signal) of the ZBP is observed when varying the tip-sample distance (Supplementary Note 3),

while its intensity quickly decays away from the MTB (Supplementary Note 4). To understand the nature of the ZBP, we investigate the influence of magnetic fields and temperature on the shape of the ZBP, shown in Fig. 2b-d. We find a clear Zeeman splitting of the ZBP with increasing magnetic field (Fig. 2b,c), while the ZBP broadens when the temperature is increased (Fig. 2d), in line with the expectation for a Kondo resonance ²¹.

Theoretically, such a Kondo system is described by the Anderson model, which is established for a single impurity level coupled to an electron bath ³¹. The dI/dV spectrum of this model is simulated using the numerical renormalization group (NRG) theory and compared to the experimental spectrum in Fig. 2a. The NRG simulation resembles the experimental spectrum with striking accuracy for both high and low energy features. This agreement is highlighted when comparing the magnetic field dependence shown for individual spectra in Fig. 2b and as a color plot in Fig. 2c. In both experiment and theory, the resonance transforms into a pronounced gap at high magnetic fields. From the splitting of the Kondo resonance with an out-of-plane magnetic field B we extract a g -factor of $g = 2.5$. A smaller splitting is observed for in-plane fields (Supplementary Note 5). An excellent match between experiment and theory is also found in the temperature-dependence of the Kondo resonance, depicted in Fig. 2d (Supplementary Note 6). Note that no additional fitting was performed to obtain the spectra in Fig. 2b-d, with the experimental magnetic field and temperature used simply as input for NRG calculations.

The Anderson model parameters required for these simulations are the splitting U of the

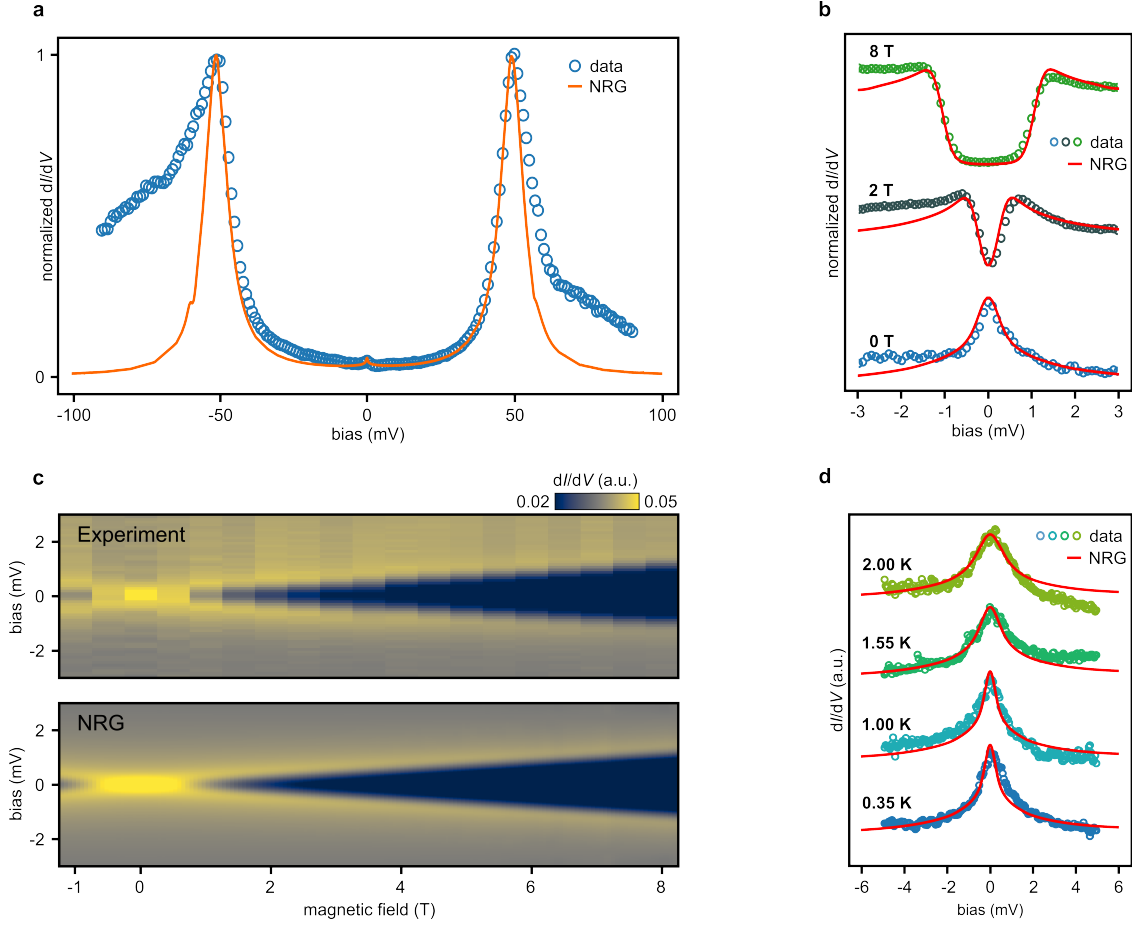


Figure 2: **Kondo resonance and NRG simulation of magnetic MTB at different magnetic fields and temperatures.** **a** dI/dV spectrum of impurity level with Kondo resonance (blue circles, $L = 8.6$ nm, $\varepsilon = -51$ meV, $U = 100$ meV, $\gamma = 10.4$ meV) and corresponding NRG simulation (orange line, $\varepsilon = -51$ meV, $U = 100$ meV, $\gamma_{\text{NRG}} = 9.35$ meV). Experimental spectra and theory are normalized to non-degenerate states. The NRG curves have been broadened by the experimental resolution. **b** dI/dV spectra of Kondo resonance at different magnetic fields (colored circles), with NRG simulation (red line). Plotted in the same scale as **a**. **c** Conductance (dI/dV signal) colormaps of the Kondo resonance as a function of bias and magnetic field, comparing experimental spectra (top) and the NRG model (bottom) with $g = 2.5$. **d** Dependence of dI/dV signal on temperature, with NRG data. STM/STS parameters: **a** $V_{\text{set}} = 90$ mV, $I_{\text{set}} = 1.0$ nA, $V_{\text{mod}} = 1.0$ mV; **b,c** $V_{\text{set}} = 10$ mV, $I_{\text{set}} = 1.0$ nA, $V_{\text{mod}} = 0.2$ mV; **d** $V_{\text{set}} = 5$ mV, $I_{\text{set}} = 1.0$ nA, $V_{\text{mod}} = 0.2$ mV

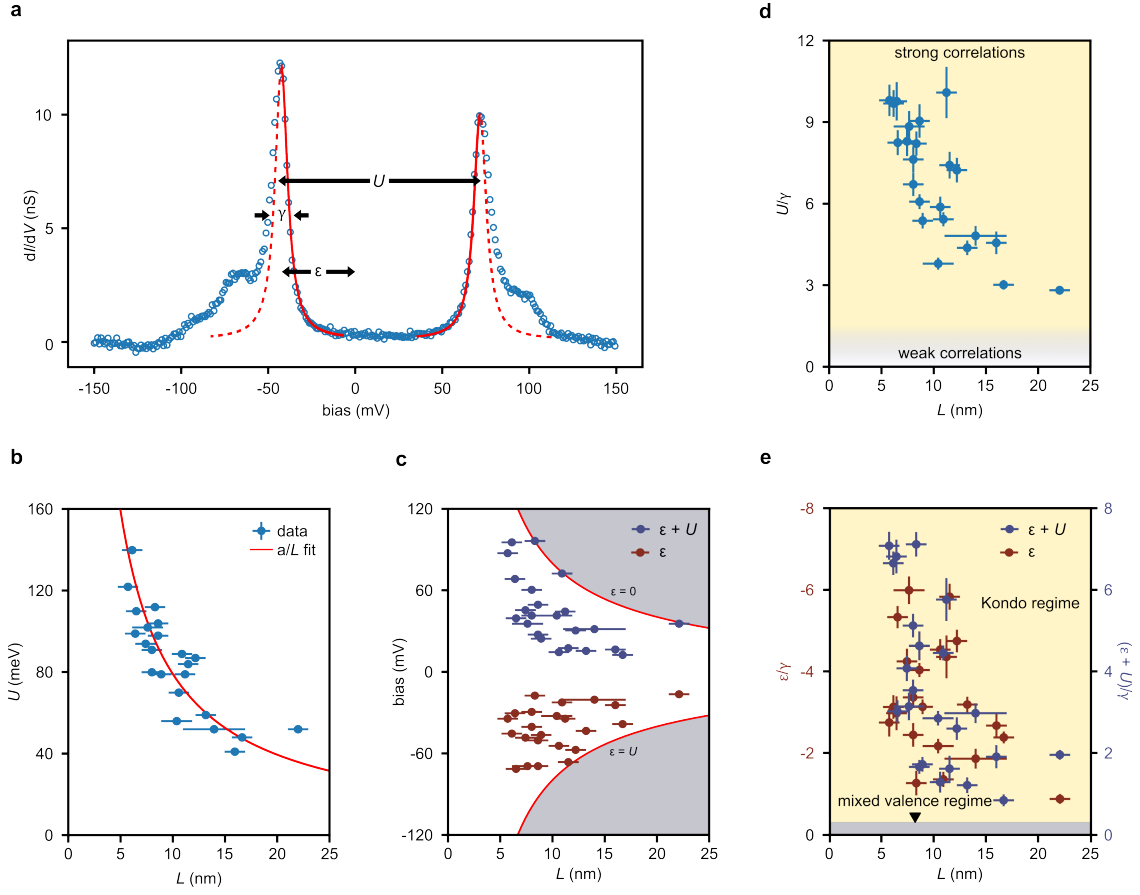


Figure 3: Tuning Kondo effect and correlations. **a** dI/dV spectrum of non-degenerate states (blue circles) of a MTB with $L = 6.5$ nm, $\varepsilon = -39$ meV, $U = 110$ meV, $\gamma = 10.8$ meV. Indicated are the Coulomb energy U , the energy spacing ε from E_F , and the full width at half maximum of the main Lorentzian peak γ , defining the parameters needed for a NRG simulation. Lorentzian functions fitted to the inner slope of the peaks are shown, from which the FWHM γ is extracted. **b** Coulomb gap (U) for MTBs of different length (L). a/L fit gives $a = 793$ meV nm $= 0.55e^2/(4\pi\varepsilon_0)$, where e is the electron charge. **c** Peak position of non-degenerate states below (ε) and above ($\varepsilon + U$) the Fermi energy. As L increases, the gap U between the states shrinks. **d** Correlation strength U/γ of MTBs, calculated for MTBs with U and γ obtained from Lorentzian fits. **e** Peak position of non-degenerate states in units of γ . For all boundaries: $|\varepsilon| \geq \gamma/4$ and $|\varepsilon + U| \geq \gamma/4$, placing them in the Kondo regime. STM/STS parameters: **a** $V_{\text{set}} = 200$ mV, $I_{\text{set}} = 0.2$ nA, $V_{\text{mod}} = 1.0$ mV. The spectra used in **b**, **c**, **d**, **e** were all measured with $V_{\text{mod}} = 1.0$ mV, but different stabilization voltages and currents.

non-degenerate states, the position ε of the impurity orbital relative to the Fermi energy and the bare width γ_0 of the impurity level (Supplementary Note 7). The first two are directly obtained from the experiment, see Fig. 3a. A crucial point concerns the extraction of γ_0 from the measured width γ . Firstly, as pointed out by Logan et al.³², spin flip processes in the Kondo regime increase the experimentally observable width γ of the non-degenerate peaks at ε and $\varepsilon + U$ by a factor of two, $\gamma = 2\gamma_0$ (Supplementary Note 8). Secondly, the broad inelastic tail related to phonons leads to a systematic overestimation of the experimental γ , which we counteract by fitting the inner tail of the non-degenerate peaks (Supplementary Notes 9 & 11). Taking this into account, we find agreement on a quantitative level between experiment and theory. Importantly, NRG is able to fully predict the magnetic field and temperature dependence of the experimental Kondo resonance purely based on parameters stemming from the impurity level.

Having the capability to predict properties of the Kondo effect using information on the impurity states, we make use of the latter to demonstrate the high tunability of our Kondo system by extracting the parameters (U, ε, γ) for 23 different MTBs of varying length L . We find a clear inverse length-dependence of U as shown in Fig. 3b, which is a consequence of the lower Coulomb energy of electrons when they are spread over a larger L (Supplementary Note 10). A fit $\tilde{U}(L) = a/L$ is shown as a solid line in Fig. 3b. Strong variations are found in ε , which can fluctuate between $-U$ and the Fermi energy. This energy range is visualized in Fig. 3c using the fit function $\tilde{U}(L)$ of Fig. 3b. The scatter in γ , which shows no indication of a length dependence (Supplementary Note 11), is most likely related to the large

momentum mismatch of electrons in the MTB and in graphene. This mismatch suppresses direct tunneling and enhances the role of defect-induced tunneling processes.

With the knowledge of (U, ε, γ) , we first point out that all our non-degenerate states cover a wide range of the strongly correlated regime $U/\gamma \gg 1$, see Fig. 3d. Furthermore, all these boundaries satisfy $-\varepsilon/\gamma \gg 1$ and $(\varepsilon + U)/\gamma \gg 1$ showing that these systems are in the Kondo regime, see Fig. 3e and Supplementary Note 5. The realization of a wide range of level energies ε and Coulomb repulsions U in these boundaries translates into a wide range of Kondo temperatures $T_K = 10^{-10} \text{ K} - 10^{-4} \text{ K}$, where $k_B T_K = w\gamma_0 \sqrt{U/4\gamma_0} \exp(-\pi|\varepsilon||\varepsilon + U|/\gamma_0 U)$ and $w = 0.4128$ is the Wilson number (Supplementary Note 12). Such small Kondo temperatures are consistent with the small density of states of the substrate and the large van-der-Waals gap between substrate and MoS₂. Since we have access to the microscopic parameters (U, ε, γ) , T_K is calculated directly and we do not require estimates of the Kondo coupling to extract T_K . The interested reader will nevertheless find a calculation of Kondo couplings in Supplementary Note 12. These results highlight that there is strong internal tuneability of the Kondo effect in MoS₂ MTBs. Without the need to change the dielectric or chemical environment, a wide range of Kondo temperatures is immediately available due to the wide range of boundary lengths and the asymmetry of the states with respect to the Fermi energy.

Finally, we investigated the spatial distribution of the Kondo resonance together with the non-degenerate states along a MTB. The non-degenerate states beat along the MTB with a wavelength related to their Fermi wave vector ^{26,30,33}, as expected for a particle in

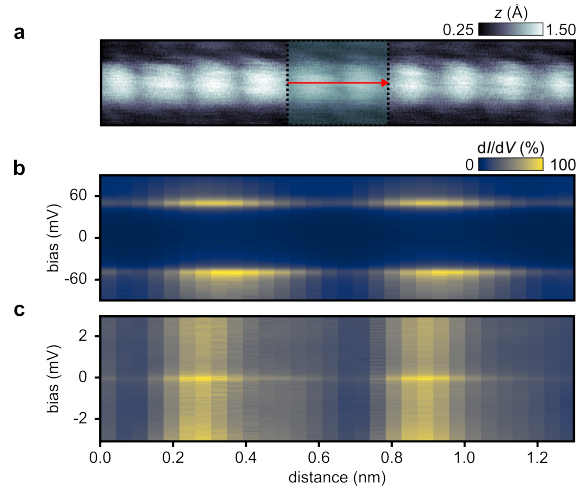


Figure 4: **Modulated Kondo screening along the particle in a box.** **a** Topography along a MTB of $L = 8.6$ nm, $\varepsilon = -51$ meV, $U = 100$ meV, $\gamma = 9.35$ meV, showing electronic beating of the confined state near E_f . The red arrow indicates where the spectra shown in **b,c** were taken. **b** Conductance colormap of constant height dI/dV spectra of the non-degenerate peaks along the MTB. **c** Conductance colormap showing constant height dI/dV spectra of the Kondo resonance along the same path. STM/STS parameters: **a** 6×1.1 nm², $V_{\text{set}} = -10$ mV, $I_{\text{set}} = 5$ pA; **b** $V_{\text{set}} = 90$ mV, $V_{\text{mod}} = 1.0$ mV; **c** $V_{\text{set}} = 10$ mV, $V_{\text{mod}} = 0.2$ mV. $I_{\text{set}} = 0.5$ nA for all spectra.

a box. This beating is apparent in the topograph of Fig. 4a. Focusing on the two maxima in the boxed area in Fig. 4a, the set of dI/dV spectra taken along the MTB in Fig. 4b shows the beating of the two non-degenerate states on either side of E_F . The two states are in phase along the MTB as they are derived from the same energy level, which is split due to Coulomb interaction. The dI/dV line scan in Fig. 4c, taken at the same location, shows the Kondo resonance. The amplitude of the Kondo resonance beats in phase with the non-degenerate peaks, compare Fig. 4b. In particular, we find that the amplitude of the resonance is linearly dependent on the peak amplitude of the MTB states, emphasizing the direct relation between these elements of the Kondo effect. These results are reminiscent of the orbital symmetries observed in Shiba states on superconductors which were attributed to anisotropic scattering due to the orbital shapes of the magnetic atom^{34,35}. We envision that using extended magnetic wave functions like those of the MTBs might enable direct access to the correlated behavior of Shiba states and wave function, as observed here for the Kondo effect.

As for the correspondence between Anderson model and experiment, further refining of the model, though outside the scope of this paper, can be envisioned. In particular, as the theoretical model does not include phonons, the inelastic tails and phonon side peaks of the high-energy peaks in Fig. 3a are not taken into account. The experimental peaks also vary slightly in height and width, which may arise from the bias dependence of the density of states neglected within our model (the Fermi energy of our graphene layer is estimated to lie 250 meV from the Dirac point³⁶, a substantially larger range than the energy scales

relevant for our experiment). Spin-orbit interactions are furthermore expected to induce an anisotropic magnetic response, while multi-channel effects arising from virtual transitions to other high-energy states of the MTB are also neglected in the current approach.

In summary, we established 1D magnetic MTBs in a 2D material as a prototypical system to characterize the Kondo effect. We presented a comprehensive study of a fully accessible spin- $\frac{1}{2}$ Kondo system allowing us to not only characterize the Kondo resonance itself, but also to quantitatively determine the impurity levels. We find that NRG calculations accurately reproduce intensity, shape, magnetic field, and temperature dependence of the Kondo resonance when simulating the impurity states. By quantitatively relating high- and low-energy features, our experiment confirms many properties of the Anderson model qualitatively and quantitatively. This includes the ratio of amplitudes of high- and low-energy peaks and an extra broadening of the high-energy peaks by a factor 2 due to spin-flip processes. In addition, our system reveals the real space relation between the impurity level wave function and the spatial dimension of the Kondo resonance. The variability of the parameters U (via boundary length), ρ (via doping ³⁷), and ε (via pulsing or gating), makes MTBs in transition metal dichalcogenides a valuable testbed for nanoscale magnetic investigations. Controlled coupling of the extended magnetic wave function to localized magnetic defects ³⁸ or adatoms represent exciting perspectives.

Methods

The MoS₂ monolayers were grown *in situ* on a graphene substrate, supported by an Ir(111) crystal, in a preparation chamber with base pressure $p < 5 \times 10^{-10}$ mbar. Ir(111) is cleaned by 1.5 keV Ar⁺ ion erosion and annealing to temperatures $T \approx 1550$ K. Gr is grown on Ir(111) by two steps. First, room temperature ethylene exposure till saturation followed by 1370 K thermal decomposition gives well-oriented Gr islands. Second, exposure to 2000 L ethylene at 1370 K for 600 s yields a complete single-crystal Gr layer³⁹. ML MoS₂ is grown by Mo deposition in an elemental S pressure of 7×10^{-9} mbar⁴⁰. Subsequently, the sample is annealed to 1050 K in the same S background pressure.

STM and STS are carried out at a base operating temperature of $T_0 = 0.35$ K after *in situ* transfer from the preparation chamber. STS is performed with the lock-in technique, at modulation frequency 907.0 Hz. STM images are taken in constant current mode. Some of the data in Fig. 3d was taken using a second STM with an operating temperature of $T = 6.5$ K.

We briefly outline the NRG procedure for the Anderson impurity model. For details, we refer the reader to reviews⁴¹⁻⁴⁴. In short, the NRG consists of iteratively diagonalizing the following equivalent linear chain form of the Anderson impurity model (Eq. (1) in Supplementary Note 5),

$$H = \sum_{\sigma} \varepsilon_{\sigma} n_{\sigma} + U n_{\uparrow} n_{\downarrow} + V \sum_{\sigma} (f_{0\sigma}^{\dagger} d_{\sigma} + \text{H.c.}) + \sum_{n=0}^{\infty} \sum_{\sigma} t_n (f_{n\sigma}^{\dagger} f_{n+1\sigma} + \text{H.c.}), \quad (1)$$

where $\varepsilon_\sigma = \varepsilon - g\mu_B B\sigma/2$ is the impurity level energy for spin σ measured relative to the Fermi energy, B is a local magnetic field, U is the Coulomb repulsion, and $\gamma_0 = 2\pi\rho V^2$ is the hybridization strength with ρ the conduction electron density of states. The iterative diagonalization is carried out on a sequence of decreasing energy scales $t_n \sim D\Lambda^{-n/2}$, $n = 0, 1, \dots$, with discretization parameter $\Lambda > 1$, by diagonalizing successive truncated Hamiltonians H_N with $N = 0, 1, \dots$ conduction electron orbitals $f_{n\sigma}$, $n = 0, \dots, N$, using the recursion relation $H_{N+1} = H_N + t_N \sum_\sigma (f_{N\sigma}^\dagger f_{N+1\sigma} + \text{H.c.}) \equiv \mathcal{T}[H_N]$. This procedure yields the many-body eigenvalues and eigenvectors and also the matrix elements of physical observables of interest. The logarithmic discretization parameter $\Lambda > 1$ separates out the many (infinite) energy scales of the conduction band, from high energies (small n) to intermediate energies (intermediate n) and low energies ($n \gg 1$), allowing the physics to be obtained iteratively on each successive energy scale. This nonperturbative approach allows essentially exact calculations for thermodynamical and dynamical quantities, including the spectral function, to be carried out on all temperature and energy scales. In fitting the calculated dI/dV to experiment, a constant elastic background of less than 1% of the total intensity takes into account direct tunneling from the substrate.

In order to compare NRG with experiment (see also Supplementary Note 13), it is important to take the experimental broadening due to temperature and lock-in modulation into account. Experimentally, we use an oscillating voltage with an amplitude of $V_{\text{mod}} = 0.2$ meV, $V(t) = V_0 + V_{\text{mod}} \cos(\omega t)$. As the experimental differential conductance (proportional to $A(\omega)$) is obtained from the standard lock-in technique, we obtain a spectral function $A(\omega)$

broadened by the experimental resolution from $\tilde{A}(V_0) = \frac{1}{2TV_{\text{mod}}} \int_0^T dt \cos(\omega t) \int_0^{V(t)} A(\omega) d\omega$. Concerning the temperature implemented in NRG, we use the experimental temperature. At or below 0.7 K, a constant $T_{\text{eff}} = 0.7$ K is implemented, which is equal to the temperature of the tunnel junction measured at the lowest experimental temperatures ⁴⁵.

Data availability

Data that support the plots within this paper and other findings of this study are available from the corresponding author upon reasonable request.

Acknowledgments

This work was funded by the Deutsche Forschungsgemeinschaft (DFG, German Research Foundation) - Project number 277146847 - CRC 1238 (subprojects A01, B06 and C02). JF acknowledges financial support from the DFG SPP 2137 (Project FI 2624/1-1) T.A.C. gratefully acknowledges the computing time granted through JARA on the supercomputer JURECA at Forschungszentrum Jülich.

Author contributions

W. J. designed the experiments. C. v. E., J. F. and W. J. carried out the measurements. C. v. E. did most of the analysis of the experimental data under the supervision of W. J. T. A. C. performed the NRG calculations and T.A.C and A.R. both gave theoretical input. C. v.

E., W. J. and T.M. mainly wrote the manuscript, with help from all the authors. All authors contributed to the discussion and interpretation of the results.

Ethics declarations

The authors declare no competing interests.

References

1. Kondo, J. Resistance Minimum in Dilute Magnetic Alloys. *Prog. Theor. Phys.* **32**, 37–49 (1964).
2. Goldhaber-Gordon, D. *et al.* Kondo effect in a single-electron transistor. *Nature* **391**, 156–159 (1998).
3. Cronenwett, S. M., Oosterkamp, T. H. & Kouwenhoven, L. P. A tunable Kondo effect in quantum dots. *Science* **281**, 540–544 (1998).
4. Borzenets, I. V. *et al.* Observation of the Kondo screening cloud. *Nature* **579**, 210–213 (2020).
5. Cronenwett, S. *et al.* Low-Temperature Fate of the 0.7 Structure in a Point Contact: A Kondo-like Correlated State in an Open System. *Phys. Rev. Lett.* **88**, 226805 (2002).
6. Iqbal, M. *et al.* Odd and even Kondo effects from emergent localization in quantum point contacts. *Nature* **501**, 79–83 (2013).

7. Rejec, T. & Meir, Y. Magnetic impurity formation in quantum point contacts. *Nature* **442**, 900–903 (2006).
8. Smith, L. W. *et al.* Electrically Controllable Kondo Correlation in Spin-Orbit-Coupled Quantum Point Contacts. *Phys. Rev. Lett.* **128**, 027701 (2022). URL <https://link.aps.org/doi/10.1103/PhysRevLett.128.027701>.
9. Nygård, J., Cobden, D. H. & Lindelof, P. E. Kondo physics in carbon nanotubes. *Nature* **408**, 342–346 (2000).
10. Liang, W., Shores, M. P., Bockrath, M., Long, J. R. & Park, H. Kondo resonance in a single-molecule transistor. *Nature* **417**, 725–729 (2002).
11. Park, J. *et al.* Coulomb blockade and the Kondo effect in single-atom transistors. *Nature* **417**, 722–725 (2002). URL <http://www.nature.com/articles/nature00791>.
12. Guo, L., Yan, Y., Xu, R., Li, J. & Zeng, C. Zero-Bias Conductance Peaks Effectively Tuned by Gating-Controlled Rashba Spin-Orbit Coupling. *Phys. Rev. Lett.* **126**, 57701 (2021). URL <https://doi.org/10.1103/PhysRevLett.126.057701>.
13. Jiao, L. *et al.* Chiral superconductivity in heavy-fermion metal UTe₂. *Nature* **579**, 523–527 (2020).
14. Vaño, V. *et al.* Artificial heavy fermions in a van der waals heterostructure. *Nature* **599**, 582–586 (2021).

15. Ruan, W. *et al.* Evidence for quantum spin liquid behaviour in single-layer 1T-TaSe₂ from scanning tunnelling microscopy. *Nat. Phys.* **17**, 1154–1161 (2021).
16. Madhavan, V., Chen, W., Jamneala, T., Crommie, M. F. & Wingreen, N. S. Tunneling into a single magnetic atom: Spectroscopic evidence of the Kondo resonance. *Science* **280**, 567–569 (1998).
17. Li, J., Schneider, W. D., Berndt, R. & Delley, B. Kondo Scattering Observed at a Single Magnetic Impurity. *Phys. Rev. Lett.* **80**, 2893–2896 (1998).
18. Trishin, S., Lotze, C., Bogdanoff, N., von Oppen, F. & Franke, K. J. Moiré Tuning of Spin Excitations: Individual Fe Atoms on MoS₂/Au (111). *Phys. Rev. Lett.* **127**, 236801 (2021).
19. Li, J., Schneider, W.-D., Berndt, R. & Crampin, S. Electron Confinement to Nanoscale Ag Islands on Ag(111): A Quantitative Study. *Phys. Rev. Lett.* **80**, 3332–3335 (1998). URL <http://link.aps.org/doi/10.1103/PhysRevLett.80.3332>.
20. Ternes, M., Heinrich, A. J. & Schneider, W.-D. Spectroscopic manifestations of the Kondo effect on single adatoms. *J. Phys. Condens. Matter* **21**, 053001 (2008).
21. Ternes, M. Spin excitations and correlations in scanning tunneling spectroscopy. *New J. Phys.* **17**, 063016 (2015).
22. Bouaziz, J., Mendes Guimarães, F. S. & Lounis, S. A new view on the origin of zero-bias anomalies of Co atoms atop noble metal surfaces. *Nat. Commun.* **11**, 6112 (2020). URL <https://doi.org/10.1038/s41467-020-19746-1>. 2003.01746.

23. Schrieffer, J. R. & Wolff, P. A. Relation between the Anderson and Kondo Hamiltonians. *Phys. Rev.* **149**, 491–492 (1966). URL <https://link.aps.org/doi/10.1103/PhysRev.149.491>.
24. Liu, H. *et al.* Dense Network of One-Dimensional Midgap Metallic Modes in Monolayer MoSe₂ and Their Spatial Undulations. *Phys. Rev. Lett.* **113**, 066105 (2014).
25. Barja, S. *et al.* Charge density wave order in 1D mirror twin boundaries of single-layer MoSe₂. *Nat. Phys.* **12**, 751–756 (2016). URL <http://dx.doi.org/10.1038/nphys3730>.
26. Jolie, W. *et al.* Tomonaga-Luttinger Liquid in a Box: Electrons Confined within MoS₂ Mirror-Twin Boundaries. *Phys. Rev. X* **9**, 11055 (2019). URL <https://doi.org/10.1103/PhysRevX.9.011055>.
27. Ma, Y. *et al.* Angle resolved photoemission spectroscopy reveals spin charge separation in metallic MoSe₂ grain boundary. *Nat. Commun.* **8**, 1–12 (2017).
28. Castro Neto, A. H., Guinea, F., Peres, N. M. R., Novoselov, K. S. & Geim, A. K. The electronic properties of graphene. *Rev. Mod. Phys.* **81**, 109–162 (2009). URL <http://link.aps.org/doi/10.1103/RevModPhys.81.109><https://link.aps.org/doi/10.1103/RevModPhys.81.109>.
29. Yang, X. *et al.* Manipulating Hubbard-type Coulomb blockade effect of metallic wires embedded in an insulator. *Natl. Sci. Rev.* (2022). URL <https://doi.org/10.1093/nsr/nwac210>. Nwac210, <https://academic.oup.com/nsr/advance-article-pdf/doi/10.1093/nsr/nwac210/46342134/nwac210.pdf>.

30. Zhu, T. *et al.* Imaging gate-tunable Tomonaga–Luttinger liquids in 1H-MoSe₂ mirror twin boundaries. *Nat. Mater.* **21**, 748–753 (2022). URL <https://doi.org/10.1038/s41563-022-01277-3>.
31. Anderson, P. W. A poor man's derivation of scaling laws for the Kondo problem. *J. Phys. C: Solid State Phys.* **3**, 2436–2441 (1970). URL <https://doi.org/10.1088/0022-3719/3/12/008>.
32. Logan, D. E., Eastwood, M. P. & Tusch, M. A. A local moment approach to the Anderson model. *J. Phys. Condens. Matter* **10**, 2673 (1998).
33. Yang, K. *et al.* Probing resonating valence bond states in artificial quantum magnets. *Nat. Commun.* **12**, 4–10 (2021). URL <http://dx.doi.org/10.1038/s41467-021-21274-5>.
34. Ruby, M., Peng, Y., von Oppen, F., Heinrich, B. W. & Franke, K. J. Orbital Picture of Yu-Shiba-Rusinov Multiplets. *Phys. Rev. Lett.* **117**, 186801 (2016). URL <https://link.aps.org/doi/10.1103/PhysRevLett.117.186801>.
35. Choi, D. J. *et al.* Building Complex Kondo Impurities by Manipulating Entangled Spin Chains. *Nano Lett.* **17**, 6203–6209 (2017).
36. Ehlen, N. *et al.* Narrow photoluminescence peak of epitaxial MoS₂ on graphene/Ir(111). *2D Mater.* **6**, 011006 (2019). URL <http://arxiv.org/abs/1809.01886>. 1809.01886.
37. van Efferen, C. *et al.* Metal-insulator transition in monolayer MoS₂ via contactless chemical doping. *2D Mater.* **9**, 025026 (2022). URL <https://dx.doi.org/10.1088/2053-1583/ac5d0f>.

38. Cochrane, K. A. *et al.* Spin-dependent vibronic response of a carbon radical ion in two-dimensional WS₂. *Nat. Commun.* **12**, 1–10 (2021).
39. Coraux, J. *et al.* Growth of graphene on Ir(111). *New J. Phys.* **11**, 023006 (2009). URL <http://stacks.iop.org/1367-2630/11/i=2/a=023006?key=crossref.41fefc8129b7d1091023ff6f80606e2b>.
40. Hall, J. *et al.* Molecular beam epitaxy of quasi-freestanding transition metal disulfide monolayers on van der Waals substrates: a growth study. *2D Mater.* **5**, 025005 (2018). URL <http://stacks.iop.org/2053-1583/5/i=2/a=025005?key=crossref.ccfb46f08c689ba275c96d24f12bc040>.
41. Wilson, J., Di Salvo, F. & Mahajan, S. Charge-density waves and superlattices in the metallic layered transition metal dichalcogenides. *Adv. Phys.* **24**, 117–201 (1975). URL <http://www.tandfonline.com/doi/abs/10.1080/00018737500101391.0410314v1>.
42. Krishna-murthy, H. R., Wilkins, J. W. & Wilson, K. G. Renormalization-group approach to the Anderson model of dilute magnetic alloys. I. Static properties for the symmetric case. *Phys. Rev. B* **21**, 1003–1043 (1980). URL <http://link.aps.org/doi/10.1103/PhysRevB.21.1003>.
43. Bulla, R., Costi, T. A. & Pruschke, T. Numerical renormalization group method for quantum impurity systems. *Rev. Mod. Phys.* **80**, 395–450 (2008). URL <http://link.aps.org/doi/10.1103/RevModPhys.80.395>.

44. Hewson, A. C. *The Kondo Problem to Heavy Fermions* (Cambridge University Press, Cambridge, 1997).
45. Bagchi, M., Brede, J. & Ando, Y. Observability of superconductivity in Sr-doped Bi₂Se₃ at the surface using scanning tunneling microscope. *Phys. Rev. Mater.* **6**, 034201 (2022).
URL <https://link.aps.org/doi/10.1103/PhysRevMaterials.6.034201>.

7.1 Supporting information

Supplementary Information of ‘Modulated Kondo screening along magnetic mirror twin boundaries in monolayer MoS₂ on graphene’

Camiel van Efferen^{1,*}, Jeison Fischer¹, Theo A. Costi^{2,3}, Achim Rosch⁴, Thomas Michely¹,
Wouter Jolie¹

¹*II. Physikalisches Institut, Universität zu Köln, Zülpicher Straße 77, 50937 Köln, Germany*

²*Peter Grünberg Institut, Forschungszentrum Jülich, 52425 Jülich, Germany*

³*Institute for Advanced Simulation, Forschungszentrum Jülich, 52425 Jülich, Germany*

⁴*Institut für theoretische Physik, Zülpicher Straße 77, 50937 Köln, Germany*

Contents

Supplementary Note 1: dI/dV maps of the confined states close to the Fermi energy	4
Supplementary Note 2: Tuning mirror twin boundary filling with voltage pulses	7
Supplementary Note 3: Influence of the tip-sample distance on the Kondo resonance	9
Supplementary Note 4: Decay of Kondo resonance away from MTBs	10
Supplementary Note 5: Anisotropy of the g -factor	12
Supplementary Note 6: Temperature dependence of Kondo resonance	13
Supplementary Note 7: Anderson impurity model and parameter regimes	15
Supplementary Note 8: Broadening of the impurity states in the spectral function	20

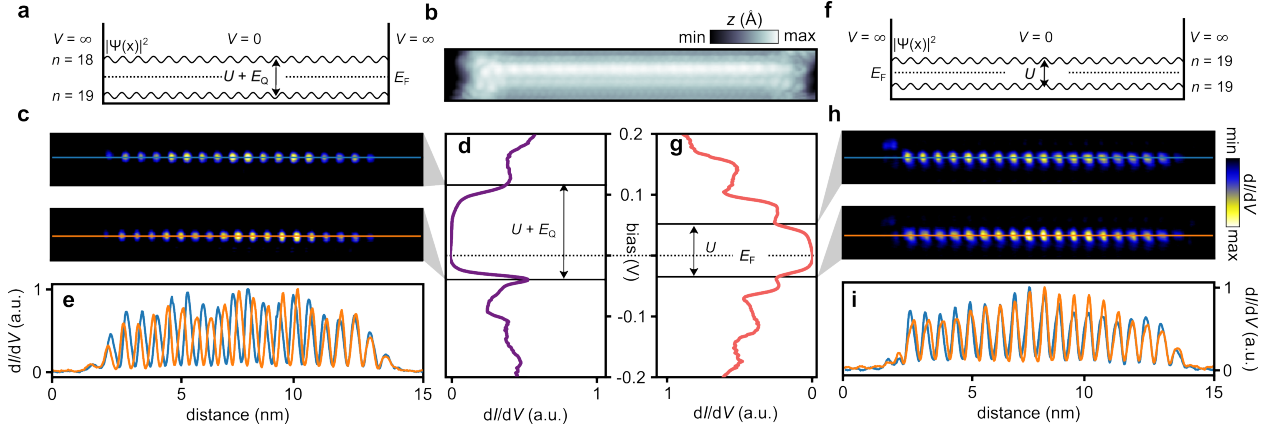
Supplementary Note 9: Comparison of spectral function and dI/dV for a mirror twin boundary with asymmetric states	22
Supplementary Note 10: Dependence of quantization energy and Coulomb gap on boundary length	23
Supplementary Note 11: Dependence of γ on fitting procedure	24
Supplementary Note 12: Kondo scales	26
Supplementary Note 13: NRG spectral function and dI/dV	35

Supplementary Note 1: dI/dV maps of the confined states close to the Fermi energy

Supplementary Figure 1 summarizes how we can experimentally distinguish a singly occupied, non-degenerate confined state from a doubly occupied degenerate state. Let us start by pointing out that mirror twin boundaries in MoS_2 host a confined Tomonaga-Luttinger liquid that displays spin and charge excitations. However, the first confined states below and above the Fermi energy, the so-called zero modes, can be viewed as single electronic levels which are either empty, singly occupied or doubly occupied. Thus, spin-charge separation does not enter the Kondo problem and consequently it does not complicate the analysis, as long as one focuses on the zero modes only.

The probability density $|\Psi(x)|^2$ of the confined zero modes is what one expects for an electron in a one-dimensional box, *i.e.* it is proportional to $\sin(x)^2$ with the boundary condition of vanishing probability density at the box ends (where we assume a potential energy barrier $V = \infty$). Supplementary Figure 1a represents a sketch for the case of two wave trains with 18 and 19 maxima. In contrast to the non-interacting particle-in-a-box situation, these two degenerate levels are spaced by an energy $E_Q + U$, where E_Q is the level spacing one would expect for non-interacting electrons and U is the Coulomb penalty when an additional electron is added to the system.

Supplementary Figure 1b shows an atomically resolved STM image of a mirror twin boundary with its highest occupied state being spin-degenerate. Maps of the dI/dV signal at



Supplementary Figure 1: Mapping the confined wave functions in mirror twin boundaries.

a Sketch of the two confined states next to the Fermi energy in a spin-degenerate state. **b** STM image of the mirror twin boundary. **c** Maps showing the dI/dV signal at the energy of the lowest unoccupied and highest occupied state along the entire length of the boundary. The number of maxima of the wave trains differ by one. **d** Corresponding dI/dV spectra averaged over the length of the boundary. **e** Linescans along the lines sketched in **c**, showing the anti-phase behavior of the two wave trains in the center of the boundary. **f** Sketch of the two states next to the Fermi energy when the highest occupied state is occupied by a single electron. **g** Spectra averaged over the length of the boundary. **h** Maps showing the dI/dV signal at the energy of the lowest unoccupied and highest occupied state along the entire length of the boundary. Both wave trains have the same number of maxima. **i** Linescans along the lines sketched in **c**, showing the in-phase behavior of the two wave trains along the entire boundary. STM/STS parameters: **b** $15 \times 2.1 \text{ nm}^2$, $V_{\text{set}} = 1.0 \text{ V}$, $I_{\text{set}} = 5 \text{ pA}$; **c** $V_{\text{set}} = 110 \text{ mV}$ (top), $V_{\text{set}} = -42 \text{ mV}$ (bottom); **d,g** $V_{\text{set}} = 200 \text{ mV}$, $I_{\text{set}} = 0.2 \text{ nA}$; **h** $V_{\text{set}} = 60 \text{ mV}$ (top), $V_{\text{set}} = -40 \text{ mV}$ (bottom); $V_{\text{mod}} = 2.0 \text{ mV}$, $f_{\text{mod}} = 833.0 \text{ Hz}$ for all spectra.

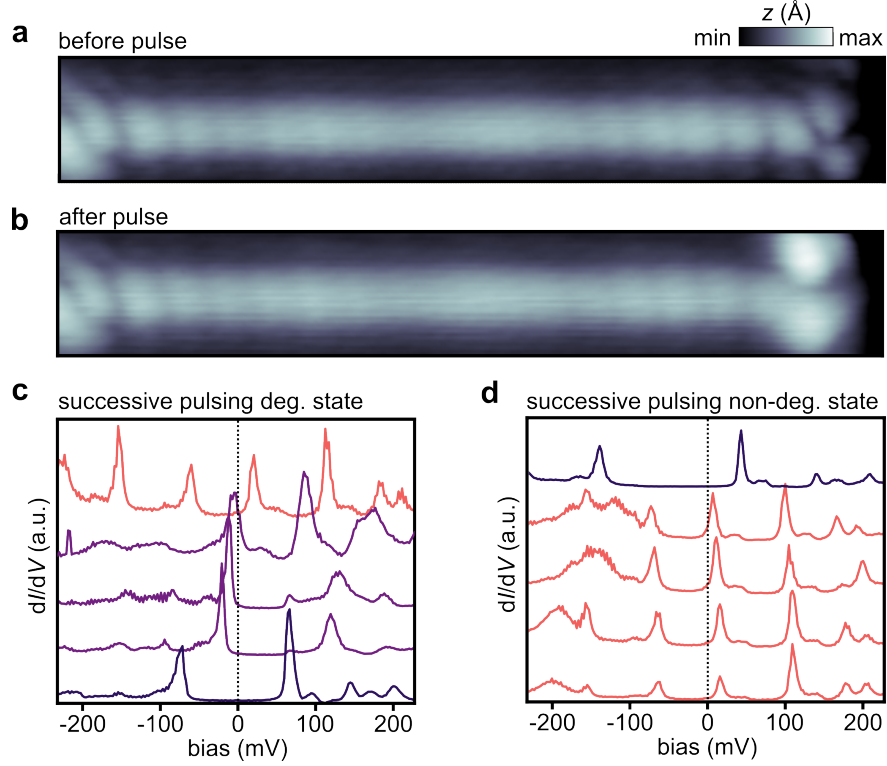
the energies of the first quantized states above and below the Fermi energy are presented in Supplementary Figure 1c. Their location in energy is deduced from dI/dV spectra measured along the boundary, see Supplementary Figure 1d. The wave trains differ by one maximum (18 at $V = 110 \text{ mV}$ and 19 at $V = -42 \text{ mV}$], best seen in the line profiles taken along the line

sketched in the dI/dV maps, shown in Supplementary Figure 1e. This difference leads to an out-of-phase behavior in the center of the boundary. Note that the number of maxima increases with decreasing energy due to the hole-like (rather than electron-like) band of the mirror twin boundary ¹. The excellent agreement with ab initio density functional theory calculations ¹, together with the ability to shift the periodicity of the states at the Fermi energy by changing the chemical potential ², further validates our assignment that these wave trains are confined states and have no other structural origin.

Next, we pulse this mirror twin boundary into the non-degenerate state, in which the highest occupied state is filled by one electron at ε , while the lowest energy state above the Fermi energy corresponds to the same quantized state filled with two electrons at $\varepsilon + U$. The sketch in Supplementary Figure 1f visualizes the wave trains above and below the Fermi energy, which have the same number of maxima (19).

After extracting the energy of the quantized states above and below the Fermi energy using dI/dV spectra measured along the boundary (Supplementary Figure 1g), we map the two wave trains and find the same number of maxima (19), see Supplementary Figure 1h. The corresponding line profiles in Supplementary Figure 1i lie on top of each other, as the wave trains would collapse to a spin-degenerate level for a vanishing U .

Supplementary Note 2: Tuning mirror twin boundary filling with voltage pulses



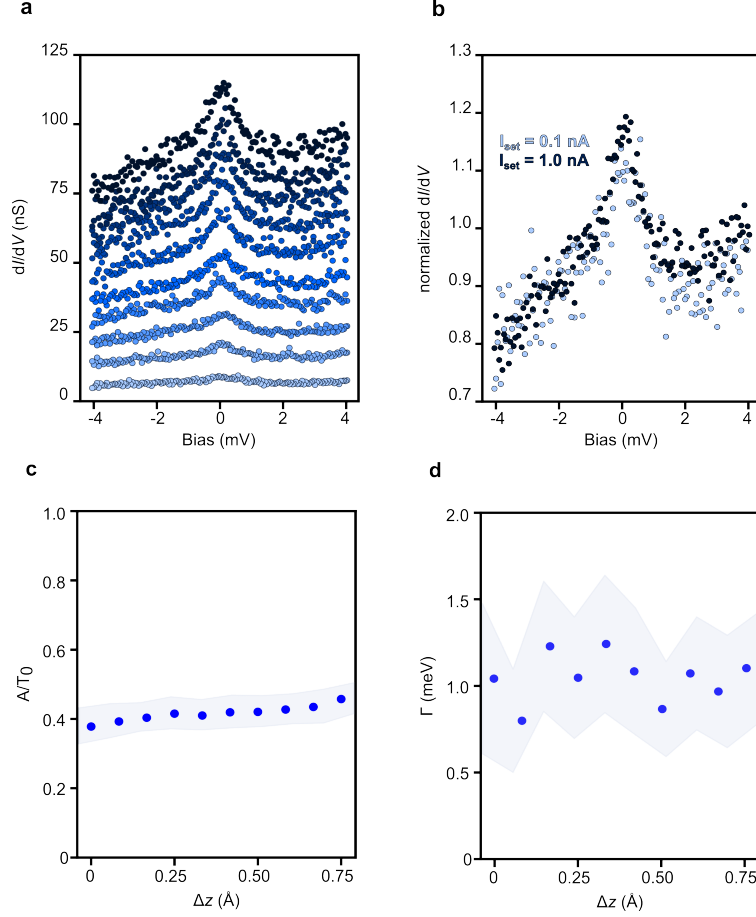
Supplementary Figure 2: Tuning mirror twin boundary filling with voltage pulses. **a** STM topograph of a mirror twin boundary before and **b** after the application of a voltage pulse at the right side of the boundary. **c** dI/dV spectra taken at the same location on a mirror twin boundary after successive voltage pulses. The highest occupied state transforms from a degenerate (bottom) to a non-degenerate state (top). **d** Sequence of dI/dV spectra taken at the same location on a mirror twin boundary. The highest occupied state transform from a non-degenerate (bottom) to a degenerate state (top). Between each spectrum from bottom to top a voltage pulse in the range $V = |1 - 2.5|$ eV was applied. STM/STS parameters: **a,b** 12.0×1.8 nm², $V_{\text{set}} = 500$ mV, $I_{\text{set}} = 10$ pA; **c** $V_{\text{set}} = 200$ mV, $I_{\text{set}} = 500$ pA; **d** $V_{\text{set}} = 200$ mV, $I_{\text{set}} = 350$ pA. $V_{\text{mod}} = 2.5$ mV, $f_{\text{mod}} = 907.0$ Hz for all spectra.

Following the method set out in Ref. 3, we change the electronic configuration of mirror twin boundaries *via* the application of voltage pulses in the range $V = |1 - 2.5|$ eV. We

find that pulses are most effective near the ends of the mirror twin boundaries, close to the edges of the MoS₂ islands. Supplementary Figure 2a,b shows the same mirror twin boundary before and after a voltage pulse performed near the right end of the boundary. Comparing the two STM images, we find that the apparent height at the edge is altered close to the location of the mirror twin boundary. This behavior is reproducibly found after pulsing and fully reversible. While we are not able to provide a microscopic model of the structure modifications at the edge of MoS₂ islands, the edge modifications induced by voltage pulses are likely related to the shifts in peak position in the mirror twin boundaries observed in dI/dV .

An example is shown in Supplementary Figure 2c, where successive pulses on a degenerate boundary (dark purple line) lead first to a shift of the quantized levels such that a single state crosses the Fermi energy (purple lines) and ultimately a transformation to a non-degenerate state (orange line). Note that when a single state overlaps with the Fermi energy, the MTB is in the so-called mixed valence regime and can no longer be regarded as a pure Kondo system (see Supplementary Note 5 for more information). Conversely, pulsing a non-degenerate boundary, as shown in Supplementary Figure 2d, can transform the lowest occupied state from non-degenerate (orange lines) into a degenerate state (dark purple line).

Supplementary Note 3: Influence of the tip-sample distance on the Kondo resonance



Supplementary Figure 3: Tip-sample distance dependence of Kondo resonance. **a** dI/dV spectra obtained with various stabilization currents averaged over the same location. The lowest stabilization current is 0.1 nA, and increases stepwise by 0.1 nA between measurements. **b** dI/dV spectra obtained with $I_{\text{set}}(10 \text{ mV}) = 0.1$ nA (blue line) and $I_{\text{set}}(10 \text{ mV}) = 1.0$ nA (green line) stabilization current, normalized so that $dI/dV(4 \text{ mV}) = 1$. **c**, **d** Normalized amplitude A/T_0 (Δz) (c) and width Γ (d) of Frota fits (blue dots), with a $2\times$ standard deviation confidence interval indicated in gray. $V_{\text{mod}} = 0.2 \text{ mV}$, $f_{\text{mod}} = 907.0 \text{ Hz}$.

To rule out that the metallic tip apex of the scanning tunneling microscope (STM) is involved in the formation of the Kondo resonance, we measured a series of dI/dV spectra with

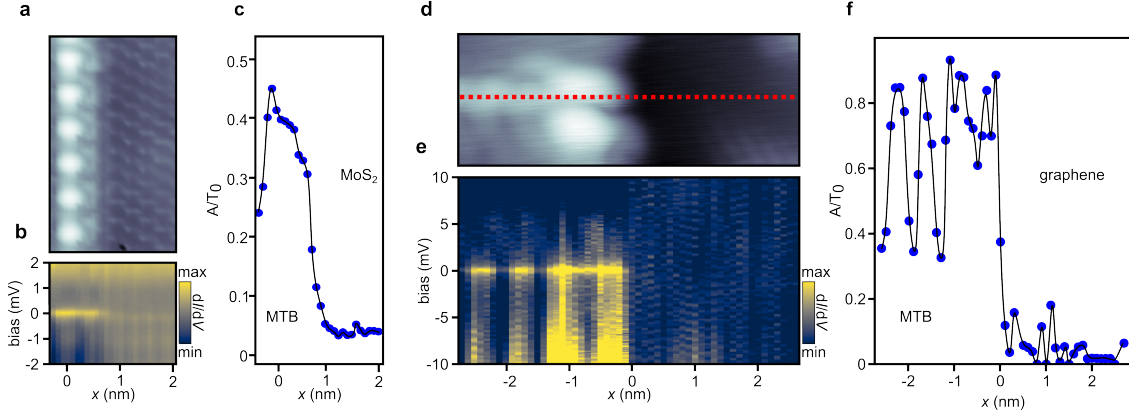
progressively higher stabilization currents $I_{\text{set}} (10 \text{ mV}) = 0.1 - 1.0 \text{ nA}$, shown in Supplementary Figure 3a.

If the electrons in the tip would contribute to Kondo screening, this effect should be enhanced when the tip is brought in close proximity to the non-degenerate states, leading to an increase in the width of the resonance peak. We find however, that an increase in the tunneling current by a factor 10, achieved by bringing the tip $\approx 0.75 \text{ \AA}$ closer to the surface, has only a minor influence on the spectral shape of the Kondo resonance, which is depicted in Supplementary Figure 3b. To quantify the dependence on tip-sample distance, we fitted the spectra with a Frota function to obtain the peak amplitude A/T_0 and width Γ . In Supplementary Figure 3c it can be seen that the amplitude slightly increases by about 10%, whereas no detectable change is observed in Γ within the confidence interval of the fit.

Supplementary Note 4: Decay of Kondo resonance away from MTB

The Kondo resonance decays rapidly when moving away from the mirror twin boundary. Moving across the boundary towards MoS_2 , we see that the Kondo resonance is quickly suppressed. This is shown in Supplementary Figure 4a-c, where the amplitude of the resonance is expressed as the ratio of the Frota amplitude A and the background conductance T_0 , using the Frota function ^{4,5}:

$$\mathcal{F}(V) \propto T_0 + \Im \left[A \times ie^{i\phi} \sqrt{\frac{i\Gamma}{eV - E_{\text{F}} + i\Gamma}} \right].$$

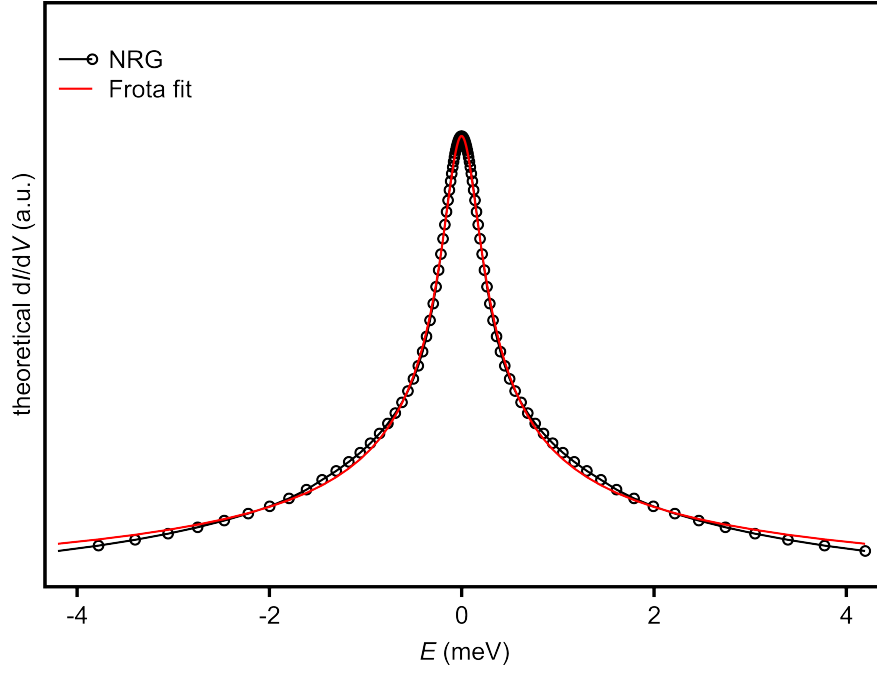


Supplementary Figure 4: Decay of Kondo resonance away from mirror twin boundaries.

a Topography of MoS₂ close to a mirror twin boundary (MTB). **b** dI/dV spectra averaged along the length of the boundary and **c** normalized amplitude A/T_0 of Frota fit as a function of sample bias and perpendicular distance x (nm) from center of MTB. **d** Topography of MoS₂ island edge. Part of a MTB is visible on the left; on the right side the graphene substrate is shown. **e** dI/dV and **f** normalized amplitude A/T_0 of Frota fit as a function of sample bias and distance x (nm) from the edge of the island. STM/STS parameters: **b** $2.3 \times 4 \text{ nm}^2$; **b,c**: $V_{\text{set}} = 5 \text{ mV}$, $I_{\text{set}} = 0.5 \text{ nA}$; **e** $5.7 \times 2.2 \text{ nm}^2$, $V_{\text{set}} = 100 \text{ mV}$, $I_{\text{set}} = 5.0 \text{ pA}$; **e** $V_{\text{set}} = 10 \text{ mV}$, $I_{\text{set}} = 1.0 \text{ nA}$. $V_{\text{mod}} = 0.2 \text{ mV}$, $f_{\text{mod}} = 907.0 \text{ Hz}$ for all spectra.

, where \Im denotes the imaginary part of the function, ϕ is a form factor describing the asymmetry of the peak and the half width at half maximum of the line is given by 2.542Γ . The resonance becomes undetectable around 1 nm away from the boundary. Similarly, we find that the Kondo resonance decays rapidly on graphene, see Supplementary Figure 4d-f.

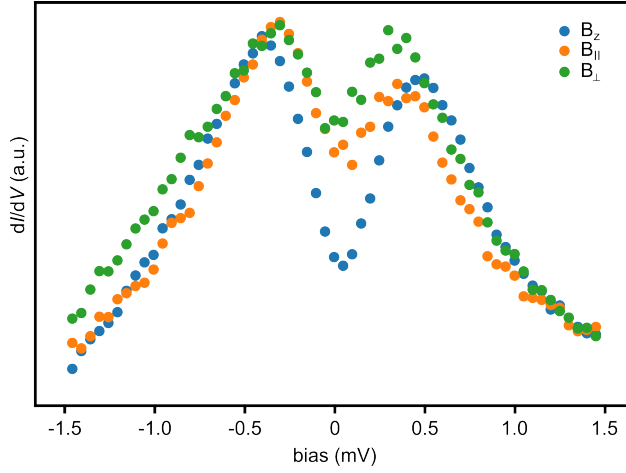
In Supplementary Figure 5 we show a comparison of the Kondo resonance as described by Frota and NRG. The good agreement confirms the Frota fit to be an adequate description of the Kondo resonance at the experimental temperatures.



Supplementary Figure 5: Comparison between NRG and Frota. NRG was performed with $U = 98$ meV, $\gamma = 9.35$ meV, $T_{\text{eff}} = 0.7$ K. The Frota fit to the NRG data used $T_0 = 0.00744$, $A = 0.00786$ and $\Gamma = 0.1997$ meV.

Supplementary Note 5: Anisotropy of the g -factor

Supplementary Figure 6 shows the splitting of the Kondo resonance for various field directions. The splitting is clearly largest for magnetic field pointing perpendicular to the MoS₂ plane (B_z), while we observe similar splitting for magnetic fields pointing in the MoS₂ plane parallel ($B_{||}$) and perpendicular (B_{\perp}) to the mirror twin boundary.

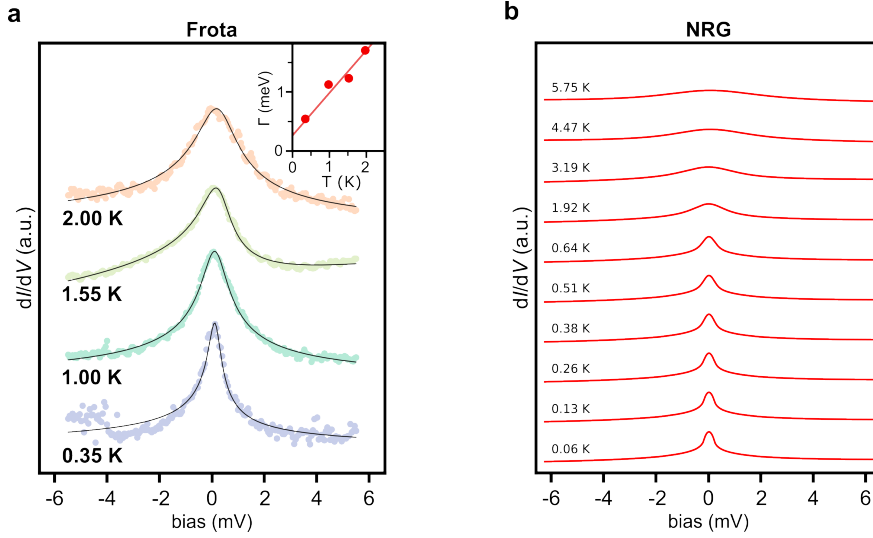


Supplementary Figure 6: Anisotropic splitting of the Kondo resonance under the influence of a magnetic field. Vectorial magnetic field-dependence of the Kondo resonance. B_z points out-of-plane, while $B_{||}$ (B_{\perp}) points along (across) the mirror twin boundary. All spectra are taken at $|B| = 0.75$ T.

Supplementary Note 6: Temperature dependence of Kondo resonance

Supplementary Figure 7 presents additional fits to the temperature-dependence of the Kondo effect of the mirror twin boundary shown in Fig. 2 of the main text. Supplementary Figure 7a represents a Frota fit (line) to the experimental data (dots). This Frota width is often used to extract the Kondo temperature T_K by fitting $\Gamma(T)$ to $\Gamma = 2\sqrt{(\pi k_B T)^2 + 2(k_B T_K)^2}$ ⁶ (a discussion on Kondo scales is found in Supplementary Note 12). At temperatures well above T_K , this function decreases linearly with decreasing temperature, while at temperatures $T < T_K$ the width should saturate at a value $\propto T_K$ ⁷. Since we find a linear temperature dependence down to our lowest temperature we can conclude that our lowest temperatures is still well above T_K , in line with our NRG calculations.

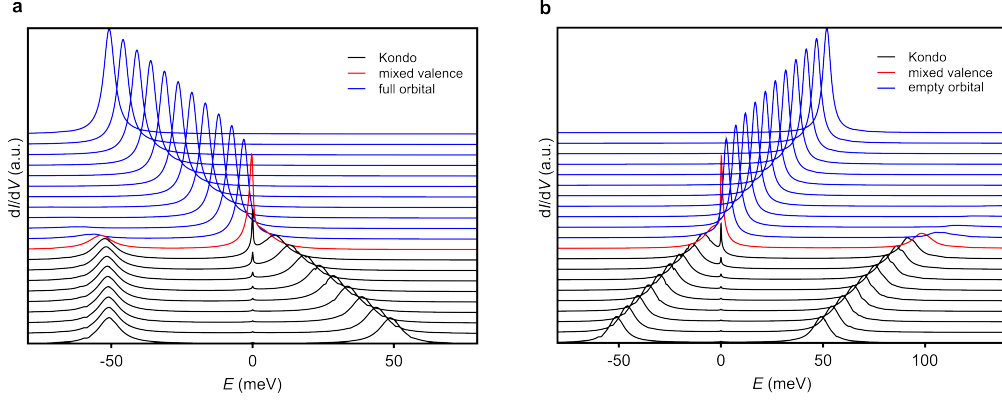
Supplementary Figure 7b shows the NRG prediction for a range of temperatures above



Supplementary Figure 7: Temperature dependence of Kondo resonance. **a** Dependence of the dI/dV signal (averaged over the length a mirror twin boundary) on temperature ($B = 0$ T). The grey lines are a Frota function fitted to the experimental data, which is represented as dots. The inset displays in red dots the width $\Gamma(T)$ obtained from the Frota fit. The red line is a linear fit to $\Gamma(T)$. **b** Additional temperature-dependent NRG simulations for this specific boundary. STM/STS parameters: $V_{\text{set}} = 5$ mV, $I_{\text{set}} = 0.5$ nA, $V_{\text{mod}} = 0.2$ mV

and below the experimental values for this mirror twin boundary. Counter-intuitively, we find that the Kondo resonance is well visible up to $T \approx 4$ K, despite its small Kondo temperature of $T_K = 2 \times 10^{-9}$ K. NRG calculations at still higher temperatures show that for $T > 45$ K the Kondo resonance is no longer discernible since the contribution at E_F coming from the tails of the non-degenerate states overwhelms that from the Kondo effect.

Supplementary Note 7: Anderson impurity model and parameter regimes



Supplementary Figure 8: Evolution of dI/dV spectra with U and ε at $T = 0.7\text{ K}$ and $B = 0\text{ T}$ ($\gamma_0 = 4.68\text{ meV}$). **a** Fixed $\varepsilon = -51\text{ meV}$ and decreasing U from 100 meV (bottom) to 0 meV (top), showing first a symmetric Kondo regime, then an asymmetric Kondo regime with a growing Kondo resonance, which eventually merges with the Hubbard peak at $\varepsilon + U$ to form a mixed valence resonance when $|\varepsilon + U| \lesssim \gamma_0/2$. Upon further reduction of U , a full orbital regime appears for $\varepsilon + U \leq -\gamma_0/2$. **b** Fixed $U = 100\text{ meV}$ and increasing ε from $-51\text{ meV} \approx -U/2$ (bottom) to $+51\text{ meV} \approx +U/2$ (top), showing first a symmetric Kondo regime, then an asymmetric Kondo regime with a growing Kondo resonance. The latter merges with the Hubbard peak at ε to form a mixed valence resonance for $|\varepsilon| \lesssim \gamma_0/2$ (charge fluctuations between $n = 0$ and $n = 1$). Empty orbital regime for $\varepsilon \geq \gamma_0/2$. NRG calculations: discretization parameter $\Lambda = 5$, z -averaging with $N_z = 192$ and retaining 1400 states per iteration. A vertical offset of 0.1 is used.

The NRG simulations of the dI/dV spectra of the MTB's are based on the single-level Anderson impurity model, given by

$$H = \sum_{\sigma} (\varepsilon - g\mu_B B\sigma/2) n_{\sigma} + U n_{\uparrow} n_{\downarrow} + \sum_{k\sigma} \varepsilon_k c_{k\sigma}^{\dagger} c_{k\sigma} + \sum_{k\sigma} V_k (c_{k\sigma}^{\dagger} d_{\sigma} + d_{\sigma}^{\dagger} c_{k\sigma}). \quad (1)$$

This describes a spin degenerate level of energy ε relative to the Fermi energy, $E_F = 0$, hybridizing with conduction electron states (ε_k) of the substrate via hybridization matrix

elements V_k . In (1), $n_\sigma = d_\sigma^\dagger d_\sigma$ is the occupation number for spin $\sigma = \uparrow, \downarrow$ electrons in the impurity level, U is a local Coulomb repulsion and B is a magnetic field acting on the impurity electrons via a Zeeman shift $-g\mu_B B\sigma/2$ with g the g-factor. We take a constant $V_k = V$ and a constant conduction electron density of states $\rho(E) = \rho = 1/2D$ with $-D \leq E \leq +D$, where D is the half-bandwidth. Hence, the hybridization function $\gamma_0(E) = 2\pi \sum_k |V_k|^2 \delta(E - \varepsilon_k)$ is a constant $\gamma_0(E) = \gamma_0 = 2\pi\rho V^2$ and equals the full-width at half-maximum (FWHM) of the $U = 0$ resonant level. The model is fully characterized by the parameters U , ε and γ_0 . For the MTB's of interest, the graphene monolayer on the iridium substrate is doped and has a metallic density of states at E_F with the Dirac point lying far above ¹. The Hubbard excitations at ε and $\varepsilon + U$ also lie far from the Dirac point. Thus, to a first approximation, NRG calculations in the wide-band limit of the Anderson impurity model, *i.e.*, $D \gg \max(U, |\varepsilon|, |\varepsilon + U|, \gamma_0)$, are justified. We note also on our use of the term Hubbard excitations to describe the excitations at ε and $\varepsilon + U$. These are otherwise known in the literature on the Anderson model as the satellite peaks in the spectral function ⁹, or in the context of molecular junctions as the HOMO (highest occupied molecular orbital) and LUMO (lowest unoccupied molecular orbital) states, respectively. In the present experiment with MTBs, these are termed the non-degenerate states.

The model is a paradigm for describing strong correlations $U/\gamma_0 \gg 1$. In this limit, a number of interesting regimes occur, such as the spin-fluctuation dominated Kondo regime for $-\varepsilon \gg \gamma_0/2$ and $(\varepsilon + U) \gg \gamma_0/2$, or the charge-fluctuation dominated mixed valence regime for $|\varepsilon| \lesssim \gamma_0/2$ ⁹. These exhibit emergent low energy scales and a strong temperature and/or

magnetic field dependence in physical quantities. In contrast, for weak correlations, $U/\gamma_0 \lesssim 1$, renormalization effects are small, and the physics is essentially that of a noninteracting resonant level with a Lorentzian spectral function $A(E) = (\gamma_0/2\pi)/((E - \varepsilon)^2 + (\gamma_0/2)^2)$. The MTB's in this paper are deep in the strongly correlated regime with $U/\gamma_0 \sim 6 - 20$, see Fig. 3b in the main text. By comparison, semiconductor quantum dots exhibiting the Kondo effect typically have $U/\gamma_0 \sim 3 - 6$ ¹⁰. Moreover, since the Hubbard peaks $-\varepsilon/\gamma_0 \gg 1$ and $(\varepsilon + U)/\gamma_0 \gg 1$ are well separated from the Fermi energy, see Fig. 3e of the main text, the impurity is singly occupied and has $S = 1/2$, i.e., the system is in the Kondo regime. Other regimes can, in principle, be realized by pulsing or gating the MTB to shift ε relative to the Fermi energy. For example, when ε (or $\varepsilon + U$) is within $\gamma_0/2$ of $E_F = 0$ the mixed valence regime is realized. When $\varepsilon \gg \gamma_0/2$ (or $\varepsilon + U \ll -\gamma_0/2$) the empty (or full) orbital regime emerges, which despite having a large U/γ_0 is effectively noninteracting because the empty (or full orbital) cannot undergo charge or spin fluctuations. However, as discussed in more detail at the end of this note, for such large ε additional levels in the MTB's need to be considered, so the simple empty (full) orbital regime is not realizable.

Figure 8 illustrates the parameter regimes of the model in terms of the trends in dI/dV , calculated within NRG, upon decreasing U for a fixed ε (Figure 8a) or upon increasing ε for a fixed U (Figure 8b). We take as reference system the MTB in Fig. 2 of the main text with the parameters given above (but allowing either U or ε to vary) and the experimental temperature $T = 0.7$ K and zero magnetic field. Decreasing U at fixed $\varepsilon \ll E_F$ drives the system from the Kondo regime (black lines) through a mixed valence regime for $|\varepsilon + U| \lesssim \gamma_0/2$ (red line),

a full orbital regime for $\varepsilon + U \leq \gamma_0/2$ with U finite and eventually to the noninteracting resonant level regime at $U = 0$ (Figure 8a). Note how the full orbital resonance with finite U continuously connects to the noninteracting ($U = 0$) resonant level. Similarly, with U fixed and increasing ε , the system is driven from the Kondo and asymmetric Kondo regimes to a mixed valence regime for $|\varepsilon| \lesssim \gamma_0/2$ and eventually to the empty orbital regime for $\varepsilon > \gamma_0/2$ (Figure 8b). Notice how the Kondo resonance grows in the asymmetric Kondo regime as ε (or $\varepsilon + U$) approaches E_F , eventually merging with this level to form the mixed valence resonance when $|\varepsilon| \lesssim \gamma_0/2$ (or $|\varepsilon + U| \lesssim \gamma_0/2$). Supplementary Figure 2d (Supplementary Note 2) shows a Hubbard excitation moving closer to the Fermi energy under pulsing. This could eventually give rise to a mixed valence resonance at E_F , either when ε or $\varepsilon + U$ is within $\gamma_0/2$ of E_F .

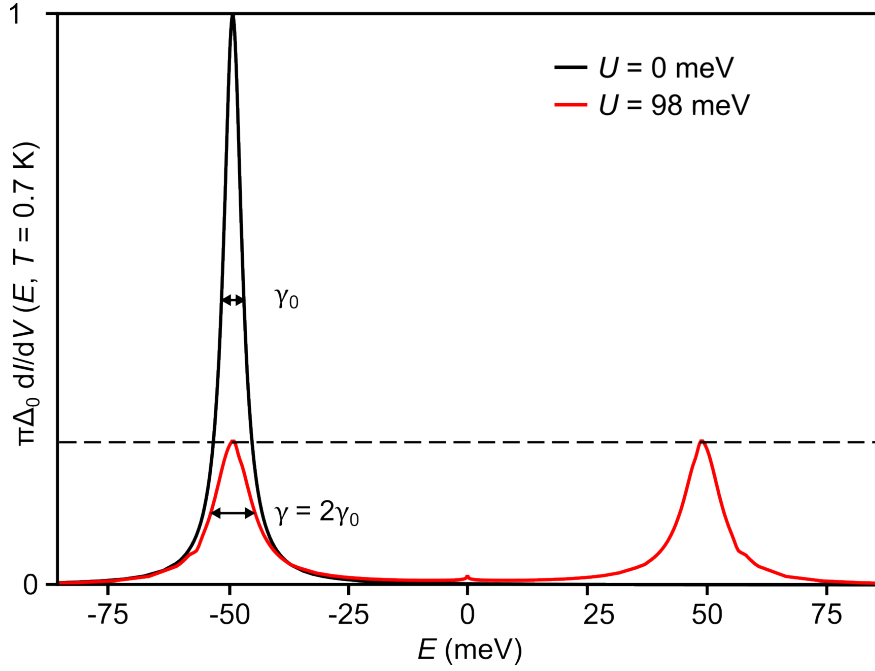
The trends in the *weights* of the high energy Hubbard excitations in dI/dV can be easily understood within the exactly solvable atomic limit $V = 0$. This gives a two peaked spectral function $A(E, T) = (2 - n)\delta(E - \varepsilon) + n\delta(E - (\varepsilon + U))$, where n is the impurity occupation. The latter changes from $n = 1$ (symmetric Kondo regime $\varepsilon = -U/2$) to $n = 2$ (full orbital regime $\varepsilon + U \leq -\gamma_0/2$) on decreasing U at fixed ε (Fig. 8a) and from $n = 1$ (symmetric Kondo regime) to $n = 0$ (empty orbital regime) on increasing ε at fixed U (Fig. 8b).

A finite $V > 0$ results, (i), in a finite width for the Hubbard peaks $\propto V^2$ and, (ii), in a low energy Kondo resonance appearing at E_F , generated by $O(V^4)$ spin-flip processes. As discussed in the main text and in Supplementary Note 8, in the Kondo regime (black

curves) the full width γ of the Hubbard peaks at ε and $\varepsilon + U$ is *twice* the bare value γ_0 as a result of spin-flip processes^{11,12}, i.e., $\gamma = 2\gamma_0$. This is important for interpreting the experiments which measure the enhanced width γ , whereas the input parameter for the model calculations is $\gamma_0 = \gamma/2$. This factor of two enhancement of the width is absent in the empty (or full) orbital regime which is effectively noninteracting so in this case $\gamma = \gamma_0$ (Figs. 8a,b). The width of the mixed valence resonance is also of order γ_0 , but its position is strongly renormalized¹³.

In real MTB's additional levels enter which will modify the above picture. The situation we described with the single level Anderson model assumes that all other levels are fully occupied or empty and do not enter the transport window as ε is changed. This assumption remains valid in the Kondo regime and in the mixed valence regime, but will break down in the empty (full) orbital regime when additional levels start to be populated (de-populated) and thus contribute to transport.

Supplementary Note 8: Broadening of the impurity states in the spectral function

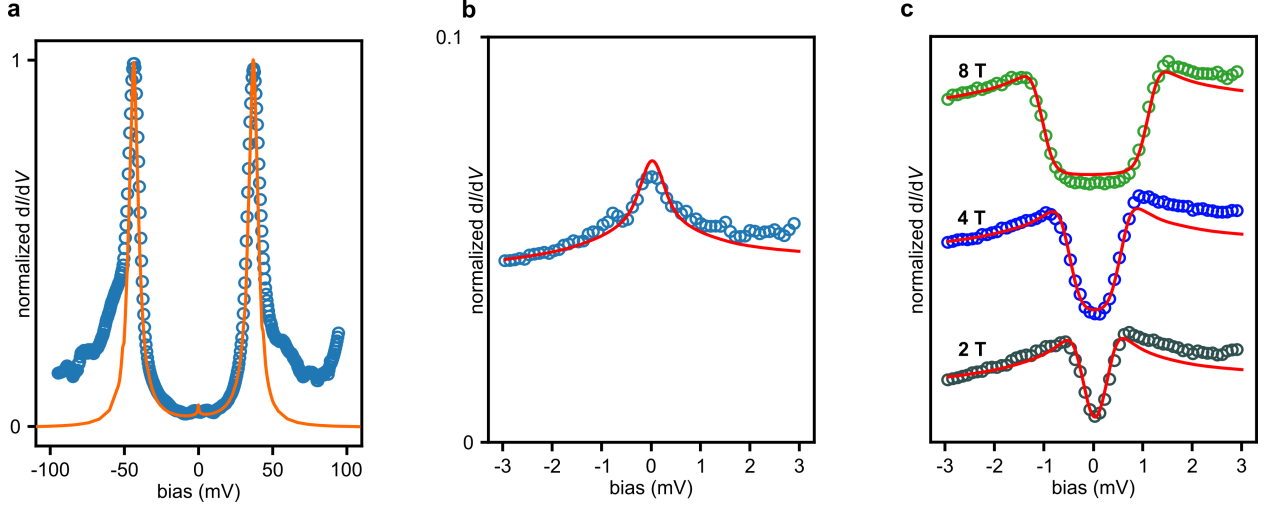


Supplementary Figure 9: Broadening of the impurity states. Influence of the impurity peak position on the broadening and Kondo resonance. NRG calculations performed with $T_{\text{eff}} = 0.7$ K, $\varepsilon = -49$ meV, $\gamma = 9.35$ meV.

The impurity states have a finite width in the spectral function. This width is composed of two terms: (i) broadening caused by hybridization of impurity states with the electron bath of the substrate, and (ii) spin-flip processes of the electron occupying the impurity state¹². While both are always present in an experimental Kondo system, NRG is able to separate the two by setting $U = 0$, shown in Supplementary Figure 9. In this limit, only hybridization contributes to the broadening of the impurity states, leading to a FWHM of γ_0 . In comparison, we find that a sizeable U redistributes the spectral weight on the lower and upper Hubbard impurity levels, leading to a reduction of the peak height by a factor of 2.

An additional reduction is due to spin-flip processes, leading to a peak height reduction by a factor of 4 and a peak width of $\gamma = 2\gamma_0$.

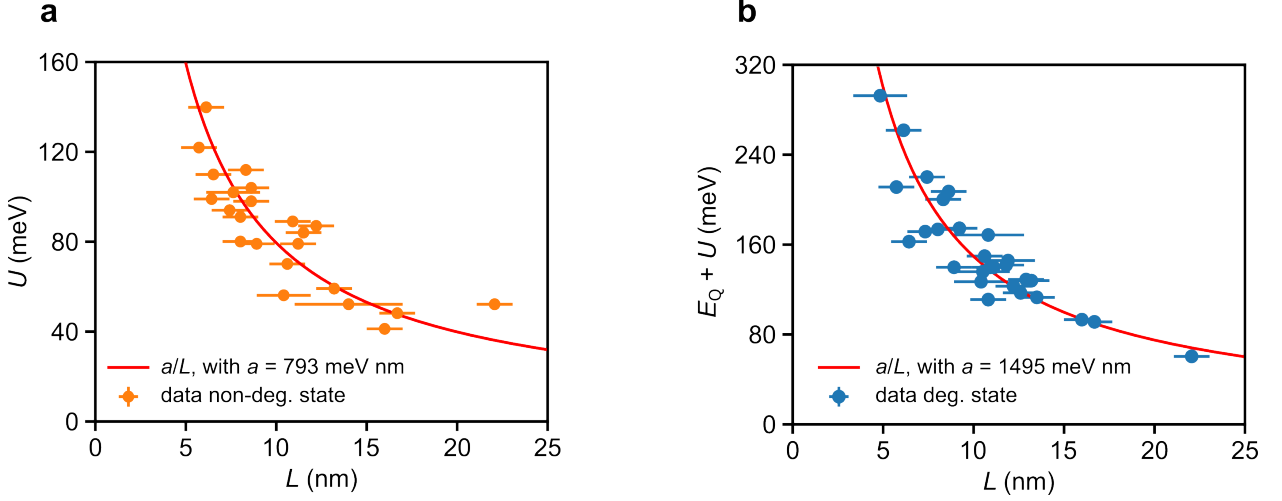
Supplementary Note 9: Comparison of spectral function and dI/dV for a mirror twin boundary with asymmetric states



Supplementary Figure 10: Comparison between NRG and dI/dV for a mirror twin boundary with asymmetric states. **a** dI/dV spectrum measured on a MTB with $L = 11.2$ nm, $\varepsilon = -44$ meV, $U = 81$ meV, $\gamma_{\text{NRG}} = \gamma = 7.8$ meV, with a NRG fit to the data (orange line). Data and fit normalized to highest peak. **b** Kondo resonance measured with STS (blue circles) with NRG fit (red line), plotted in the same scale as **a**. Note that NRG is not fitted to the Kondo resonance, only to the non-degenerate states. **c** Dependence of dI/dV signal on magnetic field ($T_{\text{eff}} = 0.7$ K), with NRG data for $g = 2.5$.

Supplementary Figure 10 presents a comparison between theoretical NRG simulations and experimental dI/dV spectra for a mirror twin boundary with asymmetric states around the Fermi energy, i.e., $\varepsilon \neq -U/2$. Due to the reduced inelastic tails, we find that for $\gamma_{\text{NRG}} = \gamma$, NRG correctly predicts the intensity, width and magnetic field dependence of the Kondo resonance, using $g = 2.5$ in the simulations.

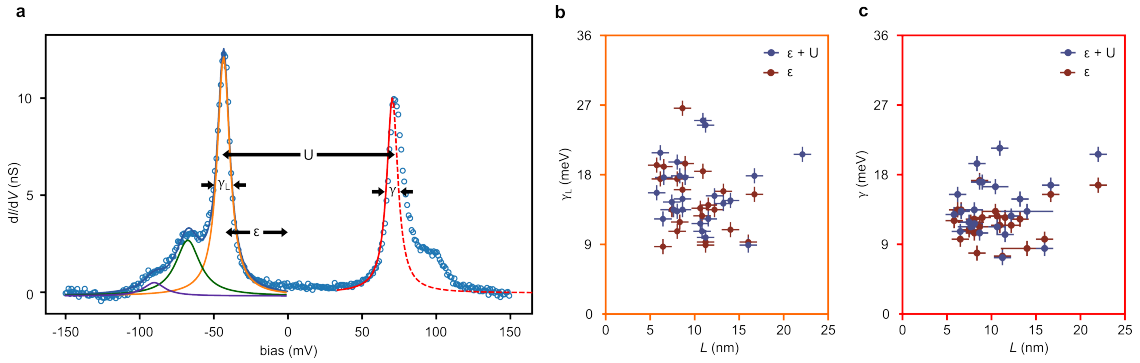
Supplementary Note 10: Dependence of quantization energy and Coulomb gap on boundary length



Supplementary Figure 11: Coulomb gap (U) and degenerate gap $E_{\text{gap}} = E_{\text{Q}} + U$ dependence on boundary length (L). **a U versus L . **b** $E_{\text{Q}} + U$ versus L . Fits $y = a/L$ are shown in red.**

The quantization energy E_{Q} of a one-dimensional system with linear dispersion is $\hbar v q_n$, with v the velocity and $q_n = (\pi/L)n$. Likewise, also the Coulomb energy U is proportional to $1/L$. As observed previously in Refs. 1, 14, we indeed find a $1/L$ dependence of U , see Supplementary Figure 11a. The sum of the quantization and the Coulomb energy, which makes up the gap $E_{\text{gap}} = E_{\text{Q}} + U$ that we find in the non-degenerate state, also scales with $1/L$, as plotted in Supplementary Figure 11b.

Supplementary Note 11: Dependence of γ on fitting procedure



Supplementary Figure 12: Dependence of hybridization γ on fitting procedure. **a** dI/dV spectrum of non-degenerate states (blue circles) of a MTB with $L = 8.6$ nm, $\varepsilon = -51$ meV, $U = 100$ meV. On the left state, a Lorentzian fit (dark blue line) with three components is shown: the non-degenerate peak (orange line) and two phonon satellites (green and purple lines). Indicated are the Coulomb energy U , the energy spacing ε from E_F , and the full width at half maximum of the main Lorentzian peak γ_L . On the right state, a single Lorentzian fitted to the inner slope of the peak is shown, giving γ . **b** FWHM of non-degenerate states obtained by a fit with three skewed Lorentzian functions γ_L . **c** FWHM γ of Lorentzians fitted to inner slope of non-degenerate states γ . STM/STS parameters: **a** $V_{\text{set}} = 200$ mV, $I_{\text{set}} = 0.2$ nA, $V_{\text{mod}} = 1.0$ mV.

The phonon excitations caused by inelastic tunneling processes lead to an artificial broadening of the confined peaks in experiment. This effect is strongest at absolute energies larger than the peak energies, leading to the appearance of inelastic tails towards higher absolute energies. Supplementary Figure 12a compares two ways to extract the width of the confined states from the experimental dI/dV spectra. One is to fit the non-degenerate states with up to three Lorentzians, dependent on the number of visible phonon peaks. This gives us a width γ_L of which the distribution of values is shown in Supplementary Figure 12b. The method applied in the main manuscript (Fig. 3e), on the other hand, is to fit the inner tail

of the peaks using a single Lorentzian with width γ , shown in Supplementary Figure 12c. Both distributions do not show a correlation with the mirror twin boundary length L , but γ_L tends to be larger than γ for the same peak. This is because the inelastic tail is not only due to discrete phonon losses at the energies of van Hove singularities in the phonon dispersion, but by phonon losses with the entire spectrum of phonon energies in the phonon dispersion. Therefore we use γ obtained from fitting to the inner slope as a more reliable estimate based on our direct comparison with NRG, instead of γ_L . Note that for both γ and γ_L , we fit both the upper and lower peak and use the average peak width $\gamma = (\gamma_{\text{lower}} + \gamma_{\text{upper}})/2$ in the Anderson model.

Supplementary Note 12: Kondo scales

The two commonly used definitions for the Kondo scale in the Anderson and Kondo models, are the low temperature strong coupling Kondo scale, denoted by $k_B T_0$, and the perturbative Kondo scale $k_B T_K$, related to the former via $T_K/T_0 = w$, where the universal Wilson number $w = e^{C+1/4}/\pi^{3/2} = 0.4128$ with $C = 0.577216$ being Euler's constant ⁹. In limiting cases, analytic expressions for T_K and T_0 can be given for the Kondo and Anderson models, as described below.

Besides these two scales, a third scale is of particular interest in STM, namely the HWHM Γ_K of the zero temperature Kondo resonance in the spectral function or in dI/dV ,

$$\frac{dI}{dV}(\text{eV}) = \int_{-D}^{+D} \frac{A(E, T)}{4k_B T \cosh^2((E - eV)/2k_B T)}. \quad (2)$$

More precisely, denoting by $\Gamma^A(T)$ and $\Gamma^G(T)$ the HWHM of the Kondo peak in $A(E, T)$ and $G(V, T) = dI/dV$ at temperature T , respectively, one clearly has in the zero temperature limit $\Gamma^G(T = 0) = \Gamma^A(T = 0) = \Gamma_K$. At finite temperature, $\Gamma^A(T)$ and $\Gamma^G(T)$ will differ due to the additional thermal broadening in dI/dV , i.e., $\Gamma^G(T) \geq \Gamma^A(T)$. Furthermore, the experimentally measured differential conductance $G_{\text{expt}}(eV, T)$ will be a convolution of the intrinsic dI/dV and the resolution in the measurement protocol (described in Methods in the main text). Deconvoluting allows to extract $\Gamma^A(T)$ and $\Gamma^G(T)$ from the measured $G_{\text{expt}}(eV, T)$ ⁵. Theoretically, however, both $\Gamma^G(T)$ and $\Gamma^A(T)$ can be accessed directly. Below, we calculate the universal curves for $\Gamma^G(T)$ and $\Gamma^A(T)$ as a function of T/T_0 and show that $\Gamma_K = \pi k_B T_0/2$ deep in the symmetric Kondo regime of the Anderson model for

$U/\gamma_0 \gg 1$. Hence, the relation between the three scales in this limit is

$$\Gamma_K = \frac{\pi k_B T_0}{2} = \frac{\pi k_B T_K}{2w}. \quad (3)$$

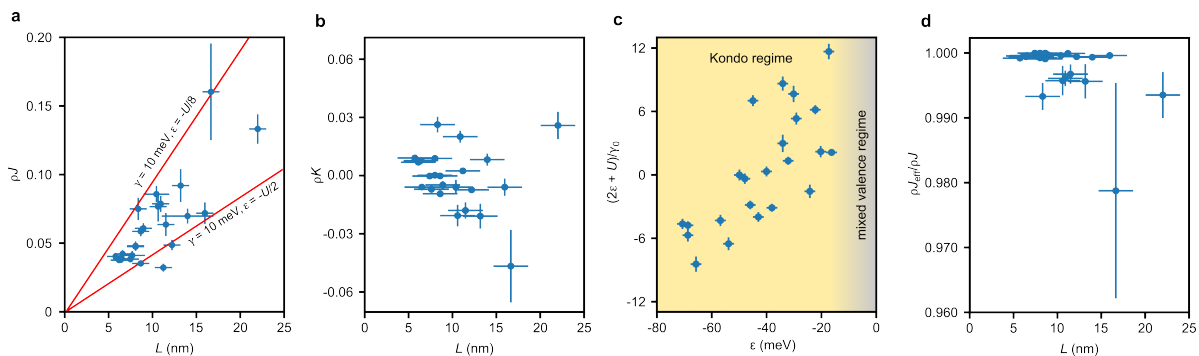
Kondo model scales The low energy behaviour of the Anderson model in the Kondo regime, i.e., for $-\varepsilon/\gamma_0 \gg 1$ and $(\varepsilon + U)/\gamma_0 \gg 1$, can be captured by the Kondo model $H_K = \sum_{k\sigma} \varepsilon_k c_{k\sigma}^\dagger c_{k\sigma} + 2J\vec{S} \cdot \vec{s}_0 + K \sum_{\sigma,\sigma'} c_{0\sigma}^\dagger c_{0\sigma'}$ with an effective antiferromagnetic exchange coupling J and a potential scattering term K related to the Anderson model parameters (U, ε and γ_0) by the Schrieffer-Wolff expression ^{9,15}

$$\rho J = \frac{\gamma_0}{2\pi} \left(\frac{1}{\varepsilon + U} - \frac{1}{\varepsilon} \right) = \frac{\gamma_0 U}{2\pi |\varepsilon| |\varepsilon + U|}, \quad (4)$$

$$\rho K = -\frac{\gamma_0}{4\pi} \left(\frac{1}{\varepsilon + U} + \frac{1}{\varepsilon} \right) = \frac{\gamma_0^2}{4\pi} \frac{\delta(\varepsilon)}{|\varepsilon| |\varepsilon + U|}, \quad (5)$$

where $\delta(\varepsilon) = (2\varepsilon + U)/\gamma_0$ measures the particle-hole asymmetry in the two models. The latter is zero at the symmetric point $\varepsilon = -U/2$, but is finite otherwise. The values of ρJ and ρK for the boundaries in the main text are shown in Figs. 13a,b together with $\delta(\varepsilon)$, a measure of their particle-hole asymmetry (Fig. 13c). The latter show that the boundaries in the main text realize both the nearly particle-hole symmetric Kondo regime ($\varepsilon \approx -U/2$) where $\delta(\varepsilon) \approx 0$ and also the asymmetric Kondo regime where $|\delta(\varepsilon)| > 0$.

A finite K has two effects, (i), it shifts the position of the Kondo resonance to either slightly above or slightly below the Fermi energy, depending on the sign of $\delta(\varepsilon)$, and, (ii), it affects the Kondo scale, defined below, by renormalizing $\rho J \rightarrow \rho J_{\text{eff}} = \rho J / (1 + (\pi \rho K)^2)$ ¹³. The latter effect, however, is very weak, since the potential scattering strength enters only



Supplementary Figure 13: Kondo coupling and potential scattering strengths. **a** Kondo coupling ρJ from Eq. (4) versus L for the boundaries in the main text. The lines simulate ρJ for the symmetric case $\varepsilon(L) = -U(L)/2$ and for an asymmetric case $\varepsilon(L) = -U(L)/8$ using constant $\gamma = 10\text{meV}$ and the $U(L)$ from Fig.3 of the main text. As expected, ρJ increases away from particle-hole symmetry. **b** Potential scattering strength ρK from Eq. (5) versus L . **c** Measure of the particle-hole asymmetry $\delta(\varepsilon) = (2\varepsilon + U)/\gamma_0$ versus L . All boundaries are in the Kondo regime (shaded yellow). The mixed valence regime $|\varepsilon| \lesssim \gamma_0/2$ is shaded grey. **d** Ratio $\rho J_{\text{eff}}/\rho J$ versus L showing that potential scattering has a negligible effect on the Kondo coupling.

quadratically in ρJ_{eff} . For the systems considered in the main text, all in the Kondo regime, the effect of potential scattering on the Kondo coupling, shown explicitly in Fig. 13d, is negligible and we have $\rho J_{\text{eff}} \approx \rho J$. Thus, even in the presence of a finite potential scattering, the usual expression for T_K of the Kondo model applies,

$$k_B T_K = D \sqrt{2\rho J} e^{-1/2\rho J + O(\rho J)} \approx D \sqrt{2\rho J} e^{-1/2\rho J}. \quad \text{for } \rho J \ll 1. \quad (6)$$

The strong coupling scale can be obtained from this as $k_B T_0 = k_B T_K/w$.

Note that from (Eq. 4), the measure for strong correlations in the Anderson model $U/\pi\gamma_0/2 \sim (4/\pi)U/\gamma \sim U/\gamma \gg 1$ ⁹ translates, in the symmetric case $\varepsilon = -U/2$, to

$U/\gamma \sim \frac{U}{\pi\gamma_0/2} = \frac{8}{\pi^2} \frac{1}{2\rho J} \approx \frac{1}{2\rho J} \gg 1$, i.e., strong correlations in the Kondo model correspond to $2\rho J \ll 1$. This condition holds for the boundaries in the main text, both in terms of U/γ_0 (see main text Fig.3d) and in terms of the Kondo coupling ρJ in Fig. 13a which shows that $0.04 \lesssim \rho J \lesssim 0.16$.

Finally, note that the factor of 2 in the dimensionless Kondo coupling $2\rho J$ holds for the above convention for the Kondo interaction ($2J\vec{S} \cdot \vec{s}_0$). This is used, for example, in the work of Kondo¹⁶ and in Ref.⁹. Wilson¹⁷ used the same notation with the opposite sign for J . The notation without the factor of 2 is also common in the literature^{13,18}.

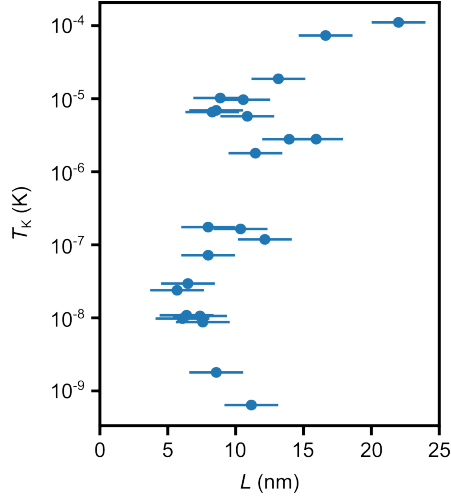
Anderson model scales For the Anderson model, $k_B T_0$ can be calculated accurately within NRG via its definition $\chi(T=0) = (g\mu_B)^2/4k_B T_0$. Analytic formulae are also available in limiting cases for $U/\gamma_0 \gg 1$. For example, for $\varepsilon = -U/2$ Bethe-Ansatz gives⁹

$$k_B T_0 = \gamma_0 \sqrt{U/4\gamma_0} e^{-\pi U/4\gamma_0 + \pi\gamma_0/4U}, \quad \text{for } \varepsilon = -U/2 \text{ and } U/\gamma_0 \gg 1, \quad (7)$$

whereas for the asymmetric Kondo regime, $\varepsilon \neq -U/2$, we have, to leading order in the exponent,

$$k_B T_0 = \gamma_0 \sqrt{U/4\gamma_0} e^{-\pi|\varepsilon||\varepsilon+U|/U\gamma_0}. \quad \text{for } \varepsilon/\gamma_0 \ll -1, (\varepsilon+U)/\gamma_0 \gg +1 \text{ and } U/\gamma_0 \gg 1. \quad (8)$$

All parameters appearing in (7) and (8) can be measured in the dI/dV of the present experiment, thereby allowing $k_B T_0$ and hence also $k_B T_K = w k_B T_0$ to be calculated. Figure 14 shows T_K calculated in this way for the boundaries in the main text using the experimentally extracted parameters $U, \varepsilon, \gamma = 2\gamma_0$.



Supplementary Figure 14: Kondo temperature $k_B T_K = w T_0 = w \gamma_0 \sqrt{U/4\gamma_0} e^{-\pi|\varepsilon||\varepsilon+U|/U\gamma_0}$ for the boundaries in the main text. The parameters U, ε, γ are extracted from the dI/dV spectra. In terms of ρJ , this T_K is equivalent to Eq. (9).

While the Anderson model parameters suffice to determine $k_B T_K$ directly, one can also express the latter in terms of the Kondo coupling ρJ analogously to the expression for T_K in terms of ρJ for the Kondo model in Eq.(6). In the symmetric Kondo regime, this can be achieved by using $k_B T_K = w k_B T_0$, with T_0 from Eq. (7), and the Schrieffer-Wolff relation between ρJ and the Anderson model parameters. One finds the result ^{18,19},

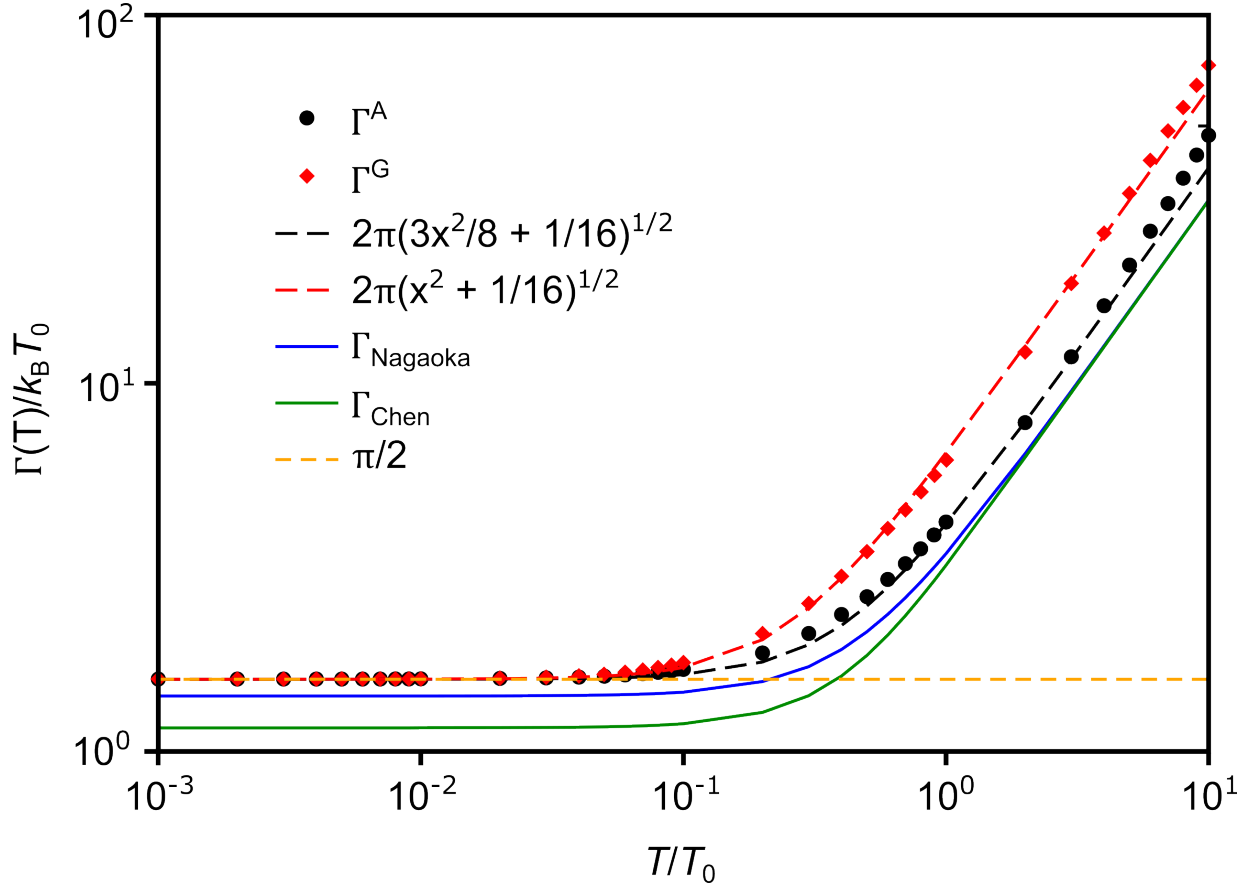
$$k_B T_K = D_{\text{eff}} \sqrt{2\rho J} e^{-1/2\rho J}, \quad \text{for } \rho J \ll 1, \quad (9)$$

where $D_{\text{eff}} = w\sqrt{\pi}U/4 \approx 0.1829U$ is the effective half-bandwidth for an Anderson model that yields the same T_K as for a Kondo model of half-bandwidth D , i.e., D_{eff} plays the same role as D in the prefactor in Eq.(6). The above expression for $k_B T_K$ holds for $D \gg U$ (wide-band limit) and in the symmetric Kondo regime of the Anderson model. It can also be applied to the asymmetric Kondo regime when both $|\varepsilon|$ and $|\varepsilon + U|$ are smaller than D , but requires

modification on approaching the mixed valence regime¹³.

Kondo scale Γ_K in dI/dV and universal linewidths In Fig. 15, we show the universal curves for $\Gamma^A(T)/k_B T_0$ and $\Gamma^G(T)/k_B T_0$ versus T/T_0 for the symmetric Anderson model in the Kondo regime with $U/\gamma_0 = 25.6$. For $\Gamma^A(T)$, we also show analytic results using Fermi liquid theory for the Anderson model by Nagaoka *et al.*⁶ and refinements of this by Chen *et al.*²⁰. Both the NRG and the Fermi liquid approaches use the strong coupling scale T_0 , allowing them to be compared.

The NRG gives $\Gamma_K = \Gamma^G(T = 0) = \Gamma^A(T = 0) = 1.5706k_B T_0 \approx \pi k_B T_0/2$, *i.e.*, the zero temperature width of the Kondo resonance clearly approaches $\pi k_B T_0$. Previous NRG estimates of Γ_K , for a smaller $U/\gamma_0 \approx 7.9$, gave $2\Gamma_K = 3.0k_B T_0$ ²¹. The Frota lineshape⁴, an interpolation of NRG data for the zero temperature spectral function, gave $2\Gamma_K \approx 2.98k_B T_0$, consistent with our estimate. The Fermi liquid approaches underestimate Γ_K : the expression of Nagaoka *et al.* gives $\sqrt{2}k_B T_0 = 1.41k_B T_0$ while the expression of Chen *et al.* gives $\Gamma_K = 1.16k_B T_0$. The reason for this is well known: the Kondo resonance lineshape is not a Lorentzian, except for $|E| \ll k_B T_0$. Instead, it has logarithmic tails which enhance its linewidth²². Estimating its linewidth requires a method like NRG which can access the crossover energy scale $E \sim \Gamma_K \sim k_B T_0$ which is outside the regime where Fermi liquid theory applies. Despite this, the Fermi liquid approaches, which give simple expressions for $\Gamma^A(T)$ and its dimensionless form $f^A(x = T/T_0) = \Gamma^A(T)/k_B T_0$, capture the qualitative aspects of the temperature dependence. The reason for this is that they can be regarded as giving a



Supplementary Figure 15: Temperature dependence of the HWHM of the Kondo resonance in $A(E, T)$ and dI/dV . $\Gamma^{A,G}/k_B T_0$ with T_0 from Eq. (7) are NRG calculations for $U/\gamma_0 = 25.6$. Fits with square root interpolations are indicated. Also shown are the expressions Γ_{Nagaoka} from Eq. (10) and Γ_{Chen} from Eq. (12). The zero temperature limit of the NRG data gives a Kondo resonance HWHM of $\pi k_B T_0/2$. The NRG calculations used $\Lambda = 5$, $N_z = 192$ and retained 1400 states per iteration.

lower bound on the line width since a Lorentzian is always narrower than the true Kondo resonance. The Nagaoka expressions for $\Gamma^A(T) = \Gamma_{\text{Nagaoka}}^A(T)$ and $f_{\text{Nagaoka}}^A(x = T/T_0)$ read

$$\Gamma_{\text{Nagaoka}}^A(T) = \sqrt{(\pi k_B T)^2 + 2(k_B T_0)^2}, \quad (10)$$

$$f_{\text{Nagaoka}}^A(x) = \sqrt{\pi^2 x^2 + 2}, \quad (11)$$

while the corresponding expressions of Chen et al. read,

$$\Gamma_{\text{Chen}}^A(T) = \frac{4\sqrt{2}}{\pi} \left[\sqrt{(k_B T_0)^4 + \left[(k_B T_0)^2 + \frac{\pi^4}{32} (k_B T)^2 \right]^2} - (k_B T_0)^2 \right]^{1/2}, \quad (12)$$

$$f_{\text{Chen}}^A(x) = \frac{4\sqrt{2}}{\pi} \left[\sqrt{1 + \left[1 + \frac{\pi^4}{32} x^2 \right]^2} - 1 \right]^{1/2}, \quad (13)$$

An attempt to fit the NRG results for $\Gamma^{A,G}(T)$ in the range $10^{-3} \leq T/T_0 \leq 10$ with a square root expression of the form $\Gamma_{\text{NRG}}^{A,G} = (1/2)\sqrt{(\alpha^{A,G}k_B T)^2 + (\beta^{A,G}k_B T_0)^2}$ yields for the specified range,

$$\Gamma_{\text{NRG}}^A(T) = \sqrt{\frac{3}{2}(\pi k_B T)^2 + \left(\frac{\pi k_B T_0}{2}\right)^2}, \quad (14)$$

$$f_{\text{NRG}}^A(x = T/T_0) = \frac{\Gamma_{\text{NRG}}^A(T)}{k_B T_0} = 2\pi \sqrt{\frac{3}{8}x^2 + \frac{1}{16}}, \quad (15)$$

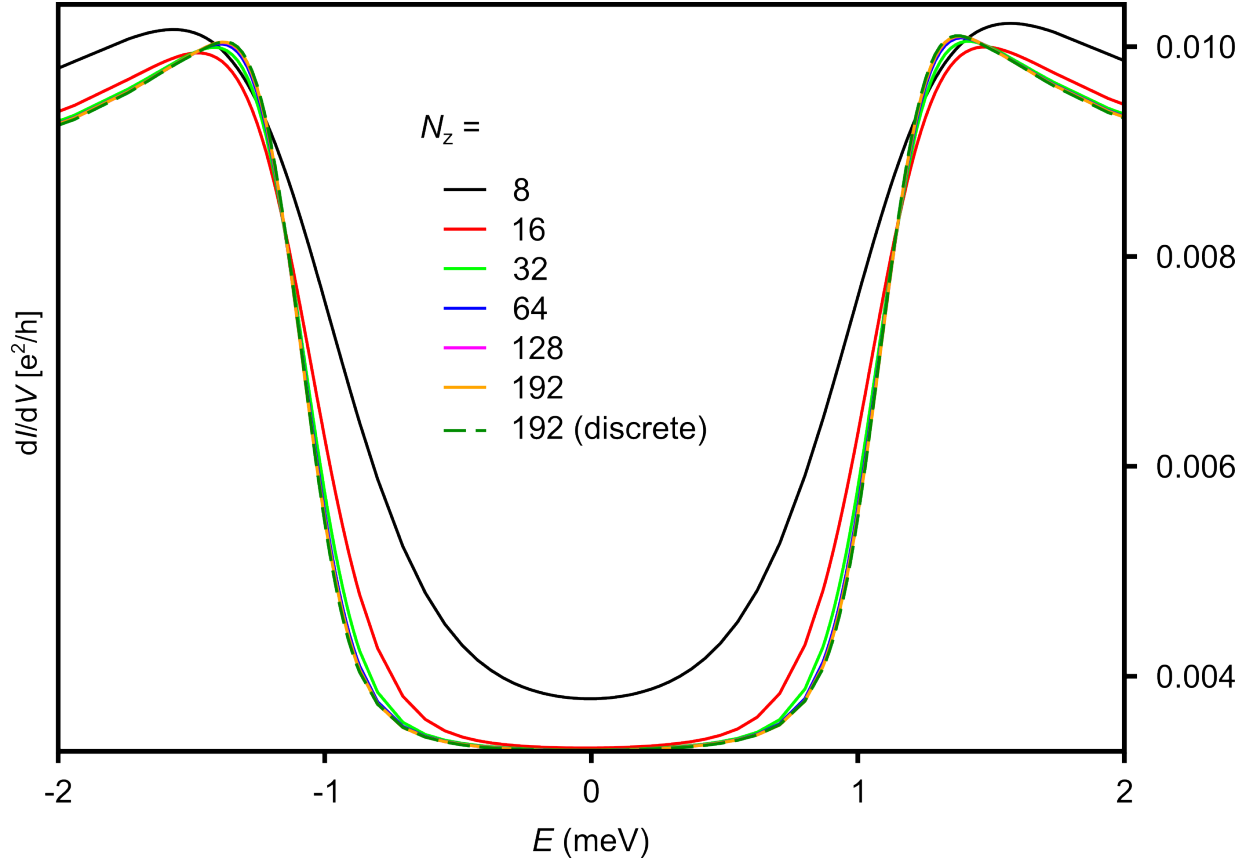
$$\Gamma_{\text{NRG}}^G(T) = \sqrt{(2\pi k_B T)^2 + \left(\frac{\pi k_B T_0}{2}\right)^2}, \quad (16)$$

$$f_{\text{NRG}}^G(x = T/T_0) = \frac{\Gamma_{\text{NRG}}^G(T)}{k_B T_0} = 2\pi \sqrt{x^2 + \frac{1}{16}}, \quad (17)$$

where the NRG coefficients $\beta^A = \beta^G = \pi$ give the correct width at $T = 0$, i.e., $f_{\text{NRG}}^{A,G}(x = 0) = \pi/2$ so $2\Gamma_K = \pi k_B T_0$. The coefficients $\alpha^A = \sqrt{6}\pi \approx 1.2 \times 2\pi$ and $\alpha^G = 4\pi$ give reasonable fits to the NRG data in the range $10^{-3} \leq T/T_0 \leq 10$. It should be emphasized that these coefficients are not chosen to reproduce exactly the NRG data in the limits $x \rightarrow 0$ (low temperature limit) or $x \gg 1$ (high temperature limit) exactly, but only to obtain a good overall fit in the above range. Indeed, outside the above range, i.e., for $x = T/T_0 > 10$, the approximate functions $f_{\text{NRG}}^{A,G}(x)$ actually deviate significantly from the NRG data (as can already be seen in Fig. 15 for $x = 10$). Even in the range $10^{-3} \leq x \leq 10^1$ where $f_{\text{NRG}}^{A,G}(x)$ fit the NRG data reasonably well, there are still significant deviations, e.g., in the range

$0.1 \leq x \leq 0.7$ for $f_{\text{NRG}}^G(x)$. The fact that the expressions $f_{\text{NRG}}^{A,G}$ do not fit the NRG data very well, shows that the true scaling functions $\Gamma_{\text{NRG}}^{A,G}$ are indeed more complicated than a square root function.

Supplementary Note 13: NRG spectral function and dI/dV



Supplementary Figure 16: Convergence of dI/dV spectra with N_z . Illustrates how the correct thermal broadening of the inelastic steps at $E = \pm B$ in dI/dV is captured with increasing number of bath realizations N_z in the z -averaging approach to spectral functions. Convergence to the numerically exact form (green dashed line) in Eq. (18), i.e., without broadening of the delta peaks, is achieved for $N_z \gtrsim 128$. The parameters used for the Anderson model calculation are for the symmetric MTB ($U = 100$ meV, $\varepsilon = -51$ meV and $\gamma = 9.35$ meV) at the largest experimental field $B = 8$ T and for $T = 0.7$ K. The NRG calculations here, and elsewhere, used $\Lambda = 5$ and retained 1400 states per iteration.

Due to the use of a logarithmically discretized conduction band, the NRG spectral function takes on a discrete form $A(E, T) = \sum_m w_m \delta(E - \varepsilon_m)$ where ε_m are the many body

excitations and w_m are weights containing matrix elements and Boltzmann factors (or within the full density matrix approach²³⁻²⁵, that we use, reduced density matrix elements). In principle, such a discrete spectral function can be directly substituted into Eq. (2) and evaluated to give

$$\frac{dI}{dV}(eV) = \sum_m \frac{w_m}{4k_B T \cosh^2((\varepsilon_m - eV)/2k_B T)}. \quad (18)$$

Since this approach just uses the raw NRG excitations and matrix elements, it is in principle exact and includes in dI/dV just the required thermal broadening. However, in practice, due to the lower logarithmic resolution of the NRG excitations ε_m at higher energies, this approach only works for $|eV| \lesssim 100k_B T$. This would suffice to obtain the low energy (Kondo) features of dI/dV in the experiment, however, an important aspect of the present dI/dV measurements is that they also probe the high energy Hubbard peak excitations at ε and $\varepsilon + U$ of the Anderson model. In practice, therefore, we proceed by first obtaining a smooth spectral function $A(E, T)$, by replacing the delta functions appearing in the discrete $A(E, T)$ by, typically, Gaussians, logarithmic Gaussians or other functions with appropriate widths. This NRG broadened $A(E, T)$ is then substituted in Eq.(2) in Supplementary Note 12 to obtain dI/dV . In this procedure, it is important to demonstrate that the NRG broadening of the discrete spectral function does not influence the widths of excitations and features in dI/dV , such as, for example, the slope of the sharp inelastic peaks in dI/dV at $E = \pm B$. This problem is overcome by using the z-averaging approach to spectral functions²⁶ with N_z realizations of the discretized conduction band, and choosing $N_z \gg 1$ sufficiently large. As illustrated in Fig. 16, for $N_z \gtrsim 128$ the NRG broadening used for $A(E, T)$, which is

proportional to $1/N_z$, no longer affects the shape of the sharp inelastic steps at $E = \pm B$ in dI/dV . As required, these are then only determined by the temperature T , which is obtained from experiment. All NRG calculations for comparison with experiment, reported in this paper, were carried out for $N_z = 192$.

References

1. Jolie, W. *et al.* Tomonaga-Luttinger Liquid in a Box: Electrons Confined within MoS₂ Mirror-Twin Boundaries. *Phys. Rev. X* **9**, 11055 (2019). URL <https://doi.org/10.1103/PhysRevX.9.011055>.
2. van Efferen, C. *et al.* Metal-insulator transition in monolayer MoS₂ via contactless chemical doping. *2D Mater.* **9**, 025026 (2022). URL <https://dx.doi.org/10.1088/2053-1583/ac5d0f>.
3. Yang, X. *et al.* Manipulating Hubbard-type Coulomb blockade effect of metallic wires embedded in an insulator. *Natl. Sci. Rev.* (2022). URL <https://doi.org/10.1093/nsr/nwac210>. Nwac210, <https://academic.oup.com/nsr/advance-article-pdf/doi/10.1093/nsr/nwac210/46342134/nwac210.pdf>.
4. Frota, H. O. Shape of the kondo resonance. *Phys. Rev. B* **45**, 1096–1099 (1992). URL <https://link.aps.org/doi/10.1103/PhysRevB.45.1096>.
5. Gruber, M., Weismann, A. & Berndt, R. The Kondo resonance line shape in scanning tunnelling spectroscopy: instrumental aspects. *J. Phys. Condens. Matter.* **30**, 424001

- (2018). URL <https://doi.org/10.1088/1361-648x/aadfa3>.
6. Nagaoka, K., Jamneala, T., Grobis, M. & Crommie, M. F. Temperature Dependence of a Single Kondo Impurity. *Phys. Rev. Lett.* **88**, 077205 (2002). URL <https://link.aps.org/doi/10.1103/PhysRevLett.88.077205>.
 7. Cronenwett, S. M., Oosterkamp, T. H. & Kouwenhoven, L. P. A tunable Kondo effect in quantum dots. *Science* **281**, 540–544 (1998).
 8. Jolie, W. *et al.* Charge density wave phase of VSe₂ revisited. *Phys. Rev. B* **99**, 115417 (2019). URL <https://link.aps.org/doi/10.1103/PhysRevB.99.115417>.
 9. Hewson, A. C. *The Kondo Problem to Heavy Fermions* (Cambridge University Press, Cambridge, 1997).
 10. Goldhaber-Gordon, D. *et al.* Kondo effect in a single-electron transistor. *Nature* **391**, 156–159 (1998).
 11. Pruschke, T. & Grewe, N. The Anderson model with finite Coulomb repulsion. *Z. Phys. B: Condens. Matter* **74**, 439–449 (1989).
 12. Logan, D. E., Eastwood, M. P. & Tusch, M. A. A local moment approach to the Anderson model. *J. Phys. Condens. Matter* **10**, 2673 (1998).
 13. Krishna-murthy, H. R., Wilkins, J. W. & Wilson, K. G. Renormalization-group approach to the Anderson model of dilute magnetic alloys. II. Static properties for the asymmetric

- case. *Phys. Rev. B* **21**, 1044–1083 (1980). URL <http://link.aps.org/doi/10.1103/PhysRevB.21.1044>.
14. Zhu, T. *et al.* Imaging gate-tunable Tomonaga–Luttinger liquids in 1H-MoSe₂ mirror twin boundaries. *Nat. Mater.* **21**, 748–753 (2022). URL <https://doi.org/10.1038/s41563-022-01277-3>.
 15. Schrieffer, J. R. & Wolff, P. A. Relation between the Anderson and Kondo Hamiltonians. *Phys. Rev.* **149**, 491–492 (1966). URL <https://link.aps.org/doi/10.1103/PhysRev.149.491>.
 16. Kondo, J. Resistance Minimum in Dilute Magnetic Alloys. *Prog. Theor. Phys.* **32**, 37–49 (1964).
 17. Wilson, J., Di Salvo, F. & Mahajan, S. Charge-density waves and superlattices in the metallic layered transition metal dichalcogenides. *Adv. Phys.* **24**, 117–201 (1975). URL <http://www.tandfonline.com/doi/abs/10.1080/00018737500101391.0410314v1>.
 18. Krishna-murthy, H. R., Wilkins, J. W. & Wilson, K. G. Renormalization-group approach to the Anderson model of dilute magnetic alloys. I. Static properties for the symmetric case. *Phys. Rev. B* **21**, 1003–1043 (1980). URL <http://link.aps.org/doi/10.1103/PhysRevB.21.1003>.
 19. Haldane, F. Theory of the atomic limit of the Anderson model. 1. Perturbation expansions re-examined. *J. Phys. C: Solid State Phys.* **11**, 5015–5034 (1978).

20. Chen, C., Sodemann, I. & Lee, P. A. Competition of spinon Fermi surface and heavy Fermi liquid states from the periodic Anderson to the Hubbard model. *Phys. Rev. B* **103**, 085128 (2021). URL <https://link.aps.org/doi/10.1103/PhysRevB.103.085128>.
21. Hsu, C. *et al.* Magnetic-field universality of the kondo effect revealed by thermocurrent spectroscopy. *Phys. Rev. Lett.* **128**, 147701 (2022). URL <https://link.aps.org/doi/10.1103/PhysRevLett.128.147701>.
22. Rosch, A., Costi, T. A., Paaske, J. & Wölfle, P. Spectral function of the kondo model in high magnetic fields. *Phys. Rev. B* **68**, 014430 (2003). URL <https://link.aps.org/doi/10.1103/PhysRevB.68.014430>.
23. Peters, R., Pruschke, T. & Anders, F. B. Numerical renormalization group approach to Green's functions for quantum impurity models. *Phys. Rev. B* **74**, 245114 (2006). URL <http://link.aps.org/doi/10.1103/PhysRevB.74.245114>.
24. Weichselbaum, A. & von Delft, J. Sum-rule conserving spectral functions from the numerical renormalization group. *Phys. Rev. Lett.* **99**, 076402 (2007). URL <http://link.aps.org/doi/10.1103/PhysRevLett.99.076402>.
25. Kugler, F. B. Improved estimator for numerical renormalization group calculations of the self-energy. *Phys. Rev. B* **105**, 245132 (2022). URL <https://link.aps.org/doi/10.1103/PhysRevB.105.245132>.

26. Campo, V. L. & Oliveira, L. N. Alternative discretization in the numerical renormalization-group method. *Phys. Rev. B* **72**, 104432 (2005). URL <http://link.aps.org/doi/10.1103/PhysRevB.72.104432>.

CHAPTER 8

Manuscript 5: Real-space observation and tunneling spectroscopy of polarons in monolayer MoS₂

This chapter wholly consists of the above-named manuscript and its supplement. Unlike the other manuscripts in this thesis, it is not yet finished. The interpretation of the experimental data and DFT calculations is therefore subject to change.

The experiments were proposed by C. van Efferen. Sample growth and STM measurements were conducted the TSTM and MSTM systems in Cologne. The measurements were carried out by C. van Efferen and W. Jolie, with assistance from T. Tounsi, M. Georger, A. Saffeer, J. Bergelt and C. Krämer. The analysis of the experimental data was performed by C. van Efferen, with support from W. Jolie. The DFT calculations were performed by A. Schobert and M. Winter, with support from R. Mozara, J. Berges and T. Wehling. The interpretation of the results was discussed in depth by C. van Efferen, A. Schobert, J. Fischer, R. Mozara, J. Berges, T. Wehling, T. Michely and W. Jolie.

C. van Efferen and A. Schobert wrote the manuscript, with advice and corrections from W. Jolie, R. Mozara and J. Berges.

Real-space observation and tunneling spectroscopy of polarons in monolayer MoS₂

Camiel van Efferen^{1,*}, Arne Schobert², Tfyeché Tounsi¹, Michael Winter², Mark Georger¹, Affan Safeer¹, Jason Bergelt¹, Christian Krämer¹, Jeison Fischer¹, Roberto Mozara², Jan Berges³, Tim Wehling^{2,4}, Thomas Michely¹, Wouter Jolie¹

¹*II. Physikalisches Institut, Universität zu Köln, Zùlpicher Straße 77, 50937 Köln, Germany*

²*I. Institut für Theoretische Physik, Universität Hamburg, Notkestr. 9-11, 22607 Hamburg, Germany*

³*U Bremen Excellence Chair, Bremen Center for Computational Materials Science, and MAPEX Center for Materials and Processes, Universität Bremen, 28359 Bremen, Germany*

⁴*The Hamburg Centre for Ultrafast Imaging, Luruper Chaussee 149, 22607 Hamburg, Germany*

Polarons are quasiparticles that arise from the interaction of electrons or holes with lattice vibrations ¹. Though polarons are extremely well-studied across multiple disciplines ², experimental observations of polarons in two-dimensional crystals are sparse. This study provides scanning tunneling microscopy (STM) and spectroscopy (STS) of polaronic states emerging from coupling of non-polar zone-boundary phonons to Bloch electrons in *n*-doped metallic monolayer MoS₂, which is kept chemically pristine by using the contactless doping method ³. Tunneling into the vibrationally coupled polaron states leads to a series of evenly-spaced peaks in STS dI/dV spectra on either side of the Fermi level. Aided by density-functional theory calculations, the energy spacing is shown to stem from

a renormalized M-phonon, responsible for the polaron formation. The binding energy of the polarons is furthermore shown to be affected by surface charge, enabling the localization of the polaron wavefunctions to a quantum well, which allows them to be visualized with STM.

In a perfect crystal, electrons can be described as periodic plane waves traveling freely through the lattice. A polaron is a quasiparticle that forms when charge carriers like electrons or holes instead interact strongly with the ionic lattice, leading to self-trapping of the carrier, creating a localized state in absence of a defect ². While the polaron is generally still able to move through the lattice, it drags a deformation of the lattice with it, enhancing its effective mass.

Polarons are ubiquitous, forming in a wide array of materials ². Their presence has been associated with a host of exotic phenomena, such as colossal magnetoresistance ^{4,5}, spin currents ⁶, magnetic transitions ⁷, the star-of-David ground state of 1T-TaS₂ and its spin-glass transition ⁸⁻¹⁰, high- T_c superconductivity ¹¹⁻¹³ and the pseudogap in transition metal oxides ¹⁴. Though their presence can be detected with many experimental techniques, local observations of polarons are rare and limited to studies of strongly localized polarons in insulating materials ¹⁵⁻²¹. In these cases, the polaron is trapped near a defect or specific lattice site, rendering it largely immobile, allowing it to be imaged directly with the scanning tunneling microscope (STM) or atomic force microscope.

Another apparent gap in the field of polaron studies concerns the relative dearth of examples of polarons forming in 2D materials. To date, they have only been unambiguously observed in a couple of materials ²⁰⁻²³. A recent DFT-based approach has explored the

conditions for forming stable Fröhlich polarons in 2D materials based on polar zone-center phonons, finding that some of the most popular transition metal dichalcogenides (TMDCs), including MoS₂, cannot host them in their monolayer, due to the weak ionic screening which is a consequence of their 2D nature²⁴. The explanation for the polaronic features in the ARPES spectra of alkali-doped bulk MoS₂, observed in Ref. 25, is accordingly sought in the coupling of Bloch electrons to non-polar zone-boundary phonons²⁶. Results for top-gated or doped bulk MoS₂ cannot however be taken as representative for metallic single-layer (SL) MoS₂, with multiple studies finding different transport properties between the two materials²⁷⁻³¹. Generally, metallic SL MoS₂ has only a single band at the K-point crossing the Fermi level^{32,33}, while metallic bulk MoS₂ has a second band at the Q-point³⁴⁻³⁷, with significant ramifications for the electron-phonon coupling³⁷. It therefore remains an open question whether SL MoS₂ and similar TMDCs can host polarons at all.

Here, we investigate polaronic effects in quasi-freestanding SL MoS₂ on a graphene (Gr) on Ir(111) substrate using STM, STS and density functional theory (DFT) theory augmented by model calculations. SL MoS₂ is grown using a two-step molecular-beam epitaxy process on Gr³⁸. Using contactless chemical doping with Eu or Cs atoms intercalated below the Gr substrate, MoS₂ is *n*-doped, shifting the conduction band (CB) into the Fermi level E_F and thus inducing a metal-insulator transition. We refer to Ref. 3 for more details about the method.

An STM topograph of metallic SL MoS₂ is shown in Fig. 1a, displaying the typical morphology. The islands are grown together forming large networks, with areas ranging in

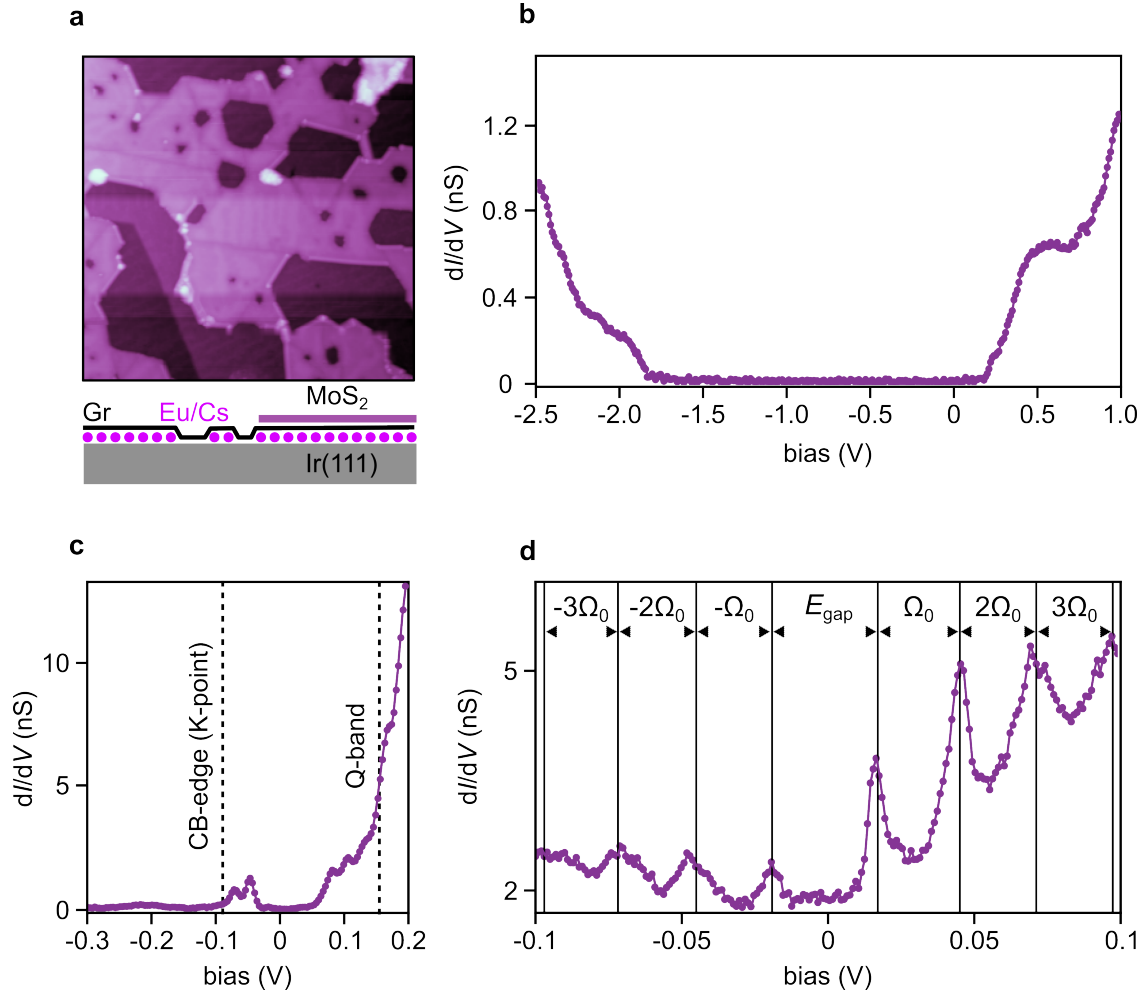


Figure 1: **Electronic structure of single-layer MoS₂.** **a** Large-scale STM image of single-layer MoS₂/Gr/Eu/Ir(111). A step edge in the Ir substrate can be seen in the bottom left. The Eu intercalation has slight density modulations which lead to the bright strips visible through MoS₂ and Gr. **b** High-bias STM dI/dV spectrum of single-layer MoS₂ on Gr/Eu/Ir(111), showing the renormalized band gap. **c** Low-bias STM dI/dV spectrum. The CB edge at the K-point of the Brillouin zone and the onset of the band near the Q-point are indicated, showing the metallic nature of MoS₂ on Gr/Eu/Ir(111). **d** Low-bias STM dI/dV spectrum, revealing peak-dip features and a gap at the Fermi level, characteristic for metallic single-layer MoS₂. STM/STS parameters: **a** $100 \times 100 \text{ nm}^2$, $V_{\text{set}} = 2.5 \text{ V}$, $I_{\text{set}} = 50 \text{ pA}$; **b** $V_{\text{set}} = 1 \text{ V}$, $I_{\text{set}} = 500 \text{ pA}$, $V_{\text{mod}} = 15 \text{ mV}$; **c** $V_{\text{set}} = 0.2 \text{ V}$, $I_{\text{set}} = 500 \text{ pA}$, $V_{\text{mod}} = 5 \text{ mV}$; **d** $V_{\text{set}} = 0.1 \text{ V}$, $I_{\text{set}} = 500 \text{ pA}$, $V_{\text{mod}} = 1 \text{ mV}$. **d** is smoothed using the Savitzky–Golay method. For all spectra $f_{\text{mod}} = 877 \text{ Hz}$.

size from 50–700 nm². These areas are separated by grain boundaries, which show up as dark stripes. Through the islands, a striped superstructure can be recognized, which stems from minor density variations in the Eu intercalation layer and has little effect on the electronic properties of MoS₂³.

A high-bias dI/dV spectrum, showing the band gap of MoS₂ is depicted in Fig. 1b. On account of the n -doping of the Gr substrate layer by the Eu atoms, the MoS₂ CB edge is shifted down. The band gap is strongly renormalized compared to SL MoS₂ on undoped Gr³⁹. The spectrum shows an apparent onset of the CB above the Fermi level. However, since the CB minimum of doped SL MoS₂ lies at the K-point^{33,37}, the high parallel momentum k_{\parallel} of the quasiparticles renders them nearly invisible to tunneling spectroscopy, unless the tip-sample distance is severely reduced^{39,40}. We therefore focus on the energies closest to E_F and decrease the distance between tip and sample. The resulting dI/dV spectrum in Fig. 1c reveals a finite density of states (DOS) in the occupied states, separated from the unoccupied states by a gap at E_F .

A particular aspect of the spectrum in Fig. 1c is the presence of peak-dip features on either side of the Fermi level. In Fig. 1d these are seen to manifest as a series of evenly-spaced peaks, nearly symmetric around E_F . The peaks are spaced by a fixed energy Ω_0 , with a larger gap E_{gap} separating the states around E_F . We note that these features are only present in metallic MoS₂ and are not found in the semiconducting state, see Supplementary Fig. 1.

To better understand the behavior of the peaks, we have analysed ≈ 3000 dI/dV spectra. The spectra were taken on islands of different size and on two different metallic MoS₂ samples

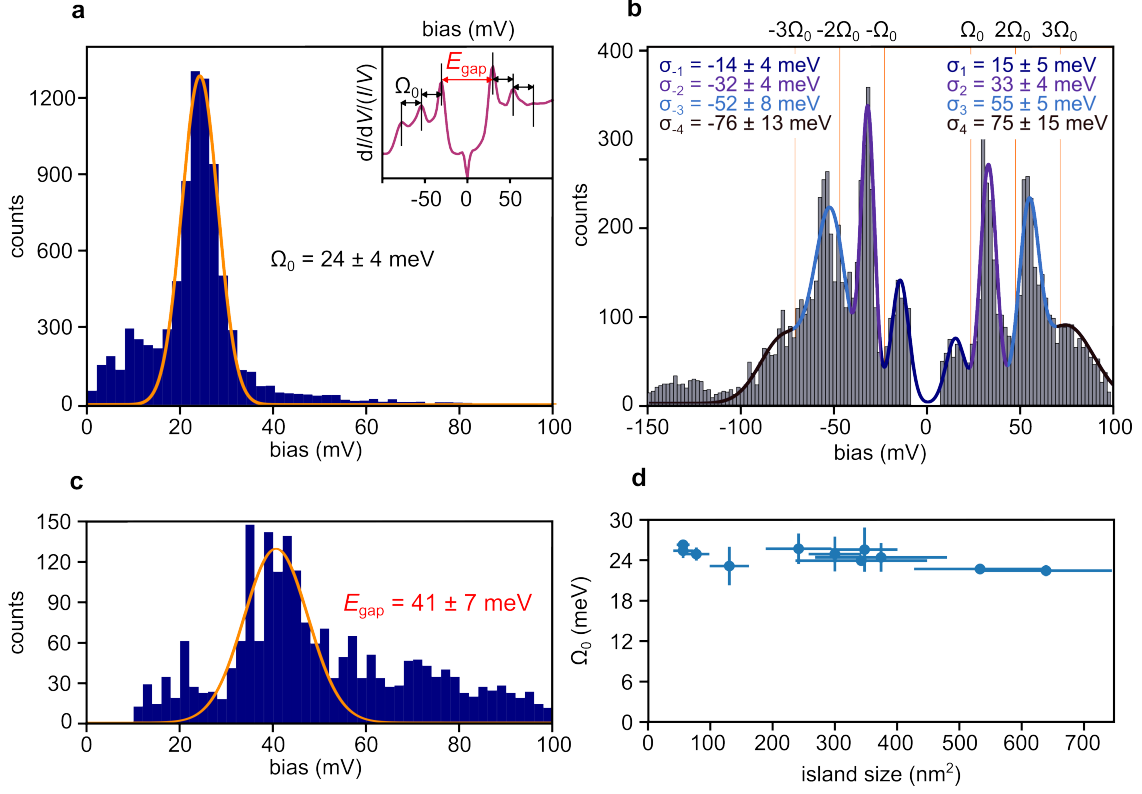


Figure 2: **Statistical analysis of peak-dip features in dI/dV spectra.** **a,b** Histograms of 2935 dI/dV spectra acquired on different locations, at different temperatures (0.4–6 K) and on MoS_2 areas of different sizes, using different samples (multiple $\text{MoS}_2/\text{Gr}/\text{Eu}/\text{Ir}(111)$ samples and one $\text{MoS}_2/\text{Gr}/\text{Cs}/\text{Ir}(111)$ sample) and tips (Au and PtIr). In **a** the energetic distances between neighbouring peaks (excepting the peaks closest to the Fermi level) are plotted. A Gaussian fit to the peak yields $\Omega_0 = 24 \pm 4$ meV. In **b** the peak locations are plotted. To each peak in the histogram a Gaussian is fitted, yielding $\sigma_{1,2,3,4}$ and $\sigma_{-1,-2,-3,-4}$ for the peaks above and below the Fermi level, respectively. To analyze the data, the dI/dV spectra were smoothed and normalized. The inset in **a** shows a dI/dV spectrum after this procedure, with the locations of peaks found by a peak finding algorithm marked. **c** Histogram of the distribution of the energetic distance between the first peaks on either side of the Fermi level. A Gaussian fit to the peak yields $\Omega_0 = 41 \pm 7$ meV. **d** Average distance between neighbouring peaks Ω_0 for spectra taken on MoS_2 islands of different sizes.

– with either Eu or Cs intercalated below Gr. We included spectra taken in a temperature range of 0.3–6 K. We find that the spacing between the peaks has a Gaussian distribution, with a mean value and standard deviation of $\Omega_0 = 24 \pm 4$ meV, see Fig. 2a. We therefore treat all peaks as harmonics of a single bosonic mode Ω_0 instead of independent excitations.

If we plot the locations of the peaks in a histogram, we see that the peaks are distributed evenly on either side of E_F , with the gaps between them located at intervals of Ω_0 , see Fig. 2b. So, while the peaks in individual spectra are spaced by Ω_0 , the peaks are less likely to be located near energies $|E = n\Omega_0|$, with $n = 1, 2, 3, \dots$. When we check for the size of E_{gap} across all investigated spectra, see Fig. 2c, we find considerably more fluctuation than for the peak spacing. The distribution does have a marked peak, which fitted with a Gaussian gives $E_{\text{gap}} = 41 \pm 7$ meV.

We have checked in Fig. 2d that there is no dependence of Ω_0 on the size of the island. Since the grain boundaries that divide the different regions of the MoS₂ islands are charged relative to their surroundings, band bending effects take place perpendicular to them, isolating the different parts of the structure from one another⁴¹. The sample is thus composed of many areas of differing size, all of which show the same peak spacing Ω_0 , ensuring that the peak-dip features are not related to area-dependent effects like confinement.

We now investigate the peak-dip features in a non-uniformly doped sample, with Cs atoms adsorbed on the metallic MoS₂ surface, acting as potential n -donors. Cs is also intercalated below Gr, n -doping Gr by a similar amount as Eu⁴³ and inducing the metal-insulator transition in MoS₂. A STM topograph of the sample is shown in Fig. 3a. The adsorbed Cs

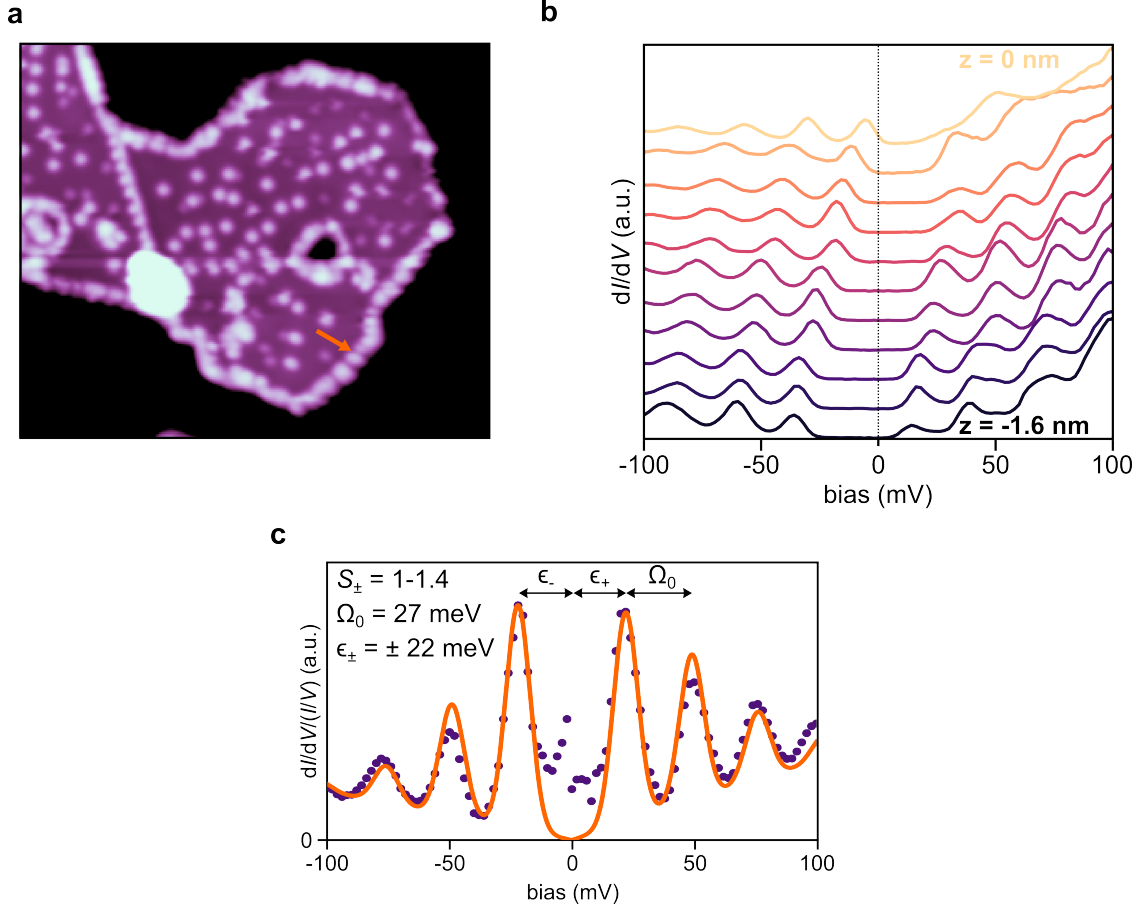


Figure 3: **Tunneling through localized polaronic states.** **a** STM image of a single-layer MoS₂ island on Gr/Cs/Ir(111). Adsorbed Cs atoms are visible on the island, grain boundaries and edges as bright dots. A small bilayer can be seen on the left bottom part of the island. **b** dI/dV spectra taken along the orange arrow in **a**, with $z = 0$ nm corresponding to the spectrum closest to the edge. Spectra are offset for clarity. **c** Symmetric low-bias $dI/dV/(I/V)$ spectrum with peaks above and below the Fermi level (purple dots). A fit based on Ref. 42 is shown as an orange line. Fitting parameters: the Huang-Rhys factor $S_- = 1$ ($S_+ = 1.4$) for the resonances in the occupied (unoccupied) states, the phonon energy $\Omega = 27$ meV, location of the polaronic state $\epsilon = \pm 22$ meV, the full width at half maximum of the states $\Gamma = 7$ meV. A linear offset is included to account for (inelastic) tunneling processes that involve the MoS₂ band. STM/STS parameters: **a** 40×33 nm², $V_{\text{set}} = 1.0$ V, $I_{\text{set}} = 100$ pA; **b,c** $V_{\text{set}} = 100$ mV, $I_{\text{set}} = 1.1$ nA, $V_{\text{mod}} = 2$ mV, $f_{\text{mod}} = 877$ Hz.

atoms are visible in the image as bright dots, preferentially sticking to grain boundaries and edges. Taking a series of dI/dV spectra along the line drawn in Fig. 3a, we can track the behavior of the peak-dip features as they move to the island edge on the right. The spectra are plotted in Fig. 3b. The peaks are seen to bend collectively upwards near the edge of the island in a range of 1.6 nm.

Given the experimental evidence, we can conclude that tunneling in metallic SL MoS₂ is strongly affected by the existence of a bosonic mode of energy $\Omega_0 = 24 \pm 4$ meV, leading to satellite peaks in the tunneling spectra. The existence of these peaks can either stem from renormalization of the electrons via virtual boson emission²⁶, or from inelastic tunneling processes which involve the emission of real bosons. Since SL MoS₂ hosts multiple flat phonon bands near the edges of its Brillouin zone, with energies of 20–30 meV⁴⁴, the bosonic mode Ω_0 is likely a phonon.

Inelastic tunneling processes can lead to characteristic sideband structures in the case of strong coupling between vibronic excitations and localized electronic states. This has been established for STM junctions in 1D and 0D systems^{45–47}, in particular for molecules on surfaces^{48–50} and in tunneling devices based on semiconductor quantum wells⁵¹. In these systems, a series of resonant peaks spaced by the energy of the vibronic mode are observed in conductance spectra. Following Ref. 42, we model the peak-dip features as the coupling of a discrete state with energy ϵ_{\pm} , with a phonon mode $\omega = \Omega_0/\hbar$:

$$A(\omega) = 2\pi \sum_{\{l_1 l_2 \dots l_n\}}^{\infty} \left[\left(e^{-S_{\pm}} \frac{S_{\pm}^l}{l!} \right) \delta(\hbar\omega - \epsilon_{\pm} - \hbar\omega l) \right], \quad (1)$$

with S_{\pm} the Huang-Rhys factor related to the state-boson coupling strength $g = \frac{\sqrt{S_{\pm}}}{\omega}$ and l an

integer. Eq. 1 is the exact solution of the Holstein Hamiltonian, which quantifies the coupling between electrons and phonons and leads to a Franck-Condon shape for the spectrum⁴². Fitting the states on both sides of E_F of a symmetric normalized conductance ($dI/dV/(I/V)$) spectrum, we find Huang-Rhys factors of $S_- = 1$ and $S_+ = 1.4$ for the resonances in the occupied and unoccupied states, respectively. Though the model is able to adequately describe the experimental spectra, the fact that the peaks in metallic MoS₂ are also present in the absence of any structural defects begs the question as to what type of localized energy state gives rise to the first peaks around E_F . To this end we performed DFT and density functional perturbation theory (DFPT) calculations augmented by a downfolded *ab-initio* lattice model which facilitates relaxations on large supercells⁵² (see Calculation Details below for more information).

We find that n -doped SL MoS₂ is unstable towards to localized deformations, as can be seen in the relaxed structure depicted in Fig. 4a. The size of the deformation corresponds to the amount of additional charge carriers in the system, as there will be a balance between charge accumulation and Coulomb repulsion and the charges will not localize indefinitely at a specific site. In Fig. 4b we show the potential energy surface (PES) in the direction of the relaxed displacements, revealing an energy gain of up to 4 meV per formula unit of MoS₂. Resolving the local occupations on Mo atoms (see Supplementary Fig. 5), we can infer that on average one electron will occupy 2.4 sites, which implies a binding energy of ≈ 10 meV per electron.

To gain insight into the momentum-resolved intensity of the electron-phonon scatterings,

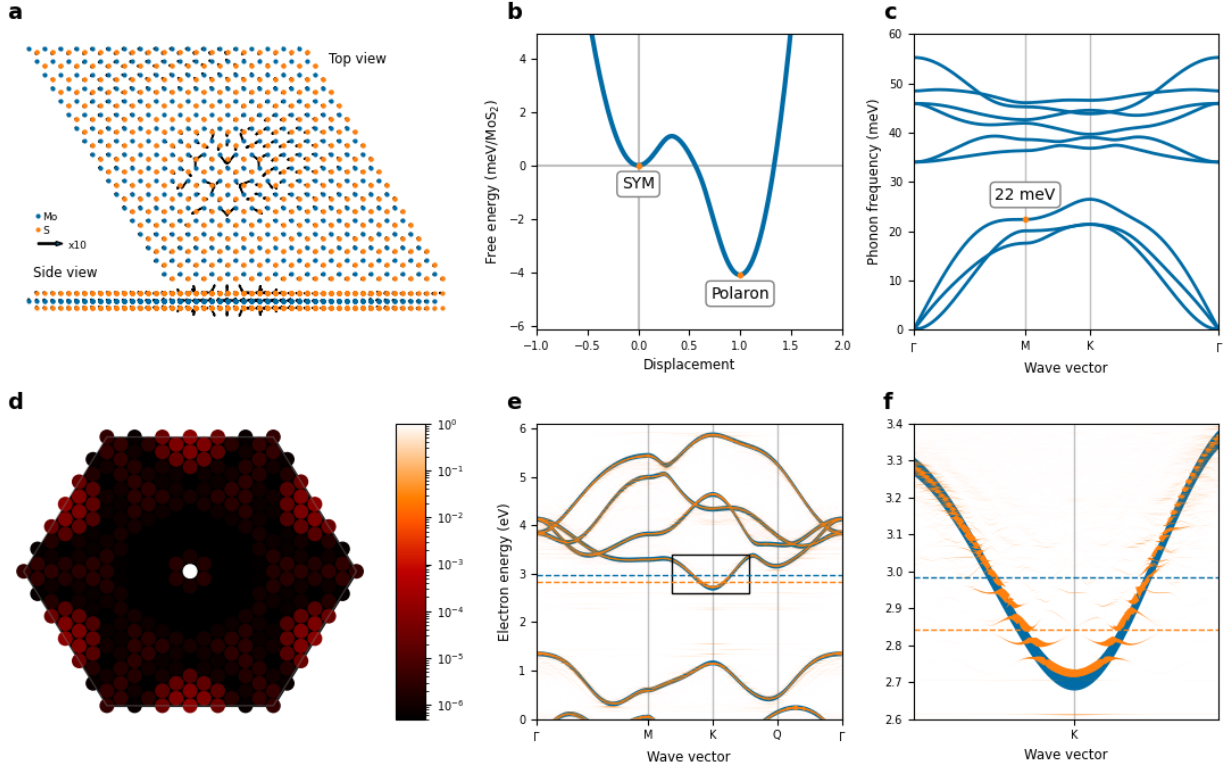


Figure 4: **Polaronic deformations in metallic single-layer MoS₂.** **a** Relaxed crystal structure based on ab-initio model calculations on an 18×18 supercell at an electronic doping of $0.12 e^-$ per formula unit of MoS₂. The displacements indicated by black arrows are rescaled by a factor of 10 for better visibility. **b** PES in the direction of the relaxed displacement seen in **a**. The relaxation started from the symmetric phase (“SYM”) and shows a minimum at the displacement corresponding to the polaronic deformation. **c** Phonon bands obtained via DFPT. The phonon mode at the M-point that contributes the most to the polaronic deformation is marked by its energy. The phonon bands are obtained at an electronic doping of $0.1 e^-/\text{MoS}_2$. **d** Structure factor $S(\mathbf{q})$ for the relaxed geometry seen in **a**. The high intensity at the M-points of the phononic Brillouin zone shows that the modes located there contribute the most to the polaronic deformation. **e** Band structure as obtained by DFT (blue) and after the ab-initio model relaxation (orange). The polaron formation is accompanied by the appearance of dispersionless states deep inside the gap which pull down the Fermi level (dashed lines). The relaxed band structure has been unfolded from the super- to the unit cell, revealing the opening of gaps associated with the symmetry breaking due to the polaronic deformation. **f** Zoom of the band structure in **e** into the region around the K-point.

we turn towards the MoS₂ phonon dispersion in Fig. 4c, which has multiple flat regions near the M- and K-points of the Brillouin zone. We evaluated the structure factor $\langle S(\mathbf{q}) \rangle$ (see Fig. 4d)⁵², which represents the Fourier transform of the relaxed lattice and thereby provides an estimation of the momentum-dependent scattering intensity. Remarkably, we found that the highest intensity occurs around the M-point in the phononic Brillouin zone. By comparing the phonon dispersions in Fig. 4c, which is calculated for the relaxed lattice, with the one in Supplementary Fig. 4c, where the lattice constant is fixed, we observe a strong softening in the third branch of the longitudinal acoustic phonons which becomes cured when the lattice constant is allowed to relax upon doping. Similar findings were reported in Ref. 26. This M-point phonon in the third branch with a frequency of ≈ 22 meV is thus mainly responsible for the displacement pattern, which is in close agreement with the experimental observation of the phonon energy of $\Omega_0 = 24 \pm 4$ meV.

The occurrence of scattering via M-point phonons suggests that the electronic states at K- and Q-points are electron-phonon coupled³⁷. It is intriguing to note that this coupling exists even though the Q-point is not occupied, with off-shell quantum excitations of electron-hole pairs via virtual phonons possible even in the absence of thermal excitations (c.f. Eq. (33) in Ref. 53). Our *ab-initio* calculations indicate that the lattice deformations concomitant with charge localization are accompanied by a particular quasi-particle property: the polarization cloud². These observations lead us to interpret the local deformations as indicative of a polaronic state in MoS₂.

To further understand the implications of the local deformations, we examined the

corresponding electronic structure. In Fig. 4e,f we depict the undistorted band structure (blue) and the unfolded band structure in the deformed phase (orange), where the linewidths of the unfolded bands were calculated as the the overlap of the electronic wavefunctions (with the same wavevector) of the distorted and the undistorted system. In both band structures the Q-point is not occupied, as illustrated by the Fermi level (dashed lines). The location of the Q-point was experimentally determined in Ref. 3 for SL MoS₂ on Gr/Ir(111). The unoccupied nature of the Q-point is also found in the case of a smaller MoS₂ lattice constant at some distance from the local deformation, only not as pronounced (see Supplementary Fig. 4). The precise position of the Q-point will thus depend on local variations in charge and lattice constant. Notably, we observe displacement-induced gaps at the K-point, see Fig. 4f, as well as other locations along the band structure, which correspond to the geometric symmetry breaking within the supercell^{54,55}.

Our calculations suggest that the first peaks separated by E_{gap} are related to polaronic bound state energies, from (or to) which electrons can tunnel elastically, while the side peaks are inelastic phonon replicas separated by the frequency of the third mode at the M-point. We find that the binding energy depends strongly on the doping level and the lattice constant, as well as on the energy window chosen for downfolding. Depending on these parameters, we find both stable and metastable polaronic states, with local minima on the PES (compare Fig. 4 and Supplementary Figs 2 and 4). Our calculations thus offer the possibility of inelastic excitations of polarons besides elastic tunneling into bound states, though our results are not conclusive on this point.

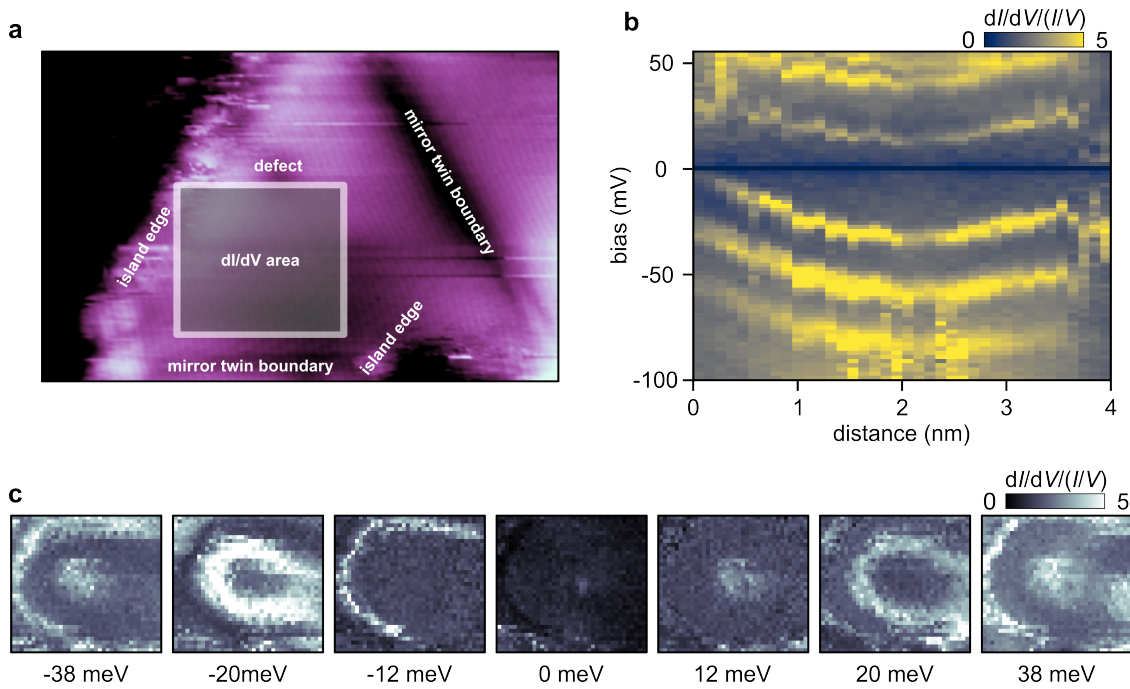


Figure 5: Polarons in a box. **a** STM image of a small area of single-layer MoS₂ on Gr/Eu/Ir(111). Indicated in the figure is the location of a dI/dV map, boxed in from multiple sides by defects (island edges, mirror twin boundaries and a point defect). **b** Colormap of dI/dV spectra taken from top to bottom along the center of the box in **a**. **c** Conductance (dI/dV) maps at different energies showing ring-like behavior of resonance peaks. STM/STS parameters: **a** $16 \times 10 \text{ nm}^2$, $V_{\text{set}} = 1.0 \text{ V}$, $I_{\text{set}} = 10 \text{ pA}$; **b,c** $V_{\text{set}} = 100 \text{ mV}$, $I_{\text{set}} = 1.0 \text{ nA}$, $V_{\text{mod}} = 2 \text{ mV}$, $f_{\text{mod}} = 907 \text{ Hz}$. **c** $4 \times 3.6 \text{ nm}^2$.

Considering that the peaks are related to tunneling into polaronic states, we can explore the local conditions for polaron formation with the STM. In large areas of MoS₂ the states are delocalized, with their presence only modulating the total background of the dI/dV signal, see Supplementary Fig. 7. However, due to the charges within edges and grain boundaries, the localized states ϵ_{\pm} become strongly location-dependent near such defects, effectively trapping them. In a similar vein oxygen vacancies in rutile TiO₂(110) were used to localize the wavefunctions of polarons¹⁶; electron localization was also observed to preferably happen near defects⁵⁶ or step edges⁵⁷. In Fig. 5 spectroscopic maps of a small confined MoS₂ area are shown, with island edges and grain boundaries functioning as the sides of a quasi-0D box, see Fig. 5a. In a dI/dV linescan across the area, shown in Fig. 5b, the localized states can be seen to bend upwards together with their resonances towards the island edge. Conductance maps shown in Fig. 5c reveal how the states travel outward towards the edges, leading to a series of concentric rings that have the same spatial character, independent of the applied bias voltage. This can be contrasted with localization of dispersing electrons, where the wavefunction of the quantized level is dependent on the electron momentum state k ⁵⁸.

Discussion

While the exact mechanism that leads to the asymmetric peaks spaced by E_{gap} is not yet fully clear, we can rule out certain scenarios based on our observations. The energetic shifts of the peaks in response to localized charges are, *e.g.*, incompatible with purely inelastic tunneling processes, which lead to the appearance of symmetrically distributed steps or peaks in the dI/dV signal on either side of the Fermi level (at energies $\pm n\Omega_0$)^{49,59,60}. In the same

vein, renormalization of the electron bands with a particular phonon mode can be excluded as the cause of the peaks, as it would lead to mass-enhanced (flatter) bands symmetrically spaced around E_F , as observed for instance in surface-doped bulk MoS₂ with ARPES²⁵. In our case, the asymmetry induced by charges within the layer, together with the statistical distribution of the peaks, which dips at energies $E \pm n\Omega_0$, strongly suggests that the first two peaks have a different origin than provided by either of these effects.

An intuitive picture relating the peaks at ϵ_{\pm} to polaron formation might be provided by two recent works on polarons in semiconducting CoCl₂, where localized polarons are created with the STM tip^{20,21}. In these works, the creation (at positive bias) or annihilation (at negative bias) of a polaron results in a sudden change in the tunneling current which would correspondingly lead to a peak or dip in the conductance. However, it is not *a priori* clear, whether the spatially localized and macroscopically stable polarons observed in those studies can be compared to the type of polaronic states in metallic SL MoS₂.

Concerning the DFT, we encountered many different (meta-)stable geometries. While all geometries contain local deformations, their associated energy gain or loss depends on the lattice constant and doping of the system (see Supplementary Figs. 2 and 3). Experimentally, the MoS₂ surface will have small variations of the lattice constant, depending on regional doping conditions and defects, but also on differences in strain when the coupling between the MoS₂ and the substrate layers varies slightly³. To account for this situation, we considered two relaxed lattice constants, a smaller one that has been obtained for the undoped unit cell, and one for the doped unit cell, which becomes larger due to electronic repulsion. Eventually

polaronic deformations will be surrounded by regions with a lattice constant closer to the smaller value, but the local physical properties of the deformation itself will be determined by the larger lattice constant. The results for both lattice constants are shown in Fig. 4 and Supplementary Fig. 4, respectively. This interplay between the lattice constant, doping and the polaronic deformations warrants further investigation.

Within the mean-field approximation the polaron is a self-consistent localization of additional charges in the system, and this localization can be captured by DFT when self-interaction errors are eliminated⁶¹ or localization is ensured otherwise². Our downfolded-model approach incorporates DFT and DFPT, but still refers to the same mean-field picture and by construction contains no self-interaction terms. This static mean-field approach can be embedded into a self-consistent many-body approach as in Refs. 53,62, and be related to the so-called polaronic self-energy responsible for the static renormalization of electronic energies due to localization. The actual formation energy of the polaron, though, contains not only static contributions from electronic energies and the polaronic self-energy, but possibly also contributions from dynamical renormalization, *e.g.*, due to the Fan-Migdal self-energy. For SL MoS₂ the latter, however, does not lead to any spectral modifications at the K-valley because the Q-point is not occupied, see Supplementary Fig. 6. Therefore, our above-mentioned estimated binding energy of ≈ 10 meV per electron will not constitute the actual formation energy, but it still provides the scale on which elastic resonances should be visible in STS. Thus, the scale of the calculated binding energy corresponds to $\epsilon_{\pm} \sim E_{\text{gap}}/2 \sim 20$ meV.

In conclusion, our results demonstrate that polaronic states emerging from coupling

of charge carriers to non-polar zone-boundary phonons can be measured with the STM in n -doped metallic SL MoS₂. A strong resonance peak is observed in dI/dV when tunneling through MoS₂, associated with the binding energy of a polaron in the material, which is estimated to be ~ 20 meV. Apart from this resonance, clear higher harmonics of this peak, spaced by an energy $\Omega_0 = 24 \pm 4$ meV, are measured on either side of the Fermi level. In DFT calculations, we find that the MoS₂ lattice has a strong tendency towards localized deformations, which can be interpreted as polarons. The formation dynamics of these polaronic states can be explored in small confined areas, allowing access to local variations in the binding energy. Our findings create new research opportunities into 2D polarons and reveal the effects of large electron-phonon coupling on tunneling spectra of 2D materials.

Methods

The samples were grown in situ in two preparation chambers with base pressure $p < 5 \times 10^{-10}$ mbar. Ir(111) is cleaned by 1.5 keV Ar⁺ ion sputtering and annealing to a temperature of 1550 K. Gr is grown on Ir(111) by two steps. First, the Ir is exposed to ethylene until saturation, followed by 1370 K thermal decomposition in order to obtain well-oriented Gr islands. Afterwards, the sample is exposed to 2000 L ethylene at 1370 K for 600 s, which yields a complete single-crystal Gr layer⁶³. SL MoS₂ is grown by Mo deposition in an elemental S pressure of 1×10^{-8} mbar³⁸. Subsequently, the sample is annealed to 1050 K in the same S background pressure. Cs intercalation was achieved by intercalation after growth of MoS₂. Cs was evaporated using a direct current evaporator to heat a Cs dispenser in UHV. During evaporation, the MoS₂/Gr/Ir(111) sample was kept at 570 K. After intercalation, the

sample was flashed to 730 K to remove residual Cs from the surface. Details about the Eu intercalation can be found in Ref. 3.

STM and STS were carried out in two ultra high vacuum systems with base temperatures 6 K and 0.35 K after in situ transfer from the preparation chamber.

Calculations details

DFT calculations were performed with QUANTUM ESPRESSO ⁶⁴ using the PBE approximation for the exchange-correlation potential ⁶⁵ and norm-conserving pseudo-potentials from the PseudoDojo database ^{66,67}. Plane waves until an energy cutoff of 100 Ry were included and a Fermi-Dirac-type smearing of 1 meV was imposed. We considered a doping of $0.1 e^-/\text{MoS}_2$ which corresponds to a dopant density of $9.56 \times 10^{-13} \text{ cm}^{-2}$. We included a vacuum of approximately 12 Å above the monolayer. We used an 18×18 \mathbf{k} -point grid for the unit cell. Relaxation of the (un)doped unit cell for fixed cell height yielded the lattice constant of 3.23 Å (3.19 Å). We used these unit cell structures and their lattice constants as the starting point of all subsequent calculations.

For the DFPT calculations via QUANTUM ESPRESSO we used a 6×6 \mathbf{q} -point grid. For the determination of the electron-phonon coupling we employed the EPW code ⁶⁸. Either three or eleven energy bands around the Fermi energy were transformed into the Wannier basis starting from orbitals of either Mo d_{z^2-} , $d_{x^2-y^2-}$, and d_{xy-} or of Mo d - and S p -character. Spectral function calculations in Supplementary Fig. 7 were carried out on-top of the three band Wannier model extended to include spin-orbit coupling within the EPW code including possible Fan-Migdal contributions to the self-energy. A dense \mathbf{q} -point grid (192×192) was

used, smearing in electron-phonon coupling summation was set to 0.002 meV, and smearing in energy-conserving delta functions was set to 0.002 eV.

The relaxations on large supercells (18×18) were facilitated by the downfolded strategies from Ref. 52, which have been implemented in the ELPHMOD package⁶⁹. The same parameters as in DFT were used except for the \mathbf{k} -point grid, which corresponds to a Γ -only calculation on the 18×18 supercell.

References

1. Emin, D. *Polarons* (Cambridge University Press, 2013).
2. Franchini, C., Reticcioli, M., Setvin, M. & Diebold, U. Polarons in materials. *Nat. Rev. Mater.* **6**, 560–586 (2021). URL <https://doi.org/10.1038/s41578-021-00289-w>.
3. van Efferen, C. *et al.* Metal-insulator transition in monolayer MoS₂ via contactless chemical doping. *2D Mater.* **9**, 25026 (2022).
4. Ramirez, A. P. Colossal magnetoresistance. *J. Phys. Condens.* **9**, 8171 (1997).
5. Teresa, J. M. D. *et al.* Evidence for magnetic polarons in the magnetoresistive perovskites. *Nature* **386**, 256–259 (1997). URL <https://doi.org/10.1038/386256a0>.
6. Watanabe, S. *et al.* Polaron spin current transport in organic semiconductors. *Nat. Phys.* **10**, 308–313 (2014).
7. Soriano, D. & Katsnelson, M. I. Magnetic polaron and antiferromagnetic-ferromagnetic transition in doped bilayer CrI₃. *Phys. Rev. B* **101**, 41402 (2020). URL <https://link.aps.org/doi/10.1103/PhysRevB.101.041402>.

8. Stojchevska, L. *et al.* Ultrafast Switching to a Stable Hidden Quantum State in an Electronic Crystal. *Science* **344**, 177–180 (2014). URL <https://doi.org/10.1126/science.1241591>.
9. Klanjšek, M. *et al.* A high-temperature quantum spin liquid with polaron spins. *Nat. Phys.* **13**, 1130–1134 (2017). URL <https://doi.org/10.1038/nphys4212>.
10. Gerasimenko, Y. A. *et al.* Quantum jamming transition to a correlated electron glass in 1T-TaS₂. *Nat. Mater.* **18**, 1078–1083 (2019). URL <https://doi.org/10.1038/s41563-019-0423-3>.
11. Salje, E. K. H., Alexandrov, A. S. & Liang, W. Y. Polarons and bipolarons in high-Tc superconductors and related materials. *Polarons and Bipolarons in High-Tc Superconductors and Related Materials* (2005).
12. Lee, P. A., Nagaosa, N. & Wen, X.-G. Doping a Mott insulator: Physics of high-temperature superconductivity. *Rev. Mod. Phys.* **78**, 17 (2006).
13. Keller, H., Bussmann-Holder, A. & Müller, K. A. Jahn–Teller physics and high-Tc superconductivity. *Mater. Today* **11**, 38–46 (2008).
14. Rønnow, H. M., Renner, C., Aeppli, G., Kimura, T. & Tokura, Y. Polarons and confinement of electronic motion to two dimensions in a layered manganite. *Nature* **440**, 1025–1028 (2006).
15. Setvin, M. *et al.* Direct view at excess electrons in TiO₂ rutile and anatase. *Phys. Rev. Lett.* **113**, 86402 (2014).

16. Yim, C. M. *et al.* Engineering polarons at a metal oxide surface. *Phys. Rev. Lett.* **117**, 116402 (2016).
17. Reticcioli, M. *et al.* Polaron-Driven Surface Reconstructions. *Phys. Rev. X* **7**, 31053 (2017). URL <https://link.aps.org/doi/10.1103/PhysRevX.7.031053>.
18. Xing, Y. *et al.* Localized spin-orbit polaron in magnetic Weyl semimetal $\text{Co}_3\text{Sn}_2\text{S}_2$. *Nat. Commun.* **11**, 5613 (2020). URL <https://doi.org/10.1038/s41467-020-19440-2>.
19. Reticcioli, M. *et al.* Competing electronic states emerging on polar surfaces. *Nat. Commun.* **13**, 4311 (2022). URL <https://doi.org/10.1038/s41467-022-31953-6>.
20. Liu, H. *et al.* Atomic-scale manipulation of single-polaron in a two-dimensional semiconductor. *Nat. Commun.* **14**, 3690 (2023). URL <https://doi.org/10.1038/s41467-023-39361-0>.
21. Cai, M. *et al.* Manipulating single excess electrons in monolayer transition metal dihalide. *Nat. Commun.* **14**, 3691 (2023). URL <https://doi.org/10.1038/s41467-023-39360-1>.
22. Chen, C. *et al.* Emergence of Interfacial Polarons from Electron–Phonon Coupling in Graphene/h-BN van der Waals Heterostructures. *Nano Lett.* **18**, 1082–1087 (2018). URL <https://doi.org/10.1021/acs.nanolett.7b04604>.
23. Jin, W. *et al.* Observation of the polaronic character of excitons in a two-dimensional semiconducting magnet CrI_3 . *Nat. Commun.* **11**, 4780 (2020). URL <https://doi.org/10.1038/s41467-020-18627-x>.

24. Sio, W. H. & Giustino, F. Polarons in two-dimensional atomic crystals. *Nat. Phys.* **19**, 629–636 (2023). URL <https://doi.org/10.1038/s41567-023-01953-4>.
25. Kang, M. *et al.* Holstein polaron in a valley-degenerate two-dimensional semiconductor. *Nat. Mater.* **17**, 676–680 (2018).
26. Garcia-Goiricelaya, P., Lafuente-Bartolome, J., Gurtubay, I. G. & Eiguren, A. Long-living carriers in a strong electron–phonon interacting two-dimensional doped semiconductor. *Commun. Phys.* **2**, 81 (2019). URL <https://doi.org/10.1038/s42005-019-0182-0>.
27. Ye, J. T. *et al.* Superconducting dome in a gate-tuned band insulator. *Science* **338**, 1193–1196 (2012).
28. Lu, J. M. *et al.* Evidence for two-dimensional Ising superconductivity in gated MoS₂. *Science* **350**, 1353–1357 (2015). URL <https://doi.org/10.1126/science.aab2277>.
29. Saito, Y. *et al.* Superconductivity protected by spin–valley locking in ion-gated MoS₂. *Nat. Phys.* **12**, 144–149 (2016). URL <https://doi.org/10.1038/nphys3580>.
30. Costanzo, D., Jo, S., Berger, H. & Morpurgo, A. F. Gate-induced superconductivity in atomically thin MoS₂ crystals. *Nat. Nanotechnol.* **11**, 339–344 (2016).
31. Fu, Y. *et al.* Gated tuned superconductivity and phonon softening in monolayer and bilayer MoS₂. *npj Quantum Mater.* **2**, 52 (2017). URL <https://doi.org/10.1038/s41535-017-0056-1>.

32. Caruso, F. *et al.* Two-dimensional plasmonic polarons in n -doped monolayer MoS_2 . *Phys. Rev. B* **103**, 205152 (2021). URL <https://link.aps.org/doi/10.1103/PhysRevB.103.205152>.
33. Khestanova, E. *et al.* Robustness of Momentum-Indirect Interlayer Excitons in $\text{MoS}_2/\text{WSe}_2$ Heterostructure against Charge Carrier Doping. *ACS Photonics* **10**, 1159–1168 (2023). URL <https://doi.org/10.1021/acsp Photonics.2c01930>.
34. Splendiani, A. *et al.* Emerging Photoluminescence in Monolayer MoS_2 . *Nano Lett.* **10**, 1271–1275 (2010). URL <https://doi.org/10.1021/nl903868w>.
35. Kuc, A., Zibouche, N. & Heine, T. Influence of quantum confinement on the electronic structure of the transition metal sulfide TM_2S_2 . *Phys. Rev. B* **83**, 245213 (2011). URL <https://link.aps.org/doi/10.1103/PhysRevB.83.245213>.
36. Ellis, J. K., Lucero, M. J. & Scuseria, G. E. The indirect to direct band gap transition in multilayered MoS_2 as predicted by screened hybrid density functional theory. *Appl. Phys. Lett.* **99**, 261908 (2011). URL <https://doi.org/10.1063/1.3672219>.
37. Ge, Y. & Liu, A. Y. Phonon-mediated superconductivity in electron-doped single-layer MoS_2 : A first-principles prediction. *Phys. Rev. B* **87**, 241408 (2013). URL <https://link.aps.org/doi/10.1103/PhysRevB.87.241408>.
38. Hall, J. *et al.* Molecular beam epitaxy of quasi-freestanding transition metal disulphide monolayers on van der Waals substrates: a growth study. *2D Mater.* **5**, 25005 (2018).

39. Murray, C. *et al.* Comprehensive tunneling spectroscopy of quasifreestanding MoS₂ on graphene on Ir(111). *Phys. Rev. B* **99** (2019).
40. Zhang, C. *et al.* Probing Critical Point Energies of Transition Metal Dichalcogenides: Surprising Indirect Gap of Single Layer WSe₂. *Nano Lett.* **15**, 6494–6500 (2015). URL <https://doi.org/10.1021/acs.nanolett.5b01968>.
41. Murray, C. *et al.* Band bending and valence band quantization at line defects in MoS₂. *ACS Nano* **14**, 9176–9187 (2020).
42. Cochrane, K. A. *et al.* Spin-dependent vibronic response of a carbon radical ion in two-dimensional WS₂. *Nat. Commun.* **12**, 7287 (2021).
43. Schröder, U. A. *et al.* Core level shifts of intercalated graphene. *2D Mater.* **4**, 15013 (2017). URL <https://dx.doi.org/10.1088/2053-1583/4/1/015013>.
44. Tornatzky, H., Gillen, R., Uchiyama, H. & Maultzsch, J. Phonon dispersion in MoS₂. *Phys. Rev. B* **99**, 144309 (2019). URL <https://link.aps.org/doi/10.1103/PhysRevB.99.144309>.
45. Lundin, U. & McKenzie, R. H. Temperature dependence of polaronic transport through single molecules and quantum dots. *Phys. Rev. B* **66**, 75303 (2002). URL <https://link.aps.org/doi/10.1103/PhysRevB.66.075303>.
46. Galperin, M., Ratner, M. A. & Nitzan, A. Inelastic electron tunneling spectroscopy in molecular junctions: Peaks and dips. *J. Chem. Phys.* **121**, 11965–11979 (2004). URL <https://doi.org/10.1063/1.1814076>.

47. Skorobogatko, G. A. Resonant polaron-assisted tunneling of strongly interacting electrons through a single-level vibrating quantum dot. *Phys. Rev. B* **85**, 75310 (2012). URL <https://link.aps.org/doi/10.1103/PhysRevB.85.075310>.
48. Stipe, B. C., Rezaei, M. A. & Ho, W. Single-molecule vibrational spectroscopy and microscopy. *Science* **280**, 1732–1735 (1998).
49. Franke, K. J. & Pascual, J. I. Effects of electron–vibration coupling in transport through single molecules. *J. Phys. Condens. Matter* **24**, 394002 (2012).
50. Krane, N. *et al.* High-resolution vibronic spectra of molecules on molybdenum disulfide allow for rotamer identification. *ACS Nano* **12**, 11698–11703 (2018).
51. Zou, N. & Chao, K. A. Inelastic electron resonant tunneling through a double-barrier nanostructure. *Phys. Rev. Lett.* **69**, 3224 (1992).
52. Schobert, A. *et al.* Ab initio electron-lattice downfolding: potential energy landscapes, anharmonicity, and molecular dynamics in charge density wave materials (2023). 2303.07261.
53. Lafuente-Bartolome, J. *et al.* Ab initio self-consistent many-body theory of polarons at all couplings. *Phys. Rev. B* **106**, 075119 (2022). URL <https://link.aps.org/doi/10.1103/PhysRevB.106.075119>.
54. Allen, P. B., Berlijn, T., Casavant, D. A. & Soler, J. M. Recovering hidden Bloch character: Unfolding electrons, phonons, and slabs. *Phys. Rev. B* **87**, 085322 (2013). URL <https://link.aps.org/doi/10.1103/PhysRevB.87.085322>.

55. Rubel, O., Bokhanchuk, A., Ahmed, S. J. & Assmann, E. Unfolding the band structure of disordered solids: From bound states to high-mobility Kane fermions. *Phys. Rev. B* **90**, 115202 (2014). URL <https://link.aps.org/doi/10.1103/PhysRevB.90.115202>.
56. Esch, F. *et al.* Electron localization determines defect formation on ceria substrates. *Science* **309**, 752–755 (2005).
57. Setvin, M. *et al.* Charge trapping at the step edges of TiO₂ anatase (101). *Angew. Chem. Int.* **53**, 4714–4716 (2014).
58. Crommie, M. F., Lutz, C. P. & Eigler, D. M. Confinement of Electrons to Quantum Corrals on a Metal Surface. *Science* **262**, 218–220 (1993). URL <https://doi.org/10.1126/science.262.5131.218>.
59. Hirjibehedin, C. F. *et al.* Large Magnetic Anisotropy of a Single Atomic Spin Embedded in a Surface Molecular Network. *Science* **317**, 1199–1203 (2007). URL <https://doi.org/10.1126/science.1146110>.
60. Natterer, F. D. *et al.* Strong asymmetric charge carrier dependence in inelastic electron tunneling spectroscopy of graphene phonons. *Phys. Rev. Lett.* **114**, 245502 (2015).
61. Sio, W. H., Verdi, C., Poncé, S. & Giustino, F. Ab initio theory of polarons: Formalism and applications. *Phys. Rev. B* **99**, 235139 (2019). URL <https://link.aps.org/doi/10.1103/PhysRevB.99.235139>.

62. Lafuente-Bartolome, J. *et al.* Unified Approach to Polarons and Phonon-Induced Band Structure Renormalization. *Phys. Rev. Lett.* **129**, 076402 (2022). URL <https://link.aps.org/doi/10.1103/PhysRevLett.129.076402>.
63. Johann Coraux *et al.* Growth of graphene on Ir(111). *New J. Phys.* **11**, 39801 (2009). URL <https://dx.doi.org/10.1088/1367-2630/11/3/039801>.
64. Giannozzi, P. *et al.* QUANTUM ESPRESSO: a modular and open-source software project for quantum simulations of materials. *J. Phys. Condens. Matter* **21**, 395502 (2009). URL <https://dx.doi.org/10.1088/0953-8984/21/39/395502>.
65. Perdew, J. P., Burke, K. & Ernzerhof, M. Generalized Gradient Approximation Made Simple. *Phys. Rev. Lett.* **77**, 3865–3868 (1996). URL <https://link.aps.org/doi/10.1103/PhysRevLett.77.3865>.
66. Hamann, D. R. Optimized norm-conserving Vanderbilt pseudopotentials. *Phys. Rev. B* **88**, 085117 (2013).
67. van Setten, M. *et al.* The PseudoDojo: Training and grading a 85 element optimized norm-conserving pseudopotential table. *Comput. Phys. Commun.* **226**, 39–54 (2018). URL <https://www.sciencedirect.com/science/article/pii/S0010465518300250>.
68. Ponc e, S., Margine, E., Verdi, C. & Giustino, F. EPW: Electron–phonon coupling, transport and superconducting properties using maximally localized Wannier functions. *Comput. Phys. Commun.* **209**, 116–133 (2016). URL <https://www.sciencedirect.com/science/article/pii/S0010465516302260>.

69. Berges, J., Schobert, A., van Loon, E. G. C. P., Rösner, M. & Wehling, T. O. elphmod: Python modules for electron-phonon models. doi.org/10.5281/zenodo.5919992 (2017).

8.1 Supporting information

Real-space observation and tunneling spectroscopy of polarons in monolayer MoS₂

Camiel van Efferen^{1,*}, Arne Schobert², Tfyeché Tounsi¹, Michael Winter², Mark Georger¹, Affan Safeer¹, Jason Bergelt¹, Christian Krämer¹, Jeison Fischer¹, Roberto Mozara², Jan Berges³, Tim Wehling^{2,4}, Thomas Michely¹, Wouter Jolie¹

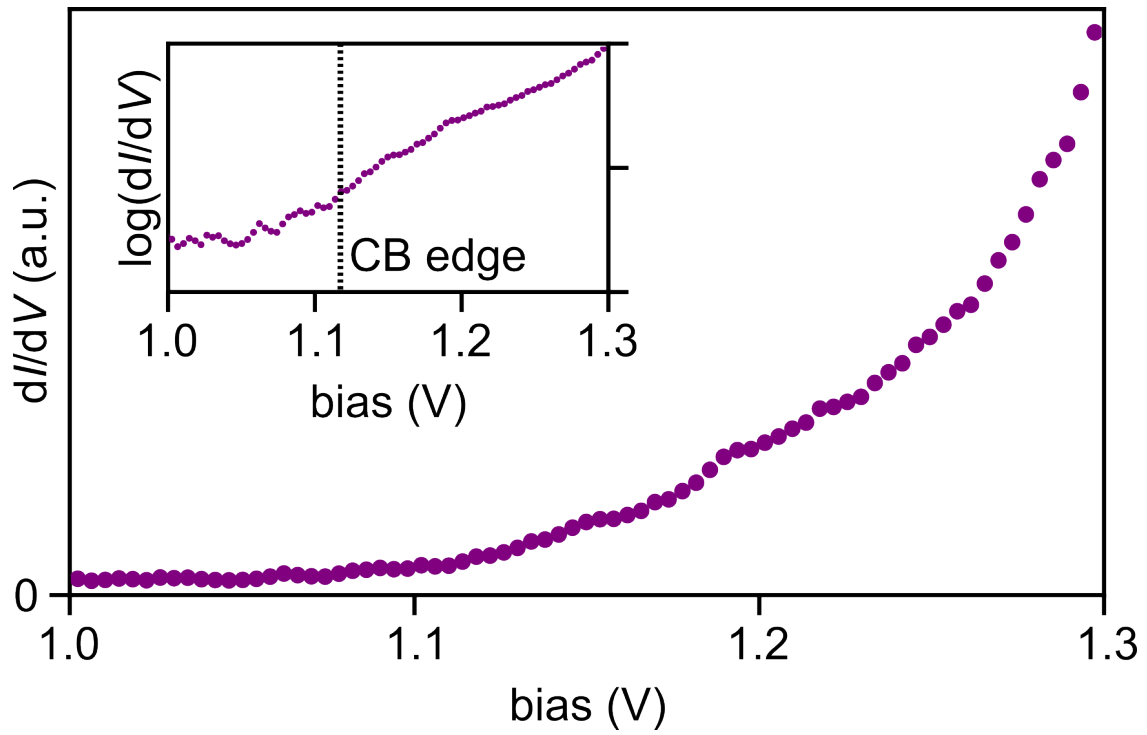
¹*II. Physikalisches Institut, Universität zu Köln, Zùlpicher Straße 77, 50937 Köln, Germany*

²*I. Institut für Theoretische Physik, Universität Hamburg, Notkestr. 9-11, 22607 Hamburg, Germany*

³*U Bremen Excellence Chair, Bremen Center for Computational Materials Science, and MAPEX Center for Materials and Processes, Universität Bremen, 28359 Bremen, Germany*

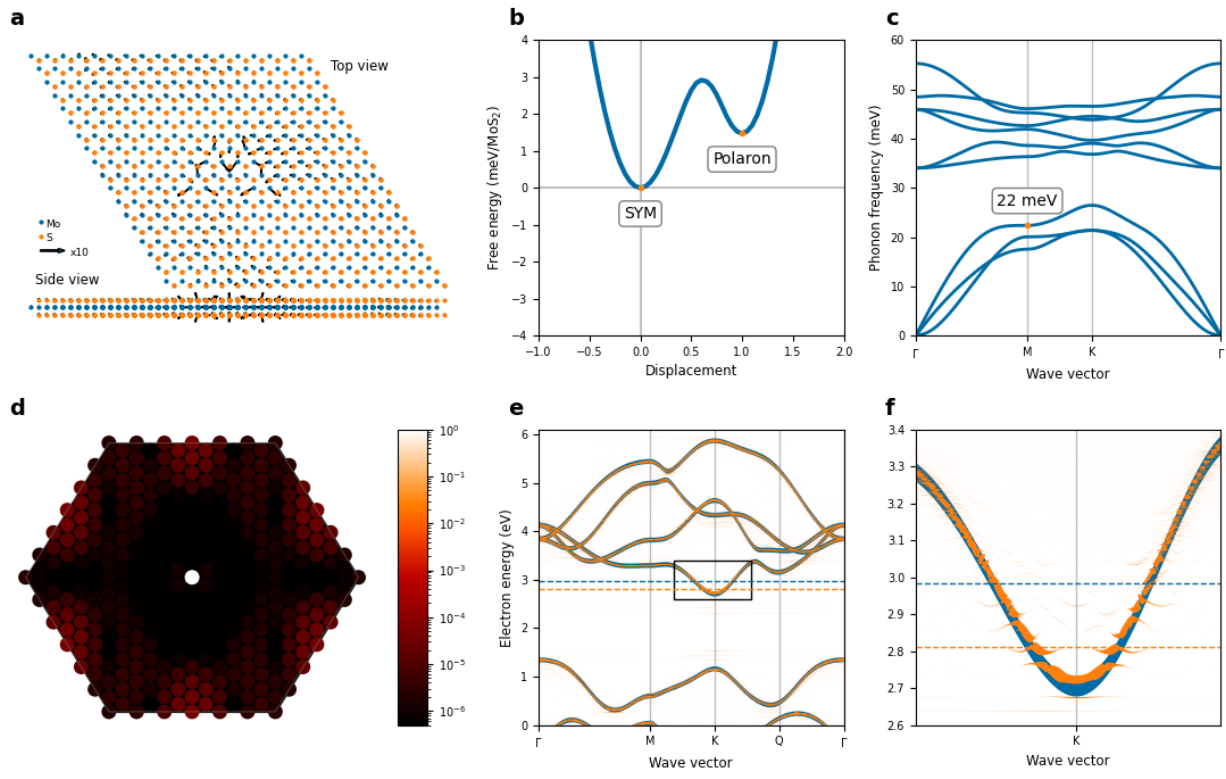
⁴*The Hamburg Centre for Ultrafast Imaging, Luruper Chaussee 149, 22607 Hamburg, Germany*

Supplementary Note 1: Absence of peak-dip features in semiconducting MoS₂



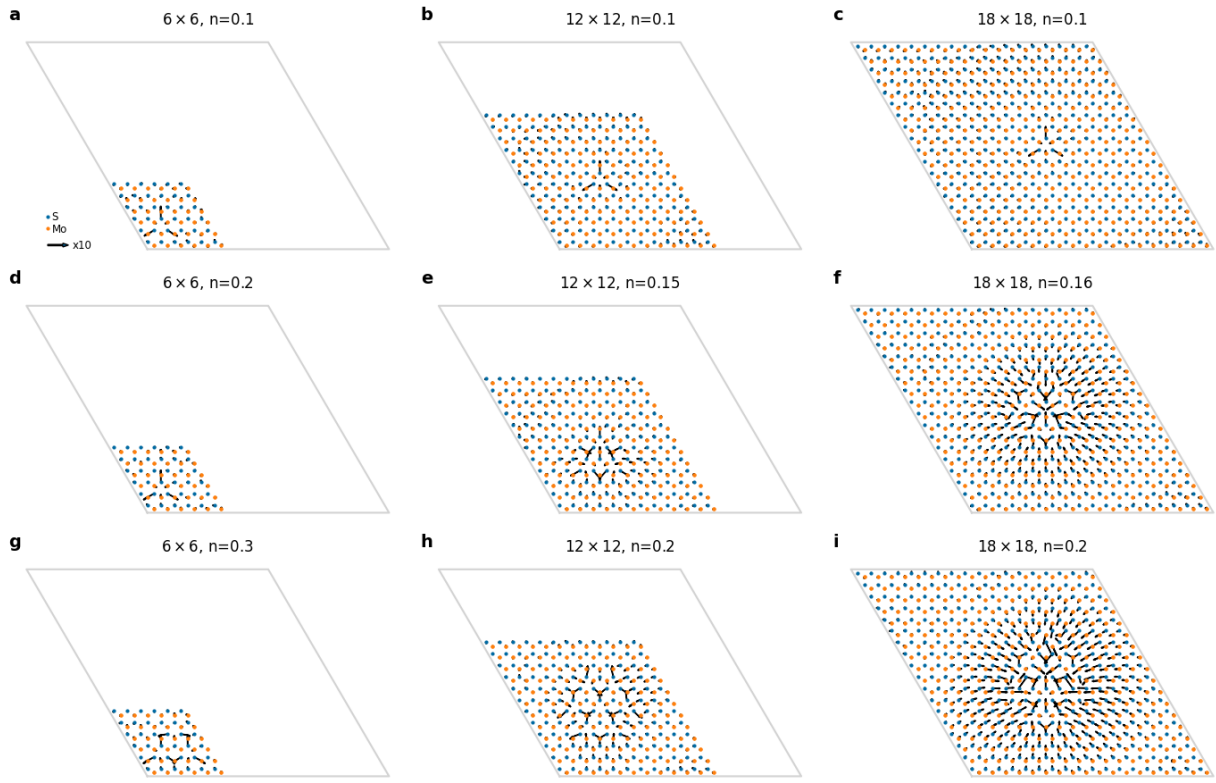
Supplementary Figure 1: **Absence of peak-dip features in semiconducting MoS₂.** In semiconducting MoS₂, here on a Gr/O/Ir(111) substrate, the band edge is smooth. No peak-dip features are seen. STM/STS parameters: **a** $V_{\text{set}} = 1.35$ V, $I_{\text{set}} = 1.0$ nA, $V_{\text{mod}} = 5$ mV.

Supplementary Note 2: Metastable polarons

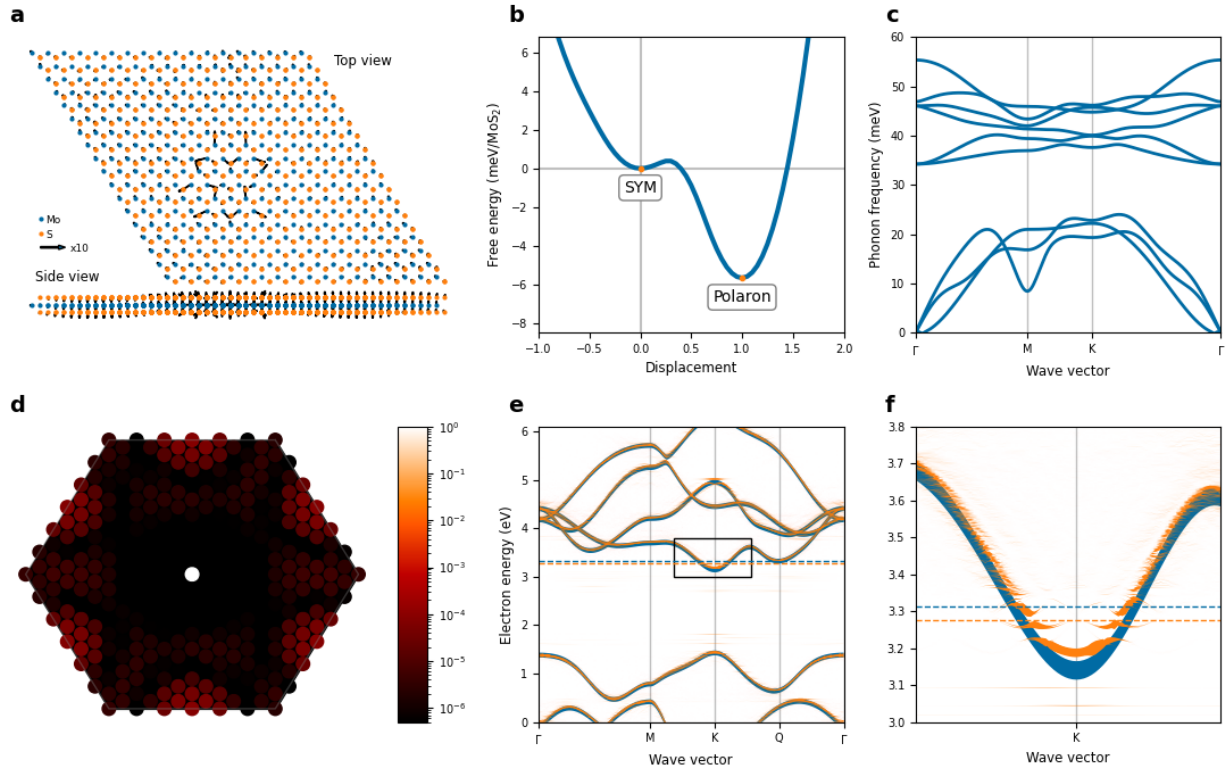


Supplementary Figure 2: **Metastable polarons.** With an electronic doping of $0.07e^-$ per formula unit of MoS₂, we find metastable polarons. See Fig. 4 of the main manuscript for detailed information on the figures.

Supplementary Note 3: Doping dependence of polarons



Supplementary Note 4: Lattice constant dependence of polarons



Supplementary Figure 4: **Lattice constant dependence of polarons.** For a fixed lattice constant after doping, i.e., not relaxing, we find polaronic deformations as well (**a** and **b**). The phonon dispersion shows a softening of the third branch at the M-point (**c**). The Q-point of the electronic band structure in the high-symmetry phase is almost occupied (blue dashed line). However, due to displacement induced in-gap states, the Fermi level is pushed down (orange dashed line) (**e** and **f**).

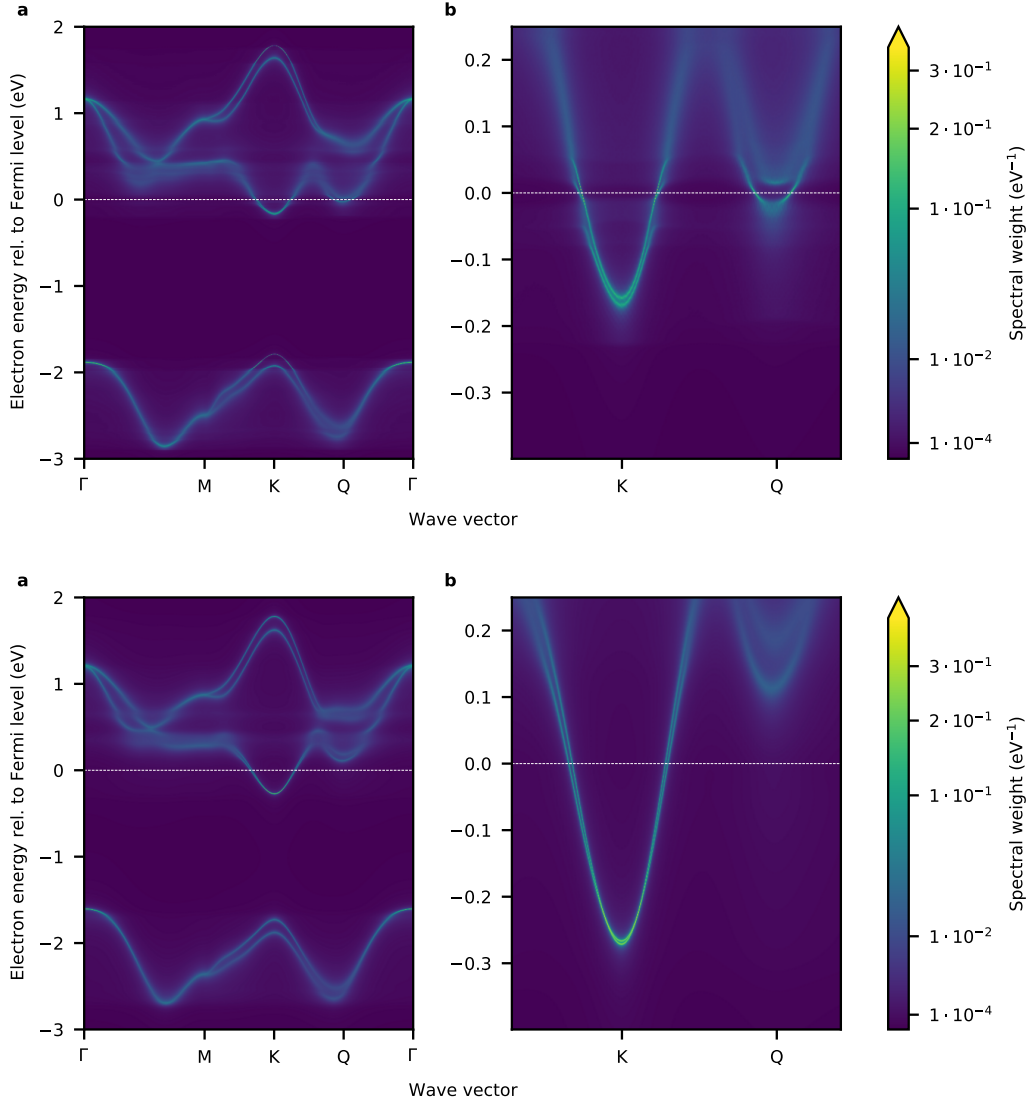
Supplementary Note 6: Spectral function with Fan-Migdal self-energy

The analytical expression for the Fan-Migdal self-energy in combination with the general formula relating the spectral function with any type of self-energy (see for instance ¹) can be used to understand the absences of phonon-cuts in the K-valley upon lattice relaxation in an electron doped system as visualised in FigS.6.

$$\Sigma_{\mathbf{k}j}(\omega) = \frac{1}{N_q} \sum_{\mathbf{q}i\nu} |g'_{ij}(\mathbf{k}, \mathbf{q})|^2 \left(\frac{f(\epsilon_i^{\mathbf{k}+\mathbf{q}})}{\omega - \epsilon_i^{\mathbf{k}+\mathbf{q}} + \omega_{i\nu}^{\mathbf{q}} + i\eta} + \frac{1 - f(\epsilon_i^{\mathbf{k}+\mathbf{q}})}{\omega - \epsilon_i^{\mathbf{k}+\mathbf{q}} - \omega_{i\nu}^{\mathbf{q}} + i\eta} \right)$$

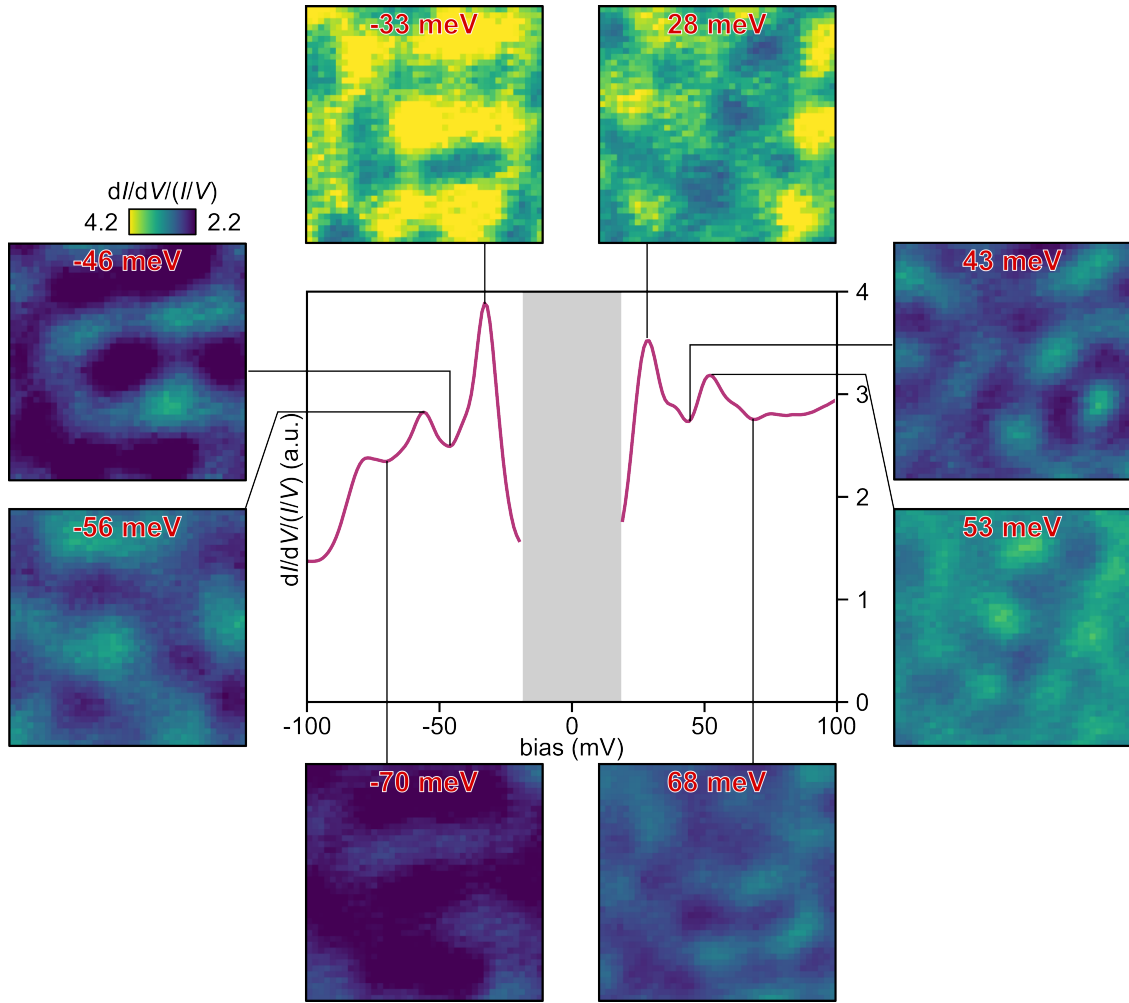
$$A(\mathbf{k}, \omega) = -\frac{1}{\pi} \sum_j \Im(G(\mathbf{k}, \omega)) = -\frac{1}{\pi} \sum_j \frac{\Im(\Sigma_{\mathbf{k}j}(\omega))}{(\omega - \epsilon_j^{\mathbf{k}} - \Re(\Sigma_{\mathbf{k}j}(\omega)))^2 + (\Im(\Sigma_{\mathbf{k}j}(\omega)))^2}$$

Focusing on the imaginary part of the spectral function, it is evident that a large imaginary self-energy leads to a low spectral weight at a given point in (\mathbf{k}, ω) . In case of a populated Q-valley (FigS6 a,b) poles can be realised for electronic energy $\omega < 0$ due to the distribution function f approaching 1 and the band dispersion $\epsilon_i^{\mathbf{k}+\mathbf{q}}$ falling below the Fermi level simultaneously. The same logic applies for an unpopulated Q-valley with $f \rightarrow 0$ and $\epsilon_i^{\mathbf{k}+\mathbf{q}}$ above the Fermi level.



Supplementary Figure 6: **Spectral function with Fan-Migdal self-energy.** Direct visualisation of lattice relaxation influence on the electronic structure and spectral function of monolayer MoS₂ doped with 0.1 e⁻ per unit cell at 15.8 K. Subfigures **a** and **b** use the lattice relaxed as an undoped system, the lattice in subfigures **c** and **d** in contrast was relaxed after doping. Via the change in lattice structure, the K- and Q-valley are pushed apart, setting the Q-minimum above the Fermi level. Hence, the phonon-cuts visible in **b** are no longer realised in **d**.

Supplementary Note 7: Delocalized quasiparticle scattering in metallic MoS₂



Supplementary Figure 7: **Delocalized quasiparticle scattering in metallic MoS₂**. Conductance maps of a large, defect free area of MoS₂. The normalized spectrum in the center is spatially averaged over the whole investigated area. While the characteristic resonances are visible, they are delocalized, leading to an increase or decrease of the conductance at any point in the area. The patterns that are visible are related to quasiparticle interference stemming from the Bloch electrons (holes) in MoS₂. STM/STS parameters: a $10 \times 10 \text{ nm}^2$, $V_{\text{set}} = 0.1 \text{ V}$, $I_{\text{set}} = 1.0 \text{ nA}$, $V_{\text{mod}} = 2 \text{ mV}$, $f_{\text{mod}} = 877 \text{ Hz}$.

References

1. Garcia-Goiricelaya, P., Lafuente-Bartolome, J., Gurtubay, I. G. & Eiguren, A. Long-living carriers in a strong electron–phonon interacting two-dimensional doped semiconductor. *Commun. Phys.* **2**, 81 (2019). URL <https://doi.org/10.1038/s42005-019-0182-0>.

PART III

Discussion

CHAPTER 9

Discussion

9.1 What makes a charge density wave: the case of single-layer VS_2

In Chapter 4 we have presented the charge density wave (CDW) of single-layer VS_2 . It is a rather remarkable CDW in three aspects: it involves spontaneous symmetry breaking, reducing the symmetry of the unit cell from hexagonal to rectangular; it persists up to room temperature; and it leads to a full gap in the DOS above the Fermi level. While VS_2 has multiple nested vectors at the Fermi surface which are all coupled to the lattice via electron-phonon coupling, including the actual CDW vector, its unique features arise from non-linear mode-mode coupling between the CDW phonon and another phonon mode at double the CDW wavevector. This latter effect drives the large displacements of the lattice, of up to 8%. If the CDW was instead purely driven by nesting, the better nested phonon at $1/2M$ would have 'won out', leading to a $4a \times 4a$ CDW.

However, the very same features that make the CDW of VS_2 unique, also prompt the question as to why it is a CDW at all (and not another type of phase transition). In this section, I would like to address that question. Afterwards, an outlook will be given on further research related to single-layer VS_2 .

The problem lies in defining what a CDW is, something that became increasingly difficult with time, as the understanding of the microscopic origins of the charge ordered patterns observed in many materials deepened over the last decades [223].

Foremost, a CDW is a structural phase transition (SPT), involving a discontinuity in an order parameter as a consequence of a lattice reconstruction [224]. Surface reconstructions like the herringbone pattern on the surface of Au(111) or the 7×7 reconstruction of Si(111) are good examples of such SPTs. Cutting a 3D material anywhere will break strong bonding interactions of the surface atoms, leading to charge transfer and stress alleviation [225], which drive the reconstruction [224]. A hallmark of such reconstructions is thus that they are purely driven by the structural properties of the surface layer. They also lead to large displacements of the atoms, which reach up to 30% of the lattice constant in the case of Au(111) [226].

Another interesting SPT takes place between different crystal groups in TMDCs, like 2H, 1T and 1T'. While under normal conditions only one of them tends to be stable, this balance can be shifted via temperature, chemical means or electrostatic doping [227–229]. As for the surface reconstructions,

the transition is argued to be purely structural as it involves large atomic displacements and bond reconstructions [229].

In contrast, a CDW *could* be defined as a structural transition primarily driven by the electronic system, with only minor lattice distortions. In its most pure form, we would only have to find a Fermi surface nesting (FSN) vector connecting a large number of electronic states and from that deduce that the lattice will distort with the wavelength associated with that vector. That is the picture sketched in Chapter 3.1, based on the 1D Peierls transition. For a 2D CDW, the argument goes, it is necessary that its Fermi surface is partially one-dimensional, so that these nested portions of the surface can lead to a large electronic susceptibility, which can then drive the transition through screening of a particular phonon mode, which softens in response and leads to the lattice distortion [194].

However, such an ideal CDW is seldom found in real systems. Most 2D CDWs are mainly driven by strong momentum \mathbf{q} -dependent electron-phonon coupling (EPC) instead of FSN [176, 223]. Nesting generally has no predictive power and even small deviations from the nesting conditions can destroy electronic instabilities [223]. Even if nesting occurs, there are almost always multiple nesting vectors, like in VS_2 ; it is the \mathbf{q} -dependent EPC that determines which of them is 'selected'. In its absence, nothing happens [195]. The CDW phases observed in 2H-NbSe_2 , CeTe_3 [195], 1T-TaS_2 , 2H-TaSe_2 and 1T-TiSe_2 can all be attributed to strong q -dependent EPC, sometimes with large displacements of the transition metal atoms of up to 7% [176], comparable to those we found in single-layer VS_2 . The case of 2H-NbSe_2 is telling: while its CDW was first explained by Fermi surface nesting [230], more recent theoretical and experimental studies have abandoned this idea in favor of strong EPC, with no gap opening at the Fermi level [231–235]. In the case of CDWs in cuprates, consensus about their origin has not yet been reached, but a FSN scenario is unlikely [223, 236]. Even in 1D, CDWs are found with no relation to the Fermi surface [237], or partly driven by electron-electron correlations [238]. DFT calculations on a 1D chain of Na atoms - the best representation of the perfect Peierls system - showed no sign of a Peierls distortion; only when the ions were allowed to move in 2D, did some distortion occur. But even then the electronic energy gap at E_F was missing [195].

To further complicate the matter, other mechanisms for CDW formation have been put forward, like the saddle band mechanism for 2H-TaSe_2 [239] and a band-type Jahn-Teller mechanism for the CDW transition in TiSe_2 [240]. The latter involves a local coordination change from 1T to 2H, blurring the line between a CDW and the transitions between different coordination phases of TMDCs [241]. Explanations for the CDW in TiSe_2 involve excitonic electron-hole interactions [241], exciton-phonon interactions [242] or an excitonic condensate [243]. In recent experimental works on more exotic materials, CDWs driven by the pair-density wave of the superconducting state [244], disorder [245] and orbital hybridization [246] have been proposed.

So, neither FSN nor EPC are necessary prerequisites for CDW formation. While FSN may be sufficient, in the sense that all systems that undergo a lattice distortion due to FSN are CDWs,

9.1 What makes a charge density wave: the case of single-layer VS₂

this does not hold for EPC, since EPC can be used as well to describe the non-CDW 2H-1T phase transition in MoS₂, on equal footing with other commensurate reconstructions like CDWs [136].

Looking at it from another direction, the size of the displacements, might be more fruitful. Some of the most studied CDW systems like 1T-TaX₂ and 1T-NbX₂ (X = S, Se) have large displacements and strong reconfigurations of their band structure [176]. In these systems, like in the prototypical metal-insulator transition material VO₂, there is strong interplay between electron-lattice (CDW) and electron-electron interactions (Mott transition), which are hard to disentangle [247–249]. Similarly, the large band gap (≈ 1 eV) of single-layer IrTe₂ was argued to stem from a combination of a CDW and local bond formation [250]. In all of these examples, like in our system 1T-VS₂, the CDW coacts with another mechanism to lead to larger structural changes than possible from the CDW alone. A case very similar to ours was published recently: in Ta₂NiSe₂ the CDW is driven by higher-order nesting at twice the CDW wavevector, while the actual CDW wavevector shows no nesting at all, suggesting that the driving force is a coupling between the two phonon modes and the electronic system [251].

The SPT in 1T-VS₂ is thus a CDW in the sense that it has multiple FSN vectors which are all coupled to the lattice via electron-phonon interactions. However, additional mode-mode coupling to one of the q -vectors leads to a larger energy gain for that vector - and larger displacements and reconstructions of the band structure. This secondary effect causes the formation of the 1D $9 \times \sqrt{3}R30^\circ$ phase, instead of the more classical $4a \times 4a$ phase which would otherwise have been the ground state. The CDW in 1T-VS₂ is thus akin to other 1T-phase TMDCs, which also have additional mechanisms coupled to the CDW transition.

Recent CDW studies have focused precisely on this class of materials, where the CDW phase coexists with other correlation-driven effects, like pair-density waves [244], spin-density waves [252], superconductivity [253,254] or magnetism [255]. The V-based Kagome materials play host to many of these phenomena [245,246,254,256]; they also lend themselves for investigations of the competition between superconductivity and CDWs [257,258]. Another novel direction of research explores the bosonic modes that emerge out of the broken-symmetry state of incommensurate CDWs, the phason and amplitudon [259–261], while in 1T-TaS₂ and 1T-NbSe₂ the chiral nature of their correlated CDWs has recently been explored [262–264].

For similar reasons, we conceive of a bright outlook for VS₂, where the combination of the CDW with strong electron-electron correlations [11] opens up multiple avenues of further research. If single-layer VS₂ turns out to be magnetic, we can imagine creating heterostructures of magnetic 2D materials, coupling VS₂ to *e.g.* Cr₂Ge₂Te₆ or CrI₃ [265,266]. Due to the lattice mismatch between the materials, this could result in moiré-modulated interlayer magnetic coupling, which can give rise magnetic phase transitions [267] and moiré skyrmions [268]. More generally, the possibility that the magnetic structure of VS₂ takes the form of a spin-density wave (SDW), is fascinating in its own right. While SDWs have been observed in high- T_c superconductors [269,270] and highly correlated materials [271], as well as in magnetic bulk crystals [252,272], they have not yet been realized in 2D

materials. If the CDW is indeed coexisting with a SDW, this would be a wonderful addition to the list of phenomena available in TMDCs.

It could also be interesting to couple the CDW to magnetic atoms, which might lead to strong location dependent Kondo screening. Since the CDW causes a strong modulation of the electronic properties of VS_2 , using it as the metal substrate for a Kondo effect would enable tuning of Kondo and spin-excitation properties, like was demonstrated for Fe atoms on moiré-modulated $MoS_2/Au(111)$ [273].

We also found multiple instabilities in the phonon dispersion of 1T- VS_2 with DFT. We could therefore expect that exchanging the substrate (for instance using hBN/Ir(111) or Gr/Ir(110)) might lead to the stabilization of a different CDW phase, as was observed in the sister compound 1T- VSe_2 , where the CDW was found to depend on the substrate, strain, and number of layers [274–278]. The effect of doping via alkali atoms or using our contactless gating method of Chapter 6 could also result in different electronic correlation effects. In particular, figuring out the conditions for suppressing the $9 \times \sqrt{3}R30^\circ$ phase in favor of the $4a \times 4a$ phase, which has been observed in bulk VS_2 , might lead to a deeper understanding of the microscopic mechanisms that underlie CDW formation. It could also unlock the predicted ferromagnetic ground state, which might be suppressed by the CDW, as was previously suggested for VSe_2 [279, 280]. Furthermore, low-temperature investigations of the low-bias properties of 1T- VS_2 might yield spectroscopic evidence for amplitudon and phason modes. Since the CDW is incommensurate, yet has strong Coulomb interactions, the phason mode should have significant mass and energy, allowing it to be resolved [260].

9.2 Mind the gap: CDW gaps measured with STM

In the standard Peierls picture of a CDW, a gap should open at the Fermi level. As a result, many STM works which observe a CDW have corroborated their topographic data with STS of a gap at the Fermi level [281–285]. While this is certainly justified in many cases, it is interesting to note that (1) other explanations for gaps at the Fermi level exist and (2) that not all CDWs are expected to have a gap at E_F and (3) not all gaps are visible with STS. Our case of single-layer VS_2 is telling: while the CDW is accompanied by the opening of a gap at the Fermi level between the M- and K-point of the Brillouin zone, we do not observe a dip at the Fermi level in tunnelling spectra. This is because the CDW leads to a reconstruction of the whole band structure, which does not preserve the idealized gap structure of the Peierls model.

Concerning (1), there have been many reports of gaps around the Fermi level arising due to inelastic tunneling via phonons [286]. A good example can be seen in graphene, which should have a flat DOS in STS, but often shows a deep gap [287], or a V-like shape [288] due to inelastic tunneling processes. Since it is difficult to tunnel into the K -states of graphene, the additional tunneling channels provided by phonons can lead to substantial enhancement of the current and the occurrence of steps in the dI/dV signal. This concept has recently been extended to the CDW

materials $2\text{H-Ta}_x\text{Nb}_{1-x}\text{Se}_2$ and NbS_2 [289, 290]. In addition, gaps can be present that have nothing to do with either phonons or the CDW, such as the inexplicable gap at E_F in the CDW phase of TiSe_2 , which has been dubbed a pseudogap [291], or the gap in FeGe [256]. The small gap in single-layer NbSe_2 could also not be straightforwardly explained from the possible mechanisms of CDW formation [27]. Another interesting aspect to consider is that an incommensurate CDW should have collective phonon modes of the broken-symmetry ordered state (amplitudon and phason), which could also contribute to the gap-like feature since they are expected to have comparable energies as CDW gaps ≈ 10 meV [260, 261].

As for (2) and (3), theoretical calculations can find changes to the DOS throughout the band structure, not necessarily limited to the Fermi level [176, 292, 293]. While a gap opening in a particular part of the BZ can be seen easily with ARPES, STM is only sensitive to the total DOS, which might change somewhere else than at E_F or in a very broad range around E_F [231–235]. A good example of this can be seen in the seemingly classical $3a \times 3a$ CDW of single-layer NbS_2 , where DFT calculations do not find a gap directly at E_F , but a constant depression of ≈ 150 meV around the Fermi level [261]. At the Fermi surface, a reconstruction can take place [294], like in the case of VS_2 . This is of particular interest to STM, since the tunnelling current is dominated by states close to the center of the Brillouin zone. Practically, this could mean that if a large gap opens near K , but some states near Γ are pushed to the Fermi level, the STS signal at E_F actually goes up as a result of the CDW formation, even if the total DOS goes down.

Care must be therefore be taken, when interpreting gaps around E_F as stemming from a CDW. Ideally, the temperature dependence of the gap is measured [295], or a careful analysis made of how the gap relates to the CDW [27].

9.3 The blessings and curses of a metastable material

In Chapter 5 we explored the many different phases that can be obtained when V and S atoms react on a graphene substrate. Their complicated phase diagram, especially when we consider all the different heights observed in the V_5S_8 -derived structures, leaves some open questions. For starters, it is unclear what happens to the bottom S layer when V_4S_7 is formed. With STM we only probe the top layer and while XPS can be used in a layer-sensitive manner - for instance by changing the angle or energy of the incoming X-rays so that the penetration depth changes - we have so far only used normal incidence at a single photon energy. A similar problem is encountered for the V_5S_8 -derived structures, where the presence of the 2×2 intercalation layer is clear from low-energy electron diffraction (LEED) measurements, but is often difficult to resolve with STM. Here, cross-sectional (scanning) transmission electron microscopy might help to definitively prove that the island are indeed V_5S_8 , as was done for thin films of V_5Se_8 [296].

Multiple open questions swarm around the $\sqrt{3} \times \sqrt{3}R30^\circ$ CDW in the lowest V_5S_8 islands. While the 2×2 intercalation structure is visible in LEED, the $\sqrt{3} \times \sqrt{3}R30^\circ$ is not, even when we performed

LEED at temperatures where the superstructure dominates the contrast in STM data (≈ 40 K). We take this as an indication, that the latter structure is mainly electronic in origin, which leads to an oversized effect on the STM tunnelling current. It is remarkable that a CDW should form at all in V_5S_8 , since it is not a layered material and most studies on bulk V_5S_8 show no evidence for a CDW transition. In addition, the lattice constant of our islands is still closer to the one of VS_2 than V_5S_8 . The increased lattice constant of the self-intercalated compound was used previously as evidence for the transition of thin films of VSe_2 to V_5Se_8 [297, 298]. It is interesting to speculate about the thickness or lateral size dependence of a transition from self-intercalated layers of VS_2 to the bulk material V_5S_8 . In any case, these discrepancies seem to suggest that the extremely thin V_5S_8 -derived islands must really be regarded as a unique 2D material.

Turning now to an outlook, the metastability of VS_2 has given us, instead of only VS_2 , two new V-S compounds to explore: V_5S_8 -derived islands and V_4S_7 . These materials hold their own promises for future research.

Let us first consider the V_5S_8 -derived islands. While bulk 1T- VS_2 is not magnetic, when intercalated with V atoms in an ordered 2×2 pattern, forming V_5S_8 , it develops antiferromagnetism. Upon being thinned down to about 5 nm, a transition to a ferromagnetic state occurs [299–301]. From this we can already conclude that it would be of great interest to probe our ultimately thin V_5S_8 -derived islands with spin-polarized STM to ascertain their magnetic state. This could be combined with averaging techniques like X-ray magnetic circular dichroism, superconducting quantum interference device or magneto-optic Kerr effect measurements to fully characterize both the local and macroscopic properties.

Going beyond the mere presence of magnetism, there have also been reports of a Kondo effect in V_5S_8 [302, 303]. Since the intercalated V atoms host magnetic moments, which can couple to the itinerant electrons in the VS_2 layers, this can lead to Kondo resonances located at the intercalation sites, provided that the long-range magnetic order is suppressed. Since the resonances would nevertheless exist in an ordered array, it is conceivable that coupling between the resonances exists, leading to a Kondo lattice. Indications of Kondo lattices and heavy fermion behavior have indeed been observed in V_5S_8 [304]. With the STM, the presence of a Kondo lattice could be investigated, probing from the metallic side of the lattice. If the Kondo lattice drives the metallic system into the heavy fermion Kondo insulator state, this should lead to a temperature-dependent heavy-fermion hybridization gap [31].

A more thorough understanding of the CDW phase of the V_5S_8 -derived islands should also prove worthwhile. Since VS_2 is a material with strong electron-electron correlations [11], CDW phases could coexist with Mott insulating phases, like in VO_2 , where the metal-insulator transition is still a subject of active research [247–249], or 1T-TaS₂, 1T-TaSe₂ or 1T-NbSe₂ [31, 248, 305, 306]. Here, temperature dependent measurements of the band structure during the transition from the normal to the CDW state could shed light on the type of CDW present in V_5S_8 , ideally combined with *ab-initio* calculations.

9.4 Doping single-layer MoS₂: a material of many phases

We can also consider intercalating other elements between the VS₂ layers, which should be easy given the large interlayer spacing [156]. With Li intercalated, the 1T-VS₂ phase could be stabilized in the bulk, with a CDW transition at 305 K [166, 167]. Intercalating alkali atoms between layers of VS₂ could enhance indirect magnetic exchange and ferromagnetic coupling [307]. In general, due to the tendency for self-intercalation, VS₂ could be a promising platform for intercalation of other magnetic atoms such as Fe, Co or Cr.

Turning now towards V₄S₇, we encounter other possibilities. Since its structure is buckled, forming 1D stripes, it would be intriguing to investigate its electronic properties. In TMDCs with a similar lattice structure, like the distorted 1T' phases of MoX₂ (X = S, Se, Te), topological properties emerge, such as the quantum spin Hall effect and Weyl semimetallicity [30, 308]. Depending on the coupling between V atoms in the structure, it could also behave as a quasi-1D material, hosting Tomonaga-Luttinger liquid or CDW physics when the temperature is lowered [309–312].

It is further within the realm of prospects, that the desulphurization affects the magnetic properties of VS₂. In monolayer 1T-VSe₂, it was shown that creating line defects of missing S atoms leads to a ferromagnetic state [91]. A low-temperature spin-polarized STM study of this material is therefore of interest. Since it can furthermore be grown in a phase pure state, it is also more suited for averaging techniques for determining its magnetic state than V₅S₈.

Finally, the patterned adsorption of Pt atoms was demonstrated on desulphurized single-layer 1T-VSe₂ [313]. With our V₄S₇ sample, the adsorption of different atom species could be tested. This can alternatively be done with noble metals, with possible applications for hydrogen evolution reaction catalysis [313], or with magnetic atoms to create spin chains, 1D metallic bands or Kondo lattices, as an alternative to creating them atom by atom on a surface.

9.4 Doping single-layer MoS₂: a material of many phases

In Chapter 6 we demonstrated our method of contactless chemical doping, using intercalation of Eu and O atoms between Gr and Ir(111) to *n*- and *p*-dope single-layer MoS₂, without chemically altering its structure. There are two important outcomes of this work. The first is general: the method set out in the manuscript should work for other TMDCs besides MoS₂. In the Supplementary Information, we already showed that we can do the same for WS₂. More importantly, in a recent publication from our group the *p*-doping of the metallic single-layer TMDC NbS₂ via O intercalation of Gr was used to track the effect of doping on its CDW [261], highlighting that the method is not restricted to semiconducting materials.

The second outcome is specific to MoS₂: using the *n*-doping provided by intercalated Eu atoms, we have made the metallic phase of single-layer 2H-MoS₂ accessible for STM. While this phase has been extensively investigated in transport experiments, the local properties and the full spectral function have remained obscure. Using the method of this Chapter has allowed us to investigate strong electron-phonon coupling effects in metallic MoS₂, discussed in Chapter 8. It has also led to

the observation of a possible electron-electron interaction driven Coulomb gap in the MoS₂ islands at 0.35 K, see Appendix A.1. Beyond what we have achieved so far, the versatility of our approach enables us to imagine a whole range of further experiments.

A crucial next step would be to achieve a measure of control over the amount of doping, so that we are not limited to a particular doping level. For this purpose, we can turn towards small mobile intercalation species like Li, K and Na. With Li, the Gr Dirac point of Gr/Ir(111) can be tuned in a continuous fashion up to $E_D = 1.63$ eV below E_F [314], with part of the doping stemming from intercalation and further doping achieved by adsorption [315]. A similar effect was found for Gr/Na/Ir(111), where after a full Na intercalation layer, additional Li could lead to a shift of the Dirac point of $E_D = 1.7$ eV [316]. With K as well, combinations of intercalation and adsorbed structures were found to be able to shift the Dirac point $E_D = 1.61$ eV below the Fermi level [317]. Not only do these methods allow a continuous tuning of the doping level, but compared to the doping we have achieved with Eu ($E_D = 1.36 - -1.43$ eV) or Cs ($E_D = 1.20$ eV) [315], the additional adsorption of Li or K after intercalation should lead to significant enhancement of the metallic properties of MoS₂. The cost would of course be that we are no longer in a completely contactless regime, so the effect of adsorption (disorder) has to be taken into account.

When single-layer MoS₂ is sufficiently doped, with high carrier densities of $n \approx 1 \times 10^{14}$ cm⁻², it becomes superconducting [9, 57]. A rough estimate of our current carrier density is $n = N_V \frac{m^*}{\pi \hbar^2} E_F = 7.7 \times 10^{13}$ cm⁻², with N_V the number of valleys, $m^* = 0.36m_e$ the effective mass of the conduction band and $E_F = 85$ meV the energy difference between the bottom of the band and the Fermi level (see Chapter 6 for the extraction of these values). It is therefore possible that we are close to the superconducting transition, which could be reached using extra Li and K doping as described above. Note, however, that in order to be superconducting, it is necessary to have large single-domain areas of MoS₂, since the superconducting transition in, *e.g.*, single-layer NbSe₂ was found to be sensitively dependent on lateral island size [318]. It is also not a priori clear whether the electronic band structure of our single-layer MoS₂ islands behaves exactly the same as that of large single-layer devices which are investigated in transport and from which the required carrier density was determined [9, 57]. The onset and transition temperature of superconductivity are linked to the Fermi-level crossing of the Q-band in theoretical studies [145, 319]. In our sample, the Q-band is still more than 100 meV away from E_F , which might necessitate considerable doping to reach E_F . The energetic difference between the K and Q bands is likely linked to strain: the difference is increased by tensile and reduced by compressive strain, with large compressive strain even causing a lowering of Q-valley so that it becomes the lowest valley [319–322]. It is thus possible that varying strain conditions for single-layer MoS₂ samples lead to different behaviors upon *n*-doping. Whether superconductivity is actually realized or not, being able to control the doping level of large domains of single-layer MoS₂, while tracking the locating of the Q-valley, might resolve the open question of whether the Q band is necessary for superconductivity.

Considerable doping of MoS₂ can also lead to a phase transition to the 1T-phase [136]. This has

been demonstrated in particular for doping using Li intercalation and adsorption [323, 324], while the 1T'-phase of MoS₂ could be stabilized with hydrogenated Li [325]. Single-layer 1T-phases of MoS₂ are predicted to have topological properties, leading to the quantum spin Hall effect, dipolar ferroelectricity, and Weyl semimetallicity [30, 308]. Although the single-layer 1T'-phase has been measured previously on Au(111) [326], a quasi-freestanding structure has not yet been realized.

Going in the other direction, a particularly difficult but satisfying challenge would be to *p*-dope MoS₂ so that the highly spin-orbit split valence band (VB) reaches the Fermi level. Graphene could be *p*-doped via intercalation with O, as we have shown, or alternatively with Cl which has a similar doping level of 0.57 eV [327], but also more drastically with boron substitution (1.2 eV) [328]. Combined with *p*-doping of MoS₂, for instance via Nb substitution [152], this might put the VB edge within reach.

We can also further experiment with the current setup without trying to increase the doping level. Even with the VB still below the Fermi level, it would be interesting to perform photoluminescence measurements of MoS₂/Gr/O/Ir(111). Since dielectric screening of the band gap should reduce both the exciton binding energy and the electronic band by roughly the same amount [197, 329], the optical band gap can be expected to be the same as for MoS₂/Gr/Ir(111) $E_{\text{opt}} = 1.945$ eV [330]. However, the possible lack of coupling to the Ir(111) substrate could enhance the lifetime of the excitons [331, 332]. It might also be possible to measure the excitons directly with the STM: exciton-assisted tunneling was reported for a range of vdWs heterostructures in a device setup [333], so the lifetime increase might enable STS observation of excitons as well. It has also been shown that other magnetic 4f-metal atoms can be intercalated between Gr and Ir(111); in the case of Dy, the graphene layer lifts Dy atoms from the Dy/Ir surface alloy and induces a giant magnetic anisotropy in the Dy atoms [334]. Probing the effect of a magnetic substrate on the Kondo resonance of Chapter 7 or the polaronic states of Chapter 8 would be captivating subjects for further study.

It is additionally possible to consider using another shielding layer, like hBN on Ir(111), where the moiré superstructure leads to a periodic arrangement of strongly chemisorbed valleys [335]. Although the growth of MoS₂ leads to the incomplete intercalation of S in the valleys, lifting the strong binding to the substrate, as discussed in Appendix A.2, and inducing disorder, this possibility of intercalation can also be exploited. We might succeed in fully intercalating the layer with Eu or Cs, suppressing the moiré potential, and end up with a truly freestanding layer of *n*-doped MoS₂. Alternatively, partially intercalating the hBN layer so that the chemisorbed valleys are left intact, might result in an enhanced potential landscape. If the periodic moiré potential is very strong, the electron bandwidth is strongly suppressed, magnifying any correlation effects. This can lead to localized states in the moiré wells, of excitonic [204–206] or polaronic [336] nature. Strong moiré effects in TMDCs can also lead to a Mott insulating [337], Wigner crystal [338–340] or excitonic insulating state [341]. To be able to reach these regimes, continuous tuning of the filling level with Li or a gate voltage would likely be necessary.

Finally, we could also exchange the metallic substrate, for instance to Ir(110), on which single-

crystal growth of graphene has been demonstrated [342]. The physisorbed hexagonal moiré of Gr/Ir(111) would be replaced with a wave pattern which is partly chemisorbed. Like in the case of hBN, this could lead to patterned intercalation or strong moiré effects.

9.5 The various uses of a tunable, fully resolved Kondo system

Current microscopic Kondo research has roughly three directions: the first goes towards ultimate control of a single resonance in quantum dot setups, with a focus on high spin Kondo systems and coupling of the Kondo system to other phenomena like superconductivity; the second goes towards combining single Kondo systems to form heavy fermion and Kondo lattices, *i.e.* emergent phenomena that arise when many Kondo impurities are combined in an ordered fashion; and the third involves single magnetic adatoms coupled to exotic states of matter, such as CDWs, superconducting substrates or spin-liquids. Our realization of the Kondo effect in MoS₂ grain boundaries, see Chapter 7, is in that sense a bit of an asynchronous event, since it involves a simple, non-interacting single spin 1/2 system. In this section, I will first give a short overview of the first two research directions. Then I will focus on how our Kondo system can be used in the context of the third direction, by replacing single magnetic adatoms with our fully resolved, delocalized Kondo system and highlight some of the advantages it holds over conventional setups.

Quantum dots quickly, after the first realization of the spin-1/2 Kondo effect in a single charge trap state [343], moved towards unprecedented control over the Kondo state in a single-electron transistor or quantum dot setup, which allowed precise tuning of the number of electrons confined to a small region [344, 345]. This was extended to more exotic interactions, such as triplet Kondo resonances [346, 347], the Kondo effect in the unitary limit [348], SU(2) and SU(4) Kondo effects [349] and the effect of spin-orbit interaction on the Kondo state [350]. Recently, a quantum dot setup allowed researchers to explore the Kondo screening cloud which is entangled with the impurity [351]; they also studied spin-orbit coupling in bilayer graphene quantum dots hosting the Kondo effect [352] and the interplay between the Kondo effect and superconductivity in a quantum dot coupled to NbSe₂ [353].

The many-impurity (Kondo lattice) front is a very active field of research. If many single-Kondo impurities are brought together in an ordered fashion, at sufficiently low temperatures and coupling between the impurities and the conduction electrons, either a coherently ordered Kondo lattice is formed or a heavy fermion system/Kondo insulator [354]. Kondo lattices can occur naturally in heavy fermion compounds like UTe₂ [355] or be artificially made using Co atoms on Cu(111) [356]. A TMDC heterostructure of 1T/1H-TaSe₂ has been argued to be a coherent 2D magnetic Kondo lattice [354], while 1T/1H-TaS₂ heterostructures have been argued to be in the heavy fermion Kondo insulator state [31, 357]. A Kondo lattice has also been realized in a MoTe₂/WSe₂ structure with half-filled moiré bands [358].

The investigation of magnetic adatoms on metallic surfaces spans more than two decades, with

9.5 The various uses of a tunable, fully resolved Kondo system

the first Kondo resonance measured in 1998 by Madhavan *et al.* using STM for Co adatoms on Au(111) [359]. A recent discussion on whether this system actually displays the Kondo effect, has a nice connection to our work. While Co on noble metal surfaces is a known Kondo system in the bulk [360, 361], the question has come up whether Co adatoms on the surface, which typically only show a dip at the Fermi level instead of peak, argued to stem from quantum mechanical interference effects [359, 362, 363], also exhibit the Kondo effect. In recent works, the zero-bias anomaly seen with STM is argued to stem from spin-excitations, which interact with electrons to form a new quasiparticle called a spinaron [364]. This assertion has been provided with some further experimental backing in the specific case of Co on Cu(111) [365, 366]. Although it is hardly a settled matter whether the new theory will displace the old, the discussion highlights the strong dependence on theory in the absence of a fully resolved system. In all the magnetic adatom setups discussed below, there is no experimental access to the impurity states, which therefore allow no clear *ab-initio* determination of the system. Added to that is the complexity of the orbital structure and spin state of many single atoms, which leads to the use of overly simplified models to describe the experiments [367]. We will therefore consider some experiments where we can use our simple, fully resolved Kondo system in place of adatoms.

We could, for instance, couple the Kondo resonances in two MTBs to each other, when they are in close enough proximity. This would allow us to explore the two-impurity Kondo problem [368], which has been investigated previously in two atom setups, either with an atom at the tip probing an atom on the surface [369] or with both atoms on the surface [370]. Recently, the Kondo states of two Mn atoms on MoS₂/Au(111) were shown to have a moiré dependent interaction [371]. However, in all these cases, only the Kondo resonance was observed, while our Kondo system would allow for easy comparison of the experiments with NRG calculations, thus eliminating the need for extra-experimental assumptions.

By growing MoS₂ on top of a superconductor, the magnetic impurity state of the MTB should induce YSR states in the superconducting gap. Theoretically, it was proposed that the orbital symmetry of the impurity state should affect the YSR states [372]. This was tentatively shown in experiment, when transition metal atoms on superconducting lead induced YSR states with a 4-fold symmetry, evocative of the d-orbitals hosting the magnetic moment [373]. Symmetries of YSR states have also been investigated in the context of molecular orbitals [374], arising due to interaction with a CDW [375], or forming bonding and antibonding states [376] or bands [377]. In experiment, a perplexing variety of YSR states is encountered, in contrast to the simplicity of popular theoretical models. This is because the high spin of transition metal atoms, the ligand and crystal fields and the magnetic anisotropy are often not taken into account [367]. Here, too, the simple nature of our Kondo system would allow us to establish the orbital nature of YSR states and their relation to the impurity orbital, in much the same way as we did for the relation between the Kondo resonance and the impurity states in Chapter 7. For our selection of a suitable superconductor, there are TMDC candidates available, like 1H-TaS₂ [378] and 2H-NbSe₂ [27]. The former was already grown in our

group on Gr/Ir(111) [284], making it an ideal choice to form a vdWs heterostructure with MoS₂.

We can also imagine placing the MTBs on top of a quantum spin liquid. Evidence for a spin liquid phase has been reported for single-layer 1T-TaSe₂ [248, 305], while the ground states of single-layer 1T-TaS₂ [31] and 1T-NbSe₂ [306] are very similar to the one from 1T-TaSe₂ and at least the former is considered another likely candidate for spin-liquid behaviour [379]. In each case, the strong electron localization in the Mott insulating state leads to unpaired magnetic moments localized in the star-of-David clusters of the CDW distortion. These have been shown to give rise to a Kondo effect when coupled to a metallic substrate [31, 305]. In a quantum spin liquid, the charge excitations of the lattice would be gapped due to the Coulomb repulsion, while the spin excitations of the lattice could travel freely, leading to a spinon band in the Mott gap of the material. These spinons have been reported to lead to a spinon-density wave in 1T-TaSe₂ [305]. Here, our delocalized Kondo impurity could be used instead of the Co atom, which was coupled to 1T-TaSe₂ in Ref. [380]. The spinons in the band crossing the Fermi level can interact with the localized impurity, creating a many-body resonance, analogous to electrons in the Kondo effect [380]. Replacing the Co atom with our MTB state would allow for a complete description of the interaction, since all relevant states are accessible with the STM. This might lead to the first unambiguous observation of spinon-impurity bound states with the STM.

The final measurement discussed here is to obtain spin-polarized STM spectra of the impurity peaks. They should reveal the complete (100%) spin-polarization of these states, with the difference between the dI/dV signal from parallel and antiparallel alignment of tip and sample only limited by the spin polarization of the tip. This would be a rare example of complete spin polarization in STS, which is generally not present in the band structure of materials and cannot be accessed in the case of single magnetic impurities.

9.6 Seeing polarons: manifestations of strong electron-phonon coupling in STM

The manuscript of Chapter 8 is still a work in progress. In particular, the question of what actually leads to the peaks in the dI/dV spectra is not completely solved. It is clear that strong coupling to a phonon mode is involved, leading to satellite peaks spaced by the phonon energy, but it is less clear what gives rise to these peaks in the first place. The explanation put forth in the manuscript involves the presence of polarons. Either there are already polarons in MoS₂, with bound states that are directly (elastically) accessible with the STM, or they are metastable, separated from the free electron state by an energy barrier which can be locally overcome (inelastically) by the electrons tunnelling from the tip. In this section, I explore first some manifestations of polarons in ARPES and STM, two techniques which allow direct visualization of polaronic states. Then I will address some further experiments that can be conducted on this system and the open problems about single-layer MoS₂ they might solve.

9.6 Seeing polarons: manifestations of strong electron-phonon coupling in STM

While there are many experimental methods for detecting or inferring the presence of polarons in materials, there are only two ways to directly see them. With ARPES the energy and \mathbf{k} -dependence of polarons can be mapped, while local probe techniques like STM and non-contact AFM access spatially resolved information on the polarons [175]. ARPES and STM (or nc-AFM) can be regarded as complementary, both in the type of information that they obtain, but also in the kind of polarons that they are able to measure.

ARPES functions best when the material hosts large polarons, which due to their size are spread over so many lattice sites that they behave as dispersive carriers. Therefore, they show up in ARPES as bands, located at multiples n of the phonon energy Ω below the conduction band of the material [186–188, 381]. The ARPES replica bands of anatase TiO_2 doped with O vacancies [186] are argued to have an analogue in STS, where they appear as peaks in dI/dV spectra taken near subsurface dopants in Nb-doped anatase TiO_2 [382].

The more metallic a material is, the better it is able to screen electron-phonon interactions and thus the less likely it is to host polarons. This can be intuitively seen as a competition between the plasma frequency of the material and the oscillation frequency of the phonons. If the carriers are responding fast enough to screen the long-range electric field stemming from the oscillation of the particular phonon mode responsible for polaron formation, the electronic energy gain associated with the polaron will rapidly diminish. Once localized polarons become unfavorable, the only remnant of EPC is a kink in the ARPES bandstructure, located at $E = -\Omega$ [174, 184, 383]. This is also argued to account for the ARPES data of surface-doped bulk MoS_2 [8], where EPC involving two phonons modes leads to three different dispersive quasiparticle states [185]. In this regime, STM is not very practical. While the kinks might be obvious in ARPES, the effect of the mass enhancement is likely too subtle to unambiguously determine their presence from STS spectra.

When the polarons are small - confined to a single or only a few lattice sites - their k -state is not a good quantum number; small polarons thus appear flat in k -space [175]. In ARPES they are visible as a broad envelope of small excitations below the Fermi level [384–387]; in principle, the bound state lying multiple eV below E_F should be visible as well, but this has not been unambiguously observed because it is difficult to separate from defect states. Here STM is perfect. It can measure the polaron states directly and compare lattice sites with and without defects to disentangle defect states from polaronic states [382]. Two recent papers have shown that small polarons can be created with the STM tip in a 2D semiconductor using voltage pulses. After creation, the polarons remained stable enough to be visualized, while a voltage pulse of opposite polarity could also erase them [388, 389]. Another interesting behavior of polarons was visualized on a polar surface, where polarons form ordered patterns due to their mutual repulsive interaction [390].

Despite what was said above, it is in practice not obvious how one should distinguish between a defect state coupling to lattice phonons and a polaron trapped near the defect. The coupling between the defect and phonons can give rise to satellite peaks in a process similar to that of molecular junctions [391, 392]. In addition, defect states can also extend to several lattice sites [393],

or lead to charging rings which can give the appearance of a larger object [394]. The crucial aspect of trapped polarons is the temperature dependence of the electronic wavefunctions observed around the defect with STM. The defining characteristic of polaronic trapping is the presence of multiple local structural minima and their thermally activated hopping. At high temperatures, hopping speeds are much faster than a typical STM measurement; one would therefore see the thermal equilibrium of the polaron states trapped around the defect. Lowering the temperature leads to the kinetic trapping of the polarons in a single, degenerate configuration, leading for instance to symmetry breaking and different appearances of the electronic wavefunctions around equivalent defects [395]. In other cases, the differences between an extended defect state and a trapped polaron could only be determined by comparing STM data with DFT calculations [382]. In most publications the distinction is not made explicitly: a polaron is taken as synonymous with localized electrons near defects [396–399]. Indeed, in many systems, polaron self-trapping cannot in any practical sense be separated from regular trapping of electrons by the potential of defects, with the effects of EPC and weak external potential generally working together to lead to the observed localization [400].

Polarons also show up in many tunneling setups, not limited to STM. The prime example is resonant tunneling through molecular wires. In the limit of strong coupling between the electronic state and vibrations of, *e.g.*, the molecular wire, a series of peaks spaced by Ω in dI/dV spectra is observed, below (for an occupied state) or above (for tunneling into an unoccupied state) the peak associated with the electronic level [401–403]. When these satellites show similar or larger conductance than the original peak, the tunneling can be called polaronic or polaron-assisted [403,404]. Similar spectra have been measured on single molecules [405,406], adatoms [407] and quantum wells [408]. Here, the word ‘polaron’ denotes a single electronic level strongly coupled to vibrational modes, instead of a band of free electrons interacting with a phonon.

STM studies of polarons are limited. Most have been performed on TiO_2 , with only the most recent papers focussing on other materials. Given the limited amount of studies, it is remarkable how varied the manifestations of polarons are that have been observed. They can show up as immobile single objects in a perfect crystal; as localized, but extended states around defects; or as delocalized bands. To get a more unified idea of the conditions that underlie how polarons appear in the STM, more data is needed. Fortunately, a recent study on polaron formation in 2D crystals predicts that many single-layer TMDCs should actually host polarons, ranging from very large (*e.g.* ≈ 40 nm in MoSe_2) to small polarons (*e.g.* $1 - 2$ nm in HfS_2) [192]. Especially the latter ones should have binding energies that should easily be observed in STS and sizes that are small compared to the island sizes obtained with MBE or CVD growth of single-layer TMDCs. They should therefore be excellent materials for further investigating the effect of strong-coupling polarons on the electronic and structural properties that can be probed with STM. Making a general study of a selection of these materials would furthermore allow us to determine how STS spectra of polarons change based on the size of the polaron and the binding energy involved.

Turning back to our sample, it would be helpful to compare our STM data with ARPES of the

9.6 Seeing polarons: manifestations of strong electron-phonon coupling in STM

same material. In ARPES, the effect of EPC would either show up as band renormalisation (no polarons), satellite bands (large polarons) or in gap states (small polarons), allowing us to interpret the peaks observed in STS within the boundaries imposed by the ARPES data. In literature, ARPES data of metallic single-layer MoS₂ is scarce. A Cs-doped sample of single-layer MoS₂ on Gr showed the K-band dipping below the Fermi level, but no high-resolution data is shown or analysed, so it is not known whether any effects of EPC were present [150]. In a more detailed study of single-layer MoS₂/sapphire, where MoS₂ is doped via S vacancy formation to very similar levels as in our sample (with the K valley up to 70 meV below E_F), strong plasmonic resonance peaks are seen with energies exceeding 100 meV, while the effective mass of the conduction band is enhanced to $0.9m_e$ [149]. Due to this discrepancy, ARPES of our samples, where MoS₂ is made metallic through contactless doping, is desired.

Transport in single-layer MoS₂ is characterized by Efros-Shklovskii variable-range hopping in its insulating state and normal electron-phonon scattering in its metallic state [70, 138, 140]. Separating these regimes, a metal-insulator transition was found, with a localization-driven quantum critical point ascribed either to strong electron-electron correlations [140] or disorder [141]. Evidence for carrier localization was also found in strong carrier density variations with temperature at a fixed gating voltage [142]. In the investigated samples, MoS₂ was annealed after being exposed to ambient conditions to improve conductivity. Vacuum annealing of CVD-grown single-layer MoS₂ leads to significant *n*-doping of the sample [138], likely due to the removal of oxygen adorbates and substitutions at S vacancy sites, which otherwise fill up the in-gap dopant states of the S vacancies [139]. This has led to the speculation that the presence of S-vacancies results in Anderson localization [73]. In highly disordered materials, Anderson localization leads to a Coulomb gap at the Fermi level [409, 410]. In materials driven by strong EPC however, even weak disorder scattering can lead to self-trapping of polarons and the opening of a localization gap [411–413]. Polaronic localization was argued to result in the gapped phase of Li-doped 2H-MoTe₂ [414]. In this context, understanding the nature of EPC effects on the electronic structure of single-layer MoS₂ becomes crucial for further device applications. If we could tune the carrier density of MoS₂ in a more continuous fashion, for instance by using a combination of Li or K intercalation and adsorption, the strength of the EPC determined from fitting the resonances observed in STS, as well as the size of the gap around the Fermi level, could be ascertained depending on the doping level. This microscopic study could help answer questions about the nature of the localization and metal-insulator transition.

Low temperature (0.35 K) STS data of MoS₂, see Appendix A.1, reveals a small ($2\Delta \approx 1$ meV), asymmetric gap around the Fermi level. The nature of this gap is as of yet unclear, but its relation to the polaronic resonances and localization effects could be a worthwhile subject for further study. Temperature and doping dependence of the gap and the resonances should be established. Possible explanations for the gap are a Coulomb gap, as was observed in small islands of single-layer NbSe₂ [318]; a localization gap due to disorder and strong EPC discussed above [411–413]; or a pseudogap as observed in high- T_c superconductors above the superconducting temperature.

In this context, the superconducting transition of single-layer MoS₂ can be investigated as well. In a previous study, the onset of superconductivity was related to an increase in the mass enhancement due to EPC in surface-doped bulk MoS₂ [8]. This is in line with theoretical considerations that predict that the superconducting transition temperature goes up as the EPC strength is increased by *n*-doping [145, 319]. Since our DFT calculations predict an increasing preference for polaron formation at high doping levels, the interplay between superconductivity and polaron formation can be investigated. This is especially interesting since the presence of polarons has been linked to (high-*T_c*) superconductivity for a long time, where the superconductivity results from the instability of polarons towards bipolaron formation, which act as bosonic carriers [415–417]

In the low-doping regime, on the other hand, achievable with a lower intercalation level of Li, so that MoS₂ is on the verge of metallicity, it might be possible to create stable polarons, like was demonstrated for CoCl₂ [388, 389]. The question is whether the lack of screening when MoS₂ is no longer metallic, which favors polaron formation, is offset by the lessened coupling between the K and Q valleys by the M phonon, when both valleys are unoccupied. In any case, tuning the EPC strength with doping would be of interest, certainly since DFT calculations for different doping regimes have already been performed for the current manuscript.

PART IV

Appendix

APPENDIX A

Scientific Appendix

A.1 Coulomb gap in metallic single-layer MoS₂

The experiments in this section were proposed by C. van Efferen and W. Jolie. The measurements were carried out by C. van Efferen, W. Jolie, A. Saffeer and J. Fischer. The analysis of the data was done by C. van Efferen, with support from W. Jolie.

Introduction

Transport measurements of single-layer MoS₂ show that a sharp metal-insulation transition (MIT) takes place upon reaching a critical carrier density $\approx 1 \times 10^{13} \text{ cm}^{-2}$ [140]. The nature of the MIT has been correlated to the presence of a soft Coulomb gap, formed as the result of strong electron-electron correlations [140] and/or disorder [141] in the insulating state. Localization effects, which can create an Anderson gap at the Fermi level [409,410], are indeed routinely observed in MoS₂ and generally linked to S-defects from CVD growth [70,138,142].

However, in materials with strong electron-phonon coupling, even weak disorder scattering can lead to self-trapping of carriers and the opening of a localization gap [411–413]. This type of polaronic localization was argued to result in the gapped phase of Li-doped 2H-MoTe₂ [414]. So, it is not a priori necessary that a Coulomb gap in single-layer MoS₂ only opens in the limit of strong disorder, since we have shown in Chapter 8, that electron-phonon interactions are sufficient to lead self-trapping of carriers (polaron formation).

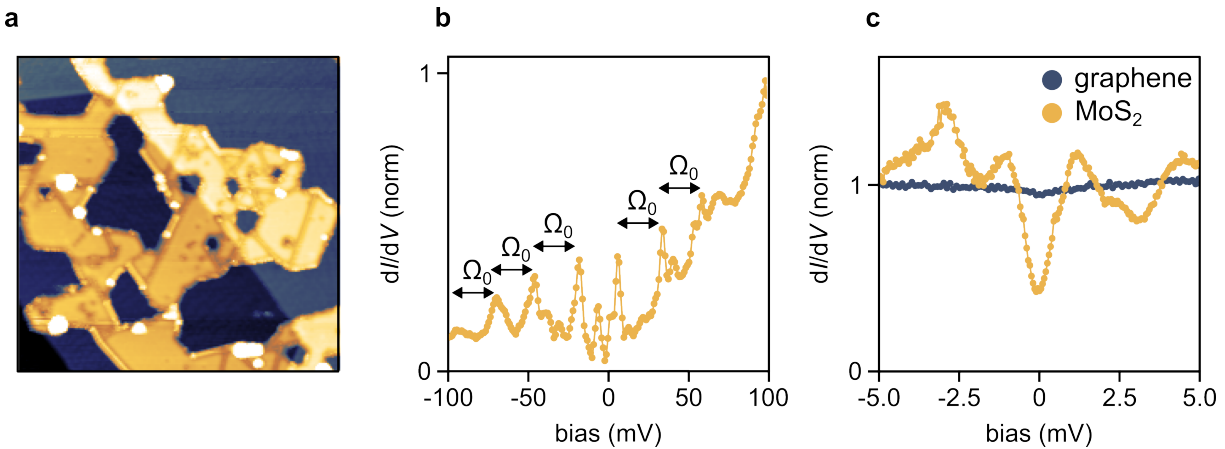


Figure A.1: Electronic structure of metallic single-layer MoS₂ at 0.35 K. **a** Large scale STM image of single-layer MoS₂ on Gr/Eu/Ir(111). Two Ir(111) step edges are visible. Some small clusters of Mo or Eu are present on top of the MoS₂. **b** Low-temperature (0.35 K) dI/dV spectrum of MoS₂. Multiple peaks spaced by the energy of a M-phonon Ω_0 are indicated. **c** Low-bias dI/dV spectra of graphene (blue) and MoS₂ (gold), taken at 0.35 K. A pronounced gap is visible in the MoS₂ spectrum. STM/STS parameters: **a** $120 \times 120 \text{ nm}^2$, $V_{\text{set}} = 2.5 \text{ V}$, $I_{\text{set}} = 5 \text{ pA}$; **b** $V_{\text{set}} = 100 \text{ mV}$, $I_{\text{set}} = 1.0 \text{ nA}$, $V_{\text{mod}} = 500 \text{ } \mu\text{V}$, smoothed using the Savitzky–Golay method; **c** $V_{\text{set}} = 5.0 \text{ mV}$, $I_{\text{set}} = 1.0 \text{ nA}$, $V_{\text{mod}} = 50 \text{ } \mu\text{V}$. For all spectra: $f_{\text{mod}} = 719 \text{ Hz}$.

In this Appendix, we investigate the properties of metallic MoS₂ at 0.35 K. We observe a gap at the Fermi level, which can differ in size from $2\Delta = 1 - -12 \text{ meV}$. It is not symmetric with respect to the Fermi level and highly location dependent. We speculate that it is a Coulomb gap, driven by

a combination of electron-electron interactions, disorder and electron-phonon coupling. At the end, we suggest some follow-up experiments that could help resolve the origin of the gap.

Results

A typical STM topograph of metallic SL MoS₂ is shown in Fig. A.1a, compare Chapters 6 and 8. The islands are grown together into large networks, separated by grain boundaries. Measuring the states in the conduction band, the onset of which lies 85 meV below the E_F [3], we observe a series of peaks on either side of E_F , see Fig. A.1b. The highest peaks are separated by $\Omega_0 = 27$ meV, which is close to the energy of the phonon mode coupling between the K and Q valleys of MoS₂, see Chapter 8. Likely due to the lower temperature (0.35 K) and reduced modulation voltage (0.5 meV), many more peaks are visible compared to the data in Chapter 8.

If we now focus on the states near the Fermi level, a pronounced gap is measured in dI/dV spectra of large islands of single-layer MoS₂, see Fig. A.1c. The gap has a V-like shape and two coherence peaks on either side of it. Beyond the gap, multiple peaks and valleys are present in the spectrum. Measured from peak to peak, the width of the gap is $2\Delta = 2.1$ meV. Using the same tip, a spectrum taken on the Gr/Eu/Ir(111) substrate far away from the island shows a completely flat density of states (DOS).

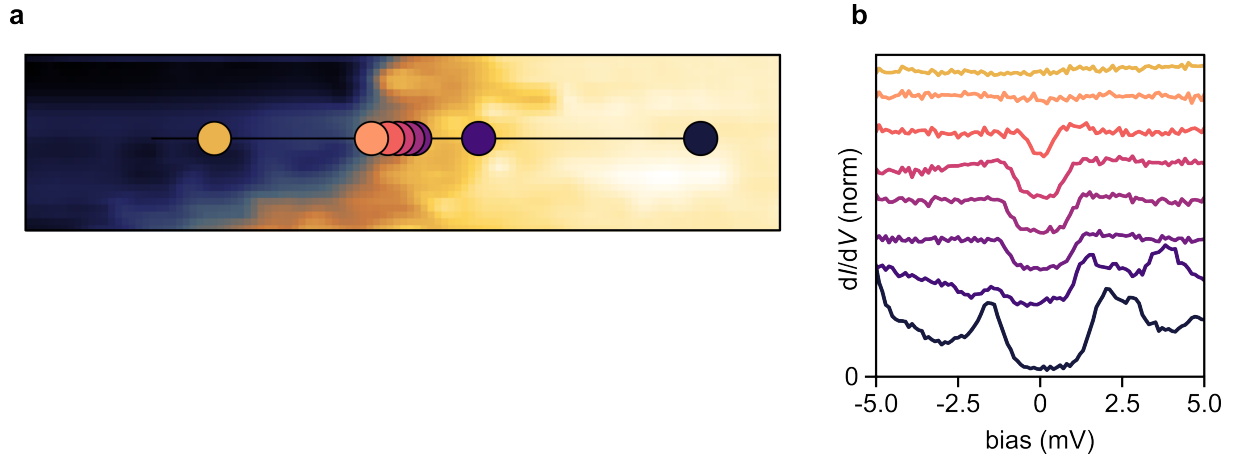


Figure A.2: Spatial dependence of low-bias dI/dV spectra. **a** STM image of MoS₂ island edge. Indicated are the locations of the spectra in **b**, marked by their respective colors. **b** Low-bias dI/dV spectra of MoS₂ along the line drawn in **a**. Spectra have been normalized and offset vertically. STM/STS parameters: **a** 13×3 nm², $V_{\text{set}} = 1.0$ V, $I_{\text{set}} = 6$ pA; **b** $V_{\text{set}} = 10.0$ mV, $I_{\text{set}} = 0.1$ nA, $V_{\text{mod}} = 50$ μ V, $f_{\text{mod}} = 907$ Hz.

To see whether the gap is located only on the MoS₂ or extends somewhat into the surrounding Gr, we take a series of spectra from the center of a MoS₂ island to the edge. In Fig. A.2a, a STM image of a MoS₂ island edge is shown, with colored dots marking the location of the spectra in Fig. A.2b. In the middle of this island a broad gap is found, with a peak-to-peak size of $2\Delta = 3.5$ meV. Closer to the edge, the depth and the width of the gap start to shrink, closing rapidly on a length scale of 1 nm. As soon as Gr is reached, the gap is gone.

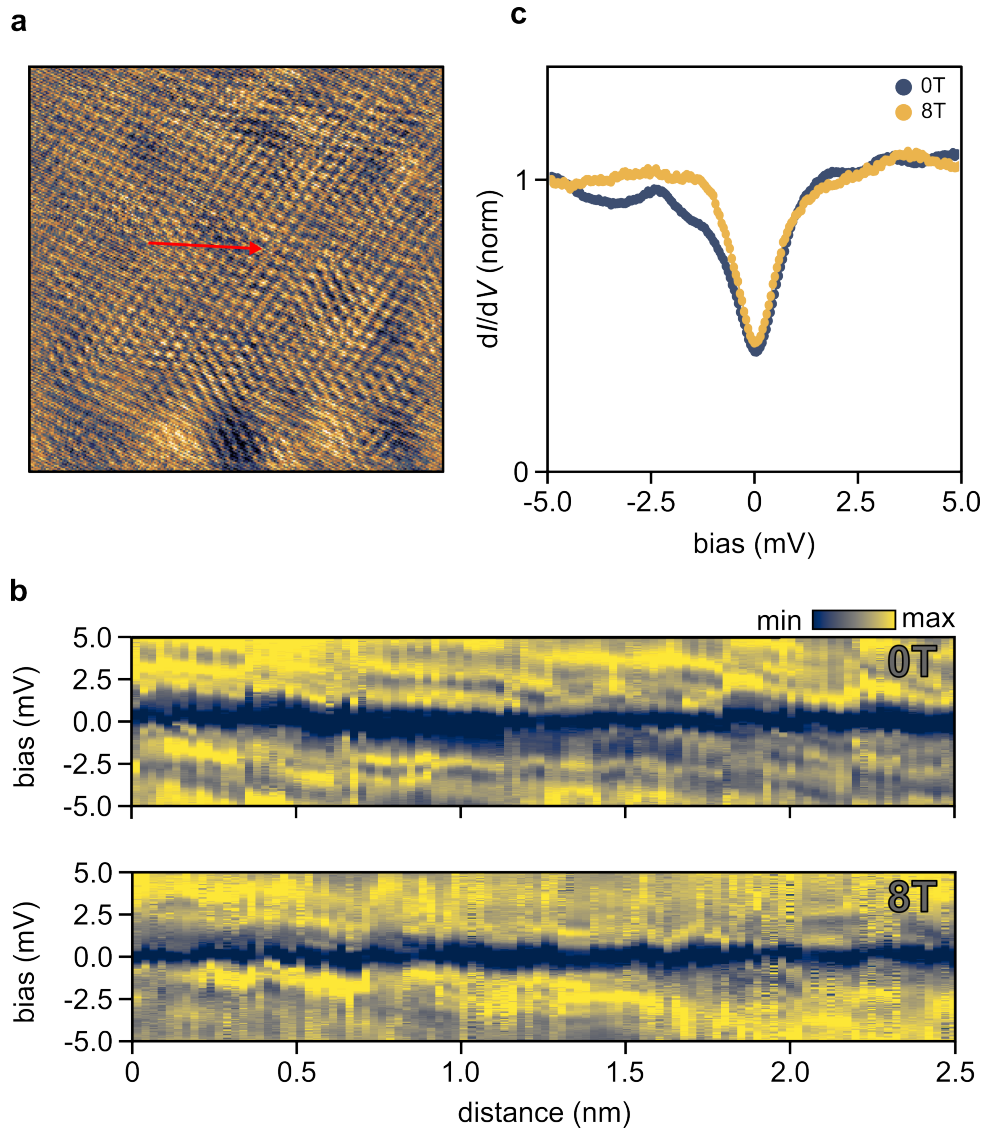


Figure A.3: Magnetic field dependence of low-bias dI/dV spectra. **a** Atomically resolved STM image of single-layer MoS₂. **b** Conductance (dI/dV) linescans taken along the red arrow in **a**. The upper panel was taken without external magnetic field (blue data), the lower panel was obtained in an out-of-plane field of 8 T (gold data). **c** Averaged spectra of the linescans in **b**. STM/STS parameters: **a** $10 \times 10 \text{ nm}^2$, $V_{\text{set}} = 100 \text{ mV}$, $I_{\text{set}} = 6 \text{ pA}$; **b,c** $V_{\text{set}} = 5.0 \text{ mV}$, $I_{\text{set}} = 1.0 \text{ nA}$, $V_{\text{mod}} = 50 \mu\text{V}$, $f_{\text{mod}} = 719 \text{ Hz}$.

We also checked the magnetic field dependence of the gap. Here, we used a large, clean area of MoS₂, see Fig. A.3a. We took series of dI/dV spectra along the line indicated in the topograph at 0 T and 8 T, following a dense-packed direction of the lattice. Presenting the spectra as colormaps in Fig. A.3b, we observe a strong spatial dependence of the gap, even in the absence of any disorder (island edges, grain boundaries, defects, adatoms, etc.). Next to the central gap, series of asymmetric conductance minima and maxima can be distinguished, which shift down in energy as the distance increases. These side features are more pronounced at 0 T than at 8 T, but this could be due to the increased noise incurred by the STM when using high fields. In the shape of the gap, no obvious

difference can be made out, compare the averaged spectra in Fig. A.3c. Only the relative strength of the side features is distinguished the two spectra, with the 8 T spectrum distinctly flatter outside of the gap than its 0 T counterpart.

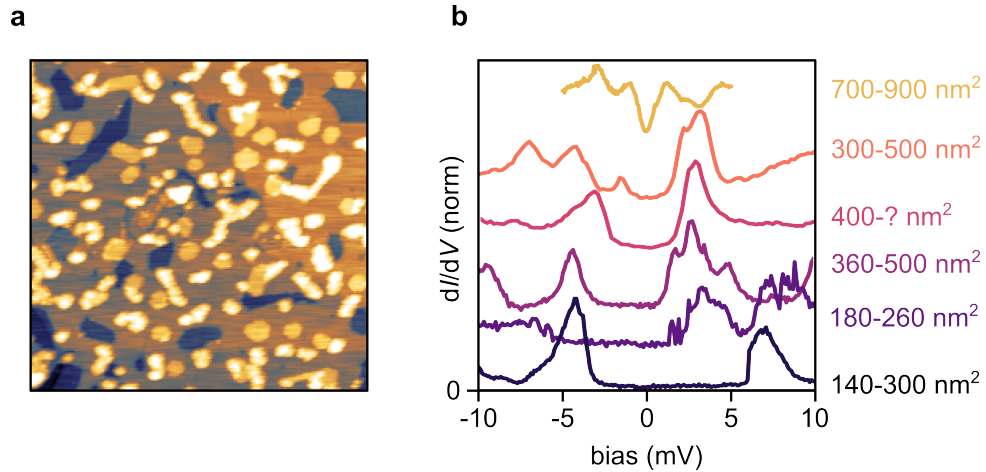


Figure A.4: Area dependence of gap. **a** Large scale STM image of high-coverage MoS₂ on Gr/Eu/Ir(111). Nearly the whole surface is covered with single-layer MoS₂, with some bilayers on top. **b** Variation of the gap with island size. Spectra have been normalized and offset vertically.

Finally, we compare the size of the gap for MoS₂ regions of different sizes. Part of data was acquired on a different sample, where we have grown > 1 ML of MoS₂, see Fig. A.4a. The larger coverage led to the presence of bilayers on top of single-layer MoS₂, while the general area size of MoS₂ seemed to go down, with grain boundaries, defects and clusters of undetermined structure (some of the larger, bright areas in Fig. A.4a) limiting average defect-free area size. On this sample, the gap was often significantly larger, with the peak-to-peak size sometimes exceeding 10 meV, see the bottom spectrum of Fig. A.4b. The patchwork appearance of MoS₂, with many small islands stitched together, allowed us to explore the dependence of gap size on area. Some selected spectra are plotted in Fig. A.4b, with the estimated island sizes of each spectrum written on the side. A clear trend can be made out, where the V-shaped spectrum investigated in Figs. A.1 and A.3 appears as the limit of the gap in large areas. In contrast, on smaller islands, the gap is flat in the center and the dI/dV signal is close to zero.

Discussion

Regarding the nature of the gap at the Fermi level found in metallic single-layer MoS₂, we can immediately rule out that is a superconducting gap, due to the lack of magnetic field-dependence, the absence of a proximity effect in graphene and the asymmetry with respect to the Fermi level. In shape and size, it can best be compared to the Coulomb gap observed in single-layer NbSe₂ [318], where the Coulomb gap was present on islands too small to host superconductivity. A clear $1/L$ dependence of the Coulomb gap was established, with L the lateral size of the island [318].

In our case as well, the gap seems to have a strong dependence on island size. Some care needs to be taken in determining to which degree bilayers, clusters or defects lead to localization of carriers in single-layer MoS₂. Bilayers should bind only weakly to the layer below and therefore not induce any localization, whereas this is not necessarily the case for metallic clusters. In the same vein, some defects have in-gap states and scatter strongly, while others are passivated and inert [139]. Whether one counts the structures on top of MoS₂ or the point defects in the islands as limiting island size or not will have a significant effect on the calculated area, as indicated by the broad ranges of island sizes given for each spectrum in Fig. A.4b. Nevertheless, the general trend of smaller gaps for larger islands seems to hold.

It would be interesting to see what happens to the Coulomb gap when the island size becomes ever larger. It could transition into a superconducting gap as was found in Ref. [318], completely vanish or reach a certain minimum width which does not change with island size. This could help distinguish localization effects stemming from electron-electron correlations (island size) from those arising due to disorder and electron-phonon coupling, since the electron-phonon coupling strength and intrinsic defect density are not dependent on island size, while electron-electron correlations scale with $1/L$ [318]. A close comparison of defect-free islands of different sizes with the same tip could help resolve this issue. We could also induce disorder by evaporating Cs atoms on the sample, as was done in Chapter 8, to check its effect. As for electron-phonon coupling, this should become stronger for single-layer MoS₂ as the doping level is increased [145, 319], while electron-electron interactions should be more effectively screened and thus go down. A doping dependence of the gap would therefore be of interest as well.

We could also check the temperature dependence of the gap. In NbSe₂, the Coulomb gap closed at 4 K. It might be possible that the temperature dependence of the gap allows us to draw some conclusions as to its origin.

Single-layer MoS₂ is a known superconductor at sufficiently high doping levels [9,57]. It is intriguing to speculate whether MoS₂/Gr/Eu/Ir(111) would be superconducting if the island size would be large enough, or whether a higher doping level needs to be reached. Higher doping levels are available, for instance using Li [316]. Growing larger islands remains an experimental challenge, with several avenues like seeded growth, growth at elevated temperatures and using lower annealing temperatures already explored to no avail.

Finally, it is interesting to note that in each spectrum, the gap is accompanied by modulations in the DOS (peaks and valleys) beside it. This is best observed in Fig. A.3b, where some of the peaks are seen to shift continuously over several Å, while sometimes undergoing more abrupt changes as well. Here, it would be relevant to check for any characteristic features of these modulations in large, defect-free islands, to determine whether they arise from some type of collective excitations [418] or coupling to a particular quasiparticle.

A.2 Single-layer MoS₂ on h-BN on Ir(111)

The experiments in this section were proposed by W. Jolie. The measurements were carried out by C. van Efferen and W. Jolie. The analysis of the data was done by C. van Efferen, with support from W. Jolie.

Introduction

While Gr/Ir(111) is in many respects a perfect substrate for MoS₂, it has a downside: Gr is metallic. Even though it is a 'bad' metal, with a low DOS, it can still screen interactions in MoS₂. As a consequence, the band gap of MoS₂ on Gr/Ir(111) is 2.53 ± 0.08 eV [82], at some distance from its predicted freestanding value of $E_g \approx 2.8$ eV [125,212]. This also leads to a wider photoluminescence peak of 18 meV for MoS₂/Gr/Ir(111) [330] compared to 5 meV for a MoS₂ layer encapsulated in hBN [419], meaning that the exciton lifetime is significantly reduced.

Exchanging Gr for hBN has the potential to enable the growth of truly freestanding MoS₂, due to the large bandgap of hBN. Its ultrathin structure should allow for tunneling through the hBN layer to the Ir substrate, which is necessary for STM. The growth of hBN on Ir(111), as well as the possibility of performing STM on this system, has been demonstrated previously by Farwick zum Hagen *et al.* [335].

At the same time, the strong moiré potential of hBN/Ir(111) [420] holds a promise of another type of physics altogether. It could lead to localized states trapped in the quantum wells created by bending of the MoS₂ bands in response to the moiré potential, of excitonic [204–206] or polaronic [336] nature. Strong moiré effects in TMDCs can also lead to a Mott insulating [337], Wigner crystal [338–340] or excitonic insulating state [341].

Results

In Fig. A.5a, a STM topograph of single-layer MoS₂/hBN/Ir(111) is shown, where we used the same MoS₂ growth parameters as for MoS₂/Gr/Ir(111). See Methods below for the growth of hBN on Ir(111). The resulting MoS₂ islands do not look too dissimilar from those grown on Gr [82]. Small MoS₂ islands have grown together to form larger clusters, separated by grain boundaries. The apparent height of the islands is about 0.65 nm, very similar to the height of MoS₂ on Gr/Ir(111) [3]. On the hBN and through the MoS₂, the hexagonal moiré of hBN/Ir(111) can be seen, which has a unit cell of size $a_{\text{moiré}} = 2.91 \pm 0.08$ nm [335]. However, unlike the clean growth on Gr, there are signs of disorder in the sample. In some parts of the hBN layer the moiré seems suppressed, while bright patches of altered apparent height are visible in MoS₂.

A closer look at a disordered MoS₂ island in Fig. A.5b, reveals that the apparent height of the bright areas is about 0.1–0.2 nm. Next to the bright spots, the moiré of hBN/Ir(111) can be seen faintly, in contrast to defect-free areas of MoS₂, like in the bottom left of Fig. A.5a, where a strong moiré modulation can be observed.

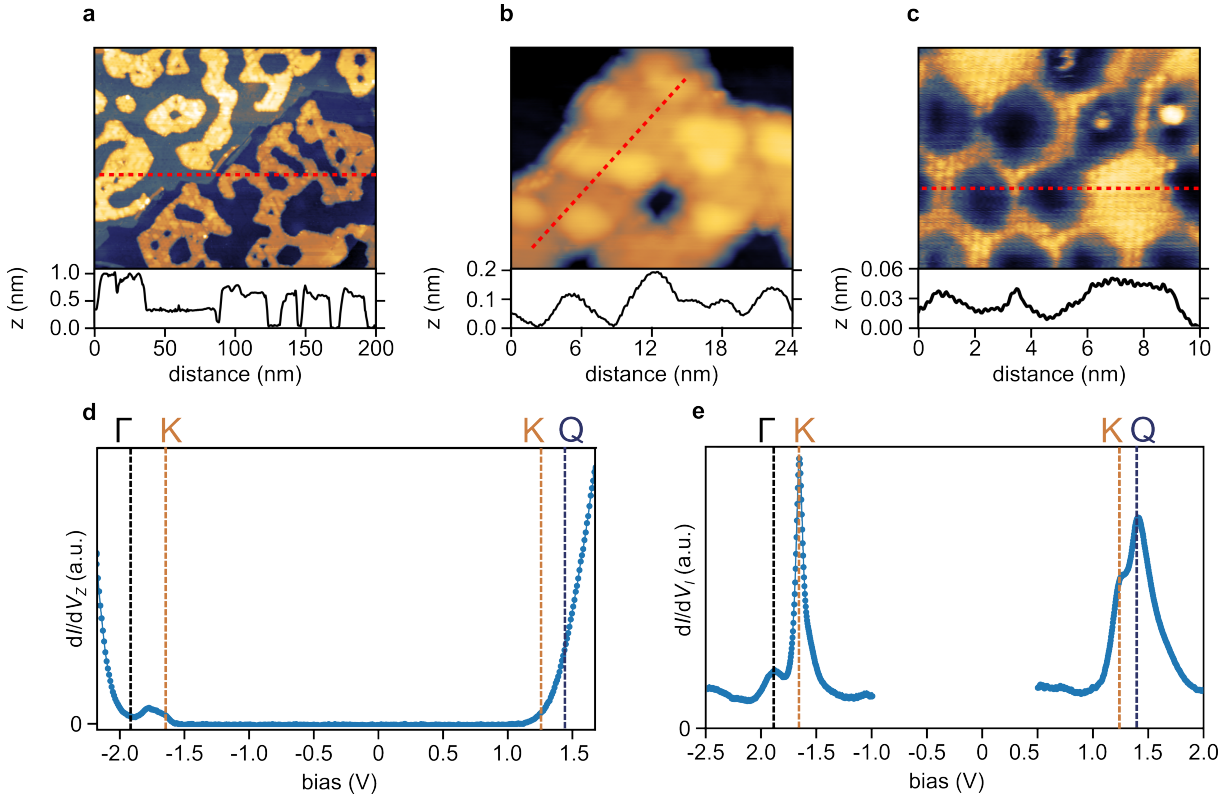


Figure A.5: Topography and electronic structure of single-layer MoS₂ on hBN/Ir(111). **a** Large scale STM image of single-layer MoS₂ on hBN/Ir(111). Two step edges in the Ir(111) substrate are visible. The moiré pattern of hBN/Ir(111) can be seen through the MoS₂ islands. **b** STM image of MoS₂ island. The bright bumps are related to S intercalation under the hBN layer. **c** STM image of hBN. S atoms stemming from the growth of MoS₂ have partially intercalated the hBN layer, lifting the hBN locally. **d** Constant height dI/dV spectrum of MoS₂ on top of a relatively flat area, showing the band gap. **e** Constant current dI/dV spectra of the valence and conduction band edges. Below the topographies **a-c** line profiles taken along the red dashed lines are shown. In the spectra **d,e**, the critical point energies at high symmetry points in the Brillouin zone are identified. STM/STS parameters: **a** $200 \times 200 \text{ nm}^2$, $V_{\text{set}} = 2.0 \text{ V}$, $I_{\text{set}} = 50 \text{ pA}$; **b** $30 \times 30 \text{ nm}^2$, $V_{\text{set}} = 2.0 \text{ V}$, $I_{\text{set}} = 50 \text{ pA}$; **c** $10 \times 10 \text{ nm}^2$, $V_{\text{set}} = 1.0 \text{ V}$, $I_{\text{set}} = 100 \text{ pA}$; **d** $V_{\text{set}} = 1.75 \text{ V}$, $I_{\text{set}} = 300 \text{ pA}$; **e** $V_{\text{set}} = -2.5 \text{ V}$, $I_{\text{set}} = 100 \text{ pA}$ [left], $V_{\text{set}} = 2.0 \text{ V}$, $I_{\text{set}} = 100 \text{ pA}$ [right]. For all spectra: $V_{\text{mod}} = 5 \text{ mV}$, $f_{\text{mod}} = 619 \text{ Hz}$.

On the hBN layer, depicted in Fig. A.5c, we see a superstructure of $(\sqrt{3} \times \sqrt{3})R30^\circ$ with respect to Ir. The superstructure seems to mostly grow around the strongly chemisorbed valley region of the moiré [335]. However, in the top right, two small atomic clusters can be seen, which are moved by the tip, while in the bottom right, a moiré valley has vanished, seemingly lifted by the superstructure. A likely explanation for the superstructure is that S atoms stemming from the growth of MoS₂ have intercalated between hBN and Ir, as was observed previously for Gr/Ir(111) [421]. While they initially grow around the valleys of the moiré, they can apparently lift the chemisorbed regions of the hBN from the Ir, which is visible in the top left and bottom right. Finally, S or Mo atoms can apparently also form clusters in the strongly bound valley regions.

It is not immediately clear which of these effects is responsible for the bright areas in MoS₂. We

speculate that they are either lifted valley regions - since the moiré is indeed invisible or suppressed near the bright areas - or S intercalated between MoS₂ and hBN.

Turning our attention to the electronic structure, by measuring constant height (CH) and constant current (CC) spectra in the flat, weakly-moiré modulated regions next to the bright areas, we find that the band gap of MoS₂ has increased substantially from its Gr/Ir(111) analogue. In CH dI/dV , see Fig. A.5d, the valence band (VB) edge is characterized by a small 'hump' at about 1.6 eV, followed by a steep rise starting at about 2.0 eV. The conduction band (CB) shows a single steep edge near 1.2 eV. Employing the comprehensive STS method, we use CC STS in Fig. A.5e to better identify the band edges [82, 422]. We observe a striking feature in the VB at 1.65 eV, marking the onset of the small 'hump' seen in CH spectroscopy, followed by a smaller peak corresponding to the large rise observed in CH. In the CB, the steep rise in CH spectroscopy can be resolved as two separate, close-lying peaks in CC spectroscopy.

We tentatively assign the large CC peak to the VB maximum at the K-point. Due to the small tunneling probability of the STM into high-momentum states, the K-point is generally only weakly resolved with STS. In the STS of MoS₂/Gr/Ir(111) the VB K-point is invisible [3, 82]. In MoSe₂ and WSe₂ on HOPG, the VB K-point was measured as a rather broad feature in CC STS [422]. It is therefore surprising that we observe such a sharp peak in CC STS. This might indicate that the increased decoupling from the substrate achieved with the insulating hBN layer, compared to Gr or HOPG, allows us to resolve states which are otherwise hidden in background tunneling into the substrate. Besides the sharp peak, there is smaller feature in the CC STS, marking the onset of the band at the Γ point, which can be recognized by the large increase in CH spectroscopy. On the other side of the K-point peak, a small shoulder can be observed, which might be due to the spin-orbit splitting of the VB K-bands. This should lead to two peaks in the CC spectrum [422].

Turning towards the CB, the two close-lying peaks in CC STS can be assigned to the K- and Q-points of the MoS₂ bandstructure. They were previously measured in much the same way on MoS₂/Gr/Ir(111) [82], though the lower-lying K-point is more pronounced here. This is in line with the enhanced intensity of the VB K-point.

Measuring now in an area of MoS₂ where there are no bright bumps, the moiré of hBN/Ir(111) is more pronounced, see the STM image of Fig. A.6a. The modulation of the apparent height is about 0.5 Å, as can be gathered from the line profile below the image. If we take constant current dI/dV linescans along the dashed lines indicated in Fig. A.6a, we see that the VB and CB of MoS₂ bend by about 100 meV going across one of the apparent moiré valleys, see Fig. A.6b,c. The bending does not seem to be continuous everywhere; instead, localized states are visible in both band edges, as well as replica peaks, especially in the VB, where besides the band edge near -2 eV, two other peaks of similar intensity are seen, 200 meV and 400 meV below it. In the CB, multiple small peaks can be seen in the moiré valley region between 1-4 nm, spaced by about 80 meV.

The moiré of hBN on Ir(111) was previously found to have a corrugation of about 0.4 Å, close to the apparent corrugation we measure on the MoS₂ [420]. However, the modulation of the work

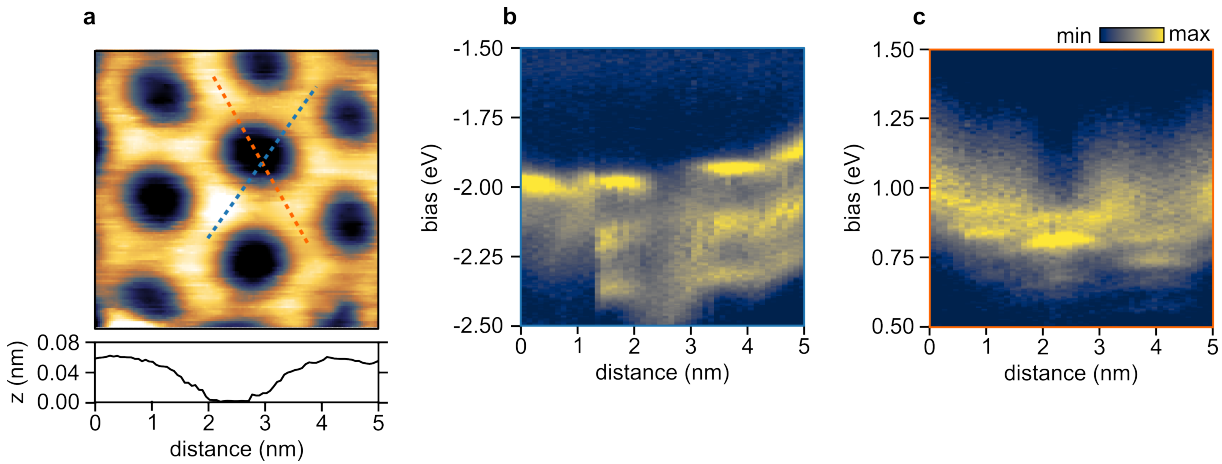


Figure A.6: Effect of hBN/Ir(111) moiré on MoS₂ band edges. **a** STM image of MoS₂, showing the hBN/Ir(111) moiré which is visible through the MoS₂ layer. The line profile below the image is taken along the orange dashed line. **b,c** Constant current dI/dV linescans taken along the colored dashed lines indicated in **a** (blue **b**, orange **c**). In both cases, the lines are taken to include top, hcp, fcc and bridge sites of the moiré [335,423], though the strong electronic effects on the apparent height make a straightforward assignment difficult. STM/STS parameters: **a** $8 \times 8 \text{ nm}^2$, $V_{\text{set}} = 2.0 \text{ V}$, $I_{\text{set}} = 100 \text{ pA}$; **b** $V_{\text{set}} = -2.5 \text{ V}$, $I_{\text{set}} = 100 \text{ pA}$; **c** $V_{\text{set}} = 1.5 \text{ V}$, $I_{\text{set}} = 100 \text{ pA}$. For all spectra: $V_{\text{mod}} = 5 \text{ mV}$, $f_{\text{mod}} = 619 \text{ Hz}$.

function within the moiré unit cell of 0.5 eV, measured using field emission resonances [420], greatly exceeds the band bending in the MoS₂ layer. This could be due to dielectric screening of the effect, reducing it substantially in MoS₂, or as a result of the partial S intercalation, which might lead to a flatter potential. Nevertheless, even with the bending weaker than might be expected, it still leads to considerable changes to the electronic structure of MoS₂, compared to the spectra in Fig. A.5d,e. The presence of replica bands in the VB and what appear to be localized states in both bands, could be signs of correlated physics and warrant further investigation.

Discussion

MoS₂ on hBN/Ir(111) is a promising system, both as a realization of an truly freestanding TMDC which can still be measured with the STM, and as a candidate for correlated moiré physics. The current setup is however plagued by inhomogeneous S intercalation, which makes a systematic investigation of its properties difficult.

Going forward, we could try to fully intercalate the hBN layer with S, so that the MoS₂ will be as close to freestanding as possible. This might enable the first observation of excitons with regular STM using inelastic tunneling spectroscopy; inelastic signatures of TMDC excitons were recently observed in tunnel junctions consisting of graphene and gold electrodes separated by hBN with an adjacent TMD monolayer [333]. It might also allow us to probe the spin-orbit split VB states in detail. It could furthermore lead to enhanced Tomonaga-Luttinger liquid physics in the MoS₂ mirror twin boundaries, since any electron-electron correlation effects are even less screened than on Gr/Ir(111) [103]. We could also aim to fully intercalate hBN with other atomic species, such as Eu or Cs. Indeed, a full

Cs intercalation of hBN/Ir(111) has been achieved [424]. Ideally, we could reach the metallic MoS₂ regime in this way, while keeping the substrate interaction to a minimum [3].

Another route would be to aim for unintercalated hBN, so that the effects of the moiré are not dampened by disorder. While this might be difficult with S, we could aim for growth of Se or Te based TMDCs, since the larger chalcogen atoms might be less inclined to intercalate. These materials might then be investigated for their potential correlated moiré properties.

Methods

Growth of hBN on Ir(111) was performed in a low-temperature STM system with a dedicated preparation chamber with a base pressure in the range of 1×10^{-10} mbar. Ir(111) was prepared using cycles of 1.5 keV Ar⁺ erosion and flash annealing to $T \approx 1550$ K. hBN is grown by dosing the Ir sample with 1×10^{-6} mbar of borazine for 10 minutes, while the sample is kept at 1250 K. For more details on the growth of hBN, see Ref. [335]. Single-layer MoS₂ was grown in the same way as on Gr/Ir(111), see for instance [82].

APPENDIX B

Software

B.1 CPlot: plotting, analysing, filtering and managing Nanonis files

CPlot is a Python program written with the idea of automating certain routines of data analysis, which can take up considerable amounts of time over the course of a PhD. Apart from the scanning tunnelling microscopy (topography) data, which can be processed with free software like WSxM [425] or Gwyddion, we are mostly concerned with scanning tunnelling spectroscopy (conductance) data, where the density of states of a sample is resolved as a function of voltage (V) and spatial coordinates (X, Y). This data is acquired either as individual spectra, where the bias voltage of the STM is swept while recording the current I and conductance dI/dV at fixed X and Y , or as a map, where the dI/dV signal for a range of X, Y coordinates is obtained while keeping V fixed.

Using CPlot, most types of spectroscopy data acquired with a Nanonis STM control system can be quickly plotted, without the need to import the data into proprietary software like Origin, Excel or Igor, which can be costly in terms of both time and money. It nevertheless provides a complete graphical user interface that allows for further signal processing (fast Fourier transform, normalization, second derivative, smoothing, interpolating, averaging), as well as presentation (color maps, linear/log scale, offsets, data range), which is lacking when doing the data analysis directly in Python or MATLAB. In this section, I will discuss some of the main features of CPlot.



Figure B.1: Main window of CPlot.

The main menu of CPlot consists of four different options: 'Spectra', 'Grid', 'Linescan' and 'Multipass', see Fig. A.7. In each case, clicking on an option will open file explorer, allowing one to select either multiple files ('Spectra', 'Linescan') or a single file ('Grid', 'Multipass') of the appropriate type: DAT in the case of 'Spectra' and 'Linescan', 3DS in the case of 'Grid' and SXM for 'Multipass'.

Spectra

After selecting a number of DAT files in file explorer, the window in Fig. A.8 will open. In this window, a list of the selected files will be present on the bottom. Clicking on the file names that should be plotted, followed by 'Set' will plot the files in the graph above. Next to the graph, some

B.1 CPlot: plotting, analysing, filtering and managing Nanonis files

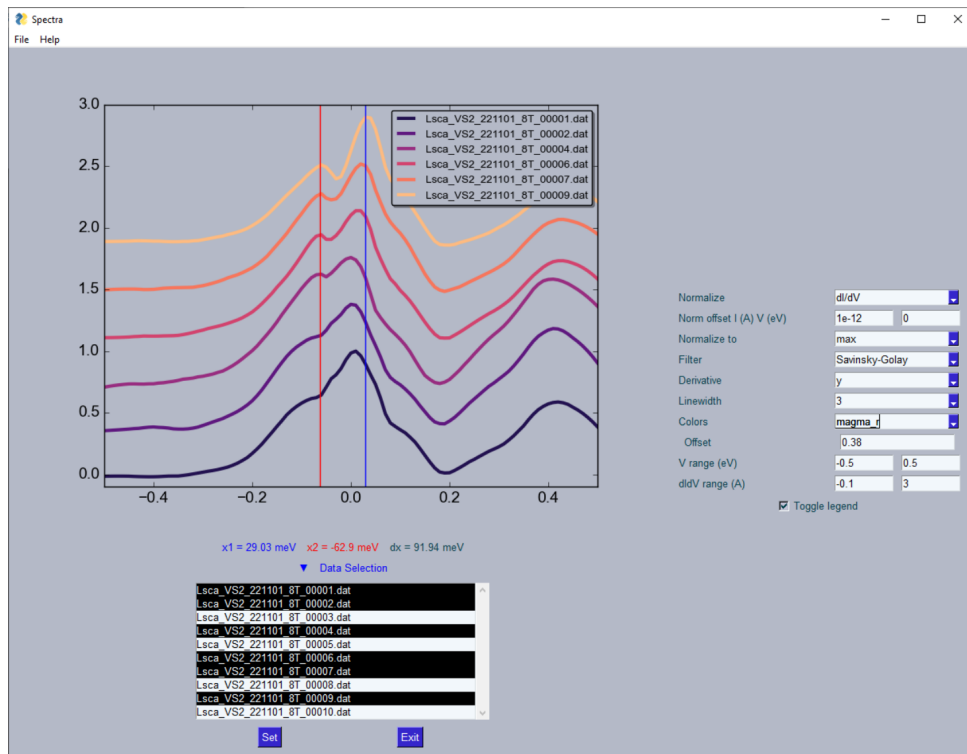


Figure B.2: Spectra module of CPlot.

options for file analysis can be found, including plotting the normalized conductance $dI/dV/(I/V)$, where both I and V can be given an offset, to account for artefacts from the procedure [426]; applying a Savinsky-Golay filter; and taking the derivative of the conductance. There are options to normalize the spectra to their maximum, minimum, start or end value, and to plot them with an offset. The range of dI/dV and V can be changed, as well as the linewidth and color scheme. After each change, they need to be applied with 'Set'.

In the graph, clicking on the lines in the legend will toggle the visibility of that spectrum on or off. The legend itself can also be toggled on and off with a selection button. If one keeps the left mouse button pressed while moving through the graph, the red and blue vertical lines can be dragged. The energy positions of both lines and the difference between them can be read off below in graph in meV.

Via the drop-down menu 'File'->'Save'->'Image', the graph can be saved. If no folder is specified with 'Save As...', the folder of the selected files will be used. If no file extension is explicitly written behind the chosen file name, it will be saved as a PNG. It is often worthwhile to save the graph as a vector graphic (SVG) file - this is done by typing '.svg' behind the name - so it can be further adapted with software like Inkscape or Powerpoint. As a vector file, nearly element of the graph can be altered and/or removed.

Linescan

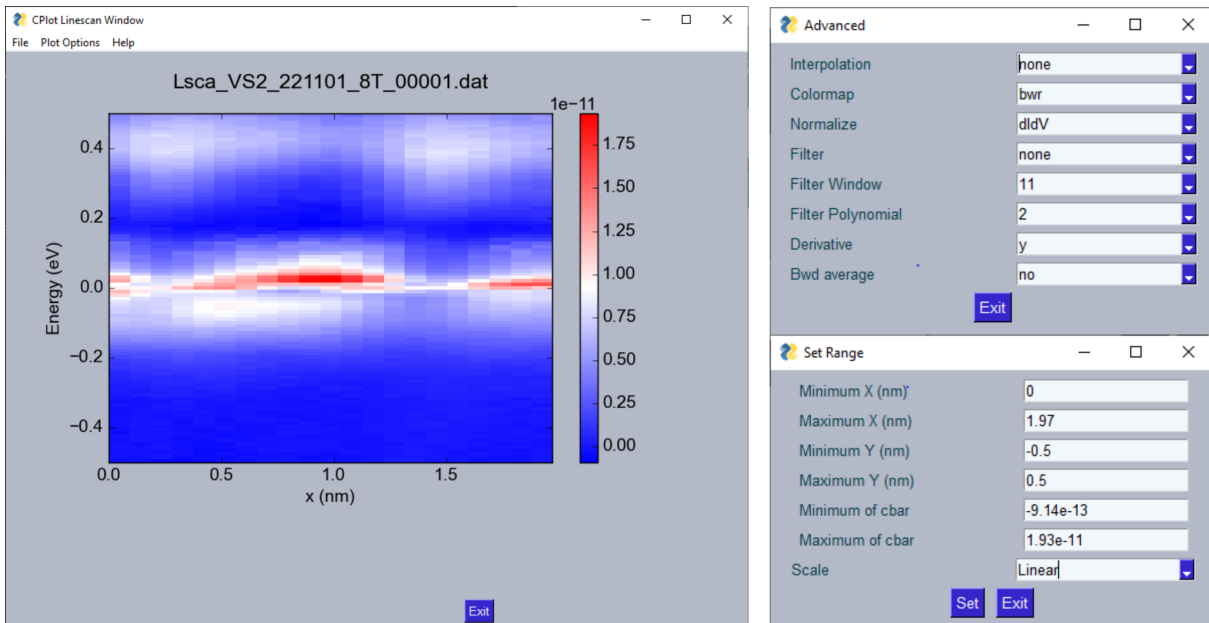


Figure B.3: Linescan module of CPlot.

After selecting a number of DAT files in file explorer, the window in the left side of Fig. A.9 will open, which shows a graph of the selected conductance spectra, plotted as a color map. The x-axis of the map is determined by the difference of the (X,Y) coordinates of the first and last spectrum, which are obtained from the Nanonis files automatically. The y-axis is set by the bias voltage range of the spectra. For this module to function at all, the selected spectra need to have same number of data points, otherwise an error window will appear. For this module to function properly, all spectra need to have the same voltage range and need to be spaced by the same distance in real space. This is done with the Nanonis software by using the 'Pattern': 'Line': 'Bias Spectroscopy ASCII' option, where spectra with the same settings are obtained along a line in real space at evenly spaced intervals.

Using the 'Plot Options' drop-down menu, various other windows can be opened. 'Plot Options'-'>'Advanced' opens the window in the upper right of Fig. A.9, which gives access to options for interpolation of the color map, different color schemes, using the normalized conductance $dI/dV/(I/V)$, applying a Savinsky-Golay filter (filter window size and polynomial order can be set by hand), and taking the derivative of the conductance. 'Plot Options'-'>'Set Range' opens the window in the bottom right of Fig. A.9, which allows one to change the voltage, distance and conductance ranges, as well as set either a linear or logarithmic scale for the conductance. 'Plot Options'-'>'FFT' opens a window with a fast Fourier transform of the color map. The FFT is performed on the $(x,dI/dV)$ signal at each voltage and can thus be used to analyse periodic modulations in real space.

'Plot Options'-'>'Spectra' opens the window in Fig. A.10. Using the slider below the graph, a

B.1 CPlot: plotting, analysing, filtering and managing Nanonis files

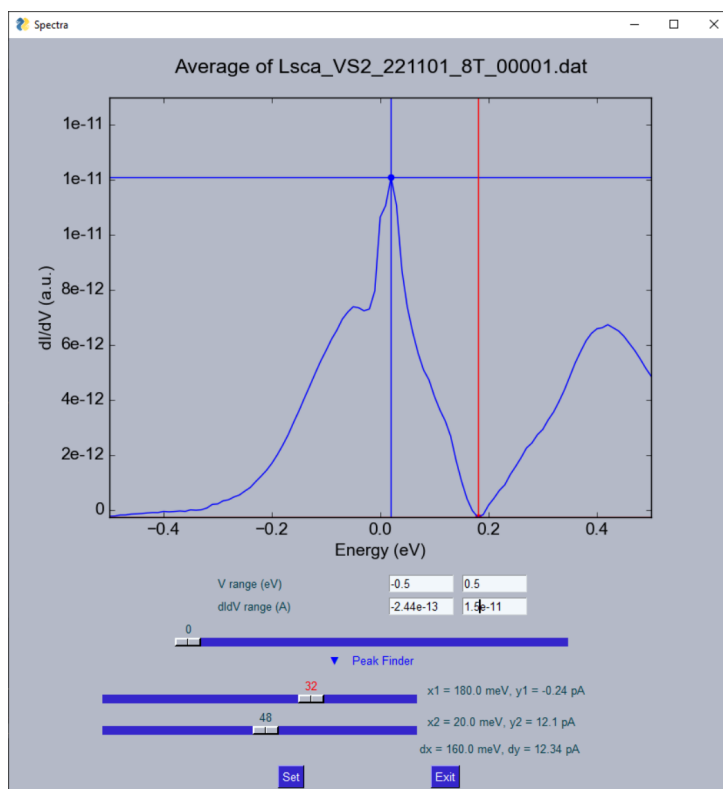


Figure B.4: Spectra window of linescan module of CPlot.

particular spectrum of the linescan can be selected, which will then be plotted in the graph. If the slider is placed all the way to the left, the averaged spectrum of the linescan is shown. The two lower sliders can be used to control the red and blue points, which read off the conductance and energy values at their position in the graph. When a particular spectrum is selected, a red vertical bar while appear in the main 'Linescan' window of Fig. A.9 at the position of that spectrum. The red and blue lines are also plotted as horizontal lines in the main graph. 'Plot Options'->'Horizontal Spectra' opens a window where the $(x, dI/dV)$ signals are plotted as line graphs, working in much the same way as the normal spectra window of Fig. A.10.

Under 'File'->'Save', several options are found. One can save PNG, SVG or JPEG images of the respective graphs of the color map, FFT, spectrum and horizontal spectrum; or one can save data as DAT files in ASCII format. Saving an image works only when the appropriate window is opened and will save the graph that is currently plotted. For instance, after opening the 'Plot Options'->'Spectra' window and selecting a certain spectrum, 'File'->'Save'->'Save Spectrum'->'Image Spec' will save the graph of that particular spectrum. Saving the data as DAT files can be done directly for be the average spectrum or average horizontal spectrum. Alternatively one can save all the individual spectra together in a single file. Note that the average spectra files generated in this way can be used with the 'Spectrum' module of CPlot just like Nanonis files.

Grid

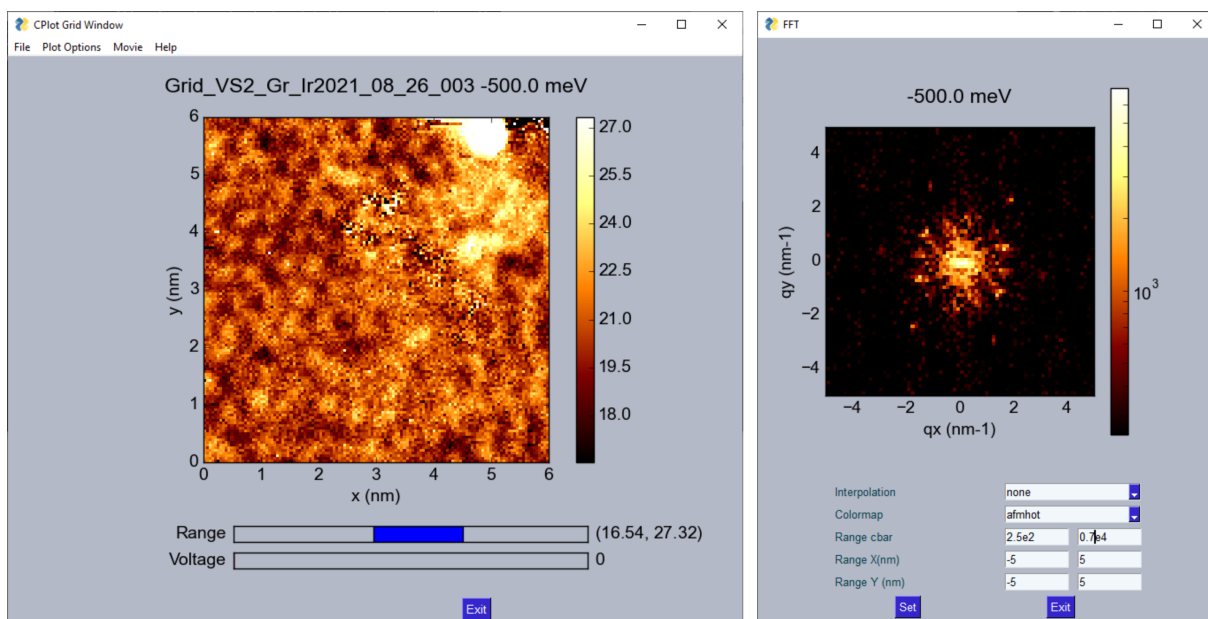


Figure B.5: Grid module of CPlot.

After selecting a 3DS Nanonis file, the window on the left side of Fig. A.11 will open. 3DS is a three-dimensional, binary file format. It is used by Nanonis to store spectra taken in a 2D real space grid, so that we obtain the conductance values as a function of (V, X, Y) . CPlot represents the data at each voltage as a 2D color map. Using the sliders below the image, the contrast on the image can be adjusted (upper slider) and the voltage selected (lower slider).

The 'Plot Options' drop-down menu works the same as for the 'Linescan' module. On the right side of Fig. A.11, the FFT window is shown, which can be adjusted for color scheme, scale and range. In the 'Plot Options'-'>'Spectra' window, two sliders allow one to select individual spectra at each X, Y point of the grid, the location of which is indicated in the main window as a blue dot. Each spectrum is named according to its row and column in the grid. Via 'Plot Options'-'>'Channel', the ' Z ', ' I ' and ' d^2I/dV^2 ' channels, if recorded during measurements, can be set instead of the dI/dV channel. 'Plot Options'-'>'Topography' shows the topography, which is automatically saved by Nanonis during the recording of the grid.

The 'Movie'-'>'GridMov' option saves the data as a GIF, showing the conductance maps at the different bias values sequentially.

Under 'File'-'>'Save', both images and ASCII files can be saved. Here, CPlot allows one to save the data in a format directly compatible with either WSxM or MountainsSPIP. Since they are ASCII files, they can also be used with Gwyddion or other programs with the right import parameters. Selecting 'File'-'>'Save All' results in a list of DAT files in ASCII format which are named according to 'gridname + voltage'. This allows for quick importing into other software while keeping track of

B.1 CPlot: plotting, analysing, filtering and managing Nanonis files

the relevant information (*i.e.* the voltage of each 2D map). It is also possible to save single spectra, rows and columns of the grid, which can then be used for the 'Spectra' or 'Linescan' modules of CPlot. In order to do that, a location/spectrum needs to be selected using the 'Plot Options'-'>'Spectra' window. Using 'File'-'>'Save Spectra'-'>'Row'/'Column'/'Spectrum' will then save the chosen object.

Multipass

The 'Multipass' module functions in the same way as the 'Grid' module. Here one opens a normal SXM Nanonis file, which is the same file format as the topography data. This can lead to issues, since CPlots cannot open the regular topography files. Trying to do so will most likely result in a crash.

In the Nanonis multipass, each scan line is taken at multiple voltage values, leading to a composite file. This mode is often used to simultaneously obtain constant current conductance maps at different bias values. CPlot reads out the voltages at which each pass was measured and plots them in order, so one can easily cycle through them. Saving the files in the same way as for the grid results in multiple DAT ASCII files labelled with their respective bias voltage, which can then be further processed with WSxM or Gwyddion.

APPENDIX C

List of Publications (*Liste der Teilpublikationen*)

The results presented in this thesis can be found in the following publications:

Teile dieser Arbeit wurden als Bestandteil der folgenden Artikel in Fachzeitschriften bereits veröffentlicht:

- [1] **Camiel van Efferen**, Jan Berges, Joshua Hall, Erik Van Loon, Stefan Kraus, Arne Schobert, Tobias Wekking, Felix Huttmann, Eline Plaar, Nico Rothenbach, Katharina Ollefs, Lucas Machado Arruda, Nick Brookes, Gunnar Schönhoff, Kurt Kummer, Heiko Wende, Tim Wehling and Thomas Michely
A full gap above the Fermi level: the charge density wave of monolayer VS₂
Nature Communications, **12**, 6837 (2021)
- [2] **Camiel van Efferen**, Joshua Hall, Virgínia Boix, Tobias Wekking, Nikolay Vinogradov, Alexei Preobrajenski, Jan Knudsen, Jeison Fischer, Wouter Jolie and Thomas Michely
Novel 2D vanadium sulphides: synthesis, atomic structure engineering and charge density waves
manuscript, submitted to ACS Nano, available as preprint
- [3] **Camiel van Efferen**, Clifford Murray, Jeison Fischer, Carsten Busse, Hannu-Pekka Komsa, Thomas Michely and Wouter Jolie
Metal-insulator transition in monolayer MoS₂ via contactless chemical doping
2D Materials, **9**, 025026 (2022)
- [4] **Camiel van Efferen**, Jeison Fischer, Achim Rosch, Thomas Michely and Wouter Jolie
Modulated Kondo screening along magnetic mirror twin boundaries in monolayer MoS₂ on graphene
manuscript, accepted at Nature Physics, available as preprint
- n/a **Camiel van Efferen**, Arne Schobert, Tfyche Tounsi, Michael Winter, Mark Georger, Affan Safeer, Jason Bergelt, Christian Krämer, Jeison Fischer, Roberto Mozara, Jan Berges, Tim

Appendix C List of publications (*Liste der Teilpublikationen*)

Wehling, Thomas Michely, Wouter Jolie

Real-space observation and tunneling spectroscopy of polarons in monolayer MoS₂
manuscript, in preparation phase

Further publications:

Weitere Publikationen:

- [82] Clifford Murray, Wouter Jolie, Jeison A Fischer, Joshua Hall, **Camiel van Efferen**, Niels Ehlen, Alexander Grüneis, Carsten Busse and Thomas Michely
Comprehensive tunneling spectroscopy of quasifreestanding MoS₂ on graphene on Ir(111)
Physical Review B, **99**, 115434 (2019)
- [284] Joshua Hall, Niels Ehlen, Jan Berges, Erik van Loon, **Camiel van Efferen**, Clifford Murray, Malte Rosner, Jun Li, Boris V Senkovskiy, Martin Hell, Matthias Rolf, Tristan Heider, Maria C Asensio, José Avila, Lukasz Plucinski, Tim Wehling, Alexander Grüneis and Thomas Michely
Environmental Control of Charge Density Wave Order in Monolayer 2H-TaS₂
ACS Nano, **13**, 10210-10220 (2019)
- [100] Clifford Murray, **Camiel van Efferen**, Wouter Jolie, Jeison Antonio Fischer, Joshua Hall, Achim Rosch, Arkady V Krasheninnikov, Hannu-Pekka Komsa and Thomas Michely
Band Bending and Valence Band Quantization at Line Defects in MoS₂
ACS Nano, **14**, 9176-9187 (2020)
- n/a T. Knispel, D. Mohrenstecher, **C. van Efferen**, V. Boix, C. Speckmann, A. Grüneis, A Preobrajensk, J. Knudsen, N. Atodiresei, T. Michely and J. Fischer
Covalent growth pathways to engineer new 2D material based on monolayer NbS₂
manuscript, in preparation phase

Conference contributions as presenting author:

Konferenzbeiträge als präsentierender Autor:

- 2023** DPG Spring Meeting, Dresden (DE), *Vanadium sulphides on graphene on Ir(111): polymorphs, charge density waves, layer dependency*. Talk
- 2022** SFB1238 workshop, Bonn (DE), *Real-space observation of Holstein polarons in monolayer MoS₂*. Poster
- 2022** DPG Condensed Matter Section, Regensburg (DE), *Real-space observation of Holstein polarons in monolayer MoS₂*. Poster
- 2022** 2DSPM (2D Scanning Probe Microscopy) Conference, San Sebastián (ES), *Real-space observation of the Kondo effect in MoS₂ mirror twin boundaries*. Poster
- 2022** EWEG-2D (5th European Workshop on Epitaxial Graphene and 2D Materials), St. Moritz (CH), *A full gap above the Fermi level: the charge density wave of monolayer VS₂*. Talk
- 2021** SFB1238 workshop, Bad Honnef (DE), *Metal-insulator transition in monolayer MoS₂ via contactless chemical doping*. Poster
- 2021** DPG Spring Meeting 2022, Online Conference, *A full gap above the Fermi level: the charge density wave of monolayer VS₂*. Poster
- 2021** International Conference On Nanoscience And Technology (ICN+T), Online Conference, *Band bending and valence band quantization at 1D line defects in MoS₂*. Talk
- 2021** SFB1238 workshop, Online Conference, *A full gap above the Fermi level: the charge density wave of monolayer VS₂*. Talk

Bibliography

- [1] C. van Efferen *et al.*, 'A full gap above the Fermi level: the charge density wave of monolayer VS₂', *Nat. Commun.* **12**, 6837 (2021). Cited on page(s) 19, 26, 33, 299, and 345
- [2] C. van Efferen, J. Hall, V. Boix, T. Wekking, N. Vinogradov, A. Preobrajensk, J. Knudsen, J. Fischer, W. Jolie and T. Michely, 'Novel 2D vanadium sulphides: synthesis, atomic structure engineering and charge density waves', *arXiv preprint arXiv:2306.16792* (2023). Cited on page(s) 65, 299, and 345
- [3] C. van Efferen, C. Murray, J. Fischer, C. Busse, H.-P. Komsa, T. Michely and W. Jolie, 'Metal-insulator transition in monolayer MoS₂ via contactless chemical doping', *2D Mater.* **9**, 25026 (2022). Cited on page(s) 117, 283, 287, 289, 291, 299, and 346
- [4] C. van Efferen, J. Fischer, A. Rosch, T. Michely and W. Jolie, 'Modulated Kondo screening along magnetic mirror twin boundaries in monolayer MoS₂ on graphene', *arXiv preprint arXiv:2210.09675* (2022). Cited on page(s) 151, 299, and 346
- [5] S. Manzeli, D. Ovchinnikov, D. Pasquier, O. V. Yazyev and A. Kis, '2D transition metal dichalcogenides', *Nat. Rev. Mater.* **2**, 17033 (2017). Cited on page(s) 4, 7, 8, 9, and 15
- [6] A. Splendiani, L. Sun, Y. Zhang, T. Li, J. Kim, C.-Y. Chim, G. Galli and F. Wang, 'Emerging Photoluminescence in Monolayer MoS₂', *Nano Lett.* **10**, 1271 (2010). Cited on page(s) 4, 14, 15, 16, and 17
- [7] D. Xiao, G.-B. Liu, W. Feng, X. Xu and W. Yao, 'Coupled spin and valley physics in monolayers of MoS₂ and other group-VI dichalcogenides', *Phys. Rev. Lett.* **108**, 196802 (2012). Cited on page(s) 4, 8, 14, and 15
- [8] M. Kang, S. W. Jung, W. J. Shin, Y. Sohn, S. H. Ryu, T. K. Kim, M. Hoesch and K. S. Kim, 'Holstein polaron in a valley-degenerate two-dimensional semiconductor', *Nat. Mater.* **17**, 676 (2018). Cited on page(s) 5, 23, 275, and 277
- [9] D. Costanzo, S. Jo, H. Berger and A. F. Morpurgo, 'Gate-induced superconductivity in atomically thin MoS₂ crystals', *Nat. Nanotechnol.* **11**, 339 (2016). Cited on page(s) 5, 16, 270, and 286

Bibliography

- [10] Y. Saito, Y. Nakamura, M. S. Bahramy, Y. Kohama, J. Ye, Y. Kasahara, Y. Nakagawa, M. Onga, M. Tokunaga, T. Nojima, Y. Yanase and Y. Iwasa, 'Superconductivity protected by spin-valley locking in ion-gated MoS₂', *Nat. Phys.* **12**, 144 (2016). Cited on page(s) 5 and 16
- [11] E. B. Isaacs and C. A. Marianetti, 'Electronic correlations in monolayer VS₂', *Phys. Rev. B* **94**, 35120 (2016). Cited on page(s) 5, 18, 19, 265, and 268
- [12] F. Arnold *et al.*, 'Novel single-layer vanadium sulphide phases', *2D Mater.* **5**, 45009 (2018). Cited on page(s) 5, 11, and 19
- [13] Y. Ma, Y. Dai, M. Guo, C. Niu, Y. Zhu and B. Huang, 'Evidence of the Existence of Magnetism in Pristine VX₂ Monolayers (X = S, Se) and Their Strain-Induced Tunable Magnetic Properties', *ACS Nano* **6**, 1695 (2012). Cited on page(s) 5 and 18
- [14] M. Gibertini, M. Koperski, A. F. Morpurgo and K. S. Novoselov, 'Magnetic 2D materials and heterostructures', *Nat. Nanotechnol.* **14**, 408 (2019). Cited on page(s) 5
- [15] J. Hall, B. Pielic, C. Murray, W. Jolie, T. Wekking, C. Busse, M. Kralj and T. Michely, 'Molecular beam epitaxy of quasi-freestanding transition metal disulphide monolayers on van der Waals substrates: a growth study', *2D Mater.* **5**, 25005 (2018). Cited on page(s) 5, 9, 10, and 12
- [16] R. Roldán, J. A. Silva-Guillén, M. P. López-Sancho, F. Guinea, E. Cappelluti and P. Ordejón, 'Electronic properties of single-layer and multilayer transition metal dichalcogenides MX₂ (M = Mo, W and X = S, Se)', *Ann. Phys.* **526**, 347 (2014). Cited on page(s) 7
- [17] J. Sun, X. Li, W. Guo, M. Zhao, X. Fan, Y. Dong, C. Xu, J. Deng and Y. Fu, 'Crystals', **7**, (2017). Cited on page(s) 7
- [18] M. Liu, Z. Zhao, W. Zhang and W. Zheng, 'Perspective of Vanadium Disulfide: A Rising Star Finds Plenty of Room in Single and Multielectron Energy Storage', *Energy Fuels* **36**, 13931 (2022). Cited on page(s) 7 and 17
- [19] A. K. Geim and K. S. Novoselov, 'The rise of graphene', *Nat. Mater.* **6**, 183 (2007). Cited on page(s) 7
- [20] J. A. Wilson and A. D. Yoffe, 'The transition metal dichalcogenides discussion and interpretation of the observed optical, electrical and structural properties', *Adv. Phys.* **18**, 193 (1969). Cited on page(s) 8 and 18
- [21] C. Liu, O. Singh, P. Joensen, A. E. Curzon and R. F. Frindt, 'X-ray and electron microscopy studies of single-layer TaS₂ and NbS₂', *Thin Solid Films* **113**, 165 (1984). Cited on page(s) 8 and 9

- [22] P. Joensen, R. F. Frindt and S. Morrison, 'Single-layer MoS₂', *Mater. Res. Bull.* **21**, 457 (1986). Cited on page(s) 8 and 9
- [23] N. D. Mermin, 'Crystalline order in two dimensions', *Phys. Rev.* **176**, 250 (1968). Cited on page(s) 8
- [24] L. D. Landau, E. M. Lifshitz and L. E. Reichl, 'Statistical physics, part 1', *Physics Today* **34**, 74 (1981). Cited on page(s) 8
- [25] K. S. Novoselov, A. K. Geim, S. V. Morozov, D.-e. Jiang, Y. Zhang, S. V. Dubonos, I. V. Grigorieva and A. A. Firsov, 'Electric field effect in atomically thin carbon films', *Science* **306**, 666 (2004). Cited on page(s) 8 and 9
- [26] K. S. Novoselov, D. Jiang, F. Schedin, T. J. Booth, V. V. Khotkevich, S. V. Morozov and A. K. Geim, 'Two-dimensional atomic crystals', *Proc. Natl. Acad. Sci. U.S.A.* **102**, 10451 (2005). Cited on page(s) 8 and 9
- [27] M. M. Ugeda, A. J. Bradley, Y. Zhang, S. Onishi, Y. Chen, W. Ruan, C. Ojeda-Aristizabal, H. Ryu, M. T. Edmonds and H.-Z. Tsai, 'Characterization of collective ground states in single-layer NbSe₂', *Nat. Phys.* **12**, 92 (2016). Cited on page(s) 8, 267, and 273
- [28] Y. Saito, T. Nojima and Y. Iwasa, 'Highly crystalline 2D superconductors', *Nat. Rev. Mater.* **2**, 1 (2016). Cited on page(s) 8
- [29] H. Zeng, J. Dai, W. Yao, D. Xiao and X. Cui, 'Valley polarization in MoS₂ monolayers by optical pumping', *Nat. Nanotechnol.* **7**, 490 (2012). Cited on page(s) 8 and 14
- [30] X. Qian, J. Liu, L. Fu and J. Li, 'Quantum spin Hall effect in two-dimensional transition metal dichalcogenides', *Science* **346**, 1344 (2014). Cited on page(s) 8, 269, and 270
- [31] V. Vaño, M. Amini, S. C. Ganguli, G. Chen, J. L. Lado, S. Kezilebieke and P. Liljeroth, 'Artificial heavy fermions in a van der Waals heterostructure', *Nature* **599**, 582 (2021). Cited on page(s) 8, 268, 272, 273, and 274
- [32] N. Briggs, S. Subramanian, Z. Lin, X. Li, X. Zhang, K. Zhang, K. Xiao, D. Geohegan, R. Wallace and L.-Q. Chen, 'A roadmap for electronic grade 2D materials', *2D Mater.* **6**, 22001 (2019). Cited on page(s) 8 and 9
- [33] K. F. Mak, C. Lee, J. Hone, J. Shan and T. F. Heinz, 'Atomically thin MoS₂: a new direct-gap semiconductor', *Phys. Rev. Lett.* **105**, 136805 (2010). Cited on page(s) 8, 14, 15, and 16
- [34] H. J. Conley, B. Wang, J. I. Ziegler, R. F. J. Haglund, S. T. Pantelides and K. I. Bolotin, 'Bandgap Engineering of Strained Monolayer and Bilayer MoS₂', *Nano Lett.* **13**, 3626 (2013). Cited on page(s) 8

Bibliography

- [35] Y. Gong *et al.*, 'Band Gap Engineering and Layer-by-Layer Mapping of Selenium-Doped Molybdenum Disulfide', *Nano Lett.* **14**, 442 (2014). Cited on page(s) 8
- [36] Y. Chen, S. Huang, X. Ji, K. Adepalli, K. Yin, X. Ling, X. Wang, J. Xue, M. Dresselhaus, J. Kong and B. Yildiz, 'Tuning Electronic Structure of Single Layer MoS₂ through Defect and Interface Engineering', *ACS Nano* **12**, 2569 (2018). Cited on page(s) 8
- [37] C. Gong, H. Zhang, W. Wang, L. Colombo, R. M. Wallace and K. Cho, 'Band alignment of two-dimensional transition metal dichalcogenides: Application in tunnel field effect transistors', *Appl. Phys. Lett.* **103**, 53513 (2013). Cited on page(s) 8
- [38] G. Fiori, F. Bonaccorso, G. Iannaccone, T. Palacios, D. Neumaier, A. Seabaugh, S. K. Banerjee and L. Colombo, 'Electronics based on two-dimensional materials', *Nat. Nanotechnol.* **9**, 768 (2014). Cited on page(s) 8 and 14
- [39] H. Katzke, P. Tolédano and W. Depmeier, 'Phase transitions between polytypes and intralayer superstructures in transition metal dichalcogenides', *Phys. Rev. B* **69**, 134111 (2004). Cited on page(s) 8
- [40] D. Voiry, A. Mohite and M. Chhowalla, 'Phase engineering of transition metal dichalcogenides', *Chem. Soc. Rev.* **44**, 2702 (2015). Cited on page(s) 9
- [41] T. H. Choudhury, X. Zhang, Z. Y. Al Balushi, M. Chubarov and J. M. Redwing, 'Epitaxial Growth of Two-Dimensional Layered Transition Metal Dichalcogenides', *Annu. Rev. Mater. Res* **50**, 155 (2020). Cited on page(s) 9 and 10
- [42] M. Acerce, D. Voiry and M. Chhowalla, 'Metallic 1T phase MoS₂ nanosheets as supercapacitor electrode materials', *Nat. Nanotechnol.* **10**, 313 (2015). Cited on page(s) 9
- [43] H. Li, Y. Li, A. Aljarb, Y. Shi and L.-J. Li, 'Epitaxial Growth of Two-Dimensional Layered Transition-Metal Dichalcogenides: Growth Mechanism, Controllability, and Scalability', *Chem. Rev.* **118**, 6134 (2018). Cited on page(s) 9
- [44] C. Backes, A. M. Abdelkader, C. Alonso, A. Andrieux-Ledier, R. Arenal, J. Azpeitia, N. Balakrishnan, L. Banszerus, J. Barjon and R. Bartali, 'Production and processing of graphene and related materials', *2D Mater.* **7**, 22001 (2020). Cited on page(s) 9 and 10
- [45] Z. Li, R. J. Young, C. Backes, W. Zhao, X. Zhang, A. A. Zhukov, E. Tillotson, A. P. Conlan, F. Ding, S. J. Haigh, K. S. Novoselov and J. N. Coleman, 'Mechanisms of Liquid-Phase Exfoliation for the Production of Graphene', *ACS Nano* **14**, 10976 (2020). Cited on page(s) 9
- [46] S. Wang, Y. Rong, Y. Fan, M. Pacios, H. Bhaskaran, K. He and J. H. Warner, 'Shape Evolution of Monolayer MoS₂ Crystals Grown by Chemical Vapor Deposition', *Chem. Mater.* **26**, 6371 (2014). Cited on page(s) 10

- [47] D. Dumcenco, D. Ovchinnikov, K. Marinov, P. Lazić, M. Gibertini, N. Marzari, O. L. Sanchez, Y.-C. Kung, D. Krasnozhan, M.-W. Chen, S. Bertolazzi, P. Gillet, A. Fontcuberta i Morral, A. Radenovic and A. Kis, 'Large-Area Epitaxial Monolayer MoS₂', *ACS Nano* **9**, 4611 (2015). Cited on page(s) 10
- [48] J. Zhou *et al.*, 'A library of atomically thin metal chalcogenides', *Nature* **556**, 355 (2018). Cited on page(s) 10, 11, and 13
- [49] J. Zhang, F. Wang, V. B. Shenoy, M. Tang and J. Lou, 'Towards controlled synthesis of 2D crystals by chemical vapor deposition (CVD)', *Mater. Today* **40**, 132 (2020). Cited on page(s) 10
- [50] J. Jiang, T. Xu, J. Lu, L. Sun and Z. Ni, 'Defect engineering in 2D materials: precise manipulation and improved functionalities', *Research* **2019**, (2019). Cited on page(s) 10
- [51] B A Joyce, 'Molecular beam epitaxy', *Rep. Prog. Phys.* **48**, 1637 (1985). Cited on page(s) 10
- [52] K. Saiki, K. Ueno, T. Shimada and A. Koma, 'Application of Van der Waals epitaxy to highly heterogeneous systems', *J. Cryst. Growth* **95**, 603 (1989). Cited on page(s) 10
- [53] A. Koma, K. Sunouchi and T. Miyajima, 'Fabrication and characterization of heterostructures with subnanometer thickness', *Microelectron. Eng.* **2**, 129 (1984). Cited on page(s) 10 and 12
- [54] A. Koma, K. Saiki and Y. Sato, 'Heteroepitaxy of a two-dimensional material on a three-dimensional material', *Appl. Surf. Sci.* **41-42**, 451 (1990). Cited on page(s) 10
- [55] S. Vishwanath, X. Liu, S. Rouvimov, P. C. Mende, A. Azcatl, S. McDonnell, R. M. Wallace, R. M. Feenstra, J. K. Furdyna and D. Jena, 'Comprehensive structural and optical characterization of MBE grown MoSe₂ on graphite, CaF₂ and graphene', *2D Mater.* **2**, 24007 (2015). Cited on page(s) 10
- [56] J.-P. Peng, J.-Q. Guan, H.-M. Zhang, C.-L. Song, L. Wang, K. He, Q.-K. Xue and X.-C. Ma, 'Molecular beam epitaxy growth and scanning tunneling microscopy study of TiSe₂ ultrathin films', *Phys. Rev. B* **91**, 121113 (2015). Cited on page(s) 10
- [57] D. Fu, X. Zhao, Y.-Y. Zhang, L. Li, H. Xu, A.-R. Jang, S. I. Yoon, P. Song, S. M. Poh and T. Ren, 'Molecular beam epitaxy of highly crystalline monolayer molybdenum disulfide on hexagonal boron nitride', *J. Am. Chem. Soc.* **139**, 9392 (2017). Cited on page(s) 10, 270, and 286
- [58] S. Tongay, D. S. Narang, J. Kang, W. Fan, C. Ko, A. V. Luce, K. X. Wang, J. Suh, K. D. Patel and V. M. Pathak, 'Two-dimensional semiconductor alloys: Monolayer Mo_{1-x}W_xSe₂', *Appl. Phys. Lett.* **104**, (2014). Cited on page(s) 11

Bibliography

- [59] K. Zhang, S. Feng, J. Wang, A. Azcatl, N. Lu, R. Addou, N. Wang, C. Zhou, J. Lerach and V. Bojan, 'Manganese doping of monolayer MoS₂: the substrate is critical', *Nano Lett.* **15**, 6586 (2015). Cited on page(s) 11
- [60] J. Wang, F. Sun, S. Yang, Y. Li, C. Zhao, M. Xu, Y. Zhang and H. Zeng, 'Robust ferromagnetism in Mn-doped MoS₂ nanostructures', *Appl. Phys. Lett.* **109**, (2016). Cited on page(s) 11
- [61] S. Qiao, X. Li, N. Wang, W. Ruan, C. Ye, P. Cai, Z. Hao, H. Yao, X. Chen and J. Wu, 'Mottness Collapse in 1T-TaS_{2-x}Se_x Transition-Metal Dichalcogenide: An Interplay between Localized and Itinerant Orbitals', *Phys. Rev. X* **7**, 41054 (2017). Cited on page(s) 11
- [62] A. Chaves, J. G. Azadani, H. Alsalman, D. R. Da Costa, R. Frisenda, A. J. Chaves, S. H. Song, Y. D. Kim, D. He and J. Zhou, 'Bandgap engineering of two-dimensional semiconductor materials', *npj 2D Mater. Appl.* **4**, 29 (2020). Cited on page(s) 11
- [63] S. Helveg, J. V. Lauritsen, E. Lægsgaard, I. Stensgaard, J. K. Nørskov, B. S. Clausen, H. Topsøe and F. Besenbacher, 'Atomic-Scale Structure of Single-Layer MoS₂ Nanoclusters', *Phys. Rev. Lett.* **84**, 951 (2000). Cited on page(s) 11
- [64] T. F. Jaramillo, K. P. Jørgensen, J. Bonde, J. H. Nielsen, S. Horch and I. Chorkendorff, 'Identification of active edge sites for electrochemical H₂ evolution from MoS₂ nanocatalysts', *Science* **317**, 100 (2007). Cited on page(s) 11 and 14
- [65] Y. Gao, Z. Liu, D.-M. Sun, L. Huang, L.-P. Ma, L.-C. Yin, T. Ma, Z. Zhang, X.-L. Ma, L.-M. Peng, H.-M. Cheng and W. Ren, 'Large-area synthesis of high-quality and uniform monolayer WS₂ on reusable Au foils', *Nat. Commun.* **6**, 8569 (2015). Cited on page(s) 11
- [66] P. Yang *et al.*, 'Epitaxial Growth of Centimeter-Scale Single-Crystal MoS₂ Monolayer on Au(111)', *ACS Nano* **14**, 5036 (2020). Cited on page(s) 11
- [67] C. E. Sanders, M. Dendzik, A. S. Ngankeu, A. Eich, A. Bruix, M. Bianchi, J. A. Miwa, B. Hammer, A. A. Khajetoorians and P. Hofmann, 'Crystalline and electronic structure of single-layer TaS₂', *Phys. Rev. B* **94**, 81404 (2016). Cited on page(s) 11 and 19
- [68] R.-M. Stan, S. K. Mahatha, M. Bianchi, C. E. Sanders, D. Curcio, P. Hofmann and J. A. Miwa, 'Epitaxial single-layer NbS₂ on Au(111): Synthesis, structure, and electronic properties', *Phys. Rev. Mater.* **3**, 44003 (2019). Cited on page(s) 11 and 19
- [69] Y. Y. Illarionov, G. Rzepa, M. Walzl, T. Knobloch, A. Grill, M. M. Furchi, T. Mueller and T. Grasser, 'The role of charge trapping in MoS₂/SiO₂ and MoS₂/hBN field-effect transistors', *2D Mater.* **3**, 035004 (2016). Cited on page(s) 11

- [70] Z. Yu, Z. Ong, Y. Pan, Y. Cui, R. Xin, Y. Shi, B. Wang, Y. Wu, T. Chen and Y. Zhang, 'Realization of room-temperature phonon-limited carrier transport in monolayer MoS₂ by dielectric and carrier screening', *Adv. Mater.* **28**, 547 (2016). Cited on page(s) 12, 16, 277, and 282
- [71] X. Cui, G.-H. Lee, Y. D. Kim, G. Arefe, P. Y. Huang, C.-H. Lee, D. A. Chenet, X. Zhang, L. Wang and F. Ye, 'Multi-terminal transport measurements of MoS₂ using a van der Waals heterostructure device platform', *Nat. Nanotechnol.* **10**, 534 (2015). Cited on page(s) 12
- [72] W. Zhou, X. Zou, S. Najmaei, Z. Liu, Y. Shi, J. Kong, J. Lou, P. M. Ajayan, B. I. Yakobson and J.-C. Idrobo, 'Intrinsic Structural Defects in Monolayer Molybdenum Disulfide', *Nano Lett.* **13**, 2615 (2013). Cited on page(s) 12 and 13
- [73] H. Qiu, T. Xu, Z. Wang, W. Ren, H. Nan, Z. Ni, Q. Chen, S. Yuan, F. Miao, F. Song, G. Long, Y. Shi, L. Sun, J. Wang and X. Wang, 'Hopping transport through defect-induced localized states in molybdenum disulphide', *Nat. Commun.* **4**, 2642 (2013). Cited on page(s) 12, 13, and 277
- [74] Y. Lin, R. Torsi, D. B. Geohegan, J. A. Robinson and K. Xiao, 'Controllable Thin-Film Approaches for Doping and Alloying Transition Metal Dichalcogenides Monolayers', *Adv. Sci.* **8**, 2004249 (2021). Cited on page(s) 12
- [75] D. K. Singh and G. Gupta, 'van der Waals epitaxy of transition metal dichalcogenides via molecular beam epitaxy: looking back and moving forward', *Mater. Adv.* **3**, 6142 (2022). Cited on page(s) 12
- [76] A. K. Geim and I. V. Grigorieva, 'Van der Waals heterostructures', *Nature* **499**, 419 (2013). Cited on page(s) 12
- [77] J. Coraux, A. T. N'Diaye, C. Busse and T. Michely, 'Structural coherency of graphene on Ir(111)', *Nano Lett.* **8**, 565 (2008). Cited on page(s) 12
- [78] J. Coraux, A. T. N'Diaye, M. Engler, C. Busse, D. Wall, N. Buckanie, F.-J. M. Zu Heringdorf, R. Van Gastel, B. Poelsema and T. Michely, 'Growth of graphene on Ir(111)', *New J. Phys.* **11**, 23006 (2009). Cited on page(s) 12
- [79] A. T. N'Diaye, J. Coraux, T. N. Plasa, C. Busse and T. Michely, 'Structure of epitaxial graphene on Ir (111)', *New J. Phys.* **10**, 43033 (2008). Cited on page(s) 12
- [80] I. Pletikosić, M. Kralj, P. Pervan, R. Brako, J. Coraux, A. T. N'Diaye, C. Busse and T. Michely, 'Dirac cones and minigaps for graphene on Ir(111)', *Phys. Rev. Lett.* **102**, 56808 (2009). Cited on page(s) 12
- [81] C. Busse, P. Lazić, R. Djemour, J. Coraux, T. Gerber, N. Atodiresei, V. Caciuc, R. Brako, A. T. N'Diaye, S. Blügel and J. Zegenhagen, 'Graphene on Ir (111): physisorption with chemical modulation', *Physical review letters* **107**, 36101 (2011). Cited on page(s) 12

Bibliography

- [82] C. Murray, W. Jolie, J. Fischer, J. Hall, C. Van Efferen, N. Ehlen, A. Grüneis, C. Busse and T. Michely, 'Comprehensive tunneling spectroscopy of quasifreestanding MoS₂ on graphene on Ir(111)', *Phys. Rev. B* **99**, (2019). Cited on page(s) 12, 28, 287, 289, 291, and 300
- [83] R. W. Siegel, 'Vacancy concentrations in metals', *J. Nucl. Mater.* **69-70**, 117 (1978). Cited on page(s) 12
- [84] F. Banhart, J. Kotakoski and A. V. Krasheninnikov, 'Structural Defects in Graphene', *ACS Nano* **5**, 26 (2011). Cited on page(s) 12
- [85] A. M. van der Zande, P. Y. Huang, D. A. Chenet, T. C. Berkelbach, Y. You, G.-H. Lee, T. F. Heinz, D. R. Reichman, D. A. Muller and J. C. Hone, 'Grains and grain boundaries in highly crystalline monolayer molybdenum disulphide', *Nat. Mater.* **12**, 554 (2013). Cited on page(s) 13
- [86] H. Nan, Z. Wang, W. Wang, Z. Liang, Y. Lu, Q. Chen, D. He, P. Tan, F. Miao, X. Wang, J. Wang and Z. Ni, 'Strong Photoluminescence Enhancement of MoS₂ through Defect Engineering and Oxygen Bonding', *ACS Nano* **8**, 5738 (2014). Cited on page(s) 13
- [87] Y.-M. He, G. Clark, J. R. Schaibley, Y. He, M.-C. Chen, Y.-J. Wei, X. Ding, Q. Zhang, W. Yao and X. Xu, 'Single quantum emitters in monolayer semiconductors', *Nat. Nanotechnol.* **10**, 497 (2015). Cited on page(s) 13
- [88] C. Chakraborty, L. Kinnischtzke, K. M. Goodfellow, R. Beams and A. N. Vamivakas, 'Voltage-controlled quantum light from an atomically thin semiconductor', *Nat. Nanotechnol.* **10**, 507 (2015). Cited on page(s) 13
- [89] G. Li, D. Zhang, Q. Qiao, Y. Yu, D. Peterson, A. Zafar, R. Kumar, S. Curtarolo, F. Hunte and S. Shannon, 'All the catalytic active sites of MoS₂ for hydrogen evolution', *J. Am. Chem. Soc.* **138**, 16632 (2016). Cited on page(s) 13
- [90] A. Avsar, A. Ciarrocchi, M. Pizzochero, D. Unuchek, O. V. Yazyev and A. Kis, 'Defect induced, layer-modulated magnetism in ultrathin metallic PtSe₂', *Nat. Nanotechnol.* **14**, 674 (2019). Cited on page(s) 13
- [91] R. Chua, J. Yang, X. He, X. Yu, W. Yu, F. Bussolotti, P. K. J. Wong, K. P. Loh, M. B. H. Breese, K. E. J. Goh, Y. L. Huang and A. T. S. Wee, 'Can Reconstructed Se-Deficient Line Defects in Monolayer VSe₂ Induce Magnetism?', *Adv. Mater.* **32**, 2000693 (2020). Cited on page(s) 13 and 269
- [92] K. Kaasbjerg, K. S. Thygesen and K. W. Jacobsen, 'Phonon-limited mobility in *n*-type single-layer MoS₂ from first principles', *Phys. Rev. B* **85**, 115317 (2012). Cited on page(s) 13

- [93] S. Najmaei, M. Amani, M. L. Chin, Z. Liu, A. G. Birdwell, T. P. O'Regan, P. M. Ajayan, M. Dubey and J. Lou, 'Electrical Transport Properties of Polycrystalline Monolayer Molybdenum Disulfide', *ACS Nano* **8**, 7930 (2014). Cited on page(s) 13
- [94] T. H. Ly, D. J. Perello, J. Zhao, Q. Deng, H. Kim, G. H. Han, S. H. Chae, H. Y. Jeong and Y. H. Lee, 'Misorientation-angle-dependent electrical transport across molybdenum disulfide grain boundaries', *Nat. Commun.* **7**, 10426 (2016). Cited on page(s) 13
- [95] Y. L. Huang, Y. Chen, W. Zhang, S. Y. Quek, C.-H. Chen, L.-J. Li, W.-T. Hsu, W.-H. Chang, Y. J. Zheng, W. Chen and A. T. S. Wee, 'Bandgap tunability at single-layer molybdenum disulphide grain boundaries', *Nat. Commun.* **6**, 6298 (2015). Cited on page(s) 13 and 28
- [96] X. Liu, I. Balla, H. Bergeron and M. C. Hersam, 'Point Defects and Grain Boundaries in Rotationally Commensurate MoS₂ on Epitaxial Graphene', *J. Phys. Chem. C* **120**, 20798 (2016). Cited on page(s) 13
- [97] H. Liu, L. Jiao, F. Yang, Y. Cai, X. Wu, W. Ho, C. Gao, J. Jia, N. Wang and H. Fan, 'Dense network of one-dimensional midgap metallic modes in monolayer MoSe₂ and their spatial undulations', *Phys. Rev. Lett.* **113**, 66105 (2014). Cited on page(s) 13
- [98] X. Zou, Y. Liu and B. I. Yakobson, 'Predicting Dislocations and Grain Boundaries in Two-Dimensional Metal-Disulfides from the First Principles', *Nano Lett.* **13**, 253 (2013). Cited on page(s) 13
- [99] M. Gibertini and N. Marzari, 'Emergence of One-Dimensional Wires of Free Carriers in Transition-Metal-Dichalcogenide Nanostructures', *Nano Lett.* **15**, 6229 (2015). Cited on page(s) 13
- [100] C. Murray, C. van Efferen, W. Jolie, J. A. Fischer, J. Hall, A. Rosch, A. V. Krasheninnikov, H.-P. Komsa and T. Michely, 'Band bending and valence band quantization at line defects in MoS₂', *ACS Nano* **14**, 9176 (2020). Cited on page(s) 13 and 300
- [101] S. Barja *et al.*, 'Charge density wave order in 1D mirror twin boundaries of single-layer MoSe₂', *Nat. Phys.* **12**, 751 (2016). Cited on page(s) 13
- [102] Y. Ma, H. C. Diaz, J. Avila, C. Chen, V. Kalappattil, R. Das, M.-H. Phan, T. Čadež, J. M. P. Carmelo, M. C. Asensio and M. Batzill, 'Angle resolved photoemission spectroscopy reveals spin charge separation in metallic MoSe₂ grain boundary', *Nat. Commun.* **8**, 14231 (2017). Cited on page(s) 13
- [103] W. Jolie, C. Murray, P. S. Weiß, J. Hall, F. Portner, N. Atodiresei, A. V. Krasheninnikov, C. Busse, H.-P. Komsa and A. Rosch, 'Tomonaga-Luttinger liquid in a box: electrons confined within MoS₂ mirror-twin boundaries', *Phys. Rev. X* **9**, 11055 (2019). Cited on page(s) 13 and 290

Bibliography

- [104] T. Zhu *et al.*, 'Imaging gate-tunable Tomonaga–Luttinger liquids in 1H-MoSe₂ mirror twin boundaries', *Nat. Mater.* **21**, 748 (2022). Cited on page(s) 13
- [105] M. R. Vazirisereshk, A. Martini, D. A. Strubbe and M. Z. Baykara, 'Solid lubrication with MoS₂: a review', *Lubricants* **7**, 57 (2019). Cited on page(s) 14
- [106] E. Furimsky, 'Role of MoS₂ and WS₂ in hydrodesulfurization', *Catal Rev Sci Eng* **22**, 371 (1980). Cited on page(s) 14
- [107] Q. Ding, B. Song, P. Xu and S. Jin, 'Efficient electrocatalytic and photoelectrochemical hydrogen generation using MoS₂ and related compounds', *Chem* **1**, 699 (2016). Cited on page(s) 14
- [108] M. Bernardi, M. Palummo and J. C. Grossman, 'Extraordinary Sunlight Absorption and One Nanometer Thick Photovoltaics Using Two-Dimensional Monolayer Materials', *Nano Lett.* **13**, 3664 (2013). Cited on page(s) 14
- [109] M. Fontana, T. Deppe, A. K. Boyd, M. Rinzan, A. Y. Liu, M. Paranjape and P. Barbara, 'Electron-hole transport and photovoltaic effect in gated MoS₂ Schottky junctions', *Sci. Rep.* **3**, 1634 (2013). Cited on page(s) 14
- [110] K. Chang and W. Chen, 'In situ synthesis of MoS₂/graphene nanosheet composites with extraordinarily high electrochemical performance for lithium ion batteries', *ChemComm* **47**, 4252 (2011). Cited on page(s) 14
- [111] H. Liu, D. Su, R. Zhou, B. Sun, G. Wang and S. Z. Qiao, 'Highly ordered mesoporous MoS₂ with expanded spacing of the (002) crystal plane for ultrafast lithium ion storage', *Adv. Energy Mater.* **2**, 970 (2012). Cited on page(s) 14
- [112] B. Radisavljevic, A. Radenovic, J. Brivio, V. Giacometti and A. Kis, 'Single-layer MoS₂ transistors', *Nat. Nanotechnol.* **6**, 147 (2011). Cited on page(s) 14
- [113] S. B. Desai, S. R. Madhvapathy, A. B. Sachid, J. P. Llinas, Q. Wang, G. H. Ahn, G. Pitner, M. J. Kim, J. Bokor and C. Hu, 'MoS₂ transistors with 1-nanometer gate lengths', *Science* **354**, 99 (2016). Cited on page(s) 14
- [114] F. Wu, H. Tian, Y. Shen, Z. Hou, J. Ren, G. Gou, Y. Sun, Y. Yang and T.-L. Ren, 'Vertical MoS₂ transistors with sub-1-nm gate lengths', *Nature* **603**, 259 (2022). Cited on page(s) 14
- [115] A. Kuc, N. Zibouche and T. Heine, 'Influence of quantum confinement on the electronic structure of the transition metal sulfide *TS₂*', *Phys. Rev. B* **83**, 245213 (2011). Cited on page(s) 14, 15, and 17

- [116] J. K. Ellis, M. J. Lucero and G. E. Scuseria, 'The indirect to direct band gap transition in multilayered MoS₂ as predicted by screened hybrid density functional theory', *Appl. Phys. Lett.* **99**, 261908 (2011). Cited on page(s) 14, 15, and 17
- [117] N. Saigal, V. Sugunakar and S. Ghosh, 'Exciton binding energy in bulk MoS₂: A reassessment', *Appl. Phys. Lett.* **108**, 132105 (2016). Cited on page(s) 14
- [118] K. Hippalgaonkar, Y. Wang, Y. Ye, D. Y. Qiu, H. Zhu, Y. Wang, J. Moore, S. G. Louie and X. Zhang, 'High thermoelectric power factor in two-dimensional crystals of MoS₂', *Phys. Rev. B* **95**, 115407 (2017). Cited on page(s) 15
- [119] T. Cao, G. Wang, W. Han, H. Ye, C. Zhu, J. Shi, Q. Niu, P. Tan, E. Wang and B. Liu, 'Valley-selective circular dichroism of monolayer molybdenum disulphide', *Nat. Commun.* **3**, 887 (2012). Cited on page(s) 14
- [120] T. Li and G. Galli, 'Electronic properties of MoS₂ nanoparticles', *J. Phys. Chem. C* **111**, 16192 (2007). Cited on page(s) 15
- [121] S. Lebegue and O. Eriksson, 'Electronic structure of two-dimensional crystals from ab initio theory', *Phys. Rev. B* **79**, 115409 (2009). Cited on page(s) 15
- [122] Z. Y. Zhu, Y. C. Cheng and U. Schwingenschlögl, 'Giant spin-orbit-induced spin splitting in two-dimensional transition-metal dichalcogenide semiconductors', *Phys. Rev. B* **84**, 153402 (2011). Cited on page(s) 15
- [123] J. E. Padilha, H. Peelaers, A. Janotti and C. G. Van de Walle, 'Nature and evolution of the band-edge states in MoS₂: From monolayer to bulk', *Phys. Rev. B* **90**, 205420 (2014). Cited on page(s) 16
- [124] L. Du, T. Zhang, M. Liao, G. Liu, S. Wang, R. He, Z. Ye, H. Yu, R. Yang, D. Shi, Y. Yao and G. Zhang, 'Temperature-driven evolution of critical points, interlayer coupling, and layer polarization in bilayer MoS₂', *Phys. Rev. B* **97**, 165410 (2018). Cited on page(s) 16
- [125] T. Cheiwchanamngij and W. R. L. Lambrecht, 'Quasiparticle band structure calculation of monolayer, bilayer, and bulk MoS₂', *Phys. Rev. B* **85**, 205302 (2012). Cited on page(s) 16, 28, and 287
- [126] A. Ramasubramaniam, 'Large excitonic effects in monolayers of molybdenum and tungsten dichalcogenides', *Phys. Rev. B* **86**, 115409 (2012). Cited on page(s) 16 and 27
- [127] K. He, N. Kumar, L. Zhao, Z. Wang, K. F. Mak, H. Zhao and J. Shan, 'Tightly Bound Excitons in Monolayer WSe₂', *Phys. Rev. Lett.* **113**, 26803 (2014). Cited on page(s) 16

Bibliography

- [128] A. Chernikov, C. Ruppert, H. M. Hill, A. F. Rigosi and T. F. Heinz, 'Population inversion and giant bandgap renormalization in atomically thin WS₂ layers', *Nat. Photonics* **9**, 466 (2015). Cited on page(s) 16
- [129] G. Wang, A. Chernikov, M. M. Glazov, T. F. Heinz, X. Marie, T. Amand and B. Urbaszek, 'Colloquium: Excitons in atomically thin transition metal dichalcogenides', *Rev. Mod. Phys.* **90**, 21001 (2018). Cited on page(s) 16
- [130] S. J. Sandoval, D. Yang, R. F. Frindt and J. C. Irwin, 'Raman study and lattice dynamics of single molecular layers of MoS₂', *Phys. Rev. B* **44**, 3955 (1991). Cited on page(s) 16
- [131] Y.-C. Lin, D. O. Dumcenco, Y.-S. Huang and K. Suenaga, 'Atomic mechanism of the semiconducting-to-metallic phase transition in single-layered MoS₂', *Nat. Nanotechnol.* **9**, 391 (2014). Cited on page(s) 16
- [132] Y. Kang, S. Najmaei, Z. Liu, Y. Bao, Y. Wang, X. Zhu, N. J. Halas, P. Nordlander, P. M. Ajayan and J. Lou, 'Plasmonic hot electron induced structural phase transition in a MoS₂ monolayer', *Adv. Mater.* **26**, 6467 (2014). Cited on page(s) 16
- [133] D. Voiry, A. Goswami, R. Koppera, C. d. C. C. e. Silva, D. Kaplan, T. Fujita, M. Chen, T. Asefa and M. Chhowalla, 'Covalent functionalization of monolayered transition metal dichalcogenides by phase engineering', *Nat. Chem.* **7**, 45 (2015). Cited on page(s) 16
- [134] G. Eda, H. Yamaguchi, D. Voiry, T. Fujita, M. Chen and M. Chhowalla, 'Photoluminescence from Chemically Exfoliated MoS₂', *Nano Lett.* **11**, 5111 (2011). Cited on page(s) 16
- [135] M. A. Lukowski, A. S. Daniel, F. Meng, A. Forticaux, L. Li and S. Jin, 'Enhanced Hydrogen Evolution Catalysis from Chemically Exfoliated Metallic MoS₂ Nanosheets', *J. Am. Chem. Soc.* **135**, 10274 (2013). Cited on page(s) 16
- [136] H. L. Zhuang, M. D. Johannes, A. K. Singh and R. G. Hennig, 'Doping-controlled phase transitions in single-layer MoS₂', *Phys. Rev. B* **96**, 165305 (2017). Cited on page(s) 16, 264, and 270
- [137] S. Shi, Z. Sun and Y. H. Hu, 'Synthesis, stabilization and applications of 2-dimensional 1T metallic MoS₂', *J. Mater. Chem.* **6**, 23932 (2018). Cited on page(s) 16
- [138] H. Schmidt, S. Wang, L. Chu, M. Toh, R. Kumar, W. Zhao, A. H. Castro Neto, J. Martin, S. Adam, B. Özyilmaz and G. Eda, 'Transport Properties of Monolayer MoS₂ Grown by Chemical Vapor Deposition', *Nano Lett.* **14**, 1909 (2014). Cited on page(s) 16, 277, and 282
- [139] S. Barja *et al.*, 'Identifying substitutional oxygen as a prolific point defect in monolayer transition metal dichalcogenides', *Nat. Commun.* **10**, 3382 (2019). Cited on page(s) 16, 277, and 286

- [140] B. Radisavljevic and A. Kis, 'Mobility engineering and a metal-insulator transition in monolayer MoS₂', *Nat. Mater.* **12**, 815 (2013). Cited on page(s) 16, 277, and 282
- [141] B. H. Moon, J. J. Bae, M.-K. Joo, H. Choi, G. H. Han, H. Lim and Y. H. Lee, 'Soft Coulomb gap and asymmetric scaling towards metal-insulator quantum criticality in multilayer MoS₂', *Nat. Commun.* **9**, 2052 (2018). Cited on page(s) 16, 277, and 282
- [142] B. W. H. Baugher, H. O. H. Churchill, Y. Yang and P. Jarillo-Herrero, 'Intrinsic Electronic Transport Properties of High-Quality Monolayer and Bilayer MoS₂', *Nano Lett.* **13**, 4212 (2013). Cited on page(s) 16, 277, and 282
- [143] D. Jariwala, V. K. Sangwan, D. J. Late, J. E. Johns, V. P. Dravid, T. J. Marks, L. J. Lauhon and M. C. Hersam, 'Band-like transport in high mobility unencapsulated single-layer MoS₂ transistors', *Appl. Phys. Lett.* **102**, 173107 (2013). Cited on page(s) 16
- [144] S. Ghatak, A. N. Pal and A. Ghosh, 'Nature of Electronic States in Atomically Thin MoS₂ Field-Effect Transistors', *ACS Nano* **5**, 7707 (2011). Cited on page(s) 16
- [145] Y. Ge and A. Y. Liu, 'Phonon-mediated superconductivity in electron-doped single-layer MoS₂: A first-principles prediction', *Phys. Rev. B* **87**, 241408 (2013). Cited on page(s) 16, 17, 270, 277, and 286
- [146] Y. Fu *et al.*, 'Gated tuned superconductivity and phonon softening in monolayer and bilayer MoS₂', *npj Quantum Mater.* **2**, 52 (2017). Cited on page(s) 16
- [147] J. M. Lu, O. Zheliuk, I. Leermakers, N. F. Q. Yuan, U. Zeitler, K. T. Law and J. T. Ye, 'Evidence for two-dimensional Ising superconductivity in gated MoS₂', *Science* **350**, 1353 (2015). Cited on page(s) 16
- [148] D. Costanzo, H. Zhang, B. A. Reddy, H. Berger and A. F. Morpurgo, 'Tunnelling spectroscopy of gate-induced superconductivity in MoS₂', *Nat. Nanotechnol.* **13**, 483 (2018). Cited on page(s) 16
- [149] F. Caruso, P. Amsalem, J. Ma, A. Aljarb, T. Schultz, M. Zacharias, V. Tung, N. Koch and C. Draxl, 'Two-dimensional plasmonic polarons in *n*-doped monolayer MoS₂', *Phys. Rev. B* **103**, 205152 (2021). Cited on page(s) 17 and 277
- [150] E. Khestanova *et al.*, 'Robustness of Momentum-Indirect Interlayer Excitons in MoS₂/WSe₂ Heterostructure against Charge Carrier Doping', *ACS Photonics* **10**, 1159 (2023). Cited on page(s) 17 and 276
- [151] T. Wang, S. Chen, H. Pang, H. Xue and Y. Yu, 'MoS₂-based nanocomposites for electrochemical energy storage', *Adv. Sci.* **4**, 1600289 (2017). Cited on page(s) 17

Bibliography

- [152] W. Li, H. M. Kheimeh Sari and X. Li, 'Emerging Layered Metallic Vanadium Disulfide for Rechargeable Metal-Ion Batteries: Progress and Opportunities', *ChemSusChem* **13**, 1172 (2020). Cited on page(s) 17, 18, and 271
- [153] J. Berges, 'Private communications', 2020. Cited on page(s) 17
- [154] Y. Jing, Z. Zhou, C. R. Cabrera and Z. Chen, 'Metallic VS₂ Monolayer: A Promising 2D Anode Material for Lithium Ion Batteries', *J. Phys. Chem. C* **117**, 25409 (2013). Cited on page(s) 18
- [155] D. B. Putungan, S.-H. Lin and J.-L. Kuo, 'Metallic VS₂ monolayer polytypes as potential sodium-ion battery anode via ab initio random structure searching', *ACS Appl. Mater. Interfaces* **8**, 18754 (2016). Cited on page(s) 18
- [156] J. Feng, X. Sun, C. Wu, L. Peng, C. Lin, S. Hu, J. Yang and Y. Xie, 'Metallic Few-Layered VS₂ Ultrathin Nanosheets: High Two-Dimensional Conductivity for In-Plane Supercapacitors', *J. Am. Chem. Soc.* **133**, 17832 (2011). Cited on page(s) 18 and 268
- [157] J. Feng, L. Peng, C. Wu, X. Sun, S. Hu, C. Lin, J. Dai, J. Yang and Y. Xie, 'Giant Moisture Responsiveness of VS₂ Ultrathin Nanosheets for Novel Touchless Positioning Interface', *Adv. Mater.* **24**, 1969 (2012). Cited on page(s) 18
- [158] L. Li *et al.*, 'Vanadium disulfide flakes with nanolayered titanium disulfide coating as cathode materials in lithium-ion batteries', *Nat. Commun.* **10**, 1764 (2019). Cited on page(s) 18
- [159] H. Liang, H. Shi, D. Zhang, F. Ming, R. Wang, J. Zhuo and Z. Wang, 'Solution Growth of Vertical VS₂ Nanoplate Arrays for Electrocatalytic Hydrogen Evolution', *Chem. Mater.* **28**, 5587 (2016). Cited on page(s) 18
- [160] Y. Qu, M. Shao, Y. Shao, M. Yang, J. Xu, C. T. Kwok, X. Shi, Z. Lu and H. Pan, 'Ultra-high electrocatalytic activity of VS₂ nanoflowers for efficient hydrogen evolution reaction', *J. Mater. Chem. A* **5**, 15080 (2017). Cited on page(s) 18
- [161] H. Zhang, L.-M. Liu and W.-M. Lau, 'Dimension-dependent phase transition and magnetic properties of VS₂', *J. Mater. Chem. A* **1**, 10821 (2013). Cited on page(s) 18
- [162] H. L. Zhuang and R. G. Hennig, 'Stability and magnetism of strongly correlated single-layer VS₂', *Phys. Rev. B* **93**, 54429 (2016). Cited on page(s) 18
- [163] M. Aras, Ç. Kılıç and S. Ciraci, 'Magnetic ground state in FeTe₂, VS₂ and NiTe₂ monolayers: Antiparallel magnetic moments at chalcogen atoms', *Phys. Rev. B* **101**, 54429 (2020). Cited on page(s) 18
- [164] W. Bensch and J. Koy, 'The single crystal structure of V₅S₈ determined at two different temperatures: anisotropic changes of the metal atom network', *Inorganica Chim. Acta* **206**, 221 (1993). Cited on page(s) 18

- [165] H. Moutaabbid, Y. Le Godec, D. Taverna, B. Baptiste, Y. Klein, G. Louprias and A. Gauzzi, 'High-Pressure Control of Vanadium Self-Intercalation and Enhanced Metallic Properties in $1T-V_{1+x}S_2$ Single Crystals', *Inorg. Chem.* **55**, 6481 (2016). Cited on page(s) 18 and 19
- [166] D. W. Murphy, C. Cros, F. J. Di Salvo and J. V. Waszczak, 'Preparation and properties of Li_xVS_2 ($0 \leq x \leq 1$)', *Inorg. Chem.* **16**, 3027 (1977). Cited on page(s) 18, 19, and 268
- [167] T. Tsuda, H. Yasuoka, Y. Kitaoka and F. J. Di Salvo, '51V NMR study of the phase transition in $1T-VS_2$ ', *J. Magn. Magn. Mater.* **31-34**, 1101 (1983). Cited on page(s) 19 and 268
- [168] X. Sun, T. Yao, Z. Hu, Y. Guo, Q. Liu, S. Wei and C. Wu, 'In situ unravelling structural modulation across the charge-density-wave transition in vanadium disulfide', *Phys. Chem. Chem. Phys.* **17**, 13333 (2015). Cited on page(s) 19
- [169] M. Mulazzi, A. Chainani, N. Katayama, R. Eguchi, M. Matsunami, H. Ohashi, Y. Senba, M. Nohara, M. Uchida, H. Takagi and S. Shin, 'Absence of nesting in the charge-density-wave system $1T-VS_2$ as seen by photoelectron spectroscopy', *Phys. Rev. B* **82**, 75130 (2010). Cited on page(s) 19
- [170] A. Gauzzi, A. Sellam, G. Rousse, Y. Klein, D. Taverna, P. Giura, M. Calandra, G. Louprias, F. Gozzo, E. Gilioli, F. Bolzoni, G. Allodi, R. De Renzi, G. L. Calestani and P. Roy, 'Possible phase separation and weak localization in the absence of a charge-density wave in single-phase $1T-VS_2$ ', *Phys. Rev. B* **89**, 235125 (2014). Cited on page(s) 19
- [171] S.-H. Lee, Y. C. Park, J. Chae, G. Kim, H. J. Kim, B. K. Choi, I. H. Lee, Y. J. Chang, S.-H. Chun and M. Jung, 'Strong electron-phonon coupling driven charge density wave states in stoichiometric $1T-VS_2$ crystals', *J. Mater. Chem. C* **10**, 16657 (2022). Cited on page(s) 19
- [172] T. Kawakami, K. Sugawara, H. Oka, K. Nakayama, K. Yaegashi, S. Souma, T. Takahashi, T. Fukumura and T. Sato, 'Charge-density wave associated with higher-order Fermi-surface nesting in monolayer VS_2 ', *npj 2D Mater. Appl.* **7**, 35 (2023). Cited on page(s) 19
- [173] X. Wang, L. Ma, C. Wang, J. Wang, J. Guo, R. Tang, J. Zhu and G. Zou, 'Seed Engineering toward Layer-Regulated Growth of Magnetic Semiconductor VS_2 ', *Adv. Funct. Mater.* **33**, 2213295 (2023). Cited on page(s) 19
- [174] F. Giustino, 'Electron-phonon interactions from first principles', *Rev. Mod. Phys.* **89**, 15003 (2017). Cited on page(s) 21, 24, and 275
- [175] C. Franchini, M. Reticcioli, M. Setvin and U. Diebold, 'Polarons in materials', *Nat. Rev. Mater.* **6**, 560 (2021). Cited on page(s) 21, 24, 25, 274, and 275
- [176] K. Rossnagel, 'On the origin of charge-density waves in select layered transition-metal dichalcogenides', *J. Condens. Matter Phys.* **23**, 213001 (2011). Cited on page(s) 21, 23, 25, 26, 264, 265, and 267

Bibliography

- [177] M. Ternes, A. J. Heinrich and W.-D. Schneider, 'Spectroscopic manifestations of the Kondo effect on single adatoms', *J. Phys. Condens. Matter* **21**, 53001 (2008). Cited on page(s) 21 and 30
- [178] L. D. Landau, 'Electron motion in crystal lattices', *Phys. Z. Sowjet.* **3**, 664 (1933). Cited on page(s) 22
- [179] T. Holstein, 'Studies of polaron motion: Part I. The molecular-crystal model', *Ann. Phys.* **8**, 325 (1959). Cited on page(s) 23
- [180] M. Capone, W. Stephan and M. Grilli, 'Small-polaron formation and optical absorption in Su-Schrieffer-Heeger and Holstein models', *Phys. Rev. B* **56**, 4484 (1997). Cited on page(s) 23
- [181] D. I. Khomskii, 'Basic aspects of the quantum theory of solids: order and elementary excitations' (Cambridge university press, No address available, 2010). Cited on page(s) 23
- [182] E. Pastor, J.-S. Park, L. Steier, S. Kim, M. Grätzel, J. R. Durrant, A. Walsh and A. A. Bakulin, 'In situ observation of picosecond polaron self-localisation in α -Fe₂O₃ photoelectrochemical cells', *Nat. Commun.* **10**, 3962 (2019). Cited on page(s) 23
- [183] D. Emin, 'Polarons' (Cambridge University Press, No address available, 2013). Cited on page(s) 24
- [184] T. Valla, A. V. Fedorov, P. D. Johnson and S. L. Hulbert, 'Many-Body Effects in Angle-Resolved Photoemission: Quasiparticle Energy and Lifetime of a Mo(110) Surface State', *Phys. Rev. Lett.* **83**, 2085 (1999). Cited on page(s) 24 and 275
- [185] P. Garcia-Goiricelaya, J. Lafuente-Bartolome, I. G. Gurtubay and A. Eiguren, 'Long-living carriers in a strong electron-phonon interacting two-dimensional doped semiconductor', *Commun. Phys.* **2**, 81 (2019). Cited on page(s) 24 and 275
- [186] S. Moser, L. Moreschini, J. Jaćimović, O. S. Barišić, H. Berger, A. Magrez, Y. J. Chang, K. S. Kim, A. Bostwick and E. Rotenberg, 'Tunable polaronic conduction in anatase TiO₂', *Phys. Rev. Lett.* **110**, 196403 (2013). Cited on page(s) 24 and 275
- [187] C. Chen, J. Avila, E. Frantzeskakis, A. Levy and M. C. Asensio, 'Observation of a two-dimensional liquid of Fröhlich polarons at the bare SrTiO₃ surface', *Nat. Commun.* **6**, 8585 (2015). Cited on page(s) 24 and 275
- [188] C. Cancellieri, A. S. Mishchenko, U. Aschauer, A. Filippetti, C. Faber, O. S. Barišić, V. A. Rogalev, T. Schmitt, N. Nagaosa and V. N. Strocov, 'Polaronic metal state at the LaAlO₃/SrTiO₃ interface', *Nat. Commun.* **7**, 10386 (2016). Cited on page(s) 24 and 275

- [189] S. Pekar, 'Local quantum states of electrons in an ideal ion crystal', *Zh. Eksp. Teor. Fiz.* **16**, 341 (1946). Cited on page(s) 24
- [190] W. H. Sio, C. Verdi, S. Ponc e and F. Giustino, 'Ab initio theory of polarons: Formalism and applications', *Phys. Rev. B* **99**, 235139 (2019). Cited on page(s) 25
- [191] W. H. Sio, C. Verdi, S. Ponc e and F. Giustino, 'Polarons from first principles, without supercells', *Phys. Rev. Lett.* **122**, 246403 (2019). Cited on page(s) 25
- [192] W. H. Sio and F. Giustino, 'Polarons in two-dimensional atomic crystals', *Nat. Phys.* **19**, 629 (2023). Cited on page(s) 25 and 276
- [193] S.-K. Chan and V. Heine, 'Spin density wave and soft phonon mode from nesting Fermi surfaces', *J. Phys. F: Met. Phys.* **3**, 795 (1973). Cited on page(s) 25
- [194] X. Zhu, J. Guo, J. Zhang and E. W. Plummer, 'Misconceptions associated with the origin of charge density waves', *Adv. Phys.: X* **2**, 622 (2017). Cited on page(s) 26 and 264
- [195] M. D. Johannes and I. I. Mazin, 'Fermi surface nesting and the origin of charge density waves in metals', *Phys. Rev. B* **77**, 165135 (2008). Cited on page(s) 25, 26, and 264
- [196] A. Raja *et al.*, 'Coulomb engineering of the bandgap and excitons in two-dimensional materials', *Nat. Commun.* **8**, 15251 (2017). Cited on page(s) 27
- [197] M. M. Ugeda, A. J. Bradley, S.-F. Shi, F. H. da Jornada, Y. Zhang, D. Y. Qiu, W. Ruan, S.-K. Mo, Z. Hussain, Z.-X. Shen, F. Wang, S. G. Louie and M. F. Crommie, 'Giant bandgap renormalization and excitonic effects in a monolayer transition metal dichalcogenide semiconductor', *Nat. Mater.* **13**, 1091 (2014). Cited on page(s) 27, 28, and 271
- [198] J. P. Echeverry, B. Urbaszek, T. Amand, X. Marie and I. C. Gerber, 'Splitting between bright and dark excitons in transition metal dichalcogenide monolayers', *Phys. Rev. B* **93**, 121107 (2016). Cited on page(s) 27
- [199] K. F. Mak, K. He, C. Lee, G. H. Lee, J. Hone, T. F. Heinz and J. Shan, 'Tightly bound trions in monolayer MoS₂', *Nat. Mater.* **12**, 207 (2013). Cited on page(s) 27
- [200] Y. Lin, X. Ling, L. Yu, S. Huang, A. L. Hsu, Y.-H. Lee, J. Kong, M. S. Dresselhaus and T. Palacios, 'Dielectric Screening of Excitons and Trions in Single-Layer MoS₂', *Nano Lett.* **14**, 5569 (2014). Cited on page(s) 27
- [201] W. Liu, B. Lee, C. H. Naylor, H.-S. Ee, J. Park, A. T. C. Johnson and R. Agarwal, 'Strong Exciton-Plasmon Coupling in MoS₂ Coupled with Plasmonic Lattice', *Nano Lett.* **16**, 1262 (2016). Cited on page(s) 27

Bibliography

- [202] W. Jin *et al.*, 'Observation of the polaronic character of excitons in a two-dimensional semi-conducting magnet CrI_3 ', *Nat. Commun.* **11**, 4780 (2020). Cited on page(s) 27
- [203] B. Datta, M. Khatoniar, P. Deshmukh, F. Thouin, R. Bushati, S. De Liberato, S. K. Cohen and V. M. Menon, 'Highly nonlinear dipolar exciton-polaritons in bilayer MoS_2 ', *Nat. Commun.* **13**, 6341 (2022). Cited on page(s) 27
- [204] C. Jin, E. C. Regan, A. Yan, M. Iqbal Bakti Utama, D. Wang, S. Zhao, Y. Qin, S. Yang, Z. Zheng, S. Shi, K. Watanabe, T. Taniguchi, S. Tongay, A. Zettl and F. Wang, 'Observation of moiré excitons in WSe_2/WS_2 heterostructure superlattices', *Nature* **567**, 76 (2019). Cited on page(s) 27, 271, and 287
- [205] E. M. Alexeev *et al.*, 'Resonantly hybridized excitons in moiré superlattices in van der Waals heterostructures', *Nature* **567**, 81 (2019). Cited on page(s) 27, 271, and 287
- [206] K. Tran *et al.*, 'Evidence for moiré excitons in van der Waals heterostructures', *Nature* **567**, 71 (2019). Cited on page(s) 27, 271, and 287
- [207] K. S. Thygesen, 'Calculating excitons, plasmons, and quasiparticles in 2D materials and van der Waals heterostructures', *2D Mater.* **4**, 22004 (2017). Cited on page(s) 27
- [208] X. Liu, I. Balla, H. Bergeron, G. P. Campbell, M. J. Bedzyk and M. C. Hersam, 'Rotationally Commensurate Growth of MoS_2 on Epitaxial Graphene', *ACS Nano* **10**, 1067 (2016). Cited on page(s) 28
- [209] J. Shi, X. Zhou, G.-F. Han, M. Liu, D. Ma, J. Sun, C. Li, Q. Ji, Y. Zhang, X. Song, X.-Y. Lang, Q. Jiang, Z. Liu and Y. Zhang, 'Narrow-Gap Quantum Wires Arising from the Edges of Monolayer MoS_2 Synthesized on Graphene', *Adv. Mater. Interfaces* **3**, 1600332 (2016). Cited on page(s) 28
- [210] C. Zhang, A. Johnson, C.-L. Hsu, L.-J. Li and C.-K. Shih, 'Direct Imaging of Band Profile in Single Layer MoS_2 on Graphite: Quasiparticle Energy Gap, Metallic Edge States, and Edge Band Bending', *Nano Lett.* **14**, 2443 (2014). Cited on page(s) 28
- [211] C.-I. Lu, C. J. Butler, J.-K. Huang, C.-R. Hsing, H.-H. Yang, Y.-H. Chu, C.-H. Luo, Y.-C. Sun, S.-H. Hsu, K.-H. O. Yang, C.-M. Wei, L.-J. Li and M.-T. Lin, 'Graphite edge controlled registration of monolayer MoS_2 crystal orientation', *Appl. Phys. Lett.* **106**, 181904 (2015). Cited on page(s) 28
- [212] H. Shi, H. Pan, Y.-W. Zhang and B. I. Yakobson, 'Quasiparticle band structures and optical properties of strained monolayer MoS_2 and WS_2 ', *Phys. Rev. B* **87**, 155304 (2013). Cited on page(s) 28 and 287

- [213] W. J. De Haas, J. De Boer and G. J. Van den Berg, 'The electrical resistance of gold, copper and lead at low temperatures', *Physica* **1**, 1115 (1934). Cited on page(s) 28
- [214] J. Kondo, 'Resistance minimum in dilute magnetic alloys', *Prog. Theor. Phys.* **32**, 37 (1964). Cited on page(s) 28
- [215] L. Kouwenhoven and L. Glazman, 'Revival of the Kondo effect', *Phys. World* **14**, 33 (2001). Cited on page(s) 29
- [216] H. R. Krishna-murthy, J. W. Wilkins and K. G. Wilson, 'Renormalization-group approach to the Anderson model of dilute magnetic alloys. I. Static properties for the symmetric case', *Phys. Rev. B* **21**, 1003 (1980). Cited on page(s) 29 and 30
- [217] P. W. Anderson, 'Localized Magnetic States in Metals', *Phys. Rev.* **124**, 41 (1961). Cited on page(s) 29
- [218] J. R. Schrieffer and P. A. Wolff, 'Relation between the anderson and kondo hamiltonians', *Phys. Rev.* **149**, 491 (1966). Cited on page(s) 29
- [219] A. C. Hewson, 'The Kondo problem to heavy fermions' (Cambridge university press, No address available, 1997), No. 2. Cited on page(s) 29
- [220] F. D. M. Haldane, 'Theory of the atomic limit of the Anderson model. I. Perturbation expansions re-examined', *J. Phys. C: Solid State Phys.* **11**, 5015 (1978). Cited on page(s) 30
- [221] J. Hall, Dissertation, 2019. Cited on page(s) 33
- [222] W. Jolie, Dissertation, 2017. Cited on page(s) 117
- [223] X. Zhu, Y. Cao, J. Zhang, E. W. Plummer and J. Guo, 'Classification of charge density waves based on their nature', *Proc. Natl. Acad. Sci. U.S.A.* **112**, 2367 (2015). Cited on page(s) 263 and 264
- [224] W. Li, X. Qian and J. Li, 'Phase transitions in 2D materials', *Nat. Rev. Mater.* **6**, 829 (2021). Cited on page(s) 263
- [225] P. Li and F. Ding, 'Origin of the herringbone reconstruction of Au(111) surface at the atomic scale', *Sci. Adv.* **8**, eabq2900 (2023). Cited on page(s) 263
- [226] J. V. Barth, H. Brune, G. Ertl and R. J. Behm, 'Scanning tunneling microscopy observations on the reconstructed Au(111) surface: Atomic structure, long-range superstructure, rotational domains, and surface defects', *Phys. Rev. B* **42**, 9307 (1990). Cited on page(s) 263
- [227] R. Kappera, D. Voiry, S. E. Yalcin, B. Branch, G. Gupta, A. D. Mohite and M. Chhowalla, 'Phase-engineered low-resistance contacts for ultrathin MoS₂ transistors', *Nat. Mater.* **13**, 1128 (2014). Cited on page(s) 263

Bibliography

- [228] D. H. Keum, S. Cho, J. H. Kim, D.-H. Choe, H.-J. Sung, M. Kan, H. Kang, J.-Y. Hwang, S. W. Kim, H. Yang, K. J. Chang and Y. H. Lee, 'Bandgap opening in few-layered monoclinic MoTe₂', *Nat. Phys.* **11**, 482 (2015). Cited on page(s) 263
- [229] Y. Wang, J. Xiao, H. Zhu, Y. Li, Y. Alsaïd, K. Y. Fong, Y. Zhou, S. Wang, W. Shi and Y. Wang, 'Structural phase transition in monolayer MoTe₂ driven by electrostatic doping', *Nature* **550**, 487 (2017). Cited on page(s) 263 and 264
- [230] T. Straub, T. Finteis, R. Claessen, P. Steiner, S. Hübner, P. Blaha, C. S. Oglesby and E. Bucher, 'Charge-Density-Wave Mechanism in 2H-NbSe₂: Photoemission Results', *Phys. Rev. Lett.* **82**, 4504 (1999). Cited on page(s) 264
- [231] T. Valla, A. V. Fedorov, P. D. Johnson, P. A. Glans, C. McGuinness, K. E. Smith, E. Y. Andrei and H. Berger, 'Quasiparticle Spectra, Charge-Density Waves, Superconductivity, and Electron-Phonon Coupling in 2H-NbSe₂', *Phys. Rev. Lett.* **92**, 86401 (2004). Cited on page(s) 264 and 267
- [232] F. Weber, S. Rosenkranz, J.-P. Castellán, R. Osborn, R. Hott, R. Heid, K.-P. Bohnen, T. Egami, A. H. Said and D. Reznik, 'Extended Phonon Collapse and the Origin of the Charge-Density Wave in 2H-NbSe₂', *Phys. Rev. Lett.* **107**, 107403 (2011). Cited on page(s) 264 and 267
- [233] D. J. Rahn, S. Hellmann, M. Kalläne, C. Sohrt, T. K. Kim, L. Kipp and K. Rossnagel, 'Gaps and kinks in the electronic structure of the superconductor 2H-NbSe₂ from angle-resolved photoemission at 1K', *Phys. Rev. B* **85**, 224532 (2012). Cited on page(s) 264 and 267
- [234] C. J. Arguello, S. P. Chockalingam, E. P. Rosenthal, L. Zhao, C. Gutiérrez, J. H. Kang, W. C. Chung, R. M. Fernandes, S. Jia, A. J. Millis, R. J. Cava and A. N. Pasupathy, 'Visualizing the charge density wave transition in 2HNbSe₂ in real space', *Phys. Rev. B* **89**, 235115 (2014). Cited on page(s) 264 and 267
- [235] U. Chatterjee *et al.*, 'Emergence of coherence in the charge-density wave state of 2H-NbSe₂', *Nat. Commun.* **6**, 6313 (2015). Cited on page(s) 264 and 267
- [236] H. Miao, R. Fumagalli, M. Rossi, J. Lorenzana, G. Seibold, F. Yakhou-Harris, K. Kummer, N. Brookes, G. Gu, L. Braicovich, G. Ghiringhelli and M. Dean, 'Formation of Incommensurate Charge Density Waves in Cuprates', *Phys. Rev. X* **9**, 31042 (2019). Cited on page(s) 264
- [237] P. Hofmann, M. M. Ugeda, A. Tamtögl, A. Ruckhofer, W. E. Ernst, G. Benedek, A. J. Martínez-Galera, A. Stróżecka, J. M. Gómez-Rodríguez, E. Rienks, M. F. Jensen, J. I. Pascual and J. W. Wells, 'Strong-coupling charge density wave in a one-dimensional topological metal', *Phys. Rev. B* **99**, 35438 (2019). Cited on page(s) 264

- [238] H. Haifeng and Z. Dianlin, 'Charge Density Wave Gap Formation of NbSe₃ Detected by Electron Tunneling', *Phys. Rev. Lett.* **82**, 811 (1999). Cited on page(s) 264
- [239] R. Liu, W. C. Tonjes, V. A. Greanya, C. G. Olson and R. F. Frindt, 'Fermi surface of 2H-TaSe₂ and its relation to the charge-density wave', *Phys. Rev. B* **61**, 5212 (2000). Cited on page(s) 264
- [240] T. E. Kidd, T. Miller, M. Y. Chou and T.-C. Chiang, 'Electron-Hole Coupling and the Charge Density Wave Transition in TiSe₂', *Phys. Rev. Lett.* **88**, 226402 (2002). Cited on page(s) 264
- [241] K. Rossnagel, L. Kipp and M. Skibowski, 'Charge-density-wave phase transition in 1T-TiSe₂: Excitonic insulator versus band-type Jahn-Teller mechanism', *Phys. Rev. B* **65**, 235101 (2002). Cited on page(s) 264
- [242] J. van Wezel, P. Nahai-Williamson and S. S. Saxena, 'Exciton-phonon-driven charge density wave in TiSe₂', *Phys. Rev. B* **81**, 165109 (2010). Cited on page(s) 264
- [243] K. Sugawara, Y. Nakata, R. Shimizu, P. Han, T. Hitosugi, T. Sato and T. Takahashi, 'Unconventional Charge-Density-Wave Transition in Monolayer 1T-TiSe₂', *ACS Nano* **10**, 1341 (2016). Cited on page(s) 264
- [244] A. Aishwarya, J. May-Mann, A. Raghavan, L. Nie, M. Romanelli, S. Ran, S. R. Saha, J. Paglione, N. P. Butch, E. Fradkin and V. Madhavan, 'Magnetic-field-sensitive charge density waves in the superconductor UTe₂', *Nature* **618**, 928 (2023). Cited on page(s) 264 and 265
- [245] D. Subires, A. Korshunov, A. H. Said, L. Sánchez, B. R. Ortiz, S. D. Wilson, A. Bosak and S. Blanco-Canosa, 'Order-disorder charge density wave instability in the kagome metal (Cs,Rb)V₃Sb₅', *Nat. Commun.* **14**, 1015 (2023). Cited on page(s) 264 and 265
- [246] S. Han, C. S. Tang, L. Li, Y. Liu, H. Liu, J. Gou, J. Wu, D. Zhou, P. Yang and C. Diao, 'Orbital-Hybridization-Driven Charge Density Wave Transition in CsV₃Sb₅ Kagome Superconductor', *Adv. Mater.* **35**, 2209010 (2023). Cited on page(s) 264 and 265
- [247] D. Lee *et al.*, 'Isostructural metal-insulator transition in VO₂', *Science* **362**, 1037 (2018). Cited on page(s) 265 and 268
- [248] Y. Chen *et al.*, 'Strong correlations and orbital texture in single-layer 1T-TaSe₂', *Nat. Phys.* **16**, 218 (2020). Cited on page(s) 265, 268, and 273
- [249] Y. Nakata, K. Sugawara, A. Chainani, H. Oka, C. Bao, S. Zhou, P.-Y. Chuang, C.-M. Cheng, T. Kawakami, Y. Saruta, T. Fukumura, S. Zhou, T. Takahashi and T. Sato, 'Robust charge-density wave strengthened by electron correlations in monolayer 1T-TaSe₂ and 1T-NbSe₂', *Nat. Commun.* **12**, 5873 (2021). Cited on page(s) 265 and 268

Bibliography

- [250] J. Hwang, K. Kim, C. Zhang, T. Zhu, C. Herbig, S. Kim, B. Kim, Y. Zhong, M. Salah, M. M. El-Desoky, C. Hwang, Z.-X. Shen, M. F. Crommie and S.-K. Mo, 'Large-gap insulating dimer ground state in monolayer IrTe₂', *Nat. Commun.* **13**, 906 (2022). Cited on page(s) 265
- [251] M. D. Watson, A. Louat, C. Cacho, S. Choi, Y. H. Lee, M. Neumann and G. Kim, 'Spectral signatures of a unique charge density wave in Ta₂NiSe₇', *Nat. Commun.* **14**, 3388 (2023). Cited on page(s) 265
- [252] Y. Hu, T. Zhang, D. Zhao, C. Chen, S. Ding, W. Yang, X. Wang, C. Li, H. Wang, D. Feng and T. Zhang, 'Real-space observation of incommensurate spin density wave and coexisting charge density wave on Cr(001) surface', *Nat. Commun.* **13**, 445 (2022). Cited on page(s) 265
- [253] H. Zhang *et al.*, 'Tailored Ising superconductivity in intercalated bulk NbSe₂', *Nat. Phys.* **18**, 1425 (2022). Cited on page(s) 265
- [254] L. Nie *et al.*, 'Charge-density-wave-driven electronic nematicity in a kagome superconductor', *Nature* **604**, 59 (2022). Cited on page(s) 265
- [255] X. Teng *et al.*, 'Magnetism and charge density wave order in kagome FeGe', *Nat. Phys.* **19**, 814 (2023). Cited on page(s) 265
- [256] Z. Chen, X. Wu, R. Yin, J. Zhang, S. Wang, Y. Li, M. Li, A. Wang, Y. Wang and Y.-J. Yan, 'Charge density wave with strong quantum phase fluctuations in Kagome magnet FeGe', *arXiv preprint arXiv:2302.04490* (2023). Cited on page(s) 265 and 267
- [257] K. Y. Chen, N. N. Wang, Q. W. Yin, Y. H. Gu, K. Jiang, Z. J. Tu, C. S. Gong, Y. Uwatoko, J. P. Sun and H. C. Lei, 'Double superconducting dome and triple enhancement of T_c in the kagome superconductor CsV₃Sb₅ under high pressure', *Phys. Rev. Lett.* **126**, 247001 (2021). Cited on page(s) 265
- [258] F. H. Yu, D. H. Ma, W. Z. Zhuo, S. Q. Liu, X. K. Wen, B. Lei, J. J. Ying and X. H. Chen, 'Unusual competition of superconductivity and charge-density-wave state in a compressed topological kagome metal', *Nat. Commun.* **12**, 3645 (2021). Cited on page(s) 265
- [259] X. Yang, J.-J. Xian, G. Li, N. Nagaosa, W.-H. Zhang, L. Qin, Z.-M. Zhang, J.-T. Lü and Y.-S. Fu, 'Possible phason-polaron effect on purely one-dimensional charge order of Mo₆Se₆ nanowires', *Phys. Rev. X* **10**, 31061 (2020). Cited on page(s) 265
- [260] S. Kim, Y. Lv, X.-Q. Sun, C. Zhao, N. Bielinski, A. Murzabekova, K. Qu, R. A. Duncan, Q. L. D. Nguyen, M. Trigo, D. P. Shoemaker, B. Bradlyn and F. Mahmood, 'Observation of a massive phason in a charge-density-wave insulator', *Nat. Mater.* **22**, 429 (2023). Cited on page(s) 265, 266, and 267

- [261] T. Knispel, J. Berges, A. Schobert, E. G. C. P. van Loon, W. Jolie, T. Wehling, T. Michely and J. Fischer, 'Unconventional charge-density-wave gap in monolayer NbS₂', *arXiv preprint arXiv:2307.13791* (2023). Cited on page(s) 265, 267, and 269
- [262] A. Zong, X. Shen, A. Kogar, L. Ye, C. Marks, D. Chowdhury, T. Rohwer, B. Freelon, S. Weathersby and R. Li, 'Ultrafast manipulation of mirror domain walls in a charge density wave', *Sci. Adv.* **4**, eaau5501 (2018). Cited on page(s) 265
- [263] X. Song, L. Liu, Y. Chen, H. Yang, Z. Huang, B. Hou, Y. Hou, X. Han, H. Yang and Q. Zhang, 'Atomic-scale visualization of chiral charge density wave superlattices and their reversible switching', *Nat. Commun.* **13**, 1843 (2022). Cited on page(s) 265
- [264] Y. Zhao, Z. Nie, H. Hong, X. Qiu, S. Han, Y. Yu, M. Liu, X. Qiu, K. Liu, S. Meng, L. Tong and J. Zhang, 'Spectroscopic visualization and phase manipulation of chiral charge density waves in 1T-TaS₂', *Nat. Commun.* **14**, 2223 (2023). Cited on page(s) 265
- [265] B. Huang, G. Clark, E. Navarro-Moratalla, D. R. Klein, R. Cheng, K. L. Seyler, D. Zhong, E. Schmidgall, M. A. McGuire, D. H. Cobden, W. Yao, D. Xiao, P. Jarillo-Herrero and X. Xu, 'Layer-dependent ferromagnetism in a van der Waals crystal down to the monolayer limit', *Nature* **546**, 270 (2017). Cited on page(s) 265
- [266] C. Gong, L. Li, Z. Li, H. Ji, A. Stern, Y. Xia, T. Cao, W. Bao, C. Wang, Y. Wang, Z. Q. Qiu, R. J. Cava, S. G. Louie, J. Xia and X. Zhang, 'Discovery of intrinsic ferromagnetism in two-dimensional van der Waals crystals', *Nature* **546**, 265 (2017). Cited on page(s) 265
- [267] A. M. León, É. A. Velásquez, F. Caro-Lopera and J. Mejía-López, 'Tuning Magnetic Order in CrI₃ Bilayers via Moiré Patterns', *Adv. Theory Simul.* **5**, 2100307 (2022). Cited on page(s) 265
- [268] Q. Tong, F. Liu, J. Xiao and W. Yao, 'Skyrmions in the Moiré of van der Waals 2D Magnets', *Nano Lett.* **18**, 7194 (2018). Cited on page(s) 265
- [269] S. A. Kivelson, I. P. Bindloss, E. Fradkin, V. Oganesyan, J. M. Tranquada, A. Kapitulnik and C. Howald, 'How to detect fluctuating stripes in the high-temperature superconductors', *Rev. Mod. Phys.* **75**, 1201 (2003). Cited on page(s) 265
- [270] P. Dai, J. Hu and E. Dagotto, 'Magnetism and its microscopic origin in iron-based high-temperature superconductors', *Nat. Phys.* **8**, 709 (2012). Cited on page(s) 265
- [271] M. Enayat, Z. Sun, U. R. Singh, R. Aluru, S. Schmaus, A. Yaresko, Y. Liu, C. Lin, V. Tsurkan, A. Loidl, J. Deisenhofer and P. Wahl, 'Real-space imaging of the atomic-scale magnetic structure of Fe_{1+y}Te', *Science* **345**, 653 (2014). Cited on page(s) 265

Bibliography

- [272] E. Fawcett, 'Spin-density-wave antiferromagnetism in chromium', *Rev. Mod. Phys.* **60**, 209 (1988). Cited on page(s) 265
- [273] S. Trishin, C. Lotze, N. Bogdanoff, F. von Oppen and K. J. Franke, 'Moiré Tuning of Spin Excitations: Individual Fe Atoms on MoS₂/Au (111)', *Phys. Rev. Lett.* **127**, 236801 (2021). Cited on page(s) 266
- [274] D. Zhang, J. Ha, H. Baek, Y.-H. Chan, F. D. Natterer, A. F. Myers, J. D. Schumacher, W. G. Cullen, A. V. Davydov, Y. Kuk, M. Y. Chou, N. B. Zhitenev and J. A. Stroscio, 'Strain engineering a $4a \times \sqrt{3}a$ charge-density-wave phase in transition-metal dichalcogenide 1T-VSe₂', *Phys. Rev. Mater.* **1**, 24005 (2017). Cited on page(s) 266
- [275] G. Duvjir, B. K. Choi, T. Thi Ly, N. H. Lam, K. Jang, D. D. Dung, Y. J. Chang and J. Kim, 'Multiple charge density wave phases of monolayer VSe₂ manifested by graphene substrates', *Nanotechnol.* **32**, 364002 (2021). Cited on page(s) 266
- [276] Z. Wang, J. Zhou, K. P. Loh and Y. P. Feng, 'Controllable phase transitions between multiple charge density waves in monolayer 1T-VSe₂ via charge doping', *Appl. Phys. Lett.* **119**, 163101 (2021). Cited on page(s) 266
- [277] R. Chua, J. Henke, S. Saha, Y. Huang, J. Gou, X. He, T. Das, J. van Wezel, A. Soumyanarayanan and A. T. S. Wee, 'Coexisting Charge-Ordered States with Distinct Driving Mechanisms in Monolayer VSe₂', *ACS Nano* **16**, 783 (2022). Cited on page(s) 266
- [278] A. O. Fumega, J. Diego, V. Pardo, S. Blanco-Canosa and I. Errea, 'Anharmonicity Reveals the Tunability of the Charge Density Wave Orders in Monolayer VSe₂', *Nano Lett.* **23**, 1794 (2023). Cited on page(s) 266
- [279] P. M. Coelho, K. Nguyen Cong, M. Bonilla, S. Kolekar, M.-H. Phan, J. Avila, M. C. Asensio, I. I. Oleynik and M. Batzill, 'Charge Density Wave State Suppresses Ferromagnetic Ordering in VSe₂ Monolayers', *J. Phys. Chem. C* **123**, 14089 (2019). Cited on page(s) 266
- [280] L. Yin, T. Berlijn, R. Juneja, L. Lindsay and D. S. Parker, 'Competing magnetic and nonmagnetic states in monolayer VSe₂ with charge density wave', *Phys. Rev. B* **106**, 085117 (2022). Cited on page(s) 266
- [281] H. Ryu *et al.*, 'Persistent Charge-Density-Wave Order in Single-Layer TaSe₂', *Nano Lett.* **18**, 689 (2018). Cited on page(s) 266
- [282] P. K. J. Wong *et al.*, 'Evidence of Spin Frustration in a Vanadium Diselenide Monolayer Magnet', *Adv. Mater.* **31**, 1901185 (2019). Cited on page(s) 266
- [283] W. Jolie, T. Knispel, N. Ehlen, K. Nikonov, C. Busse, A. Grüneis and T. Michely, 'Charge density wave phase of VSe₂ revisited', *Phys. Rev. B* **99**, 115417 (2019). Cited on page(s) 266

- [284] J. Hall *et al.*, 'Environmental Control of Charge Density Wave Order in Monolayer 2H-TaS₂', *ACS Nano* **13**, (2019). Cited on page(s) 266, 273, and 300
- [285] G. Miao, S. Xue, B. Li, Z. Lin, B. Liu, X. Zhu, W. Wang and J. Guo, 'Real-space investigation of the charge density wave in VTe₂ monolayer with broken rotational and mirror symmetries', *Phys. Rev. B* **101**, 35407 (2020). Cited on page(s) 266
- [286] M. A. Reed, 'Inelastic electron tunneling spectroscopy', *Mater. Today* **11**, 46 (2008). Cited on page(s) 266
- [287] Y. Zhang, V. W. Brar, F. Wang, C. Girit, Y. Yayan, M. Panlasigui, A. Zettl and M. F. Crommie, 'Giant phonon-induced conductance in scanning tunnelling spectroscopy of gate-tunable graphene', *Nat. Phys.* **4**, 627 (2008). Cited on page(s) 266
- [288] F. D. Natterer, Y. Zhao, J. Wyrick, Y.-H. Chan, W.-Y. Ruan, M.-Y. Chou, K. Watanabe, T. Taniguchi, N. B. Zhitenev and J. A. Stroscio, 'Strong asymmetric charge carrier dependence in inelastic electron tunneling spectroscopy of graphene phonons', *Phys. Rev. Lett.* **114**, 245502 (2015). Cited on page(s) 266
- [289] X.-Y. Hou, F. Zhang, X.-H. Tu, Y.-D. Gu, M.-D. Zhang, J. Gong, Y.-B. Tu, B.-T. Wang, W.-G. Lv, H.-M. Weng, Z.-A. Ren, G.-F. Chen, X.-D. Zhu, N. Hao and L. Shan, 'Inelastic Electron Tunneling in 2H-Ta_xNb_{1-x}Se₂ Evidenced by Scanning Tunneling Spectroscopy', *Phys. Rev. Lett.* **124**, 106403 (2020). Cited on page(s) 266
- [290] C. Wen, Y. Xie, Y. Wu, S. Shen, P. Kong, H. Lian, J. Li, H. Xing and S. Yan, 'Impurity-pinned incommensurate charge density wave and local phonon excitations in 2H-NbS₂', *Phys. Rev. B* **101**, 241404 (2020). Cited on page(s) 266
- [291] P. Chen, W. W. Pai, Y.-H. Chan, A. Takayama, C.-Z. Xu, A. Karn, S. Hasegawa, M. Y. Chou, S.-K. Mo, A.-V. Fedorov and T.-C. Chiang, 'Emergence of charge density waves and a pseudogap in single-layer TiTe₂', *Nat. Commun.* **8**, 516 (2017). Cited on page(s) 267
- [292] M. Calandra, I. I. Mazin and F. Mauri, 'Effect of dimensionality on the charge-density wave in few-layer 2H-NbSe₂', *Phys. Rev. B* **80**, 241108 (2009). Cited on page(s) 267
- [293] J. Á. Silva-Guillén, P. Ordejón, F. Guinea and E. Canadell, 'Electronic structure of 2H-NbSe₂ single-layers in the CDW state', *2D Mater.* **3**, 35028 (2016). Cited on page(s) 267
- [294] S.-H. Kang, H. Li, W. R. Meier, J. W. Villanova, S. Hus, H. Jeon, H. W. S. Arachchige, Q. Lu, Z. Gai and J. Denlinger, 'Emergence of a new band and the Lifshitz transition in kagome metal ScV₆Sn₆ with charge density wave', *arXiv preprint arXiv:2302.14041* (2023). Cited on page(s) 267

Bibliography

- [295] S. Kolekar, M. Bonilla, Y. Ma, H. C. Diaz and M. Batzill, 'Layer-and substrate-dependent charge density wave criticality in 1T-TiSe₂', *2D Mater.* **5**, 15006 (2017). Cited on page(s) 267
- [296] M. Nakano, Y. Wang, S. Yoshida, H. Matsuoka, Y. Majima, K. Ikeda, Y. Hirata, Y. Takeda, H. Wadati, Y. Kohama, Y. Ohigashi, M. Sakano, K. Ishizaka and Y. Iwasa, 'Intrinsic 2D Ferromagnetism in V₅Se₈ Epitaxial Thin Films', *Nano Lett.* **19**, 8806 (2019). Cited on page(s) 267
- [297] Q. Meng, J. Zong, Q. Tian, W. Chen, X. Xie, F. Yu, X. Qiu, K. Wang, Y. Zhang, P. Wang, F.-S. Li, C. Wang and Y. Zhang, 'Selectable Growth and Electronic Structures of Monolayer 1T-VSe₂ and V₅Se₈ Films on Bilayer Graphene', *Phys. Status Solidi - Rapid Res. Lett.* **16**, 2100601 (2022). Cited on page(s) 268
- [298] K. Sumida, S. Kusaka, Y. Takeda, K. Kobayashi and T. Hirahara, 'Formation of monolayer V₅Se₈ from multilayer VSe₂ films via V- and Se-desorption', *Phys. Rev. B* **106**, 195421 (2022). Cited on page(s) 268
- [299] W. J. Hardy, J. Yuan, H. Guo, P. Zhou, J. Lou and D. Natelson, 'Thickness-Dependent and Magnetic-Field-Driven Suppression of Antiferromagnetic Order in Thin V₅S₈ Single Crystals', *ACS Nano* **10**, 5941 (2016). Cited on page(s) 268
- [300] J. Niu, B. Yan, Q. Ji, Z. Liu, M. Li, P. Gao, Y. Zhang, D. Yu and X. Wu, 'Anomalous Hall effect and magnetic orderings in nanothick V₅S₈', *Phys. Rev. B* **96**, 75402 (2017). Cited on page(s) 268
- [301] R.-Z. Zhang, Y.-Y. Zhang and S.-X. Du, 'Thickness-dependent magnetic order and phase transition in V₅S₈*', *Chin. Phys. B* **29**, 77504 (2020). Cited on page(s) 268
- [302] Z. Zhou, X. Zhao, L. Wu, H. Liu, J. Chen, C. Xi, Z. Wang, E. Liu, W. Zhou, S. J. Pennycook, S. T. Pantelides, X.-G. Zhang, L. Bao and H.-J. Gao, 'Dimensional crossover in self-intercalated antiferromagnetic V₅S₈* nanoflakes', *Phys. Rev. B* **105**, 235433 (2022). Cited on page(s) 268
- [303] I. Kar, S. Routh, S. Ghorai, S. Purwar and S. Thirupathaiah, 'Observation of weak Kondo effect and angle dependent magnetoresistance in layered antiferromagnetic V₅S₈ single crystal', *Solid State Commun.* **369**, 115209 (2023). Cited on page(s) 268
- [304] J. Niu, Z. Li, S. Yang, W. Zhang, D. Yan, S. Chen, Z. Zhang, Y. Zhang, X. Ren and P. Gao, 'V₅S₈: a Kondo lattice based on intercalation of van der Waals layered transition metal dichalcogenide', *arXiv preprint arXiv:1809.04213* (2018). Cited on page(s) 268
- [305] W. Ruan *et al.*, 'Evidence for quantum spin liquid behaviour in single-layer 1T-TaSe₂ from scanning tunnelling microscopy', *Nat. Phys.* **17**, 1154 (2021). Cited on page(s) 268, 273, and 274

- [306] M. Liu, J. Leveillee, S. Lu, J. Yu, H. Kim, C. Tian, Y. Shi, K. Lai, C. Zhang, F. Giustino and C.-K. Shih, 'Monolayer 1T-NbSe₂ as a 2D-correlated magnetic insulator', *Sci. Adv.* **7**, eabi6339 (2023). Cited on page(s) 268 and 273
- [307] H. M. R. Ahamd and J. Zhou, 'Intercalation induced ferromagnetism in group-V transition metal dichalcogenide bilayer', *AIP Adv.* **10**, 45323 (2020). Cited on page(s) 268
- [308] S. N. Shirodkar and U. V. Waghmare, 'Emergence of ferroelectricity at a metal-semiconductor transition in a 1T monolayer of MoS₂', *Phys. Rev. Lett.* **112**, 157601 (2014). Cited on page(s) 269 and 270
- [309] K. Nakayama, Z. Wang, C. X. Trang, S. Souma, E. D. L. Rienks, T. Takahashi, Y. Ando and T. Sato, 'Observation of Dirac-like energy band and unusual spectral line shape in quasi-one-dimensional superconductor Tl₂Mo₆Se₆', *Physical Review B* **98**, 140502 (2018). Cited on page(s) 269
- [310] L. S. Wu, S. E. Nikitin, Z. Wang, W. Zhu, C. D. Batista, A. M. Tselik, A. M. Samarakoon, D. A. Tennant, M. Brando and L. Vasylechko, 'Tomonaga–Luttinger liquid behavior and spinon confinement in YbAlO₃', *Nat. Commun.* **10**, 698 (2019). Cited on page(s) 269
- [311] S. E. Nikitin, S. Nishimoto, Y. Fan, J. Wu, L. S. Wu, A. S. Sukhanov, M. Brando, N. S. Pavlovskii, J. Xu, L. Vasylechko, R. Yu and A. Podlesnyak, 'Multiple fermion scattering in the weakly coupled spin-chain compound YbAlO₃', *Nat. Commun.* **12**, 3599 (2021). Cited on page(s) 269
- [312] J. Klein *et al.*, 'The Bulk van der Waals Layered Magnet CrSBr is a Quasi-1D Material', *ACS Nano* **17**, 5316 (2023). Cited on page(s) 269
- [313] Z.-L. Liu, B. Lei, Z.-L. Zhu, L. Tao, J. Qi, D.-L. Bao, X. Wu, L. Huang, Y.-Y. Zhang, X. Lin, Y.-L. Wang, S. Du, S. T. Pantelides and H.-J. Gao, 'Spontaneous Formation of 1D Pattern in Monolayer VSe₂ with Dispersive Adsorption of Pt Atoms for HER Catalysis', *Nano Lett.* **19**, 4897 (2019). Cited on page(s) 269
- [314] P. Pervan, P. Lazić, M. Petrović, I. Šrut Rakić, I. Pletikosić, M. Kralj, M. Milun and T. Valla, 'Li adsorption versus graphene intercalation on Ir(111): From quenching to restoration of the Ir surface state', *Phys. Rev. B* **92**, 245415 (2015). Cited on page(s) 270
- [315] U. A. Schröder, M. Petrović, T. Gerber, A. J. Martínez-Galera, E. Grånäs, M. A. Arman, C. Herbig, J. Schnadt, M. Kralj and J. Knudsen, 'Core level shifts of intercalated graphene', *2D Mater.* **4**, 15013 (2016). Cited on page(s) 270
- [316] P. Pervan and P. Lazić, 'Adsorbed or intercalated: Na on graphene/Ir(111)', *Phys. Rev. Mater.* **1**, 44202 (2017). Cited on page(s) 270 and 286

Bibliography

- [317] C. Struzzi, C. S. Praveen, M. Scardamaglia, N. I. Verbitskiy, A. V. Fedorov, M. Weinl, M. Schreck, A. Grüneis, S. Piccinin, S. Fabris and L. Petaccia, 'Controlled thermodynamics for tunable electron doping of graphene on Ir(111)', *Phys. Rev. B* **94**, 85427 (2016). Cited on page(s) 270
- [318] S. C. Ganguli, V. Vaňo, S. Kezilebieke, J. L. Lado and P. Liljeroth, 'Confinement-Engineered Superconductor to Correlated-Insulator Transition in a van der Waals Monolayer', *Nano Lett.* **22**, 1845 (2022). Cited on page(s) 270, 277, 285, and 286
- [319] S. Zeng, Y. Zhao, G. Li and J. Ni, 'Strongly enhanced superconductivity in doped monolayer MoS₂ by strain', *Phys. Rev. B* **94**, 24501 (2016). Cited on page(s) 270, 277, and 286
- [320] Y. Ge, W. Wan, W. Feng, D. Xiao and Y. Yao, 'Effect of doping and strain modulations on electron transport in monolayer MoS₂', *Phys. Rev. B* **90**, 35414 (2014). Cited on page(s) 270
- [321] M. Hosseini, M. Elahi, M. Pourfath and D. Esseni, 'Strain induced mobility modulation in single-layer MoS₂', *J. Phys. D Appl. Phys.* **48**, 375104 (2015). Cited on page(s) 270
- [322] I. M. Datye, A. Daus, R. W. Grady, K. Brenner, S. Vaziri and E. Pop, 'Strain-Enhanced Mobility of Monolayer MoS₂', *Nano Lett.* **22**, 8052 (2022). Cited on page(s) 270
- [323] M. A. Py and R. R. Haering, 'Structural destabilization induced by lithium intercalation in MoS₂ and related compounds', *Can. J. Phys.* **61**, 76 (1983). Cited on page(s) 270
- [324] D. Nasr Esfahani, O. Leenaerts, H. Sahin, B. Partoens and F. M. Peeters, 'Structural Transitions in Monolayer MoS₂ by Lithium Adsorption', *J. Phys. Chem. C* **119**, 10602 (2015). Cited on page(s) 270
- [325] S. J. R. Tan, I. Abdelwahab, Z. Ding, X. Zhao, T. Yang, G. Z. J. Loke, H. Lin, I. Verzhbitskiy, S. M. Poh and H. Xu, 'Chemical stabilization of 1T' phase transition metal dichalcogenides with giant optical Kerr nonlinearity', *J. Am. Chem. Soc.* **139**, 2504 (2017). Cited on page(s) 270
- [326] H. Xu, D. Han, Y. Bao, F. Cheng, Z. Ding, S. J. R. Tan and K. P. Loh, 'Observation of Gap Opening in 1T' Phase MoS₂ Nanocrystals', *Nano Lett.* **18**, 5085 (2018). Cited on page(s) 271
- [327] N. A. Vinogradov, K. A. Simonov, A. V. Generalov, A. S. Vinogradov, D. V. Vyalikh, C. Laubschat, N. Mårtensson and A. B. Preobrajenski, 'Controllable p-doping of graphene on Ir (111) by chlorination with FeCl₃', *J. Phys. Condens. Matter* **24**, 314202 (2012). Cited on page(s) 271
- [328] J. Gebhardt, R. J. Koch, W. Zhao, O. Höfert, K. Gotterbarm, S. Mammadov, C. Papp, A. Görling, H.-P. Steinrück and T. Seyller, 'Growth and electronic structure of boron-doped graphene', *Phys. Rev. B* **87**, 155437 (2013). Cited on page(s) 271

- [329] Z. Qiu *et al.*, 'Giant gate-tunable bandgap renormalization and excitonic effects in a 2D semiconductor', *Sci. Adv.* **5**, eaaw2347 (2023). Cited on page(s) 271
- [330] N. Ehlen, J. Hall, B. V. Senkovskiy, M. Hell, J. Li, A. Herman, D. Smirnov, A. Fedorov, V. Yu Voroshnin, G. Di Santo, L. Petaccia, T. Michely and A. Grüneis, 'Narrow photoluminescence and Raman peaks of epitaxial MoS₂ on graphene/Ir(111)', *2D Mater.* **6**, 11006 (2019). Cited on page(s) 271 and 287
- [331] R. Larciprete, S. Ulstrup, P. Lacovig, M. Dalmiglio, M. Bianchi, F. Mazzola, L. Hornekær, F. Orlando, A. Baraldi, P. Hofmann and S. Lizzit, 'Oxygen Switching of the Epitaxial Graphene–Metal Interaction', *ACS Nano* **6**, 9551 (2012). Cited on page(s) 271
- [332] E. Grånäs, J. Knudsen, U. A. Schröder, T. Gerber, C. Busse, M. A. Arman, K. Schulte, J. N. Andersen and T. Michely, 'Oxygen Intercalation under Graphene on Ir(111): Energetics, Kinetics, and the Role of Graphene Edges', *ACS Nano* **6**, 9951 (2012). Cited on page(s) 271
- [333] L. Wang, S. Papadopoulos, F. Iyikanat, J. Zhang, J. Huang, T. Taniguchi, K. Watanabe, M. Calame, M. L. Perrin, F. J. García de Abajo and L. Novotny, 'Exciton-assisted electron tunnelling in van der Waals heterostructures', *Nat. Mater.* (2023). Cited on page(s) 271 and 290
- [334] A. Herman, S. Kraus, S. Tsukamoto, L. Spieker, V. Caciuc, T. Lojewski, D. Günzing, J. Dreiser, B. Delley and K. Ollefs, 'Tailoring magnetic anisotropy by graphene-induced selective skyhook effect on 4f-metals', *Nanoscale* **14**, 7682 (2022). Cited on page(s) 271
- [335] F. H. Farwick zum Hagen *et al.*, 'Structure and Growth of Hexagonal Boron Nitride on Ir(111)', *ACS Nano* **10**, 11012 (2016). Cited on page(s) 271, 287, 288, 290, and 291
- [336] A. J. Campbell, M. Brotons-Gisbert, H. Baek, V. Vitale, T. Taniguchi, K. Watanabe, J. Lischner and B. D. Gerardot, 'Exciton-polarons in the presence of strongly correlated electronic states in a MoSe₂/WSe₂ moiré superlattice', *npj 2D Mater. Appl.* **6**, 79 (2022). Cited on page(s) 271 and 287
- [337] E. C. Regan, D. Wang, C. Jin, M. I. Bakti Utama, B. Gao, X. Wei, S. Zhao, W. Zhao, Z. Zhang and K. Yumigeta, 'Mott and generalized Wigner crystal states in WSe₂/WS₂ moiré superlattices', *Nature* **579**, 359 (2020). Cited on page(s) 271 and 287
- [338] Y. Xu, S. Liu, D. A. Rhodes, K. Watanabe, T. Taniguchi, J. Hone, V. Elser, K. F. Mak and J. Shan, 'Correlated insulating states at fractional fillings of moiré superlattices', *Nature* **587**, 214 (2020). Cited on page(s) 271 and 287
- [339] H. Li, S. Li, E. C. Regan, D. Wang, W. Zhao, S. Kahn, K. Yumigeta, M. Blei, T. Taniguchi and K. Watanabe, 'Imaging two-dimensional generalized Wigner crystals', *Nature* **597**, 650 (2021). Cited on page(s) 271 and 287

Bibliography

- [340] X. Huang, T. Wang, S. Miao, C. Wang, Z. Li, Z. Lian, T. Taniguchi, K. Watanabe, S. Okamoto and D. Xiao, 'Correlated insulating states at fractional fillings of the WS_2/WSe_2 moiré lattice', *Nat. Phys.* **17**, 715 (2021). Cited on page(s) 271 and 287
- [341] D. Chen *et al.*, 'Excitonic insulator in a heterojunction moiré superlattice', *Nat. Phys.* **18**, 1171 (2022). Cited on page(s) 271 and 287
- [342] S. Kraus, F. Huttmann, J. Fischer, T. Knispel, K. Bischof, A. Herman, M. Bianchi, R.-M. Stan, A. J. Holt and V. Caciuc, 'Single-crystal graphene on Ir (110)', *Phys. Rev. B* **105**, 165405 (2022). Cited on page(s) 271
- [343] D. C. Ralph and R. A. Buhrman, 'Kondo-assisted and resonant tunneling via a single charge trap: A realization of the Anderson model out of equilibrium', *Phys. Rev. Lett.* **72**, 3401 (1994). Cited on page(s) 272
- [344] D. Goldhaber-Gordon, H. Shtrikman, D. Mahalu, D. Abusch-Magder, U. Meirav and M. A. Kastner, 'Kondo effect in a single-electron transistor', *Nature* **391**, 156 (1998). Cited on page(s) 272
- [345] S. M. Cronenwett, T. H. Oosterkamp and L. P. Kouwenhoven, 'A tunable Kondo effect in quantum dots', *Science* **281**, 540 (1998). Cited on page(s) 272
- [346] S. Sasaki, S. De Franceschi, J. M. Elzerman, W. G. van der Wiel, M. Eto, S. Tarucha and L. P. Kouwenhoven, 'Kondo effect in an integer-spin quantum dot', *Nature* **405**, 764 (2000). Cited on page(s) 272
- [347] J. Paaske, A. Rosch, P. Wölfle, N. Mason, C. M. Marcus and J. Nygård, 'Non-equilibrium singlet–triplet Kondo effect in carbon nanotubes', *Nat. Phys.* **2**, 460 (2006). Cited on page(s) 272
- [348] W. G. van der Wiel, S. D. Franceschi, T. Fujisawa, J. M. Elzerman, S. Tarucha and L. P. Kouwenhoven, 'The Kondo Effect in the Unitary Limit', *Science* **289**, 2105 (2000). Cited on page(s) 272
- [349] A. Makarovski, A. Zhukov, J. Liu and G. Finkelstein, 'SU (2) and SU (4) Kondo effects in carbon nanotube quantum dots', *Phys. Rev. B* **75**, 241407 (2007). Cited on page(s) 272
- [350] F. Kuemmeth, S. Ilani, D. C. Ralph and P. L. McEuen, 'Coupling of spin and orbital motion of electrons in carbon nanotubes', *Nature* **452**, 448 (2008). Cited on page(s) 272
- [351] I. V. Borzenets, J. Shim, J. C. H. Chen, A. Ludwig, A. D. Wieck, S. Tarucha, H.-S. Sim and M. Yamamoto, 'Observation of the Kondo screening cloud', *Nature* **579**, 210 (2020). Cited on page(s) 272

- [352] A. Kurzmann, Y. Kleeorin, C. Tong, R. Garreis, A. Knothe, M. Eich, C. Mittag, C. Gold, F. K. de Vries, K. Watanabe, T. Taniguchi, V. Fal'ko, Y. Meir, T. Ihn and K. Ensslin, 'Kondo effect and spin-orbit coupling in graphene quantum dots', *Nat. Commun.* **12**, 6004 (2021). Cited on page(s) 272
- [353] T. R. Devidas, T. Dvir, E. Rossi and H. Steinberg, 'Kondo effect in defect-bound quantum dots coupled to NbSe₂', *Phys. Rev. B* **107**, 94502 (2023). Cited on page(s) 272
- [354] W. Wan, R. Harsh, A. Meninno, P. Dreher, S. Sajan, I. Errea, F. de Juan and M. M. Ugeda, 'Magnetic order in a coherent two-dimensional Kondo lattice', (2022). Cited on page(s) 272
- [355] L. Jiao, S. Howard, S. Ran, Z. Wang, J. O. Rodriguez, M. Sigrist, Z. Wang, N. P. Butch and V. Madhavan, 'Chiral superconductivity in heavy-fermion metal UTe₂', *Nature* **579**, 523 (2020). Cited on page(s) 272
- [356] J. Figgins, L. S. Mattos, W. Mar, Y.-T. Chen, H. C. Manoharan and D. K. Morr, 'Quantum engineered Kondo lattices', *Nat. Commun.* **10**, 5588 (2019). Cited on page(s) 272
- [357] C. G. Ayani, M. Pizarra, I. M. Ibarburu, M. Garnica, R. Miranda, F. Calleja, F. Martín and A. L. V. de Parga, 'Two-dimensional Kondo lattice in a TaS₂ van der Waals heterostructure', *arXiv preprint arXiv:2205.11383* (2022). Cited on page(s) 272
- [358] W. Zhao, B. Shen, Z. Tao, Z. Han, K. Kang, K. Watanabe, T. Taniguchi, K. F. Mak and J. Shan, 'Gate-tunable heavy fermions in a moiré Kondo lattice', *Nature* **616**, 61 (2023). Cited on page(s) 272
- [359] V. Madhavan, W. Chen, T. Jamneala, M. F. Crommie and N. S. Wingreen, 'Tunneling into a single magnetic atom: spectroscopic evidence of the Kondo resonance', *Science* **280**, 567 (1998). Cited on page(s) 272
- [360] M. D. Daybell and W. A. Steyert, 'Localized Magnetic Impurity States In Metals: Some Experimental Relationships', *Rev. Mod. Phys.* **40**, 380 (1968). Cited on page(s) 272
- [361] W. Wei, R. Rosenbaum and G. Bergmann, 'Magnetic scattering in AuCo and AgCo with weak localization', *Phys. Rev. B* **39**, 4568 (1989). Cited on page(s) 272
- [362] N. Knorr, M. A. Schneider, L. Diekhöner, P. Wahl and K. Kern, 'Kondo effect of single Co adatoms on Cu surfaces', *Phys. Rev. Lett.* **88**, 96804 (2002). Cited on page(s) 272
- [363] P. Wahl, L. Diekhöner, M. A. Schneider, L. Vitali, G. Wittich and K. Kern, 'Kondo Temperature of Magnetic Impurities at Surfaces', *Phys. Rev. Lett.* **93**, 176603 (2004). Cited on page(s) 272

Bibliography

- [364] J. Bouaziz, F. S. Mendes Guimarães and S. Lounis, 'A new view on the origin of zero-bias anomalies of Co atoms atop noble metal surfaces', *Nat. Commun.* **11**, 6112 (2020). Cited on page(s) 273
- [365] N. Noei, R. Mozara, A. M. Montero, S. Brinker, N. Ide, F. S. M. Guimarães, A. I. Lichtenstein, R. Berndt, S. Lounis and A. Weismann, 'Spin excitation of Co atoms at monatomic Cu chains', *arXiv preprint arXiv:2303.03317* (2023). Cited on page(s) 273
- [366] F. Friedrich, A. Odobesko, J. Bouaziz, S. Lounis and M. Bode, 'Spin-resolved spectroscopic evidence for spinarons in Co adatoms', *arXiv preprint arXiv:2306.16084* (2023). Cited on page(s) 273
- [367] F. von Oppen and K. J. Franke, 'Yu-Shiba-Rusinov states in real metals', *Phys. Rev. B* **103**, 205424 (2021). Cited on page(s) 273
- [368] C. Jayaprakash, H. R. Krishna-murthy and J. W. Wilkins, 'Two-Impurity Kondo Problem', *Phys. Rev. Lett.* **47**, 737 (1981). Cited on page(s) 273
- [369] J. Bork, Y.-h. Zhang, L. Diekhöner, L. Borda, P. Simon, J. Kroha, P. Wahl and K. Kern, 'A tunable two-impurity Kondo system in an atomic point contact', *Nat. Phys.* **7**, 901 (2011). Cited on page(s) 273
- [370] A. Spinelli, M. Gerrits, R. Toskovic, B. Bryant, M. Ternes and A. F. Otte, 'Exploring the phase diagram of the two-impurity Kondo problem', *Nat. Commun.* **6**, 10046 (2015). Cited on page(s) 273
- [371] S. Trishin, C. Lotze, F. Lohss, G. Franceschi, L. I. Glazman, F. von Oppen and K. J. Franke, 'Tuning a Two-Impurity Kondo System by a Moiré Superstructure', *Phys. Rev. Lett.* **130**, 176201 (2023). Cited on page(s) 273
- [372] C. P. Moca, E. Demler, B. Jankó and G. Zaránd, 'Spin-resolved spectra of Shiba multiplets from Mn impurities in MgB₂', *Phys. Rev. B* **77**, 174516 (2008). Cited on page(s) 273
- [373] M. Ruby, B. W. Heinrich, Y. Peng, F. von Oppen and K. J. Franke, 'Wave-Function Hybridization in Yu-Shiba-Rusinov Dimers', *Phys. Rev. Lett.* **120**, 156803 (2018). Cited on page(s) 273
- [374] L. Farinacci, G. Ahmadi, M. Ruby, G. Reecht, B. W. Heinrich, C. Czekelius, F. von Oppen and K. J. Franke, 'Interfering Tunneling Paths through Magnetic Molecules on Superconductors: Asymmetries of Kondo and Yu-Shiba-Rusinov Resonances', *Phys. Rev. Lett.* **125**, 256805 (2020). Cited on page(s) 273
- [375] E. Liebhaber, S. Acero González, R. Baba, G. Reecht, B. W. Heinrich, S. Rohlf, K. Rossnagel, F. von Oppen and K. J. Franke, 'Yu-Shiba-Rusinov States in the Charge-Density Modulated Superconductor NbSe₂', *Nano Lett.* **20**, 339 (2020). Cited on page(s) 273

- [376] D.-J. Choi, C. G. Fernández, E. Herrera, C. Rubio-Verdú, M. M. Ugeda, I. Guillamón, H. Suderow, J. I. Pascual and N. Lorente, 'Influence of Magnetic Ordering between Cr Adatoms on the Yu-Shiba-Rusinov States of the β -Bi₂Pd Superconductor', *Phys. Rev. Lett.* **120**, 167001 (2018). Cited on page(s) 273
- [377] L. Schneider, P. Beck, T. Posske, D. Crawford, E. Mascot, S. Rachel, R. Wiesendanger and J. Wiebe, 'Topological Shiba bands in artificial spin chains on superconductors', *Nat. Phys.* **17**, 943 (2021). Cited on page(s) 273
- [378] V. Vaño, S. C. Ganguli, M. Amini, L. Yan, M. Khosravian, G. Chen, S. Kezilebieke, J. L. Lado and P. Liljeroth, 'Evidence of nodal f-wave superconductivity in monolayer 1H-TaS₂ with hidden order fluctuations', (2021). Cited on page(s) 273
- [379] K. T. Law and P. A. Lee, '1T-TaS₂ as a quantum spin liquid', *Proc. Natl. Acad. Sci. U.S.A.* **114**, 6996 (2017). Cited on page(s) 273
- [380] Y. Chen *et al.*, 'Evidence for a spinon Kondo effect in cobalt atoms on single-layer 1T-TaSe₂', *Nat. Phys.* **18**, 1335 (2022). Cited on page(s) 274
- [381] Z. Wang *et al.*, 'Tailoring the nature and strength of electron-phonon interactions in the SrTiO₃(001) 2D electron liquid', *Nat. Mater.* **15**, 835 (2016). Cited on page(s) 275
- [382] M. Setvin, C. Franchini, X. Hao, M. Schmid, A. Janotti, M. Kaltak, C. G. Van de Walle, G. Kresse and U. Diebold, 'Direct view at excess electrons in TiO₂ rutile and anatase', *Phys. Rev. Lett.* **113**, 86402 (2014). Cited on page(s) 275 and 276
- [383] C. Verdi, F. Caruso and F. Giustino, 'Origin of the crossover from polarons to Fermi liquids in transition metal oxides', *Nat. Commun.* **8**, 15769 (2017). Cited on page(s) 275
- [384] J. Ranninger, 'Spectral properties of small-polaron systems', *Phys. Rev. B* **48**, 13166 (1993). Cited on page(s) 275
- [385] M. Knupfer, M. Merkel, M. S. Golden, J. Fink, O. Gunnarsson and V. P. Antropov, 'Satellites in the photoemission spectra of A₃C₆O (A=K and Rb)', *Phys. Rev. B* **47**, 13944 (1993). Cited on page(s) 275
- [386] L. Perfetti, H. Berger, A. Reggiani, L. Degiorgi, H. Höchst, J. Voit, G. Margaritondo and M. Gioni, 'Spectroscopic Indications of Polaronic Carriers in the Quasi-One-Dimensional Conductor (TaSe₄)₂I', *Phys. Rev. Lett.* **87**, 216404 (2001). Cited on page(s) 275
- [387] L. Perfetti, S. Mitrovic, G. Margaritondo, M. Gioni, L. Forró, L. Degiorgi and H. Höchst, 'Mobile small polarons and the Peierls transition in the quasi-one-dimensional conductor K_{0.3}MoO₃', *Phys. Rev. B* **66**, 75107 (2002). Cited on page(s) 275

Bibliography

- [388] M. Cai, M.-P. Miao, Y. Liang, Z. Jiang, Z.-Y. Liu, W.-H. Zhang, X. Liao, L.-F. Zhu, D. West, S. Zhang and Y.-S. Fu, 'Manipulating single excess electrons in monolayer transition metal dihalide', *Nat. Commun.* **14**, 3691 (2023). Cited on page(s) 275 and 278
- [389] H. Liu, A. Wang, P. Zhang, C. Ma, C. Chen, Z. Liu, Y.-Q. Zhang, B. Feng, P. Cheng, J. Zhao, L. Chen and K. Wu, 'Atomic-scale manipulation of single-polaron in a two-dimensional semiconductor', *Nat. Commun.* **14**, 3690 (2023). Cited on page(s) 275 and 278
- [390] M. Reticcioli, Z. Wang, M. Schmid, D. Wrana, L. A. Boatner, U. Diebold, M. Setvin and C. Franchini, 'Competing electronic states emerging on polar surfaces', *Nat. Commun.* **13**, 4311 (2022). Cited on page(s) 275
- [391] Y. Xing *et al.*, 'Localized spin-orbit polaron in magnetic Weyl semimetal $\text{Co}_3\text{Sn}_2\text{S}_2$ ', *Nat. Commun.* **11**, 5613 (2020). Cited on page(s) 275
- [392] K. A. Cochrane, J.-H. Lee, C. Kastl, J. B. Haber, T. Zhang, A. Kozhakhmetov, J. A. Robinson, M. Terrones, J. Repp and J. B. Neaton, 'Spin-dependent vibronic response of a carbon radical ion in two-dimensional WS_2 ', *Nat. Commun.* **12**, 7287 (2021). Cited on page(s) 275
- [393] B. Schuler *et al.*, 'How Substitutional Point Defects in Two-Dimensional WS_2 Induce Charge Localization, Spin-Orbit Splitting, and Strain', *ACS Nano* **13**, 10520 (2019). Cited on page(s) 275
- [394] B. Schuler, D. Y. Qiu, S. Refaely-Abramson, C. Kastl, C. T. Chen, S. Barja, R. J. Koch, D. F. Ogletree, S. Aloni, A. M. Schwartzberg, J. B. Neaton, S. G. Louie and A. Weber-Bargioni, 'Large Spin-Orbit Splitting of Deep In-Gap Defect States of Engineered Sulfur Vacancies in Monolayer WS_2 ', *Phys. Rev. Lett.* **123**, 76801 (2019). Cited on page(s) 275
- [395] C. M. Yim, M. B. Watkins, M. J. Wolf, C. L. Pang, K. Hermansson and G. Thornton, 'Engineering polarons at a metal oxide surface', *Phys. Rev. Lett.* **117**, 116402 (2016). Cited on page(s) 276
- [396] F. Esch, S. Fabris, L. Zhou, T. Montini, C. Africh, P. Fornasiero, G. Comelli and R. Rosei, 'Electron localization determines defect formation on ceria substrates', *Science* **309**, 752 (2005). Cited on page(s) 276
- [397] A. C. Papageorgiou, N. S. Beglitis, C. L. Pang, G. Teobaldi, G. Cabailh, Q. Chen, A. J. Fisher, W. A. Hofer and G. Thornton, 'Electron traps and their effect on the surface chemistry of TiO_2 (110)', *Proc. Natl. Acad. Sci. U.S.A.* **107**, 2391 (2010). Cited on page(s) 276
- [398] M. Setvin, X. Hao, B. Daniel, J. Pavelec, Z. Novotny, G. S. Parkinson, M. Schmid, G. Kresse, C. Franchini and U. Diebold, 'Charge trapping at the step edges of TiO_2 anatase (101)', *Angew. Chem. Int.* **53**, 4714 (2014). Cited on page(s) 276

- [399] M. Gerosa, F. Gygi, M. Govoni and G. Galli, 'The role of defects and excess surface charges at finite temperature for optimizing oxide photoabsorbers', *Nat. Mater.* **17**, 1122 (2018). Cited on page(s) 276
- [400] A. M. Stoneham, J. Gavartin, A. L. Shluger, A. V. Kimmel, D. Muñoz Ramo, H. M. Rønnow, G. Aeppli and C. Renner, 'Trapping, self-trapping and the polaron family', *J. Phys. Condens. Matter* **19**, 255208 (2007). Cited on page(s) 276
- [401] H. Ness and A. J. Fisher, 'Quantum Inelastic Conductance through Molecular Wires', *Phys. Rev. Lett.* **83**, 452 (1999). Cited on page(s) 276
- [402] N. B. Zhitenev, H. Meng and Z. Bao, 'Conductance of Small Molecular Junctions', *Phys. Rev. Lett.* **88**, 226801 (2002). Cited on page(s) 276
- [403] M. Galperin, M. A. Ratner and A. Nitzan, 'Inelastic electron tunneling spectroscopy in molecular junctions: Peaks and dips', *J. Chem. Phys.* **121**, 11965 (2004). Cited on page(s) 276
- [404] U. Lundin and R. H. McKenzie, 'Temperature dependence of polaronic transport through single molecules and quantum dots', *Phys. Rev. B* **66**, 75303 (2002). Cited on page(s) 276
- [405] H. Park, J. Park, A. K. L. Lim, E. H. Anderson, A. P. Alivisatos and P. L. McEuen, 'Nanomechanical oscillations in a single-C60 transistor', *Nature* **407**, 57 (2000). Cited on page(s) 276
- [406] X. H. Qiu, G. V. Nazin and W. Ho, 'Vibronic States in Single Molecule Electron Transport', *Phys. Rev. Lett.* **92**, 206102 (2004). Cited on page(s) 276
- [407] M. Berthe, A. Urbieto, L. Perdigão, B. Grandidier, D. Deresmes, C. Delerue, D. Stiévenard, R. Rurali, N. Lorente, L. Magaud and P. Ordejón, 'Electron Transport via Local Polarons at Interface Atoms', *Phys. Rev. Lett.* **97**, 206801 (2006). Cited on page(s) 276
- [408] V. J. Goldman, D. C. Tsui and J. E. Cunningham, 'Evidence for LO-phonon-emission-assisted tunneling in double-barrier heterostructures', *Phys. Rev. B* **36**, 7635 (1987). Cited on page(s) 276
- [409] P. W. Anderson, 'Absence of Diffusion in Certain Random Lattices', *Phys. Rev.* **109**, 1492 (1958). Cited on page(s) 277 and 282
- [410] F. Evers and A. D. Mirlin, 'Anderson transitions', *Rev. Mod. Phys.* **80**, 1355 (2008). Cited on page(s) 277 and 282
- [411] F. X. Bronold and H. Fehske, 'Anderson localization of polaron states', *Phys. Rev. B* **66**, 73102 (2002). Cited on page(s) 277 and 282

Bibliography

- [412] D. Di Sante and S. Ciuchi, 'Strong interplay between electron-phonon interaction and disorder in low-doped systems', *Phys. Rev. B* **90**, 75111 (2014). Cited on page(s) 277 and 282
- [413] D. Di Sante, S. Fratini, V. Dobrosavljević and S. Ciuchi, 'Disorder-Driven Metal-Insulator Transitions in Deformable Lattices', *Phys. Rev. Lett.* **118**, 36602 (2017). Cited on page(s) 277 and 282
- [414] T. Han, L. Chen, C. Cai, Z. Wang, Y. Wang, Z. Xin and Y. Zhang, 'Metal-Insulator Transition and Emergent Gapped Phase in the Surface-Doped 2D Semiconductor 2H-MoTe₂', *Phys. Rev. Lett.* **126**, 106602 (2021). Cited on page(s) 277 and 282
- [415] D. Emin, 'Formation, motion, and high-temperature superconductivity of large bipolarons', *Phys. Rev. Lett.* **62**, 1544 (1989). Cited on page(s) 278
- [416] A S Alexandrov and A B Krebs, 'Polarons in high-temperature superconductors', *Sov. phys., Usp.* **35**, 345 (1992). Cited on page(s) 278
- [417] N. F. Mott, 'Polaron models of high-temperature superconductivity', *Phys. C: Supercond.* **205**, 191 (1993). Cited on page(s) 278
- [418] W. Wan, P. Dreher, D. Muñoz-Segovia, R. Harsh, H. Guo, A. J. Martínez-Galera, F. Guinea, F. de Juan and M. M. Ugeda, 'Observation of Superconducting Collective Modes from Competing Pairing Instabilities in Single-Layer NbSe₂', *Adv. Mater.* **34**, 2206078 (2022). Cited on page(s) 286
- [419] F. Cadiz *et al.*, 'Excitonic Linewidth Approaching the Homogeneous Limit in MoS₂-Based van der Waals Heterostructures', *Phys. Rev. X* **7**, 21026 (2017). Cited on page(s) 287
- [420] F. Schulz, R. Drost, S. K. Hämäläinen, T. Demonchaux, A. P. Seitsonen and P. Liljeroth, 'Epitaxial hexagonal boron nitride on Ir(111): A work function template', *Phys. Rev. B* **89**, 235429 (2014). Cited on page(s) 287, 289, and 290
- [421] B. Pielić, J. Hall, V. Despoja, I. Š. Rakić, M. Petrović, A. Sohani, C. Busse, T. Michely and M. Kralj, 'Sulfur Structures on Bare and Graphene-Covered Ir(111)', *J. Phys. Chem. C* **124**, 6659 (2020). Cited on page(s) 288
- [422] C. Zhang, Y. Chen, A. Johnson, M.-Y. Li, L.-J. Li, P. C. Mende, R. M. Feenstra and C.-K. Shih, 'Probing Critical Point Energies of Transition Metal Dichalcogenides: Surprising Indirect Gap of Single Layer WSe₂', *Nano Lett.* **15**, 6494 (2015). Cited on page(s) 289
- [423] E. N. Voloshina, E. Fertitta, A. Garhofer, F. Mittendorfer, M. Fonin, A. Thissen and Y. S. Dedkov, 'Electronic structure and imaging contrast of graphene moiré on metals', *Sci. Rep.* **3**, 1072 (2013). Cited on page(s) 290

- [424] J. Cai, W. Jolie, C. C. Silva, M. Petrović, C. Schlueter, T. Michely, M. Kralj, T.-L. Lee and C. Busse, 'Modifying the geometric and electronic structure of hexagonal boron nitride on Ir(111) by Cs adsorption and intercalation', *Phys. Rev. B* **98**, 195443 (2018). Cited on page(s) 291
- [425] I. Horcas, R. Fernández, J. M. Gomez-Rodriguez, J. Colchero, J. Gómez-Herrero and A. M. Baro, 'WSXM: A software for scanning probe microscopy and a tool for nanotechnology', *Rev. Sci. Instrum.* **78**, (2007). Cited on page(s) 292
- [426] R. M. Feenstra, G. R. Frazier, Y. Pan, S. Fölsch, Y.-C. Lin, B. Jariwala, K. Zhang and J. A. Robinson, 'Acquisition and analysis of scanning tunneling spectroscopy data—WSe₂ monolayer', *J. Vac. Sci. Technol.* **39**, 11001 (2020). Cited on page(s) 293

Acknowledgements

(Danksagung)

During my PhD, I have never really been able to shake the feeling that I am particularly lucky. Except for some days of fiddling around with impossibly thin wires, I fully enjoyed working as a scientist. Most of the projects I have worked on had a positive outcome, which is definitely not guaranteed when taking them up. I have been to a conference on a cruise ship. But it is ultimately the people I have worked with and who have supported me that contribute most to this feeling. At this point, I would like to thank them to the best of my abilities.

First off, I want to thank my doctoral advisor Prof. **Thomas Michely**. I never planned to do a PhD in physics. At the time of my Masters project in Thomas' group, I had just started with my Masters in philosophy. But it turns out that there is a quite unique thrill to understanding the inner workings of the material plane and by the end of that first year, I was hooked. Thomas gave me the freedom to pursue the topics that captivated me, while always taking an interest in what I was doing. He took the time to discuss whatever problems came up, be it of scientific, technical or personal nature. I have learned an incredible amount about solid-state physics, experimental techniques and proper scientific writing from him and I am grateful that he gave me the opportunity to pursue a PhD, even at the personal risk of having to read another over-long thesis from me.

I wish to thank Prof. **Alexander Khajetoorians** for agreeing to referee the thesis of the hapless student he once cross-examined on the topic of bilayer TaS₂, during my first poster presentation at the DPG.

I also wish to thank Prof. **Paul van Loosdrecht**, who promptly accepted to be a referee and who has provided me with some of the few exchanges in my own language I've had in the institute, fumbling for the correct Dutch words for things I, by now, only know how to say in English.

I extend my gratitude furthermore to Prof. **Sanjay Mathur**, who has accepted the position as chair my thesis defence committee and to Dr. **Wouter Jolie**, who has taken on the role as thesis committee observer.

During the course of my PhD, I have had the pleasure to work with many collaborators. Though I am indebted to all of them, I wish to extend my thanks some in particular.

Thanks to Prof. **Tim Wehling** and the members of his group, notably Dr. **Jan Berges**, **Arne Schobert** and Dr. **Erik van Loon**, with whom we have unravelled some of the mysteries of electron-phonon interactions in TMDCs.

Acknowledgements (*Danksagung*)

Thanks also to Dr. **Theo A. Costi**, for his sublime knowledge of all things Kondo and with whom I have emailed back and forth more than with anyone else, fitting his NRG calculations to our Kondo peaks. I also wish to thank Prof. **Achim Rosch**, who embodies the kind of universal physicist long thought extinct.

I wish to thank Dr. **Hannu-Pekka Komsa**, who invited us to Helsinki, where his crash course on DFT made me wonder whether I should not have pursued a career as a theoretical physicist, and who has provided us with many helpful discussions on the properties of MoS₂.

Furthermore I'd like to thank Prof. **Jan Knudsen**, who taught me about XPS, almost doubling the total amount of measurement techniques employed during this thesis; **Alexei Preobrajenski** for patiently guiding us during our beam time at MaxIV in Lund; **Nikolay Vinogradov** for measuring the self-intercalated VS₂ sample out of his own volition; and **Virgínia Boix** for living up to her reputation as a great companion during long night shifts.

From our group I would like to thank first Dr. **Jeison Fischer** for his guidance during the whole course of my PhD on matters both scientific and beyond. I also thank him for fixing the evaporator that I roughly transported over the hexagonal cobblestones of Flensburg and for letting me have the night shift in Lund, even though he had so looked forward to a lack of sleep and the absence of sunlight.

I also thank Dr. **Wouter Jolie** for his undying patience with me running into his office to discuss whatever weird idea I'd come up with - and generally having a better one. Also for starting journal club, which I briefly tried to introduce to my friends from outside the university as well, with mixed results.

Dr. **Joshua Hall** I thank for all his work on VS₂, without which this thesis would have been very monotonous. The metaphor about the shoulders of giants is pretty apt in this specific instance. He also taught me, during my first DPG conference, about the importance of a life outside the lab, which I have tried my best to keep in mind over the years.

Dr. **Clifford Murray** deserves a special thanks, for teaching me the ways of STM and science during my Masters. Also for always treating me with kindness and patience, even when I was at my most annoying. The time I spent with him, both in the lab and outside, is one of the best things to have come out of this whole endeavour.

I want to thank my long-time office and conference room-mate **Tobias Hartl**, who started one month before me with his doctorate and was thus an invaluable source of wisdom for PhD-related matters. He also owns a Nintendo Switch, which might have led to the occasional scheduling conflict during conferences. Most importantly: he knighted me, for which I am eternally grateful.

Special thanks go to Dr. **Timo Knispel**, for urging me to do my Masters research within the group, derailing my planned career as a rather aimless philosopher, and being thus directly responsible for these last four and a half years. I believe that I am the better for it.

I extend my thanks to **Stefan Schulte**, for being an excellent person to get lost with in Dresden; to Dr. **Mahasweta Bagchi**, for filling Tobias' empty spot in the office for these last months in

Cologne; to **Daniel Jansen**, who I enjoyed practising with for the Unilauf, where he went on to dastardly defeat me in the last seconds; to **Pascal Hurth**, for providing me with support during the - for me - most difficult parts of my PhD, whenever the STM was broken or a pernicious noise invaded our tunneling current; to **Carsten Speckmann**, my barbaric friend, who I wish all the best for his PhD in Vienna; and to the rest of the **AG Michely**, which somehow manages to always contain a wonderful group of people throughout the inevitable permutations of short-spanned scientific life.

Thanks should go in particular to **Wouter, Jeison, Sweta** and Dr. **Charlotte Kiessling** who took the time to read and correct parts of this thesis.

I also want to thank everyone for their patience, who had to listen to me say the word 'polaron' far too many times.

Special thanks also to my former colleagues and now friends **Stefan Kraus** and **Moritz Will**, who have turned Cologne from an old Roman outpost into a place where I feel at home. I also thank **David Kobold** for hosting many great evenings filled with barbecue and, when the stars aligned, Looping Louie.

I thank my friends from the Netherlands, in particular **Abe Jukema** and **Patrick Birken**, who have never felt far away and whose friendship is one of the pillars on which I build my life.

I thank my family, who have wholeheartedly supported me throughout my time in Cologne - content, perhaps, to finally see me dedicate myself fully to something.

At the close, a thank you to **Charlotte**. Above all else, I am lucky because I am with you. For the first time in my life, I did not hesitate when making a choice, when I decided to come to Cologne with you. I have not regretted a single day. In closing this chapter of our lives, I look forward to all those yet to be written.

Erklärung zur Dissertation

gemäß der Promotionsordnung vom 12. März 2020

Hiermit versichere ich an Eides statt, dass ich die vorliegende Dissertation selbstständig und ohne die Benutzung anderer als der angegebenen Hilfsmittel und Literatur angefertigt habe. Alle Stellen, die wörtlich oder sinngemäß aus veröffentlichten und nicht veröffentlichten Werken dem Wortlaut oder dem Sinn nach entnommen wurden, sind als solche kenntlich gemacht. Ich versichere an Eides statt, dass diese Dissertation noch keiner anderen Fakultät oder Universität zur Prüfung vorgelegen hat; dass sie - abgesehen von unten angegebenen Teilpublikationen und eingebundenen Artikeln und Manuskripten - noch nicht veröffentlicht worden ist sowie, dass ich eine Veröffentlichung der Dissertation vor Abschluss der Promotion nicht ohne Genehmigung des Promotionsausschusses vornehmen werde. Die Bestimmungen dieser Ordnung sind mir bekannt. Darüber hinaus erkläre ich hiermit, dass ich die Ordnung zur Sicherung guter wissenschaftlicher Praxis und zum Umgang mit wissenschaftlichem Fehlverhalten der Universität zu Köln gelesen und sie bei der Durchführung der Dissertation zugrundeliegenden Arbeiten und der schriftlich verfassten Dissertation beachtet habe und verpflichte mich hiermit, die dort genannten Vorgaben bei allen wissenschaftlichen Tätigkeiten zu beachten und umzusetzen. Ich versichere, dass die eingereichte elektronische Fassung der eingereichten Druckfassung vollständig entspricht.

Teilpublikationen:

- [1] **Camiel van Efferen**, Jan Berges, Joshua Hall, Erik Van Loon, Stefan Kraus, Arne Schobert, Tobias Wekking, Felix Huttmann, Eline Plaar, Nico Rothenbach, Katharina Ollefs, Lucas Machado Arruda, Nick Brookes, Gunnar Schönhoff, Kurt Kummer, Heiko Wende, Tim Wehling and Thomas Michely
A full gap above the Fermi level: the charge density wave of monolayer VS₂
Nature Communications, **12**, 6837 (2021)

- [2] **Camiel van Efferen**, Joshua Hall, Virginia Boix, Tobias Wekking, Nikolay Vinogradov, Alexei Preobrajenski, Jan Knudsen, Jeison Fischer, Wouter Jolie and Thomas Michely
Novel 2D vanadium sulphides: synthesis, atomic structure engineering and charge density waves
manuscript, submitted to ACS Nano, available as preprint

Erklärung zur Dissertation

- [3] **Camiel van Efferen**, Clifford Murray, Jeison Fischer, Carsten Busse, Hannu-Pekka Komsa, Thomas Michely and Wouter Jolie
Metal-insulator transition in monolayer MoS₂ via contactless chemical doping
2D Materials, **9**, 025026 (2022)
- [4] **Camiel van Efferen**, Jeison Fischer, Achim Rosch, Thomas Michely and Wouter Jolie
Modulated Kondo screening along magnetic mirror twin boundaries in monolayer MoS₂ on graphene
manuscript, accepted at Nature Physics, available as preprint
- n/a **Camiel van Efferen**, Arne Schobert, Tfyeché Tounsi, Michael Winter, Mark Georger, Affan Safeer, Jason Bergelt, Christian Krämer, Jeison Fischer, Roberto Mozara, Jan Berges, Tim Wehling, Thomas Michely, Wouter Jolie
Real-space observation and tunneling spectroscopy of polarons in monolayer MoS₂
manuscript, in preparation phase

Köln, den 08.08.2023

Camiel van Efferen

Datenverfügbarkeit:

Die in dieser Dissertation gezeigten Primärdaten sind bei der Arbeitsgruppe von Prof. Dr. Thomas Michely am II. Physikalischen Institut der Universität zu Köln hinterlegt.

Lebenslauf (*Curriculum Vitae*)

Persönliche Daten

Camiel van Efferen
Geburtstag 30.06.1993
Geburtsort Delft, die Niederlande
Staatsangehörigkeit Niederländisch

Ausbildung

01/2020 – heute Promotionsstudium
II. Physikalisches Institut, Universität zu Köln
Arbeitsgruppe Prof. Dr. Thomas Michely

10/2016 – 12/2019 M. Sc. Physik
Universität zu Köln
Durchschnittsnote: 1,2
Masterarbeit: "Investigating and manipulating electronic phenomena
in transition metal dichalcogenides" (Note: sehr gut 1,0)
II. Physikalisches Institut, Universität zu Köln
Arbeitsgruppe Prof. Dr. Thomas Michely

09/2012 – 07/2016 B. Sc. Physik
Universiteit Leiden
Durchschnittsnote: 1,9
Bachelorarbeit: "Back-Action Evading Measurements on a Trampoline Resonator"
(Note: sehr gut 1,0)
Leiden Institute of Physics, Universiteit Leiden
Arbeitsgruppe Prof. Dr. Dirk Bouwmeester

06/2011 Allgemeine Hochschulreife, Gymnasium Haganum, Den Haag (NL)
Durchschnittsnote: 2,1